INTERNATIONAL SOCIETY FOR PHOTOGRAMMETRY AND REMOTE SENSING
INTERNATIONALE GESELLSCHAFT FÜR PHOTOGRAMMETRIE UND FERNERKUNDUNG
SOCIÉTÉ INTERNATIONALE DE PHOTOGRAMMÉTRIE ET DE TÉLÉDÉTECTION

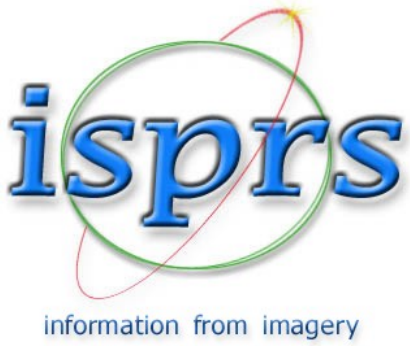

THE INTERNATIONAL ARCHIVES OF THE PHOTOGRAMMETRY, REMOTE SENSING AND SPATIAL INFORMATION SCIENCES
ARCHIV FÜR PHOTOGRAMMETRIE, FERNERKUNDUNG UND RAUMBEZOGENE INFORMATIONSWISSENSCHAFTEN
ARCHIVES INTERNATIONALES DES SCIENCES DE LA PHOTOGRAMMÉTRIE, DE LA TÉLÉDÉTECTION ET DE L'INFORMATION SPATIALE

ISSN 0246-1840

VOLUME / VOLUME / BAND **XXXIV** PART / TOME / TEIL **3/W4** COMMISSION / COMMISSION / KOMMISSION **III**

ISPRS WORKSHOP

LAND SURFACE MAPPING AND CHARACTERIZATION USING LASER ALTIMETRY

22ND TO 24TH OCTOBER 2001
ANNAPOLIS, MARYLAND

Editor
Michelle A. Hofton

ORGANIZED AND SPONSORED BY
ISPRS WG III/3: 3D Reconstruction from airborne laser scanner and InSAR data
ISPRS WG III/6: Multi-source vision
The Vegetation Canopy Lidar (VCL) Project, University of Maryland, College Park, USA
Airborne 1 Corporation, Los Angeles, CA, USA
The Ohio State University, Columbus, OH, USA
NASA Goddard Space Flight Center, Greenbelt, MD, USA

Workshop Organization

The workshop was hosted by the following Working Groups and Organizations:

ISPRS WG III/3 **3D Reconstruction from airborne laser scanner and InSAR data**
Chairs: G. Vosselman, Delft University of Technology, Delft, The Netherlands
H.-G. Maas, Dresden University of Technology, Dresden, Germany
ISPRS WG III/6 **Multi-source vision**
Chairs: O. Hellwich, Technische Universitat Munchen, Germany
B. Csatho, The Ohio State University, Columbus, OH, USA
The Vegetation Canopy Lidar (VCL) Project, University of Maryland College Park, USA
Airborne 1 Corporation, 5777 West Century Blvd., #725, Los Angeles, CA, USA
The Ohio State University, Columbus, OH, USA
NASA Goddard Space Flight Center, Greenbelt, MD, USA

Scientific Committee

M. Hofton, chair, Department of Geography, University of Maryland College Park, USA.
B. Csathó, co-chair, Byrd Polar Research Center, The Ohio State University, Columbus, USA.
B. Blair, Laser Remote Sensing Branch, NASA/Goddard Space Flight Center, Greenbelt MD, USA.
O. Hellwich, Photogrammetry and Remote Sensing, Technische Universität München, Germany.
H.-G. Maas, Institute of Photogrammetry and Remote Sensing, Dresden University of Technology, Germany.
J.-B. Minster, Cecil H. and Ida M. Green Institute of Geophysics and Planetary Physics, Scripps Institution of Oceanography, La Jolla CA, USA.
T. Schenk, Civil & Environmental Engineering and Geodetic Science, The Ohio State University, Columbus, USA.
G. Vosselman, Department of Geodesy, Delft University of Technology, The Netherlands.

Published by

Department of Geography, University of Maryland, College Park, MD, USA.

Copies of this book are available from

RICS Books
Surveyor Court
Westwood Way
Coventry CV4 8JE U.K.
E-mail: order@ricsbooks.org
Tel.: +44 (0) 20 7222 7000
Fax.: +44 (0) 20 7334 3851

Preface

Laser altimetry is rapidly establishing itself as a useful technique for many mapping, surface characterization and 3D reconstruction purposes. With successful flights of the Shuttle Laser Altimeter (SLA), planned launches of multi-year missions such as NASA's Vegetation Canopy Lidar (VCL) and Ice, Cloud and land Elevation Satellite (ICESat), as well as numerous commercial and research airborne activities, extensive observations are increasingly available. The objective of the workshop **Land Surface Mapping and Characterization Using Laser Altimetry** was to bring together an interdisciplinary group of scientists, engineers, and end users working in the field of laser remote sensing of the solid earth, oceans, and other planets, to exchange scientific research and technology development involving laser remote sensing. In addition to formal presentations, open forum discussions were held to facilitate the exchange of experience and to identify problems and potential solutions.

The three-day event brought together ~80 participants from various backgrounds, expertise and affiliations. Forty-five papers were presented covering theoretical and conceptual topics and applications. Invited contributions highlighted the diversity of applications of laser altimetry systems and data. Nearly all presentations are contained in this volume, organized in the sequence of the workshop sessions.

The workshop was held at the "Historic Inns of Annapolis", three restored inns in the center of Annapolis, Maryland, USA. The workshop was hosted by the **International Society for Photogrammetry and Remote Sensing (ISPRS),** the **University of Maryland,** the **Ohio State University,** and **NASA Goddard Space Flight Center.** Financial support was provided by **Airborne 1 Corporation** and the **Vegetation Canopy Lidar** (VCL) mission.

This workshop is the second ISPRS workshop dedicated to the theory and applications of laser altimetry. The last workshop, which was held in November of 1999 in La Jolla, California, brought together ~70 researchers from several countries to discuss a broad spectrum of lidar topics, and we look forward to continuing this series in the near future.

I would like to thank all the authors for their very valuable contributions, and everyone who contributed to the success of the workshop.

Michelle A. Hofton

Editor

CONTENTS

ii Workshop Organization
iii Preface

SESSION 1 SYSTEM OVERVIEWS

3 **Lidar Activities and Research Priorities in the Commercial Sector**
M. Flood

9 **Design and Performance of an Airborne Multikilohertz Photon-Counting Microlaser Altimeter**
J. Degnan, J. McGarry, T. Zagwodzki, P. Dabney, J. Geiger, R. Chabot, C. Steggerda, J. Marzouk and A. Chu

17 **Wide-Swath Imaging Lidar Development for Airborne and Spaceborne Applications**
J.B. Blair, M.A. Hofton and S. Luthcke

SESSION 2 SURFACE RECONSTRUCTION I

23 **Advanced DTM Generation from Lidar Data**
K. Kraus and N. Pfeifer

31 **Creation of High Resolution, Precise Digital Elevation Models (DEM) of Ocean City and Assateague Island, MD**
B. Csathó, Y.-R. Lee, T. Schenk, W. Krabill, and J. McGarry

37 **3D Building Model Reconstruction from Point Clouds and Ground Plans**
G. Vosselman

45 **Scanline Forced Delauney-TENs for Surface Representation**
E. Verbree and P.J. van Oosterom

53 **On the Use of Pulse Reflectance Data for Laserscanner Strip Adjustment**
H.-G. Maas

57 **3D Perceptual Organization From Laser Altimetry Data**
I. Lee and T. Schenk

67 **Comparing Probabilistic and Geometric Models on Lidar Data**
R. Fraile and S. Maybank

SESSION 3 DATA GEOLOCATION

73 **Aspects of Processing Extra-terrestrial Lidar Data: Clementine, NEAR, MOLA**
G. A. Neumann

81 **Spaceborne laser Altimeter Instrument Parameter Calibration from Integrated Residual Analysis**
S. Luthcke, D. Rowlands and C. Carabajal

85 **Recovery of Systematic Biases in Laser Altimeters Using Natural Surfaces**
S. Filin

SESSION 4 DATA FUSION

95 **Integration of Lidar and Landsat ETM Data**
A. T. Hudak, M. A. Lefsky, and W. B. Cohen

105 **High Resolution Surface Geometry and Albedo by Combining Laser Altimetry and Visible Images**
R. D. Morris, U. von Toussaint and P. C. Cheeseman

113 **Accuracy Study of Airborne Laser Scanning Data with Photogrammetry**
S. Seo, T. Schenk, and B. Csathó

SESSION 5 DATA MODELING

121 **Modeling Lidar Waveforms Using a Radiative Transfer Model**
B. Peterson, W. Ni, B. Blair, M. Hofton, P. Hyde, and R. Dubayah

125 **Evaluation of Geoscience Laser Altimeter System (GLAS) Waveforms For Vegetated Landscapes Using Airborne Laser Altimeter Scanning Data**
C. C. Carabajal and D. J. Harding

SESSION 6 FORESTRY APPLICATIONS

131 **Measuring Forest Canopy Height Using a Combination of Lidar and Aerial Photography Data**
B. A. St-Onge and N. Achaichia

139 **Investigation of Measuring Accuracy of Forest Area by Means of Airborne Laser Scanner**
M. Funahashi, M. Setojima, Y. Akamatsu, Y. Imai, M. Amano, T. Katsuki, M. Takahashi, and M. Fukuda

147 **Relationships Between Lidar Metrics and Above-Ground Biomass in Closed-Canopy Neotropical Forests** (invited)
J. Drake, R. Dubayah, R. Knox, and R. Condit

155 **Lidar Remote Sensing of Aboveground Biomass in Three Biomes**
M. A. Lefsky, W. B. Cohen, D. J. Harding, G. G. Parker, S. A. Acker, and S. T. Gower

SESSION 7 MAPPING GEOSURFICIAL PROCESSES

163 **Laser Monitoring of Ice Elevations and Sea-Ice Thickness in Greenland**
R. Forsberg, K. Keller and S. M. Jacobsen

169 **Quantifying River Bank Erosion With Scanning Laser Altimetry**
D. Thoma, S. C. Gupta and M. E. Bauer

175 **Mapping the Surface of Sheet Flow Water in the Everglades**
W. E. Carter, R. L. Shrestha, D. Bloomquist, and M. Sartori

181 **Laser Pulse Correlation: A Method For Detecting Subtle Topographic Change Using Lidar Return Waveforms**
M. Hofton and J. B. Blair

185 **Precise Airborne lidar surveying for Coastal Research and Geo-Hazards Applications**
R. Gutierrez, J. Gibeaut, R. Smyth, T. Hepner, J. Andrews, C. Weed, W. Gutelius, and M. Mastin

SESSION 8 SURFACE RECONSTRUCTION II

195 **Digital Terrain Models in dense urban areas**
F. Dell'Acqua, and P. Gamba

203 **Filtering of Laser Altimetry Data Using a Slope Adaptive Filter**
G. Sithole

211 **Some Algorithms for Virtual Deforestation (VDF) of LIDAR Topographic Survey Data**
R. A. Haugerud and D. J. Harding

219 **Terrain Modelling and Analysis Using Laser Scanner Data**
M. Elmqvist, E. Jungert, F. Lantz, Å. Persson, and U. Söderman

227 **Airborne Laser Scanning – Clustering in Raw Data**
M. Roggero

233 Conference Program
237 List of Participants
243 Author Index

LAND SURFACE MAPPING AND CHARACTERIZATION USING LASER ALTIMETRY

SESSION 1

SYSTEM OVERVIEWS

LIDAR ACTIVITIES AND RESEARCH PRIORITIES IN THE COMMERCIAL SECTOR

Martin Flood
Airborne 1 Corporation
5777 West Century Blvd. #725
Los Angeles, CA
USA, 90045
flood@airborne1.com

Commission III, Working Group 3

KEY WORDS: laser altimetry; airborne laser mapping; airborne laser scanning; commercial laser instruments

ABSTRACT

Laser altimetry, more commonly referred to in the commercial sector as LiDAR mapping, is becoming a commonplace operational tool in photogrammetry, survey and mapping firms. Its use has grown rapidly over the past five years due to the increasing availability of commercial off-the-shelf sensors, advancements in the design and capabilities of the sensors themselves and an increased awareness of the advantages of using LiDAR technology for elevation data capture by end users. As a result LiDAR mapping has been experiencing strong growth, which in turn has spurred further developments in the technology and even greater demand for the data products. Due to the relatively small size of the lidar mapping sector, capital investment in internally funded research and development appears to be limited. As a result further growth and development of the technology in the commercial sector will depend heavily on the ability to work cooperatively with the academic and research sector to define common research priorities and objectives, especially as relates to specific applications. Education of end users to increase awareness and acceptance of the technology along with establishing approved methodologies and quality control guidelines are also areas of overlap between the commercial and government sectors. Potential research priorities given commercial sector needs will be discussed and ranked with an emphasis on software tools. Undeveloped aspects of research-oriented laser altimetry, especially as relates to waveform capture and analysis will be discussed in the context of potential commercial markets.

1 INTRODUCTION

Laser altimetry, more commonly referred to in the commercial sector as lidar mapping[1], is becoming a commonplace operational tool in the fields of remote sensing, photogrammetry, surveying and mapping. Laser altimetry is capable of rapidly generating dense, accurate, digital models of the topography and vertical structure of a target surface. It is an attractive tool for data end users in various application areas since the cost to produce the elevation data, point for point, can be significantly less than other forms of traditional data collection. For any application with a need for high density, high accuracy elevation models, laser altimetry offers unique technical capabilities, lower field-operation costs and reduced post-processing time and effort compared to traditional survey methods.

The use of lasers as remote sensing instruments has an established history going back more than 30 years. Townes and Schawlow first put the theory of the optical maser or laser forward in 1958. Maiman demonstrated the first successful laser – a ruby laser – in 1960. Through the 1960s and 70s various experiments demonstrated the power of using lasers in remote sensing including lunar laser ranging, satellite laser ranging, atmospheric monitoring and oceanographic studies. During the 1980s laser altimetry – essentially the measurement of height using a laser rangefinder - developed as airborne instruments such as NASA's Atmospheric Oceanographic Lidar (AOL)[1] and Airborne Topographic Mapper (ATM)[2] were deployed. Laser altimetry has been successfully demonstrated from a variety of airborne platforms and from near Earth orbit during the Shuttle Laser Altimeter (SLA) missions[3]. NASA currently has two satellite missions planned that will deploy laser altimetry; the Vegetation Canopy Lidar mission (VCL)[4] and the Geosciences Laser Altimeter (GLAS)[5]. Laser altimetry has also been used to provide us with spectacular images and detailed maps of Mars via the Mars Observer Laser Altimeter (MOLA)[6].

Today two distinct techniques in laser altimetry are being actively investigated by the research community; small footprint, time-of-flight laser altimetry and large footprint, waveform-digitizing techniques that analyze the full return waveform to capture a complete elevation profile within the target footprint. In addition to these research activities, a strong commercial sector is developing to address the demand for widespread access to lidar mapping capabilities and services in the private sector.

[1] The terms *laser altimetry* and *lidar* will be used interchangeable in this article with the additional understanding that in general we are referring to small footprint, time-of-flight topographic lidars not waveform-capture or bathymetric lidars. The term *small* is subjective but is generally taken to mean a footprint on the ground no larger than 1 m.

As of July 1st 2001 there were ~ 75 organizations worldwide operating ~60 sensors for commercial applications not including sensors being deployed by research groups. Growth rates in the commercial sector in terms of installed instrument base have been averaging ~25% per year since 1998 with projections for an installed instrument base of 150 – 200 sensors by 2005[7]. There are also a growing number of value-added resellers and product developers that include lidar mapping and lidar data analysis as an integral part of their activities. The majority of lidar mapping done in the commercial sector is based on time-of-flight systems that minimize footprint size and maximize repetition rate. Awareness of waveform capture techniques is far less common and it is not being actively deployed except in the much smaller laser bathymetry sector. Consequently research priorities in the commercial sector tend to focus on the analysis and manipulation of the massive data point clouds rather than waveform analysis or interpretation. However the background and skill sets of commercial practitioners of laser altimetry are predominantly from the survey and mapping fields, led by aerial photography and photogrammetry firms. As a result the depth of specific knowledge about laser altimetry in the commercial sector is less than in the research sector. Combined with other business drivers this is limiting investment in internal R&D, creating a greater need for co-operation between private sector firms and research institutes.

2 COMMERCIAL SECTOR ACTIVITIES

Prior to 1995 laser altimetry was generally conducted using custom-designed sensors operated by research groups or built by commercial survey firms to exploit niche markets. Such custom-developed sensors required organizations to dedicate significant resources to the effort and develop expertise in various normally unrelated disciplines. The majority of these efforts were based on single prototype designs, limiting their ability to create and service a broad, sustainable, sector-wide demand for the technology. However, since 1995 a commercial off-the-shelf (COTS) instrument market has developed which has removed many of these constraints for organizations wanting to incorporate laser altimetry in their operations. The availability of COTS sensors has increased access and driven a much more rapid adoption of the technology.

Today the commercial deployment of laser altimetry continues to expand rapidly due to the increasing availability of commercial off-the-shelf sensors, advancements in the design and capabilities of the sensors themselves and an increased awareness by end users and contracting agencies of the advantages of using lidar technology for elevation data capture. Commercial laser altimetry is in the process of establishing itself as a robust, cost-effective operational tool, although application-specific methodologies are still being developed in many areas.

Unlike research organizations, which are primarily driven by scientific goals and objectives, the commercial sector is driven by the need to define and address profitable markets for the various data products. Due to the relatively recent introduction of the technology many of these end products are still being defined and there is on-going research and analysis by both private and public groups in to the best methodologies for addressing each application.

In practice commercial work is currently dominated by small footprint, time-of-flight techniques. In time-of-flight lidar instruments the distance or range from the sensor to any reflective surface beneath the platform is determined by measuring the elapsed time between the generation and return of each laser pulse. By scanning the laser across the path of the platform, a wide swath of laser range data is captured along the flight path. These laser ranges are combined with platform position and orientation information during post-processing to create a geo-referenced point cloud that is essentially a digital 3D model of the surface beneath the platform. In the commercial sector small footprint, time-of-flight lidar mapping has established itself as a robust, cost-effective operational tool, but the technology is still developing and the commercial sector is still developing appropriate business models for effectively delivering this type of data to the end-users. While full waveform capture is being used in commercial laser bathymetry, its use in topographic applications is still limited to scientific and research programs.

Depending on the particular application, laser altimetry can be viewed as either a complementary or a competitive technology when compared to existing survey methods. For many applications, airborne laser altimetry is currently deployed in conjunction with other more traditional sensors including standard aerial film cameras, digital cameras, hyperspectral scanners or thermal imagery. Integration of multiple sensors in to a single platform – sensor fusion – is a relatively high priority in the commercial sector. In general, laser altimetry is best viewed as an addition to the remote sensing toolbox that can add significant value to the data products produced, either independently or in conjunction with other sensor systems. Deploying airborne laser altimetry within a field survey can provide additional value depending on project specific goals and deliverables. Since each individual end user has particular needs and specifications that they expect to be met, laser altimetry may not meet these expectations without support from traditional survey methods. However, in certain applications, such as forestry or coastal engineering, laser altimetry offers unique capabilities not achievable with any other technology. Several reviews of the main commercial application areas have been published.[8,9,10]

Approximately 60% of the commercial activity conducted today is focused on generating bare earth DTMs for orthorectification of imagery and the generation of contour maps in the 5′ to 2′ c.i. range. Significant additional work is being done using lidar-derived DTMs in hydrological modeling and flood risk assessment and urban modeling for a variety of applications such as telecommunications. Two major projects that serve as examples of how commercial lidar mapping capabilities are being applied to large government-funded mapping efforts are the Puget Sound Lidar Consortium; Kitsap County Survey[11] and the North Carolina - Floodplain Mapping Program[12] - both of which can act as guidelines and benchmarks for organizing large area lidar surveys.

3 PROCESS FLOW AND CHALLENGES

In the commercial sector a high priority must be placed on meeting client and end user expectations for data quality, accuracy and delivery schedules. As a result, many of the challenges and research priorities identified by commercial firms focus on

optimizing the workflow from mission planning through field data collection to post-processing and final QA/QC. There can be significant differences between the planning and execution of a commercial mapping project and a research field campaign, most notably in scope, size, volume of data acquired and the need to operate to the professional standards and practices as established by the survey and mapping community. Automation, increased reliability, rigorous quantification and appropriate reporting procedures are all key areas of importance to commercial entities. A secondary priority is the manipulation of the data in to an application-specific mapping product for the end user. To understand the research priorities from the commercial perspective, it is useful to review a typical workflow on a commercial project:

1. Flight planning.
2. Sensor calibration.
3. Field data collection.
4. Preliminary QA/QC in field.
5. Repeat 3 and 4 as required; often for 20+ days on larger projects while workflow continues.
6. Post-processing:
    a. GPS quality check.
    b. Trajectory generation.
    c. Geo-referencing.
    d. Full point cloud generation.
    e. Project segmentation in to manageable area/file sizes and terrain/feature classifications.
    f. Automated Classification.
    g. Initial QA/QC.
    h. Manual Classification.
    i. Final QA/QC.
    j. Deliverables (girding).
7. Reflight, rework.

Private sector firms are generally not open about their internal process efficiency, but evidence strongly suggests that anywhere from 60% - 80% of the labor on a given project is allocated to steps 6(h) and 6(i); manual classification and final QA/QC. This is especially true on very large area mapping projects. As a result, most research by commercial data providers, funded either internally or by partnering with research groups, is focused on reducing the amount of time to complete the QA/QC process by minimizing the amount of manual classification that is required. More efficient algorithms for extracting the bare earth surface – automated feature extraction - combined with better tools for effective manual review of the data after automated filtering are a high priority.

In addition sensor development by the instrument vendors is an area of on-going activity with the primary focus on higher repetition rate time-of-flight instruments, higher operating altitudes and effective integration of digital cameras and other sensors with the laser sensor. Repetition rate promises to be a continuing benchmark. 50 kHz sensors are already being field-tested and it is likely that 100 kHz sensors will be online by 2005 at the latest. Reliability of the instruments in the field is also becoming a priority as a larger installed base of instruments and competition between data providers serves to shift the focus from the novelty of the technology to providing a quality data product on budget and on schedule.

4 RESEARCH PRIORITIES

From a commercial perspective the research priorities can be broken in to five key areas:

1. Automated or semi-automated sensor calibration in the field to an accepted and approved methodology.
2. Efficient automated feature extraction for various end user applications.
3. Development and integration of new techniques in sensor design and capabilities.
4. Software tools.
5. Training.

Calibration

Unlike aerial photography which has a well-defined set of procedures and metrics for quantifying the accuracy and calibration of a given camera, commercial lidar sensors are not yet required to be calibrated by a third-party. As a result each operator has established their own in-house calibration process and procedures, usually against different standards and test ranges. While there are similarities between many of these ad-hoc procedures, a more formal methodology needs to be developed and made standard across the commercial sector. Issues need to be resolved such as what organizations should be responsible for managing this independent calibration process, what test ranges need to be established and where, and how the results should be presented and reported to assure end users of proper sensor calibration. However the research sector can play a key role by investigating and analyzing independent verification methods and design-independent sensor calibration techniques that can be easily transferred to the private sector. Professional organizations such as ISPRS and ASPRS clearly have a role to play here as well.

Automated Feature Extraction

Automated feature extraction is an area of key interest to the commercial sector. Various firms have internal programs to develop proprietary algorithms to accomplish these tasks, or work in conjunction with research institutes on development programs, however such efforts restrict the access to the techniques developed and are rarely peer-reviewed. The underlying theoretical basis for these proprietary algorithms is often not known by the end user. A more open source approach to defining, manipulating and classifying lidar data would help spread the use of the technology. However it is unlikely that private sector firms will spearhead such an effort. Research or academic institution that are developing such techniques can play a role in ensuring such valuable tools are widely reviewed and critiqued and then made available to the end user community. A major area of interest is how to effectively integrate the object information contained in intensity data in to automated classification routines. While intensity information, the strength of the return signal, has been available for several years and research groups are looking at its applications, it use in the commercial workflow has not been addressed. In addition to

actual algorithm development, the establishment of benchmark tests to quantify the accuracy and efficiency of existing and future algorithms against common data sets would be extremely useful. With the arrival over the next few years of even higher density data sets, development of software tools and algorithms capable of handling the data are a necessity. In addition investigation in to information extraction from dense data could be useful.

Software Tools

The emergence of robust, reliable software tools that are available to the entire community will be one of the most significant areas of change in the commercial sector in the next five years. Currently, the vast majority of the processing, manipulation and classification of lidar data is conducted using proprietary software developed independently by researchers, the data providers or provided by the sensor manufacturer to its clients but not available as a separate package (e.g. Optech's REALM software). The current situation presents a significant barrier to end users as lidar processing is presented as "black box" with limited insight in to the actual manipulation of the data and a very limited ability of the end user to recreate, reclassify, manipulate or modify the data sets they are provided. The fact that few of these proprietary classification algorithms have been published or opened up to peer review is also a concern among academics and researchers. However, by its very nature as open-format data representing a well-defined geospatial point cloud, lidar data is relatively easy to manipulate by third-party software. To date there are only a few software products on the market that can efficiently handle the large point densities generated by state-of-the-art lidar sensors – easily in excess of 100s of millions of points for even moderately sized projects - but this situation is changing rapidly. Third-party products specifically designed for manipulating lidar data are starting to appear and existing mainstream software developers such as ESRI are moving to integrate lidar data manipulation in their existing product suites. The availability of appropriate software tools for the entire end user community will eventually replace the proprietary, black box solutions common today. This will open up the post-processing workflow and fundamentally change the existing value chain, presenting a serious challenge to the "status quo" of the first generation of commercial data providers. By 2005 the availability of a suite of commercial off-the-shelf software tools will shift the primary product requested of lidar data providers from bare earth DTMs to the more basic geo-referenced, all-points laser point cloud.

New Techniques in Sensor Design: Waveform Capture

While there are several areas of development being investigated in sensor design, waveform capture promises to be the most interesting. An alternative technique to the basic time-of-flight method that dominates the commercial sector, waveform capture involves recording the entire return waveform from the laser pulse rather than just the time-of-flight. By capturing the full return waveform, detailed information on the entire vertical structure within the laser footprint is obtained and ground topography can be detected even with canopy openings of only a few percent. This type of waveform characterization of the complete canopy profile can have significant value in scientific research and may have commercial importance in the forestry industry. Perhaps more important for the commercial sector, waveform capture from large footprint sensors has been demonstrated as an effective method of determining the ground surface underneath even the densest canopy. Experimental flights of NASA's Laser Vegetation Imaging Sensor (LVIS)[13] were able to successfully and accurately record the topography beneath dense rainforest in Costa Rica[14]. Small footprint time-of-flight sensors become suspect in dense, complex canopy as not only must they successfully penetrate through the gaps in the canopy to the ground surface, but post-processing of the point cloud must employ filtering algorithms to correctly classify those returns that are from the ground from those that are from canopy or other features. Even the most advanced algorithms have difficulty accurately extracting the ground surface with 100% fidelity, especially in areas of low, dense ground cover, significant relief or where sudden changes in topography such as gullies or sharp grade breaks mimic man-made features. The complex interaction of the laser pulse with the distributed vertical target is also a concern when trying to determine the point of reference for a time-of-flight sensor. As a result, waveform-capture sensors offer a powerful alternative approach to map the bare earth beneath dense canopy.

Based on the state-of-the-art in commercial sensor design today, it is likely that by 2005 waveform-capture sensors will be in operation in the commercial sector. Such sensors will likely address niche commercial markets such as scientific research in forestry, topographic mapping beneath very dense canopy and calibration/validation of global lidar data sets available from satellites such as VCL. They may also find a market in large area topographic mapping, such as statewide mapping efforts, when grid-spacing requirements do not require the high-density capabilities of a high repetition rate time-of-flight sensor.

Training

While not a specific area of research, the training of highly qualified persons and the introduction of laser altimetry in to remote sensing and mapping curriculums at both the graduate and undergraduate level is a priority for the private sector. Due to the fact laser altimetry is relatively new technology there is a gap between the commercial sectors staffing needs and the available talent pool of experienced, trained personnel. This gap covers both highly qualified persons with experience in laser altimetry at the graduate level and qualified data analysis staff at an undergraduate level, as well as knowledgeable field personnel. The resulting shortfall is causing some staffing shortages as well as promoting a relatively high turnover of staff as people move from firm-to-firm within the sector. As with any high-tech sector, such a cycling of people from firm-to-firm can have short term benefits as it helps to spread best practices and improve the overall depth of knowledge in the sector but if the underlying shortages are not address, further adoption of the technology can suffer.

However this shortage is being addressed as more universities and colleges incorporate laser altimetry and lidar mapping as part of their remote sensing and GIS curriculums. Over the past few years lidar technology has been introduced at the post-graduate and graduate levels, the undergraduate level and even in some cases the high school level. This development is extremely encouraging however the introduction of the material is being addressed at different paces in different areas, a key factor

apparently being the co-location of a principal investigator actively pursuing research in laser altimetry. It can be assumed that given the anticipated growth in laser altimetry as a common operational tool, the need for trained personnel will increase and students with at least some exposure to lidar technology will be better equipped to secure these opportunities. A national or regional scholarship program to support and promote research and education in laser altimetry would be beneficial to both the private and public sectors.

5 CONCLUSIONS

Laser altimetry is becoming a commonplace operational tool in remote sensing, photogrammetry, survey and mapping. As the underlying technology is still dynamic and capital investment in private sector R&D is limited, a strong, co-operative relationship between the commercial sector and research organizations will be important to furthering the adoption of the technology. Recognition of research priorities from the private sector point-of-view balanced against the scientific objectives and research goals of government and academic institutions will lead to a mutually beneficial development of the technology and a widerspread adoption of laser altimetry as an every day tool.

REFERENCES

[1] See http://aol.wff.nasa.gov/ for details and publication references related to the AOL sensor.

[2] Krabill et. al., 1984. Airborne laser topographic mapping results. *Photogrammetric Engineering and Remote Sensing*, 50(6), pp. 685-694.

[3] Garvin, J.B. et. al., 1998. Observations of the Earth's topography from the Shuttle Laser Altimeter (SLA); laser-pulse echo-recovery measurements of terrestrial surfaces. Phys. Chem. Earth 23 (9-10), 1053-1068

[4] Dubayah, R. et. al., 1999. The Earth as Never Seen Before: VCL and the Lidar Revolution in Land Surface Characterization. In Proc. Amer. Geo. Phys. Union, 1999 Fall Meeting

[5] Schutz, B. E. and J.H. Zwally, Geosciences Laser Altimeter System (GLAS): A Spaceborne Laser Altimeter for Ice Sheet Mass Balance Applications, Eos Trans. AGU, 74, 181, 1993.

[6] Smith, D.E., et. al., 1998. Topography of the northern hemisphere of Mars from the Mars Orbiter Laser Altimeter. Science 279 (5357), 1686-1692

[7] Flood, M., 2001. Commercial Lidar Technology: The Next Five Years. in Proc. ASPRS Conference 2001 (St. Louis)

[8] Flood, M., 1999. Review of airborne laser technology. EARSel Newsletter, June 1999, pp. 20-23

9 Flood, M., Gutelius, B., 1997. Commercial Implications of Topographic Terrain Mapping Using Scanning Airborne Laser Radar. Photogrammetric Engineering and Remote Sensing, 63(4), pp. 327-329 and 363-366.

10 Gutelius, B., 1998. Engineering applications of airborne scanning lasers; reports from the field. Photogrammetric Engineering and Remote Sensing, 64(4), pp. 246-253.

[11] For details see http://duff.geology.washington.edu/data/raster/lidar/index.htm

[12] For details see http://www.ncfloodmaps.com/

[13] Blair, J.B., et. al., 1999. The Laser Vegetation Imaging Sensor: a medium-altitude, digitization only, airborne laser altimeter for mapping vegetation and topography. *ISPRS Journal of Photogrammetry and Remote Sensing* 54, 115-122

[14] M. A. Hofton, et. al., 2001 Validation of Vegetation Canopy Lidar sub-canopy topography measurements for a dense tropical forest. To be published in *Journal of Geodynamics*.

DESIGN AND PERFORMANCE OF AN AIRBORNE MULTIKILOHERTZ PHOTON-COUNTING, MICROLASER ALTIMETER

John Degnan, Jan McGarry, Thomas Zagwodzki, Phillip Dabney, Jennifer Geiger*
Code 920.3 (*Code 588)
NASA Goddard Space Flight Center
Greenbelt, MD 20771 USA
jjd@ltpmail.gsfc.nasa.gov, jan@ltpmail.gsfc.nasa.gov, tzagwodz@pop900.gsfc.nasa.gov, pdabney@ltpmail.gsfc.nasa.gov, jgeiger@pop700.gsfc.nasa.gov

Richard Chabot, Charles Steggerda
Honeywell TSI
7515 Missions Dr.
Lanham, MD 20706 USA
rchabot@pop900.gsfc.nasa.gov, Charles.Steggerda@Honeywell-TSI.com

Joseph Marzouk, Anderson Chu
Sigma Research and Engineering Corporation
9801 Greenbelt Rd., Suite 103
Lanham, MD 20706 USA
joe.marzouk@sigmaspace.com, andy.chu@sigmaspace.com

ABSTRACT

The present paper reports on the design and performance of a scanning, photon-counting laser altimeter, capable of daylight operations from aircraft cruise altitudes. In test flights, the system has successfully recorded high repetition rate, single photon returns from clouds, soils, man-made objects, vegetation, and water surfaces under full solar illumination. Following the flights, the signal was reliably extracted from the solar noise background using a Post-Detection Poisson Filtering technique. The passively Q-switched microchip Nd:YAG laser measures only 2.25 mm in length and is pumped by a single 1.2 Watt GaAs laser diode. The output is frequency-doubled to take advantage of higher detector counting efficiencies and narrower spectral filters available at 532 nm. The transmitter produces a few microjoules of green energy in a subnanosecond pulse at few kilohertz rates. The illuminated ground area is imaged by a 14 cm diameter, diffraction-limited, off-axis telescope onto a segmented anode photomultiplier. Each anode segment is input to one channel of "fine" range receiver (5 cm resolution), which records the times-of-flight of individual photons. A parallel "coarse" receiver provides a lower resolution (>75 cm) histogram of all scatterers between the aircraft and ground and centers the "fine" receiver gate on the last set of returns.

KEY WORDS: laser ranging**,** laser altimetry, photon-counting, microchip lasers, subnanosecond pulse, segmented anode photomultipliers, detector arrays, optical scanners

1. INTRODUCTION

Spaceborne laser altimeters typically use modest energy (50 to 100 mJ) solid state lasers, large telescopes (50 to 100 cm diameter), and high detection thresholds to achieve unambiguous surface returns with few or no “false alarms” resulting from solar background noise. Examples of such systems include the Mars Orbiter Laser Altimeter (Ramos-Izquierdo, L., et al, 1994), the Geoscience Laser Altimeter System (Abshire, J., 2000), and the Vegetation Canopy Lidar (Dubayah, R., et al, 1997). As a result of this conventional design philosophy, spacecraft prime power and weight constraints typically restrict spaceborne operations to low repetition rates on the order of a few tens of Hz which, at typical planetary orbital ground velocities of a few Km/sec, limits along-track spatial sampling to one sample every few hundred meters. There is great scientific interest in obtaining higher along-track resolution and/or better cross-track coverage, but achieving this capability through a simple scaling of the laser fire rate (power) is not practical.

It has been demonstrated theoretically (Degnan, 2000) that the conventional high Signal-to-Noise Ratio (SNR) approach to laser altimetry does not make efficient use of the available laser photons. The surface return rate of an orbiting altimeter can be increased by up to two orders of magnitude for a given laser output power by emitting the available photons in a high frequency (few KHz) train of low energy (< 1 mJ) pulses, as opposed to a low frequency train of high energy pulses, and by employing single photon detection (Degnan et al, 1998). Besides improving overall lidar efficiency, this mode of operation reduces the risk of internal optical damage to the laser, thereby improving long-term reliability, and makes the beam inherently more eyesafe to a ground-based observer. In addition, high return rates can be accomplished with much smaller telescope apertures on the order of 10 to 20 cm diameter. Indeed, the contrast of the terrain “signal” against the solar-induced noise background is actually enhanced through the use of small receive telescopes. Relatively simple onboard software algorithms, loosely based on post-detection Poisson filtering techniques previously used in lunar laser ranging (Abbott et al, 1973), can be employed to identify and extract the surface sampling data from solar background noise prior to onboard data storage or transmission of the data to a ground station.

The near order of magnitude reduction in telescope diameter greatly simplifies the mechanics of scanned systems and allows the use of relatively inexpensive, modest diameter

optical wedges or holographic optical elements to simultaneously scan both the transmit and receive beams for cross-track interrogation of the terrain while still maintaining a narrow receiver field of view for background noise suppression. In addition, since the volume and weight of a telescope and its support structure nominally varies as $D^{2.3}$, where D is the telescope diameter, a two order of magnitude reduction in weight and volume and a comparable reduction in fabrication cost can be realized.

Further unique performance enhancements are also possible when operating in a photon-counting mode. In conventional laser altimeters, multiple photons reflected from anywhere within the illuminated spot must be recorded by power-hungry waveform digitizers and deconvoluted using complex (and often fallible) algorithms in order to decipher the results and obtain a single range measurement. However, commercial and developmental photon-counting detectors now exist which are capable of providing centimeter level ranging resolution as well as angularly resolving the source of a single photon event within the receiver field-of-view. These devices can be realized either as segmented anode photomultipliers, available commercially from Hamamatsu with up to 10 x 10 pixels, or as Avalanche PhotoDiode (APD) arrays (Vasile, S., et al, 1997). With sufficiently high angular resolution of the single photon source, the measured range becomes nearly a point-to-point range measurement, i.e. from the internal altimeter reference point to a small area of uncertainty on the surface. The transverse spatial resolution is determined by the angular resolving power of the receiver/photodetector combination, which, for highly pixellated detectors, can be quite small compared to the total beam area on the ground. The vertical resolution is in turn limited by the laser pulsewidth, the timing capabilities of the range receiver, and the much-reduced residual spreading of the return waveform , or "Poisson generating function" in photon counting mode, caused by surface roughness and slope within this smaller zone of uncertainty. This ability to measure the near "point-to-point time-of-flight" of an individual photon removes much of the range ambiguity inherent in conventional altimeters and, as we shall demonstrate, produces high resolution 2D profiles and/or 3D topographic images.

We believe that a spaceborne microlaser altimeter, or "microaltimeter", can address many of the same Earth science issues as the aforementioned MOLA, GLAS, and VCL systems. Potential advantages of the microaltimeter approach include significantly greater spatial resolution in either the along-track or cross-track directions (or both) as well as greatly reduced demands on spacecraft resources such as prime power, volume and weight allocations, etc. Potential microaltimeter targets are the usual land, ice, and water surfaces as well as distributed or soft targets such as clouds, planetary boundary layers, tree canopies, and other vegetation (Ho, C., et al, 1995). The much-reduced signal levels of the microaltimeter relative to conventional altimeters are largely offset by a corresponding reduction in the detection threshold to about one photoelectron so that instrument sensitivity is largely maintained or even enhanced. As a result, geoscience applications include the development of a high resolution, high accuracy topographic database of land surfaces useful for studying hydrological runoff; the effects of clouds on radiation balance; changes in sea, lake, or reservoir levels; changes in ice sheet thickness; tree canopy heights and biomass assessment, etc. Applications to extraterrestrial science missions are both obvious and numerous and include the low power, high resolution topographic mapping of other planets, moons, asteroids, and comets within the Solar System. Commercial applications include aerial surveying of cities and towns and/or the generation of local topographic maps from aircraft cruise altitudes (6 to 12 km) using relatively small and inexpensive lasers. Even with their higher pulse energies, most conventional airborne laser altimeters must fly at altitudes below 1 km, which usually requires a special waiver from the FAA and makes the mapping of hilly or mountainous terrain both difficult and hazardous.

Under NASA's Instrument Incubator Program (IIP), the Goddard Space Flight Center has been developing an airborne multikilohertz microlaser altimeter ("microaltimeter") as a technology demonstration, which hopefully will lead to future space missions. Instrument development was initiated in December 1998. One engineering and two science flights were conducted in January, May, and August of 2001. The goals of the IIP program are to:

- Develop and demonstrate the necessary technologies and the operational and analytical software.
- Confirm the validity of the mathematical modeling and surface data extraction algorithms.
- Collect high spatial resolution topographic data over a variety of surfaces (land, ice, water, biomass, clouds) from a high altitude aircraft under both night and day conditions and evaluate its scientific usefulness relative to data from conventional laser altimeters.
- Demonstrate the technical and economic advantages of the microaltimeter concept for future Earth and planetary missions.

2. INSTRUMENT OVERVIEW

In order to improve the compatibility and portability of the instrument between different host aircraft, the microaltimeter has been designed to attach to a standard Lyca camera mount, commonly used in aerial surveying and photogrammetric missions and to operate at typical aircraft cruise altitudes between 6 and 12 km (20,000 to 40,000 ft).

The airborne microaltimeter is designed to operate at up to 10 kHz single photon sampling rates. Our choice of a 10 kHz fire rate was driven by several factors:

1. We wanted to match the return rates of the best conventional altimeters but with a lower power-aperture product instrument operating at higher altitudes in order to demonstrate the technical and economic advantages of the microaltimeter approach.
2. The 10 kHz rate allows system demonstrations to be carried out at aircraft cruise altitudes as high as 15 km (50,000 ft) without having to contend with multiple pulses in flight; this greatly simplifies the receiver design.
3. 10 kHz appeared to be a comfortable rate for modern data acquisition systems and would be compatible with the projected near term capabilities of space-qualified CPU's or Programmable Array Logic (PAL) processors.

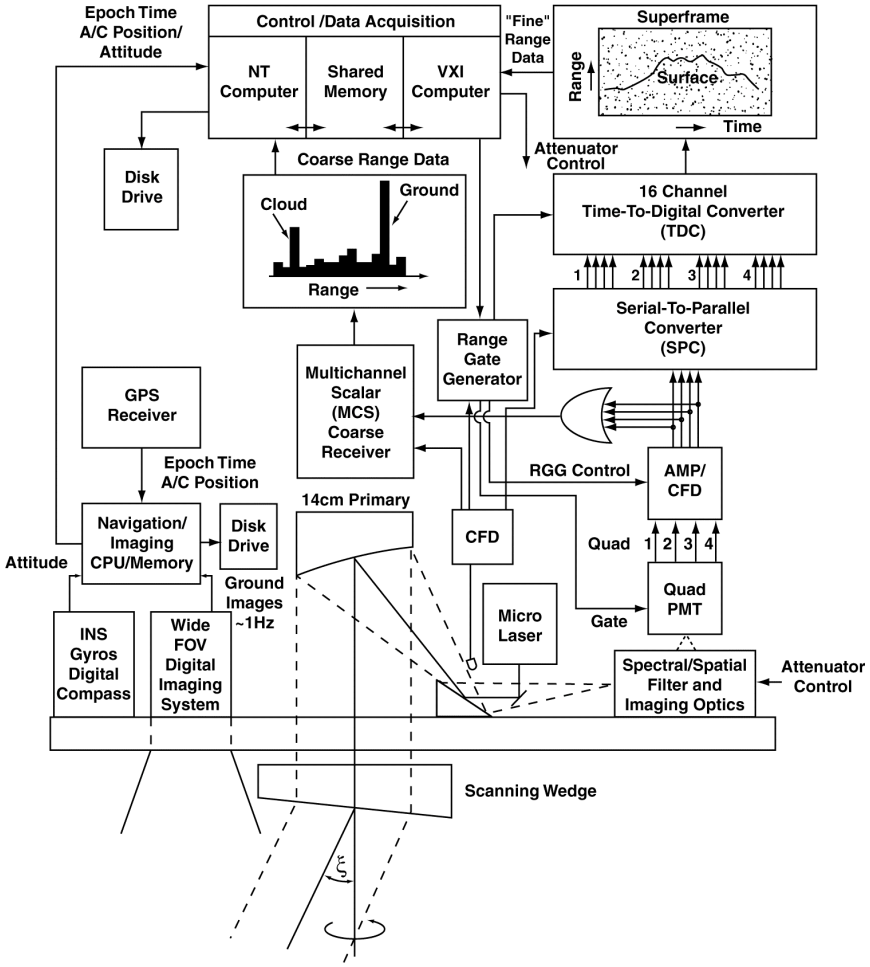

Figure 1: Block diagram of the IIP microlaser altimeter

A block diagram of the NASA IIP instrument is presented in Figure 1. In test flights carried out to date, a commercial microchip Nd:YAG laser, powered by a single 1.2 W CW laser diode and frequency doubled by a passive LBO nonlinear crystal, provides a low energy (few μJ), few kHz train of subnanosecond laser pulses at a visible green wavelength of 532 nm. The package, shown in Figure 2, contains a thermoelectric cooler, a 1.2 watt CW laser pump diode, the passively Q- switched Nd;YAG microchip laser, and an LBO nonlinear crystal for converting the infrared radiation to the visible.

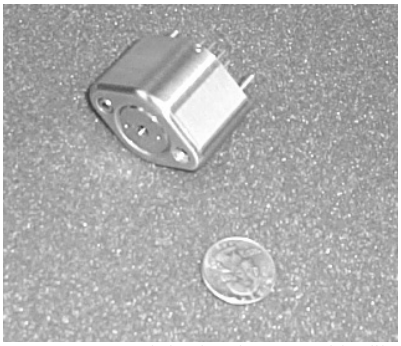

Figure 2: Commercial microlaser used in flight experiments compared to US quarter.

The microchip laser oscillator itself measures 2 mm x 2mm x 2.25 mm and consists of a Nd:YAG gain medium) segment diffusion-bonded to, or grown onto, a thin crystal of Cr^{4+}-doped YAG, which acts as a passive saturable absorber Q-switch and produces the sub-nanosecond pulses. The matching indices of refraction and diffused nature of the interface results in low internal optical loss. The monolithic laser resonator is formed by polishing opposite sides of the microchip optically flat and parallel and applying reflective coatings (Zayhowski, J., 1998). The resulting microlaser requires no active switching components and, because of the monolithic structure, can never go out of alignment. A small pick-off mirror injects the transmitter beam, following some initial divergence, into the central 5 cm of the common transmit/receive telescope, which uses a 20 cm off-axis parabola as the telescope primary mirror. Optical leakage from the outgoing laser pulse is sampled by a fast photodiode, which time-tags the start pulse with a Berkeley Nucleonics Corporation (BNC) Time-to-Digital Converter (TDC) and starts the range gate generator (BNC) Model B940). The TEM_{00} spatial mode quality (M^2 <1.3) of the end-pumped microlaser allows an extremely narrow transmit beam (< 20 arcsec) to be generated with a correspondingly small receiver FOV, which in turn reduces the solar noise count rate. The laser spot diameter on the ground

varies between 30 and 100 cm, depending linearly on aircraft altitude.

An internal computer-controlled aperture restricts the receiver to the central 14 cm of the primary or less. The receiver utilizes the remaining 87% of the available aperture that is not blocked by the injection mirror to gather photons reflected from the surface. Stray light rejection within the receive telescope and interface optics severely restricts the number of off-axis photons reaching the stop detector. The laser pickoff mirror effectively blocks the scattered return from within the aircraft and, combined with good spectral and spatial filtering, permits the detector to operate in an ungated mode, even in daylight.

The returning photons pass through spectral (0.4 nm) and spatial (~140 μrad) filters and are imaged onto a 2x2 element Hamamatsu Model R5900U metal channel dynode Photo-Multiplier Tube (PMT). Because the primary timing unit, the BNC Model B945 TDC, can accommodate up to 16 stop events (one in each of 16 channels), the receiver design permits 4 stop events to occur within the range gate for each of the 4 detector elements. Provisions have also been made in the design to incorporate either a single element Model R7400U (1 channel, 16 stops) or a 4x4 Model H6568 PMT (16 channels, 1 stop per pixel) as alternate detectors. Use of commercial segmented anode photomultipliers provides an inexpensive demonstration of the potential advantages of "quasi-imaging" or "point-to-point ranging". For example, at 12 km altitude where the ground beam diameter is about 120 cm, the 4x4 array allows the source of the received photon to be resolved within a roughly 30cm x 30 cm cell on the ground. In a 600 km Earth orbit, a roughly 20 m diameter beam would be dissected into 5 x 5 meter cells by a 4x4 array leading to a higher resolution ground "image". Of course, improved spatial resolution could be achieved through higher pixellation..

Each detector pixel output is input to a high speed amplifier/constant fraction discriminator (AMP/CFD) module (Phillips Scientific Model 6908). The CFD provides a fast timing pulse to both a "coarse" and a "fine" range receiver. The function of the coarse receiver is to simultaneously capture all of the "soft" scattering surface returns (e.g. clouds, boundary or fog layers) as well as the ground return and to provide an initial estimate of the range to the ground and near-ground scatterers (e.g. tree canopies and sub-canopies or man-made structures). The last "ground" return of the coarse receiver is used to center the range gate of the fine receiver in real time so that it can concentrate on resolving surface features with a minimum of noise background counts.

The "coarse" receiver is an EG&G Ortec Turbo- Multi-Channel Scalar (MCS) which bins all of the photons received over virtually the entire fire interval and creates a histogram of photon stop events. The best coarse range resolution of 75 cm is determined by the minimum MCS bin size of 5 nsec. Since this level of range accuracy is more than adequate for clouds or other meteorological layers and there is similarly no need for high spatial resolution in the transverse dimension, the "stop" outputs of all the pixels are ORed together at the input to the MCS.

The "fine" range receiver time-of-flight (TOF) measurement is determined by differencing the time tags of the laser fire ("start") event and the photon return ("stop") events in the TDC. Although the TDC has a timing resolution of 50 psec (7.5 mm), the range resolution of the fine receiver is limited by the detector impulse response to about 5 cm RMS. Furthermore, since the TDC is capable of measuring only one stop event per channel, the serial "stop" pulses (up to a maximum of four) from each of the four pixels must first be separated into parallel lines by a 4 channel Serial-to-Parallel Converter (SPC). The SPC output fans out to the 16 channels of the TDC, thereby preserving pixel identification.

In order of decreasing duration, individual gating pulses can be applied to the PMT, the MCS, and the TDC respectively by the multi-channel range gate generator as in Figure 1. In current flights of the prototype instrument, all photon “times-of-arrival” within the range gate, relative to the start pulse, are measured by the "fine" range receiver and recorded on the system hard disk for later analysis. However, our data extraction algorithms will be running in parallel to validate them in preparation for later operational flights, where software algorithms will identify the signal photons in flight and strip away most of the noise photons in near real-time.

There are three computers used in the flight system: the Ranging System Operator Interface (RGUI), the Ranging System Data Collector (RDATA), and the Navigational and Camera Control (NAV). A common timing reference is input to all three computers in the form of the current laser shot counter, which allows post-flight coordination of data recorded on separate computers.

The Ranging System Graphical User Interface (RGUI) is a 500 Mhz Pentium III processor running Windows NT 4.0. The system has 128 Mbytes of memory and two 13 Gbyte IDE Ultra ATA hard drives. One of the drives is used for system and program files; the other is mounted in a receiving frame for easy removal and will be used to record the flight data. The operator display is an LCD 20" rack mounted monitor with a pixel resolution of 1280 x 1024. The RGUI computer is responsible for operator interface, data logging, signal processing, and control of the EG&G Turbo-MCS Histogrammer. In addition this computer picks up a small data set from the NAV computer at 1 Hz using internet file sharing, and it reads 720 Kbytes of shared memory data from the RDATA computer at 1 Hz. Signal processing in RGUI provides visual feedback to the operator and can be used to provide control of the range window. All of the data is logged to the removable hard disk once per second. The amount of data recorded is approximately 3 Gigabytes per hour.

The basis of the RGUI software is NTGSE, which is a software package originally developed at GSFC for other missions. NTGSE has been modified for our application and has allowed a quicker software development cycle.

The Ranging System Data Collector (RDATA) is a 233 Mhz Pentium processor running DOS 6.22. The processor is an embedded module in a National Instruments VXI crate, which also contains a MXI interface to the RGUI computer (with 32Mbytes of shared memory), a digital I/O module (National Instruments DIO-128), and two Berkeley Nucleonics modules for ranging interface: the B940 digital delay generator (DDG) and the B945 16-channel time to digital converter (TDC). The embedded CPU contains 32 Mbytes of memory, a 4 Gbyte hard disk, as well as ethernet, SCSI, serial and parallel interfaces. RDATA uses an interrupt from the TDC module at the end of each range gate to trigger the reading of the laser fire time, the 16 range returns, the scan angle, and the shot counter. Interrupts are generated at laser fire rates up to 10 Khz. Data is placed in a shared memory buffer for the RGUI

computer to pick up when it can. The shared memory buffer is a circular buffer and currently holds 5 seconds worth of data. Commands from the RGUI to the RDATA computer are also sent across shared memory. These include the range delay, the size of the range window, and the scan commands and are picked up by RDATA at 2 Hz.

The instrument has been flown with and without the scanner operating in order to demonstrate both contiguous 2D linear profiling of the underlying terrain as well as the 3D mapping of larger swaths during a single pass of the aircraft. Because of the small size of the microaltimeter transmit/receive optics, an inexpensive optical wedge roughly 15 cm in diameter is rotated at rates up to 20 Hz to superimpose a circular scan (0.26 degree conical half angle) on the linear flight path motion. The rotating wedge simultaneously deflects both the transmitter beam and narrow receiver FOV Because of the small scan angle, the returning photons from the illuminated ground spot remain within the receiver FOV but, at higher aircraft altitudes, become increasingly displaced from the center due to the longer roundtrip transit time to the surface.

3. POST-FLIGHT DATA PROCESSING

In order to generate an accurate topographic map, it is essential for any laser altimeter that we know both the instantaneous position and attitude of the instrument on each laser fire in addition to the pulse time-of-flight and any fixed timing biases within the instrument. The latter bias can be determined by ranging to a target whose distance from the instrument reference point is well known. For the quasi-imaging and scanning microaltimeter, one must also make corrections based on the instantaneous off-nadir angle of the scanner and the X-Y coordinate (or pixel) which recorded the photon event.

Multiple GPS geodetic receivers are used (one in the aircraft and one or more on the ground) to provide post-flight dynamic differential positioning at the few decimeter level. The fixed offset vector between the GPS antenna phase center and the altimeter reference point in the aircraft reference frame is measured and corrected by three-axis attitude data to accurately locate the altimeter reference point in the Earth reference frame during flight. Instantaneous instrument attitude is provided by a three-axis fiber-optic gyro mounted directly on the altimeter optical bench and calibrated pre-flight. To counter or monitor gyro drift errors, independent updates of attitude are obtained in-flight by (1) a digital compass (for heading) supplemented by two collocated and orthogonal bench-mounted inclinometers and (2) repeatedly over-flying a set of four "ground stars", whose relative positions have been precisely located at the few mm level using geodetic GPS receivers. These "ground stars" are generally located near the center of the interrogated region to accommodate frequent overflights and arranged in a square or diamond pattern a couple of km on a side. Thus, when the aircraft is near the center of the pattern, they can all be viewed simultaneously by the wide FOV camera attached to the altimeter instrument, providing adequate angular resolution for updating the aircraft attitude at the few arcsecond level. The ground stars consist of small battery-powered Light Emitting Diode (LED) arrays, which are pulsed by the 1pps output of a GPS Timing Receiver. The onboard digital camera, boresighted with the range receiver and synchronized with the wide-angle ground star emission by the 1pps output of the onboard GPS receiver, then records the spectrally narrow images of the ground stars through a bandpass filter. The deviation of the ground stars from their predicted positions in the camera FOV, based on the few decimeter accuracy aircraft positioning, allows the instrument attitude to be updated post-flight with few arcsecond accuracy.

The instantaneous angular position of the scanning wedge is obtained by an encoder, time-tagged and recorded in the data file along with the ranging data. As mentioned previously, the detector pixel producing a given photon event is recorded by the "fine" range receiver and can be used to correct the measured elevation for the transverse location of the photon source within the ground spot.

To summarize, a "start" pulse and potentially one or more "stop" pulses (noise and/or signal counts) are recorded, for each laser fire, by the coarse and fine receivers, both of which can be viewed as correlation range receivers but with vastly different range gates and resolutions. A Post-Detection Poisson Filter (Degnan, J., 2000) identifies which cells in the coarse and fine receivers are most likely to contain signal counts. The photon times-of-flight for the echos selected as signal must then be subtracted from the aircraft altitude and corrected for pitch, roll, and yaw in order to determine the terrain heights. Additional corrections for the fixed offset of the GPS antenna from the instrument reference, the imposed off-nadir pointing due to the rotating scanner, attitude biases, and individual timing channel delays must also be made. Approximate X-Y locations, as determined by the pixellated or imaging detector, further allow more accurate placement of the measured terrain heights in the transverse dimension. The final analysis data product will be a three dimensional plot (and corresponding data files) of the terrain or sea heights for the scanned swaths obtained over multiple flight paths.

4. PRELIMINARY FLIGHT RESULTS

On January 4 and May 16 respectively of this year, the engineering and first science flight of the microaltimeter were respectively conducted on the NASA P3B aircraft housed at the Wallops Flight Facility (WFF). Both flights were conducted in full daylight under conditions of near maximum solar illumination. These flights have concentrated on target areas convenient to WFF which have already been accurately mapped by conventional altimeters, such as the area around Ocean City, Maryland, and Assateague Island, Virgina. The area offers a wide range of target types - tree canopies, water bodies, beach areas, and man-made structures. Barren terrain represents the simplest target for the microaltimeter and is useful in evaluating and optimizing the technique for future extraterrestrial planetary topographic mapping missions. Highly vegetated surfaces are much more complex and provide a test on whether or not the microaltimeter can successfully penetrate tree canopies to detect the ground and recover canopy and sub-canopy heights via statistical interpretation of the high repetition rate data. Towns and cities test the ability of the instrument and data processing algorithms to record and adapt to frequent and large elevation changes and assess its value as an aerial commercial surveying tool. Finally, overflights of beach areas evaluate its capability for monitoring beach erosion and wave heights and for performing shallow water bathymetry at single photon levels. Ultimately, detailed comparisons between existing Digital Elevation Models, produced by repeated flights of the Wallops Airborne Topographic Mapper, and our own terrain measurements will be produced, giving point-to-point height differences and an overall measure of terrain difference.

Figure 3 provides a summary of the instrument parameters for the first engineering flight and some sample profiling data, taken between noon and 2 pm at three altitudes (3.3, 5.5, and 6.7 km). At the highest altitude of 6.7 km (22,000 ft), the mean signal strength per laser fire was computed to be less than 0.88 photoelectron (pe) per laser fire; at no altitude did the calculated mean signal exceed 3 pe per laser fire. Crosstalk between the receiver channels forced us to limit our observations to the first stop observed in any quadrant. Nevertheless, the system successfully generated high resolution profiles of buildings, tree canopies and underlying terrain, and even performed shallow water bathymetry over the Chesapeake Bay. Each of the figures shows approximately 2 seconds of altimetry data and is uncorrected for aircraft motion or attitude.

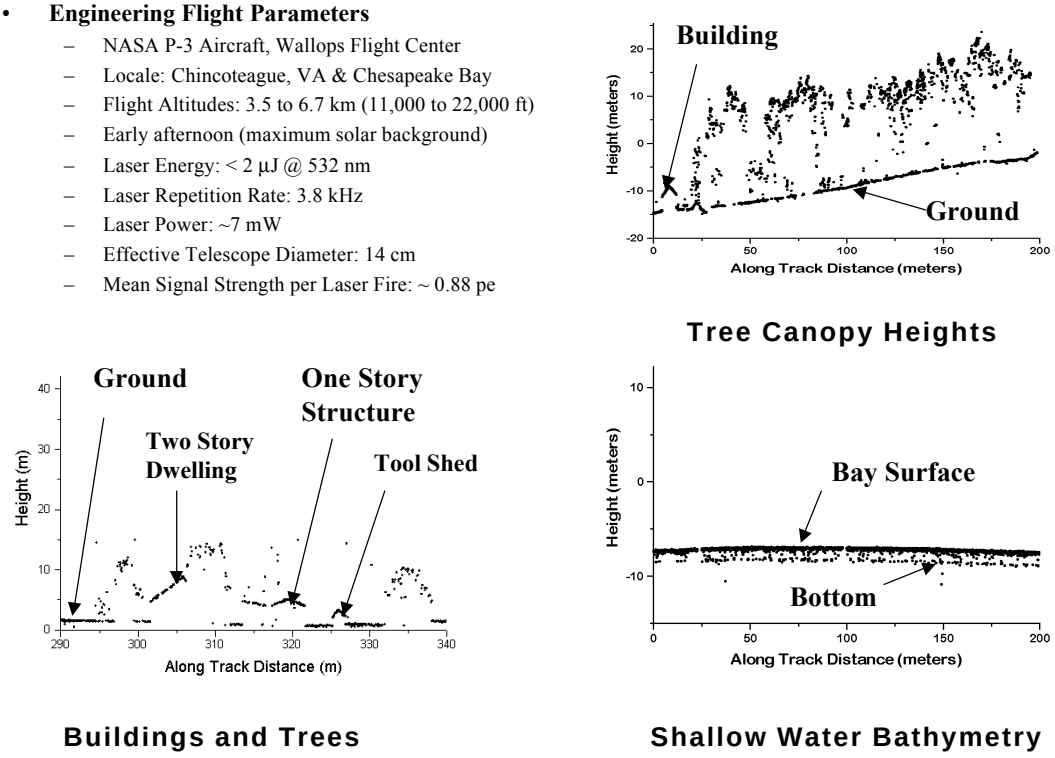

Figure 3: Engineering flight configuration plus sample profiling data from: small buildings and trees in the town of Chincoteague, VA, from 6.7 km altitude; tree lines and underlying terrain from 3.4 km altitude; and shallow water bathymetry over the Chesapeake Bay from 3.4 km altitude.

During the first science flight on the morning of May 16, both the scanner and the digital camera were available. Furthermore, the receiver crosstalk issues, which plagued the earlier engineering flight, were resolved. A single run over Assateague Island and Ocean City was made in both unscanned (2D profiling) and scanned (3D topographic) mode at a relatively low altitude of 1.6 km due to a failure in the laser's thermoelectric cooler which negatively impacted its performance. Figure 4 provides an example of the profiling data and corresponding digital images collected by the instrument. On the left hand side of the figure, we reproduce, from top to bottom: (1) a small segment of the aerial photograph taken by the onboard digital camera of a house in Ocean City, Maryland; (2) a ground photo of the house showing a tree in the rear yard (upper left of photo) , and a small shrub in the front of the house; and (3) approximately 0.3 seconds of altimeter data which clearly outlines the tree, rooftop, and shrub (plus some backyard shrubs not visible in the ground photo). Similarly, on the right hand side of the figure, we see two apartment houses (plus a portion of a third) outlined in the box in another aerial photo, followed by a ground image of the two buildings, and about one second of altimeter data. The ground photo shows a multi-tiered roof structure with single and dual chimney structures, which can also be clearly seen in the altimeter profiling data.

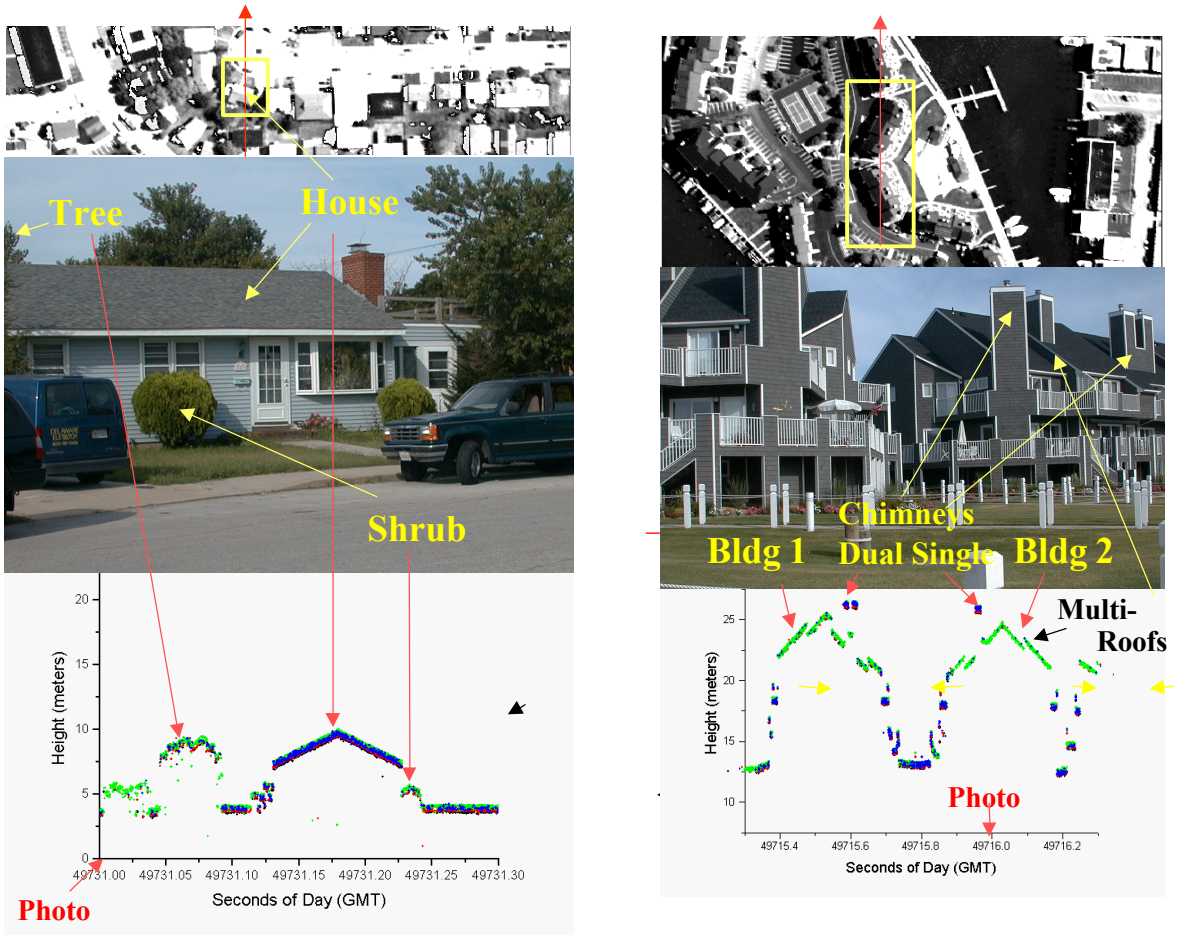

Figure 4: Profiling examples from the May 16 science flight showing (from top to bottom) an aerial photo taken by the onboard digital camera, a ground photo of the object, and the profile image as seen by the altimeter. The first example on the left is a single story home in a residential community while the second is a pair of apartment buildings with multi-tiered roofs and single and dual chimney stacks. The different color lidar points correspond to individual photons detected by different detector quadrants and have not been corrected for small differential channel delays to show the consistency between channels

5. CONCLUSIONS

Upcoming flights will make multiple passes over Ocean City and Assateague Island in order to build up a detailed topographic map which can then be compared to an existing Digital Elevation Model (DEM) of the region (Csatho, B., et al, 2001) to check the absolute accuracy of the instrument. The DEM was previously obtained by repeated flights of an existing, low altitude, laser altimeter - the Airborne Topographic Mapper- operated by Goddard's Wallops Flight Facility.

The productivity of the current instrument can be greatly improved through the use of somewhat higher power lasers and more efficient detectors. The average power of the commercial microchip lasers available for these experiments was quite low (7 to 20 mW). Passively Q-switched microchip Nd:YAG oscillators less than a cm in length and end-pumped via fiber bundles by a single linear diode array have produced output powers of greater than 1 W at 1064 nm (>600 mW at 532 nm) with repetition rates as high as 16 kHz and pulsewidths as short as 300 psec (Zayhowski, J., 1998). The commercial segmented-anode, metal dynode chain photomultiplier used in these experiments has a quantum efficiency of about 10% and an overall counting efficiency of 7% due to its internal geometry. Commercial tubes of this type with up to 100 (10x10) anodes are available from Hamamatsu. However, a segmented anode microchannel plate PMT with a GaAsP photocathode could potentially achieve a counting efficiency close to 40% at 532 nm without introducing the added complexity, expense, and long quenching times associated with avalanche photodiode (APD) arrays. By combining single photon ranging with efficient pixellated detectors and multistop, multichannel range receivers with low dead times (Degnan, J., 2000), the path to an efficient, few centimeter resolution, imaging 3D lidar seems clear. Unlike conventional laser altimeters, which rely on the deconvolution of complex multiphoton waveforms produced by a large laser ground spot, photon-counting lidars can provide efficient "point-to-point" ranging with excellent horizontal and vertical registration of multiple photon "events", even from vertically distributed or "soft" targets such as tree canopies.

REFERENCES

Abbott, R. et al, 1973. Laser observations of the Moon: Identification and construction of normal points for 1969-1971, The Astronomical Journal 78, pp. 784-793.

Abshire,J., et al, 2000. The Geoscience Laser Altimeter System (GLAS) for the ICEsat Mission , Proc. CLEO/QELS 2000, San Francisco, CA, May 7-12.

Csatho, B., et al, 2001. Creation of High Resolution, Precise Digital Elevation Models (DEM) of Ocean City and Assateague Island, these proceedings.

Dubayah, R. et al, 1997, The Vegetation Canopy Lidar Mission, Proceedings: Land Satellite Information in the Next Decade II: Sources and Applications, 1997, American Society for Photogrammetry and Remote Sensing, Bethesda, MD, December.

Degnan, J., 2000. Photon-counting multikilohertz microlaser altimeters for airborne and spaceborne topographic measurements, submitted to J. Geodynamics

Degnan, J. et al, 1998. Feasibility study of multikilohertz spaceborne microlaser altimeters, European Geophysical Society (EGS) Annual Symposium, Nice, France, April 20-24. (Abstract: Annales Geophysicae, Part I Society Symposia, Solid Earth Geophysics and Geodesy, Supplement 1 to Volume 16, p. C379)

Ho, C., et al, 1995. Volumetric measurement of plant canopies using laser ranging and mapping technique with a photon counting detector, Los Alamos National Laboratory, Internal Memorandum, NIS-2-95-206, Sept. 12.

Ramos-Izquierdo, L., et al, 1994. Optical system design and integration of the Mars Observer Laser Altimeter, Applied Optics, 33, pp. 307-322.

Vasile, S., et al, 1997. Photon detection with high gain avalanche photodiode arrays, IEEE Trans. Nuclear Science, 45, pp. 720-723.

Zayhowski, J., 1998. "Passively Q-switched microchip lasers and applications", Rev. Laser Eng., 26, pp. 841-846.

WIDE-SWATH IMAGING LIDAR DEVELOPMENT FOR AIRBORNE AND SPACEBORNE APPLICATIONS

J. Bryan Blair
Laser Remote Sensing Branch
NASA/Goddard Space Flight Center, Greenbelt, MD 20771, USA
(bryan@arthur.gsfc.nasa.gov)

Michelle Hofton
Department of Geography
University of Maryland, College Park, MD 20742

Scott B. Luthcke
Space Geodesy Branch
NASA/Goddard Space Flight Center, Greenbelt, MD 20771, USA

KEY WORDS: laser altimetry, lidar, altimetry, mapping.

ABSTRACT

With laser altimetry becoming increasingly accepted by the global Earth science community as a source for accurate topographic data, there is now a desire to apply this technology to large area mapping. Commonly, airborne laser systems provide data at several meter resolution and across swaths up to 1-2 km in width. Economic factors drive commercial systems to widen swaths further, but off-nadir incident angles degrade accuracy and significantly diminish the ability to penetrate dense vegetation canopies effectively limiting swath width. Higher operational altitudes (e.g., 10 km vs. 1 km) can provide up to a factor of ten increase in swath width within a selected angular range. However, higher altitude operations require significantly more laser output power, smaller divergence angles and higher beam quality to achieve smaller footprints. At NASA Goddard Space Flight Center, we have been prototyping spaceborne instrumentation and science applications of wide-swath lidar in aircraft for the last several years. This experience has led to the development of several satellite laser altimeters such as the Shuttle Laser Altimeter (SLA) and Vegetation Canopy Lidar (VCL). Technologies and methods utilized in the spaceborne environment are prototyped in the wide-swath, full-waveform airborne Laser Vegetation Imaging Sensor (LVIS). This sensor will undertake a large-area mapping mission in Brazil in June-August 2002. The sensor will use a 3 km-wide data swath and plans are underway to increase the swath width further. Spaceborne imaging applications require significantly higher effective rep-rates than airborne systems and are much less tolerant of unreliable mechanical scanning and equipment maintenance requirements. Unique scanning and ranging techniques for medium-large footprint, full-waveform mapping laser altimeters are currently under development to enable a spaceborne, wide-swath operational mapping laser altimeter capable of full-Earth mapping and dense vegetation penetration. A sample of some of the techniques being developed at NASA Goddard Space Flight Center for future airborne and spaceborne imaging lidar will be presented, including methods for achieving MHz scanning rates.

1. BACKGROUND

Lidar remote sensing of the Earth's surface for topography and vegetation mapping is becoming increasingly prevalent in airborne and spaceborne activities. Advanced lidar systems record the waveform of the returning laser pulse to provide a record of the interaction of the light pulse with the ground surfaces. Each waveform includes returns from the highest elements of any vegetation and the underlying ground (e.g., Blair et al., 1994). The full illumination (waveform) lidar technique is capable of making high resolution, high accuracy, independent topographic measurements on land, beneath vegetation, and over oceans (e.g., Hofton et al., 2001a). Spaceborne lidar systems such as the Shuttle Laser Altimeter (SLA) (Garvin et al., 1998) have demonstrated sub-meter absolute vertical accuracies for Earth topographic measurements (Luthcke et al., 2001). NASA's future dedicated Earth observing lidar missions, the Vegetation Canopy Lidar (VCL) (Dubayah et al., 1997) and ICESat, will provide unequaled decimeter level vertical absolute accuracies of "true ground" even in highly vegetated regions. NASA's airborne LVIS instrument (Blair et al., 1999), with its wide swath, cm ranging accuracy and the full waveform recording, has provided a wealth of engineering data to prototype space-based lidars and to develop and test data processing algorithms and analysis methodologies.

While the advantages of spaceborne laser active remote sensing are apparent, the major limitation remains data coverage. Both current (SLA) and future (VCL and ICESat) spaceborne lidar missions employ profiling instruments that only illuminate a small portion of the planetary surface (1-2%). Current expectations are that microwave mapping of the Earth's surface from synthetic aperture radar (SAR) interferometry (InSAR) presents the *only* practical method of fully illuminating and characterizing the 3D surface of the planet. While the InSAR measurement technology does provide for full global illumination, the backscattering within canopies, de-correlation of the phase images (caused by vegetation/land cover changes, surface slope, surface freezing/thawing, and random movement of scatterers whose sizes are on the scale of the wavelength of the SAR system), as well as the need for sub-pixel (meter-level) alignment of images limits the overall absolute accuracy of the observations and means accurate topographic and topographic change measurements are impossible in some areas of the Earth. Lidar mapping has distinct advantages in accuracy, resolution,

and vegetation penetration. However, there is a clear need to expand these distinct advantages of a lidar system to a spaceborne landscape scale imaging instrument capable of providing full global coverage and monitoring of surface change.

2. AIRBORNE WIDE-SWATH LIDAR

LVIS is a wide-swath, high-altitude, full-waveform airborne laser altimeter developed at NASA Goddard Space Flight Center. LVIS employs mechanical scanning using galvanometer motors to separately scan both the transmitted laser beam and the receiver field-of-view (FOV). LVIS scans in a raster pattern with each mirror coming to a full stop for each laser footprint. Using evolving scan techniques and scan patterns, we can support laser rep-rates of up to 5,000 Hz with this system. This approach has the potential for doubling or quadrupling the swath width, but spaceborne operations and order of magnitude swath increases will require a different approach. Our goal is to begin scanning at 100,000 Hz in the next year with a no-moving-parts scanner system. To support these high laser repetition rates, a different approach toward receiver scanning is required. One option is to segment the receiver FOV across the swath to simulate receiver FOV scanning just by switching detectors and combine this with multiple laser transmitters.

Numerous airborne, swath mapping laser altimeters are currently operational using swath widths from 200 – 2,000 m. To become more cost effective, these systems need to collect data faster and over larger areas. Increasing the swath width requires either operations at higher altitude or increasing the angular swath. Both of these options have negative side effects. Wide angular swaths experience increased sensitivity to errors in attitude knowledge at the swath edges and systems with incident angles >10-15° have increased difficulty penetrating closed vegetation canopies. Further, higher altitude operations also increase sensitivity to attitude errors and require significantly higher laser power to achieve the same performance as that at low altitude.

3. SPACEBORNE WIDE-SWATH LIDAR

Spaceborne implementation of a wide-swath imaging lidar will enable the high accuracy landscape-scale surface observations (Table 1) necessary to answer one of NASA's Earth Science Enterprise (ESE) key questions: *How is the Earth's surface being transformed and how can such information be used to predict future changes?* Wide-swath imaging lidar's high accuracy, high resolution measurements of topography and surface change will lead to significant near-term advances in such fields as the quantification of surface morphology (the first step to understanding constructional and erosional processes and rates) and the mitigation of natural hazards caused by, for example, landslides, flooding and earthquakes. Knowledge of crustal deformation aids in developing and understanding earthquake cycle mechanics and other plate boundary processes (at co, post and inter-event stages). Observations lead to the understanding of volcanic processes particularly for detecting pre-eruption signs and monitoring during/after an eruption, monitoring land subsidence related to human activities such as groundwater, petroleum and coal removal, coastal erosion processes, glacial/ice sheet thickness changes and flow, and post-glacial rebound. Systematic observations of these processes will lead to improved models and forecasting, for example, of eruptive and seismic events, and provide rapid response to emergencies and early warning of hazards. Existing and planned global topographic data sets contain errors (e.g., Wolf and Wingham, 1992), are of insufficient accuracy, resolution, and coverage, or do not fully characterize the true "bare earth" topography needed for global achievement of these science goals. Topographic change measurements are limited to areas where InSAR is possible, or restricted by the poor spatial coverage of techniques such as GPS.

One of the most promising and unique capabilities of laser altimetry is the potential for sensing topography beneath closed vegetation. This is one application that seems to benefit from full-waveform collection. Full-waveform laser altimetry is the only proven method for penetrating the densest of forest canopies. The canopy height and vertical structure information obtained from a full-waveform, wide-swath imaging lidar produce ecological measurements such as biomass and carbon density (Drake et al., 2001; Means et al., 1999), which do not appear to saturate as measurements from SAR technologies do (Imhoff, 1995; Kasischke et al., 1997). These data are important to the ESE Ecology/carbon cycle program. Furthermore, very high-resolution geoid measurements of oceans, topographic corrections for gravity reduction, and coastal oceanography (where radars "lose lock") are possible. For the military (and others), the wide-swath spaceborne imaging lidar can provide data at the DTED3 level (10m posting) with accuracies exceeding DTED5 levels (5m absolute) by an order of magnitude.

Wide-swath imaging lidar measurement technology provides the best characteristics of current InSAR and lidar technologies, enabling the complete illumination of the Earth's surface while maintaining high absolute accuracy (elevation measurements that are 2 orders of magnitude more accurate than the latest InSAR SRTM implementation) mapping of vegetation vertical structure and topography, as well as centimeter level change detection (Hofton and Blair, 2001). Table 1 shows an example of the capabilities of a spaceborne implementation of this technology.

Table 1:
A spaceborne implementation of the proposed wide-swath imaging lidar technology will enable:

- Landscape scale (10km swath) imaging
- Full Earth imaging at <10m pixels within 1 year
  - Near-100% coverage/illumination
- Topography measurements at decimeter-level absolute vertical accuracy
- Vegetation canopy height and structure measurements
- Change detection measurements at sub-centimeter relative vertical accuracy
  - Subtle topographic change beneath vegetation,
- Vegetation and land cover changes.

To enable spaceborne imaging lidar requires that we advance the readiness of several key technologies associated with laser scanning and laser range recovery, as well as advance post

processing techniques to allow cm-level change detection and improve signal to noise ratio within the lidar footprints. Efforts are currently underway to develop: no-moving-parts scanning systems, large aperture deployable telescopes (Browell, et al., 2001), and high-efficiency laser transmitters.

4. SUMMARY

At NASA Goddard Space Flight Center, ongoing development of wide-swath airborne laser altimeters support future development of a spaceborne imaging lidar system for fully mapping the Earth's surface topography (including sub-canopy) and vegetation vertical structure. Several techniques for achieving wide data swaths from a spaceborne laser altimeter are under investigation. An airborne demonstration of 100 kHz, no-moving-parts, high-rate laser scanning coupled with a segmented FOV receiver is planned for the near future. Ultimately, an operational spaceborne swath imaging laser altimeter system will require sampling rates of 1 MHz or greater.

5. REFERENCES

Blair, J.B., Coyle, D.B., Bufton, J.L., and Harding, D.J., 1994. Optimization of an airborne laser altimeter for remote sensing of vegetation and tree canopies. In: Proceedings of the International Geoscience and Remote Sensing Symposium – IGARSS 1994. ESA Scientific and Technical Publications, Noordwijk, pp. 939-941.

Blair, J.B., Rabine, D.L., and Hofton, M.A., The Laser Vegetation Imaging Sensor: a medium-altitude digitization-only, airborne laser altimeter for mapping vegetation and topography, ISPRS Journal of Photogrammetry and Remote Sensing, 54, 115-122, 1999.

Browell, E., Peri, F., and Connerton, R., Light-weight deployable UV/Visible/IR telescopes, presented at ESE Technology Planning workshop, 2001.

Dubayah, R., Blair, J.B., Bufton, J.L., Clark, D.B., Ja Ja, J., Knox, R., Luthcke, S.B., Prince, S., and Weishampel, J., The Vegetation Canopy Lidar mission. In: Land Satellite Information in the Next Decade II: Sources and Applications, American Society for Photogrammetry and Remote Sensing, Bethesda MD, pp. 100-112, 1997.

Drake, J., Dubayah. R., Clark, D., Knox, R., Blair, J.B., Hofton, M.A., Chazdon, R.L., Weishampel, J. F., and Prince, S., Estimation of tropical forest structural characteristics using large-footprint lidar, in press, Remote Sensing of Environment, 2001.

Garvin, J. B., Bufton, J., Blair, J., Harding, D., Luthcke, S., Frawley, J., and Rowlands, D., Observations of the Earth's topography from the Shuttle Laser Altimeter (SLA): Laser pulse echo-recovery measurements of terrestrial surfaces, Physics and Chemistry of the Earth, 23, 1053-1068, 1998.

Hofton, M. A., Blair, J. B., Minster, J.-B., Ridgway, J. R., Williams, N.P., Bufton, J.L., and Rabine, D.L., An airborne scanning laser altimetry survey of Long Valley, CA, International Journal of Remote Sensing, 21, 2413-2437, 2000a.

Hofton, M.A., and Blair, J.B., Detecting vertical ground surface change using laser pulse correlation, submitted to Journal of Geodynamics, 2001.

Imhoff, M.L., 1995. Radar backscatter and biomass saturation-ramifications for global biomass inventory. IEEE Transactions on Geoscience and Remote Sensing, 33, 511-518.

Kasischke, E.S., Melack, J.M., and Dobson, M.C., 1997. The use of imaging radars for ecological applications – a review. Remote Sensing of the Environment, 59, 141-156.

Luthcke, S.B., Rowlands, D.D., McCarthy, J.J., Stoneking, E. and Pavlis, D.E., Spaceborne Laser Altimeter Pointing Bias Calibration From Range Residual Analysis, Journal of Spacecraft and Rockets, 37, 2000.

Means, J.E., Acker, S.E., Harding, D.J., Blair, J.B., Lefsky, M.A., Cohen, W.B., Harmon, M.E., and McKee, W.A., use of large footprint scanning airborne lidar to estimate forest stand characteristics in the western Cascades of Oregon, Remote Sensing of the Environment, 67, 298-308, 1999.

Wolf, M., and Wingham, D.J., The status of the world's public-domain digital topography of the land and ice, Geophysical Research Letters, 19, 2325-2328, 1992.

LAND SURFACE MAPPING AND CHARACTERIZATION USING LASER ALTIMETRY

SESSION 2

SURFACE RECONSTRUCTION I

ADVANCED DTM GENERATION FROM LIDAR DATA

K. Kraus and N. Pfeifer
Institute of Photogrammetry and Remote Sensing
Vienna University of Technology
A-1040 Vienna, Austria
email:{kk, np}@ipf.tuwien.ac.at

Commission III, Working Group 3

KEY WORDS: laser scanning, digital terrain model, interpolation, filtering, break lines

ABSTRACT

The introduction of laser scanning has triggered off a revolution in topographic terrain capturing, especially in the generation of digital terrain models (DTM). In this article refined methods for the restitution of airborne LIDAR data are presented which have been developed at the Institute of Photogrammetry and Remote Sensing (Institut für Photogrammetrie und Fernerkundung, I.P.F.) at Vienna University of Technology. First, a technique for the calibration of laser scanner data is introduced. The (height) discrepancies between overlapping strips, as well as control points with known co-ordinates are utilised for a simultaneous adjustment and transformation of all strips into a state wide co-ordinate system. The next step of LIDAR data processing are the filtering (elimination of vegetation and building points, generally off-terrain points) and the interpolation of the (bald earth) surface. The method, developed at the I.P.F., distinguishes itself in the integration of filtering and terrain interpolation in one process (advantage: even in steep terrain ground points are classified correctly) as well as in the application of data pyramids (advantage: even in very dense forest areas and on large buildings, off-terrain points are eliminated). In order to generate a terrain model with high geo-morphological quality, methods are required for deriving structural line information (e.g. break lines) from laser scanner data. The first method which will be presented, proceeds by a simulation of rain fall over the preliminary DTM (water flow analysis). This yields an identification of the pits with their pit base and the outflow (overflow) point. Subsequently, the terrain shape is changed in order to eliminate the pits. In a further method 3D break lines are derived from the original laser scanner points. The precondition is that the ground plan of the break line is known approximately. The result of this step are 3D-splines which are integrated in the hybrid DTM, combining raster and vector data.

KURZFASSUNG

Das Laser-Scanning hat die topographische Geländeaufnahme, insbesondere die Erstellung digitaler Geländemodelle (DGM) revolutioniert. In diesem Beitrag werden verfeinerte Auswertemethoden vorgestellt, die am Institut für Photogrammetrie und Fernerkundung der TU Wien (I.P.F.) in den letzten Jahren entwickelt wurden. Zuerst wird ein Verfahren zur Kalibrierung von Laser-Scanner-Daten angegeben. Anhand von (Höhen-)Diskrepanzen zwischen den überlappenden Streifen und von koordinatenmäßig bekannten Passpunkten wird eine simultane Einpassung aller Streifen in das Landeskoordinatensystem vorgenommen.

Der nächste Abschnitt ist der Filterung (Elimination der Vegetations- und Gebäudepunkte) und Interpolation der Geländeoberfläche gewidmet. Das am I.P.F. entwickelte Verfahren zeichnet sich dadurch aus, dass einerseits die Filterung gemeinsam mit der Interpolation erfolgt (Vorteil: Auch im steilen Gelände werden Bodenpunkte als DGM-Punkte erkannt) und dass andererseits Datenpyramiden verwendet werden (Vorteil: Auch Laser-Scanner-Punkte in großen dichten Waldgebieten und auf großflächigen Gebäuden werden eliminiert).

Im letzten Abschnitt werden aus Laser-Scanner-Daten Strukturlinien abgeleitet. Im ersten Verfahren werden mittels Regensimulationen im (vorläufigen) Laser-DGM abflusslose Mulden detektiert. Anschließend wird die Form des DGM so verändert, dass die abflusslosen Mulden verschwinden. Im zweiten Verfahren werden 3D-Geländekanten aus den originären Laser-Punkten abgeleitet. Voraussetzung ist dabei, dass die Geländekanten im Grundriss näherungsweise bekannt sind. Das Ergebnis sind 3D-Splines, die im hybriden DGM, das ist ein DGM mit Raster- und Vektordaten, integriert werden.

1 INTRODUCTION

In Europe the term “Airborne Laser Scanning” instead of LIDAR is used frequently. Airborne laser scanning for topographic mapping is a widely used technology. The pros and cons of LIDAR vs. aerial photogrammetry, up to now the method of choice for topographic mapping, are well known. Airborne laser scanning has gained utmost significance for the generation of digital terrain models (DTM). A prospering technology stimulates a continual development and improvement of methods and algorithms. In this article advanced methods for the generation of DTMs from LIDAR data are presented. It will be confined to methods which have been developed at the Institute of Photogrammetry and

Remote Sensing of the Vienna University of Technology (I.P.F.), which have been (and still are) realised in software and put to the test in pilot projects. We will start with a contribution to the system calibration.

2 SYSTEM CALIBRATION

For transforming laser scanner strips into the national ground survey co-ordinate system using dGPS and INS, we principally need only one ground reference station with known ground survey co-ordinates. Moreover, we also need the form of the geoid. But, in practice, we should not be satisfied with that minimal solution because:

- The form of the geoid is not sufficiently (up to some few cm) known in many regions.
- Nowadays the on-the-fly-initialisation for solving the GPS phase ambiguities is possible for fast moving objects like aircrafts with a r.m.s.e. of about 10cm; this might result in errors of some dm. Usually, neighboring precision of dGPS is better by one order of magnitude.
- The attitudes as delivered from IMUs in use are prone to errors of about $\pm 0.01^\circ$. Errors of IMU attitude also introduce some torsion of the laser scanner strips inducing errors in height on both borders of the strip. Equally, IMU attitudes have a high neighboring precision based on the gyros used; nevertheless, they show drifting phenomena.
- System failure or system instabilities shall be mentioned, too: e.g. the change of the set of available GPS satellites during a strip might cause some displacement; however, IMU data helps to bridge such critical gaps.
- Last, but not least, the missing supervision of the whole measuring process has to be mentioned.

Instead of the minimal solution cited above (single ground reference station and geoid) the subsequent alternative is proposed which eliminates the shortcomings of the above:

- Use of more GPS ground reference stations surrounding the area of interest. Knowing the ground survey co-ordinates of all these ground reference stations, this also eliminates the (unknown) linear portion of the geoid's undulation. The undulations of higher degree remain; they might be neglected for the usually relative small extent of practical projects.
- Some of the GPS ground reference stations may be replaced by ground reference points which can be "identified" somehow in the point clouds of the laser scanner strips. For height fitting, horizontal areas free of vegetation are recommended. In photogrammetric terminology, we usually call those reference points control points.
- Monitoring many height discrepancies in the overlapping areas of neighboring laser scanner strips. The systematic portion of these discrepancies should be eliminated. This can be achieved by computing correction polynomials (of probably quite low degree) for each strip: one strip - one polynomial. This procedure preserves the high neighboring precision of both system components and copes with any drifting phenomena. The adjustment of all these sets of coefficients of the polynomials has to be done simultaneously for all strips of a block (key word: block adjustment by strips) – using the heights of corresponding points in the overlapping areas as observations. The height residuals are to be minimised in the adjustment.

The principles of the height fitting of all laser scanner strips simultaneously can be found in fig. 1. XY-positions are defined in a scheme which is – on the one hand – related to the strip borders and – on the other hand – controllable from outside. This control is performed by selection of an interval of the profiles crossing the strips and of a point interval inside the profiles. The first distance is measured (more or less) along the flying track, the second one perpendicular to the first one. Points are preferably chosen in areas of much overlap. Starting from every scheme point, a search for *suitable homologous patches* is done; 'suitable' means that there is as few vegetation as possible and the area is as horizontal as possible, 'homologous' means that the patch has the same position in every involved strip, 'patch' means a rectangular area (externally controllable) of e.g. 20 points.

The set of surfaces inside a patch region is approximated by a set of parallel (tilted) planes:

$$v_{t,s,p} = a_t \left(\bar{X}_{t,s,p} - X_t\right) + b_t \left(\bar{Y}_{t,s,p} - Y_t\right) + c_{t,s} - \bar{Z}_{t,s,p}$$

$\bar{X}_{t,s,p}, \bar{Y}_{t,s,p}, \bar{Z}_{t,s,p}$	...	point p in patch t of strip s; "raw" co-ordinates
X_t, Y_t	...	center of patch t; constant; modulated as given below
a_t, b_t	...	tilting of patch t
$c_{t,s}$	...	height of patch t in strip s; the only parameter of interest
$v_{t,s,p}$	...	residuals of the least squares adjustment

The search for (X_t, Y_t) follows a spiral pattern in the surrounding of the scheme point until certain quality criteria are satisfied: e.g. freedom of vegetation or other disturbances is judged by a tolerance of the r.m.s.e. of the above adjustment problem. Horizontality can be judged on a_t, b_t. Freedom of vegetation can be accomplished by a sort of robust estimation procedure as outlined in the next section by using a skew (asymmetric) weighting function for the above observation equations. The patch size is chosen in accordance with the geometry of the scanner (point density along and across the strip) to contain about 20 to 150 points per strip overlay. Planimetric discrepancies between the strips don't play a remarkable role as long as the terrain is flat enough.

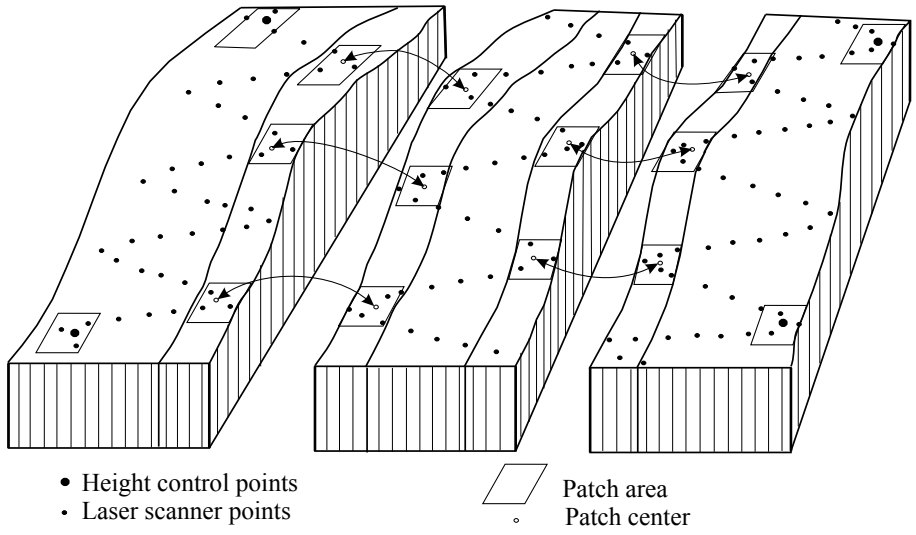

Figure 1: Principle of height block adjustment with laser scanner strips

Subsequently, the points $P_{t,s} = (X_t, Y_t, \bar{Z}_{t,s} := c_{t,s})$ are used as observations in the block adjustment. The unknowns are, as mentioned before, the coefficients of the correction polynomials. The details of the block adjustment with the ORIENT software are described in [Kager and Kraus, 2001].

For a pilot project with the „Bundesanstalt für Gewässerkunde“ in Koblenz (Germany), the “German Federal Institute of Hydrology” we had no suitable control points available. Thus, an absolute fit to the national ground survey co-ordinate system was not possible (no datum given). Nevertheless, the aim of the project was a homogenisation of the block of 56 strips by diminution of the discrepancies between overlapping strips. The scheme points for the automatic measurement of tie points were arranged in profiles at right angles to the main direction of the strips with profile distances of 1000m. (Experiments with smaller profile distances yield approximately the same results.) The height discrepancies between the laser scanner strips prior to adjustment were determined for 1495 patches. The r.m.s.e. was ±10.7cm. By the block adjustment we got a reduction of the factor 2.

In a second pilot project – in the framework of European Union INTERREG projects – we obtained an improvement by the block adjustment of the factor 2.5.

3 FILTERING OF LIDAR DATA AND INTERPOLATION OF THE TERRAIN SURFACE

For the time being, filtering shall be used for the elimination of off-terrain points (points on buildings and trees or bushes) in a LIDAR data set. Such a filtering is a classification in terrain points and off-terrain points. Often, the filtering is performed independently from the interpolation of the terrain surface. If the shape of the terrain is not regarded during the filter process – especially in steep terrain – this can lead to wrong classification results.

Fig. 2 can be used to illustrate this. If the points are only analysed with respect to their absolute terrain height, then off-terrain points can be lower than surrounding ground points. In the upper part of the figure this is the case in the second interval, where a point on the low vegetation is lower than the real ground points in the interval. Of course, this can also be the case for points on the higher vegetation and on buildings.

At the I.P.F. a solution has been found, which combines filtering and interpolation of the terrain. It is called a robust interpolation or robust linear prediction. This algorithm was originally designed for laser data in wooded areas. For a comprehensive description see [Kraus and Pfeifer, 1998] and [Pfeifer et al., 2001]. The algorithm is embedded in a hierarchial approach, however, the filtering of the laser scanner data on one level will be described first.

In this algorithm a rough approximation of the surface is computed first. Next, the residuals, i.e. the oriented distances from the surface to the measured points, are computed. Each (z-)measurement is given a weight according to its distance value, which is the parameter of a *weight function*. The surface is then recomputed under the consideration of the weights. A point with a high weight will attract the surface, resulting in a small residual at this point, whereas a point that has been assigned a low weight will have little influence on the run of the surface. During these iterations a classification is preformed, too. If an oriented distance is above a certain value, the point is classified as off–terrain point and eliminated completely from this surface interpolation. This process of weight iteration is repeated until all gross errors are eliminated (a stable situation) or a maximum number of iterations is reached.

There are two important entities in this algorithm. On one hand, the stochastic model, which is defined by the weight function, on the other hand, the functional model, which describes the way the surface is interpolated. Obviously, the weight function must assign high values (close to 1) to ground points, which are below or on the averaging surface, and low values (weights close to 0) to the vegetation points which are above the averaging surface. The standard weight

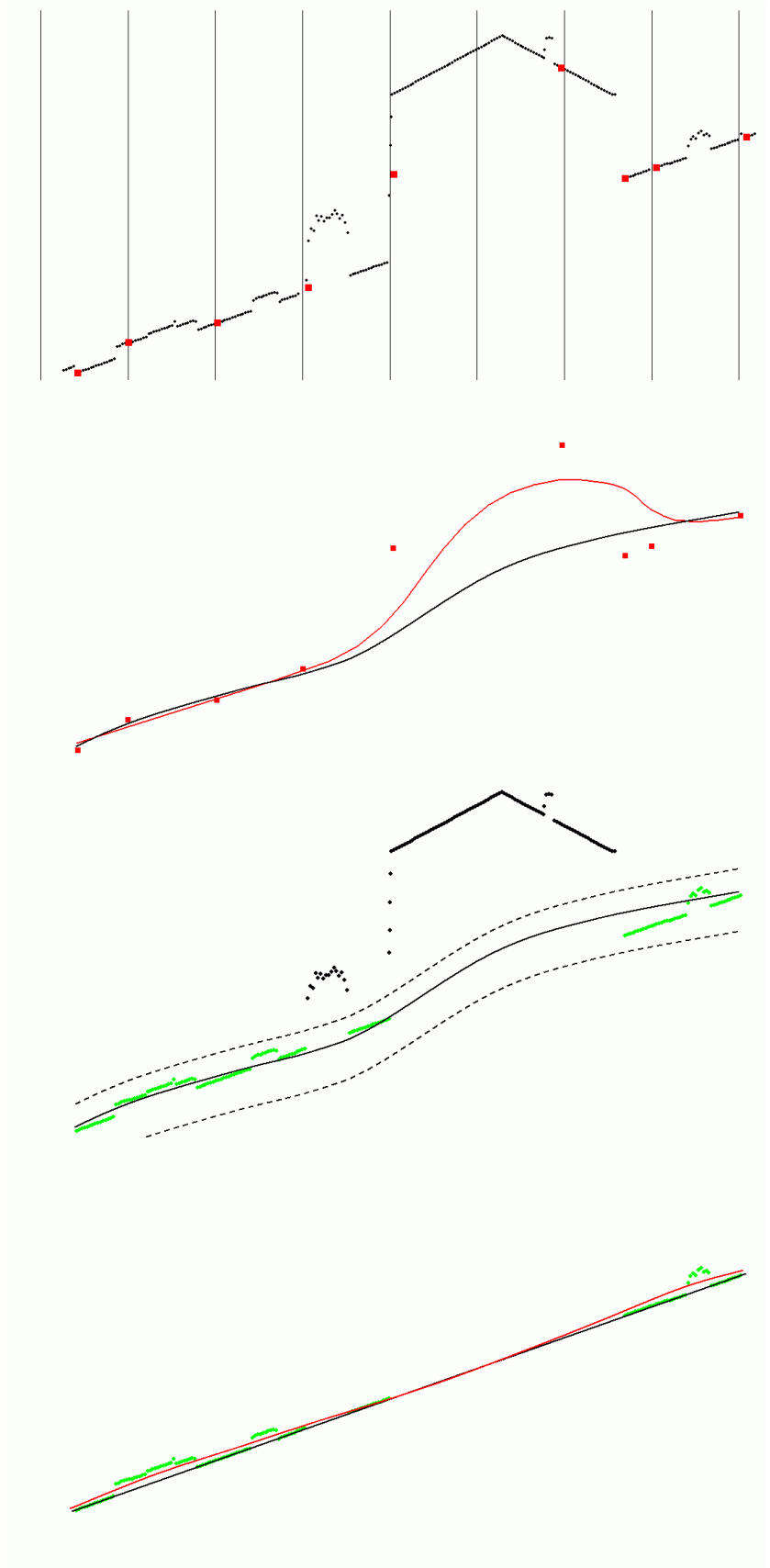

Figure 2: Schematic explanation of hierarchic robust interpolation by means of a profile of laser scanner points.
First image: original points, the lowest point in a regular 5m interval (grid in 3D) is marked as larger (red) square.
Second image: selection of points in a regular interval, averaging surface shown as thin (red) line, surface (DTM) after robust filtering with skew gross error distribution as thick line.
Third image: surface of previous step (rough terrain approximation) and original points. The dashed lines delimit a buffer zone around the DTM of the precious step. Points within this buffer are selected.
Fourth image: selected points, averaging surface approximation as thin (red) line, surface (DTM) after robust filtering as thick line. This final surface is the DTM computed from the original ground points.

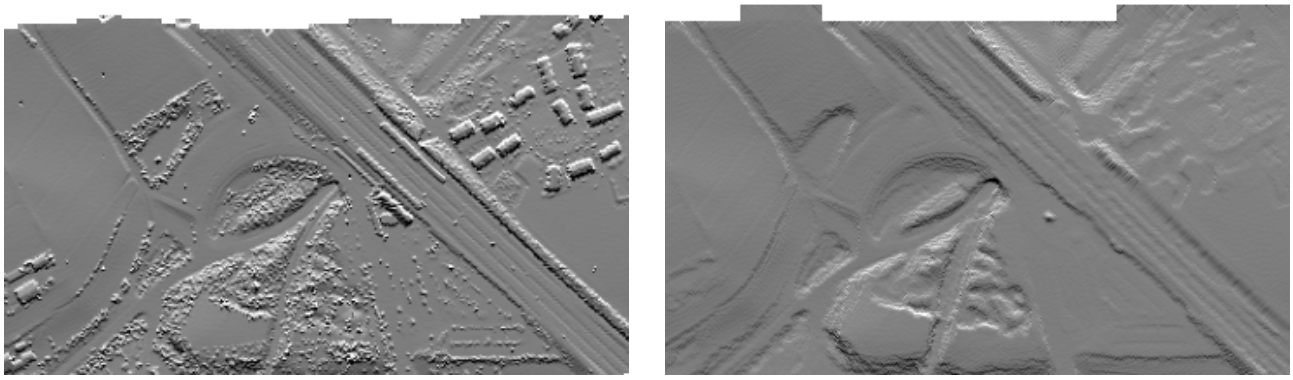

Figure 3: Vaihingen, original (left) vs. filtered data (right) in a shading

function of robust adjustment (used for example in bundle block triangulation) can be adapted to suit the needs for the interpolation and classification of laser scanner data. The function we use is not symmetrical, allowing a sharper decline for values above its origin (residuals belonging to vegetation points), and a slower decline – or no decline at all – for the ground point residuals. Furthermore, the weight function does not need to be centered on the zero-point of the real axis. It can be shifted to the left (into the negative) for the interpolation of laser scanner data. What is more, the shift of the origin can be determined automatically, depending on the given data itself.

For the interpolation (functional model) we use linear prediction which is very similar to kriging [Kraus, 1998]. The covariance function (i.e. the basis function, corresponding to the variogram of kriging) is determined automatically, depending on the data itself. In this method the classification and DTM generation are performed in one step, there is no assumption that the terrain is horizontal. It is applied patch wise to the data, which results in an adaptive setting of the shift of the origin of the weight function. Furthermore, the basis functions are determined for each patch separately, too. The process yields a smooth surface, that means that the accidental (random) measurement errors have also been filtered.

However, the algorithm relies on a 'good mixture' of ground and off–terrain (vegetation) points, which can also be seen as a high frequency of change from ground to vegetation points. This is necessary for a reliable determination of the shift value for the origin of the weight function. If this high frequency is not given, we need to provide the input data (i.e. the points) in a suitable form. This can be achieved by inserting the robust linear prediction in a hierarchic environment.

The approach is comparable to a hierarchical setup using image pyramids, in our case data pyramids. The structure of these pyramids is regular (as in image processing) and typically two or three levels are sufficient. However, in comparison to image analysis, the reduction function operates on point data, not on pixels. (If the laser scanner data is provided as a digital geo-coded image where the grey values represent the terrain heights, the pyramids would indeed be image pyramids.) The method proceeds as follows (see fig. 2):

1. Create the data sets with the lower resolutions,
2. filter the data with robust linear prediction and generate a DTM,
3. compare the DTM to the data of higher resolution and take points within a certain interval.

This process is repeated for each level. The *surface of a level with lower resolution* is used for a computation of the next surface with the *points of a higher resolution*. Of course, this procedure can be applied to any data set of laser scanner data. However, its advantages become more and more important if the data sets become more and more dense. The method speeds up the filter process, enforces the elimination of houses and dense vegetation and makes the process more robust.

Details of the hierarchical approach, the implementation in the SCOP software and the results of some examples are described in [Pfeifer et al., 2001] and [Pfeifer and Briese, 2001]. Fig. 3 is an example of the OEEPE test Vaihingen. On the left we see the surface interpolated using the original data (0.23 points/m^2). On the right is the DTM derived by the hierarchical approach without any manual intervention.

4 DERIVATION OF STRUCTURE LINES

The laser scanner data are a point cloud without structural line information. A qualified terrain model, on the other hand, excels in the inclusion of structure lines, esp. break lines. A terrain model, integrating a close drawn grid (raster data) and structure lines (vector data), is called a hybrid DTM. The raster data as well as the vector data are smoothed, the hybrid DTM shows discontinuities in the first derivation at the break lines (details: [Kraus, 2000]).

4.1 Water Flow Analysis

DTMs which are derived from filtered and interpolated laser scanning data have low geo-morphological quality. In valleys there are many spurious pits. The hydrological and geo-morphological tradition suggests that fluvially dominated

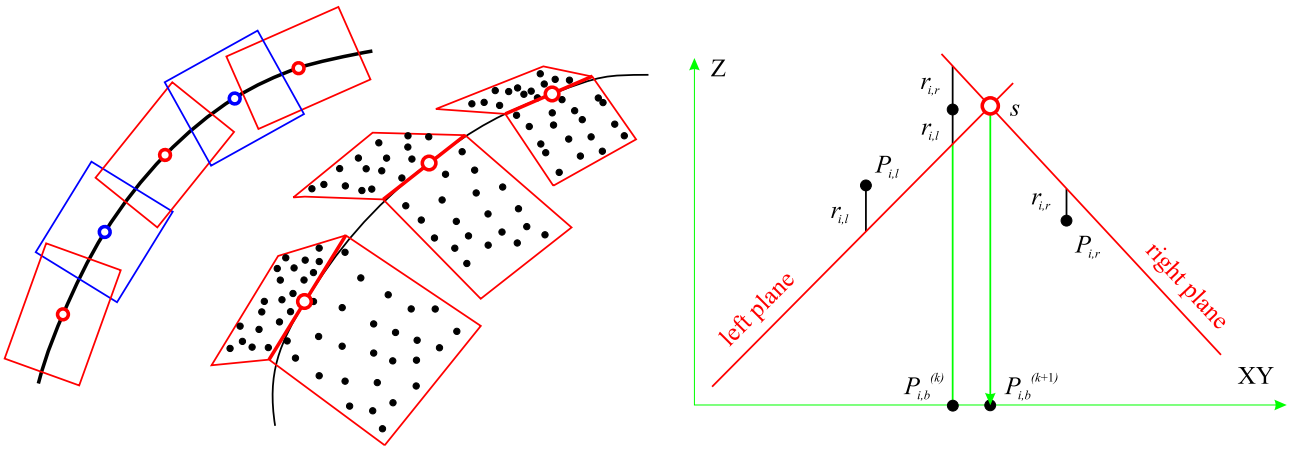

Figure 4: Left and middle: overlapping plane pairs along a break line in a ground plan and axonometric view. Right: one plane pair, the intersection line s appears as a point in this view.

landscapes rarely contain pits since the process of water transport and erosion precludes their development. Thus, the spurious pits in the DTMs must be removed. One standard method of identifying morphometric features is to apply a water flow analysis on the DTM [Rieger, 1992]. As a result of such a procedure 3D structure lines – i.e. river lines, which show the highest amount of water transport within a catchment area – are obtained. These lines are included in the following interpolation process as break lines. The new DTM has no (artificial) pits anymore. Details on this method and its performance for laser scanner data can be found in [Gaisky, 2000].

4.2 Derivation of Break Lines

In the course of a diploma thesis – carried out by Mr. A. Brzank from Dresden University of Technology at out institute – a new method for the derivation of break lines emerged. This method requires that the run of the break line is known approximately in the ground plan. For this task, the planimetric derivation of break lines, different solutions exist (e.g. [Rieger et al., 1999] and [Brügelmann, 2000]), which use digital image processing tools.

The principle is sketched in fig. 4 (left part). The approximation of the break line provides a classification (separation) of the laser scanner points in 'left' and 'right' (subscripts $_l$ and $_r$). Furthermore, the points are grouped into overlapping patches along the break line. In each patch a so-called 'plane pair' is determined. It consists of two planes which intersect in the line s. The two planes of one pair are determined simultaneously with the following equations for a least squares adjustment (right part of fig. 4).

The equations for the adjustment are (r are the residuals):

3D points $P_{i,l}$, left side:	$r_{i,l}$	=	$+\underline{a_l}X_{i,l}$	$+\underline{b_l}Y_{i,l}$	$+\underline{c_l}$						$-Z_{i,l}$
3D points $P_{i,r}$, right side:	$r_{i,r}$	=					$+\underline{a_r}X_{i,r}$	$+\underline{b_r}Y_{i,r}$	$+\underline{c_r}$		$-Z_{i,l}$
2D points $P_{i,b}$, prel. break line:	$r_{i,l}$	=	$+\underline{a_l}X_{i,b}$	$+\underline{b_l}Y_{i,b}$	$+\underline{c_l}$	$-\underline{Z_i}$					
	$r_{i,r}$	=				$-\underline{Z_i}$	$+\underline{a_r}X_{i,b}$	$+\underline{b_r}Y_{i,b}$	$+\underline{c_r}$		

Each 3D-point contributes with one equation to the least squares adjustment, each 2d-point (the ones on the preliminary break line) with two equations. The unknowns, underlined in the equations, are

- the six parameters of the two planes,
- the heights $\underline{Z_i}$ of the break lines points. (These unknowns can be eliminated easily from the equation system, which allows a faster computation. However, a different weighting of these two equations would not be possible anymore.)

Minimising the residuals r results in a plane pair, which approximates the given 3D-points $P_{i,l}$ and $P_{i,r}$ as good as possible on one hand, and on the other hand has an intersection line s which keeps close to the points $P_{i,b}$ of the preliminary break line in the ground plane. The intersection line s found in such an adjustment is used for the second adjustment as an improved approximation for the break line in the ground plan. Potentially this leads to a new classification in left and right points. After the second adjustment a third one might follow. The result of this iteration process is an intersection line s in 3-space. At this intersection line a 3D-point is computed in the middle of the patch.

The 3D-points and the intersection lines of all patches describe the 3D-break line as spline function. The points are the vertices and the lines are the tangents in these points. Break lines found in this manner can be regarded subsequently in the derivation of the hybrid DTM.

Fig. 5 shows an example. In the upper part the shaded DTM without special treatment of the terrain data is shown, in the lower part, the terrain under special consideration of the break lines is presented. The success can be assessed better

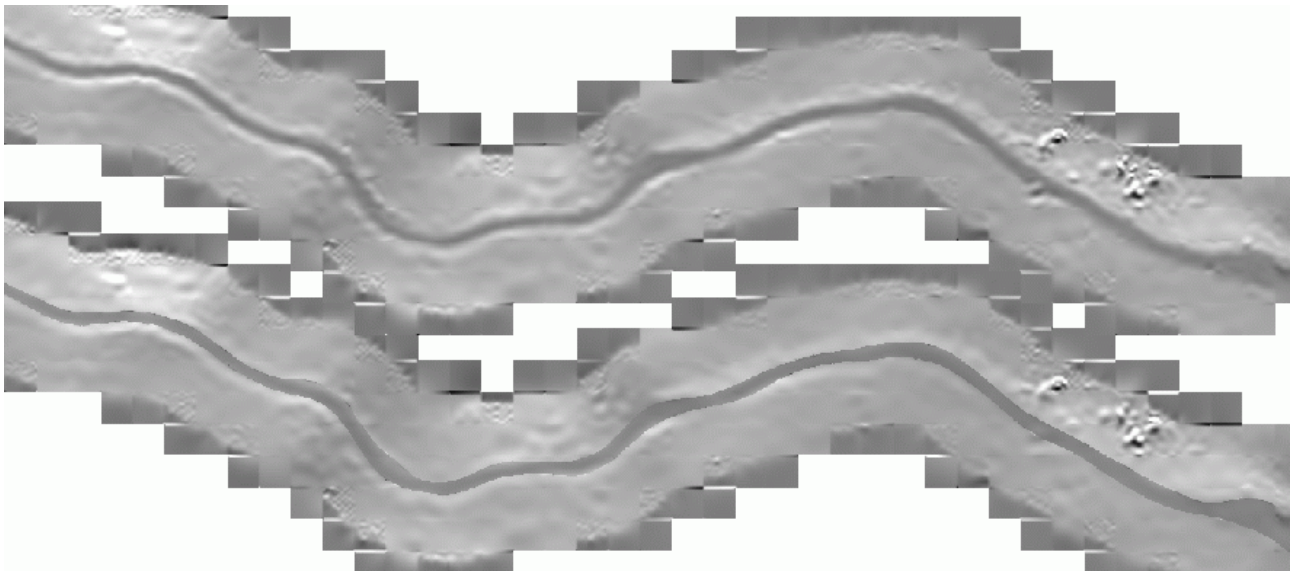

Figure 5: Shading of the DTM without break line (upper part) and with the break line (lower part)

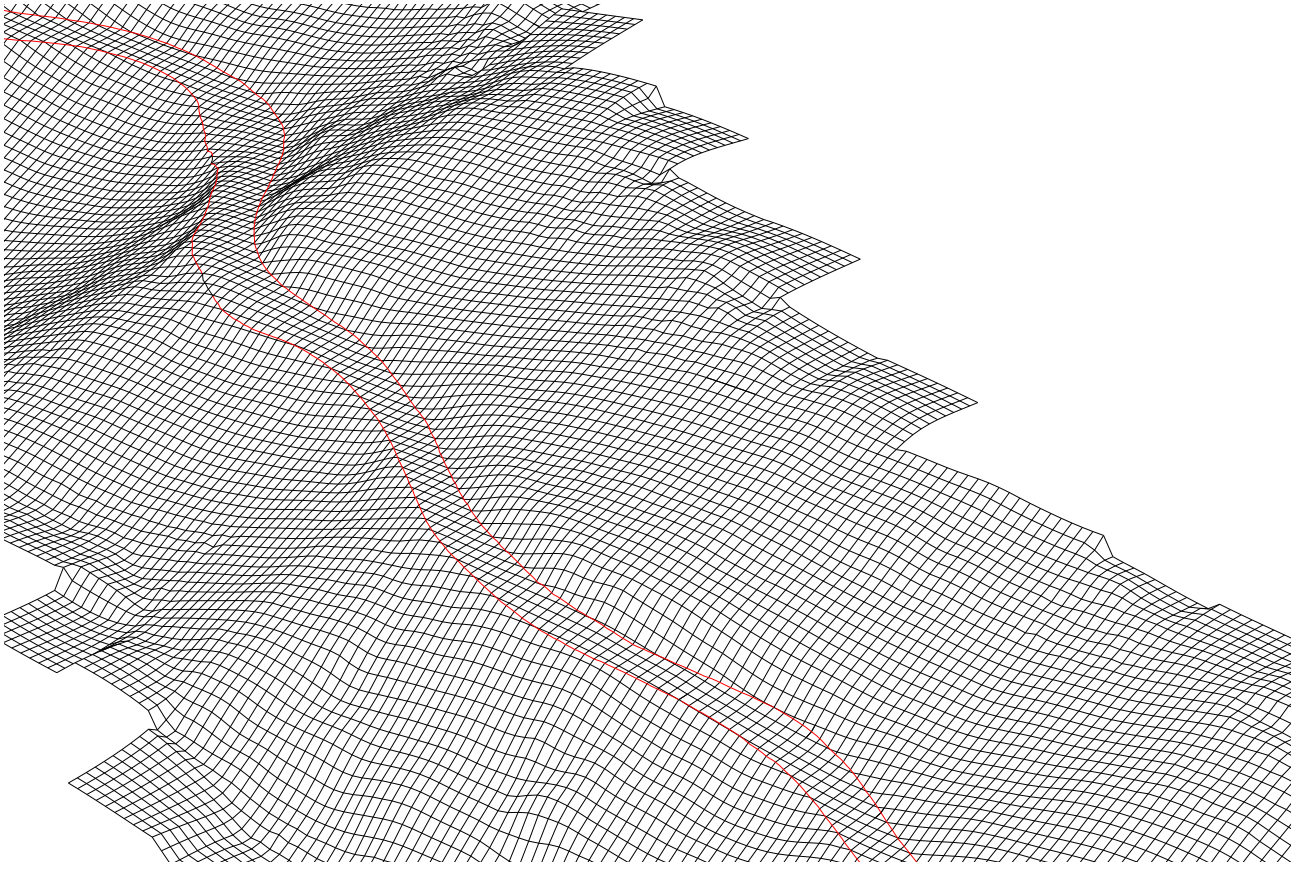

Figure 6: Perspective view of the DTM with automatically measured break lines

by looking at a perspective view of the terrain with the break lines. In fig. 6, which is a view from north west on the DTM of fig. 5, the discontinuities of the first derivatives in the hybrid model stands out clearly.

Empirical investigations on the accuracy improvement are currently running. The gain in absolute accuracy is less important than the strongly improved geo-morphological quality, which can be achieved by this method.

Concluding this section, two extensions should be noted: First, instead of planes polynomials of higher degree could be used, especially in areas with higher curvature. Second, not only plane pairs, but also triples or n-tuples of planes can be determined with this method simultaneously. For example, for a dike and its crest the usage of 3 planes (one horizontal

and two sloped) stands to reason. Another setup with three (or even more) planes can be found at the intersection of break lines (network of break lines).

5 CONCLUSION

The geometric component of airborne laser scanning has stimulated many research groups to solve problems which have been restricted to photogrammetry so far. In this article methods have been presented, which have been developed at the Institute of Photogrammetry and Remote Sensing of the Vienna University of Technology.

Three domains of LIDAR data processing have been touched in this article. The first one, the *elimination of systematic errors* originating from the measurement system, can be extended in many ways. So far, the algorithm is confined to height correction, but planimetric correction could be performed, too. The algorithms of the second domain, the *filtering and classification* of LIDAR data have been applied in many projects at our institute and have proven to be efficient and reliable tools. The last area mentioned, the *derivation of structural line information*, will play an important role in our research to come.

Other groups around the world have solved similar tasks, but different problems (e.g. automatic building modelling) have been approached as well. With (airborne) laser scanning photogrammetry has been provided a new tool. The advancements in the instruments (registration of first and last pulse and of the intensities, increased flying height, ...) as well as the methodical developments supplement each other very well and envisage a promising future.

Acknowledgements

This research has been supported by the Austrian Science Foundation (FWF) under Project No. P14083–MAT. Additionally, we are deeply grateful to Mr. Ch. Briese for his contribution to this article.

References

[Brügelmann, 2000] Brügelmann, R. (2000). Automatic breakline detection from airborne laser range data. In *International Archives of Photogrammetry and Remote Sensing, Vol. XXXIII, Part B3*, pages 109–115, Amsterdam, Netherlands.

[Gaisky, 2000] Gaisky, D. (2000). Goemorphologic improvement of DTMs especially as derived from laser scanner data. In *International Archives of Photogrammetry and Remote Sensing, Vol. XXXII/6W8*, pages 70–75, Ljubljana, Slovenia.

[Kager and Kraus, 2001] Kager, H. and Kraus, K. (2001). Height discrepancies between overlapping laser scanner strips – simultaneous fitting of aerial laser scanner strips. In *Fifth Conference on Optical 3-D Measurement Techniques*, Vienna, Austria.

[Kraus, 1998] Kraus, K. (1998). Interpolation nach kleinsten Quadraten versus Krige-Schätzer. *Österreichische Zeitschrift für Vermessung & Geoinformation*, 1.

[Kraus, 2000] Kraus, K. (2000). *Photogrammetrie, Band 3, Topographische Informationssysteme*. Dümmler. An english edition by Taylor and Francis (translator: H. Rüther) is in preparation.

[Kraus and Pfeifer, 1998] Kraus, K. and Pfeifer, N. (1998). Determination of terrain models in wooded areas with airborne laser scanner data. *ISPRS Journal of Photogrammetry and Remote Sensing*, 53:193–203.

[Pfeifer and Briese, 2001] Pfeifer, N. and Briese, C. (2001). Airborne laser scanning and derivation of digital terrain models. In *Fifth Conference on Optical 3-D Measurement Techniques*, Vienna, Austria.

[Pfeifer et al., 2001] Pfeifer, N., Stadler, P., and Briese, C. (2001). Derivation of digital terrain models in the SCOP++ environment. In *Proceedings of OEEPE Workshop on Airborne Laserscanning and Interferometric SAR for Detailed Digital Terrain Models*, Stockholm, Sweden.

[Rieger, 1992] Rieger, W. (1992). Automated river line and catchment area extraction from dem data. In *International Archives of Photogrammetry and Remote Sensing, Vol. XXIX/B4*, pages 642–649, Washington, DC.

[Rieger et al., 1999] Rieger, W., Kerschner, M., Reiter, T., and Rottensteiner, F. (1999). Roads and buildings from laser scanner data within a forest enterprise. In *International Archives of Photogrammetry and Remote Sensing, Vol. XXXII, Part 3-W14*, pages 185 –191, LaJolla, CA, USA.

CREATION OF HIGH RESOLUTION, PRECISE DIGITAL ELEVATION MODELS OF OCEAN CITY AND ASSATEAGUE ISLAND, MD

Bea Csathó[1], Young-Ran Lee[2], Tony Schenk[2], William Krabill[3], and Jan McGarry[4]

[1] Byrd Polar Research Center
[2] Department of Civil and Environmental Engineering
The Ohio State University, Columbus, OH 43210
[3] Laboratory of Hydrospheric Processes, NASA GSFC
Wallops Flight Facility, Building N-159, Wallops Island, VA 23337
[4] Code 920.3, NASA GSFC, Greenbelt, MD 20771

KEY WORDS: DEM generation, outlier detection, validation site

ABSTRACT

Researchers of NASA's GSFC are currently developing a scanning airborne photon-counting laser altimeter. This paper summarizes the creation of high resolution, precise DEMs from repeat passes of airborne laser scanning surveys to validate this new system. To study coastal erosion several sections of the Atlantic and Pacific coast have been mapped by NASA's Airborne Topographic Mapper (ATM) conical scanning altimeter. We selected two 5 km long and about 1 km wide stretches of the coast in Maryland to create precise Digital Elevation Models. One site is urban area (southern Ocean City) and the other is characterized by coastal marshes and beaches (northern Assateague Island). To obtain a dense data set, we combine laser altimetry data from 21 swaths acquired in 4 different missions. Laser points over planar surfaces, such as flat roofs and parking lots were analyzed to check the the repeatibility of the measurements. The absolute accuracy of the laser scanning was assessed by comparing surfaces extracted from the laser point cloud with GPS and photogrammetry results. These studies confirm the 0.1-0.2 m vertical and submeter horizontal accuracy of the ATM system. At the heart of the interpolation procedure is a bilinear interpolation that determines the surface elevation at the grid posts from planes fitted through the points located within 2 m by 2 m grid cells. Outlier observations are detected by using a robust estimator. The residual of the plane fitting and the uniformity of the distribution of the observations within the grid cells are used to assess the accuracy of the DEM. These parameters suggest an accuracy of 0.3 m or better for 90.4 % of the DEM points on the urban area, and 48.5 % of the points have an accuracy of 0.1 m or better. Similar accuracy is achieved on the site covered by natural vegetation on Assateague Island.

1 Introduction

NASA GSFC is currently developing a photon-counting laser scanning system, capable of daylight operations from altitudes of 6-12 km ([Degnan01]). The nominal footprint size of the system is 0.5-1 meter. This report summarizes the creation of a DEM from airborne laser scanning data over the Ocean City-Assateague area to validate this new system. The area is well suited for laser altimetry calibration purposes, because of its proximity to NASA Wallops Flight Facility and the repeat laser altimetry coverage during 1996-1999.

2 Study Site and Data Acquisition

To study coastal erosion several sections of the Atlantic and Pacific coast have been mapped by NASA's Airborne Topographic Mapper (ATM) laser system ([Sallenger99] and [Krabill99]). The ATM conical laser scanning system was developed by NASA's Arctic Mapping group from the Goddard Space Flight Center's Wallops Flight Facility to measure surface elevation changes of the Greenland ice sheet as part of NASA's Global Climate Change program ([Krabill95], [Krabill00]).

The main sensor of the ATM-II system is a Spectra Physics TFR (Tightly Folded Resonator) laser transmitter that provides a 7 nsec wide, 250 mJ pulse at frequency-doubled wavelength of 523 nm in the blue-green spectral region. The laser beam of the ATM is reflected toward the surface by a nutating mirror that has adjustable off-nadir settings of 5, 10 and 15 degrees. The scan mirror is spun at 10 or 20 Hz, producing a series of overlapping spirals of data points as the aircraft moves forward. For the missions used in this study the pulse rate was selected to 3,000 or 5,000 Hz. The nominal operating altitude of 600 m lead to an illuminated footprint size of approximately 1.5 m on the ground. The laser altimeter suite, which also includes geodetic GPS receivers and an INS unit is mounted on NASA's P-3 aircraft. A vertical accuracy of better than 10 cm has been achieved by the ATM system on polar ice sheets and coastal beaches (for example [Krabill00], [Krabill99]) and preliminary studies indicated submeter horizontal accuracy ([Schenk99]).

To create precise Digital Elevation Models for the Microlaser altimeter calibration we selected two 5 km long and about 1 km wide stretches of the coast in Maryland (Figure 1). The northern site covers part of Ocean City. Ocean City occupies a a barrier island with high-rise buildings on the east and residential areas on the west side. Along the east coast are a number of sandy beaches while harbors and docks are found on the west coast (Figure 3.d). Our southern test site comprises the coastal marshes and beaches of Assateague National Seashore Beach on northern Assateague Island.

The most important technical parameters of the 21 laser altimeter survey flights used in this study are summarized in Table 1. These surveys were primarily flown as functionality checks prior to conducting polar or beach mapping missions. Interested researchers can obtain the data acquired on April 25 and 30, 1997, through ISPRS WG III/6. Since large scale

aerial photography and multispectral data was also collected at the same time, the combined data set is frequently used for accuracy and data fusion studies (for example [Schenk99], [Csatho99], [McIntosh99]).

3 Accuracy of laser scanning data

The accuracy of the ATM system has been rigorously evaluated by comparison with surface elevations obtained by ground GPS surveys and photogrammetry ([Csatho98], [Schenk99]). These studies confirmed the 0.1-0.2 m vertical and submeter horizontal accuracy of the ATM system ([Krabill00]).

Prior to the DEM generation we examined the data sets for unremoved bias between the different laser surveys. First planar, horizontal surfaces, such as parking lots and flat roofs were identified on the aerial photographs. Then the parameters of the planar surface patches were estimated from each laser survey. The excellent agreement between the plane parameters suggests that there is no bias between the different surveys. A random elevation error of 8 cm (RMS) is indicated by the residuals of the plane fitting.

4 Generation of Digital Elevation Models

The DEMs cover the southern 5 km of Ocean City and the northern 5 km of the Assateague Island (Figure 1). Each area contains more than 2 million irregularly distributed points with an average point density of 1.5 points/m^2.

At the heart of the interpolation procedure is a bilinear interpolation that determines the surface elevation at the grid posts from planes fitted through all points within the 2 m by 2 m grid cells. Outlier observations are detected by using a robust estimator, the Least Median of Squares (LmedS) technique ([Köster00]). This approach provides a robust model estimate in data sets with up to 50 percent of the data heavily corrupted by outliers and it also performs well for small data sets. The residual of the plane fitting and the uniformity of the distribution of the observations within the grid cells are used to assess the accuracy of the DEM. Nearest neighbor interpolation is used if the number of observations is not sufficient for plane fitting or if their distribution is not isotropic enough.

Each grid post is classified into one of the following categories:

- PLANE IN 10 (label:0)
  Elevation is interpolated by fitting planes through points that are distributed in at least 3 quadrants. All residuals are less than 10 cm.
- PLANE IN 30 (label:1)
  Elevation is computed by plane fitting interpolation. Points are distributed in at least 3 quadrants. All residuals are between 10 and 30 cm.
- PLANE B IN 10 (label:2)
  Elevation is computed by plane fitting interpolation. Points are distributed in at least 3 quadrants. Blunders are detected and removed by using LmedS before plane fitting. All residuals (except blunders) are less than 10 cm.
- PLANE B IN 30 (label:3)
  Elevation is computed by plane fitting interpolation. Points are distributed in at least 3 quadrants. Blunders are detected and removed by using LmedS before plane fitting. All residuals (except blunders) are between 10 and 30 cm.
- PLANE TH (label:4)
  Elevation is computed by plane fitting. Points are distributed in at least 3 quadrants. There is at least onw observation with a residual larger then 30 cm.
- NN IN (label:5)
  Elevation is computed by using nearest neighbor interpolation. There are not enough observations for plane fitting (less than 6 points) or the distribution of points is not sufficient (points in one or two quadrants only). The distance between the grid post and its nearest neighboring point is smaller than $1/3$ cell size (0.6 m).
- NN DIST (label:6)
  Elevation is computed by using nearest neighbor interpolation. There are not enough observations for plane fitting (less than 6 points) or the distribution of points is not sufficient (points in one or two quadrants only). The distance between the grid post and its nearest neighbor is larger than $1/3$ cell size.
- NA (label:7)
  No elevation is computed. There are no points within the DEM cell.
- NN OUTRANGE (label:8)
  Elevation is computed by using nearest neighbor interpolation. Although the number of points and their distributions sufficient, the z value estimated by fitting a plane is larger than the predefined elevation range of [-50m, 50m]. These points are usually on object boundaries.

Figure 2.a-b depicts the Ocean City DEM as color-coded imagery and an aerial photograph of the southern part of the DEM is shown in Figure 3.d.

5 Evaluation of the DEMs

From the residuals of the plane fitting and the distribution of the laser points within the grid cells we infer an accuracy of 0.3 m or better for 90.4 $\%$ of the DEM points on the urban area, and 48.5 $\%$ of the points have an accuracy of 0.1 m or better. Similar accuracy is achieved on the site covered by natural vegetation on Assateague Island. Points in categories 4-8 have larger errors. For the sake of completeness these points are included in the original DEM (Figure 2.b), but a DEM including only the precise grid points is also created (Figure 2.a). This filtered DEM, which does not include the DEM points classified in categories 4-8, is used for most of the subsequent analysis, for example to compile the profiles in Figure 3.a-c.

Surface elevation profiles along extended, planar surface patches, such as roads indicate a random error of 0.03-0.04 m RMS for the DEM (Figure 3.a-b). Error propagation also confirms this accuracy:

$$\sigma_{\mathrm{DEM}} = \frac{\sigma_L}{\sqrt{n}} = \frac{0.08\,\mathrm{m}}{\sqrt{6}} = 0.033\,\mathrm{m} \qquad (1)$$

where σ_L is the vertical error of the individual laser points and n is the number of laser points per grid cell.

The elevation profiles extracted from the DEM reveal many interesting details. Notice for example the small (0.2 m deep)

depressions at several road crossings (numbered locations in Figure 3.a and 3.d). Roofs and outline of large buildings are depicted very accurately (Figure 3.c and 3.d). Building that are too small compared to the grid size are often distorted or neighboring buildings are merged.

The ATM data set has been acquired in the course of several years. Therefore errors can occur in the DEM on areas with significant surface elevation changes. Elevation changes effecting the DEM include surface erosion on the beach exceeding 0.5 m/year in several places, and new or demolished buildings. For example see the large tents set up for a fair on the southern tip of the island in April 1997 (Figure 3.d), which were not there during the subsequent flights. Comparison of the original and the filtered DEMs shows that large fitting errors occurs in this area (Figure 2.a-b).

6 Conclusion and future work

To validate NASA's microlaser altimeter we have compiled two DEMs covering a total of 7 km^2 on Ocean City and Assateague island. The interpolation is based on plane fitting in local neighborhood. Outlier observations are eliminated by a robust estimator evaluating the same local area. The accuracy of the elevations at the grid posts is derived by the goodness of the planar fit and the distribution of the laser data around the grid post. The resulted DEM is very suitable for calibrating the new laser system, since the estimated vertical accuracy is 0.3 m or better for 90.4 $\%$ of the DEM points on the urban area, and 48.5 $\%$ of the points have an accuracy of 0.1 m or better. This study is also very useful for research aiming at the automation of DEM generation from laser points in urban areas. The proposed procedure has several advantages. For example no domain knowledge is needed, and no manual thinning or editing is performed. Very accurate DEMs (absolute accuracy of 0.05 m or better) have several applications, for example precise mapping of drainage systems, neotectonic features, or road networks.

The main use of this DEM for the microlaser altimeter validation is to assess the accuracy of the the surface elevation. The combined laser and photogrammetry data set would also allow us to analyze the time-of-flight distribution of the photons measured by the microlaser altimeter. For example the microlaser altimeter footprints can be backprojected to the aerial images to determine the type of objects illuminated and their detailed structure ([Schenk01]). This will also allow to view the laser points stereoscopically for more detailed analysis.

7 Acknowledgements

The authors thank Serdar Manizade of EG $\&G$, Impyeong Lee and Samuel Megenta of Department of Civil Engineering, The Ohio State University, for assistance in data processing and analyzis. The research was sponsored by NASA, GSFC (Code 920.3) under grant S-42971-G to the first author. This contribution is 1235 of the Byrd Polar Research Center.

REFERENCES

[Csatho98] Csathó, B., W. Krabill, J. Lucas and T. Schenk, 1998.A multisensor data set of an urban and coastal scene. *International Archives of Photogrammetry and Remote Sensing*, **32**(3/2), 588-592.

[Csatho99] Csathó, B. M., T. Schenk, D.-C. Lee and S. Filin, 1999. Inclusion of multispectral data into object recognition. *International Archives of Photogrammetry and Remote Sensing*, **32**(7-4-3 W6), 53-61.

[Degnan01] Degnan, J., and 8 others. Design and performance of an airborne multikilohertz photon-counting microlaser altimeter. In this proceedings.

[Köster00] Köster, K., and M. Spann, 2000. Mir: an approach to robust clustering-application to range image segmentation. *IEEE Transactions on Pattern Analysis and Machine Intelligence*, **22**(5), 430-444.

[Krabill95] Krabill, W., R. Thomas, C. Martin, R. Swift and E. Frederick, 1995. Accuracy of airborne laser altimetry over the Greenland ice sheet. *Int. J. Remote Sensing*, **16**(7), 1211-1222.

[Krabill99] Krabill, W. and 10 others, 1999. Airborne Laser Mapping of Assateague National Seashore Beach. *Photogrammetric Engineering and Remote Sensing*, **66**(1)

[Krabill00] Krabill, W. and 9 others, 2000. Greenland ice sheet: high-elevation balance and peripherial thinning. *Science*, **289**, 428-430.

[McIntosh99] McIntosh, K., A. Krupnik, and T. Schenk, 1999. Utilizing airborne laser altimetry for the improvement of automatically generated DEMs over urban areas. *International Archives of Photogrammetry and Remote Sensing*, **32**(3-W14), 89-94.

[Sallenger99] Sallenger, A. H., et al., 1999. Airborne laser study quantifies El Nino-induced coastal changes. *EOS*, **80**(8), 89, 92-93.

[Schenk99] Schenk, T., B. Csatho and D. C. Lee, 1999. Quality control issues of airborne laser ranging data and accuracy study in an urban area. *International Archives of Photogrammetry and Remote Sensing*, **32**(3/W14), 101-108.

[Schenk01] Schenk, T., S. Suyoung, and B. Csathó, 2001. Accuracy study of airborne laser scanning data with photogrammetry. In this proceedings.

Figure 1. Location od DEMs: Ocean City S (dashed box) and Assateague Island N (solid box)

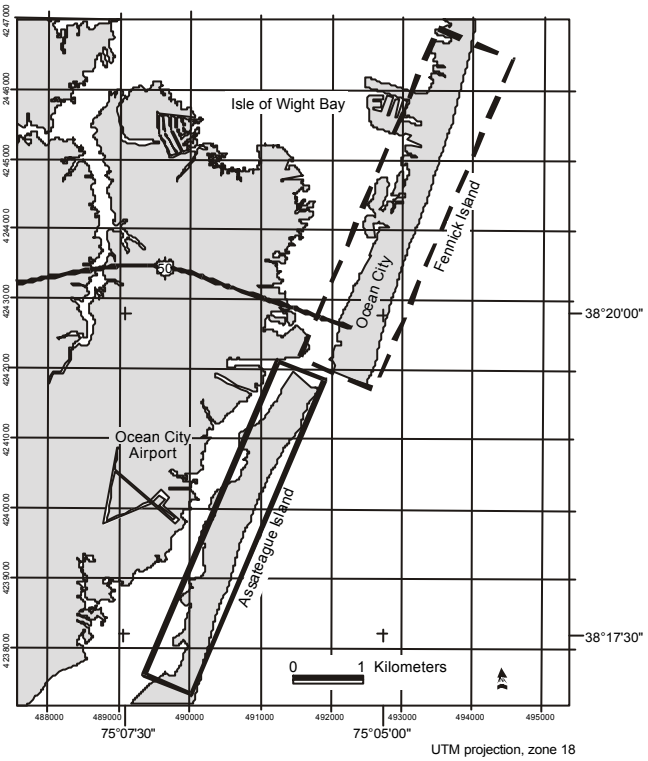

Figure 2.a Southern part of Ocean City S DEM. Grid cells with large error or uncertainty are masked (categories 4-8, black)

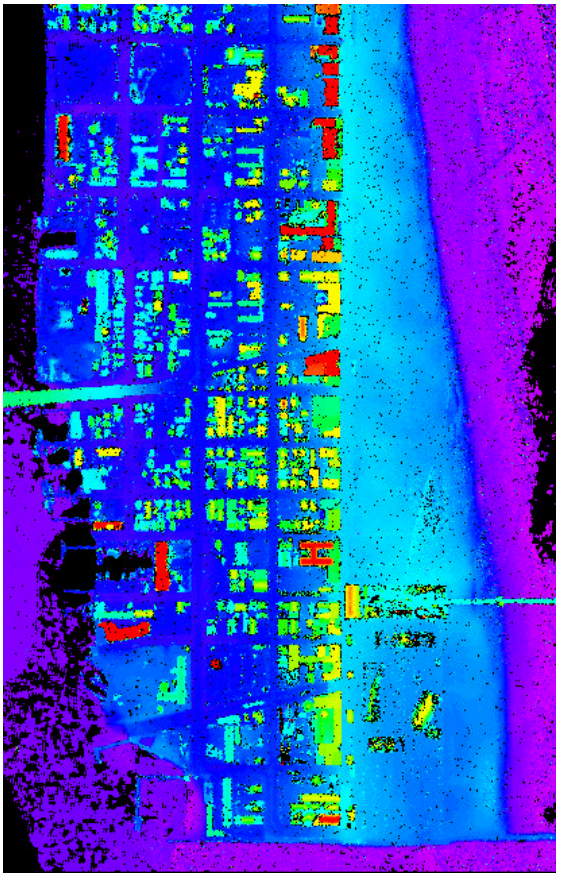

Figure 2.b Ocean City S DEM
Low elevations: blue
High elevations: red

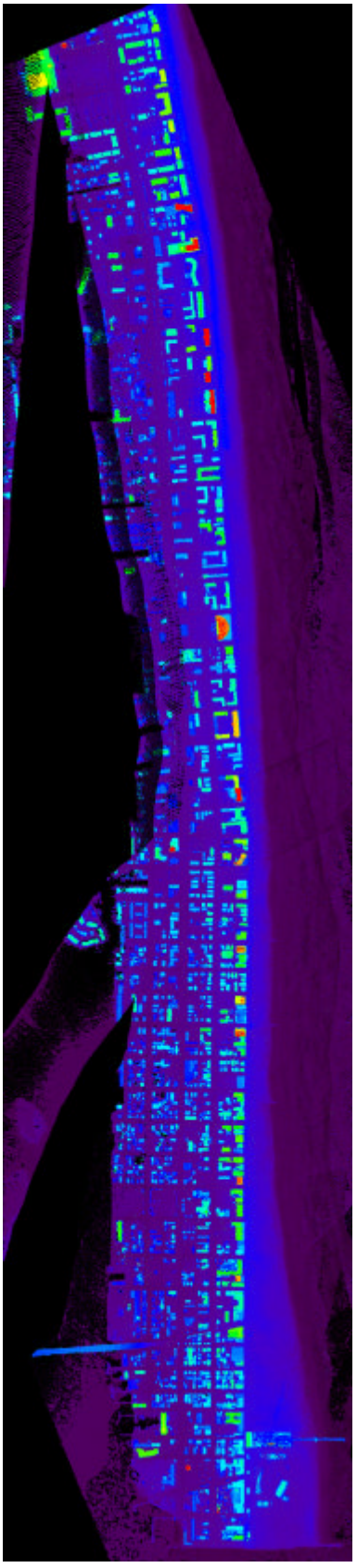

Table 1. Airborne Topographic Mapper surveys used for creating the DEMs

Date	Sensor	Frequency [Hz]	Scan frequency [Hz]	Distance		Swath width [m]	Number of missions	Density [points/m^2]
				along track [m]	across track [m]			
4/25/97	ATM-1	3000	20	5	5	300	4	0.15
4/25/97	ATM-II	3000	10	2	10	210	3	0.23
4/30/97	ATM-I	3000	20	5	5	300	2	0.15
4/30/97	ATM-II	3000	10	2	10	210	2	0.23
9/15/97	ATM-II	5000	20	4	3	310	2	0.18
10/01/99	ATM-II	5000	20	4	3	310	8	0.18

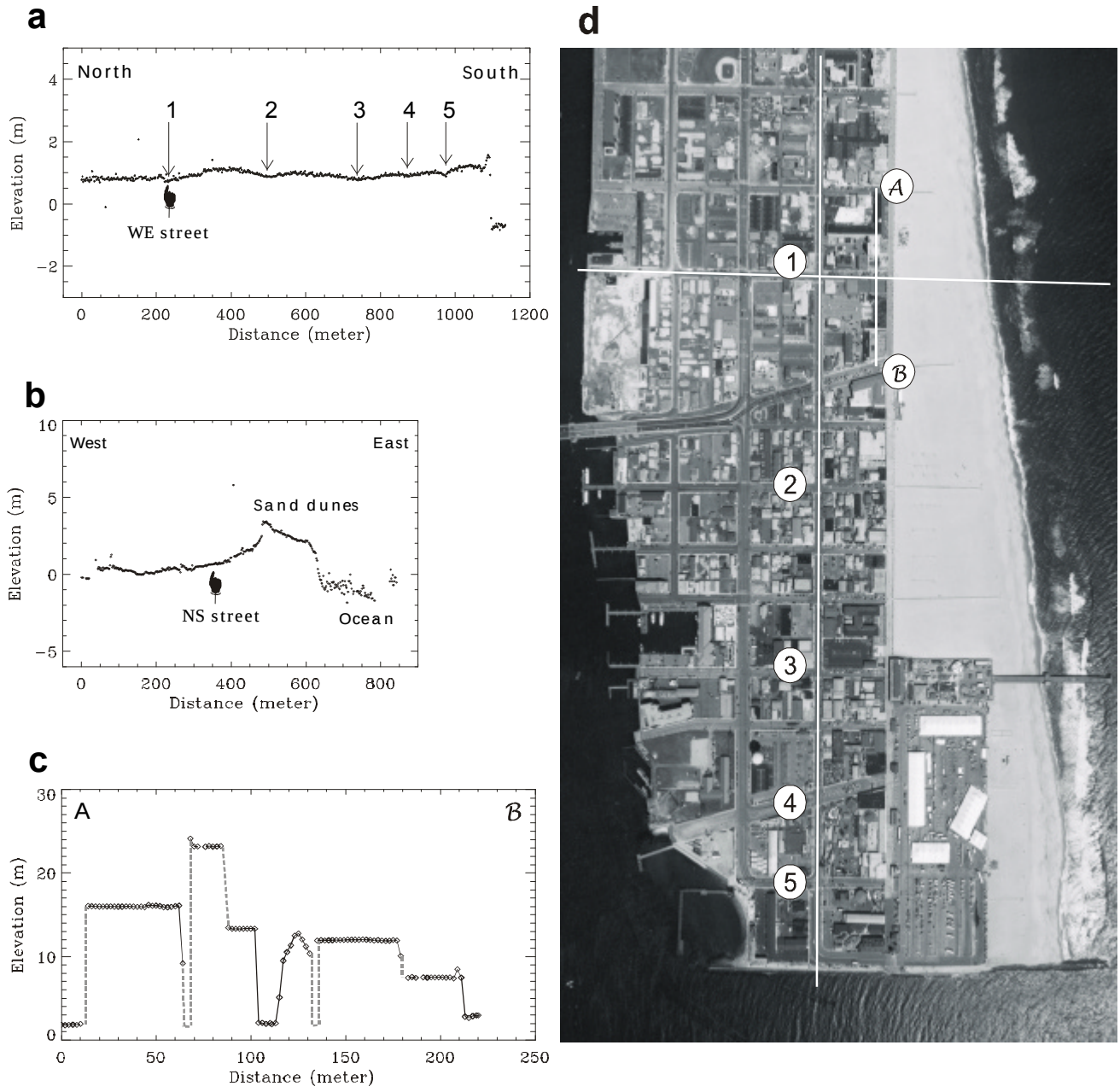

Figure 3. a-b Surface elevation profiles from DEM along streets, **3.c** Surface elevation profiles from DEM across high-rise buildings, **3.d** Aerial photograph of southern part of Ocean City. White lines show location of profiles in Figure 2.a-c.

3D BUILDING MODEL RECONSTRUCTION FROM POINT CLOUDS AND GROUND PLANS

George Vosselman and Sander Dijkman
Department of Geodesy
Delft University of Technology
The Netherlands
g.vosselman@geo.tudelft.nl

KEY WORDS: Building reconstruction, laser altimetry, Hough transform.

ABSTRACT

Airborne laser altimetry has become a very popular technique for the acquisition of digital elevation models. The high point density that can be achieved with this technique enables applications of laser data for many other purposes. This paper deals with the construction of 3D models of the urban environment. A three-dimensional version of the well-known Hough transform is used for the extraction of planar faces from the irregularly distributed point clouds. To support the 3D reconstruction usage is made of available ground plans of the buildings. Two different strategies are explored to reconstruct building models from the detected planar faces and segmented ground plans. Whereas the first strategy tries to detect intersection lines and height jump edges, the second one assumes that all detected planar faces should model some part of the building. Experiments show that the second strategy is able to reconstruct more buildings and more details of this buildings, but that it sometimes leads to additional parts of the model that do not exist. When restricted to buildings with rectangular segments of the ground plan, the second strategy was able to reconstruct 83 buildings out of a dataset with 94 buildings.

1 INTRODUCTION

3D city models become increasingly popular among urban planners and the telecommunication industry. Analysis of propagation of noise and air pollution through cities and estimation of real estate taxes are some other potential applications of 3D city models.

Currently 3D city models are produced by conventional aerial photogrammetry or by semi-automated procedures for measurements in aerial imagery. The high point densities of airborne laser scanners triggered research into the automated reconstruction of 3D building models. This paper reports on our progress in this area.

With the increasing point densities that can be achieved by modern laser scanners, the detection of planar roof faces in the generated point clouds has become easier. Many laser scanners mounted in aeroplanes can nowadays achieve point densities of up to one point per square meter. Surveys with systems mounted in helicopters have been conducted with point densities of five to ten points per square meter [Baltsavias, 1999]. These high point densities usually result in a large number of points on a single roof face. By analysis of the point clouds these roof faces can be detected automatically. Due to the overwhelming evidence provided by the large number of points, the detection of planar roof faces is quite reliable. For the detection of planar point clouds we extended the well-known Hough transform to a three dimensional transformation [Vosselman, 1999].

While the orientation and height of a roof face can be estimated accurately, the outline of a roof face is more difficult to determine. To improve this part of the 3D building model reconstruction we make use of building ground plans that are available for many cities. The outlines of the buildings as given in such ground plans give the precise locations of the building walls. By intersecting the walls with the detected roof planes, some of the bounds of the roof faces can be reconstructed. Other bounds are to be found by the intersection of pairs of adjacent roof faces and by the detection of height jump edges in the point clouds.

The ground plans not only support the accurate location of the outer roof face edges. Often a ground plan reveals information on the structure of a building [Haala and Anders, 1997, Haala and Brenner, 1997]. When modelling buildings by constructive solid geometry, buildings can be regarded as compositions of a few components with simple roof shapes (like flat roofs, gable roofs and hip roofs). The corners in the building outlines of the ground plans often give an indication on the position of these building components within the ground plan. Thus, the ground plan is also useful for the accurate location of some of the roof face edges in the interior of the building.

The paper presents results on the extraction of the roof faces and the generation of 3D building models by combining the extracted roof faces with the ground plans. Section two describes the extraction of the planar faces from the laser data and the usage of the ground plans for this purpose. In the next two sections two different strategies for the reconstruction of the building model are presented. The first strategy refines an initial ground plan segmentation until every segment corresponds to only one planar face. The second strategy starts with a course 3D model and refines this model based on the analyse of point clouds that do not fit well to the course model. Results and a comparison of the two strategies are presented and discussed in the last section.

2 EXTRACTION OF ROOF PLANES

Several algorithms have been proposed for the segmentation of range data [Hoover et al., 1996, Geibel and Stilla, 2000]. Many of those algorithms require the computation of surface normal vectors. Since these vectors tend to be very noisy in the case of laser datasets with high point densities, we prefer algorithms that do not require normal vectors. One such algorithm is the Hough transform extended to 3D [Vosselman, 1999]. Geibel and Stilla [2000] presented a split and merge algorithms that also shows to be suitable for laser data segmentation.

2.1 3D Hough transform

In the classical Hough transform [Hough, 1962] a given point (x,y) in an image defines a line $y = ax + b$ in the parameter space with axes for the parameters a and b. If an image contains several points on a straight line, the lines of these points in the parameter space will intersect and the position of the intersection yields the parameters of the line in the image.

This principle can easily be extended to three dimensions. Each point (x,y,z) in a laser dataset defines a plane $z = s_x x + s_y y + d$ in the 3D parameter space spanned by the axes of the parameters s_x, s_y, and d, where s_x and s_y are the slopes in x- and y-direction and d denotes the vertical distance of the plane to the origin. If a laser dataset contains points in a planar face, the planes of these points in the parameter space will intersect at the position that corresponds to the slopes and distance of the planar face. For the detection of this intersection point the standard procedure of sampling the parameter space and searching for the bin with the highest number of planes can be used [Ballard and Brown, 1982].

The Hough transform does not check whether the points that are found to be in the same plane indeed make up a continuous face. It may as well find some scattered points that are in one plane by coincidence. To check this, the TIN of all laser points is used. Only those points of the detected plane are used that form a connected piece of the TIN of a minimum size. Points that are now assigned to a planar face are removed from the parameter space before looking for the next best plane.

2.2 Usage of partitioned ground plans

In the case of buildings with many roof faces the Hough transform may find spurious planes. Each bin of the parameter space corresponds to a more or less planar area in the object space. It may happen that some arbitrary planar area contains more points than the areas around one of the roof planes. This is shown in figure 1. In such cases wrong planes are detected.

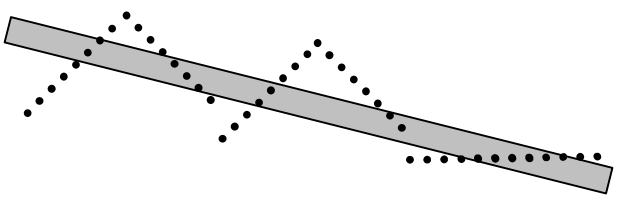

Figure 1: Planar region with most points does not coincide with a roof face.

To prevent this, we split the dataset into smaller parts (figure 2) and apply the Hough transform to the points of each part separately (figure 3). By splitting the dataset the chance that a part will contain many faces is diminished. For a useful segmentation of the dataset we make use of a segmented ground plan of the building. By extending the edges of the building outline at the concave corners a segmentation is obtained (figure 2). This segmentation often has edges that correspond to the location of roof face bounds. Thus these edges are likely to separate the points of different roof faces. This further reduces the likelihood of finding many roof faces within a single segment.

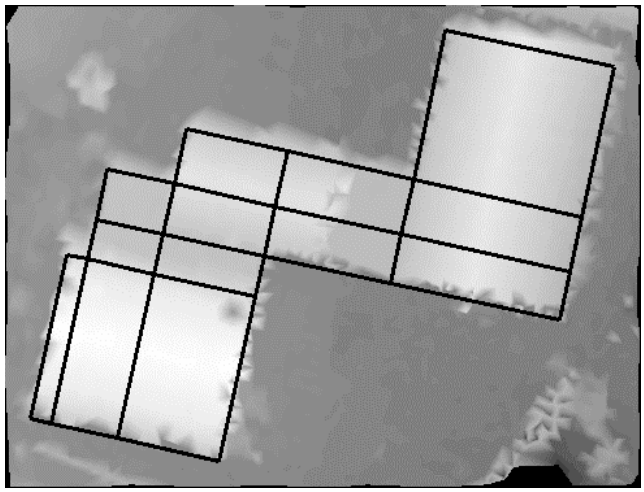

Figure 2: Partitioned building outline as overlay on grey value coded heights.

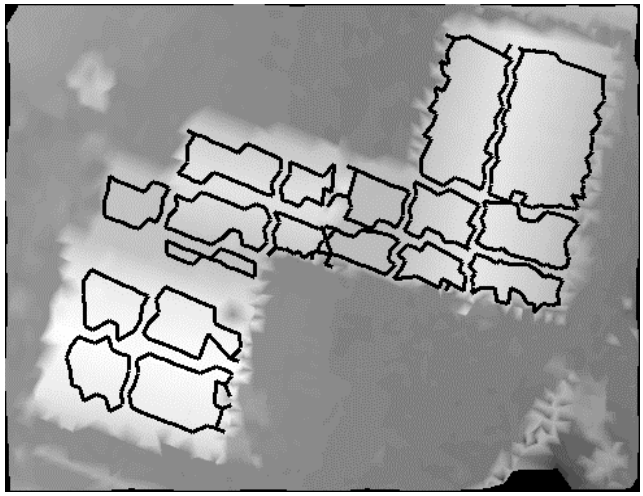

Figure 3: Bounds of planar faces detected by the 3D Hough transform within the partitions.

For many buildings the roof faces are parallel to one of the edges of the segmented ground plan [Haala and Brenner, 1997]. One can make use of this heuristic to reduce the parameter space. After projecting all points inside a segment onto a vertical plane through a segment edge, the Hough transform can again be done in 2D. Figure 4 shows a point cloud of a gable roof building with a dorm that is projected onto two perpendicular vertical planes. After performing the Hough transform on both 2D datasets it will become obvious that the lines found in the first projection correspond to the desired roof faces.

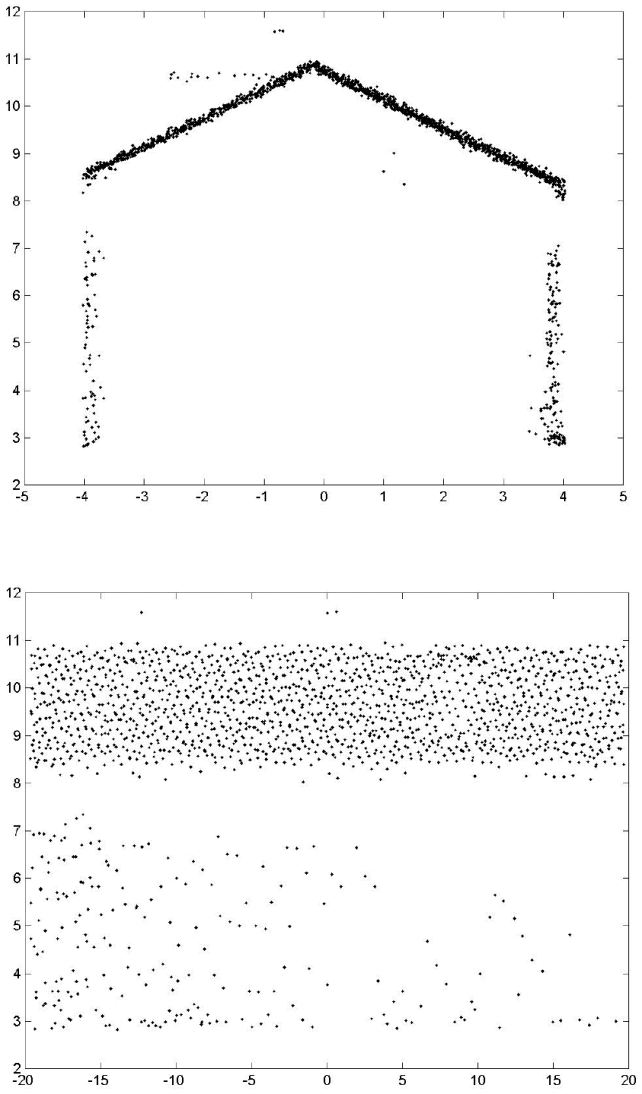

Figure 4: Points of a gable roof projected onto two wall planes.

2.3 Growing planar faces

As shown in figure 3, several planar faces will be found in multiple segments of the ground plan. In some segments no planar face can be found, because the segment only contains a few points. To find better descriptions the planar faces need to be merged over the bounds of the segments and, if possible, to be extended to a few points that are unclassified until now. The result of this procedure is shown in figure 5. For each roof plane one planar point cloud has been identified.

The final determination of the plane parameters follows from a least squares adjustment using all points that are assigned to a plane. As an alternative to growing the planar faces, one could also perform a least squares adjustment within each segment and merge the planar faces over the segments using statistical tests on the similarity of the estimated plane parameters. This strategy is faster, but has the disadvantage that unclassified points are not considered for membership of a planar face that was found in another segment.

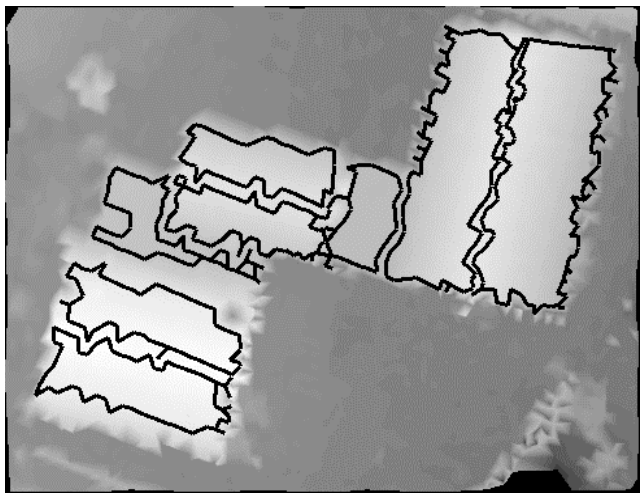

Figure 5: Bounds of planar faces after merging and expanding the faces detected inside the segments.

2.4 Least squares estimation of planes

To estimate accurate plane parameters all points assigned to a planar face are used in a least squares adjustment. For the estimation in 2D using the projection as in figure 4a, the most simple model would be

$$\mathrm{E}\left\{\begin{pmatrix} z_1 \\ z_2 \\ \vdots \\ z_n \end{pmatrix}\right\} = \begin{pmatrix} x_1 & 1 \\ x_2 & 1 \\ \vdots & \vdots \\ x_n & 1 \end{pmatrix}\begin{pmatrix} s \\ d \end{pmatrix} \quad \text{with} \quad Q_y = \sigma_z^2 I_n \qquad (1)$$

with slope s and distance d as line parameters and σ_z as standard deviation of the height measurements. This model, however, ignores that the planimetric coordinates of the laser points are stochastic too. They usually even have a higher standard deviation. To take this into account the model is linearised to

$$\mathrm{E}\left\{\begin{pmatrix} \Delta x_1 \\ \Delta x_2 \\ \vdots \\ \Delta x_n \\ \Delta z_1 \\ \Delta z_2 \\ \vdots \\ \Delta z_n \end{pmatrix}\right\} = \begin{pmatrix} 1 & & & 0 & 0 & 0 \\ & 1 & & & 0 & 0 \\ & & \ddots & & \vdots & \vdots \\ 0 & & & 1 & 0 & 0 \\ s^0 & & & 0 & x_1^0 & 1 \\ & s^0 & & & x_2^0 & 1 \\ & & \ddots & & \vdots & \vdots \\ 0 & & & s^0 & x_n^0 & 1 \end{pmatrix}\begin{pmatrix} \Delta x_1 \\ \Delta x_2 \\ \vdots \\ \Delta x_n \\ \Delta s \\ \Delta d \end{pmatrix}$$

with (2)

$$Q_y = \begin{pmatrix} \sigma_x^2 I_n & 0 \\ 0 & \sigma_z^2 I_n \end{pmatrix}$$

where the upper index ^{0} denotes an approximate value. The slope values estimated with (2) differed up to 1.3^0 from the values estimated with (1). Assuming σ_z = 5 cm and σ_x = 19 cm (based on [Vosselman and Maas, 2001]), the estimated parameter standard deviations are about 1/5 higher using the linearised equations (2) for slopes around 35^0.

3 REFINEMENT OF GROUND PLAN PARTITIONING

Unless the number of points in a segment is very small, one or more planes will have been found by the above procedure. Segments with only one planar face can be fully assigned to that plane. By combining the planimetric bounds of the ground plan segment with the detected plane, a 3D model for that segment can be constructed.

For those segments that contain points of multiple planar faces further splitting of the segment is attempted until only one planar face is left per segment. A segment is split if evidence is found for the presence of an intersection line of two adjacent planar faces or a height jump edge between two such faces.

3.1 Detection of intersection lines

To detect the intersection lines, all (non-parallel) pairs of planar faces are intersected. An intersection line is considered to be found if the following requirements are met:

- The intersection line is inside the ground plan segment.
- The contours of both planar faces are near the intersection line over some range.
- These ranges overlap over some minimum distance.

The example building in the figures has three gable roofs. The detected ridge lines are shown in figure 6. They are a little shorter than the actual ridges since the point clouds usually do not extend until the very end of a roof face. The accuracy of these reconstructed ridge lines is very high, since it results from the intersection of two planes that have been determined using many points (typically > 100) [Vosselman, 1999].

3.2 Detection of height jump lines

The detection of height jump edges is the most difficult part of the reconstruction. The accurate location of a height jump edge requires a high point density. To simplify the detection it is assumed that the height jump edge is parallel to one of the edges of the ground plan segment. For each planar face within a segment, hypotheses for locations of height jump edges are generated based on the orientations of the segment edges and the extent of the planar face. If other planar faces exist within the segment and their contours are near a hypothesised height jump edge, this hypothesis is accepted. The range over which the contour points are found near the height jump edge determines the range of this edge.

In the middle of the example building there is a clear height jump edge. In two segments of the ground plan this edge is detected (figure 6). A little to the right a short height jump edge is found. This edge is caused by a few points of the gable roof on the right hand side of this edge that were present inside the segment left of the gable roof. Since the location of this edge is very near to an edge of the ground plan segment, the height jump edge is assumed to be slightly dislocated and is not taken into account in the further processing.

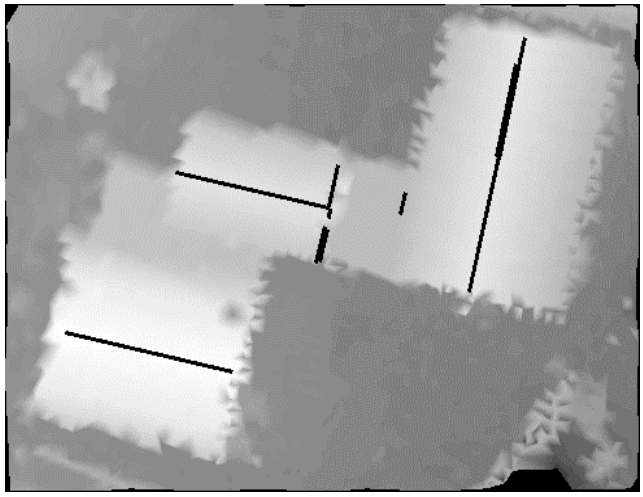

Figure 6: Detected intersection lines and height jump edges.

3.3 Splitting and merging of segments

The final steps of constructing the 3D model of a building consist of splitting and merging the ground plan segments until there is a one-to-one relationship between the segments and the roof faces. Once a intersection line or height jump edge has been detected inside a segment, this segment is split into two parts. For both resulting segments it is again evaluated whether there are possibilities to further split the segment. For the example building the ground plan segmentation resulting after the splitting is shown in figure 7.

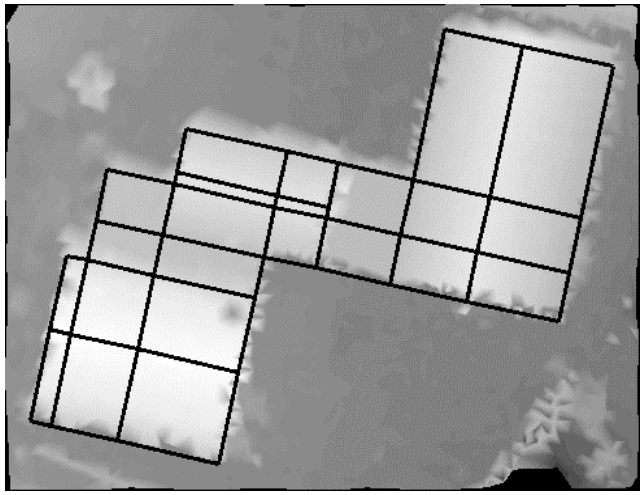

Figure 7: Refined segmentation after splitting segments at positions of intersection lines and height jump edges.

If no further splitting is possible, all segments are assigned to an detected planar face. In some segments there still may be points belonging to different planar faces. In that case the face with the largest number of points is selected. All adjacent segments of the ground plan that are assigned to the same planar face are merged. This results in the final partitioning of the ground plan where

each segment corresponds to a roof face (figure 8). By combining this partitioning with the parameters of the detected planes, the 3D building model can be constructed (figure 9).

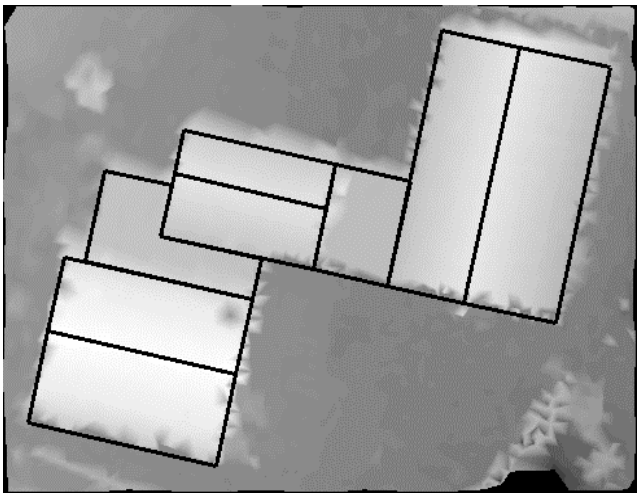

Figure 8: Final partitioning after merging segments assigned to the same planar faces.

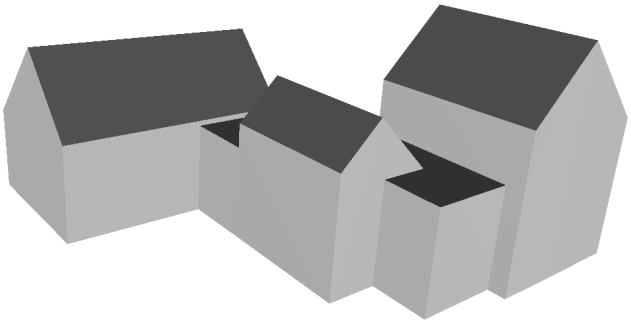

Figure 9: Reconstructed 3D building model.

4 REFINEMENT OF AN INITIAL MODEL

The strategy described above relies on the detection of intersection lines and height jump edges. For this detection the presence of points of two different planar faces near the hypothesised line or edge is required. In particular for small faces these hypotheses can often not be confirmed. The resulting under-segmentation of the ground plan then leads to a generalisation of the building model.

In order to preserve more detail in the model, another reconstruction strategy has been explored. In this strategy we start with a relatively coarse 3D building model that is derived by fitting shape primitives to the original segments of the ground plan. By analysing the clouds of points that do not correspond to this model, refinements are estimated.

4.1 Creation of an initial model

Based on the Hough transform as described in section two, planar faces are detected within each segment. Assuming rectangular segments, hypotheses for five different roof models for the segment are generated: flat roof, slanted roof with two perpendicular orientations, and two gable roofs with perpendicular orientations.

Figure 10 shows a building with four ground plan segments. The building has a cropped hip roof with a dormer and a perpendicular part with another hip roof. Choosing from the four models, gable roofs are found to be the best fit for each of the segments. By analysing the estimated parameters of the gable roofs, it is concluded that three gable roofs have collinear ridges and eaves. The corresponding segments are merged and the parameters of the gable roof are re-estimated using all points of the three segments. The initial model for this building consist of two adjacent gable roofs with perpendicular orientation.

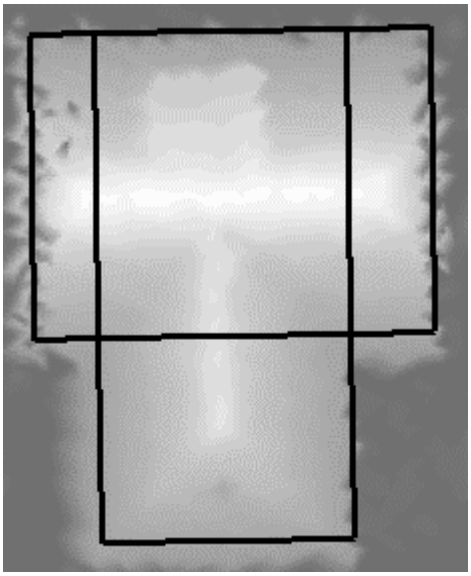

Figure 10: Building with two hip roofs and a dormer.

4.2 Analysis of remaining point clouds

This building model is then refined by modelling the point clouds that do not fit to the initial model [Maas, 1999]. If one of the five models fits to a point cloud a local correction is made to the initial model. Most often this means a small object (like a box modelling a dormer) is put on top of the initial model. Sometimes, a small part needs to be subtracted from the initial model. This is the case, e.g., if a gable roof is corrected to a hip roof. The extent of the additional models is determined by the bounding box of the examined point clouds. The orientation of such a bounding box is taken to be parallel to the bounds of the segment of the ground plan.

For the merged top three segments in figure 10 a gable roof was assumed as the initial model. Figure 11 shows that four clusters of points that do not fit this model can be discerned. The left and right cluster fit best to the slanted roof model and are situated below the gable roof model. Consequently, the gable roof is adapted to a (cropped) hip roof. The top cluster is also modelled best by a slanted roof. The point cloud is higher than the initial gable roof and therefore leads to a model for the dormer with a rectangular ground plan. Finally the lower cluster is best modelled by a gable roof. It is found that the parameters of this roof correspond to the gable roof that was already found in

another segment of the ground plan. The parameters of this gable roof are therefore re-estimated using the points of from both segments. The resulting model is shown in figure 12.

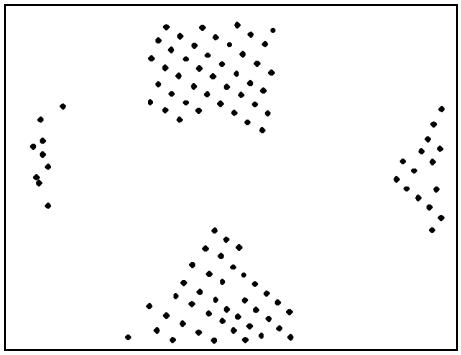

Figure 11: Clusters of points that do not fit the initial model.

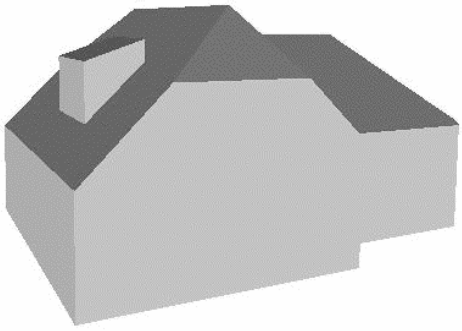

Figure 12: Reconstructed model and a photograph of the building from the same perspective.

5 RESULTS AND CONCLUSIONS

In the paper two strategies for the reconstruction of building models were described. The first strategy relied on the detection of intersection lines and height jump edges between planar faces. The second strategy adopted coarse initial models that were refined on the bases of fitting models to point clouds that did not correspond to the initial models. Overall, the latter strategy shows a larger number of reconstructed details. In datasets with a high point density (5-6 pts/m^2) even chimneys were often reconstructed. In particular in datasets with a lower point density, the second strategy leads to better results, since a few points provide enough evidence for the correctness of a model. In such cases the first strategy would often not find sufficient evidence for the presence of intersection lines or height jump edges and therefore fail to further refine the initial ground plan segmentation. In some cases the second strategy leads to small details that are incorrect. Figure 13 shows an incorrect extension of the gable roof into the rectangle with a flat roof. This extension was caused by a few points of the gable roof that were situated inside the ground plan segment of the flat roof due to a small misalignment between the ground plan and the laser data.

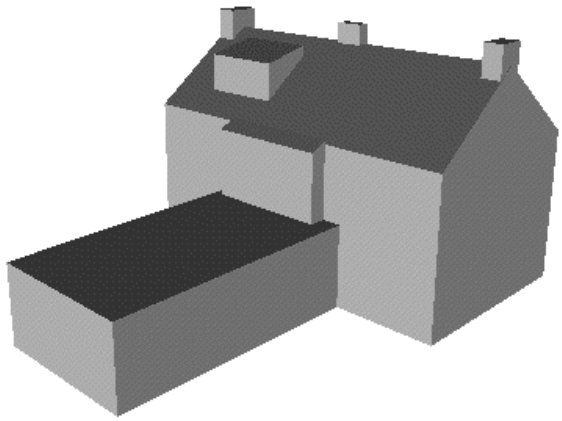

Figure 13: Building model with reconstructed dormer and chimneys and an incorrect extension of the gable roof.

A dataset of 106 buildings has been processed with the second strategy. Twelve buildings did not meet the assumptions of the method. In most of those cases the ground plan segmentation did not yield rectangular segments which is a restriction in the current implementation. 83 out of the remaining 94 buildings were reconstructed successfully (figure 14). The errors were mostly caused by an insufficient number of points within a ground plan segment. This is due to the sometimes very small size of a segment or bad reflection properties of the roof surface [Vosselman and Suveg, 2001]. To improve these results a more global reasoning strategy that incorporate knowledge on the common shapes of buildings needs to be developed.

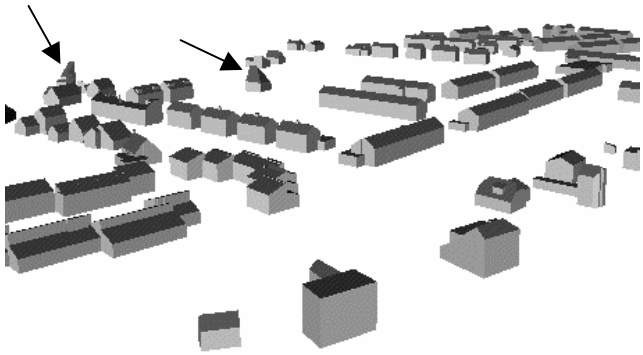

Figure 14: Part of the reconstructed buildings. The arrows indicate two apparent errors in this area.

The point density of the dataset was reduced from 5-6 points per m^2 to 1.25-1.5 points per m^2 to study the possibility to reconstruct the same buildings from datasets that can nowadays be acquired by laser scanners in aeroplanes. Obviously, the amount of detail that can be reconstructed is lower (figure 15). It was further found

that six more buildings could not be reconstructed. The other 77 buildings were reconstructed correctly, be it with less details.

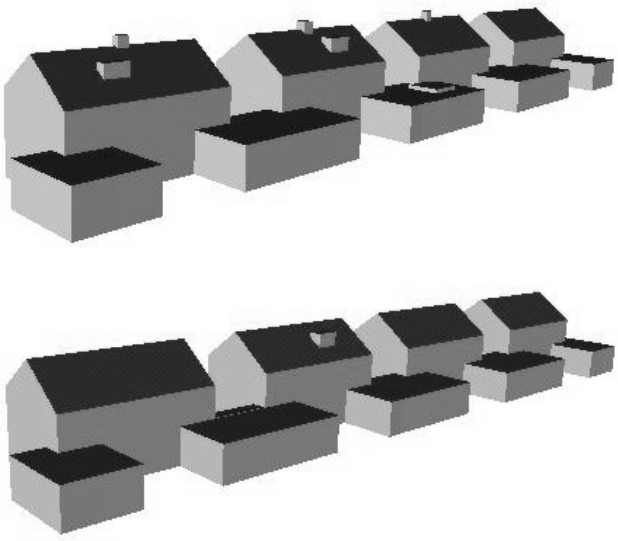

Figure 15: Effects of reducing the point density from 5-6 points per m^2 (top) to 1.25 - 1.5 points per m^2 (bottom) on the amount of reconstructed details.

ACKNOWLEDGEMENT

The FLI-MAP laser data were provided by the Survey Department of the Ministry of Transport, Public Works and Water Management of the Netherlands. The large scale map data (GBKN) was provided by the Dutch Cadastre. The authors thank both organisations for making these data available.

REFERENCES

Ballard, D.H. and C.M. Brown, 1982: Computer Vision. Prentice-Hall, Englewood Cliffs, NJ.

Baltsavias, E., 1999: Airborne laser scanning: existing systems and firms and other resources. ISPRS Journal of Photogrammetry and Remote Sensing, 54 (2-3): 164-198.

Dijkman, S.T., 2001: Automatic building reconstruction from laserscanner data and GBKN data (in Dutch). M.Sc.-thesis Delft University of Technology, 66 p.

Geibel, R. and U. Stilla, 2000. Segmentation of Laser Altimeter Data for Building Reconstruction: Different Procedures and Comparison. International Archives of Photogrammetry and Remote Sensing, vol. 33, part B3, pp. 326-334.

Haala, N. and K.-H. Anders, 1997: Acquisition of 3D urban models by analysis of aerial images, digital surface models and existing 2D building information. SPIE Conference on Integrating Photogrammetric Techniques with Scene Analysis and Machine Vision III, SPIE Proceedings vol. 3072, pp. 212-222.

Haala, N. and C. Brenner, 1997: Generation of 3D city models from airborne laser scanning data. Proceedings EARSEL workshop on LIDAR remote sensing on land and sea, pp. 105-112, Tallin, Estonia.

Hoover, A., Jean-Baptiste, G., Jiang, X., Flynn, P.J., Bunke, H., Goldgof, D.B., Bowyer, K., Eggert, D.W., Fitzgibbon, A. and Fisher, R.B., 1996: An experimental comparison of range image segmentation algorithms. IEEE Transactions on Pattern Analysis and Machine Intelligence 18 (7) : 673-689.

Hough, P.V.C., 1962: Method and Means for Recognizing Complex Patterns. U.S. Patent 3.069.654.

Maas, H.-G., 1999: Closed Solutions for the Determination of Parametric Building Models from Invariant Moments of Airborne Laserscanner Data. International Archives of Photogrammetry and Remote Sensing, vol. 32, part 3-2W5, pp. 193-199.

Maas, H.-G. and G. Vosselman, 1999: Two algorithms for Extracting Building Models from Raw Laser Altimetry Data. ISPRS Journal of Photogrammetry and Remote Sensing 54 (2-3): 153-163.

Vosselman, G., 1999: Building Reconstruction using Planar Faces in Very High Density Height Data. International Archives of Photogrammetry and Remote Sensing, vol. 32, part 3-2W5, pp. 87-92.

Vosselman, G. and H.-G. Maas, 2001: Adjustment and filtering of raw laser altimetry data. OEEPE workshop on Airborne Laserscanning and Interferometric SAR for Detailed Digital Elevation Models, Stockholm, 1-3 March, 11 p.

Vosselman, G. and I. Suveg, 2001: Map based building reconstruction from laser data and images. In: Automatic Extraction of Man-Made Objects from Aerial and Space Images (III), Swets & Zeitlinger Publishers, to appear.

Scanline forced Delaunay TENs for surface representation

ir. Edward Verbree and prof.dr.ir. Peter van Oosterom
Department of Geodesy – Section GIS-technology
Delft University of Technology
the Netherlands
e.verbree@geo.tudelft.nl

Commission III, Working Group 3

KEY WORDS: Delaunay Tetrahedron Networks (TEN), TIN, Surface reconstruction

ABSTRACT

The general idea that a Delaunay TIN (DT) is more appropriate than non-Delaunay TINs, due to 'better' shaped triangles, might be true for many applications, but not for height dependent analytical queries. This is because the distribution of the triangle tessellation is defined in the two-dimensional XY-plane, by ignoring the Z-value in the Delaunay empty circum circle criterion. Alternatively, Data Dependent Triangulations (DDT) aim to identify which triangulation of a given function z=f(x,y) over a given set of points will optimize some quality, i.e. the minimal spatial area of the surface or the volume below the resulting surface. This might be a good approach, but still there is no certainty the TIN represents the actual surface. Besides that, a 2D-TIN (Delaunay or not) is only capable to solve 2D (or 2.5D) data distributions. The reconstruction of the surface given by a set of surface points alone is therefore not unambiguous.

This paper describes a surface reconstruction method based on the scanlines, the lines-of-sight or measurements between the observer (or the measurement platform) and the target (the measured point). As the scanlines do not belong to the surface, we have to use a 'real' 3D triangulation construction method, resulting in a Tetrahedronized Irregular Network. This TEN is capable to store all kinds of surface-features (as the target-points) and the scanlines as well. The scanlines are forced to split by adding Steiner points until they are part of the Delaunay TEN. This procedure gives us the additional information needed to use the TEN to reconstruct the surface. The method is demonstrated by the non-trivial case of a set of measured points in a regular square distribution showing the improved surface reconstruction technique.

1 INTRODUCTION

Triangulated Irregular Networks are commonly used for Digital Terrain Modeling. These models are needed for several applications, in which the height value is often an important factor in the calculations and analyses. Visibility computations and line-of-sight communication problems require an appropriate representation of the 'real' terrain-surface.

The advantage of a TIN above other tessellations, like regular square grids (RSG), is the possibility to incorporate the exact position of the measured heightpoints, contourlines and breaklines into the model. In that, the actual measurements are well represented. But, one thing we often forget is the fact that the distribution of the triangle-tessellation is defined in the two-dimensional XY-plane, by ignoring the Z-value in the Delaunay empty circum circle criterion (Lawson, 1977).

The general idea that a Delaunay-TIN is more appropriate than non-Delaunay TINs because of well-formed triangles might be true for many applications, but not for height dependent analytical queries. An alternative is to use a data dependent triangulation for surface representation (Dyn, 1990). This might be a better direction to look for, but still there is no certainty that the TIN represents the actual surface. Besides that, a 2D-TIN (Delaunay or not) is only capable to solve 2D or 2.5D data distributions.

We can however use an additional observation: the scanline. One property of an observation is the line-of-sight; no surface is allowed between the observation-point and the target-point (the actual point on the surface). Hence, we consider a method for triangulations forced by scanlines, which means that not only the measured heightpoints are included into the TIN, but the measurements as well.

As the scanlines do not contribute to the representation of the surface, they cannot be treated as the surface features types like breaklines and contourlines. They could even be perpendicular, which makes it impossible to incorporate them into a 2D TIN. So we have to use a 'real' 3D triangulation construction method, resulting in a TEN (Tetrahedronized Irregular Network). A TEN is also known as a 3D-TIN, indicating the 3D conditions taken into account at the construction, i.e. in case of a Delaunay TEN the empty circum sphere criterion in contradiction to the empty circle criterion in the 2D or 2.5D case. This TEN is capable of storing all kinds of surface-features, including the scanlines. The final scanline forced TEN gives us the information needed to construct the triangles, which will define the surface we are looking at and the body (volume) of that object as a set of tetrahedrons.

In section 2, we will recall some basics of Delaunay Triangulations (DT) and Data Dependent Triangulations (DDT). Section 3 presents the ideas and some examples for scanline constrained TENs in more detail. Section 4 contains some

concluding remarks, where section 5 gives some directions for further research.

2 DELAUNAY TRIANGULATIONS AND DATA DEPENDENT TRIANGULATIONS

Most commercial GISs are capable to model surfaces by TINs. These surfaces provide insight, reveal trends and solve problems. Simple geometry features like masspoints and in addition breaklines en contourlines are the input for the TIN construction. The Z-value (or an attribute representing a heightvalue) of these features is stored as the Z-value of the nodes of the TIN.
A Delaunay TIN fulfils the 'empty circum circle criterion' (Lawson, 1977). If the point distribution is regular, for example if all points are on a regular square or rectangle (figure 1a), this criterion has two equal choices.

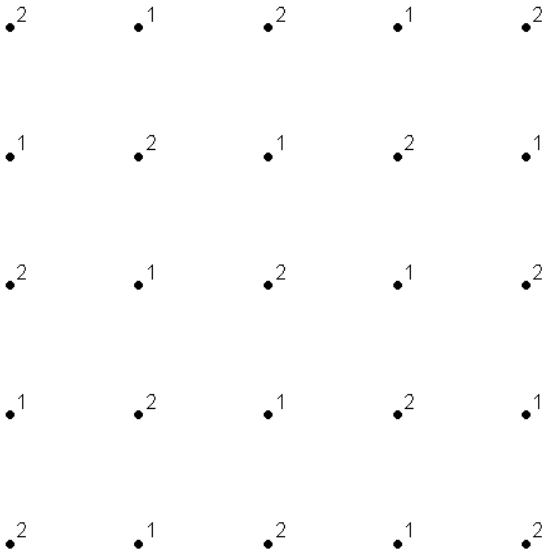

fig 1a: regular datapoint distribution, labels indicate heightvalues

In figure 1b the diagonal of all the triangles is directed northwest to southeast. This could be, under the same Delaunay criterion as four points are located on the common circum circle of a grid cell, for all squares from north-east to south-west, or even randomly chosen.

One has to realize that the given height values (or the Z-value of the nodes) do have consequences for derivatives like slope and aspect, visualization (like hill-shading) and volume statistics (like viewsheds and cut and fill calculations). However they are not used to control the 2D Delaunay triangulation process.

An other artifact is the possible occurrence of so-called 'flat' triangles. Especially TINs based on input of contourlines are known for this problem. Introducing derived drainage channels and ridges by examining the skeleton or medial axes can solve this problem, see for example (Tinghua, 2001).

One can argue that the 2D-Delaunay TIN is just one of the possibilities to triangulate a set of points (nodes) and lines (edges). In fact any triangulation could be a candidate for a 2.5D terrain surface representation. Extensive research on Data Dependent Triangulations (DDT) proves this observation. The idea is either to maximize or to minimize some cost-function that expresses certain local, regional or global properties of the resulting surface (Dyn, 1990; Bern 1992; Yu, 2001; Lenk, 2001).

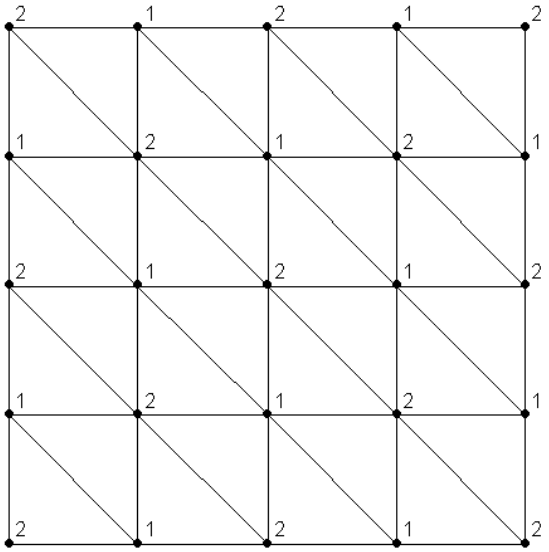

fig 1b: a possible Delaunay TIN of regular datapoint distribution

A few possible options are:
- total surface area minimum
- total content below surface (volume) minimal
- total content above surface minimal
- angles within 3D triangle minimum
- angles / bends between two triangles minimal
- no points in 3D sphere of any triangle

The results of DT can be ambiguous. This is illustrated by the following simple example: determine the surface-area and volume for the surface given by: p1=(0,0,0); p2=(0,1,0); p3=(1,1,10); p4=(1,0,0).

If the diagonal is chosen as edge (p1,p3), the surface-area equals to:
`area(p1,p2,p3) + area(p3,p4,p1) =`
`½*1*sqrt(101) + ½*1*sqrt(101) = sqrt(101) ~ 10.05`
The volume (regarding to 0-level) equals to:
`volume(p1,p2,p3) + volume(p3,p4,p1) =`
`½*½*10 + ½*½*10 = 5`
If the diagonal is chosen as edge (p2,p4), the surface-area equals to:
`area(p1,p2,p4) + area(p2,p3,p4) =`
`½*1*1 + ½*sqrt(2)*sqrt(101-½) =`
`½(1+sqrt(201) ~ 7.59`
The volume (regarding to 0-level) equals to:
`volume(p1,p2,p4) + volume(p2,p3,p4) =`
`½*½*0 + ½*½*10 = 2.5`
If we minimize the surface-area we will chose for diagonal-edge (p2,p4), but if we maximize the volume below the surface, edge (p1,p3) was preferred. As said, the 2D Delaunay TIN has no preferred edge.

In this case it could be argued that the 2D Delaunay criterion could not make the choice and that the better solution is also according to the criterion. However, it is possible to construct other situation in which the 2D Delaunay solution results in a less good 2.5D TIN than a certain alternative; e.g. assume the points p1 = (0,1,0), p2 = (1,0,0), p3 = (3,1,0) and p4 = (1,2,10). The surface-area on the Delaunay based TIN equal to:
`½*(sqrt(204) + sqrt(516))`which is clearly more than the non-Delaunay alternative: `1.5*(1+sqrt(101))`

These local optimizations could disregard regional phenomena, like ridges and faults, and as long a projection is made to the XY-plane, no overhanging cliffs or other disturbances are possible. And these disturbances could be the surface-phenomena we are looking for, like (near) vertical walls of buildings or viaducts.
We will therefor forget for the moment the data independent (like 2D Delaunay TINs) and data dependent TIN and concentrate on Delaunay 3D-TINs or TENs for surface reconstruction.

3. SCANLINE FORCED TRIANGULATION

Height datapoints are more and more collected by laserscanning from a platform at an airplane or helicopter, but scanning from a ground platform is also possible. The result of this process is a point cloud of target-points. To calculate these target-points, the position of the observer (i.e. the laser itself) has to be known and thus the scanline between the observer point and the target point. In our approach we will use these scanlines for the reconstruction of the surface at an increasing complexity demonstrated by a 1.5D, 2D and a 2.5D scenario.

3.1 1.5D Case

In exploring this problem, first a step back was taken as we consider the 1.5 scenario, where 1D-points are taken, and together with the height value and the scanline a surface is reconstructed. This could be quite trivial to do, because we can order the datapoints on their X-value. But as, later on, in two dimensions this is not straightforward, we have to use an algorithm, which will not take this ordering as a precondition.

The aim of the algorithm is to find the object and boundary defined by a set of heightpoints and scanlines The volume is bounded by the points left and right of the dataset, both given the heightvalue of zero. The scanlines are shortened to a given value above the most extreme heightvalue, and for these examples dropped as perpendiculars.

We will give the algorithm in pseudo-code:

Algorithm 'Scanline_TIN'

```
step 1: Construct TIN
input target-points
create 'scanline forced' Delaunay TIN

step 2: Transform Edges
for each scanline
  get target-point-A
  create list of connected scanlines
  for each connected scanline
    get target-point-B
    create edge(target-point-A,
                                target-point-B)
  end for
end for
```

Step 1: Construct TIN

First a regular Delaunay TIN is created by the set of target-points. and observer-points. Then, an iterative process is started. Each scanline not being an TIN-Edge is forced to sub-divide into parts. The newly formed nodes are included as points into the TIN. This procedure ends when all scanline-parts are represented by an TIN-Edge in the Delaunay TIN (fig 2a).

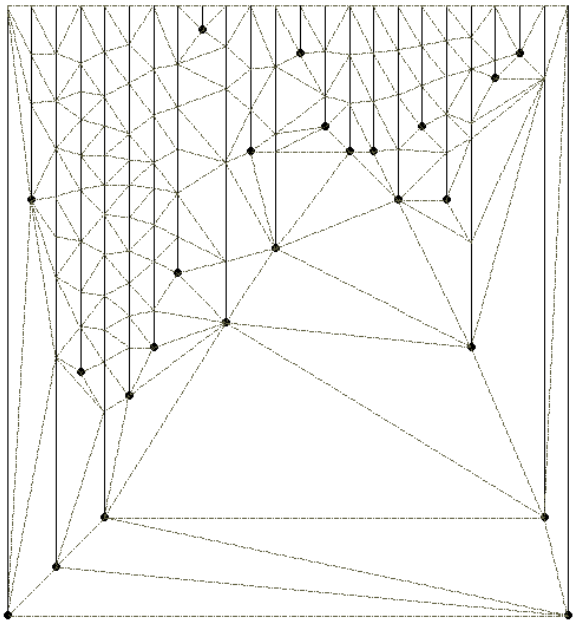

fig 2a: 'scanline forced' Delaunay TIN

This is an alternative to normal constrained triangulations, but a defendable approach, because the added nodes (Steiner points) are used to reconstruct the surface (see next step). The addition of Steiner points to a Delaunay Triangulation is a powerful concept in computational geometry which allows quite theoretical investigations. It forms the basis for many provable optimal triangulation algorithms for various quality criteria (Fleischmann, 1999).

Step 2: Transform Edges

The actual interior and boundary of the object given by the target-points and scanlines is found by the procedure in which for each scanline the connected scanlines are determined by examine the TIN-Edges. All TIN-Edges with one node known as a target-point and one node known as an added Steiner point or an other target-point are selected. If a TIN-Edge links two target-points this TIN-Edge is stored, else the TIN-Edge is dropped and replaced

by a new TIN-Edge. This new TIN-Edge is created by the original target-point and the target point at the end of the scanline belonging to the Steiner point (fig 2b).

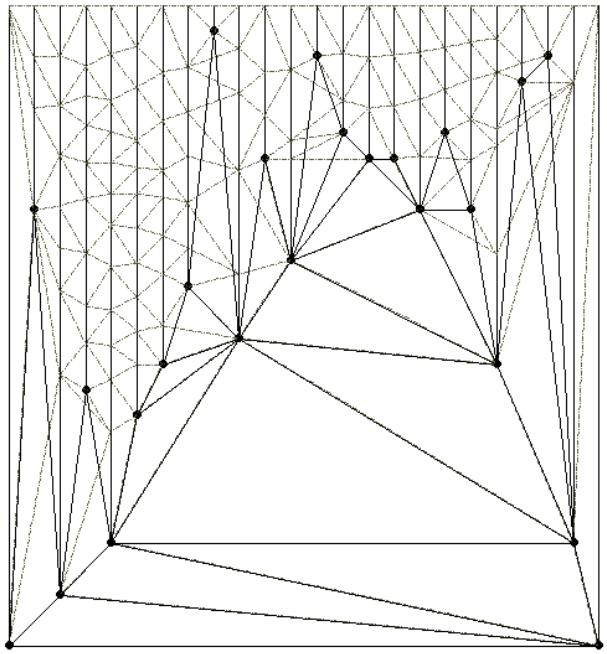

fig 2b: reconstructed solid and surface of 1.5D dataset

The 1.5D-case is quite trivial, but it explains the use of the sub-divided scanlines. The dataset is 1.5D as the Z-value is a property (measurement) of the XY-values. The TIN is Delaunay for that part where the newly formed TIN-Edges do not intersect with the original TIN; the other part is non-Delaunay.

This algorithm is implemented as a prototype, written in the object-based Language Avenue of ESRI ArcView3.2, extended by 3D-Analyst (ESRI, 2001).

3.2 The 2D Case

One can argue that the applied algorithm for the 1.5D (X, Z) example given in the previous section is a little 'over the edge', as we can simple sort the datapoints on their X-value. To show the possible use of the 'scanline forced' triangulation for 2.5D and 3D applications, the same algorithm is applied for the reconstruction of a 2D-polygon with concavities.

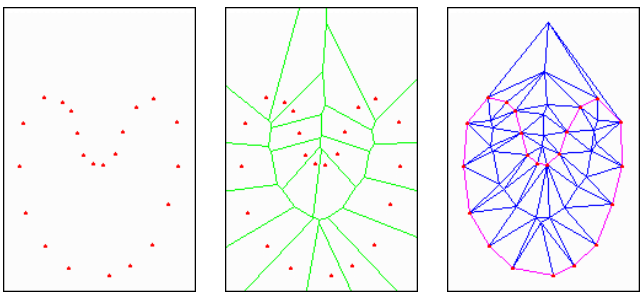

fig 3a: A point set, its Voronoi Diagram and its crust

This method has the same goal as the crust and skeleton method, see fig 3a (Zhang, 2001), where the existents of concavities is not derived by the Voronoi Diagram, but by the given set of scanlines.

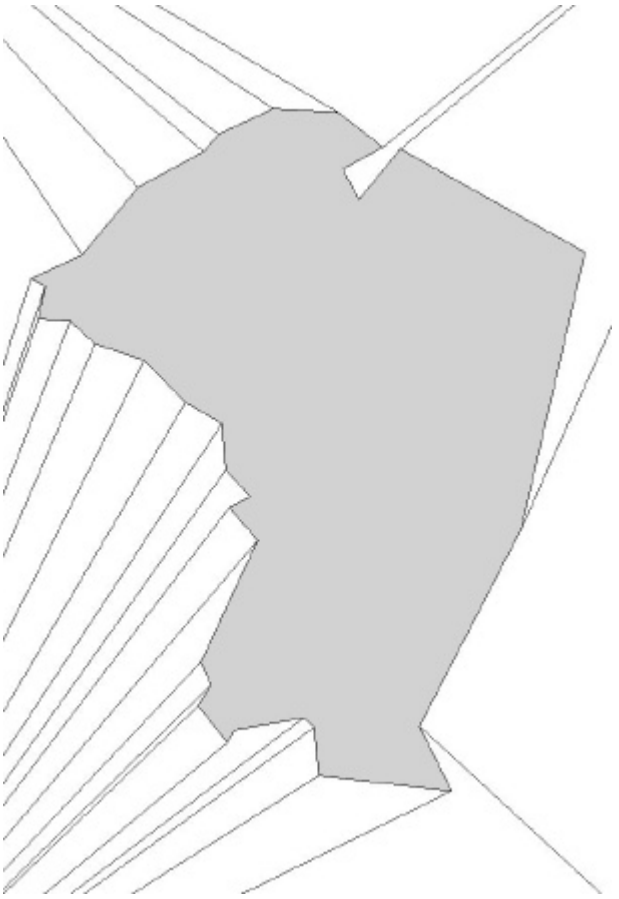

fig 3b: vertices of polygon observed from four corners

For this example a given polygon (the boundary of Annepolis' country Anne Arunde) is observed from four corners, see fig. 3b. We apply the same algorithm *Scanline_TIN* as in section 3.1. Only the scanlines (connections of target-points and observation-points) are known and used as input. Fig. 3c gives the 'scanline forced' Delaunay TIN. Now we perform Step 2 of the algorithm to reconstruct the boundary and interior by a TIN. Again, the resulting TIN is not Delaunay, as some newly formed Edges will cross the original ones.

3.3 The 2.5D Case

The 2.5D Case is not as trivial as the 1.5D or the 2D examples given in the previous paragraphs. Storing and manipulating the surface-points and scanlines by well-known 2D Delaunay TIN constructors could easily solve these cases.

In this 2.5D scenario, the heightvalue of the surface-points could be considered as one possible attribute value of the planimetric co-ordinates (X,Y). As the scanlines do not belong to the surface, we have to use a 'real' 3D triangulation construction method, resulting in a Tetrahedronized Irregular Network.

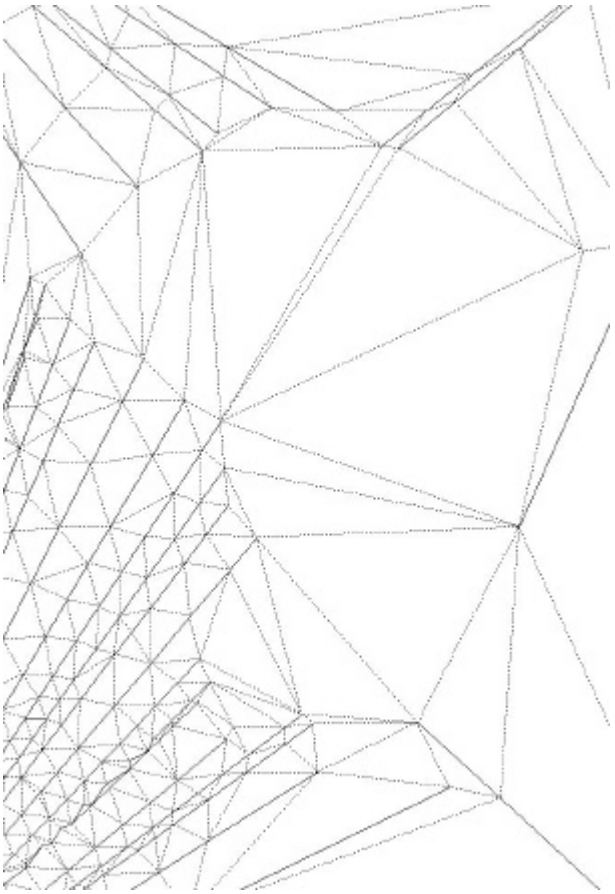

fig 3c: 'scanline forced' Delaunay TIN

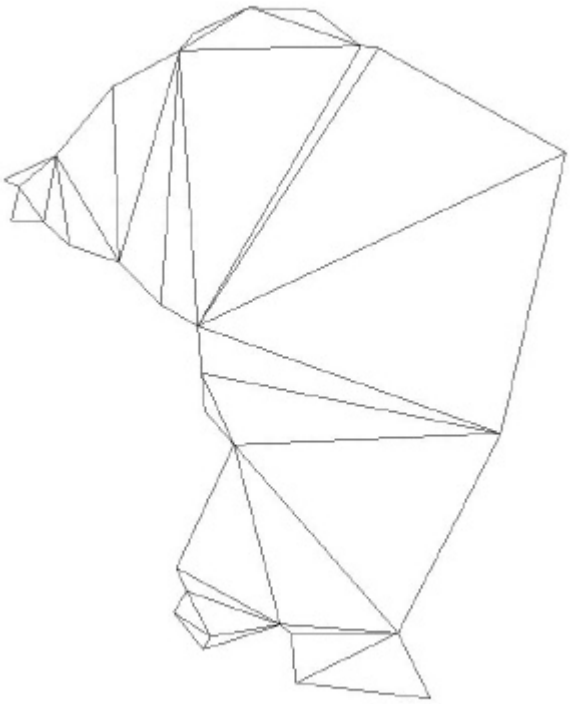

fig 3d: reconstructed boundary and interior of polygon

The triangulation should result in a set of non-overlapping tetrahedrons, which together fill a convex solid. Each network of tetrahedrons should adhere to the following:

a) Of each tetrahedron its four vertexes should not be located in the same plane;
b) Each tetrahedron should not contain any other points of the dataset;
c) A TEN-Face (triangle) is on the boundary of the solid or is exactly shared by two internal tetrahedrons.

To create a set of Delaunay tetrahedrons one condition has to be added:

d) For each of the tetrahedrons in a Delaunay TEN the circum-sphere should not contain any other point of the dataset.

To create a scanline-forced Delaunay TEN the last condition taken into account is:

e) All scanlines are identified as edges in the Delaunay TEN.

We will apply the same algorithm as given in section 3.1, but all operations are one dimension higher.

Algorithm 'Scanline_TEN'

```
Step 1: Construct TEN

input target-points and scanlines
create 'scanline forced' Delaunay TEN

Step 2: Transform Faces

for each Face in TEN
  if (two Nodes on Face are target-points)
                                        then
    if (third Node is on scan-line) then
      get third target-point at end of
                                    scanline
      construct object-Face
        (first target-point, second target-
                  point, third target-point)
    end if
  end if
end for

Step 3: 'Reconstruct Surface

for each object-Face-A
  for each other object-Face-B
    if (center object-Face-A below object-
                                    Face-B)
                                       then
      remove object-Face-A
    end if
  end for
end for
```

Step 1: Construct TEN

3D-TIN or TEN construction algorithms are not as common as 2D-TIN constructors, so we can not use a standard GIS-

environment. Recent developments in Computational Geometry Algorithms Library (CGAL, 2001) are promising, but we have used an own 3D implementation of the incremental point algorithm, given in (Lee, 1980).

This same program is used by one of the authors to create animated time series (Kraak, 1992). Here an interface to this program is written in the object-based language Avenue to control the program and visualize the results in ArcView 3.2 (ESRI, 2001).

To be Delaunay, the scanlines are divided until each part is an edge in the TEN, in contradiction to a constrained TEN, where the Delaunay-criterion is loosen to hold the scanline as one part. However, some objects exists that can not be divided into tetrahedrons without adding extra Steiner vertices (Eppstein, 2001).
The obtained Delaunay TEN holds many possible boundary solutions. We will use the added 'Steiner' vertices at the scanlines to reconstruct the surface as in the 1.5D example.

The volume of the object is controlled by an added ground point at a given height value for each target-point.

To illustrate the algorithm the same datapoints as in fig. 1a. are used (see fig 4a).

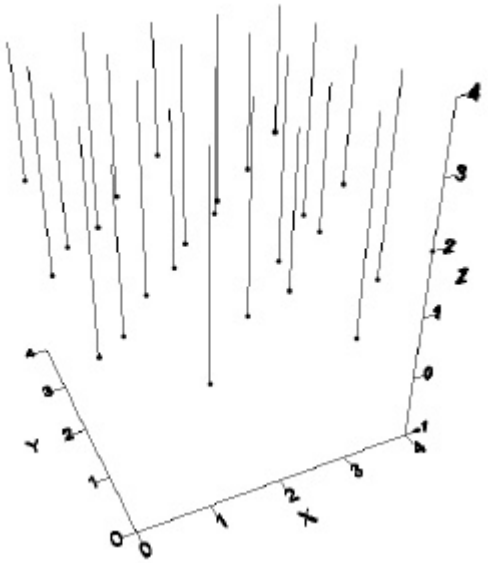

fig 4a: datapoints and scanlines of 2.5D dataset

Step 2: Transform Faces

The actual interior (solid) and boundary (surface) of the object given by the target-points and scanlines is found by the procedure in which for each scanline the connected scanlines are determined by examine the TEN-Faces. All TEN-Faces with two nodes known as a target-points and one node known as an added Steiner point or another target-point are selected. If a TEN-Face links three target-points this TEN-Face is stored, else the TEN-Face is dropped and replaced by a new TEN-Face. This new TEN-Face is created by the original two target-points and the target point at the end of the scanline belonging to the Steiner point (fig 4b).

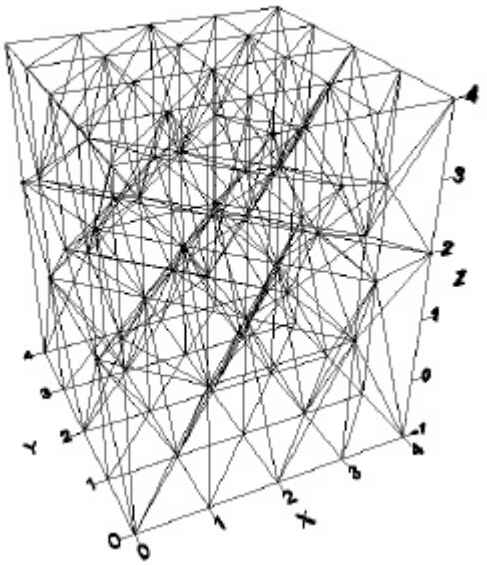

fig 4b: 'scanline forced' Tetrahedron Network (TEN)

Step 3: Reconstruct Surface

Finally a hidden-face removal algorithm finds the surface. Each newly created face is checked whether or not it is above the other faces. If not, this face will be discarded; else it is restored as an surface face.

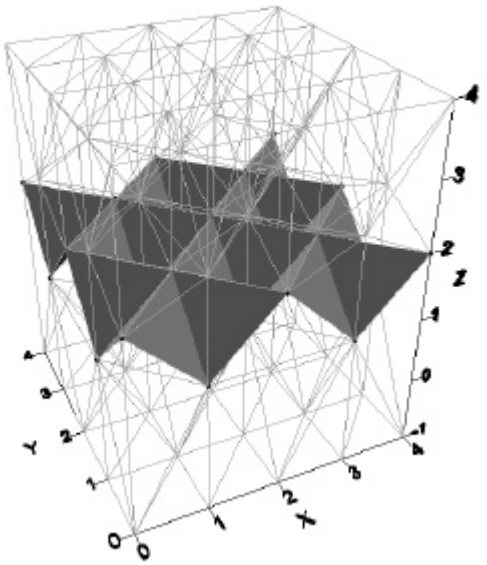

fig 4c: reconstructed surface of 2.5D dataset

If we compare the obtained surface TEN with the 'normal' TIN solution (fig. 4d, fig 1b) we will see the volume below the surface has its maximum obtained.

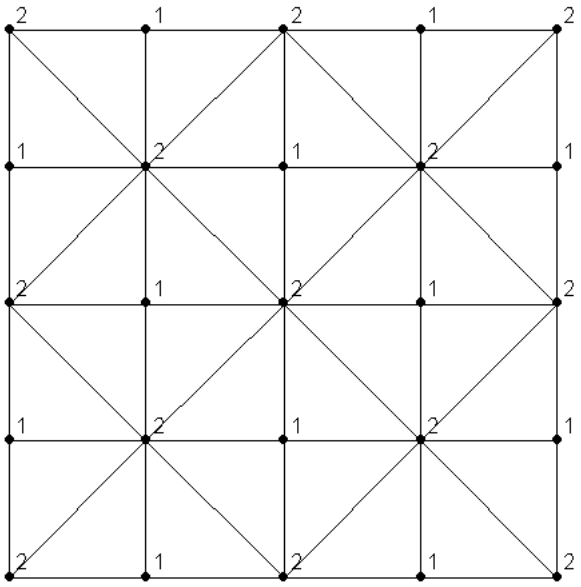

fig 4d: reconstructed TEN-surface

4. CONCLUSIONS

The use of scanline forced TENs gives us the possibilitie to construct data dependent TINs without the need for predefined and ambiguous data-dependent criteria like surface-area or volume.

The reconstruction of the surface with scanlines is a more complex method than the normal data dependent and data independent algorithms, because of the need to triangulate in three-dimensional space.

The proposed algorithm is capable not only to better reconstruct the surface, but also the volume underneath. This gives us good opportunities for real 3D-calculations (cut-and-fill of caves and other irregular shapes).

5. FURTHER RESEARCH

The surface obtained by the scanline forced Delaunay TENs has to be compared in detail with surfaces obtained by Data Dependent Triangulations for 2.5D datasets with respect to several existing optimization criteria.

The described method for 2.5D surface representation by scanline forced Delaunay TENs has to be tested in further detail for topological correctness (complete and non-overlapping partitioning) of the obtained surface.

As with 2D-TINs the surfaces obtained by the scanline forced Delaunay TENs should be able to store known surface features as breaklines and contourlines.

The (to be derived) angle of the scanline and the obtained surface could give reason to an iterative approach, where only accurate measured datapoints (given by a more or less perpendicular scanline) are taken into account.

The proposed algorithm is able to reconstruct 2D boundaries given a set of surface points and their scanlines (section 3.2). Although directions are given for higher dimensions (compare section 3.1 and section 3.3), this concept has to be proven for 3D-datasets and to be compared to existing methods like the crust and skeleton approach.

REFERENCES

[Bern, 1992] M. Bern, Herbert Edelsbrunner, David Eppstein, Scott A. Mitchell, Tiow-Seng. *Edge Insertion for Optimal Triangulations*, in: Proc. Latin Amer. Sympos. Theoret. Informatics (LATIN '92).

[CGAL, 2001] www.cgal.org

[Dyn, 1990] N. Dyn, D. Levin and S. Rippa. *Data dependent triangulations for piecewise linear interpolation.* IMA J. Numer. Anal. 10 (1990), pp. 137-154.

[Eppstein, 2001] www.ics.uci.edu/~eppstein/junkyard/untetra/

[ESRI, 2001] www.esri.com

[Kraak 1992] Menno-Jan Kraak and Edward Verbree. *Tetrahedrons and animated maps in 2D and 3D space*. In: Proceedings of the 5th Int. Sym. On Spatial Data Handling, Charleston, USA, pp. 63 – 71.

[Fleischmann, 1999] Peter Fleischmann. *Mesh Generation for Technology CAD in Three Dimensions*. Dissertation Technische Universität Wien, 1999

[Lawson, 1977]: C.L. Lawson. *Software for C^1 Surface Interpolation*, in: Rive, J. (Ed.) Mathematical Software III, pp. 161-194.

[Lee, 1980] Lee, D.T. and Schachter, B.J. *Two algorithms for constructing a Delaunay Triangulation.* International Journal of Computer and Information Sciences, vol. 9, no. 3, pp. 219-242

[Lenk, 2000] Ulrich Lenk, *Optimisation Criteria for Degenerated Delaunay Triangulations*, proceedings GIScience 2000, Savannah, Georgia, USA, October 28-21, 2000

[Yu, 2001]: Xiaohua Yu, Bryan S. Morse, and Thomas W. Sederberg, *Image Reconstruction Using Data-Depandent Triangulation*, IEEE Computer Graphics and Applications, May/June 2001, pp62-68

[Tinghua 2001]: Tinghua Ai, *Extraction of landform structure lines based on vector band analysis*, to be publicized, 2001

[Zhang, 2001] www.cim.mcgill.ca/~yzhang/skeleton.htm

On the use of pulse reflectance data for laserscanner strip adjustment

Hans-Gerd Maas
Institute of Photogrammetry and Remote Sensing
Dresden Technical University
Helmholtzstr. 10
D-01062 Dresden, Germany
e-mail hmaas@rcs.urz.tu-dresden.de

Commission III, Working Group 3

KEY WORDS: Airborne laserscanning, accuracy, pulse reflectance.

ABSTRACT

The precision of airborne laserscanner data is strongly influenced by the limited accuracy potential of the integrated GPS/INS pose determination system. Errors of kinematic GPS height determination will often be in the order of one to two decimeters and propagate directly into the height coordinates of digital surface models, digital terrain models and 3-D object models derived from these data. The planimetric accuracy of ground points is influenced by the kinematic GPS accuracy as well as by drift effects of the INS system and is in the order of a few decimeters. Errors become evident at check points or as discrepancies between neighboring strips of laserscanner data. Vice versa, these discrepancies can be used to apply corrections to laserscanner data in a strip adjustment procedure.

Tie points for laserscanner strip adjustment can be determined with high precision by least-squares matching applied to the original non-interpolated ground point clouds organized in stripwise TINs. This procedure provides useful results in regions with sufficient surface slopes in both coordinate directions, but fails over flat terrain if both height and planimetry coordinate discrepancies are to be determined. In such situations, image contrast in the laserscanner pulse reflectance data, simultaneously recorded by some laserscanner systems and perfectly co-registered with the height data in the TIN structure, can replace non-existent height contrast and provide a solution. The paper describes the extension of least-squares-matching to the alternative use of height and reflectance values of irregularly distributed laserscanner points for the determination of laserscanner strip discrepancies in flat regions with existing local image intensity contrast. The practical applicability and precision potential of the technique will be discussed.

1. Introduction

Beyond its original application field in the generation of digital terrain models and digital surface models, airborne laserscanning is meanwhile being used for a number of general 3-D object modeling tasks. While early systems captured datasets with a typical resolution of one point per ten square meters, recent systems can acquire datasets with a resolution of one point per square meter and beyond.

The accuracy potential of airborne laserscanning is mainly influenced by laser range measurement, the deflecting mirror unit and the GPS/INS aircraft pose determination system. In many cases, the latter depicts the largest error source, typically influencing the height coordinate of laserscanner ground points with one to two decimeters and the planimetric coordinates with up to half a meter. While only the height accuracy is relevant in pure digital terrain model applications over terrain with limited steepness, the planimetric coordinates become equally important in high density datasets used for general 3-D object reconstruction tasks such as 3-D building modeling. These errors become evident at ground control points or as discrepancies between overlapping or crossing strips of laserscanner data. Several authors suggested the development of laserscanner data adjustment procedures based on ground control points and tie points between strips (Kilian, 1994; Crombaghs et al., 2000; Burman, 2001; Vosselman/Maas, 2001). While height discrepancy measurements are sufficient in adjustment procedures for use in digital elevation model applications, discrepancies in all three coordinates have to be determined in general applications.

A procedure for the precise determination of tie point discrepancies has been presented by (Maas, 2000). The method is applied to non-interpolated raw laserscanner data points organized in a TIN structure, thus avoiding biases in occlusion regions introduced by the interpolation to a regular grid. It requires the selection of patches containing significant height contrast in orthogonal coordinate directions. This requirement is for instance fulfilled by roof patches with more than one ridge direction. Typical laserscanner datasets will, however, contain large regions where no suitable patches for full 3-D discrepancy measurement can be found, leading to incomplete input to laserscanner strip adjustment routines.

In such regions of insufficient height contrast, an alternative may be provided by the intensity signal recorded by several laserscanner systems. This intensity signal depicts a monochromatic image in the wavelength of the laser, perfectly co-registered with the height data and in an orthogonal projection. This reflectance value is sometimes being used in segmentation tasks (e.g. Oude Elberink and Maas, 2000). An example of a laserscanner height and reflectance image, both interpolated to a 0.5m regular grid and scaled to 8 bit for visualization, is shown in Figure 1. If a flat patch of laserscanner data contains sufficient image contrast, the intensity information may be used for the determination of planimetric coordinate differences. Combined with height discrepancies obtained from the height data in the patch, this allows for the measurement of full tie point discrepancies even over flat terrain.

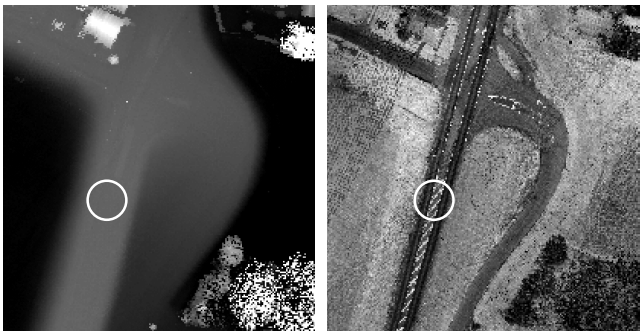

Figure 1: Height and reflectance image of a road crossing in a high-density laserscanner dataset

2. Least squares matching on laserscanner reflectance data

Least squares matching is used regularly in many applications in photogrammetry, for instance for the measurement of tie points in raster image data. The procedure for least squares matching applied to $2^1/_2$-D laserscanner height data in a TIN structure described in (Maas, 2000) uses the heights of laserscanner ground points as observations and derives patch gradients from the normals of TIN meshes. Matching is performed between discrete points in one patch and points interpolated in the corresponding mesh of a TIN structure in the other patch. One observation equations is written for every original data point of both patches, and the input for the observation vector is obtained by subtraction of a height computed by linear interpolation at the same location in the corresponding mesh of the TIN structure of the other patch. It can be shown, that this procedure is superior to matching applied to laserscanner data interpolated to a regular grid, as it allows extensions to avoid significant biases in occlusion regions (Maas, 2000).

In the case of reflectance matching, the reflectance value is used as an observation in least squares matching rather than the height value; this is in analogy to matching in optical greyvalue images with the difference that the data are not on a raster structure.

Obviously, the reflectance image will only allow for the determination of the two planimetric shift parameters. Therefore, a two-step procedure is introduced:

- Height discrepancies between patches are determined by least squares matching constrained to vertical shift determination by using height as observation and keeping the planimetric shifts fixed.
- Planimetric discrepancies between patches are determined by least squares matching constrained to horizontal shift determination by using reflectance as observation and keeping the height shift fixed.

Thus, the determination of all three components of the shift between two patches of neighboring or crossing laserscanner data strips becomes possible.

3. Practical results

The combined height and reflectance data matching technique was applied to a high-density dataset of an area in The Netherlands acquired by the FLI-MAP 1 airborne laserscanner system (Pottle, 1998), installed on a helicopter. The dataset consists of first-pulse height measurement and 6-bit reflectance data; the point density is in the order of five points per square meter. Figure 2 shows a part of the dataset in three strips, containing a road crossing with white markings. Due to the absence of sufficient height contrast, the height data in the test area along the road allows only for the determination of a vertical shift between strips. The reflectance image can be considered complementary to the height image and seems well suited for the determination of horizontal shift parameters. Matching was applied to a total of 20 tie points between the strips, choosing circular patches with a radius of three meters containing texture provided by the white road markings.

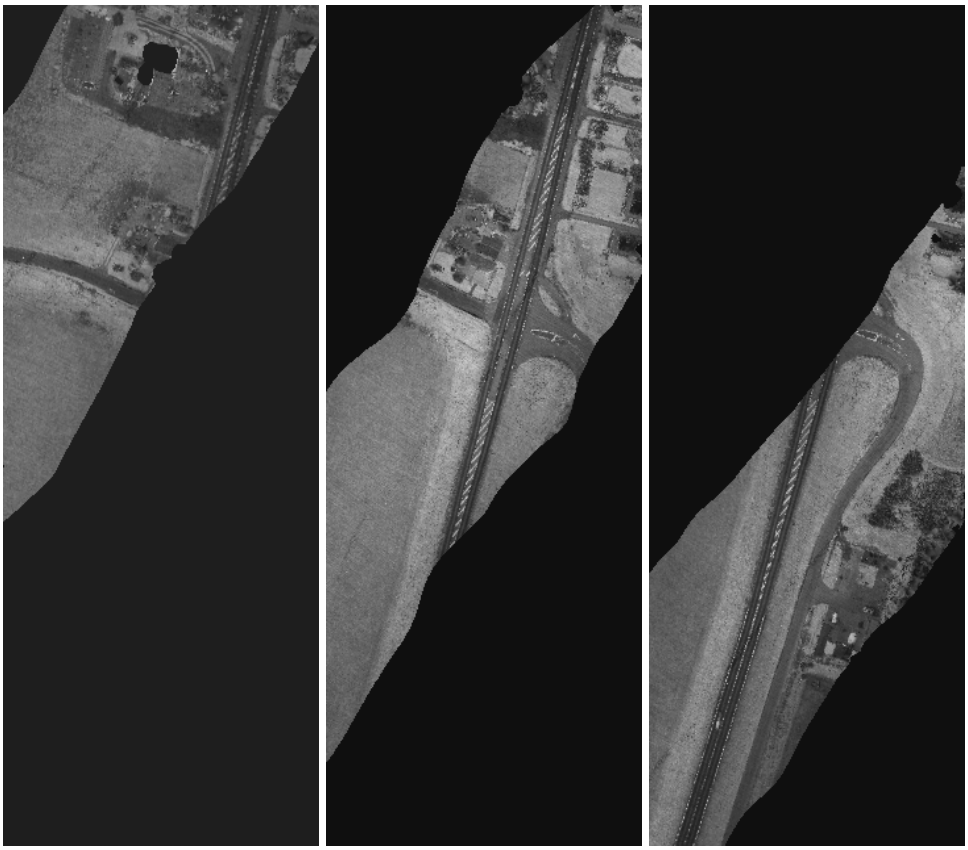

Figure 2: Reflectance image of a road crossing in three neighboring strips

The results of the application of the technique are listed in Table 1. The discrepancies over a 50 meter section of Figure 2 are shown in Figure 3. The amplitude of height discrepancies is in the order of 10-15 cm, while planimetric discrepancies of more than 40 cm occur. As discussed in (Maas, 2000), the estimated standard deviation of the planimetric shift parameters is too optimistic as a consequence of the stochastic properties in the covariance matrix – this is an inherent problem of least squares matching. Instead, variance measures in a local linear regression analysis based on a set of neighboring patches were used to obtain more realistic precision figures. Due to the fact that the data was obtained by a laserscanner system without INS, this assumption of linear strip deformation is probably not justified (cmp. Figure 3), so that the latter precision figure is contaminated by flightpath deviations and is thus too pessimistic as a measure for the accuracy potential of least squares matching. Roughly, the standard deviation of the horizontal shift parameters obtained from reflectance data can be estimated in the order of 10 cm, compared to an average point spacing of 40-50 cm in the dataset at hand. The estimation of the precision of the height shift parameter does not suffer from the limitations mentioned above; standard deviations of less than 1 cm can be obtained here.

Shift parameters [mm]			
	Planimetry (from reflectance)		Height
	X	Y	Z
strip M - L	-190 … 140	-460 … -100	-93 … -6
strip M - R	-180 … 220	-210 … +80	-46 … 91
Average standard deviation of shift parameters [mm]			
strip M - L	23	33	4
strip M - R	10	10	4
RMS from regression analysis of shift parameters [mm]			
strip M - L	123	136	36
strip M - R	70	80	33

Table 1: Results of height and reflectance matching from 20 patches in the section

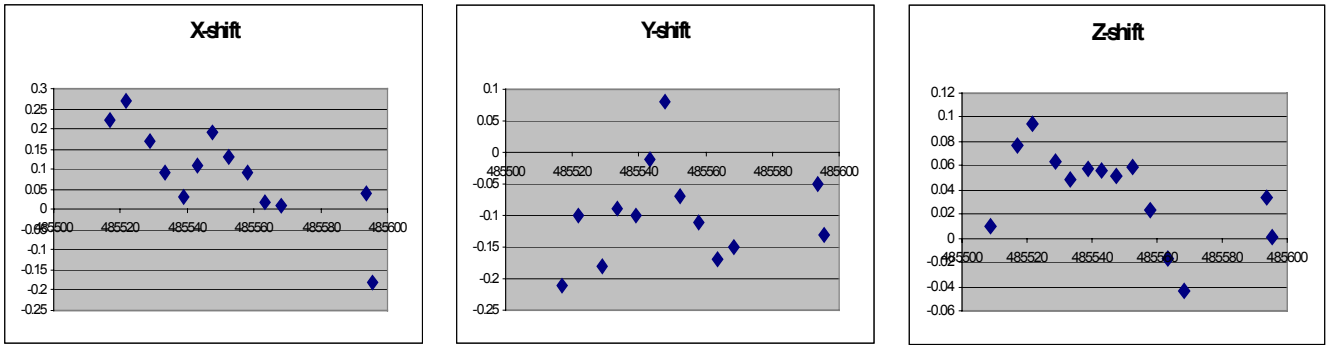

Figure 3: Patch shifts over 50 meter section in Figure 2

In addition to the road markings, a few well defined corners of fields and meadows were selected for reflectance-based matching. The results obtained from these points were only slightly worse than those of obtained from the road markings. The probe was, however, too small for secure statements.

4. Conclusion

Reflectance values of airborne laserscanner data may provide an interesting option for the determination of planimetric strip discrepancies in regions with poor height contrast. The possibility of simultaneous matching in height and reflectance data is especially relevant in flat areas, where the patch contrast situation in height data only allows the determination of the vertical shift parameter.

Limiting factors are given by the resolution of datasets and by the noise characteristics of laserscanner intensity data: The option is mainly relevant for high density datasets with point densities of at least one point per square meter. The high noise in laserscanner intensity data and the inherent undersampling of the technique will not allow to reach a precision potential which is comparable to the precision often achieved by matching applied to raster images obtained by solid state sensor cameras. Nevertheless, a precision significantly smaller than the average point spacing could be achieved in the practical tests, providing valuable input to laserscanner strip adjustment procedures.

More effort has to be spent on the suitability of different types of reflectance contrast and on the automatic selection of appropriate patches. Further research should also address the combined use of the full information of a laser pulse return in least squares matching, automatically balancing weight depending on height and reflectance contrast.

Acknowledgement:

The author would like to thank the Rijkswaterstaat Survey Department (RWS-MD, Delft, The Netherlands) for providing the Overijssel dataset used for the practical experiments.

References:

- Crombaghs, M.J.E., R. Brügelmann, E.J. de Min, 2000. On the adjustment of overlapping strips of laser-altimeter height data. In: International Archives of Photogrammetry and Remote Sensing, Vol. 33, Part B3/1, pp. 224-231.
- Burman, H., 2001: Calibration and orientation of laser scanner data. OEEPE workshop on Airborne Laserscanning and Interferometric SAR for Detailed Digital Elevation Models, Stockholm
- Kilian, J., 1994: Calibration methods for airborne laser systems. International Archives of Photogrammetry and Remote Sensing, Vol. 30, Part 1, pp. 42-46
- Maas, H.-G., 2000: Least-Squares Matching with Airborne Laserscanning Data in a TIN Structure. International Archives of Photogrammetry and Remote Sensing Vol. 33, Part 3A, pp. 548-555
- Oude Elberink, S., Maas, H.-G., 2000: The use of anisotropic height texture measures for the segmentation of laserscanner data. International Archives of Photogrammetry and Remote Sensing, Vol. 33, Part B3
- Pottle, D., 1998: Helicopter-based observations replace traditional surveying. Geodetic Info Magazine 2/98, pp. 62-65
- Vosselman, G., Maas, H.-G., 2001: Adjustment and filtering of raw laser altimetry data. OEEPE Workshop on Airborne Laserscanning and Interferometric SAR for Detailed Digital Elevation Models, Stockholm

3D Perceptual Organization of Laser Altimetry Data

Impyeong Lee, Toni Schenk
Dept. of Civil & Environmental Engineering and Geodetic Science
The Ohio State University
USA
lee.1517@osu.edu, schenk.2@osu.edu

Commision III, Working Group 3

KEY WORDS: Perceptual Organization, Segmentation, Merging, Grouping, LIDAR, Laser Altimetry, Points, 3D

ABSTRACT

Perceptual organization is to group sensory primitives arising from a common underlying cause by imposing structural organization on sensory data. It has been emphasized as a robust intermediate-level grouping process toward object recognition and reconstruction since it imparts robustness and computational efficiency to the perceptual process. Sarkar and Boyer (1993) proposed a classificatory structure for perceptual organization and clarified what should be done under each class. Despite intensive research on 2D data, 3D perceptual organization is still in its infancy, however. Increasing research efforts are needed to understand 3D data from various range sensors such as laser altimetry systems. Therefore, the purpose of this research is to develop a robust approach for constructing 3D perceptual organization from irregularly distributed 3D points acquired from laser altimetry systems. The scope of perceptual organization presented in this paper is limited to signal, primitive and structural levels. At the signal level, we organize raw 3D points into spatially coherent surface patches. Then, at the primitive level, we merge the patches into co-parametric surfaces and detect breaklines and occlusions. Finally, at the structural level, we derive useful surface combinations such as polyhedral structures. The approach has been successfully applied to real laser altimetry data. The organized output is on a much more abstract level than the raw data and makes information explicit. Thus, it serves as a valuable input to higher order perceptual processes, including the generation and validation of hypotheses in object recognition tasks.

1 INTRODUCTION

Perception is the process by which organisms interpret and organize sensory stimulus to produce a meaningful description of the world. Especially, the ability to impose organization on sensory data in human perception started to be emphasized by Gestalt psychologists from the early 20th century (Koffka, 1935; Khler, 1929). It has been recognized as a crucial component that makes human perception powerful and volatile. Hence, many systems in computer vision organize primitive sensor data into perceptually meaningful groups before advancing to higher-level processing such as object recognition. These grouping processes are known as perceptual organization, formally defined as a process that groups sensory primitives arising from a common underlying cause by imposing structural organization on sensory data (Sarkar and Boyer, 1993).

Since the roles of perceptual organization were emphasized as a robust intermediate-level vision process by Witkin and Tenenbaum (1983) and Lowe (1985), many researchers have demonstrated the importance of perceptual organization in the tasks under many levels and domains of computer vision, e.g., figure-ground discrimination (Herault and Horaud, 1993), motion-based grouping (Allmen and Dyer, 1993; Chang and Aggarwal, 1997), object recognition (Havaldar et al., 1996; Modayur and Shapiro, 1996; Nelson and Selinger, 1998; Zisserman et al., 1995), building detection (Henricsson, 1998; Lin et al., 1994) and change detection (Sarkar and Boyer, 1998).

Sarkar and Boyer (1993) propose a classificatory structure of perceptual organization based on the dimension over which organization is sought and the abstraction level of features to be grouped. The structure has two axes: one axis denotes 2D, 3D, 2D plus time and 3D plus time; and the other axis represents signal, primitive, structural and assembly level. For example, surface segmentation from laser altimetry data can be classified into 3D signal level perceptual organization. In addition, further grouping of the segmented surfaces falls under 3D primitive or structural level perceptual organization.

Even though they suggest what should be done under every class, the previous work has mainly concentrated on 2D organization, dealing with all the abstraction levels and emphasizing the structural level. In addition, some researchers also consider 2D plus time (Sarkar, 1995) but profound research is still required for successfully applying the organization to interpreting motion sequences. In 3D organization, most previous studies falls under signal level only, particularly focusing on range image segmentation. However, the need of perceptual organization in the various levels of 3D will significantly increase because 3D sensors become cheaper and more available. Hence, "perceptual organization in 3D" are emphasized as one of the most important research directions (Boyer and Sarkar, 1999).

The most important 3D sensors recently widely used in many photogrammetric applications are laser altimetry systems. A chain of photogrammetric processes traditionally starts from images. Inference of 3D information from images involves a matching process to find conjugated features from images (Schenk, 1999). However, matching is a highly intelligent process that cannot be easily archived by computers in spite of the astonishing development in artificial intelligence and computer vision during the last several decades. Therefore, the automation of the entire processes is still extremely challenging.

Laser altimetry data have been thus recently noticed as alternative or supportive to images, since laser altimetry systems produce 3D points by sampling directly physical surfaces. They provide a cloud of irregularly distributed raw sur-

face points consisting of the x, y, z coordinates for each laser footprint without radiometric information. In addition, multiple echo data, radiometric values at the laser wave length, the waveforms of returned laser pulses are also available depending on the systems but not considered in this research.

Applications using the laser altimetry data are rapidly increasing, ranging from DEM (Digital Elevation Model) construction to urban modelling. Many post-processing algorithms are reviewed by Tao and Hu (2001). Most of the algorithms typically involve interpolating into regular grid data, separating the ground surface, detecting upper-ground objects such as buildings (Gamba and Houshmand, 2000; Maas and Vosselman, 1999), trees (Hyyppa et al., 2001) and other objects (Axelsson, 1999) and further identifying their changes (Murakami et al., 1999).

Instead of introducing another application oriented algorithm, we intend to establish a middle-level process which are less dependent on an application and hence sufficiently general for various applications. Using this process, we will derive a robust, explicit and computationally efficient description from raw data, which usually include many redundancies and outliers. As the most suitable approach to perform this, we propose 3D perceptual organization, which has been proved as a robust intermediate process for various tasks in computer vision.

We significantly benefit from the use of 3D perceptual organization as an intermediate step toward various applications of laser altimetry data. Main advantages are summarized as follows:

- Explicitness: perceptual organization provides more abstract and explicit description of raw data. For example, we do not need 50 points sampled from a planar roof of a building and prefer to have explicitly the boundary and the parameters of the plane.
- More information available: according to the principle of Gestalt laws, one plus one is not just two but much more than two. We can compute from a segmented surface various additional information, which is not meaningful to a point, such as point density, surface roughness, outlier ratio, area, orientation, surface normal and so on.
- Robustness: a grouping process contributes to identifying outliers since it tries to group mutually consistent entities and non-grouped entities usually corresponds to outliers. Hence, grouped entities are a robust description of the original data.
- Reduced complexity: perceptual organization significantly reduces the number of entities thanks to its explicitness and abstractness. For example, when we detect buildings from laser altimetry data, if we search from perpendicular surface combinations rather than from all surfaces (or extremely all points), the number of entities that we should check with a building hypothesis is much smaller.

In summary, the objective of this research is to present a framework that computes 3D perceptual organization from laser altimetry data. Here, the computed organization should be a robust, explicit and computationally efficient description of the original data so that they can be flexibly used as an input for various higher-level processes. The problem is more formally stated in the next subsection.

The problem statement is followed by three sections which describe the proposed approach, show the experimental results and conclude with discussion and future research, respectively.

1.1 Problem Statement

Given a set of irregularly distributed 3D surface points acquired from laser altimetry systems, compute perceptual organization at signal, primitive and structural levels. At the signal level, we organize the raw points into spatially coherent surface patches with their boundaries. Then, at the primitive level, we merge the patches into co-parametric surfaces, refine the boundaries and identify breaklines and occlusions. Finally, at the structural level, we derive useful surface combination such as parallel surfaces and continuous surfaces, identify the ground surface and generate hypothesized surfaces for the occluded areas. Table 1 summarizes the inputs and outputs at each organization level.

Table 1: Inputs and outputs at each organization level

Level	Inputs	Outputs
Signal	Points	Patches with their boundaries
Primitive	Patches	Surfaces with refined boundaries, breaklines and occlusions
Structural	Surfaces	Surface combinations with hypothesized surface

2 THE PROPOSED APPROACH

As acknowledged from the objective of this research presented in section 1, we have been focusing on developing an overall framework rather than inventing a new specific algorithm to constitute the framework. It is because the use of perceptual organization for the post-processing of laser altimetry data has been rare with our best knowledge and also the 3D perceptual organization is still in infancy although tremendous research has been performed for 2D data (Boyer and Sarkar, 1999). Thus, our fundamental strategy for this work is to review various research efforts in 2D data and extend them for 3D data, particulary in the domain of laser altimetry data, even though we developed inevitably new pieces in several cases.

Despite the lack of previous studies, we managed to introduce two representative studies. At the signal level, Ahuja and Tuceryan (1989) extracted perceptual organization from irregularly distributed 2D points called dot patterns. They classified dots into interior dots, border dots, curve dots, and isolated dots using their relationships with the neighborhood defined by Vornoi diagram. They also used a probabilistic relaxation process to produce a globally optimal result. At the primitive and structural level, Fisher (1989) grouped surfaces reconstructed from 2D images into 'surface clusters', that is, perceptually meaningful surface combinations. Since the surfaces are reconstructed from 2D images, they have many different aspects from those from 3D laser points. However, his research is a valuable basis for this work.

Based on the relevant studies including not only these representative studies but also many valuable research regarding 2D perceptual organization, range image segmentation and unsupervised point clustering, we establish a framework comprised of three grouping processes at the signal, primitive, and

structural levels, where the inputs and outputs at each level are previously summarized in Table 1.

The process at each level includes preprocessing, main processing and postprocessing. Preprocessing performs the task supportive to grouping such as defining the adjacency among features and computing the attributes of features. Postprocessing complements grouping outcomes, for example, by filling gaps, determining boundaries, identifying breaklines and occlusions, adding hypothesized surfaces, and inferring more complex entities such as the ground surface.

The main processing at each level is designated as segmentation, merging, and grouping, respectively. Although we use three different terms so that they can be more appropriate for the features to be grouped at each level, all of them are actually classified to grouping processes.

The grouping process consists of three components which should be deliberately selected mainly based on the features to be grouped and the groups to be sought. The components are "grouping cues", "testable feature subsets", and "cue integration method" (called grouping mechanism here), as described by Berengolts and Lindenbaum (2001). Grouping cues are the information that indicates whether two or more entities arise from an object, such as proximity, connectedness, continuity, similarity, parallelism, symmetry, common region and closure (Sarkar and Boyer, 1994b). Testable feature subsets indicate a subset of features, inside of which we examine the validity of the grouping cues. The size of the subset can be determined by considering the meaningful range of the cues and the computational complexity. Grouping mechanism is the means by which we produce globally optimized grouping of the entire set by integrating the grouping cues locally computed inside the testable feature subsets. The method is frequently implemented as an optimization process that minimizes a cost function.

One should also determine how to represent the perceptual information being processed during the grouping process. Representation using a graph structure where nodes indicate the entities to be grouped and arcs describe perceptual information between the entities is a promising choice as indicated by many other researchers (Zahn, 1971; Geman et al., 1990; Herault and Horaud, 1993; Matula, 1997; Shaashua and Ullman, 1988; Shapiro and Haralick, 1979; Wu and Leahy, 1993).

2.1 Signal Level

At the signal level, we group raw 3D surface points into surface patches (or point clusters). The process is summarized in Figure 1.

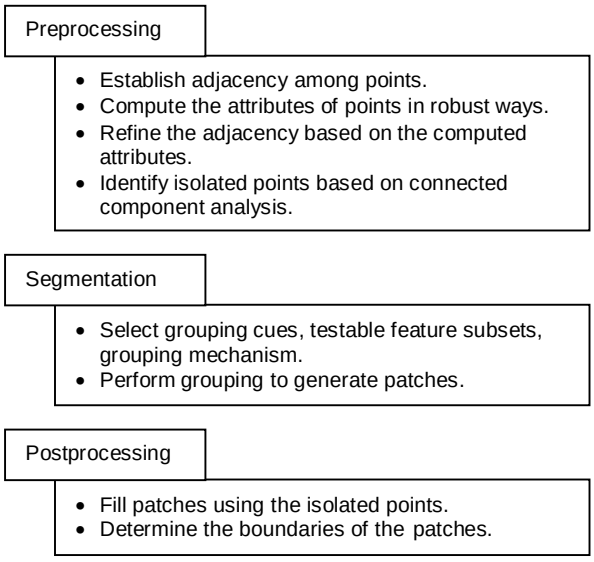

Figure 1: Signal level process

Adjacency: neighborhood of a point Adjacency defining the neighborhood of a point is required for a grouping process, which often access the neighborhood to compute multi-feature grouping cues and check them with grouping criteria. Neighborhood in a set of irregularly distributed points is not obvious, however. Various neighborhood concepts are well reviewed early by Ahuja and Tuceryan (1989) and recently by Chaudhuri (1996). We describe several examples here. The best one among them is determined according to the size and distribution of a data set.

The Delaunay triangulation is a acceptable choice since the region of influence of a point is determined by the Voronoi diagram and the adjacency of the regions is then expressed by the edges of the Delaunay triangulation. Some researchers use 2D Delaunay triangulation considering only horizontal coordinates (Maas and Vosselman, 1999) while others also use 3D Delaunay triangulation (Lee and Schenk, 2001). The computational requirement constructing the Delaunay triangulation is the hindrance to its use in a large data set.

Simple approaches such as selecting the k nearest points and the points inside a sphere of a fixed radius are thus useful in such sets. In addition to proximity considered by these approaches, the distribution of neighboring points is important. With the idea that neighborhood should be not only as near but also as symmetric as possible, Chaudhuri (1996) propose 'nearest centroid (or median) neighborhood'.

Attributes of points Attributes of points are the fundamental information which we can use to examine grouping hypotheses. The most primitive attribute of a point is its 3D coordinates. We frequently require more complex information such as point density, roughness, surface normal, plane parameters, outlier ratio and other properties which can be defined with a set of points rather than a single point. Such complex attributes are meaningful since the laser footprint of a point is actually not a zero-dimensional point but a two-dimensional elliptical area.

Although they can be considered as the attributes of a point, they cannot be defined or computed from only a point. Therefore, we compute them from a small patch defined around a point. The patch should be large enough to include the points from which the attribute can be computed. For example, at least three points are required for determining surface normal. Contrarily, the patch should be small enough to represent a point and its local area. In addition, the patch should consist of the neighboring points which locate not only near to its representing point but also symmetrically around the point. The nearest centroid (or median) neighborhood can be thus a strong candidate.

To compute an attribute of a patch, we establish a system of the equations, which formalizes the contribution of the interior points to the attribute. For example, if we compute plane parameters from a patch, each equation shows a plane equation substituted by the three coordinates of a point with the noises associated with each coordinate.

The computation of the attributes from this established system (usually overdetermined) should be equipped with a robust estimation approach rather than the least mean squares approach, because every small patch can include outliers, which result in an significantly different attribute comparing to the others. For example, Least Median Square Error (LMedS) estimation is a promising alternative since it allows up to 50 % outlier ratio in theory (Koster and Spann, 2000).

In addition, we measure the tendency of a point to be an outlier from every computation of the attribute. After the computation of all the attributes, we conservatively classify some points into outliers by synthesizing the outlier tendency measured from each computation.

Refined adjacency The points classified as outliers with significant evidence should not maintain its adjacency to at least the representing point of the patch. Accordingly, we refine the adjacency established before so that the outliers cannot be linked to the inliers.

Isolated points Based on the refined adjacency, we classify isolated points by the connected component analysis. This analysis produces groups of connected points based on the adjacency. Some of the groups may include very small number of points, which can be labelled isolated points.

Grouping cues among points Another aspect of grouping is the selection of grouping cues. At the signal level, proximity, similarity and continuity are typically considered. It is natural to group points which locate near to each other and show similar attributes. Grouping cues can be defined on at least two points. The more entities considered, the stronger cues can be realized. For example, if we intend to group the points expected to be on the same plane, we can check the similarity of the fitted plane parameters of the points. If we have more points involved, the similarity is stronger evidence for grouping. However, such multi-feature cues cannot be explicitly represented in a graph structure, since it can only include as arcs the bi-feature cues. To overcome this, Amir and Lindenbaum (1998) propose a procedure that enhances the strength of the bi-feature cues based on the multi-feature cues founded. They increase the strength of a bi-feature cue of two entities if multi-feature cues around the entities support the bi-feature cues and decrease them otherwise.

Testable feature subsets If we compute the grouping cues from all the points in a set, we would be confronted with the combinatorial explosion. Furthermore, some cues such as proximity are meaningless for two distant points. Hence, we have to specify a certain range named testable feature set, only the entities inside which we consider to compute these grouping cues. The range is deliberately determined by considering the validity of the cues and the computational complexity. At the signal level organization, a point and its connected points in terms of the refined adjacency are considered as the testable feature set.

Grouping mechanism Another component to be determined for a grouping process is grouping mechanism. The mechanisms range from optimized processes such as simulated annealing and probabilistic relaxation, usually involving heavy computation, to the connected component clustering of only linear time complexity.

According to the performance of the connected component clustering assessed by Berengolts and Lindenbaum (2001), it can be suitable for many practical applications requiring less computation complexity and medium quality of grouping. Iterative growing is also a strong candidate, which is similar to connected component clustering since it also follows the connection among the entities. Its uniqueness comes from performing iteratively testing a new point, including (or discarding) the point, and updating the attributes of a growing group (Lee and Schenk, 2001). In addition, some researchers use scalar or vector voting (Sarkar and Boyer, 1994a; Guy and Medioni, 1997; Tang and Medioni, 1998; Lee and Medioni, 1999) and graph spectral partition (Sarkar and Soundararajan, 2000).

Although the selection of a mechanism depends on the allowable computation complexity and the application to be sought, we are not willing to choose a complex time-consuming process in general. It is because grouping as a middle-level process should reduce the overall complexity of a whole process. Consequently, iterative growing is a reasonable choice.

Segmented patches: point clusters Based on the grouping cues, the testable feature sets, and the grouping mechanism considerately selected, the segmentation process is applied to a set of points. The segmented outputs are spatially coherent surface patches represented by the interior points and the surface parameters shared by them.

Filling The segmented patches may have small holes. Some of them are filled if they are matched to their close isolated points. Similar approach is used by Boyer et al. (1994).

Boundaries Additional useful description of the segmented patches are their boundaries which can be computed as a post-processing from the distribution of the interior points. It is a intricate problem that many researchers have attacked because the interior points are irregularly distributed on a 2D surface locating in 3D space.

An option is the convex hull (Berg, 2000), which represents the outlines of the minimum convex area covering all the interior points. It is good for representing an overall coverage of a patch but weak for describing the actual boundaries which may include concave shapes and holes. To accommodate concave shape and holes in a certain degree, Richards and Mullins (1977) presented the space filling hull defined as the union of the discs, each of which is associated with a point. The radius of the disc is a parameter to be determined and can be selected as the half distance between a point and its nearest point (Toussaint, 1988). Edelsbrunner et al. (1983) proposed α-shape as a general description of the boundaries. It is a family of graphs, each of which is a subset of Delaunay triangulation (Berg, 2000). The parameter α varies ∞ to 0 and controls the level of details. It conceptually corresponds to the radius of the space filling hull. It is extended to weighted α-shape for accommodating the variable density of points (Edelsbrunner, 1992). By synthesizing the ideas of the space filling hulls and α shapes, Melkemi and Djebali (2000) and Melkemi and Djebali (2001) propose more sophisticated description such as "A-shapes" and "weighted A-shapes", respectively. While most of these description are subsets of the Delaunay triangulation or a regular triangulation, Chaudhuri et al. (1997) propose "r-shape" based on a regular grid defined over the points with the intervals prudently selected by considering the point density.

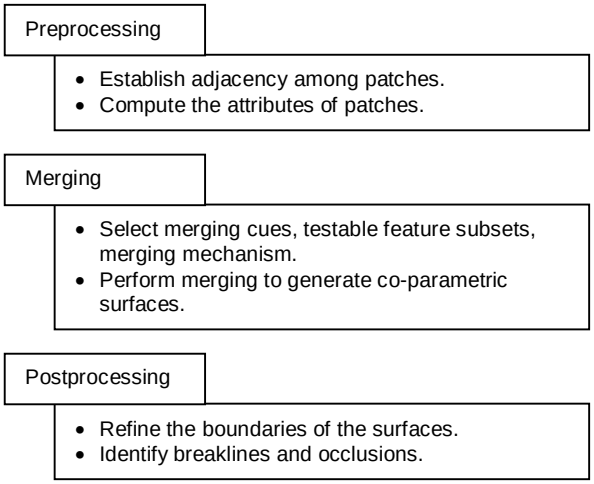

Figure 2: Primitive level process

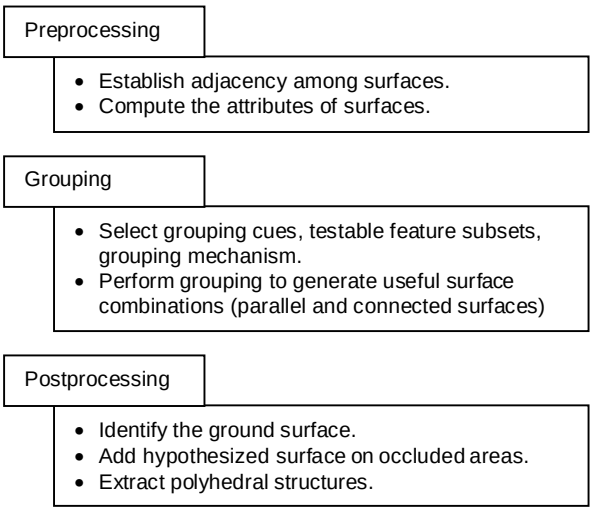

Figure 3: Structural level process

2.2 Primitive Level

At the primitive level, we merge the patches segmented at the signal level into co-parametric surfaces, refine the boundaries of the merged surfaces and identify the breaklines and occluded areas, as shown in Figure 2

Adjacency: neighborhood of a patch The adjacency established among points at the signal level is extended for defining the adjacency between edges and between patches. If at least a point of an edge is adjacent to a point of another edge, we define that the two edges are adjacent each other. The boundaries of a patch computed at the signal level are a set of the edges, each of which links two boundary points. If at least a boundary edge of a patch is adjacent to a boundary edge of another patch, we define that the two patches are adjacent each other. Furthermore, we define the ratio between the total length of adjacent boundary edges and the total length of all boundary edges as a measure indicating the degree of adjacency between patches.

Attributes of patches The attributes of patches are various, ranging from those already described at the signal level such as point density and roughness to those associated with the shape of the boundaries such as the orientation and the aspect ratio. The most useful attributes for the merging process are the surface parameters indicating the shape of the patch (for example, plane parameters) and their associated fitting errors.

Merging cues among patches The merging cues we selected are proximity and similarity so that we can merge two patches which are sufficiently near and shows the similar attributes, that is, the surface parameters and their fitting errors.

Testable feature sets Testable feature sets are simply defined based on the adjacency among patches. We intend to check every pair of adjacent patches with a merging hypothesis.

Merging mechanism We use iterative growing approach similar to the approach that Koster and Spann (2000) utilize for range image segmentation. It iteratively proceeds until no adjacent patches meet merging criteria. At each iteration, it investigates every pair of adjacent patches and computes a measure indicating how well each pair satisfies the merging criteria. For example, if we use a statistical test such as F-test to check a merging hypothesis, the p-value is the measure. Then, merging starts from the pair with the largest measure in a descending order of the measure. This contributes to producing a globally optimal merged set.

Merged surfaces The iterative growing approach equipped with the merging criteria based on adjacency and similarity produces a set of merged co-parametric surfaces. Their preliminary boundaries are computed using the same method as at the signal level. Based on the boundaries, we refine the adjacency among them.

Refined boundaries Refined boundaries are interesting outcomes supporting the Gestalt argument that one plus one is much more than two. Since no laser pulse can be reflected from only 0 or 1-dimensional entities in general (extraordinarily, from electrical power transmission lines, see (Axelsson, 1999)), we never directly extract from a set of laser points such information as the boundary of a roof. However, we can accurately infer the boundaries from two adjacent surfaces produced under the Gestalt principles. The boundaries of all adjacent surfaces are refined using their intersections.

Breaklines and occlusions The boundary edges of a surface which are not adjacent to other surface are identified as breaklines. Every breakline invokes a hypothesis for occlusion. The empty space between the breaklines and the nearest boundary of other surfaces are thus hypothesized as occlusions.

2.3 Structural Level

At the structural level, we group the merged co-parametric surfaces organized at the primitive level into useful surface combinations. Furthermore, we identify the ground surface, add hypothesized surfaces over occlusions and extract polyhedral structures. The process is summarized in Figure 3.

Adjacency: Neighborhood of a surface The adjacency among surfaces is also defined using the adjacency among their boundaries, which is already computed during the post-processing stage at the primitive level. In addition to the 3D adjacency, we establish in a similar way the 2D adjacency, that is, the adjacency defined by considering only the horizontal locations.

Attributes of surfaces All the same attributes as defined at the primitive level are meaningful at this level. Roughness, surface normal and many parameters describing the shape of the boundary are particularly useful.

Grouping cues among surfaces Several cues can be selected from various choices such as proximity, connectedness, continuity, similarity, parallelism, symmetry, common region and closure depending on the properties of the group to be sought. For example, proximity, connectedness and continuity are particularly useful to group the surfaces into the ground surface.

Testable feature subsets While we use just the adjacent features at the signal and primitive level, we should define the testable subsets by deliberately considering the selected attributes and cues. For example, the range where we check parallelism should be proportional to the area of the surface rather than just constant.

Grouping mechanism The mechanism can be also selected among the various ones described at the signal level. The connected component analysis is very useful in many applications such as identifying the ground surface and polyhedral structures.

Connected surfaces They are easily found by the connected component analysis on the 3D adjacency graph.

Parallel surfaces We define for every surface a testable feature subset, the size of which is proportional to the area of each surface. We examine the parallelism based on the similarity of the surface normal with every entity inside this subset. Based on the result, we construct a parallelism graph where an arc indicates the parallelism of the two surface linked through the arc. Parallel surfaces are thus identified by the connected component analysis on the parallelism graph.

The ground surface We examine continuity with the same testable feature subset as used for parallel surfaces and construct a continuity graph. The largest connected components of the graph is detected as the ground surface.

Hypothesized surfaces For each occlusion detected at the primitive level, we add a hypothesized surface and update the adjacency. For example, a roof of a building is adjacent to the ground surface not in 3D but in 2D. This inconsistency triggers a hypothesis of a vertical surface between them.

Polyhedral structures We perform the connected component analysis on the graph constructed by subtracting the detected ground surface and the very rough surfaces from the adjacency graph. Each connected surfaces corresponds a polyhedral structure.

3 THE EXPERIMENTAL RESULTS

The proposed approach was applied to constructing perceptual organization from a real data set. As a test area we selected a sub-site of the Ocean City test site. A more detailed description of this test site is presented by Csatho et al. (1998). The sub-site includes 4633 points with a point density of 1.2 points/m^2.

The data set, acquired by an airborne laser altimetry system, covers a small portion of an urban area in Ocean City. As Figure 4 illustrates, the sub-site contains a large building with complex roof structures.

The patches segmented at the signal level are visualized with the boundaries in Figure 5. The adjacency is defined by a sphere of a fixed radius (2.5 m) and then refined by eliminating the links between the outliers and inliers. The similarity of the plane parameters and the roughness are used as the grouping criteria. Each patch thus indicates a plane with certain roughness. The boundaries are then computed using the α-shape algorithm with $\alpha = 2.5$.

The merged surfaces with the preliminary and the refined boundaries are shown in Figure 6. The similarity of plane parameters and roughness with less strict threshold is used as merging criteria. The criteria are checked with the F-test and the resulting p-value is used for a measure indicating the tendency of merging. Merging starts from the patches with the highest measure. The merging process iteratively repeats until no adjacent patches can satisfy the criteria. The boundaries are also refined based on the intersections between surfaces. The breaklines and the occlusions are also identified.

The ground surface and polyhedral structure organized at the structural level are shown in Figure 7. The ground surface are polyhedral structures are identified based on the continuity graph and the 2D adjacency graph, respectively.

4 CONCLUSIONS

We recognized the need of an intermediate process common toward various applications using laser altimetry data. As the common process, we proposed generating a robust, abstract and explicit description from the raw data, called perceptual organization. For the process, we established a framework comprised of three organization processes at the signal, primitive and structural levels, represented as segmentation, merging and grouping, respectively. Furthermore, we elaborated the diverse components constituting the framework, inspired by the previous work on perceptual organization in various levels and domains.

The experimental results based on real data illustrate the outcomes expected at each level, demonstrate the good performance of the proposed approach and emphasize the need of perceptual organization as an intermediate process. A complete quantitative and computational analysis using various synthetic and real data will be performed for a reliable assessment about the performance. Furthermore, we will demonstrate the effectiveness of the proposed perceptual organization to higher-level processing by applying them to building reconstruction from urban data.

REFERENCES

Ahuja, N., Tuceryan, M., 1989. Extraction of early perceptual structure in dot patterns: integrating region, boundary, and component gestalt. Computer Vision, Graphics, and Image Processing 48 (3), 304–356.

Allmen, M., Dyer, C. R., 1993. Computing spatiotemporal relations for dynamic perceptual organization. CVGIP: Image Understanding 58 (3), 338–351.

Amir, A., Lindenbaum, M., 1998. A generic grouping algorithm and its quantitative analysis. IEEE Transactions on Pattern Analysis and Machine Intelligence 20 (2), 168–185.

Axelsson, P. E., 1999. Processing of laser scanner data - algorithms and applications. ISPRS Journal of Photogrammetry and Remote Sensing 54 (2-3), 138–147.

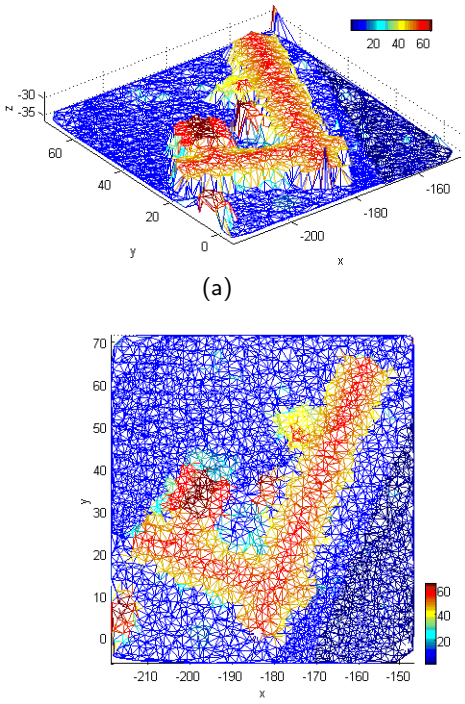

Figure 4: The test data is visualized as the mesh graph based on the Delaunay triangulation in (a) 3D and (b) 2D view.

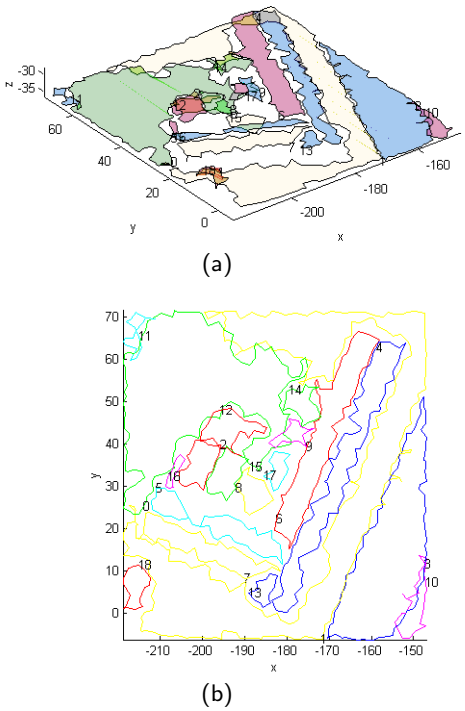

Figure 5: The segmented patches organized at the signal level are visualized with the boundaries in (a) 3D and (b) 2D view.

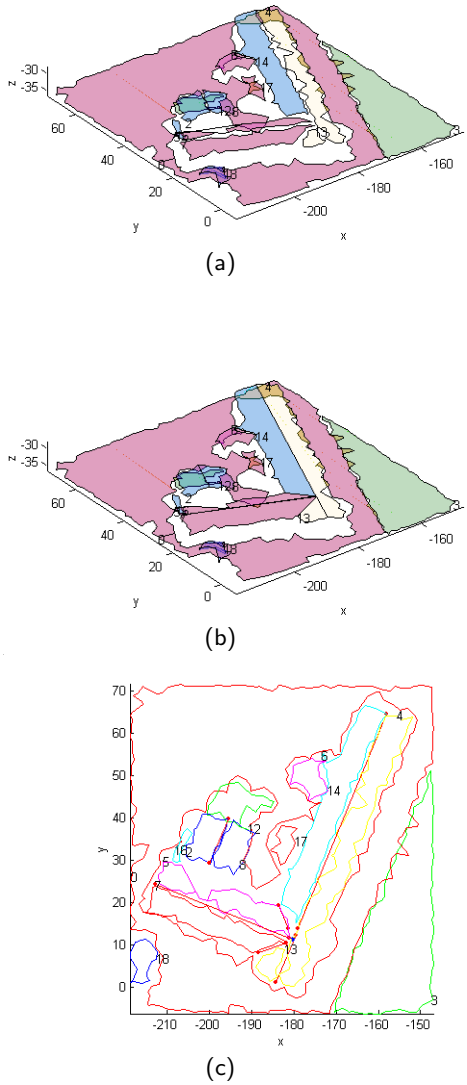

Figure 6: The merged surfaces organized at the primitive level are visualized with the preliminary boundaries in (a) and with the refined boundaries (b). The preliminary boundaries, the intersections (red lines and dots) and the corners (blue dots) are also indicated in (c).

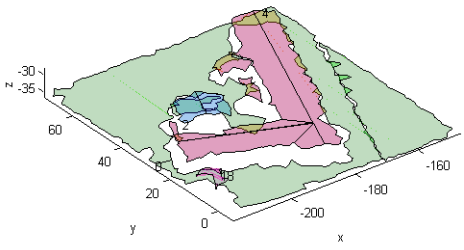

Figure 7: The ground surfaces (green) and the polyhedral structure organized at the structural level are visualized. The same color indicates the same group.

Berengolts, A., Lindenbaum, M., 2001. On the performance of connected components grouping. International Journal of Computer Vision 41 (3), 195–216.

Berg, M. d., 2000. Computational geometry : algorithms and applications, 2nd Edition. Springer, Berlin ; New York.

Boyer, K. L., Mirza, M. J., Ganguly, G., 1994. The robust sequential estimator: a general approach and its application to surface organization in range data. IEEE Transactions on Pattern Analysis and Machine Intelligence 16 (10), 987–1001.

Boyer, K. L., Sarkar, S., 1999. Perceptual organization in computer vision: status, challenges, and potential. Computer Vision and Image Understanding 76 (1), 1–5.

Chang, Y.-L., Aggarwal, J. K., 1997. Line correspondences from cooperating spatial and temporal grouping processes for a sequence of images. Computer Vision and Image Understanding 67 (2), 186–201.

Chaudhuri, A. R., Chaudhuri, B. B., Parui, S. K., 1997. A novel approach to computation of the shape of a dot pattern and extraction of its perceptual border. Computer Vision and Image Understanding 68 (3), 257–75.

Chaudhuri, B. B., 1996. A new definition of neighborhood of a point in multi- dimensional space. Pattern Recognition Letters 17 (1), 11–17.

Csatho, B., Krabill, W., Lucas, J., Schenk, T., 1998. A multisensor data set of an urban and coastal scene. International Archives of Photogrammetry and Remote Sensing 32 (3/2), 26–31.

Edelsbrunner, H., 1992. Weighted alpha shape. Tech. Rep. UIUCDCS-R-92-1760, University of Illinois at Urbana-Champaign.

Edelsbrunner, H., Kirkpatrick, D. G., Seidel, R., 1983. On the shape of a set of points in the plane. IEEE Transactions on Information Theory 29 (4), 551–559.

Fisher, R. B., 1989. From surfaces to objects : computer vision and three dimensional scene analysis. J. Wiley, Chichester ; New York.

Gamba, P., Houshmand, B., 2000. Digital surface models and building extraction: a comparison of ifsar and lidar data. IEEE Transactions on Geoscience and Remote Sensing 38-2 (4), 1959–1968.

Geman, D., Geman, S., Graffigne, C., Dong, P., 1990. Boundary detection by constrained optimization. IEEE Transactions on Pattern Analysis and Machine Intelligence 12 (7), 609–628.

Guy, G., Medioni, G., 1997. Inference of surfaces, 3d curves, and junctions from sparse, noisy, 3d data. IEEE Transactions on Pattern Analysis and Machine Intelligence 19 (11), 1265–1277.

Havaldar, P., Medioni, G., Stein, F., 1996. Perceptual grouping for generic recognition. International Journal of Computer Vision 20 (1-2).

Henricsson, O., 1998. The role of color attributes and similarity grouping in 3d building reconstruction. Computer Vision and Image Understanding 72 (2), 163–184.

Herault, L., Horaud, R., 1993. Figure-ground discrimination: a combinatorial optimization approach. IEEE Transactions on Pattern Analysis and Machine Intelligence 15 (9), 899–914.

Hyyppa, J., Kelle, O., Lehikoinen, M., Inkinen, M., 2001. A segmentation-based method to retrieve stem volume estimates from 3-d tree height models produced by laser scanners. IEEE Transactions on Geoscience and Remote Sensing 39 (5), 969–975.

Khler, W., 1929. Gestalt psychology. H. Liveright, New York.

Koffka, K., 1935. Principles of gestalt psychology, lst Edition. International library of psychology, philosophy and scientific method. Harcourt Brace and Company, New York,.

Koster, K., Spann, M., 2000. Mir: an approach to robust clustering-application to range image segmentation. IEEE Transactions on Pattern Analysis and Machine Intelligence 22 (5), 430–444.

Lee, I., Schenk, T., 2001. Autonomous extraction of planar surfaces from airborne laser scanning data. In: Proc. ASPRS conference. St. Louis, MO, USA.

Lee, M.-S., Medioni, G., 1999. Grouping ., -, to , theta , into regions, curves, and junctions. Computer Vision and Image Understanding 76 (1), 54–69.

Lin, C., Huertas, A., Nevatia, R., 1994. Detection of buildings using perceptual grouping and shadows. In: Proc. IEEE Conference on Computer Vision and Pattern Recognition. Los Alamitos, CA, USA, pp. 62–69.

Lowe, D. G., 1985. Perceptual organization and visual recognition. Kluwer Academic Publishers, Hingham, MA, U.S.A.

Maas, H. G., Vosselman, G., 1999. Two algorithms for extracting building models from raw laser altimetry data. ISPRS Journal of Photogrammetry and Remote Sensing 54 (2-3), 153–163.

Matula, D., 1997. Graph theoretic techniques for cluster analysis algorithms. In: Classification and clustering. Academic Press, pp. 95–129.

Melkemi, M., Djebali, M., 2000. Computing the shape of a planar points set. Pattern Recognition 33 (9), 1423–36.

Melkemi, M., Djebali, M., 2001. Elliptic diagrams: application to patterns detection from a finite set of points. Pattern Recognition Letters 22 (8), 835–44.

Modayur, B. R., Shapiro, L. G., 1996. 3d matching using statistically significant groupings. In: Proc. International Conference on Pattern Recognition. Los Alamitos, CA, USA, pp. 238–242 vol.231.

Murakami, H., Nakagawa, K., Hasegawa, H., Shibata, T., Iwanami, E., 1999. Change detection of buildings using an airborne laser scanner. ISPRS Journal of Photogrammetry and Remote Sensing 54 (2-3), 148–152.

Nelson, R. C., Selinger, A., 1998. A cubist approach to object recognition. In: International Conference on Computer Vision. New Delhi, India, pp. 614–621.

Richards, F. M., Mullins, L. J., 1977. Areas, volumes, packing, and protein structure. In: Annual review of biophysics and bioengineering, vol.6. Palo Alto, CA, USA, pp. 151–76.

Sarkar, S., 1995. Tracking 2d structures using perceptual organizational principles. In: Proc. International Symposium on Computer Vision. Los Alamitos, CA, USA, pp. 283–288.

Sarkar, S., Boyer, K. L., 1993. Perceptual organization in computer vision: a review and a proposal for a classificatory structure. IEEE Transactions on Systems, Man and Cybernetics 23 (2), 382–399.

Sarkar, S., Boyer, K. L., 1994a. A computational structure for preattentive perceptual organization: graphical enumeration and voting methods. IEEE Transactions on Systems, Man and Cybernetics 24 (2), 246–267.

Sarkar, S., Boyer, K. L., 1994b. Computing perceptual organization in computer vision. Series in machine perception and artificial intelligence ; v. 12. World Scientific, New Jersey, USA.

Sarkar, S., Boyer, K. L., 1998. Quantitative measures of change based on feature organization: eigenvalues and eigenvectors. Computer Vision and Image Understanding 71 (1), 110–136.

Sarkar, S., Soundararajan, P., 2000. Supervised learning of large perceptual organization: graph spectral partitioning and learning automata. IEEE Transactions on Pattern Analysis and Machine Intelligence 22 (5), 504–525.

Schenk, T. F., 1999. Digital photogrammetry. TerraScience, Laurelville, OH, USA.

Shaashua, A., Ullman, S., 1988. Structural saliency: the detection of globally salient structures using a locally connected network. In: Proc. International Conference on Computer Vision. Washington, DC, USA, pp. 321–327.

Shapiro, L. G., Haralick, R. M., 1979. Decomposition of two-dimensional shapes by graph-theoretic clustering. IEEE Transactions on Pattern Analysis and Machine Intelligence (1), 10–20.

Tang, C.-K., Medioni, G., 1998. Inference of integrated surface, curve and junction descriptions from sparse 3d data. IEEE Transactions on Pattern Analysis and Machine Intelligence 20 (11), 1206–1223.

Tao, C. V., Hu, Y., 2001. A review of post-processing algorithms for airborne lidar data. In: Proc. ASPRS conference. St. Louis, MO, USA.

Toussaint, G. T., 1988. A graph-theoretical primal sketch. In: Toussaint, G. T. (Ed.), Computational Morphology. North-Holland, Amsterdam, pp. 229–260.

Witkin, A., Tenenbaum, J., 1983. On the role of structure in vision. In: Beck, J., Hope, B., Rosenfeld, A. (Eds.), Human and Machine Vision. Academic Press, New York, pp. 481–543.

Wu, Z., Leahy, R., 1993. An optimal graph-theoretic approach to data clustering - theory and its application to image segmentation. IEEE Transactions on Pattern Analysis and Machine Intelligence 15 (11), 1101–1113.

Zahn, C. T., 1971. Graph-theoretical methods for detecting and describing gestalt clusters. IEEE Transactions on Computers (1), 64–82.

Zisserman, A., Mundy, J., Forsyth, D., Liu, J., Pillow, N., Rothwell, C., Utcke, S., 1995. Class-based grouping in perspective images. In: Proc. International Conference on Computer Vision. Los Alamitos, CA, USA, pp. 183–188.

Comparing Probabilistic and Geometric Models On Lidar Data

Roberto Fraile and Steve Maybank
The University of Reading, UK

September 2001

Abstract

A bottleneck in the use of Geographic Information Systems (GIS) is the cost of data acquisition. In our case, we are interested in producing GIS layers containing useful information for river flood impact assessment.

Geometric models can be used to describe regions of the data which correspond to man-made constructions. Probabilistic models can be used to describe vegetation and other features.

Our purpose is to compare geometric and probabilistic models on small regions of interest in lidar data, in order to choose which type of models renders a better description in each region. To do so, we use the Minimum Description Length principle of statistical inference, which states that best descriptions are those which better compress the data. By comparing computer programs that generate the data under different assumptions, we can decide which type of models conveys more useful information about each region of interest.

1 Introduction

High density sources of information, such as lidar, compare with traditional topographic surveys on the vast amount of information available. Automation in the processing of lidar data is not only required for reasons of speed and accuracy, but it also helps to find new ways of understanding the data. The initial assumption is that the best descriptions of objects are the shortest ones, when those descriptions are built taking into account the context information required to reproduce those objects [4, 5] Our purpose is to produce constructive models, in the form of computer programs, that can reproduce the data, are as compact as possible, convey the knowledge we have about the data, and which we can compare using a single measure, their length in bits. This approach is based in the theory of Kolmogorov Complexity, most popular under the perspective of the Minimum Description Length (MDL) principle [8].

A proportion of past work in reconstruction from range images [1, 2] starts from the assumption that the range data represented surfaces with continuity properties. This is not the case with the lidar data we have, representing not only topographic features of terrain but also buildings and vegetation, which are not suitable for representation in terms of curvatures.

In this paper present work towards the selection of appropriate models, with examples on the classification of lidar data using a narrow family of models. Similar work in applications of MDL has spanned over a wide range of applications, for example [3] is a review of MDL from the point of view of machine learning. See [6] for an application to computer vision.

The interest of this approach is in the way it could help to handle increasingly complex models, by helping in the comparison between heterogenous families of models, and in the explicit use of prior knowledge.

We introduce the principle and report an application in which lidar images are segmented in quadtrees [9] and the resulting cells are classified.

2 Model Selection

Constructive models allow us to compare between very heterogenous alternatives. A constructive model leads to a description of the data, which has a length in bits. This length is weakly dependent on the language in which the description is written. If that description is close enough to the Kolmogorov complexity [4] of the data, which is the result of compressing the data as much as possible, then we are obtaining a measure of the complexity of the data.

The data D is represented by a program that corresponds to its structure P, and some error E which we expect to be small. The description of D is P together with S. It is the size of P and S what we use as measure of complexity. If the structure chosen to represent the data is the appropriate one, then the size of the error should be small. But it could be the case that the structure is not very correct but very simple, and still leading to a small description.

These are the families of models we are looking at

geometric representing buildings, dykes and any other feature usually formed by straight lines combined in simple forms. Our aim is to describe geometric features using programs that reconstruct the features, and short codes to represent the error.

probabilistic representing vegetation, areas that are better described by giving the probability distribution, with non-zero standard deviation, that generated them. Our aim is to identify the distributions involved.

The features of interest in our data are characterised in very simple geometric and probabilistic terms, compared to the study of range images in general [1]. But the models that represent such types of features are fundamentally very different: a geometric model that describes well the shape of a building in terms of facets and edges, will fail to describe accurately the shape of vegetation; a probabilistic distribution, more appropriate for vegetation, will not capture most essential characteristics of built environment.

In order to compare such models, they must be defined in a generative form: in our case, we have implemented them as computer programs that can generate the data. The data is described using a computer program to generate it. That means that the model itself is encoded, and its size taken into account. This is an important feature of this method. When the models to compare are fairly similar, the size of the model is irrelevant, and reduces to Maximum Likelihood. This method departs from plain Bayes when the size of the model varies and affects our decision on which model is best.

Probabilistic models consist on data that is draw from a particular distribution. This is equivalent to assume that the data is described in shorter form by a code that associates shortest programs to the data with higher probability. For example, we use a uniform distribution in our experiments, and we implement it by encoding all data using the same amount of bits.

In the case of geometric models, in particular, we expect the model to approximate the data fairly well. In our experiments we consider flat surfaces. To encode the errors for such a model we use the $\log^*$ code [7], which is just one case of a code that associates shorter programs to shorter numbers while filling the tree of codewords.

3 Experiments

The pilot site of our project is a 25 km stretch of the river Váh in Slovakia, chosen for the purpose of flood simulation and impact assessment. Our experiments are centered in a patch of terrain around the canal that include in a cross section. The features under consideration are industrial buildings and vegetation.

These experiments were carried in two steps. First the image was segmented into a quadtree using a homogeneity criterion, then the resulting quadtree cells, of different sizes, were classified according to a description length criterion.

4 Segmentation

The first step in the labeling is the segmentation of the images. The segmentation structure are quadtrees, which are recursive division of a cell c into four equal cells c_1, c_2, c_3, c_4, whenever a homogeneity test is negative over the cell. The first cell is the complete image. Quadtrees were chosen expecting to obtain somehow a transition between probabilistic models (quadtrees with small cells) to geometric models, which in our case correspond to flat areas of the terrain and large tiles.

Two main types of homogeneity test were tried in the segmentation (see Figure 1 and below); the simplest one is the variance test, $v(c)$, in which the cell is divided whenever the variance is above a threshold. The second type of test consists on describing the area as if it was flat with small perturbations, $\log^*(c)$, and dividing the cell if the amount of bits per pixel is above a threshold. The third type of test consists on describing the cell c as if it a flat area with small perturbations, $\log^*(c)$, encoding the mean value and the small perturbations using a special code, then doing the same considering now the four sub-cells independently $\log^*(c_1) \ldots, \log^*(c_4)$. Both descriptions of the same data are compared and those shortest one is chosen: if dividing the cells leads to a shortest description, then the recursion goes on.

Only the first two tests lead to significant results, both $v(c)$ and $\log^*(c)$ produce clusters of small cells in the vegetation areas and lines of small cells in the edges. The $\log^*$ description did not lead to a significative improvement over the variance.

This leads to an illustration of the fact that a variety of common model selection methods are in fact computable approximations of the Kolmogorv Complexity. The variance function $v(c)$ corresponds to an encoding in the similar way that our

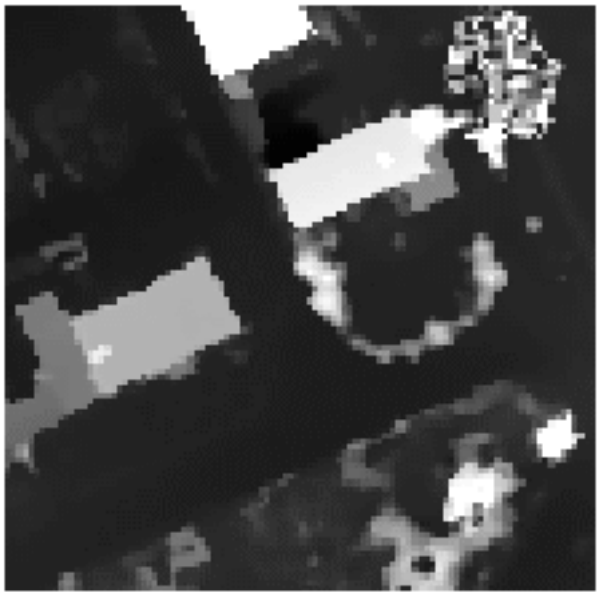

Figure 1: Lidar tile 100 meter side

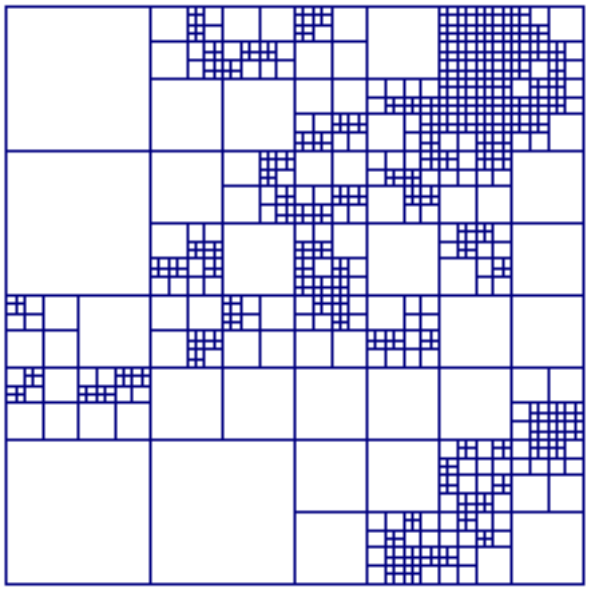

Figure 2: Quadtree segmentation of Figure 1 based on variance, cells with variance below 20000 are not split

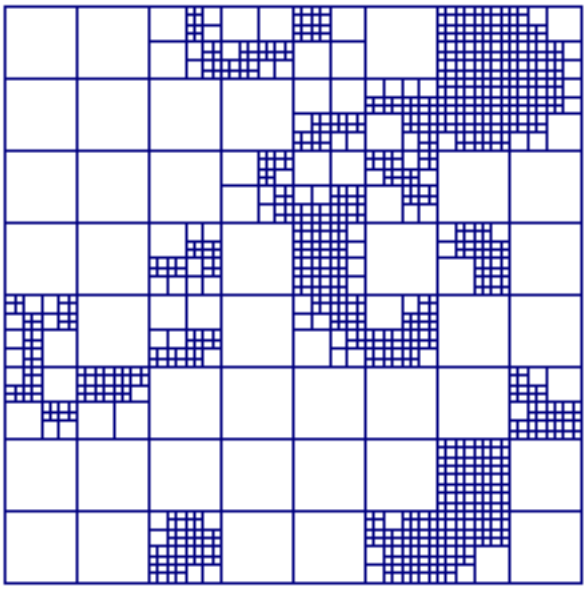

Figure 3: Quadtree segmentation of Figure 1 based on description size using $\log^*$, cells with 14 bits per pixel or less are not split

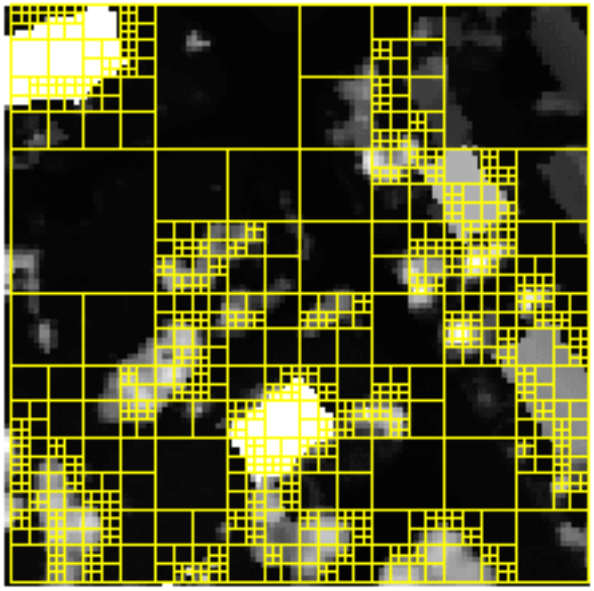

Figure 4: A lidar tile (100 meter side) after variance-based segmentation into a quadtree

$\log^*(c)$ encoding:

$$v(c) = \frac{\sum_i (s_i - \mu)^2}{n}$$

(where μ is the mean and $c = \{s_i, \ldots, s_n\}$ the data available), is the code length when each datum is represented using $(s_i - \mu)^2$ bits. The actual $\log^*$ function we have used is:

$$\log^*(c) = \frac{\sum_i \log^*(s_i - \mu)^2}{n}$$

5 Classification

For the classification, a wider family of models were compared: each of them was used to describe the cells, and the model that produced the shortest description of the cell was used to label it. Two families of models were considered: the data was produced by a uniform distribution, which means that it is evenly distributed within its range of values, or the data was flat with small perturbations, subject to short description by $\log^*$.

Two models were dominant, and are used to label Figure 5. The cells that correspond to the vegetation and building corners were better described by the $\log^*$ code. The rest of the cells, including flat areas, were better described by the assumption of a uniform distribution. This fact contradicts the fact that $\log^*$ should encode better flat areas, and it is just a direct effect of the size of the cell.

6 Conclusion

We are applying the concept of length of description to compare very heterogenous models when interpreting lidar data. This method would also help in handling models of varying complexity.

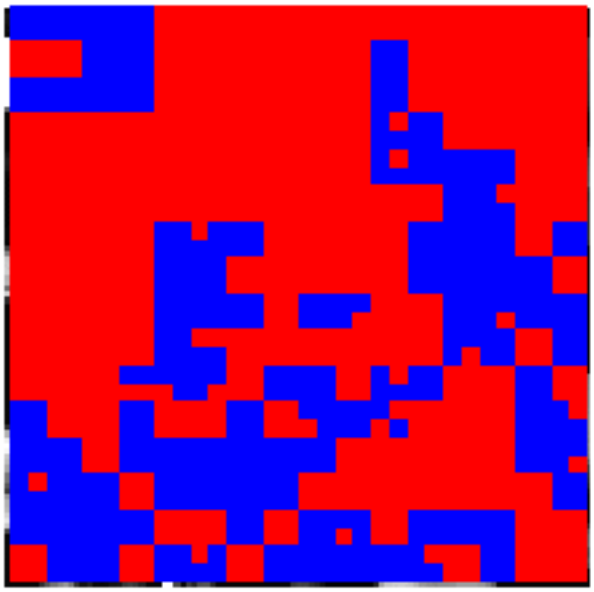

Figure 5: A classification of the pixels from the segmentation in Figure 4, according to the shortest description. Large (lighter) blocks are better represented by a uniform distribution, small (darker) blocks's description is shorter when using a $\log^*$ code

Applications of this technique are in the development of extensible, flexible methods for off-line feature extraction, as a result of the ability of this algorithm to compare between very heterogenous models.

We also expect this sort of metrics to be robust against outliers, a requirement for automatic feature extraction.

We are also looking for alternatives for the segmentation, such as region growing, that produce structures with a clearer geometric meaning. This would produce complex models that better represent the reality, while keeping a grasp on a wider range of models by means of the code length metric.

REFERENCES

[1] Farshid Arman and J. K. Aggarwal. Model-based object recognition in dense-range images — a review. *ACM Computing Surveys*, 25(1), March 1993.

[2] Brian Curless. *New Methods for Surface Reconstruction from Range Images*. PhD thesis, Stanford University, 1997.

[3] Peter D. Grnwald. *The Minimum Description Length Principle and Reasoning Under Uncertainty*. PhD thesis, CWI, 1998.

[4] Ming Li and Paul Vitányi. Inductive reasoning and Kolmogorov complexity. *Journal of Computer and System Sciences*, 44:343–384, 1992.

[5] Ming Li and Paul Vitányi. *An Introduction to Kolmogorov Complexity and Its Applications*. Springer, 2nd edition, 1997.

[6] S. J. Maybank and R. Fraile. Minimum description length method for facet matching. In Jun Shen, P. S. P. Wang, and Tianxu Zhang, editors, *Multispectral Image Processing and Pattern Recognition*, number 44 in Machine Perception and Artificial Intelligence, pages 61–70. World Scientific Publishing, 2001. Also published as special issue of the International Journal of Pattern Recognition and Artificial Intelligence.

[7] Jonathan J. Oliver and David Hand. Introduction to minimum encoding inference. Technical Report 4-94, Department of Statistics, Open University Walton Hall, 1994.

[8] Jorma Rissanen. *Encyclopedia of Statistical Sciences*, volume 5, chapter Minimum-Description-Length Principle, pages 523–527. Wiley New York, 1983.

[9] Milan Sonka, Vaclav Hlavac, and Roger Boyle. *Image Processing, Analysis and Machine Vision*. PWS Publishing, second edition, 1999.

LAND SURFACE MAPPING AND CHARACTERIZATION USING LASER ALTIMETRY

SESSION 3

DATA GEOLOCATION

SOME ASPECTS OF PROCESSING EXTRATERRESTRIAL LIDAR DATA: CLEMENTINE, NEAR, MOLA

Gregory A. Neumann[1,2]

[1]Laboratory for Terrestrial Physics, NASA/Goddard Space Flight Center
[2]Department of Earth, Atmospheric and Planetary Sciences, Massachusetts Institute of Technology
neumann@tharsis.gsfc.nasa.gov

KEYWORDS: Laser altimetry, planetary mapping, topography, geolocation, crossover analysis

ABSTRACT

The increasing volume of planetary lidar data is creating global datasets of unprecedented resolution and accuracy, and presenting new challenges. From 1971-72, when three Apollo missions carried laser altimeters to the Moon, to the Mars Global Surveyor mission operating the MOLA instrument for nearly 1000 days, the number of planetary ranges has increased by more than 5 orders of magnitude, and accuracy by nearly 3 orders. Significant refinements to orbital and attitude knowledge result from the use of millions of altimetric crossover constraints.

1 INTRODUCTION

Table 1 shows the dramatic improvement in laser terrain mapping since the first use of lasers by the Apollo Orbiters. The NEAR Laser Rangefinder (NLR) returned 16 million ranges and the Mars Orbiter Laser Altimeter (MOLA) instrument returned over 600 million ranges, five orders of magnitude more than the first altimeters flown by the Apollo lunar orbiters. Over a time span of 25 years, this represents a doubling of yield every 18 months, similar to Moore's law for transistors! The Geoscience Laser Altimeter System and MultiBeam Laser Altimeter instruments are expected to increase yield and accuracy by another factor of 10.

This paper compares Clementine, Shuttle Laser Altimeter (SLA), NLR and MOLA from the perspective of data analysis and validation. Apollo, Clementine, SLA, NLR, and MOLA operations span nearly three decades. The small number of orbital lidar missions is surprising in view of their success and modest cost. Planetary terrain mapping depends on coverage, instrument calibration and performance, timing, pointing, and precise orbital analysis. We review each of these factors over the course of these missions. We then describe some of the unique characteristics of long duration laser altimetric missions, focusing on the geolocation of NLR and MOLA ranges.

1.1 Coverage

Despite numerous orbital missions, lunar topography remains poorly known at scales less than 100 km. Optical and radar ground-based mapping of landmarks is limited to the nearside and has only recently achieved good resolution [*Margot et al.*, 1999, and references therein]. High-resolution regional contour maps were created from Apollo metric camera stereo images, using control from laser altimeters, but coverage was modest. The Apollo laser transmitters were short-lived. Pulse width was controlled mechanically, and their flashlamp exciters required 16-32 s to recharge. In the low-inclination (26°) orbits used for landing approaches, only a limited region of terrain was sampled (Figure 3). Apollo 17's laser outlasted the others, enduring 12 revolutions as the command module grazed within a few kilometers of the surface. Had the astronauts persisted and the lasers not failed, orbital decay would soon have ended the missions.

Two decades later, Clementine [*Nozette et al.*, 1994], a joint mission of NASA and the Ballistic Missile Defense Organization, spent two months in a 5-hour eccentric lunar orbit, with a 400-km periapse placed first at 30°S, then 30°N. Clementine obtained useful lidar data from 284 of its revolutions [*Smith et al.*, 1997]. With a hardware limited maximum of 640 km, the moon was within lidar range for at most 30 minutes per orbit. The detector system shared optics with the camera and was poorly tuned for mapping, so that few laser shots were returned from rough terrain. Laser shots were interleaved with imaging sequences, limiting firing rate. Coverage was spotty at best in the rough topography of the lunar highlands, where the shot-to-shot variance exceeded 1 km [*Smith et al.*, 1997].

Clementine demonstrated new, efficient, diode-pumped laser technology. Its significance might have been less had the Mars Observer mission not been lost the previous year. The Mars Observer Laser Altimeter (MOLA) was a redesigned lunar altimeter (not surprisingly called LOLA) sharing heritage with Clementine, optimized for planetary mapping [*Zuber et al.*, 1992]. Lacking an immediate reflight, MOLA spares were assembled with ancillary electronics to create the Shuttle Laser Altimeter. SLA was a Hitchhiker payload on STS-72 and later on STS-85 [*Garvin et al.*,

Table 1. Laser Altimetry Missions[a]

Mission Name	Launch Date	Type	Firing Rate, Hz	Shots fired	Geolocated Ranges	Horizontal accuracy	Vertical precision	Vertical accuracy
Apollo 15, 16, 17	1971-1972	Ruby	0.06	7,080	5,140	30 km	4 m	400 m
Clementine	1994	Cr:Nd:YAG[b]	0.6	600,000	72,300	3 km	40 m	90 m
SLA-01	01/1996	Cr:Nd:YAG	10	3,000,000	1,203,000	40 m	0.75 m	2.78 m
SLA-02	08/1997	Cr:Nd:YAG	10	3,000,000	2,090,000	40 m	0.75 m	6.74 m
NLR	02/1996	Cr:Nd:YAG	1-2	20,000,000	15,868,304	20 m	0.31 m	10 m
MOLA	11/1996	Cr:Nd:YAG	10	675,000,000	583,000,000	100 m	0.38 m	1 m

[a]The number of geolocated ground returns does not necessarily reflect the instrument's ability to range. Spacecraft off-pointing, data loss, gaps in tracking, clouds, as well as range failure limit the altimetric product.

[b]Chromium:neodymium-doped yttrium-aluminum-garnet

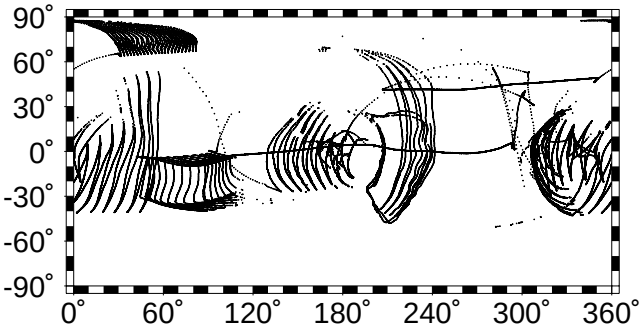

Figure 1. NLR coverage of 433 Eros on day 2000-111. Typically most of the coverage was acquired in rapid off-nadir scans.

1997, 1998]. SLA-01 and 2 demonstrated the effectiveness of orbital laser altimeters for terrestrial geodesy despite relatively short flights and the inconvenience of using the shuttles as an orbital platform. SLA-01 obtained excellent land and sea data between 28°N/S, and SLA-02 from 57°N/S. *Carabajal et al.* [1999] provides details of data processing and coverage.

NEAR-Shoemaker and Mars Global Surveyor (MGS) were launched successfully in 1996, carrying NLR and MOLA-2. Each achieved their planned orbits after some delay, but with all instruments performing well. NEAR orbited the asteroid 433 Eros for nearly one year before landing. Figure 1 shows a typical day's data acquired at 1 Hz at a range of 100 km. The NLR instrument [*Cole et al.*, 1997] had an 11 m spot size in the nominal 50 km orbit, and operated at ranges from 300 km to 17 m. Low-altitude orbits of 35 and 25 km radius allowed higher resolution mapping, with shots 3-4 m apart. NEAR-Shoemaker performed rapid scans and traverses for imaging purposes with NLR "riding along", ranging to nadir only a fraction of the time. Figure 2 shows the global dataset of observations. The coverage was highly nonuniform due to the asteroid's irregular shape and mission constraints. Data recovery was nearly perfect, with full attitude and timing reconstructions provided. Many track crossings were obtained.

The delayed MGS mission allowed limited coverage of the northern hemisphere of Mars in 1997-98. During aerobraking MOLA ranged intermittently from 170 km to 785 km in an elliptical orbit [*Zuber et al.*, 1998]. In mapping orbit, MOLA operated continuously at elevations of 365 to 430 km for a total of 26 months [*Smith et al.*, 2001b] before losing a critical oscillator signal on June 30, 2001. More than 98% of laser shots returned ground ranges. About 8% of ranges were unusable due to telemetry losses, attitude reconstruction gaps, and other events. The MGS orbital inclination of 92.7° allowed nadir coverage of 99.9% of the planet, with a few off-nadir observations of the poles. So many returns were obtained that in many regions topographic terrain models are better than Viking-era images [*Withers and Neumann*, 2001]. With shot spacing typically 300 m along track, nearly 50 profiles cross the equator for each degree of longitude (about 60 km). In some places on Mars, several profiles traverse a single square kilometer (Figure 4). Mapping was nominally in an 88-cycle near-repeat orbit, with a ground track offset that eventually transitioned from positive to negative. Some tracks overlapped, enabling direct temporal comparisons of topography between seasons [*Schmerr et al.*, 2001]. Most importantly the regular crossings of ascending and descending tracks provided many internal consistency checks.

1.2 Instrument performance and calibration

The Apollo altimeters were more than adequate for their primary purpose, giving ranges for photographs, with a precision of about 4 m. While the 15 MHz oscillator of Clementine's laser rangefinder was calibrated within 1 part in 10^5, or a few meters of range, only a 14-bit range count was returned, since full 16-bit hardware was not available on an accelerated development schedule. To reach a 640-km-distant target, ranges were quantized to 40 m, as illustrated in Fig-

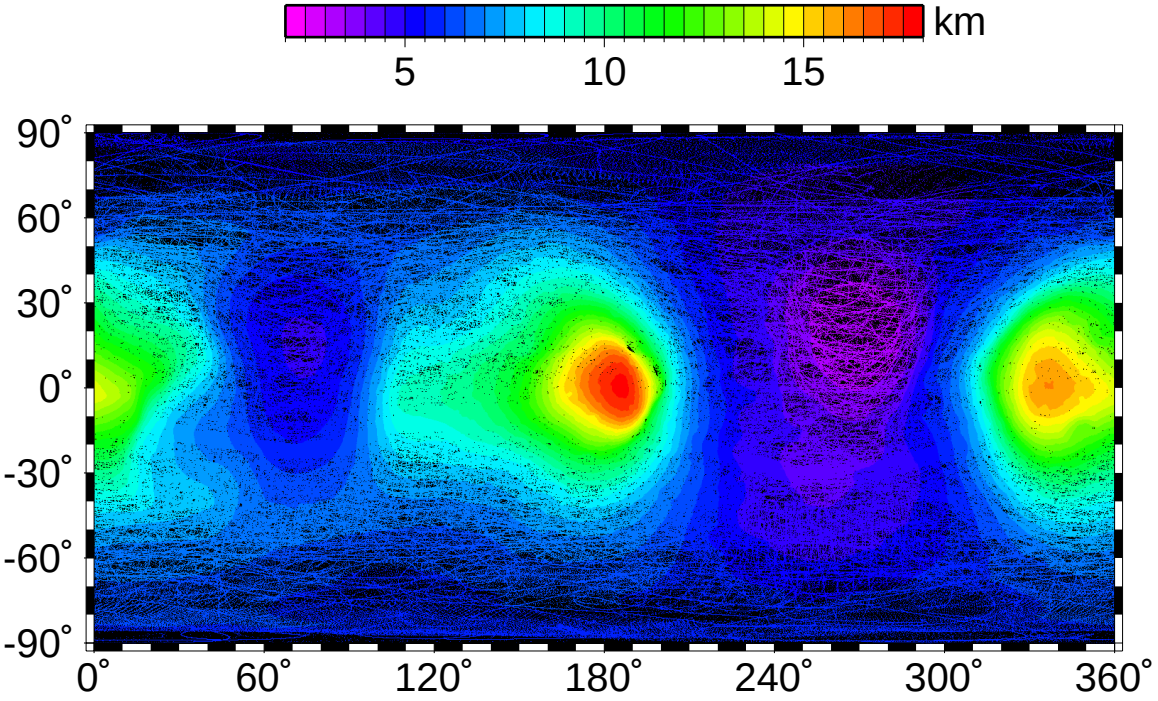

Figure 2. NLR altimetric coverage of asteroid 433 Eros. Regions lacking data shown in black.

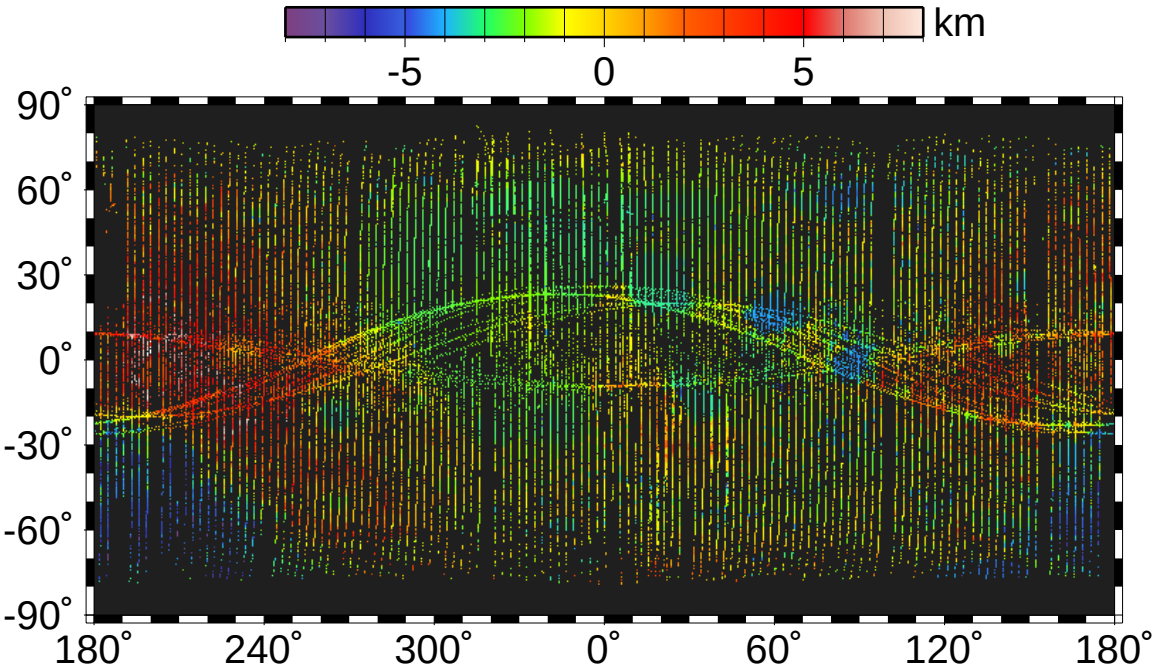

Figure 3. Lunar topographic coverage from Apollo orbiters and Clementine [*Smith et al.*, 1997].

ure 5. The laser could range at 8 Hz for about 1 minute until overheating. The only good 8-Hz profile taken under ideal conditions over smooth Mare terrain shows shot-to-shot variation of about 40 m. Comparison with a MOLA profile over level terrain (lower curve) shows that precision was limited due to quantization and electronic jitter.

Another problem was Clementine's low signal-to-noise ratio. Elevations had to be processed with a range-correlation filter to edit the nearly 50% noise triggers, and many errors remain. Finally, the orientation of the laser transmitter was uncertain. The laser was boresighted to a detector within the camera telescope, so that ranges were nominally pointed at spacecraft nadir, but the amount of offset was not known at the time of the analysis. Information obtained since from the

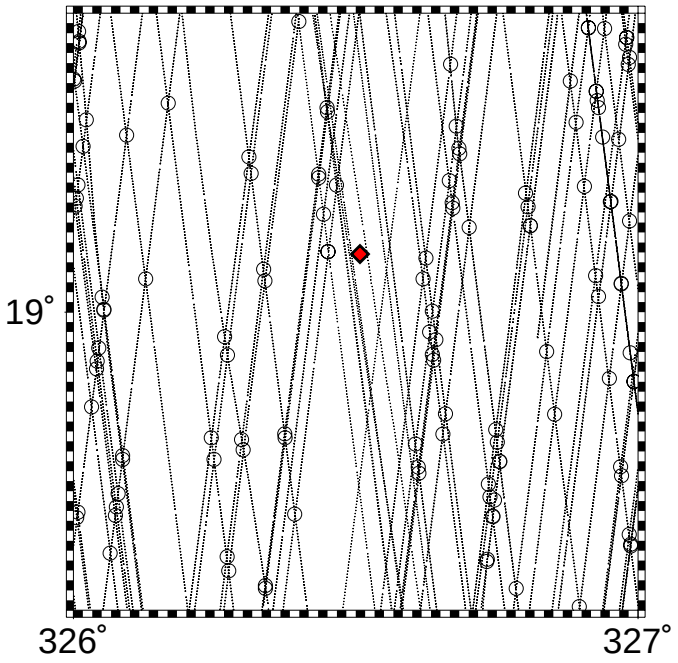

Figure 4. Coverage in a 1° by 1° area around the Pathfinder landing site (solid diamond) acquired by MOLA. Border markings are 1 minute (roughly 1 km). Individual shot elevations (crosses) are compared at crossovers (circles).

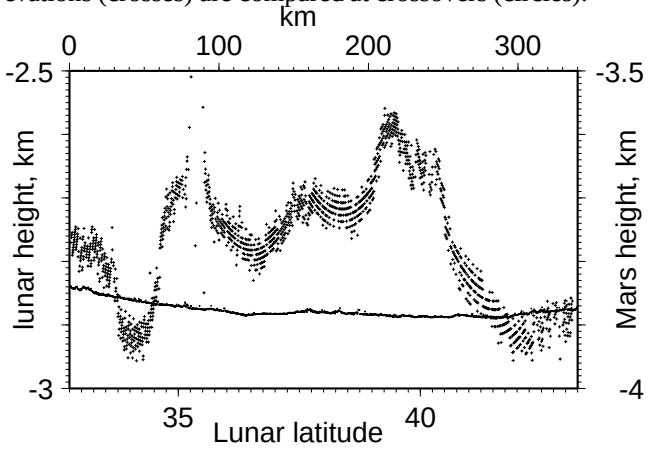

Figure 5. Clementine high-resolution rangefinder profile extending 340 km across northwest Mare Procellarum (crosses). Vertical exaggeration ∼400:1. MOLA profile 10061 across Amazonis Planitia, one of the flattest places in the solar system, shown for comparison.

SPICE archives at JPL shows a 5 mrad deviation in camera orientation along-track and 1 mrad across-track. This offset was also indicated by a comparison with ground-based radar interferometry [*Margot et al.*, 1999], showing a 3-km offset along-track.

NLR was rigorously calibrated, and drift of the instrument after launch was monitored via an optical delay fiber [*Cheng et al.*, 2000]. Ranging performance from shot-to-shot approached the limiting resolution of 31 cm, and noise was negligible at all but the lowest operating threshold. The largest single source of range error was due to pulse dilation on non-ideal target surfaces, or "range walk". Dilation causes the leading edge of a pulse to be detected early, introducing range bias as much as 6 m error on sloping terrain [*Zuber et al.*, 1997].

MOLA is a fully calibrated [*Abshire et al.*, 2000], all-terrain lidar with direct (leading edge of pulse) detection. MOLA pulse waveforms vary due to interaction with the surface of Mars, and their energy varies with atmospheric transmission and surface reflectivity. MOLA-2 addressed the issue of range walk by measuring the echo pulse width at a preset threshold, and the echo energy. Time of flight was corrected to the centroid of the pulse using half the measured pulse width. With this approach, calculated range errors due to detector noise were less than 1 m over slopes of up to 3°. This calibration enables unbiased comparison of measurements from different altitudes, laser outputs, and atmospheric conditions. The situation was complicated by the use of four parallel low-pass filters to maximize the probability of detection under all conditions, and the generally saturated condition of the detector over the unusually flat martian terrain seen in Figure 5. For saturated pulses, the pulse width measurement was unreliable. The leading-edge to centroid timing delay was estimated based on terrain slope, while interchannel calibration at the sub-meter level was obtained empirically [*Neumann et al.*, 2001].

The MOLA timing interval clock controls firing rate as well as range measurement. By monitoring the firing rate, an absolute calibration of range units over the course of the mission was obtained, adding to the stability of the range measurement. The calibration changed by several parts per million over the course of the mission [*Smith et al.*, 2001b], accelerating in the final weeks before the clock signal was lost.

By averaging over many shots, MOLA can measure temporal changes in the height of the Martian surface with decimeter precision. MOLA elevation measurements have recently been used to map 1-2 m seasonal changes due to the deposition and sublimation of CO_2 ice [*Smith et al.*, 2001a] associated with the planet's seasonal cycle of CO_2 exchange. Unfortunately in polar regions, many of MOLA's returned pulses were saturated, which greatly compromises the measurement of pulse energy. In some regions there may be significant unmodeled range walk due to albedo changes. A global 1064 nm albedo map being generated as part of the investigation will permit an improved estimate of echo pulse energy. This will enable a more accurate correction of range walk effects and therefore improve the ability to detect subtle patterns of topographic change in the polar regions.

1.3 Orbit determination

Orbital analysis during the Apollo era was crude by today's standards and the lunar gravity field was largely unknown. Many archives have been lost or contain only partial information. Position errors of 30 km or more were not uncom-

mon. Reanalysis of historical lunar tracking [*Lemoine et al.*, 1997] together with sophisticated force modeling reduced Clementine's orbital uncertainties to 10's of meters. Some improvement in orbits might be obtained from using gravity fields derived from Lunar Prospector [*Konopliv et al.*, 1998, 2001], but the issues with ranging accuracy mentioned earlier would remain.

SLA used a combination of Global Positioning Satellite (GPS) and Tracking/Data Relay Satellite System (TDRSS) together with TOPEX-Poseidon to TDRSS tracking [*Rowlands et al.*, 1997] to generate orbits with meter-level radial precision. Long-wavelength orbital errors remained but were masked by pointing uncertainty [*Luthcke et al.*, 2000].

Orbit determination for NEAR-Shoemaker at Eros remains problematic. The small gravitational pull of the body provided weak dynamic constraints, while tracking range data were biased by uncertainty in the asteroid ephemeris. Altimetry was required to constrain the orbits, as well as optical landmark tracking [*Yeomans et al.*, 1999; *Zuber et al.*, 2000]. Only partial altimetry were included in orbit solutions, using a low-degree shape model to provide an apriori constraint. Altimetric residuals were $\sim$60-110 m, depending on orbital phase. In this situation, much improvement may be gained from the use of crossovers, described in a following section.

MGS tracking was intermittent during aerobraking. Orbit solutions typically had 5-10 m errors, occasionally more. After reaching a circular mapping orbit, a period of tracking was dedicated to refining knowledge of the martian gravity field. The MGS orbital total position was subsequently determined to an accuracy of 1.7 m, and 0.3 m radially [*Lemoine et al.*, 1999]. Exceptions occurred when propulsive momentum desaturation occurred during long gaps in tracking and could not be adequately modeled. During these gaps, radial orbit error sometimes exceeded 20 m [*Neumann et al.*, 2001].

1.4 Timing bias estimation

Timing is another source of uncertainty in geolocation, since the spacecraft ephemeris is determined from Earth-based tracking. Clementine timing was corrupted by recurrent computer resets, and had to be corrected by as much as 32 seconds. Timing reconstruction was not available until more than a year after the mission ended. Thus an empirical approach to corrections was required for the analysis of the Laser Rangefinder data. Since in a polar orbit there were no crossing tracks and little other data, the only comparisons available were with nearby tracks taken during the second monthly mapping cycle over relatively smooth basins (cf. Figure 5). These revealed some mundane timing software issues and prompted a full timing reconstruction.

Global Positioning Satellites provide accurate timing in earth orbit, although SLA used the shuttle precision clock for a reference. The interface to this clock was problematic, and some time periods contained invalid tags [*Carabajal et al.*, 1999]. At the 1-2 AU distances to 433 Eros, time transfer is nontrivial. The NEAR-Shoemaker spacecraft was aided by solutions for times of cosmic gamma ray burst events observed by multiple platforms. Timing accuracy was within 100 ms, more than adequate for a slow-moving spacecraft. Instrument firing was synchronized to the spacecraft clock, and timing bias was not anticipated.

The MGS spacecraft clock had a small and stable rate of drift throughout the mission and was monitored, but was not tied to the Ultra-Stable Oscillator instrument which could have maintained millisecond accuracy. The MGS Project specified a worst-case 30 ms timing uncertainty, although it was typically better than 10 ms. The orbital velocity of MGS during aerobraking ranged from 3.3-4.5 km/s, and a 10 ms error in timing resulted in up to 16 m of vertical error in an eccentric orbit. During the aerobraking mission phase, an observation timing bias of 117 ms was estimated[*Rowlands et al.*, 1999], the cause of which remains unknown. In addition there was an attitude timing bias of 1.15 s, discussed below.

1.5 Attitude bias and uncertainty

Pointing bias and uncertainties must be minimized as far as possible in the space environment. The importance of this was seen in the context of Clementine. Star trackers provide the inertial reference, supplemented by attitude gyros. When performing maneuvers, trackers may lose lock, and knowledge degrades rapidly. The alignment of laser boresight with respect to star trackers is liable to change in flight, and may be perturbed by thermal distortion. Different approaches may be taken to improve attitude knowledge and minimize bias. For the SLA missions, a joint solution for alignment bias together with orbit determination was undertaken, using the oceans as a reference [*Luthcke et al.*, 2000]. Independent verification was provided by comparison with well-controlled terrestrial terrain models.

The NEAR-Shoemaker spacecraft provided attitude data at 1 Hz throughout the mission. NLR and cameras were aligned prior to flight along the X-axis with respect to the Spacecraft Bus Prime coordinate system. The Multi-spectral Imager (MSI) was able to verify its alignment through star observations, and variations were detected that appeared to correlate with instrument deck temperature. The coalignment of NLR with MSI could not be determined by directly imaging the laser spot, despite several attempts. Indirect measurements were obtained by observing the time at which ranges were lost as the imager scanned across the asteroid limb [*Cheng et al.*, 2001]. Further information was obtained by laboriously comparing images of boulders with altimetric features, providing a location within two camera pixels ($\sim$0.2 mrad). It became apparent that the instrument had shifted from its pre-flight orientation. The laser mounting was thermally better isolated than that of the camera. Alignment was therefore investigated independently for NLR in the course of altimetric processing, as described in Section 2.

MGS attitude reconstruction from Lockheed-Martin in Den-

ver was provided by the Project in the form of spacecraft quaternions at approximately 4-second intervals. During aerobraking, images were taken of various landmarks (e.g., the Face on Mars) by means of rapid off-nadir slews. These slews revealed a timing bias in the reconstruction of attitude data. Such delays can lead to substantial errors in geolocation due to the ∼1 mrad/s pitch motion of MGS as it tracks nadir. In nadir mapping, timing biases trade off with alignment bias, but are distinguishable in the altimetry taken during maneuvers. *Rowlands et al.* [1999] found a shift in boresight of approximately 0.024° (0.42 mrad) from preflight, primarily in the roll direction.

MGS telemetry transmitted attitude quaternions after onboard processing with a causal delay due to two-pole, recursive digital filter. The filter characteristics included a phase shift equivalent to 1.15 s delay at low frequencies. Upon commencement of mapping, the solar panels oscillated slowly as they tracked the sun. A 6-s notch filter with two additional poles was added to damp the oscillations. Calculations suggested that the mapping filter should have induced a 2.3 s delay. We found that the delay was the same as before the commencement of mapping, both during normal operation and during high-rate slews. This apparent contradiction with theory remains unresolved, but MOLA alignment continued to be monitored throughout the mission.

2 ALTIMETRIC CROSSOVERS

Abundant crossovers in lidar mapping provide a powerful constraint on orbital and attitude knowledge. During the course of the NLR investigation, over ∼16,000,000 altimetric points were acquired. Distinct orbital phases permitted observations over northern and southern hemispheres, using nadir and off-nadir observations. In order to assess their accuracy, ∼3,800,000 crossovers were analyzed. A shot point (x,y,z) in Cartesian space is expressed in polar coordinates. Two sequential shot points define a small track segment, parameterized by time. Crossovers occur at the intersection of two such segments projected onto a sphere. The radius r is linearly interpolated along each track. At each crossover we obtain the altimetric residual

$$d(t, t') = r(t) - r(t') \quad (1)$$

at a time-ordered pair of crossover times t, t', as well as the crossing latitude, longitude, and a pair of headings and slopes.

A local surface normal perpendicular to both segments is estimated in Cartesian coordinates. This unit normal vector represents the change in radius at the time of intersection resulting from an adjustment of the track in the X, Y, and Z directions. There are six adjustments, three per track, for each crossover residual. Such an underdetermined problem may be solved by constraining the adjustment to vary as a smooth function of time. Using the approach of *Neumann et al.* [2001], tracks were adjusted to minimize the crossover residual via least-squares. The effort to obtain a solution in this simplified approach depends only linearly on the number of crossovers considered and thus can handle a very large dataset. The adjustment is made in body-fixed coordinates, and does not truly represent a single error in orbit, range, timing, or alignment, but rather the combined effects of each.

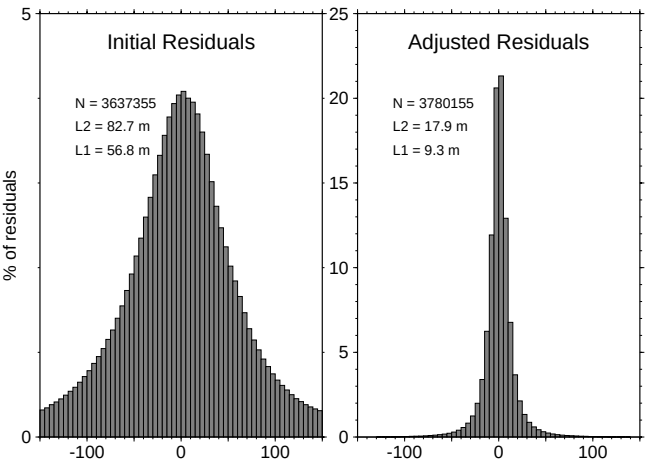

Figure 6. Initial and final crossover residuals for NLR altimetry, using a crossover adjustment with temporal resolution of four cycles per asteroid revolution. Residuals >200 m are edited.

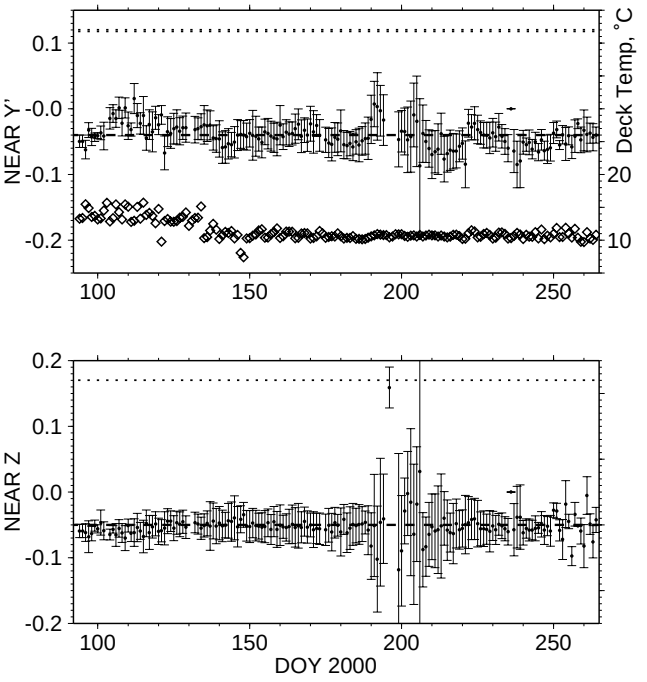

Figure 7. Boresight positions of crossovers after adjustment as a function of time. Error bars show the median daily dispersion about the median value. Dotted line shows initial value, while dashed lines show the nominal fit. Instrument deck temperatures (diamonds) declined early in the mission, but boresight did not appear to be correlated.

The relocated crossovers generally have smaller residuals. Figure 6 shows the initial and final residual after three iterations. An adjustment of four cycles per asteroid revolution reduced the RMS residuals d from 82.7 to 17.9 m, after excluding grossly mislocated data. A more typical measure of residual is the L_1 residual, the median absolute residual scaled to a normal distribution. Using this measure, a sixfold improvement in crossover error results from a quasi-periodic adjustment with a period of $\sim$1.25 hours. Obviously there are sources of error that vary more rapidly, but errors in the slow-moving NEAR orbit typically show up as errors at multiples of the 5-hour rotational period of Eros.

If one assumes that all but one of the sources of error are minor and randomly distributed, the relocated crossover indicates the amount of the chief source of error. For example, the position of the adjusted crossover in the instrument plane provides an estimate of true boresight direction. At each crossover the relocated range vector may be projected to the Y-Z plane (recall that instruments point in the platform X-direction). The median locus of these points shows the degree to which the boresight deviates from nominal, while the dispersion shows the relative contribution from other sources of error. Several iterations with improved boresight alignment successively reduce the crossover residual. Figure 7 shows the preflight boresight direction and daily averages of the apparent true boresight. No correlation with instrument deck temperature was seen. The spacecraft orbit remained illuminated by the Sun during all mission phases, keeping temperatures stable. The analysis used orbit solutions from day 2000-094 through day 264. The Euler angles obtained for the instrument were -0.04° about the Z-axis, and -0.05° about the Y-axis. These angles map a unit X-vector along the lidar boresight to the vector
`(0.999999376, -6.98131378E-04, 8.726645E-04)`^{T}
in the spacecraft frame. This boresight alignment offset was assumed for the remainder of the analysis. A final analysis using all 351 days of observations should refine this, but the uncertainty in pointing on a given day appears to be $\sim$0.01°, or 0.2 mrad.

Altimetric crossovers have been employed in the MOLA investigation to monitor the stability of pointing as well as orbital precision [*Neumann et al.*, 2001]. That study found that significant adjustments in three orthogonal directions were required to fit the crossover data. The regular mapping geometry allows the adjustments to be expressed in radial, along-track, and across-track components. Quasi-cyclic, once- and twice-per-rev adjustments dramatically reduced residuals. These cyclic errors were traced to unconstrained propulsive momentum dumps that perturbed the MGS orbit. A shorter-duration signal was seen when the spacecraft transitioned between night and day sides of Mars, inducing a thermal distortion of alignment between the MOLA beam and the inertial reference system.

Longer term drift can be characterized via daily averages. Figure 8 shows the average deviation from nominal alignment over the life of the mission. Some of the variation is correlated with spacecraft thermal environment as Mars' elliptical orbit circles the Sun. Drift in timing, spacecraft maneuvers, and gradual shift in spacecraft center-of-mass are also suspected.

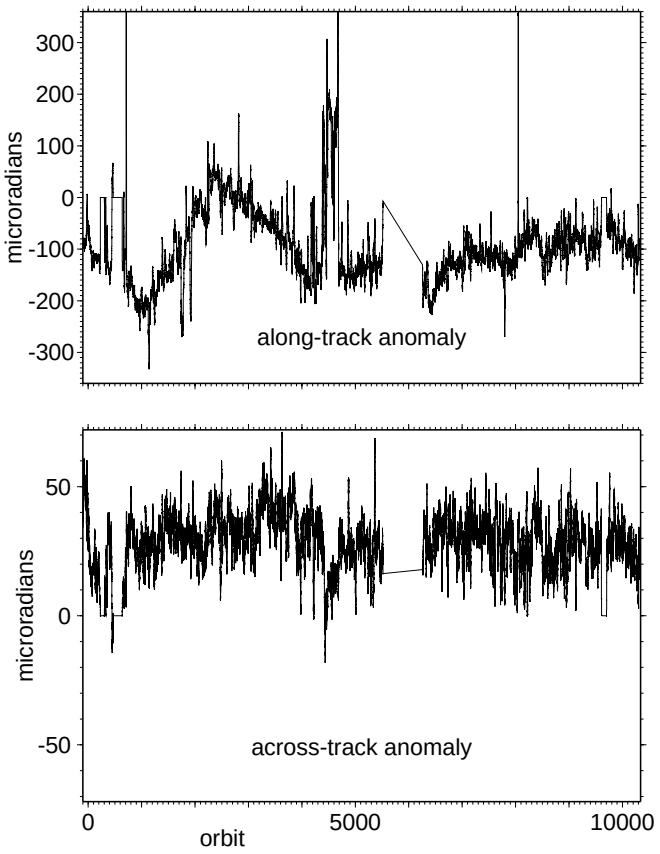

Figure 8. MOLA along-track and across-track misalignment as a function of orbit. Adjustment value from crossover analysis, averaged over one day. At a nominal altitude of 400 km, 100 μrad = 40 m. Some offsets result from targeting maneuvers affecting attitude knowledge, others from variations in beam alignment.

3 DISCUSSION

The Moon was the first extraterrestrial body to be ranged with lasers. The extant data are contaminated with instrument defects and other uncertainties, and are simply inadequate in quantity for detailed regional studies. Lunar topography awaits a fully calibrated, high-performance altimetric study by the next generation of laser altimeters.

The NLR and MOLA investigations have revealed the power of rigorous orbital processing within the GEODYN software system [*Rowlands et al.*, 1999] combined with full crossover analysis. The pointing bias on NLR has been characterized within 0.2 mrad and the topographic uncertainty reduced to $\sim$10 m via the use of crossovers [*Zuber et al.*, 2000]. An even better level of precision may be attainable given the capabilities of the NLR instrument.

MOLA had many more observations than any other mis-

sion, in a highly stable geometry, with more than 38 million topographic crossovers. Radial topographic accuracy of 1 m and horizontal position accuracy better than 100 m has been achieved. Where known positions of landers have been traversed, essentially identical topography is measured. Martian topography is referenced to an equipotential surface. Formal uncertainty in the martian geoid height, as currently defined by spherical harmonics to degree and order 60 [*Lemoine et al.*, 2001], is 1.8 m. At present the most uncertain element of martian cartography is the position of the prime meridian [*Davies et al.*, 1996], defined by the crater Airy-0, in inertial space.

Acknowledgments. Supported by the NASA Mars Exploration Program MOLA Investigation. The Generic Mapping Tools software [*Wessel and Smith*, 1998] greatly assisted the analysis.

REFERENCES

Abshire, J. B., X. Sun, and R. S. Afzal, Mars Orbiter Laser Altimeter: Receiver model and performance analysis, *Appl. Opt.*, *39*, 2440–2460, 2000.

Carabajal, C. C., D. J. Harding, S. B. Luthcke, W. Fong, S. C. Rowton, and J. J. Frawley, Processing of Shuttle Laser Altimeter range and return return pulse data in support of SLA-02, *International Archives of Photogrammetry and Remote Sensing*, *32*, 65–72, 1999.

Cheng, A. F., T. D. Cole, M. T. Zuber, Y. Guo, and F. Davidson, Inflight calibration of the Near-Earth Asteroid Rendezvous Laser Rangefinder, *Icarus*, *148*, 572–576, 2000.

Cheng, A. F., et al., Laser altimetry of small-scale features on 433 Eros from NEAR-Shoemaker, *Science*, *292*, 488–491, 2001.

Cole, T. D., M. T. Boies, A. F. C. A. S. El-Dinary, M. T. Zuber, and D. E. Smith, The Near Earth Asteroid Rendezvous laser altimeter, *Space Sci. Rev.*, *82*, 217–253, 1997.

Davies, M. E., et al., Report of the IAU/IAG/COSPAR working group on cartographic coordinates and rotational elements of the planets and satellites: 1994, *Cel. Mech. and Dynam. Astron*, *63*, 127–148, 1996.

Garvin, J. B., J. L. Bufton, J. B. Blair, S. B. Luthcke, J. J. Frawley, and J. A. Marshall, Observations of the Earth's topography from the Shuttle Laser Altimeter (SLA): Laser pulse echo recovery measurements of terrestrial surfaces, in *Proc. European Geophys. Soc. Mtg.*, Vienna, 1997.

Garvin, J. B., J. L. Bufton, J. B. Blair, D. Harding, S. B. Luthcke, J. J. Frawley, and D. D. Rowlands, Observations of the Earth's topography from the Shuttle Laser Altimeter (SLA): Laser pulse echo recovery measurements of terrestrial surfaces, *Phys. Chem. Earth*, *23*, 1053–1068, 1998.

Konopliv, A. S., A. Binder, L. Hood, A. Kucinskas, W. L. Sjogren, and J. G. Williams, Gravity field of the moon from lunar prospector, *Science*, *281*, 1476–1480, 1998.

Konopliv, A. S., A. Binder, L. Hood, A. Kucinskas, W. L. Sjogren, and J. G. Williams, Gravity field of the moon from lunar prospector, *submitted to Journal of Geophysical Research*, 2001.

Lemoine, F. G., D. E. Smith, M. T. Zuber, G. A. Neumann, and D. D. Rowlands, A 70th degree and order lunar gravity model from Clementine and historical data, *J. Geophys. Res.*, *102*, 16,339–16,359, 1997.

Lemoine, F. G., D. D. Rowlands, D. E. Smith, D. S. Chinn, D. E. Pavlis, S. B. Luthcke, G. A. Neumann, and M. T. Zuber, Orbit determination for Mars Global Surveyor during mapping, in *AAS/AIAA Astrodynamics Specialist Conference, Girdwood, Alaska, 16-19 August 1999*, pp. 99–328, 1999.

Lemoine, F. G., D. E. Smith, D. D. Rowlands, M. T. Zuber, G. A. Neumann, D. S. Chinn, and D. E. Pavlis, An improved solution of the gravity field of Mars (GMM-2B) from Mars Global Surveyor, *J. Geophys. Res.*, *in press*, 2001.

Luthcke, S. B., D. D. Rowlands, J. J. McCarthy, E. Stoneking, and D. E. Pavlis, Spaceborne laser-altimeter-pointing bias calibration from range residual analysis, *J. Spacecr. Rockets*, *37*, 374–384, 2000.

Margot, J.-L., D. B. Campbell, R. F. Jurgens, and M. A. Slade, The topography of Tycho Crater, *J. Geophys. Res.*, *104*, 11,875–11,882, 1999.

Neumann, G. A., D. D. Rowlands, F. G. Lemoine, D. E. Smith, and M. T. Zuber, Crossover analysis of Mars Orbiter Laser Altimeter data, *J. Geophys. Res.*, *in press*, 2001.

Nozette, S., et al., The Clementine mission to the moon: Scientific overview, *Science*, *266*, 1835–1839, 1994.

Rowlands, D. D., S. B. Luthcke, J. A. Marshall, C. M. Cox, R. G. Williamson, and S. C. Rowton, Space shuttle precision orbit determination in support of SLA-1 using TDRSS and GPS tracking data, *J. Astro. Sci.*, *45*, 113–129, 1997.

Rowlands, D. D., D. E. Pavlis, F. G. Lemoine, G. A. Neumann, and S. B. Luthcke, The use of crossover constraint equations derived from laser altimetry in the orbit determination of Mars Global Surveyor, *Geophys. Res. Lett.*, *26*, 1191–1194, 1999.

Schmerr, N., G. A. Neumann, S. E. H. Sakimoto, and J. B. Garvin, Seasonal changes in thickness of martian crater deposits from the Mars Orbiter Laser Altimeter, *Eos Trans. AGU*, *82*, *Fall Meet. Suppl.*, to appear, 2001.

Smith, D. E., M. T. Zuber, G. A. Neumann, and F. G. Lemoine, Topography of the Moon from the Clementine lidar, *J. Geophys. Res.*, *102*, 1591–1611, 1997.

Smith, D. E., M. T. Zuber, and G. A. Neumann, Seasonal variations of snow depth on Mars, *submitted to Science*, 2001a.

Smith, D. E., et al., Mars Orbiter Laser Altimeter: Experiment summary after the first year of global mapping of Mars, *J. Geophys. Res.*, *in press*, 2001b.

Wessel, P., and W. H. F. Smith, New, improved version of Generic Mapping Tools released, *Eos Trans. AGU*, *79*, 579, 1998.

Withers, P., and G. A. Neumann, Enigmatic northern plains of Mars, *Nature*, *410*, 651, 2001.

Yeomans, D. K., et al., Estimating the mass of asteroid 433 Eros during the NEAR spacecraft flyby, *Science*, *285*, 560–561, 1999.

Zuber, M. T., D. E. Smith, S. C. Solomon, D. O. Muhleman, J. W. Head, J. B. Garvin, J. B. Abshire, and J. L. Bufton, The Mars Observer Laser Altimeter investigation, *J. Geophys. Res.*, *97*, 7781–7797, 1992.

Zuber, M. T., D. E. Smith, A. F. Cheng, and T. D. Cole, The NEAR laser ranging investigation, *J. Geophys. Res.*, *102*, 23,761–23,773, 1997.

Zuber, M. T., D. E. Smith, R. J. Phillips, S. C. Solomon, W. B. Banerdt, G. A. Neumann, and O. Aharonson, Shape of the northern hemisphere of Mars from the Mars Orbiter Laser Altimeter (MOLA), *Geophys. Res. Lett.*, *25*, 4393–4396, 1998.

Zuber, M. T., et al., The shape of 433 Eros from the NEAR-Shoemaker Laser Rangefinder, *Science*, *289*, 2097–2101, 2000.

Spaceborne Laser Altimeter Instrument Parameter Calibration From Integrated Residual Analysis – A Brief Overview

S.B. Luthcke and D.D. Rowlands
NASA Goddard Spaceflight Center, Space Geodesy Branch
USA
sluthcke@geodesy2.gsfc.nasa.gov
Claudia Carabajal
NVI, Inc., Greenbelt, MD, USA

KEY WORDS: spaceborne laser altimeter, geolocation, instrument parameter calibration

ABSTRACT

To take advantage of the unique observing capabilities of lidar technology, two NASA dedicated Earth observing laser altimeter missions are scheduled for launch in the near future: the Vegetation Canopy Lidar (VCL) and the Ice, Cloud and land Elevation Satellite (ICESat). To properly geolocate the surface returns it will be necessary to verify and calibrate pointing, ranging, timing and orbit parameters once the instrument is in orbit. In preparation for these spacborne lidar missions, detailed algorithms and methodologies have been developed and tested to precisely geolocate the surface returns. Rigorous laser direct altimetry, dynamic crossover and geolocation measurement models have been implemented within NASA's state of the art Precision Orbit Determination (POD) and geodetic parameter estimation software, GEODYN. The algorithms and their implementation provide an integrated range residual analysis capability to simultaneously estimate orbit, pointing, ranging and timing parameters from a combined reduction of direct altimetry, dynamic crossover and spacecraft tracking data. The following is a brief overview of the integrated residual analysis methodology and implementation. In addition, results of simulations and error analyses along with the application of the technique to the processing of Shuttle Laser Altimeter (SLA) data will be briefly discussed. The topics discussed are detailed within several papers currently in print and in review. The following is meant simply as an overview and to provide the reader with the necessary background and references to pursue the work in more detail.

1 INTRODUCTION

Two NASA dedicated Earth observing laser altimeter missions are scheduled for launch in the near future: the Vegetation Canopy Lidar (VCL) and the Ice, Cloud and land Elevation Satellite (ICESat). The ground spot size of these spaceborne laser altimeters is as small as the VCL footprint of 25m, and is on the order of 20-80 times smaller than the footprint of spaceborne radar altimeters now in use (TOPEX, GFO, ERS-2). The small laser footprints and the small spatial scale over which the surface characteristics of interest vary require precise geolocation, typically significantly smaller than the footprint itself.

One approach to spaceborne laser altimeter data geolocation is to independently obtain laser pointing, spacecraft body attitude, spacecraft orbit, range bias and time tag corrections and to simply combine these elements along with the range observation to obtain the geolocated surface return. However, these data have errors and their pre-launch parameter values and models must either be verified or more likely corrections must be estimated once the instrument is on orbit. Towards this end, the laser range observations can be fully exploited in an integrated residual analysis to accurately calibrate these corrections or geolocation/instrument parameters (Luthcke et al., 2000 and Rowlands et al., 2000). Our "integrated residual analysis" approach allows for the simultaneous estimation of orbit and geolocation parameters from a combined reduction of laser range and spacecraft tracking data.

While this technique is not entirely new for spaceborne radar altimetry, what is new is the implementation and application of the laser altimeter measurement models that take into account the additional complexities of the spaceborne laser altimeter observation. Laser altimeter measurement models must precisely consider the pointing of the instrument, the small lidar footprint and the highly varying surface characteristics from which the data are collected. The laser altimeter range measurement model algorithms have been implemented within NASA/GSFC's GEODYN precise orbit and geodetic parameter estimation system (Pavlis et al., 1999). Therefore, the laser altimeter range processing can take advantage of GEODYN's high fidelity reference frame modeling, detailed geophysical modeling and estimation process. The GEODYN implementation allows for the simultaneous estimation of the geometric and dynamic parameters of the orbit and laser range measurement model through the reduction of a combination of spacecraft tracking and laser altimeter range data residuals.

2 IMPLEMENTATION and METHOD OVERVIEW

Three laser altimeter measurement models have been implemented within the GEODYN system. The first is a rigorous implementation of the classic geolocation measurement model that takes into account the motion of the laser tracking points over the round trip light time of the laser pulse. While the geolocation measurement model cannot be used to directly estimate parameters, it is used to construct the "dynamic

crossover" measurement model (discussed below) and provides the geolocation data for any particular solution.

The second measurement model implemented is an altimeter "crossover" capability, termed "dynamic crossover". The dynamic crossover measurement model is discussed in detail, along with its application to orbit and attitude determination for Mars Global Surveyor (MGS), in Rowlands et al. (1999). This crossover measurement model has been implemented to take into account the small footprint of the laser altimeter along with the observed sloping terrain, and therefore the horizontal sensitivity of these data. The formulation can exploit change in horizontal crossover location as well as change in radial position of the satellite.

The third measurement model implemented is the "direct altimetry" measurement model. A detailed discussion and mathematical description of the direct altimetry measurement model is presented in Luthcke et al. (2000). The round trip range is computed using knowledge of the spacecraft position, laser pointing, timing and ranging parameters along with the surface height. Multiple surface height grids representing the ocean surface and various land areas can be used.

The GEODYN implementation of these measurement models supports Multi-Beam-Laser-Altimeters (MBLA), like that to be flown on VCL, as well as single beam instruments like ICESat's Geosciences Laser Altimeter System (GLAS). Laser range observation time tag bias, spacecraft attitude time tag bias, range observation bias and scale, and laser pointing parameters can be estimated. These parameters can be recovered on a time period basis where different parameter sets can be estimated for each distinct time period within a data reduction arc. Multiple time periods of user-defined length can be employed. The pointing parameterization is sufficiently complex to allow for the estimation of both laser and spacecraft body pointing bias, drift, quadratic and periodic terms. This level of detail facilitates the calibration of pointing effects due to thermal and environmental drivers and not simply constant pointing bias misalignments. The pointing parameterization is discussed in detailed in Luthcke et al. (2000).

3 ANALYSIS and RESULTS OVERVIEW

Several pre-launch simulations and error analyses have been conducted to gauge the performance of the integrated residual analysis algorithms and methodology. Luthcke et al. (2000) detail an extensive pre-launch error analysis and set of simulations to quantify the performance of "ocean sweep" maneuvers in calibrating VCL and ICESat pointing and range corrections. Practical design considerations, the impact of various error sources and performance results are discussed. The paper shows how the recovery of pointing corrections can be made to the sub-arcsecond level for a single maneuver under the worst expected conditions taking into account a detailed error model. The paper also shows how complex variations in pointing misalignment (e.g. orbital period and laser "warm-up" temporal variations) can be recovered using the calibration maneuver and the resultant direct altimeter ranges.

Additional simulations have been conducted to gauge the performance of land direct altimetry and dynamic crossovers. While these simulations were not performed to the same rigor as the ocean sweep error analysis described in Luthcke et al. (2000), they do provide important insight. An ICESat 8-day repeat crossover simulation was performed to quantify the ability of the dynamic crossovers to recover a simple pointing misalignment bias. Both land and ocean crossovers were simulated (6,797 land and 8,106 ocean). Only nadir pointing direct altimeter ranges were considered in the crossover simulation, and no errors other than ranging noise were simulated. The GTOPO-30 DEM was used to simulate the land ranges, while an ellipsoid was used to simulate the ocean ranges. The simulation showed that the dynamic crossovers were capable of recovering a simple pointing misalignment to 0.34 arcsecond (noise only) as compared to 0.06 arcseconds (noise only) for a single ocean sweep maneuver. Although, it should be noted again, that this is a nadir pointing only case, and it is expected that the results would be further improved if there were some variation in pointing during the 8-day repeat. Additionally, another simple (noise only) simulation was performed to look at the ability to recover ICESat pointing misalignment using direct altimetry from highly accurate 50km to 1600 km land Digital Elevation Model "patches". This land DEM direct altimetry technique is capable of recovering a simple pointing misalignment to the 0.15 arcsecond (noise only) level.

Although, these simulations and detailed error analyses show the power of each separate technique, the real strength in the integrated residual analysis approach is the ability to simultaneously estimate the instrument/geolocation parameters from a combination of calibration data including direct altimetry from ocean surface and detailed land calibration site DEMs, and dynamic crossovers. While data from a few, small (~100 km pass length) detailed calibration sites provides an opportunity to estimate simple geolocation parameter biases for that particular time and location, by combining these data with global crossovers and long duration ocean sweeps we can further the accuracy and observe complex environmental and system related variations in the calibrated geolocation parameters.

While it is important to perform the various pre-launch error analyses and simulations, these studies do not fully test the laser altimeter measurement model algorithms and processing software. Systematic errors in the software and algorithms can cancel and may not be detected in pre-launch simulations. In preparation for VCL and ICESat, it is imperative that these algorithms are rigorously tested. Complete testing includes the processing of actual Earth observing spaceborne laser altimetry to fully test the algorithms, reference frames and geophysical models. While the dynamic crossover capability was exercised on MGS data, still further testing is needed to verify the algorithms for the processing of an Earth orbiting laser altimeter's data in conjunction with the direct altimetry algorithms. In addition, the application of intra-mission crossovers must also be tested and verified. Towards this end, the data from two Shuttle Laser Altimeter missions (SLA-01 and 02) have been reprocessed and analyzed in detail. Applying the new integrated residual analysis measurement model algorithms and capabilities has resulted in an

Enhanced Data Product (EDP) geolocation, which represents a significant improvement over the current SLA Standard Data Products (SDP). The details of this SLA/EDP analysis, and the results obtained are discussed in Luthcke et al. (2001). A brief overview of the analysis and results found in Luthcke et al. (2001) are provided below.

Data from several SLA-01 and SLA-02 observation periods, representing a good sampling of the mission data, have been reprocessed using the integrated residual analysis algorithms, software and analysis methodologies. Residual and overlap performance have been used as metrics to determine the optimal data weighting (between tracking and altimeter data) and orbit, pointing, ranging and timing parameterization. Significant improvements in geolocation have been achieved from a combined reduction of laser altimeter range observations and spacecraft tracking data simultaneously estimating pointing, ranging and orbit parameters. Intra-mission dynamic crossovers with TOPEX/Poseidon (T/P) (constructed from SLA laser and T/P radar direct altimeter ranges) have been used to contribute to the orbit and geolocation parameter recovery, and both inter- (constructed from SLA only direct altimeter ranges) and intra-mission crossovers have been used to assess the solution performance. Resultant SLA-01 enhanced geolocation precision is on the order of 40 m RMS horizontal and 26 cm RMS in elevation. Independent DEM profile accuracy assessments show similar performance at 60 m horizontal positioning. Ocean range residuals show the SLA ranging performance is now at the 1m level. Overall improvement over the SLA-01 SDP geolocation is nearly a factor of two. Orbit precision and accuracy have also been improved by more than a factor of 2 over the SDP orbits and are at the 30cm radial RMS level. Detailed analyses of SLA-02 enhanced data geolocation, also obtained from a combined solution, show significant improvement in resultant overlap, residual and DEM profile comparison performance. Finally, the analysis presented in Luthcke et al. (2001) shows that complex temporal variations in pointing, and not just simple biases, can and must be recovered for accurate geolocation.

4 CONCLUDING REMARKS

While the shuttle is not a geodetic satellite and the SLA does not possess the ranging performance that both VCL and ICESat will achieve, the data has been invaluable in developing, validating and assessing our processing algorithms, software and methodologies. Furthermore, when taking into account the SLA data limitations and the various simulations and error analyses performed, the results achieved show that the integrated residual analysis algorithms, software and methodologies can, and will meet VCL and ICESat geolocation performance requirements. A truly combined calibration solution for VCL and ICESat instrument and geolocation parameters will be made processing direct altimetry from “ocean sweeps” and detailed land calibration sites along with land and ocean dynamic crossover (both inter- and intra-mission) and spacecraft tracking data.

REFERENCES

[Luthcke et al., 2000] Luthcke, S.B., D.D Rowlands, J.J. McCarthy, D.E. Pavlis, and E. Stoneking, “Spaceborne Laser-Altimeter-Pointing Bias Calibration from Range Residual Analysis,” *Journal of Spacecraft and Rockets*, Vol. 37, No. 3, May-June 2000.

[Luthcke et al., 2001] Luthcke, S.B., C.C. Carabajal, D.D. Rowlands, “Enhanced geolocation of spaceborne laser altimeter surface returns: parameter calibration from the simultaneous reduction of altimeter range and navigation tracking data,” *Journal of Geodynamics, Special Issue on Laser Altimetry*, in review, 2001.

[Pavlis et al., 1999] Pavlis, D. E., Moore, D., Luo, S., McCarthy, J. J., and Luthcke, S. B., “GEODYN Operations Manual: 5 volumes," Raytheon ITSS, Greenbelt, MD, December, 1999.

[Rowlands et al., 1999] Rowlands, D.D., Pavlis, D.E., Lemoine, F.G., Neumann, G.A., and Luthcke, S.B., “The Use of Laser Altimetry in the Orbit and Attitude Determination of Mars Global Surveyor,” *Geophysical Research Letters*, Vol. 26, No. 9, May, 1999, pp. 1191-1194.

[Rowlands et al., 2000] Rowlands, D.D., Carabajal, C.C., Luthcke, S.B., Harding, D.J., Sauber, J.M. and Bufton, J.L., “Satellite Laser Altimetry: On-Orbit Calibration Techniques for Precise Geolocation,” The Review of Laser Engineering, Vol. 28, No. 12, December 2000, pp. 796-803.

Recovery of Systematic Biases in Laser Altimeters Using Natural Surfaces

Sagi Filin
Department of Civil and Environmental Engineering and Geodetic Science, The Ohio State University
Department of Geodesy, Faculty of Civil Engineering and Geosciences, Delft University of Technology, The Netherlands*
s.filin@citg.tudelft.nl

Commision 3, Working Group 3

KEY WORDS: Laser Altimetry, Error model, Calibration

ABSTRACT

Elements of accuracy of LIDAR systems and the corrections of systematic errors have received growing attention in recent years. The expected level of accuracy and the additional processing that is needed for making the raw data ready to use are affected directly by the systematic errors in the laser data. It is evident that calibration of the LIDAR system, both laboratory and in-flight, are mandatory to alleviate these deficiencies. This paper presents an error recovery model that is based on modeling the system errors and on defining adequate control information. The association of the observations and control information, and configurations that enhance the reliability of the recovered parameters, are also studied here in detail.

1 Introduction

Laser altimetry has emerged in recent years as a leading technology for capturing data of physical surfaces. Properties like the relatively high accuracy, the expected short turnout time, and a detailed and almost ready-made digital surface model (DSM) that is generated by the system, ensure the growing interest in this technology. While a detailed coverage of the surveyed surface is achieved by an increased system sampling rate and thereby the point density, achieving the expected level of accuracy and ensuring a short turnout time depend in large on maintaining the potential quality of the data. A major factor that affects the data quality is the existence, and thus removal, of the systematic errors in the data.

A growing number of publications in recent years report the existence of systematic errors in the laser data and their effect on the accuracy and on the processing of laser data. For example, Huising and Gomes Pereira (1998) report about systematic errors of 20 cm in elevation and of several meters in position between overlapping laser strips, Crombaghs et al. (2000) and Vosselman and Mass (2001) identify systematic trends between overlapping strips, and Hofton et al. (2000) report about identifying systematic errors in NASA's Scanning Lidar Imager of Canopies by Echo Recovery (SLICER) (Blair et al., 1994). The systematic errors have several effects on the laser data. Clearly they degrade the accuracy of the geolocation of the laser footprint. Furthermore, they distort the surface that is reconstructed by the laser data in several ways, some of them linear (shifts and rotations) but others not. One consequence of the distortions is that surveyed objects in the overlapping areas of different laser swaths may not coincide. Corrections then require a relatively long preprocessing time that, in turn, increases the turnout time. Reducing the effect of such errors requires pre-flight system calibration (Krabill et al., 1995; Ridgway et al., 1997) as well as in-flight calibration.

To eliminate the effect of the systematic errors, several procedures have been proposed so far. One group can be categorized as data driven. The motivation is to correct the laser points by transforming them so that the difference between their values and the reference control information is minimized, namely,

$$\| (x_w, y_w, z_w) - T(x_l, y_l, z_l) \| = min \qquad (1)$$

where the subscripts l, w denote laser and world respectively, and $\| \ \|$ is the l_2 norm. Mostly, the corrections are modeled by means of the similarity transformation (Postolov et al., 1999; Crombaghs et al., 2000; Mass, 2000), which involves translations and rotations of the laser points. Another approach is based on recovering the systematic *system* errors. Several authors report recovering the errors by conducting different flight patterns over flat locally horizontal surfaces and "flattening" the surface as a function of the systematic errors (Vaughn et al., 1996; Ridgway et al., 1997; Hofton et al., 2000). Others (e.g., Kilian et al., 1996) base their calibration procedure on control, height, and tie points, in a fashion similar to photogrammetric block adjustment, or propose to reconstruct the elevation model (Burman, 2000) around distinct landmarks to tie the overlapping strips.

The correction of laser points by means of a linear transformation focuses on the effect of the systematic errors but not on their causes. This may not always be appropriate; an analysis of the similarity transformation (Filin et al., 2001) reveals that not all error effects can be modeled, and thus removed, by this transformation. Therefore, some accuracy may be lost, and more complicated algorithms may be needed. Calibration approaches that are based on flying over flat locally horizontal surfaces have their own limitations. For one, planar surfaces are not always available, and furthermore they cannot model the effects of several error sources, like the positional offsets. In general, the concept of control information has not been fully explored. The information carried by laser points is rather limited as it consists of the 3–D coordinates of the laser point without any additional information such as radiometric intensity. The laser points position is, however, distorted by the errors, and identifying the footprint location (the actual location of the laser point) is practically impossible. Flattening the reconstructed surface is one way to circumvent the lack of information and identifying distinct control landmarks is another one. The limitations are, however, clear; both approaches require the existence of such objects, and in the case of distinct control features, they also depend on the altimeter sampling rate.

*The research was conducted while the author was with the department of Civil and Environmental Engineering and Geodetic Science at The Ohio-State University. The author is currently with the Department of Geodesy at Delft University of Technology.

The strategy presented in this paper is based on utilizing natural and man-made surfaces to recover the calibration parameters. The approach has several advantages. It is relatively simple to apply even in areas that traditionally are not considered favorable for calibration, and does not require control points or flat locally horizontal surfaces. The algorithm also simplifies the sought correspondence between the laser points and ground control information and offers a more general solution that does not depend on well-defined control landmarks. In addition, the formulation enables one to model the outcome of different systematic effects and to analyze the preconditions for their recovery. Thereby, an analytical look into the potential recovery of different biases is made possible.

The paper is organized as follows. The next section presents the approach for the error recovery, it consists of the error modeling and the recovery model. Following is an analysis of the model properties, and of elements that enhance the reliability of the recovered parameters. Results and discussion conclude the presentation.

2 Error recovery

In-flight calibration of laser systems is complicated. The error model involves the intrinsic errors of each system component as well as errors that are a consequence of their integration. A detailed error model is provided by Schenk (2001), but it is clear that the error model is not yet fully understood. In addition, the calibration procedure involves more than the formulation of an analytical error model. System calibration belongs, in general, to the class of inverse problems. For many of them knowledge about the relation between the target and domain data (dubbed here correspondence) is assumed to be known, so the focus is on solving the inverse problem. With laser mapping, however, it is impossible to know the exact footprint location, and thus establishing a relation between the domain (a laser point) and the target data (the footprint). Solving the inverse problem requires to find first the correspondence by some method. This problem indicates that the calibration is in fact a strategy rather than a formulation of the calibration equation. The geometric realization of the data acquisition system poses another problem. In general, from each firing point only one beam is being transmitted and therefore leaves no intrinsic redundancy. One potential effect of this configuration is an increased correlation of the calibration parameters that implies that not all the systematic errors may be recovered independently. Therefore, another question is which errors can be recovered and how to solve for them.

The approach taken here is focused on the geolocation of the laser footprint. The goal is finding the best geolocation of the laser points in terms of minimizing the l_2 norm of the differences between the laser point coordinates and the ground. Two spatial relations are involved in this modeling – the laser geolocation equation and the surface model. The geolocation and the error modeling are presented first.

2.1 Footprint geolocation and error modeling

The laser geolocation equation models the incorporation of the different components of a laser altimeter system by means of the transformations between the different reference frames. The form is well established (see e.g., Vaughn et al., 1996; Schenk, 2001) and is given in eq. 2.

$$\begin{bmatrix} x_l \\ y_l \\ z_l \end{bmatrix} = \begin{bmatrix} X_0 \\ Y_0 \\ Z_0 \end{bmatrix} + R_W R_G R_{INS} \left(\begin{bmatrix} \delta_x \\ \delta_y \\ \delta_z \end{bmatrix} + R_m R_s \begin{bmatrix} 0 \\ 0 \\ -\rho \end{bmatrix} \right) \tag{2}$$

where:

- x_l, y_l, z_l – location of the footprint in WGS-84 geocentric coordinate system.
- X_0, Y_0, Z_0 – location of the phase center of the GPS receiver.
- R_W – rotation from the local ellipsoidal system into the WGS-84 geocentric reference frame.
- R_G – rotation from reference system defined by the local vertical, to the ellipsoidal reference frame.
- R_{INS} – rotation from body reference frame to reference frame defined by local vertical. Rotations are defined according to the INS angles.
- δ_x, δ_y, δ_z – offset vector between the phase center of the GPS antenna and laser firing point, defined by the body frame.
- R_m – the mounting bias, which designate rotation between the altimeter and the body frame.
- R_s – rotation between laser beam and laser system defined by scanning angles.
- ρ – range measured by laser system.

The systematic errors are analytically modeled by their effect on the geolocation equation. A standard error model is yet to be set, and the literature shows that the type of modeled errors vary from one author to another. Schenk (2001) lists as many as six potential groups of error sources. They include (i) ranging errors, (ii) scan angle errors that consist of an error in the swath angle, and in the determination of the scan plane, (iii) mounting errors that consist of errors in determining the alignment between altimeter and the INS, and of an error in the determination of the offset between the phase center of the GPS antenna and the laser system, (iv) INS errors (v) position errors, and (vi) timing errors. Some of these errors may be fixed during the flight mission, while others may vary over time or as a function of position. Identifying the effect of each error source is not always possible and under given conditions several groups of the errors can have similar effects. A detailed study of the effects and conditions for the recovery of the errors can be found in Schenk (2001) and Filin (2001). In this paper, two error sources that are considered to have the major effect on the geolocation (see e.g., Vaughn et al., 1996; Hofton et al., 2000; Ridgway et al., 1997) are studied. They consist of the mounting bias and the range bias. The effect of the mounting bias was modeled already in eq. 2, and the range bias models a constant offset in the range determination. An interesting effect of the range bias is that it may result in a nonlinear surface deformation. The mounting bias can be approximated, in general, by measurements prior to the mission and can be treated as composed of a measured part and am unknown part (thus modeled as $\Delta R_m R_m$, with ΔR_m as the unknown part). For simplicity it is modeled here as a single entity with the measured part considered as a first

approximation. The modified geolocation equation with the two error sources, and the effect of the random errors is given in eq. 3

$$\begin{bmatrix} x_l \\ y_l \\ z_l \end{bmatrix} = \begin{bmatrix} X_0 \\ Y_0 \\ Z_0 \end{bmatrix} + R_W R_G R_{INS} \left(\begin{bmatrix} \delta_x \\ \delta_y \\ \delta_z \end{bmatrix} + R_m R_s \begin{bmatrix} 0 \\ 0 \\ -(\rho + \delta\rho) \end{bmatrix} \right) + \begin{bmatrix} \bar{e}_x \\ \bar{e}_y \\ \bar{e}_z \end{bmatrix} \quad (3)$$

with $\delta\rho$ – the range bias, $\bar{e}_x, \bar{e}_y, \bar{e}_z$ – and the random errors for the x, y, and z coordinates respectively. The mounting bias can be described by the three Euler angles, and, together with the range bias, there are four unknowns. Performing the following derivations in a geocentric reference frame does not contribute much to the problem formulation. As the term $R_W R_G$ can be approximated by a constant for a relatively large surface size, it is multiplied out and the reference frame is also shifted to the surface elevation, thereby forming a local reference frame.

2.2 Error recovery model

To recover the systematic biases the surface is introduced as a constraint. A general expression for a surface is given in eq. 4

$$f(x, y, z) = 0 \quad (4)$$

The footprint coordinates can be viewed as a vector-valued function g of the observations – Y, the systematic errors – Ξ, and the random errors - $\overline{e}$ that is written in the following form – $\mathbf{l} = g(Y, \Xi, \bar{e})$, with $\mathbf{l} = [x_l, y_l, z_l]^T$. Consequently, the following relation can be written

$$f(x_l, y_l, z_l) = h(Y, \Xi, \bar{e}) = 0 \quad (5)$$

with h the implicit representation of the surface as a function of the observations, and the systematic and the random errors. The obvious target function is minimizing the l_2-norm of the residual vector, which also has the property of providing the best linear uniformly unbiased estimate for the parameters.

An explicit form of the surface function is, in general, not known. It is more realistic to assume that the surface consists of a set of surface elements, each with its analytical form. The current modeling assumes that the surface can be represented by a set of a planar surfaces

$$s_1 x + s_2 y + s_3 z + s_4 = 0 \quad (6)$$

although any other surface model can be used. In this form $\mathbf{s} = [s_1, s_2, s_3]$ is the surface normal direction and s_4 is the intercept point. The surface parameters are considered here to be known a priori. Incorporation of the surface constraint and geolocation equation (eq. 3) is given in eq. 7

$$\mathbf{s} \left[\begin{bmatrix} X_0 \\ Y_0 \\ Z_0 \end{bmatrix} + R_{INS} \left(\begin{bmatrix} \delta_x \\ \delta_y \\ \delta_z \end{bmatrix} + R_m R_s \begin{bmatrix} 0 \\ 0 \\ -(\rho + \delta\rho) \end{bmatrix} \right) \right] + \mathbf{s} \begin{bmatrix} \bar{e}_x \\ \bar{e}_y \\ \bar{e}_z \end{bmatrix} + s_4 = 0 \quad (7)$$

The relation in eq. 7 is the scalar product between the representation of the laser point in homogeneous coordinates and the surface, namely,

$$\bar{\mathbf{s}} \cdot \bar{\mathbf{l}} = 0 \quad (8)$$

with $\bar{\mathbf{s}} = \begin{bmatrix} s_1 & s_2 & s_3 & s_4 \end{bmatrix}$ and $\bar{\mathbf{l}} = \begin{bmatrix} x_l & y_l & z_l & 1 \end{bmatrix}$.

Linearization of this form is given in eq. 9. First approximations can either be set to zero or to the prior information values if ones exist.

$$\bar{\mathbf{s}} \cdot \bar{\bar{\mathbf{l}}} = (\mathbf{s} R_{INS} \mathbf{U})_{1\times 3} \begin{bmatrix} \kappa \\ \phi \\ \omega \end{bmatrix}_{3\times 1} + (\mathbf{s} R_{INS} R_s)_{1\times 3} \begin{bmatrix} 0 \\ 0 \\ \delta\rho \end{bmatrix} + \mathbf{s}\bar{e} \quad (9)$$

with ω, ϕ, κ, the bias angles along the x, y, and z-axes, respectively; $\bar{\bar{\mathbf{l}}}$, the approximation for the geolocation of the laser point (according to the current knowledge of the biases), and $\mathbf{U}_{3\times 3}$ a matrix of the form

$$\mathbf{U} = \begin{bmatrix} -v & w & 0 \\ u & 0 & -w \\ 0 & -u & v \end{bmatrix} \quad (10)$$

where

$$\begin{bmatrix} u \\ v \\ w \end{bmatrix} = R_s \begin{bmatrix} 0 \\ 0 \\ -\rho \end{bmatrix} \quad (11)$$

Notice that each laser point contributes one equation. The model parameters are recovered via the Gauss-Helmert model,

$$w_n = A_{n\times m}\xi_m + B_{n\times 3n} e_{3n} \quad , \quad e \sim \{0, \sigma_0^2 P^{-1}\} \quad (12)$$

with w, the transformed observation vector; A, the coefficient matrix; B, the conditions matrix; ξ, the vector of unknowns; e, the observational noise; P, the weight matrix; σ_0^2, the variance component; n, the number of laser points; and m, the number of unknowns. The least-squares criterion results in

$$\hat{\xi} = (A^T (B P^{-1} B^T)^{-1} A)^{-1} A^T (B P^{-1} B^T)^{-1} w \quad (13)$$

with:

$$\hat{D}\{\hat{\xi}\} = \hat{\sigma}_0^2 (A^T (B P^{-1} B^T)^{-1} A)^{-1} \quad (14)$$

$$\hat{\sigma}_0^2 = \frac{(B\tilde{e})^T (B P^{-1} B^T)^{-1} (B\tilde{e})}{n - m} \quad , \; B\tilde{e} = w - A\hat{\xi}. \quad (15)$$

Notice that with this formulation the essence of the problem is modeled; the 3–D laser points and the surface are constrained. Furthermore, an explicit surface model incorporates additional information about the terrain, such as slopes, into the calibration model. In addition, with this formulation, no

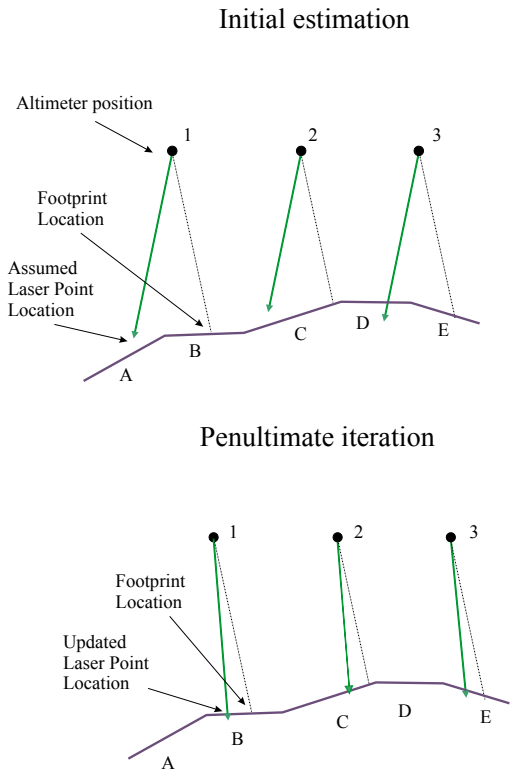

Figure 1: The iteration process – second level

restriction on the surface type, e.g., flat locally horizontal surfaces, is needed. The approach is also independent of the altimeter system sampling rate. Instead of focusing on the reconstructed surface the model concerns the laser points themselves. Therefore, distinct landmarks such as breaklines and corners are not needed; the focus, here, is on minimizing the distances between the points to the ground, the density of the laser points is, therefore, not as significant.

Extension of this model to accommodate for other types of errors can be carried out by modifying the laser geolocation equation. The extension however does not mean that all the errors are recoverable; further analysis of recoverability conditions is required.

3 Model Analysis

The construction of the error recovery model enables one to study of several aspects in greater detail. One aspect is establishing a more general model for the correspondence between the laser points and the surface. Another is analyzing the configurations that enhance the reliability of the parameter recovery.

3.1 Detection of the correspondence

The proposed model simplifies significantly the detection of the correspondence between the laser points and the control information; the association here is between the laser points and the surface elements that contain the footprint. That is a subtle but important difference between association of the laser points and their corresponding ground position. The current association is less restrictive insofar as it does not require well-defined 3–D landmarks for calibrating the system. In fact, laser points that fall "inside" ordinary surfaces (i.e., not "on" or near breaklines) are as good or even better than any other points in terms of accuracy.

Nevertheless, simplifying the correspondence does not guarantee that the initial association between the laser points, before being corrected for the systematic errors, and the surface elements is indeed correct. It is still possible that the laser points will fall inside wrong surface elements; see, for example the initial estimations in Figure 1. Here, point **1** is initially associated with surface element **A** instead of surface element **B**, point **2** is correctly associated with surface element **C**, and point **3** is, again, wrongly associated with surface element **D** instead of **E**. The approach presented here solves this problem by an iterative convergence to the true solution. The approach resembles the concepts of deformable templates, and the Iterative Closest Point (ICP) algorithm (Besl and McKay, 1992). The algorithm works as follows. Correspondence is established by the initial location of the laser points; surface parameters are then derived for each laser point. After construction of the observation and condition matrices and the transformed observation vector, the parameters are estimated by the Gauss-Helmert model (eq. 12). In the following iteration the correspondence is updated according to the modified position of the laser point, and the computation of the systematic errors repeats itself. Convergence is reached when the errors are not updated further, which occurs when the points fall on the true surfaces, see the penultimate iteration in figure 1. The algorithm below summarizes the steps that are taken

1. initialize $\hat{\Xi}$ and $\hat{\xi}$
2. **while** $\hat{\xi} \neq 0$, **do**
3. **for each** laser point, $\mathbf{l}_j$, **do**
4. compute the incident point – $\{x_j, y_j, z_j\} = g(\mathbf{l}_j, \hat{\Xi}_i)$
5. compute $\mathbf{s}_j = f(x_j, y_j, z_j)$
6. Solve for $\hat{\xi}_i$ using eq. 13
7. $\hat{\Xi} = \hat{\Xi} + \hat{\xi}$
8. **endwhile**
9. declare convergence,

Problems may be encountered with points near breaklines between surfaces with a relatively big height discontinuity. The large differences are likely to bias the solution to compensate for the differences. This problem can be circumvented either by robust estimation techniques, or by removing error prone points prior to the adjustment, for example, by evaluating the homogeneity of points' neighborhood.

3.2 Configuration and Reliability

The analytical error recovery model that was derived in Section 2.2 provides a closed form that incorporates the laser points, the errors and the surface parameters. It enables the analysis of the elements that influence the recovery of the systematic biases and the study of configurations that provide a better and more reliable estimation of the systematic errors. The analysis begins with the linearized form of the observation equations given in equation 9. An explicit form is given by

$$w = -(c_2\omega_i + c_3)\delta\rho + (-c_1 v + c_2 u)\kappa + (c_1 w - c_3 u)\phi + (-c_2 w + c_3 v)\omega + s_1\bar{e}_x + s_2\bar{e}_y + s_3\bar{e}_z \quad (16)$$

with $\mathbf{c} := \begin{bmatrix} c_1 & c_2 & c_3 \end{bmatrix} = \mathbf{s}R_{INS}$. The vector $\mathbf{c}$ can be viewed as a modified surface slope determined as a function of the aircraft attitude and the surface slope. The values for u, v, w are defined by eq. 11.

The form in equation 16 is general and can be applied to different types of scanning systems. We analyze it with respect to a linear scanner configuration which is widely used in laser mapping. For a linear scanning system the rotation matrix R_s is given by $R_s = R_x(\omega_i)$. Consequently the laser beam pointing direction can be approximated by $\begin{bmatrix} u & v & w \end{bmatrix} \approx \begin{bmatrix} 0 & -\omega_i\rho & -\rho \end{bmatrix}$. Equation 16 can be written then as

$$w = -(c_2\omega_i + c_3)\delta\rho + c_1\omega_i\rho\kappa - c_1\rho\phi + \\ - (c_2 + c_3\omega_i)\rho\omega + s_1\bar{e}_x + s_2\bar{e}_y + s_3\bar{e}_z \quad (17)$$

The recovery of the calibration parameters depends in large on the modified surface slope and on the scanning angle; the positional dependency shows itself only through the range, but this effect is not big. The dependency on the angular quantities vary, however, from one parameter to another. Equation 17 shows that the pitch bias, ϕ, depends on the modified slope c_1 along the flight direction while the coefficients for the mounting bias in the roll direction, ω, depends on the modified surface slope across the flight direction. This coefficient can be viewed as the sum of the surface tilt across the flight direction and the scanner pointing angle. The coefficient for the heading bias, κ, depends on the product of the slope along the flying direction and the pointing angle and is expected to be smaller by an order of magnitude compared to the other two. The coefficient for the range bias can be regarded fixed up to variations as a function of surface slope along the flying direction and the scanning angle.

To recover the four biases simultaneously, the observation matrix, A, should have neither zero nor linear dependent columns. Equation 17 shows that zero columns can occur if the modified surface slopes in the roll direction c_1 is constantly equal to zero, namely a zero slope along the flying direction. It is very unlikely to encounter situations in which the roll bias coefficients are all zero or close to zero, unless c_2 and ω_i constantly cancel one another. The scanner angle contribution indicates that no slope variation across the flying direction is needed to recover the roll bias. Notice also that the slope variations can be achieved by aircraft maneuvers, so theoretically the recovery of the four parameters can be performed by flying over a flat horizontal surface. This is however not an optimal configuration because maneuvers may introduce additional errors that will degrade the quality of the estimated parameters. It is, therefore, recommended to recover the errors by using observations taken over sloping surfaces. Configurations that result in a linear dependency or in columns that are almost similar are possible to construct. One example, is using observations in which the value of the scan angle, ω_i is almost fixed. With this configuration the coefficients for κ and ϕ are similar. Another configuration that may result in similar columns occurs when calibrating the system over a single surface or surfaces with almost the same slope. Under such configuration high similarity is expected between the range and the pitch bias coefficients, and if c_2 is equal to zero, also between the heading and the roll bias. It is therefore recommended to use observations from the two sides of the swath and to use surface elements with different slopes.

Conf.	Slope		Cond.	
	s_1	s_2	Number	$tr\{N^{-1}\}$
I	0.01	0	236758.035	243.1
	-0.01	0		
II	0.1	0	13834.425	10.3
	0.2	0		
III	-0.1	0	2309	2.4
	0.1	0		
IV	-0.15	0	1050	1.1
	0.15	0		
V	-0.2	0	587	0.6
	0.2	0		
VI	-0.2	0.1	580	0.6
	0.2	-0.1		
VII	-0.2	0.1	650	0.6
	0.2	0.1		

Table 1: Effect of slope distribution

Configurations that enhance the reliability of the recovered parameters should minimize the trace of the dispersion matrix

$$tr\{D\{\hat{\xi}\}\} = min \quad (18)$$

and results, in general, in a relatively small condition number and small correlation between the estimated parameter. The term configuration refers here to the slopes of the surface rather than to their spatial organization. Big surface slopes, and surface slopes in different directions have the effect of increasing the diagonal elements of the normal equations while reducing the off diagonal ones. Thus, smaller correlations and a smaller trace can be achieved this way.

The effect of different surface configurations is demonstrated in Table 1. The configurations are analyzed by the conditions number and by the trace of the cofactor matrix, $N^{-1} := (A^T(BP^{-1}B^T)^{-1}A)^{-1}$. With the first configuration the errors are recovered by flying over a surface with very mild slopes (one percent). The condition number is large and so is the trace of the cofactor matrix; the results are therefore less reliable. With the second configuration the errors are recovered by flying over surfaces with relatively big slopes, but ones that are pointing in the same direction. Comparing the results to those obtained by the third configuration demonstrates the effect of using surfaces that point in opposite directions. The trace of the cofactor matrix for configuration III is five times smaller than the one for configuration II, even though the surface slopes in configuration II are bigger. Configurations III-V show the effect of using steeper slopes. As can be seen, the trace decreases from 2.4 to 0.6 as the slopes change from 10 percent to 20 percent. In general, steeper slopes are preferable than smaller ones, however, the rang-

1.00	0.94	-0.08	0.08
0.94	1.00	-0.08	0.08
-0.08	-0.08	1.00	-0.94
0.08	0.08	-0.94	1.00

Table 2: Correlation matrix for configuration II, surface slopes pointing in the same direction

1.00	-0.10	-0.08	0.02
-0.10	1.00	-0.02	0.09
-0.08	-0.02	1.00	-0.04
0.02	0.09	-0.04	1.00

Table 3: Correlation matrix for configuration III, surface slopes pointing in positive and negative directions

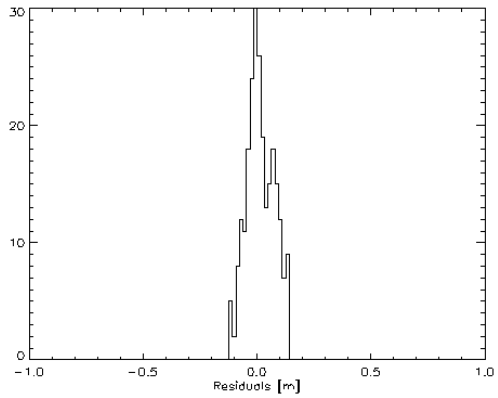

Figure 2: Frequency of residuals after removal of systematic errors

ing accuracy decreases as a function of the slope increase, so the effect of steeper slopes is balanced by smaller weights. Configuration VI and VII show that surface slopes across the flight direction do not contribute to the quality of parameter estimation. The effect of the estimation of the κ angle on the condition number and the trace was evaluated in regards to configuration III. When recovering only the three parameters (assuming no bias in the heading direction) the condition number was reduced to 25 and the trace to 0.4. Eliminating other angular biases did not change much the original values.

The effect of the pointing direction of the surface slopes on the parameters correlation is demonstrated with respect to configurations II and III. Tables 2 and 3 list the correlation matrices of the estimated parameters for these two configurations. The order of parameters is - the range, the pitch, the roll, and the heading biases. The results show that the use of surfaces that point in positive and negative directions has also the effect of reducing the correlation, and thus making the recovery of each systematic error almost independent. Notice also that the high correlation in configuration II is between the range and the pitch bias and the heading and the roll bias. This type of correlation was anticipated when calibrating the system over surfaces with similar slopes (see the discussion above about configurations that result in high similarity between columns). The results show that even when variations in the surface slope are significant (but in the same direction) the similarity between the coefficients of the different parameters is high.

4 Discussion and results

The results of the analysis show that recovering the systematic error of LIDAR system is a manageable task, and one that can result in reliable estimates. The results show that by fairly simple means, like surfaces pointing in different directions solutions with a low condition number, and low correlation can be generated. Utilizing natural surfaces or man-made objects to resolve the systematic errors make this formulation advantageous to the existing methods as it neither limits the solution to flat surfaces nor requires distinct control features. Notice that the need for preliminary knowledge about the correspondence between laser points and the ground is removed; the proposed formulation solves for the calibration parameters and the correspondence simultaneously. In addition, with this model the solution to the correspondence problem is an integral part of the calibration model; no additional algorithms are needed to solve this part.

Experiments with the recoverability of the potential error sources shows that solutions with a minimum correlation and small variance can be achieved. The approach was applied to recover the calibration parameters of the NSF-SOAR (National Science Foundation Support Office for Aerogeophysical Research) laser altimetry system. The NSF-SOAR system is a unique suite of geophysical, mapping and navigational instruments, mounted in a ski-equipped aircraft. The system was flown in Antarctica to map surface elevation changes on the West Antarctica Ice Shelf (WAIS) ice streams (Spikes et al., 1999). The calibration of the NSF-SOAR laser system posed a challenge for existing calibration approaches since the whole mission was performed in the interior of the WAIS where neither flat surfaces nor distinct features were available. The profiling configuration also meant a relatively sparse sampling – one point per eight meters – and the comparison of a two dimensional object to a three dimensional one. Ground control information was available from snowmobile-mounted GPS surveys that was conducted along the skiways and their surroundings. Control surfaces were formed by a triangulation of the points, and planar surface parameters were computed using plane fitting. The site was overflown several times including flights with constant attitude as well as with pitch or roll maneuvers. Data from flight segments that contributed to achieving the optimal configuration were used as observations. The parameters were recovered in a fairly high level of accuracy. Figure 2 presents the residual distribution after the system calibration. Evaluating the statistical characteristics shows that $\hat{\sigma}_0 = 0.06$m, the condition number for this calibration configuration is $C = 800$, and the highest correlation is 30 percent and the others are less than ten. These values validate the analysis in Section 3.2 and show than solutions with small variance and low correlation can be achieved even under less than optimal conditions.

5 Concluding remarks

This research studied the calibration of a laser altimeter system. An analysis of the data characteristics and the data acquisition concept has indicated a need for a model that is different from the traditional data registration concepts, e.g.,

the ones applied in photogrammetry. It was identified that the two prevailing problems are the nonredundant determination of laser points and the unknown correspondence between laser points and the spot they illuminate on the ground.

By analyzing the properties of the proposed method, it has been demonstrated that moderate slopes are sufficient to generate reliable solutions. The only requirement consists in having the surface elements oriented in different directions. The compelling conclusion is that natural terrain will yield results that are accurate and reliable.

Acknowledgment

The author would like to acknowledge Dr. Bea Csathó for making the NSF-SOAR data available and for her help in processing the data. This work was funded in part by the National Science Foundation grant OPP- 9615114.

REFERENCES

Besl, P. J. and N. D. McKay (1992). A method for registration of 3–D shapes. *IEEE Trans. on PAMI*, **14**(2): 239–256.

Blair, B., B. Coyle, J. L. Bufton and D. Harding (1994). Optimization of an Airborne Laser Altimeter for Remote Sensing of Vegetation and Tree Canopy. *Proceedings of IEEE*, 939–941.

Burman, H. (2000). Adjustment of laser scanner data for correction of orientation errors. *International Archives of Photogrammetry and Remote Sensing*, **33**(B3/1): 125–132.

Crombaghs, M., E. De Min and R. Bruegelmann (2000). On the Adjustment of Overlapping Strips of Laser Altimeter Height Data. *International Archives of Photogrammetry and Remote Sensing*, **33**(B3/1): 230–237.

Filin, S. and B. Csathó (1999). A Novel Approach for Calibration of Satellites Laser Altimeters. *International Archives of Photogrammetry and Remote Sensing*, **32**(3–W14): 47–54.

Filin, S., (2001), Calibration of spaceborne and airborne laser altimeters using natural surfaces. PhD Dissertation Department of Civil and Environmental Engineering and Geodetic Science, the Ohio-State University, Columbus, OH. To be published as a report in Geodetic Science and Surveying

Filin, S., Csathó, B., Schenk T., (2001), An Analytical Model for In-flight Calibration of Laser Altimeter Systems Using Natural Surfaces, Proceedings of the Annual Conference of the American Society of Photogrammetry and Remote Sensing (ASPRS), St. Louis MS., published on CD-ROM.

Hofton, M., B. Blair, J. B. Minster, J. R. Ridgway, N. Williams, J. L. Bufton and D. L. Rabine (2000). An Airborne Laser Altimetry Survey of Long Valley, California. *Int. J. Remote Sensing* **21**(12): 2413–2437.

Huising, E. J. and L. M. Gomes Pereira (1998). Errors and accuracy estimates of laser data acquired by various laser scanning systems for topographic applications. *ISPRS J. of Photogrammetry and Remote Sensing*, **53**(5): 245–261.

Kilian, J., N. Haala and M. Englich (1996). Capture of Elevation of Airborne Laser Scanner Data. *International Archives of Photogrammetry and Remote Sensing*, **31**(B3): 383-388.

Krabill, W. B., R. H. Thomas, C. F. Martin, R. N. Swift and E. B. Frederick (1995). Accuracy of Airborne Laser Altimetry over the Greenland Ice Sheet. *Int. J. Remote Sensing*, **16**(7): 1211–1222.

Maas, H. G. (2000). Least-Squares Matching with Airborne Laserscanning Data in a TIN Structure. *International Archives of Photogrammetry and Remote Sensing*, **33**(B3/1): 548–555.

Postolov, Y., A. Krupnik and K. McIntosh (1999). Registration of airborne laser data to surface generated by photogrammetric means. *International Archives of Photogrammetry and Remote Sensing*, **32**(3–W14): 95–100.

Ridgway, J. R., J. B. Minster, N. Williams, J. L. Bufton and W. B. Krabill. 1997. Airborne laser altimeter survey of Long Valley California. *Int. J. Geophys.,* **131**, 267-280.

Schenk, T. (2001). Modeling and analyzing systematic errors of airborne laser scanners. *Technical Notes in Photogrammetry* No. 19, Department of Civil and Environmental Engineering and Geodetic Science, The Ohio State University, Columbus, OH., 40 pages.

Spikes, B., B. Csathó and I. Whillans (1999). Airborne laser profiling of Antarctic ice streams for change detection. *International Archives of Photogrammetry and Remote Sensing*, **32**(3–W14): 169–175.

Vaughn, C. R., J. L. Bufton, W. B. Krabill and D. L. Rabine (1996). Georeferencing of Airborne Laser Altimeter Measurements. *Int. J. Remote Sensing*, **17**(11): 2185–2200.

Vosselman G., and Maas, H. G. (2001). Adjustment and filtering of raw laser altimetry data. *In Proceeding of OEEPE workshop on Airborne laser scanning and interferometric SAR for detailed digital elevation model.*, Stockholm, Sweden.

LAND SURFACE MAPPING AND CHARACTERIZATION USING LASER ALTIMETRY

SESSION 4

DATA FUSION

INTEGRATION OF LIDAR AND LANDSAT ETM+ DATA

Andrew T. Hudak
Research Forester
Rocky Mountain Research Station
USDA Forest Service
United States of America
ahudak@fs.fed.us

Michael A. Lefsky
Assistant Professor
Department of Forest Science
Oregon State University
United States of America
lefsky@fsl.orst.edu

Warren B. Cohen
Research Forester
Pacific Northwest Research Station
USDA Forest Service
United States of America
wcohen@fs.fed.us

Mercedes Berterretche
Masters Degree Recipient
Department of Forest Science
Oregon State University
Uruguay
mebeae@adinet.com.uy

KEYWORDS: regression, kriging, cokriging, sampling, spatial model, geostatistics

ABSTRACT

Lidar data provide accurate measurements of forest canopy structure in the vertical plane however current lidar sensors have limited coverage in the horizontal plane. Landsat data provide extensive coverage of generalized forest structural classes in the horizontal plane but are relatively insensitive to variation in forest canopy height. It would therefore be desirable to integrate lidar and Landsat data to improve the measurement, mapping, and monitoring of forest structural attributes. We tested five aspatial and spatial methods for predicting canopy height, as measured by an airborne lidar system (Aeroscan), from Landsat ETM+ data: regression, kriging, cokriging, and kriging and cokriging of regression residuals. Our 200 km^2 study area in western Oregon encompassed Oregon State University's McDonald-Dunn Research Forest, which is broadly representative of the age and structural classes common in the region. We sampled our continuous lidar coverage in eight systematic patterns to determine which lidar sampling strategy would optimize lidar-Landsat integration: transects sampled at 2000, 1000, 500 and 250 m frequencies, and points sampled at these same spatial frequencies. The aspatial regression model results, regardless of sampling strategy, preserved actual vegetation pattern, but underestimated taller canopies and overestimated shorter canopies. The spatial models, kriging and cokriging, produced less biased results than regression but poorly reproduced vegetation pattern. The integrated models that kriged or cokriged regression residuals were preferable to either the aspatial or spatial models alone, because they preserved the vegetation pattern like regression yet improved estimation accuracies above those predicted from the regression models alone. We concluded that in our study landscape, an integrated modeling strategy is most suitable for estimating and mapping canopy height at locations unsampled by lidar, and that a 250 m point sampling strategy would be more useful for lidar-Landsat ETM+ integration than sparser transect sampling strategies planned for satellite missions.

1. INTRODUCTION

Lidar data provide detailed information on forest canopy structure in the vertical plane but over a limited spatial extent (Lefsky et al., in press). Landsat data provide useful structural information in the horizontal plane (Cohen and Spies, 1992) but are relatively insensitive to canopy height. Lidar-Landsat ETM+ integration is therefore a very logical goal to pursue. No remote sensing instrument is suited for all applications, and there have been several calls for improving the applicability of remotely sensed data through multisensor integration. Most multisensor integration studies published up to this point have involved Landsat imagery (e.g. Oleson

et al., 1995; Asner et al., 1997) but none have integrated Landsat imagery with lidar data.

Lidar-Landsat ETM+ integration has immediate relevance due to the anticipated launches of the Ice, Cloud, and Land Elevation Satellite (ICESat) and Vegetation Canopy Lidar (VCL) satellite missions. The global sampling of the earth's forests, as VCL should provide, will be a huge boon for forest resource assessments. For example, the VCL mission has potential to greatly narrow the uncertainty surrounding estimates of global C pools. Discontinuous lidar data will need to be integrated with continuous optical imagery to produce comprehensive maps that have practical value to forest ecologists and forest resource managers (Lefsky et al., 1999c). Given the continued demand for Landsat imagery, the growing supply of imagery from Landsat 7, and the recent decommissioning of Landsats 4 and 5 (and thus any further TM or MSS data), ETM+ imagery from Landsat 7 is a logical choice for integrating with lidar sample data.

In this study, our first objective was to estimate canopy height at locations unsampled by lidar, based on the statistical and geostatistical relationships between the lidar and Landsat ETM+ data at the lidar sample locations. We used the most basic data from lidar (maximum canopy height) and Landsat ETM+ (raw band values) and tested widely used, straightforward empirical estimation methods: ordinary least squares regression, ordinary kriging, and ordinary cokriging.

Prior research has shown that landscape pattern varies principally as a function of the areal size of individual stands in the heavily managed forests of western Oregon, or at a typical scale of 250-500 m (Cohen et al., 1990; Milne and Cohen, 1999). Thus, we hypothesized that VCL may undersample the landscape relative to the spatial scale at which most canopy variation occurs in western Oregon forests, and in perhaps most other forested regions. Our second (yet equally important) objective was to determine what spatial sampling design would optimize the integration of lidar and Landsat ETM+ data for accurate mapping.

2. BACKGROUND

2.1 Lidar

Lidar (LIght Detection and Ranging) is an active remote sensing technology like radar but operating in the visible or near-infrared region of the electromagnetic spectrum. Lidar at its most basic level is a laser altimeter that determines the distance from the instrument to the physical surface by measuring the time elapsed between a laser pulse emission and its reflected return signal. This time interval multiplied by the speed of light measures twice the distance to the target; dividing this measurement by two can thus provide a measure of surface elevation (Bachman, 1979). Processing of the return signal may identify multiple pulses and returns. As a result, trees, buildings, and other objects are apparent in the lidar signal, permitting accurate calculation of their heights (Nelson et al., 1984). Studies using coincident field data have indicated that lidar data can provide non-asymptotic estimates of structural attributes such as basal area, biomass, stand volume (Nilsson, 1996; Nelson et al., 1997; Lefsky et al., 1999a,b; Means et al., 1999, 2000), and leaf area index (LAI) (Lefsky et al., 1999b), even in high-biomass forests. Lidar allows extraordinary differentiation between young, mature, and old-growth stand structure that is currently unrivaled by any other remote sensing technology (Lefsky et al., 1999b; Weishampel et al., 2000).

Lidar instruments can be divided into two general categories: discrete return and waveform sampling (Lefsky et al., in press). They are distinguished in part by the size of the laser illumination area, or footprint, which typically is smaller with discrete-return systems (0.25-1 m) than with waveform-sampling systems (10-100 m). Waveform-sampling systems compensate for their coarser horizontal resolution with finer vertical resolution, providing sub-meter vertical profiles, while discrete-return systems record only 1-5 returns per laser footprint. Discrete-return systems are more suited for supplying the demand for accurate, high-resolution topographic maps and digital terrain models, and are therefore becoming widely available in the commercial sector (Lefsky et al., in press). The most advanced vegetation application of waveform-sampling lidar data to date has been the development of a canopy volume profile in high-biomass forests, which provides a more direct measure of physical canopy structure than any other remote sensing technology so far (Lefsky et al., 1999b).

VCL is a spaceborne, waveform-sampling lidar system that will inventory canopy height and structure between ±68° latitude for an estimated 2 years. VCL footprints will be approximately 25 m in diameter and arrayed in single file along transects. Originally, VCL was designed to acquire along 3 parallel transects spaced at 2 km intervals. More recently, this spacing was broadened to 4 km (http://essp.gsfc.nasa.gov/vcl). The ground track of the VCL satellite will be randomly placed on the Earth's surface; the juxtaposition of the ascending and descending orbital paths will form a web of transects sampling the Earth's surface (Dubayah et al., 1997).

ICESat is a spaceborne, waveform-sampling lidar system that will measure and monitor ice-sheet topography as well as cloud and atmospheric properties. Like VCL, it will acquire data in the near-infrared region at 1064 nm, but ICESat will also acquire data in the visible green region at 532 nm (http://ltpwww.gsfc.nasa.gov/eib/glas.html). It has a 70 m footprint that will likely prove too large for measuring tree heights in areas with steep slopes. However the 175 m spacing of the lidar point samples could be better for integrating with passive optical imagery.

2.2 Landsat ETM+

Landsat imagery is the most common satellite data source used in terrestrial ecology. This is in large part due to its widespread availability and unrivaled length of record (since 1972), but also because the grain, extent, and multispectral features make Landsat suitable for a variety of environmental applications at landscape-regional scales. Landsat spectral data are typically related to vegetation structural attributes

via spectral vegetation indices (SVIs). Ecologically relevant structural attributes such as LAI have been estimated from SVIs of croplands (e.g. Wiegand et al., 1979; Asrar et al., 1984), grasslands (e.g. Friedl et al., 1994), shrublands (e.g. Law and Waring, 1994), and forests (e.g. Chen and Cihlar, 1996; Fassnacht et al., 1997; Turner et al. 1999). Sensitivity of SVIs to variation in LAI or biomass generally declines, however, as foliar densities increase between ecosystems (e.g. Turner et al., 1999). The greater structural complexity of forests requires, not surprisingly, more complex image processing techniques. For instance, Cohen and Spies (1992) used all 6 Landsat radiance bands, rather than just the red and near-infrared bands as with most SVIs. Other notable yet more complicated approaches to enhancing the extraction of canopy structure information from Landsat imagery include using multi-temporal TM data to capture variable illumination conditions (Lefsky et al., 2001) and spectral mixture analysis to quantify canopy shadows (e.g. Adams et al., 1995; Peddle et al., 1999). The new ETM+ instrument on board Landsat 7 features enhanced radiometric resolution over its TM predecessor, which should aid all of the empirical methods just described. Yet there are fundamental limitations to the utility of passive optical sensors for characterizing vertical forest canopy structure, which will probably make them perpetually inferior to lidar for this task (Lefsky et al., 2001).

2.3 Estimation methods

All of the estimation methods we employed are empirical and were chosen for their broad use and general applicability: ordinary least squares regression (OLS), ordinary kriging (OK), and ordinary cokriging (OCK). The literature documents many variations on these aspatial (e.g. Curran and Hay, 1986) and spatial (e.g. Journal and Rossi, 1989; Stein and Corsten, 1991; Pan et al., 1993; Knotters et al., 1995) estimation methods. We deemed it less useful to conduct an exhaustive study of them all than to concentrate on the three methods just named because they broadly represent the basic empirical estimation techniques.

3. METHODS

3.1 Study Area

The 200 km^2 study area features Oregon State University's McDonald-Dunn Research Forest in the eastern foothills of the Coast Range in western Oregon. The area has elevations ranging from 58-650 m. Most of the area is coniferous forest dominated by *Pseudotsuga menziesii* and co-dominated by *Tsuga heterophylla*, but hardwood stands featuring *Acer macrophyllum* and *Quercus garryana* also are common. Stands span the full range of successional stages: young, intermediate, mature, and old-growth, and three management themes: even-aged, two-storied, and uneven-aged (http://www.cof.orst.edu/resfor/mcdonald/purpose.sht).

3.2 Image Processing

Small-footprint lidar data were acquired from an airborne platform (Aeroscan, Spencer B. Gross, Inc., Portland, OR) in January 2000. The Aeroscan instrument records 5 vertical returns within small footprints having an average diameter of 60 cm and geolocated in real time using an on-board, differential global positioning system to an accuracy of 75 cm (horizontal) and 30 cm (vertical). North-south paths were flown to provide continuous lidar coverage of the entire area. Maximum canopy height values were calculated for each footprint as the difference between the first (canopy top) and last (ground) returns using waveform processing algorithms developed in IDL (Research Systems Inc., Boulder, CO) by coauthor Lefsky. Maximum height values in each footprint were then aggregated into 25 x 25 m bins to produce a maximum canopy height image of 25 m spatial resolution. Every pixel was assigned a maximum canopy height value from a population of 10-764 lidar footprints, with a median of 26 footprints per pixel.

A Landsat ETM+ image (USGS-EROS Data Center, Sioux Falls, SD) acquired on 7 September 1999 was coregistered to a 1988 base image using 90 tie points selected through an automated spatial covariance procedure (Kennedy and Cohen, in review). Georegistration was performed in Imagine (ERDAS, Cambridge, U.K.) using a first-order polynomial function with nearest neighbor radiometric resampling, with a root mean square error of ±14.3 m.

3.3 Sampling strategies

Possession of an actual height image across a large area allowed us to sample across a range of spatial frequencies. We simulated not only the original VCL sampling interval (2000 m) but also doubled the sampling frequency three times to 1000, 500 and 250 m; we sampled not only along transects (as VCL) but also in point patterns (as ICESat) at these same 4 spatial frequencies, or the intersections of the mentioned transects. The total of 8 height datasets were sampled in ERDAS Imagine.

3.4 Estimation methods

The histogram of the maximum canopy height data exhibited a strong positive skew. We therefore normalized each of the 8 height datasets with a square root transformation (SQRTHT) prior to applying any of the estimation methods; afterwards, all estimated SQRTHT values were backtransformed (squared) before comparing to measured height values.

3.4.1 Aspatial. The SQRTHT sample data were regressed on the raw ETM+ bands 1-7, as well as the Universal Transverse Mercator (UTM) X and Y locations, using stepwise multiple linear regression. Variables were assigned only if they added significantly to the model ($\alpha = 0.05$).

3.4.2 Spatial. The SQRTHT sample data were normal-score transformed prior to modeling. This non-linear, ranked transformation normalizes the data to produce a standard Gaussian cumulative distribution function with mean equal to zero and variance equal to one (Deutsch and Journel, 1998). After modeling, the estimates were backtransformed to the

original SQRTHT data distribution; the estimates at the sample locations were an exact reproduction of the original SQRTHT sample data.

Ordinary kriging and ordinary cokriging operations were performed using algorithms in GSLIB (Statios, San Francisco, CA). We modeled the sample semivariograms by nesting nugget estimates with two exponential models. Only a model semivariogram for the primary variable was needed for ordinary kriging. For cokriging, a model semivariogram was also required for the secondary variable, along with a cross semivariogram modeling the spatial cross correlation between the primary and secondary variables. The ETM+ panchromatic band was the logical choice to serve as a secondary variable for cokriging, since this band has the highest resolution (15 m) among the ETM+ bands and therefore the highest spatial information content. The secondary data were also normal-score transformed before modeling. We were careful to observe the positive definiteness constraint on the linear model of coregionalization while developing the 3 semivariogram models required for each cokriging operation (Isaaks and Srivastava, 1989; Goovaerts, 1997).

3.4.3 Integrated. Residuals from the OLS regression models were exported from IDL as ASCII files and imported into GSLIB for kriging/cokriging. The same rules and procedures were followed for modeling the residuals as for modeling the SQRTHT data.

3.5 Validation. A comprehensive image of lidar-measured height values allowed exhaustive validation of the 5 estimation methods and 8 sampling strategies tested. To ensure comparability, the same validation points were used to evaluate all estimation methods and sampling strategies. Two sets of validation points were systematically selected to compare measured and estimated height values using Pearson's correlation statistic. One set of validation points was designed to assess the height estimates for the study area as a whole, with no regard to distance from sample locations; the other set was designed to assess the height estimates as a function of distance from sample locations.

Histograms, scatterplots, and graphs of measured versus estimated height values were graphically compared, and correlation coefficients were calculated in IDL. Estimated height and estimation error images were mapped in Arc/Info GRID (ESRI, Redlands, CA). Moran's Coefficient (I) calculations for spatial autocorrelation in the model residuals were performed using S-PLUS (Insightful, Seattle, WA) functions developed by Dr. Robin Reich (Colorado State University, Fort Collins, CO). The significance test to evaluate each I statistic assumed normality in 700 residual values sampled from the population of errors. The theory underlying Moran's I statistic can be pursued more thoroughly in Moran (1948) and Cliff and Ord (1981).

4. RESULTS

4.1 Empirical models

Separate stepwise multiple regression models were developed for the 8 sampling strategies tested. In every case, ETM+ band 7 was the first variable selected. All 9 independent variables contributed significantly, and were therefore included, in the 4 transect cases. The number of variables included in the point models decreased as sample data volume decreased, with only one variable selected in the lower extreme case (2000 m point strategy).

For the spatial and integrated models, unique semivariogram models of the height and height residual datasets were generated for all 8 of the sampling strategies tested. The range and sill parameters, and the shape of the semivariograms, were very similar among the 8 height datasets, and among the 8 height residual datasets. Nugget variance increased in the cases of the relatively sparse 1000 and 2000 m point samples. For cokriging, each of the 8 sampling strategies also required unique model semivariograms of the secondary data semivariograms and the respective cross semivariograms. As with the primary datasets, the range and sill parameters and semivariogram shapes were consistent amongst all 8 sample datasets, and nugget variance was again greater in the 1000 and 2000 m point samples. There was less spatial autocorrelation to exploit in the residual data than in the SQRTHT data. Similarly, the spatial cross correlation between the primary and secondary data was considerable with regard to the SQRTHT datasets, but relatively low with regard to the residual datasets. Very tight model fits were achieved for all of the primary, secondary, and cross semivariograms by nesting a nugget value and two exponential models.

4.2 Estimation accuracy

4.2.1 Global. Histograms of the full populations of estimated height values were used to evaluate global accuracy. Deviations in the estimated height histograms away from the measured height histograms were a good indicator of estimation biases at various heights. These biases were most pronounced in all of the regression results, and in the kriging/cokriging results based on sparse point samples (1000 or 2000 m). Biases in the estimates from the integrated methods were relatively minor, and decreased as sampling frequency increased. Correlations between measured and estimated heights were always better using the integrated models than using either the regression or spatial models alone. Cokriging produced slightly higher correlations than kriging. Correlations also were higher with the transect samples than with the point samples at each spatial sampling frequency.

Scatterplots of measured vs. estimated height values were also generated to compare the 5 models and 8 sampling strategies tested. Deviations in the slope of the fitted trendlines away from the 1:1 line helped show that the regression models suffered the most from underestimating the taller heights while overestimating the shorter heights. These deviations corresponded closely with the deviations in the estimated height histograms from the measured height histogram. Furthermore, correlations between measured and

estimated height values in the scatterplots agreed well with the correlations calculated from the global height estimates. It is thus safe to conclude that the 700 points in these scatterplots were highly representative of the full population of height estimates, and their errors.

4.2.2 Local. Local estimation accuracy was also assessed according to Pearson's correlation statistic. Accuracy decreased as the distance from sample locations increased. The spatial models were more accurate than the regression models below distances of approximately 200 m from the sample locations. The integrated models preserved the accuracy of the regression estimates beyond this distance to the nearest sample. A sampling interval of 250 m ensured that all estimates were <180 m from the nearest sample, which improved estimation accuracies of the spatial and integrated models above those of regression, at all locations.

4.3 Mapping. Regression-based maps were virtually indistinguishable regardless of the sampling strategy or number of variables included. In dramatic contrast, the sampling strategy caused obvious artifacts in the kriging or cokriging maps that were most pronounced at the sparser sampling frequencies. These artifacts were however greatly attenuated in the maps produced from the integrated models. The kriging and cokriging maps were virtually indistinguishable when the same primary data were modeled.

Maps of estimation errors were produced by subtracting the actual height map from the estimated height maps. Overall, every model underestimated canopy height, although the estimation bias was an order of magnitude greater for the regression models than for any of the spatial or integrated models. The standard deviation of the estimation errors for the spatial and integrated models decreased as the spatial sampling frequency increased.

Spatial patterns in the error maps for the spatial and integrated models became less apparent as sampling density increased, while sampling density had no effect on error patterns for the aspatial regression models. Moran's I statistic was useful for quantifying the significance of the spatial autocorrelation remaining in the height estimation errors for all models. All regression models, and all models derived from the two sparser point sample datasets (2000 and 1000 m), failed to remove the spatial dependence from the residuals. The spatial models applied to the 2000 m transect sample dataset also left significant spatial autocorrelation in the residual variance, although the integrated models did not. All other models successfully accounted for spatial autocorrelation in the sample data.

5. DISCUSSION

5.1 Ordinary Least Squares Regression

The high similarity among all regression estimates of height indicates the insensitivity of the regression models to sample size, sample pattern, sampling frequency, or number of ETM+ bands selected. Regression suffered the worst from a consistent estimation bias, overestimating shorter stands while underestimating taller stands. On the other hand, regression did preserve the spatial pattern of stands across the study landscape.

We included the UTMX and UTMY location variables in the regression models as an easy way to account for a potential geographic trend across our study area, following the approach of Metzger (1997). Yet most of the height data variance explainable with regression was explained by ETM+ band 7 alone. The location variables (particularly UTMY) were selected by some of the stepwise regression models but only for those sampling strategies with a high data volume. In these cases, the addition of the location variables and other ETM+ bands as explanatory variables carried statistical significance but probably lacks biological significance.

Regression models of canopy height from future VCL-Landsat ETM+ integration will likely be less accurate than in this study. We developed a multiple regression model for estimating canopy height in southern Washington at the Wind River Canopy Crane Research Area (Hudak, unpublished), an area with canopy structure and composition very similar to the McDonald-Dunn Research Forest. The regression model was developed from a 1995 Landsat TM scene (bands 1-7, plus UTMX and UTMY locations) and lidar data acquired in 1995 by the SLICER instrument, a waveform-sampling lidar system more similar to VCL than the discrete-return Aeroscan lidar used in this study. The correlation between measured and estimated height values at Wind River was substantially less ($r = 0.57$) than at McDonald-Dunn ($r = 0.76$). Whether height estimates after adding a kriged/cokriged VCL residual surface to the regression surface will also be less accurate remains to be seen, but should not comprise the utility of our integrated modeling approach.

5.2 Ordinary Kriging/Cokriging

In stark contrast to regression, height estimates from the spatial methods were only slightly biased, but were highly sensitive to sampling frequency and pattern, which produced spatial discontinuities in the resulting maps. These discontinuities were visually distracting when the modeled variable (canopy height in this case) was undersampled relative to the spatial frequency at which it actually varies; the semivariograms indicate that the range of spatial autocorrelation in canopy height is no more than 500 m in this landscape. Beyond 500 m from the nearest sample, the semivariograms carried little or no weight in the estimation; this produced the smoothing effect visible especially in the 2000 and 1000 m kriged/cokriged maps. At sampling intervals of 500 or 250 m, all estimates were at or below the range of spatial autocorrelation for this landscape, so little smoothing occurred.

Stein and Corsten (1991) found that kriging/cokriging estimates differ only slightly from each other, and that the advantage of cokriging is greater when a highly correlated secondary variable is sampled intensely. We found cokriging slightly more advantageous than kriging at all sampling

frequencies, perhaps because canopy height and the ETM+ panchromatic band were only weakly correlated (r = -0.43).

Journel and Rossi (1989) showed how ordinary kriging or cokriging is capable of modeling a trend component in interpolation situations, which is confirmed in our study by the lack of any visible trend or anisotropy in the error maps from the spatial models. Ordinary kriging or cokriging is advisable only in interpolation situations such as in this study; in extrapolation situations, it may be better to use universal kriging (Journel and Rossi, 1989; Stein and Corsten, 1991) or ordinary kriging with an external drift (Berterretche, 2001). In cases where anisotropy exists in the landscape, anisotropic kriging models having a directional component can be employed. Goovaerts (1997) thoroughly presents the many kriging/cokriging procedures available.

5.3 Integrated Method

Most of the bias in the regression estimates was eliminated in the integrated models, where the regression residuals were subsequently kriged and added back to the regression surface. We found the advantage of cokriging over kriging to be greater with the height residuals than with the height values. Perhaps because the regression models explain such a large proportion of the total variation in canopy height ($r^2 = 0.58$), the height residuals may correspond more closely than the height values to the fine-scale structural features in the panchromatic image.

The integrated methods proved superior because they preserved the spatial pattern in canopy height, like the regression models, while also improving global and local estimation accuracy, like the spatial models. They have no apparent disadvantage relative to aspatial or spatial methods alone.

The estimation methods applied to lidar canopy height data in this analysis are applicable to field data, as has already been demonstrated by Atkinson (1992, 1994). The samples need not be situated along a systematic grid; the methods are as applicable to random or subjective sampling strategies, as long as the samples represent the population in both statistical and geographical space.

5.4 Alternative Modeling Techniques

For estimation, inverse regression models (Curran and Hay, 1986) should be considered when the explanatory variables are dependent on the variable of interest. Surface radiance is influenced by canopy height, however Landsat imagery is much more sensitive to the spectral properties of the surface materials than to their height. Another criticism of standard regression is that it accounts for errors in only the explanatory variables (Landsat bands 1-7) and assumes a lack of measurement error in the independent variable (lidar height). All remotely sensed data including lidar are subject to several sources of error: irradiance variation, sensor calibration, sensor radiometric resolution, sensor drift, signal digitization, atmospheric attenuation, and atmospheric path radiance. An alternative approach that accounts for errors in both the independent and dependent variables is reduced major axis (RMA) regression (Curran and Hay 1986). Regardless of the regression method selected, we argue against using regression models alone to estimate canopy height. Our regression equations were useful for explaining a large proportion of the total variance in canopy height due to high covariance with measured radiance, but not due to any functional relationship. As stated in our objectives, we considered it most useful to present the most commonly used techniques for this paper, and OLS regression is clearly the standard empirical modeling tool.

For mapping, conditional simulation can be a good alternative to the estimation methods presented here (Dungan, 1998, 1999). Conditional simulation "conditions" stochastic predictions of the modeled variable within the spatial range of the sample data, as defined by the same semivariogram model used for kriging. Although locally inaccurate, conditional simulation preserves the global accuracy and spatial pattern of the data modeled. These qualities can be important for some applications, such as modeling variables as input for ecological process models. For example, Berterretche (2001) simulated LAI values across a boreal forest, for the purpose of informing a spatial model of net primary production (NPP). A single eddy flux tower centered at the site predicted NPP from a continuous stream of trace gas, light, temperature, and humidity measurements (Running et al., 1999). LAI is the key structural parameter driving NPP, yet one of the largest sources of uncertainty for modeling NPP at the ecosystem level. Conditional simulation provided multiple realizations (maps) of LAI, each map having a pattern of LAI values similar to remotely sensed indices of canopy structure (Berterretche, 2001). This set of maps provided a probability distribution of LAI predictions for every pixel (except those "conditional" locations where LAI was measured in the field, where the field value was preserved). Such multiple realizations of LAI provide a spatial measure of uncertainty, which could prove important for assessing the sensitivity of ecosystem NPP to spatial variation in LAI.

A sensitivity analysis was not possible with the single map realizations created in this study, but neither was it necessary. We ran conditional stochastic simulations of canopy height, and height residuals, from our 8 sample datasets. In every case, local accuracy was markedly lower than for any of the estimation methods we tested. Since local accuracy was important for our objectives, while multiple realizations were not, we pursued simulation methods no further for this paper. The decision of which estimation or simulation methods to use for modeling LAI, height, or any other variable ultimately depends on user objectives.

5.5 Sampling Strategy

Traditionally, most remote sensors have afforded analysts with a certain luxury by sampling the entire population within the extent of coverage. This has precluded any need to apply spatial interpolation strategies such as kriging, yet imagery is full of underexploited spatial information. A number of studies have demonstrated the value of geostatistical analysis tools such as semivariograms (e.g. Curran, 1988; Glass et al., 1988; Woodcock et al., 1988;

Cohen et al., 1990; Hudak and Wessman, 1998). As remote sensing technology has advanced towards increasing spectral, spatial, and temporal resolution, data processing and storage technologies have kept pace, enabling the continued availability of comprehensive data even as those data volumes have exponentially increased. While these trends may very well continue, it is instructive and useful to consider the applicability of remote sampling instruments such as ICESat and VCL.

We found that a 2000 m transect sampling strategy simulating the original VCL sampling design is not optimal for vegetation mapping of dense coniferous forests. The more recent, 4000 m transect sampling design of VCL would be even more problematic, at least in western Oregon where forest structure predominantly varies at the scale of individual stands with spatial frequencies of <500 m (Cohen et al., 1990). Better maps of canopy height could be achieved with less lidar data if a 250 m point sampling strategy were used. This reduced data volume would alleviate data transmission, storage, and processing loads. Processing time is proportional to data volume when running geostatistical models in particular. Whether or not a point sampling strategy could be feasibly designed into the next lidar satellite for vegetation applications is an engineering issue and beyond the scope of this paper, but the point sampling design of ICESat suggests that this technology already exists. Future lidar missions designated for vegetation inventories should be designed by engineers and vegetation ecologists who have given due consideration to application of the data.

6. CONCLUSION

Integration of lidar and Landsat ETM+ data using straightforward empirical modeling procedures can be used to improve the utility of both datasets for forestry applications. Our integrated technique of ordinary cokriging of the height residuals from an OLS regression model proved the best integration method for estimating and mapping canopy height. We encourage the use of our integrated modeling approach in a variety of ecosystems once lidar sample data become readily available. Results strongly support our hypothesis that the VCL satellite will undersample the highly managed forest landscapes of western Oregon and probably many other regions. Future lidar satellites for vegetation mapping in this region should sample points at spatial intervals of 250 m or less. This would ensure that every estimate is no more than 180 m from the nearest sample while also keeping the sample data volume to a manageable level and therefore maximizing the efficiency of our integrated modeling approach. An equitable distribution of sample data is critical for lidar-Landsat ETM+ integration.

7. ACKNOWLEDGEMENT

This work was funded by the NASA Terrestrial Ecology Program (NRA-97-MTPE-08). Aeroscan data were provided courtesy of Mike Renslow of Spencer B. Gross, Inc., Portland, Oregon.

8. REFERENCES

Adams, J. B., Sabol, D. E., Kapos, V., Filho, R. A., Roberts, D. A., Smith, M. O., & Gillespie, A. R. (1995). Classification of multispectral images based on fractions of endmembers: application to land-cover change in the Brazilian Amazon. *Remote Sensing of Environment,* 52, 137-154.

Asner, G. P., Wessman, C. A., & Privette, J. L. (1997). Unmixing the directional reflectances of AVHRR sub-pixel landcovers. *IEEE Transactions on Geoscience and Remote Sensing,* 35, 868-878.

Asrar, G., Fuchs, M., Kanemasu, E. T., & Hatfield, J. L. (1984). Estimating absorbed photosynthetic radiation and leaf area index from spectral reflectance in wheat. *Agronomy Journal*, 76, 300-306.

Atkinson, P. M., Webster, R., & Curran, P. J. (1992). Cokriging with ground-based radiometry. *Remote Sensing of Environment,* 41, 45-60.

Atkinson, P. M., Webster, R., & Curran, P. J. (1994). Cokriging with airborne MSS imagery. *Remote Sensing of Environment,* 50, 335-345.

Bachman, C. G. (1979). *Laser radar systems and techniques* (193 pp.). Norwood, MA: Artech House.

Berterretche, M. (2001). *Comparison of regression and geostatistical methods to develop LAI surfaces for NPP modeling.* Master's Thesis (169 pp.), Oregon State University, Corvallis, OR.

Chen, J. M., & Cihlar, J. (1996). Retrieving leaf area index of boreal conifer forests using Landsat TM images. *Remote Sensing of Environment,* 55, 153-162.

Cliff, A. D., & Ord, J. K. (1981). *Spatial processes: models and applications* (266 pp.). London: Pion Ltd.

Cohen, W. B., & Spies, T. A. (1992). Estimating structural attributes of Douglas-fir / western hemlock forest stands from Landsat and SPOT imagery. *Remote Sensing of Environment,* 41, 1-17.

Cohen, W. B., Spies, T. A., & Bradshaw, G. A. (1990). Semivariograms of digital imagery for analysis of conifer canopy structure. *Remote Sensing of Environment,* 34, 167-178.

Cohen, W. B., Harmon, M. E., Wallin, D. O., & Fiorella, M. (1996). Two decades of carbon flux from forests of the Pacific Northwest. *BioScience*, 46, 836-844.

Curran, P. J. (1988). The semivariogram in remote sensing: an introduction. *Remote Sensing of Environment,* 24, 493-507.

Curran, P. J., & Hay, A. M. (1986). The importance of measurement error for certain procedure in remote sensing of optical wavelengths. *Photogrammetric Engineering and Remote Sensing,* 52, 229-241.

Deutsch, C. V., & Journel, A. G. (1998). *GSLIB geostatistical software library and user's guide* (369 pp.). New York: Oxford University Press.

Dubayah, R., Blair, J. B., Bufton, J. L., Clark, D. B., JaJa, J., Knox, R., Luthcke, S. B., Prince, S., & Weishampel, J. (1997). The vegetation canopy lidar mission. In: *Land satellite information in the next decade: II. sources and applications* (pp. 100-112). Washington, DC: ASPRS.

Dungan, J. L. (1998). Spatial prediction of vegetation quantities using ground and image data. *International Journal of Remote Sensing,* 19, 267-285.

Dungan, J. L. (1999). Conditional simulation: an alternative to estimation for achieving mapping objectives. In: A. Stein, F. van der Meer, & B. Gorte (Eds.), *Spatial statistics for remote sensing* (pp. 135-152). Dordrecht: Kluwer Academic Publishers.

Fassnacht, K. S., Gower, S. T., MacKenzie, M. D., Nordheim, E.V., & Lillesand, T. M. (1997). Estimating the LAI of North Central Wisconsin forests using the Landsat Thematic Mapper. *Remote Sensing of Environment,* 61, 229-245.

Friedl, M. A., Michaelsen, J., Davis, F. W., Walker, H., & Schimel, D. S. (1994). Estimating grassland biomass and leaf area index using ground and satellite data. *International Journal of Remote Sensing*, 15, 1401-1420.

Glass, C. E., Carr, J. R., Yang, H. –M., & Myers, D. E. (1988). Application of spatial statistics to analyzing multiple remote sensing data sets. In: A.I. Johnson, & C.B. Pettersson (Eds.), *Geotechnical appliations of remote sensing and remote data transmission*, ASTM STP 967 (pp. 138-150). Philadelphia: American Society for Testing and Materials.

Goovaerts, P. (1997). *Geostatistics for natural resources evaluation* (483 pp.). New York: Oxford University Press.

Hudak, A. T., & Wessman, C. A. (1998). Textural analysis of historical aerial photography to characterize woody plant encroachment in South African savanna. *Remote Sensing of Environment*, 66, 317-330.

Isaaks, E. H., & Srivastava, R. M. (1989). *Applied Geostatistics* (561 pp.). New York: Oxford University Press.

Journel, A. G., & Rossi, M. E. (1989). When do we need a trend model in kriging? *Mathematical Geology* 21, 715-739.

Kennedy, R. E., & Cohen, W. B. Automated designation of tie-points for image-to-image registration. *International Journal of Remote Sensing,* in review.

Knotters, M., Brus, D. J. & Voshaar, J. H. O. (1995). A comparison of kriging, co-kriging and kriging combined with regression for spatial interpolation of horizon depth with censored observations. *Geoderma*, 67, 227-246.

Law, B. E., & Waring. R. H. (1994). Remote sensing of leaf area index and radiation intercepted by understory vegetation. *Ecological Applications*, 4, 272-279.

Lefsky, M. A., Harding, D., Cohen, W. B., Parker, G. & Shugart, H. H. (1999a). Surface lidar remote sensing of basal area and biomass in deciduous forests of Eastern Maryland, USA. *Remote Sensing of Environment,* 67, 83-98.

Lefsky, M. A., Cohen, W. B., Acker, S. A., Parker, G. G., Spies, T. A. & Harding, D. (1999b). Lidar remote sensing of the canopy structure and biophysical properties of Douglas-fir western hemlock forests. *Remote Sensing of Environment,* 70, 339-361.

Lefsky, M. A., Cohen, W. B., Hudak, A. T., Acker, S. A., & Ohmann, J. L. (1999c). Integration of lidar, Landsat ETM+ and forest inventory data for regional forest mapping. In: *International Archives of Photogrammetry and Remote Sensing*, Vol. 32, Part 3W14, 119-126.

Lefsky, M. A., Cohen, W. B., & Spies, T. A. (2001). An evaluation of alternate remote sensing products for forest inventory, monitoring, and mapping of Douglas-fir forests in western Oregon. *Canadian Journal of Forest Research*, 31, 78-87.

Lefsky, M. A., Cohen, W. B., Parker, G. G., & Harding, D. J. Lidar remote sensing for ecosystem studies. *Bioscience*, in press.

Means, J. E., Acker, S. A., Harding, D. J., Blair, J. B., Lefsky, M. A., Cohen, W. B., Harmon, M. E., & McKee, W. A. (1999). Use of large-footprint scanning airborne lidar to estimate forest stand characteristics in the Western Cascades of Oregon. *Remote Sensing of Environment,* 67, 298-308.

Means, J. E., Acker, S. A., Fitt, B. J., Renslow, M., Emerson, L., & Hendrix, C. J. (2000). Predicting forest stand characteristics with airborne scanning lidar. *Photogrammetric Engineering and Remote Sensing*, 66, 1367-1371.

Metzger, K.L. (1997). *Modeling forest stand structure to a ten meter resolution using Landsat TM data.* Master's

thesis (123 pp.), Colorado State University, Fort Collins, CO.

Milne, B. T., & Cohen, W. B. (1999). Multiscale assessment of binary and continuous landcover variables for MODIS validation, mapping, and modeling applications. *Remote Sensing of Environment,* 70, 82-98.

Moran, P. (1948). The interpretation of statistical maps. *Journal of the Royal Statistical Society*, 10B, 243-251.

Nelson, R., Krabill, W., & Maclean, G. (1984). Determining forest canopy characteristics using airborne laser data. *Remote Sensing of Environment,* 15, 201-212.

Nelson, R., Oderwald, R., & Gregoire, T. G. (1997). Separating the ground and airborne laser sampling phases to estimate tropical forest basal area, volume, and biomass. *Remote Sensing of Environment,* 60, 311-326.

Nilsson, M. (1996). Estimation of tree heights and stand volume using an airborne lidar system. *Remote Sensing of Environment,* 56, 1-7.

Oleson, K.W., Sarlin, S., Garrison, J., Smith, S., Privette, J. L., & Emery, W. J. (1995). Unmixing multiple land-cover type reflectances from coarse spatial resolution satellite data. *Remote Sensing of Environment,* 54, 98-112.

Pan, G., Gaard, D., Moss, K., & Heiner, T. (1993). A comparison between cokriging and ordinary kriging: case study with a polymetallic deposit. *Mathematical Geology*, 25, 377-398.

Peddle, D. R., Hall, F. G., & LeDrew, E. F. (1999). Spectral mixture analysis and geometric-optical reflectance modeling of boreal forest biophysical structure. *Remote Sensing of Environment*, 67, 288-297.

Running, S. W., Baldocchi, D. D., Turner, D. P., Gower, S. T., Bakwin, P. S., & Hibbard, K. A. (1999). A global terrestrial monitoring network integrating tower fluxes, flask sampling, ecosystem modeling and EOS satellite data. *Remote Sensing of Environment,* 70, 108-127.

Stein, A., & Corsten, L. C. A. (1991). Universal kriging and cokriging as a regression procedure. *Biometrics*, 47, 575-587.

Turner, D. P., Cohen, W. B., Kennedy, R. E., Fassnacht, K. S., & Briggs, J. M. (1999). Relationships between LAI and Landsat TM spectral vegetation indices across three temperate zone sites. *Remote Sensing of Environment,* 70, 52-68.

Weishampel, J. F., Blair, J. B., Knox, R. G., Dubayah, R., & Clark, D. B. (2000). Volumetric lidar return patterns from an old-growth tropical rainforest canopy. *International Journal of Remote Sensing,* 21, 409-415.

Wiegand, C. L., Richardson, A. J., & Kanemasu, E. T. (1979). Leaf area index estimates for wheat from LANDSAT and their implications for evapotranspiration and crop modeling. *Agronomy Journal*, 71, 336-342.

Woodcock, C. E., Strahler, A. H., & Jupp, D. L. B. (1988). The use of variograms in remote sensing: II. real digital images. *Remote Sensing of Environment,* 25, 349-379.

HIGH RESOLUTION SURFACE GEOMETRY AND ALBEDO BY COMBINING LASER ALTIMETRY AND VISIBLE IMAGES

Robin D. Morris, Udo von Toussaint and Peter C. Cheeseman,
NASA Ames Research Center, MS 269-2, Moffett Field, CA 94035
[rdm,udt,cheesem]@email.arc.nasa.gov

KEY WORDS: Bayesian inference; surface geometry; albedo; computer vision;

ABSTRACT

The need for accurate geometric and radiometric information over large areas has become increasingly important. Laser altimetry is one of the key technologies for obtaining this geometric information. However, there are important application areas where the observing platform has its orbit constrained by the other instruments it is carrying, and so the spatial resolution that can be recorded by the laser altimeter is limited. In this paper we show how information recorded by one of the other instruments commonly carried, a high-resolution imaging camera, can be combined with the laser altimeter measurements to give a high resolution estimate both of the surface geometry and its reflectance properties. This estimate has an accuracy unavailable from other interpolation methods. We present the results from combining synthetic laser altimeter measurements on a coarse grid with images generated from a surface model to re-create the surface model.

RÉSUMÉ

Le besoin d'informations géométriques et radiométriques précises couvrant de grandes étendues devient de plus en plus important. L'altimétrie laser est une des technologies principales pour obtenir ces informations géométriques. Cependant, il est des domaines d'application importants où la plateforme d'observation a son orbite contrainte par les autres instruments qu'elle porte, ce qui limite la résolution spatiale qui peut être enregistrée par l'altimètre. Dans cet article nous montrons comment l'information enregistrée par un des autres instruments communément embarqués, une caméra photographique à haute résolution, peut être combinée avec les mesures de l'altimètre laser pour donner une estimation haute résolution à la fois de la géométrie de surface et de ses propriétés de réflectivité. Cette évaluation offre une exactitude inégalée par d'autres méthodes d'interpolation. Nous présentons les résultats obtenus en combinant des mesures synthétiques d'altimètre laser sur une grille grossière avec des images produites à partir d'un modèle de surface pour recréer le modèle de surface.

KURZFASSUNG

Präzise geometrische und radiometrische Informationen über grosse Areale ist zunehmend von Bedeutung. Die Laser Altimetrie ist eine der Schlüsseltechnologien zur Gewinnung dieser Daten. Allerdings ist in wichtigen Anwendungsfällen die Laser Altimetrie Messung durch weitere Instrumente behindert und daher die räumliche Auflösung eingeschränkt. In dieser Veröffentlichung zeigen wir auf wie die von einer hochauflösenden Kamera (einer fast immer installierten Diagnostik) gewonnenen Bilder mit den Daten der Laser Altimetrie kombiniert werden können um eine präzise Bestimmung der Oberflächenform und ihrer Reflektivitätseigenschaften zu ermöglichen. Diese Art der Oberflächenbestimmung erweist sich einer Splineinterpolationen der Laser Altimetriedaten überlegen. Wir zeigen die Ergebnisse der Oberflächenrekonstruktion aus der Kombination von synthetischen, niedrig aufgelösten Laser Altimetriedaten und Bildern.

1 INTRODUCTION

The need for accurate geometric information for a variety of problems has grown rapidly in the last decades. These needs cover a broad field, from monitoring of environmental changes such as the deformation rates of glaciers, to the creation of 3-dimensional digital city models, and the determination of the shapes of asteroids and features on planets. The demands with respect to the required accuracy are steadily increasing (Rees 1990).

Laser altimetry systems have been able to respond to these demands. However, for many applications, only coarse resolution sampling is available. This is especially true for planetary and small body observations, where the sampling of the surface is constrained by the orbit of the sensor, and this orbit is often determined by the other instruments carried by the spacecraft.

These other instruments usually include a high-resolution optical imager. These images have been previously used to infer a surface reconstruction, solving this inverse problem using Bayesian probability theory (Smelyanskiy 2000, Morris 2001). The accuracy of the reconstruction of the 3-dimensional surface depends on the geometric information content of the images and on additional prior knowledge. Often images from mapping orbits do not contain much geometric information as the baseline is very small compared to the distance to the surface.

In this paper we show that a dense surface geometry estimate can be made by combining the information from a coarse but highly accurate grid of height field points from Laser altimetry measurements and the limited geometrical information from a set of optical images. The resulting surface estimate (both geometry and albedo) has a precision unavailable from other interpolation methods. At the same time far fewer images are needed for a surface reconstruction than without the data

from the laser altimetry measurements.

The calculation is a two step process: Using the images and a spline interpolation of the laser altimetry data, an approximate albedo field of the surface is inferred. This albedo field and the spline interpolated surface are the starting points for the Bayesian surface reconstruction. The varying accuracy of the height field points is taken into account by assigning different uncertainty values to the individual points. The uncertainty of the laser altimetry measured points is very much lower compared with the interpolated values. This approach also offers an easy way to combine measurements with different accuracy. The height field points between the grid points of the laser altimetry measurements are updated by the additional geometrical constraints of the optical images. We present results of the inference of surface models from simulated height field grids and aerial photographs. The influence of different number of images and varying grid resolution is shown.

2 THEORY

The objective here is to infer a *surface model* using the available data, in this case, laser altimeter measurements. Bayesian inference has, for some time now, been the method of choice for many inference problems, enabling accurate estimation of parameters of interest from noisy and incomplete data (Bernardo 1994). It also provides a consistent framework for the incorporation of multiple, distinct, data sets into the inference process. The general approach is illustrated in figure 1. The figure shows that synthetic observations of the model are made using a computer simulation of the observation process, and that these are compared with the actual observations. The error between the actual and the simulated observations is used to adjust the parameters of the model, to minimize the errors. Bayes theorem tells us directly how much weight to assign to the two sources of errors, those coming from the image measurements and those coming from the laser altimeter measurements.

The surface model we use here is a triangulated mesh. At each vertex of the mesh we store the height and the albedo. As discussed above, to be able to infer the surface heights and albedos, we must first be able to simulate the data that would be recorded from the surface.

Generating images from the surface model is the area of computer graphics known as *rendering* (Foley 1990). It is important to note, however, that much recent work in computer graphics is unsuitable for our purpose, as it works in *image space*, where the fundamental unit is the image pixel, and any given pixel is coloured by light from one and only one surface element. This results in artefacts due to the relative sizes of the projections of the surface elements onto the image plane and their discretization into pixels. These artefacts are particularly noticeable along the edges of the surface elements (aliasing). For this work we require the renderer to operate in *object space*, and below we will briefly describe such a system. We also note that an object-space renderer can also compute the *derivatives* of the pixel values with respect to the surface model parameters. This is crucial in enabling efficient estimation of the surface model parameters, and will be described in more detail below.

We are also required to produce synthetic laser altimeter measurements. We make the approximation that the laser altimeter makes point measurements of the surface, and so producing these synthetic observations is straightforward. We also assume that the error in these measurements are known.

3 A BAYESIAN FRAMEWORK

In this paper the surface geometry is represented by a triangular mesh and the surface reflectance properties (albedos) are associated with the vertices of the triangular mesh. We will consider the case of Lambertian surfaces. We will also assume that the camera parameters (position and orientation, and internal calibration) and the parameters of the lighting are known. It is possible to estimate these parameters in a similar Bayesian framework, but it is beyond the scope of this paper (Morris 2001, Smelyanskiy 2001).

Thus we represent the surface model by the pair of vectors $[\vec{z}\ \vec{\rho}]$. The components of these vectors correspond to the height and albedo values defined on a regular grid of points

$$[\vec{z}\ \vec{\rho}] = \{(z_{\mathbf{i}}, \rho_{\mathbf{i}}), \quad \mathbf{i} = \ell\ (q\,\hat{\mathbf{x}} + p\,\hat{\mathbf{y}})\} \quad q, p = 0, 1, \ldots \quad (1)$$

where ℓ is the elementary grid length, $\hat{\mathbf{x}}$, $\hat{\mathbf{y}}$ are an orthonormal pair of unit vectors in the (x,y) plane and $\mathbf{i}$ indexes the position in the grid. The pair of vectors of heights and albedos represents a full vector for the surface model

$$\mathbf{u} = [\vec{z}\ \vec{\rho}]. \quad (2)$$

To estimate the values of $\vec{z}, \vec{\rho}$ from the laser altimeter and image data, we apply Bayes theorem which gives

$$p(\vec{z}, \vec{\rho}|L, I_1 \ldots I_F) \propto p(L, I_1 \ldots I_F|\vec{z}, \vec{\rho})\, p(\vec{z}, \vec{\rho}), \quad (3)$$

where L is the laser altimeter data I_f $(f = 1, \ldots, F)$ is the image data. This states that the posterior distribution of the heights and the albedos is proportional to the likelihood – the probability of observing the data given the heights and albedos – multiplied by the prior distribution on the heights and albedos.

Given the surface description, the images and the laser altimeter measurements are *conditionally independent*, and equation 3 can be written as

$$p(\vec{z}, \vec{\rho}|L, I_1 \ldots I_F) \propto p(L|\vec{z}, \vec{\rho})\, p(I_1 \ldots I_F|\vec{z}, \vec{\rho})\, p(\vec{z}, \vec{\rho}),$$

where we now have two independent likelihood terms, one for each data stream.

The prior distribution is assumed to be Gaussian

$$p(\vec{z}, \vec{\rho}) \propto \exp\left(-\frac{1}{2}\mathbf{u}\Sigma^{-1}\,\mathbf{u}^T\right), \quad (4)$$
$$\Sigma^{-1} = \begin{bmatrix} \hat{Q}/\sigma_h^2 & 0 \\ 0 & \hat{Q}/\sigma_\rho^2 \end{bmatrix},$$

where the vector of the surface model parameters $\mathbf{u}$ is defined in (2). The inverse covariance matrix is constructed to enforce a smoothing constraint on local variations of heights and albedos. We penalize the integral over the surface of the curvature factor $c(x, y) = z_{xx}^2 + z_{yy}^2 + 2z_{xy}^2$, and similarly for albedos. The two hyperparameters σ_h and σ_ρ in equation (4) control the expected values of the surface-averaged curvatures for heights and albedos.

This prior is placed directly over the height variables, z, but albedos are only defined over the range $[0-1]$. To avoid this,

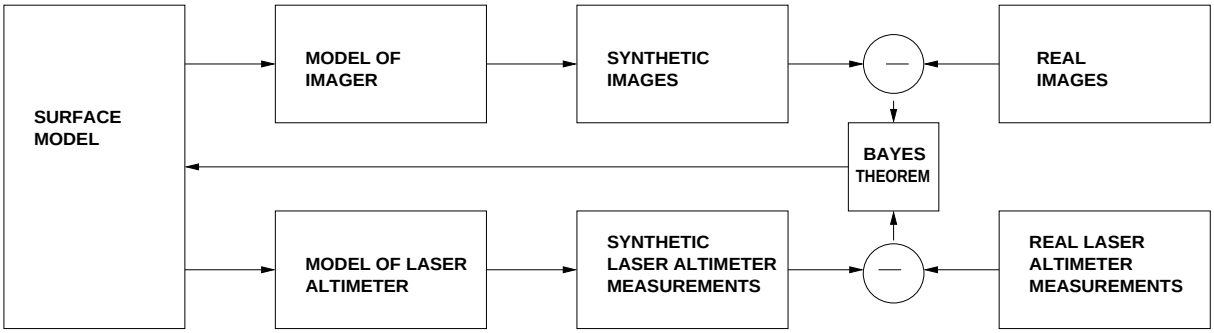

Figure 1: Outline of the Bayesian approach to surface reconstruction from images and laser altimeter measurements

we use transformed albedos $\rho'_{\mathbf{i}}$ in the Gaussian (4), where $\rho'_{\mathbf{i}}$ are defined by:

$$\rho'_{\mathbf{i}} = \log(\rho_{\mathbf{i}}/(1-\rho_{\mathbf{i}})), \quad \mathbf{u} \rightarrow [\vec{z}\ \vec{\rho}\,'\,]. \tag{5}$$

In the vector of model parameters $\mathbf{u}$ values of $\vec{\rho}$ are replaced by values of $\vec{\rho}'$.

For both the likelihoods we make the usual assumption that the differences between the observed data and the data synthesized from the model have a zero mean, Gaussian distribution. So for the laser altimeter measurements we have

$$p(L|\vec{z},\vec{\rho}) \propto \exp\left(-\frac{\sum_l (L_l - \hat{L}_l(\vec{z},\vec{\rho}))^2}{2\sigma_l^2}\right) \tag{6}$$

where the summation is over the individual measurement points L_l, and $\hat{L}_l(\vec{z},\vec{\rho})$ denotes the laser altimeter measurements synthesized from the model. The parameter σ_l^2 is the variance of the laser altimeter measurement system.

We also assume that the images I_f comprising the data are conditionally independent, giving

$$p(I_1 \ldots I_F|\vec{z},\vec{\rho}) \propto \exp\left(-\frac{\sum_{f,p}(I_{f\,p} - \hat{I}_{f\,p}(\vec{z},\vec{\rho}))^2}{2\sigma_e^2}\right)$$

where $\hat{I}_{f\,p}(\vec{z},\vec{\rho})$ denotes the pixel intensities in the image f synthesized from the model, σ_e^2 is the noise variance and the summation is over the pixels (p) and over all images (f) used for the inference.

Consider the negative log-posterior.

$$\begin{aligned}\mathcal{L}(\vec{z},\vec{\rho}) \quad \propto \quad & \frac{\sum_{f,p}(I_{f\,p} - \hat{I}_{f\,p}(\vec{z},\vec{\rho}))^2}{\sigma_e^2} \\ & + \frac{\sum_l (L_l - \hat{L}_l(\vec{z},\vec{\rho}))^2}{\sigma_l^2} \\ & + \mathbf{x}\Sigma^{-1}\,\mathbf{x}^T,\end{aligned} \tag{7}$$

where $\mathbf{x} = \mathbf{u} - \mathbf{u}_0$ is a deviation from a current estimate $\mathbf{u}_0$. $\mathcal{L}$ is a nonlinear function of $\vec{z},\vec{\rho}$ and the MAP estimate is that value of $\vec{z},\vec{\rho}$ which minimizes $\mathcal{L}(\vec{z},\vec{\rho})$.

The crux of the problem is thus how to minimize $\mathcal{L}$. We apply a gradient method, using an initialization based on a spline interpolation of the laser altimeter measurements.

Making the assumption that the laser altimeter makes point measurements of one of the vertices of the mesh, equation 6 can be written as

$$p(L|\vec{z},\vec{\rho}) \propto \exp\left(-1/2(\mathbf{l}-\mathbf{l}_0)\Sigma_l^{-1}(\mathbf{l}-\mathbf{l}_0)^T\right)$$

where $\mathbf{l}_0$ is the vector of actual laser altimeter observations, and $\mathbf{l}$ are the corresponding entries taken from the $\vec{z}$ vector. The inverse covariance matrix σ_l^{-1} is a diagonal matrix with $1/\sigma_l^2$ on the leading diagonal.

The term for the image measurements is more complex, as $\hat{I}(\vec{z},\vec{\rho})$ is the rendering process. To make progress with minimizing $\mathcal{L}(\vec{z},\vec{\rho})$ we linearize $\hat{I}(\vec{z},\vec{\rho})$ about an initial estimate, $\vec{z}_0,\vec{\rho}_0$

$$\hat{I}(\vec{z},\vec{\rho}) = \hat{I}(\vec{z}_0,\vec{\rho}_0) + \mathbf{D}\,\mathbf{x}, \quad \mathbf{D} \equiv \left\{\frac{\partial \hat{I}_{f\,p}}{\partial z_{\mathbf{i}}}, \frac{\partial \hat{I}_{f\,p}}{\partial \rho'_{\mathbf{i}}}\right\} \tag{8}$$

where $\mathbf{D}$ is the matrix of derivatives evaluated at z_0,ρ_0. Then the minimization of $L(\vec{z},\vec{\rho})$ is replaced by minimization of the quadratic form:

$$\begin{aligned}\mathcal{L}' &= \frac{1}{2}\mathbf{x}\,\hat{A}\,\mathbf{x} - \mathbf{b}\,\mathbf{x}, \quad \mathbf{x} \equiv \mathbf{u} - \mathbf{u}_0, \\ \hat{A} &= \Sigma^{-1} + \frac{\mathbf{D}\mathbf{D}^T}{\sigma_e^2} + \hat{\Sigma}_l^{-1}, \\ \mathbf{b} &= \frac{(I - \hat{I}(\vec{z}_0,\vec{\rho}_0))}{\sigma_e^2}\mathbf{D}\end{aligned} \tag{9}$$

where $\hat{\Sigma}_l^{-1}$ is now a large square matrix (of dimension length($\vec{z}$) + length($\vec{\rho}$)), where the diagonal elements corresponding to the vertices for which there are laser altimeter measurements take values $1/\sigma_l^2$ and all other entries are zero. The entries of $\mathbf{u_0}$ corresponding to the laser altimeter measurements are set to the observed values, and the remaining height values are initialized using a spline interpolation. This interpolation and the albedo initialization will be described below.

In equation 9 $\hat{A}$ is the Hessian matrix of the quadratic form and vector $\mathbf{b}$ is the gradient of the likelihood $\mathcal{L}$ computed at the current estimate. We search for the minimum in $\mathbf{x}$ using a conjugate-gradient method (Press 1992).

Thus the most difficult part of finding the MAP is the requirement to render the image and compute the derivatives for any values of the surface model parameters. We discuss this computation in some detail in the next sections. Here it is sufficient to note that while forming $\hat{I}$ using only object space computation (see section 4) is computationally expensive, we can compute $\mathbf{D}$ at the same time for little additional computation. Also the derivative matrix is sparse with the number of nonzero entries a few times the number of model parameters. This makes the process described above a practical one.

The log-posterior is potentially multi-modal, and so it is important to begin the optimization from a good initialization.

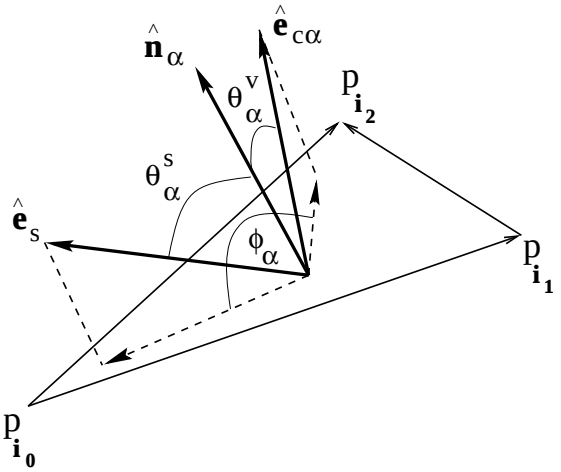

Figure 2: Geometry of the triangular facet, illumination direction and viewing direction. $\hat{\mathbf{z}}_s$ is the vector to the illumination source; $\hat{\mathbf{z}}_v$ is the viewing direction.

In order to do this, the high resolution surface estimation proceeds as follows.

1. Use a spline interpolation of the laser altimeter measurements to produce an initial height field estimate at the desired high resolution.
   Also produce the matrix $\hat{\Sigma}_l^{-1}$, with zeros everywhere except those diagonal entries corresponding to the points of the high resolution surface grid that are measured by the laser altimeter. These values are $1/\sigma_e^2$.
   Initialism all the albedos to 0.5.
2. Render the surface generated in step 1 and compute the derivative matrices **D** (one for each image). Set to zero all the derivatives with respect to the surface heights. This fixes the heights at their current values in the optimization step (below), so that only the surface albedo values are inferred.
   Starting from the surface from step 1, and using the derivative matrices calculated above, use the conjugate gradient algorithm to minimize the linearization of the log-posterior in equation 9. This produces a good initialization for the final optimization.
3. Render the surface generated in step 2 and compute the derivative matrices **D**.
   Starting from the surface in step 2, use the conjugate gradient algorithm to minimize the linearization of the log-posterior.
4. Repeat step 3 until convergence.
   The minimum found is the final surface estimate, which combines the information from the laser altimeter measurements and the visible images.

4 FORMATION OF THE IMAGE AND THE DERIVATIVE MATRIX.

The task of forming an image, $\hat{I}$, given a surface description, $\vec{z}, \vec{\rho}$, and camera and illumination parameters is the area of computer graphics known as rendering (Foley 1990). Most current rendering technology is focused on producing images which are *visually* appealing, and producing them very quickly. As discussed in the introduction, this results in the use of image-space algorithms, with the fundamental assumption that each triangle making up the surface, when projected onto the image plane, is much larger than a pixel. This makes reasonable the assumption that any given pixel receives light from only one triangle, but does produce images with artifacts at the triangle edges. Standard rendering also produces inaccurate images if the triangles project into areas much smaller than a pixel on the image plane, as the pixel will then be colored with a value coming from just *one* of the triangles.

Clearly this approach is not suitable for high-resolution 3D surface reconstruction from multiple images. The triangles in a high-resolution surface may project onto an area much smaller than a single pixel in the image plane (sub-pixel resolution). Therefore, as discussed in the introduction, for our system we implemented a renderer for triangular meshes which performs all computation in *object space*. At present we neglect the blurring effect due to diffraction and due to the role of pixel boundaries in the CCD array. Then the light from a triangle as it is projected into a pixel contributes to the brightness of the pixel with a weight factor proportional to the fraction of the area of the triangle which projects into that pixel. This produces anti-aliased images and allows an image of any resolution to be produced from a mesh of arbitrary density, as required when the system performing the surface inference may have no control over the image data gathering.

Our renderer computes brightness $\hat{I}_p$ of a pixel p in the image as a sum of contributions from individual surface triangles $\triangle$ whose projections into the image plane overlap, at least partially, with the pixel p.

$$\hat{I}_p = \sum_{\triangle} f^p_{\triangle}\, \Phi_{\triangle}. \tag{10}$$

Here $\Phi_{\triangle}$ is a radiation flux reflected from the triangular facet $\triangle$ and received by the camera, and $f^p_{\triangle}$ is the fraction of the flux that falls onto a given pixel p in the image plane. In the case of Lambertian surfaces and a single spectral band $\Phi_{\triangle}$ is given by the expression

$$\begin{aligned} &\Phi_{\triangle} = \rho\, E(\alpha^s)\, \cos\alpha^v\, \cos^\kappa\theta\, \Delta\Omega, \\ &E(\alpha^s) = \rho\, \mathcal{A}\, (\mathcal{I}^s\, \cos\alpha^s + \mathcal{I}^a)\,. \\ &\Delta\Omega = S/d^2. \end{aligned} \tag{11}$$

Here ρ is an average albedo of the triangular facet. Orientation angles α^s and α^v are defined in figure 2. $E(\alpha^s)$ is the total radiation flux incident on the triangular facet with area $\mathcal{A}$. This flux is modeled as a sum of two terms. The first term corresponds to direct radiation with intensity $\mathcal{I}^s$ from the light source at infinity (commonly the sun). The second term corresponds to ambient light with intensity $\mathcal{I}^a$. The parameter θ in equation. (11) is the angle between the camera axis and the viewing direction (the vector from the surface to the camera); κ is the lens falloff factor. $\Delta\Omega$ in (11) is the spatial angle subtended by the camera which is determined by the area of the lens S and the distance d from the centroid of the triangular facet to the camera.

We identify the triangular facet $\triangle$ by the set of 3 indices $(\mathbf{i_0}, \mathbf{i_1}, \mathbf{i_2})$ from the vector of heights (1) that determines the vertices of the triangle in a counterclockwise direction (see figure 2). In the r.h.s of equation (11) we have omitted for brevity those indices from all the quantities associated with individual triangles. The average value of albedo for the

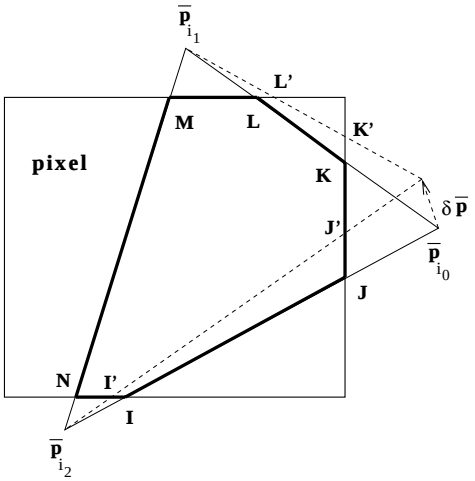

Figure 3: The intersection of the projection of a triangular surface element $(\mathbf{i_0}, \mathbf{i_1}, \mathbf{i_2})$ onto the pixel plane with the pixel boundaries. Bold lines corresponds to the edges of the polygon resulting from the intersection. Dashed lines correspond to the new positions of the triangle edges when point $\mathbf{P_{i_0}}$ is displaced by $\delta\mathbf{P}$

triangle in (11) is computed based on the components of the albedo vector ρ corresponding to the triangle indices

$$\rho_{\triangle} \equiv \rho_{\mathbf{i_0},\mathbf{i_1},\mathbf{i_2}} = \frac{1}{3}(\rho_{\mathbf{i_0}} + \rho_{\mathbf{i_1}} + \rho_{\mathbf{i_2}}). \tag{12}$$

We note that using average albedo (12) in the expression for $\Phi_{\triangle}$ is an approximation which is justified when the albedo values vary smoothly between the neighboring vertices of a grid.

The area $\mathcal{A}$ of the triangle and the orientation angles in (11) can be calculated in terms of the vertices of the triangle $\mathbf{P_i}$ (see figure 2) as follows:

$$\hat{\mathbf{n}} \cdot \hat{\mathbf{z}}^s = \cos\alpha^s, \quad \hat{\mathbf{n}} \cdot \hat{\mathbf{z}}^v = \cos\alpha^v, \tag{13}$$
$$\hat{\mathbf{n}} = \frac{\mathbf{v_{i_0,i_1}} \times \mathbf{v_{i_1,i_2}}}{2\mathcal{A}}, \quad \mathbf{v_{i,j}} = \mathbf{P_j} - \mathbf{P_i}$$

Here $\hat{\mathbf{n}}$ is a unit normal to the triangular facet and vectors of the edges of the triangle $\mathbf{v_{i,j}}$ are shown in figure 2.

We use a standard pinhole camera model with no distortion in which coordinates of a 3D world point $\mathbf{P} = (x, y, z)$ are first rotated with the rotation matrix $\hat{\mathbf{R}}$ and then translated by the vector $\mathbf{T}$ into camera coordinates, yielding $\mathbf{P_c} = (x_c, y_c, z_c)$

$$\mathbf{P_c} = \hat{\mathbf{R}}\,\mathbf{P} + \mathbf{T} \tag{14}$$

($\hat{\mathbf{R}}$ and $\mathbf{T}$ are expressed in terms of the camera registration parameters (Hartley 2000). We do not give them explicitly here). After the 3D transformation given in (14), point $\mathbf{P_c}$ in the camera coordinate system is transformed using a perspective projection into the 2D image point $\bar{\mathbf{P}} = (\bar{x}, \bar{y})$ using a focal length f and aspect ratio a.

$$\begin{bmatrix} \bar{x} \\ \bar{y} \end{bmatrix} = -\frac{f}{z_c} \begin{bmatrix} a\,x_c \\ y_c \end{bmatrix}. \tag{15}$$

We use 2D image projections of the triangular vertices $\mathbf{P_i}$ to compute the area fraction factors $f^p_{\triangle}$ for the surface triangles (cf. Eq. (10))

$$f^p_{\triangle} = \frac{\bar{A}_{\text{polygon}}}{\bar{A}_{\triangle}}. \tag{16}$$

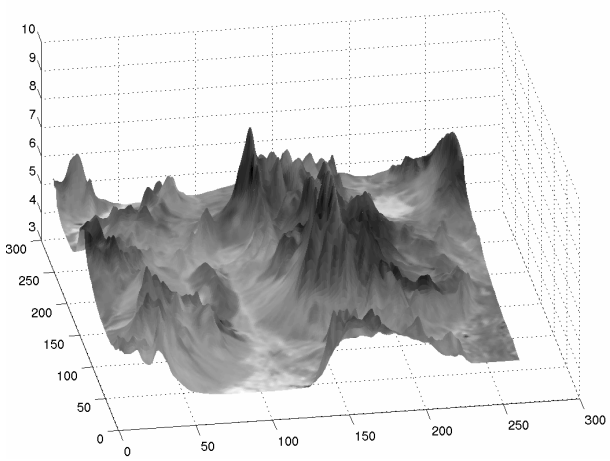

Figure 4: The initial synthetic surface model (Duckwater, NV).

Here $\bar{A}_{\triangle}$ is the area of the projected triangle on the image plane and $\bar{A}_{\text{polygon}}$ is the area of the polygon resulting from the intersection of the projected triangle and boundary of the pixel p (see figure 3).

4.1 Computation of the derivative matrix.

The inference of the surface model parameters depends on the ability to compute the derivatives of the modeled observations $\hat{I}$ with respect to the model parameters. According to equation (10), the intensity $\hat{I}_p$ of a pixel p depends on the subset of the surface parameters, (heights and albedos), that are associated with the triangles whose projections overlap the pixel area.

The derivatives $\hat{I}_p$ with respect to logarithmically transformed albedo values are easily derived from equations (5), (10) and (11).

In our object-space renderer, which is based on pixel-triangle geometrical intersection in the image plane, the pixel intensity derivatives with respect to the surface heights have two distinct contributions

$$\frac{\partial \hat{I}_p}{\partial z_{\mathbf{i}}} = \sum_{\triangle} \left(f^p_{\triangle}\, \frac{\partial \Phi_{\triangle}}{\partial z_{\mathbf{i}}} + \Phi_{\triangle} \frac{\partial f^p_{\triangle}}{\partial z_{\mathbf{i}}} \right) \tag{17}$$

Variation of the surface height $z_{\mathbf{i}}$ gives rise to variations in the normals of the triangles associated with this height (in a general triangular mesh, on average 6 triangles are associated with each height) and this produces the derivatives of the total radiation flux $\Phi_{\triangle}$ to the camera from those triangles. This is the first term in equation (17). Also, height variation gives rise to the displacement of the corresponding point which is the projection of this vertex on the image plane. This results in changes to the areas of the triangles and polygons with edges containing this point (see figure 3). This produces the derivatives of the fractions $f^p_{\triangle}$, the second term in equation 17. Details of these derivatives can be found in (Smelyanskiy 2000, Morris 2001, Smelyanskiy 2001).

5 RESULTS

Figure 4 shows the synthetic surface that we will use to demonstrate our methodology. The topography is taken from the USGS DEM of Duckwater, Nevada. A LANDSAT-TM

image 1	camera	$(75, 150, 2000)$
	look at	$(150, 150, 0)$
	view up	$(0, 1, 0)$
image 2	camera	$(225, 150, 2000)$
	look at	$(150, 150, 0)$
	view up	$(0, 1, 0)$

Table 1: Camera parameters used to generate the images in figure 5

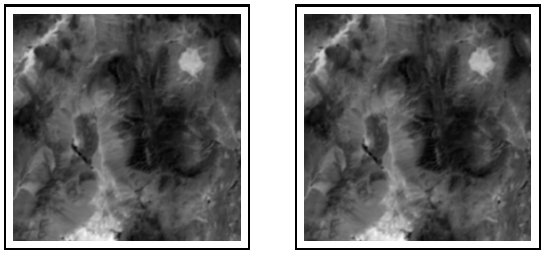

Figure 5: Images of the synthetic surface

image was co-registered with the DEM, and the values of one band were used in place of the true albedos. This results in the surface shown. One unit is approximately 180 meters.

Figure 5 shows two images rendered from the surface, and table 1 gives the positions and orientations of the (synthetic) cameras. The cameras were positioned to approximate satellite observations. The two images look very realistic. Note that the image appear very similar due to the proximity of the two camera positions. There is limited geometric information available from the images alone.

Figure 6 shows a surface from a grid of 9×9 points extracted from the surface in figure 4. The major terrain features have all been sampled, but clearly it is a very poor representation of the surface. This is taken as the laser altimeter observations of the surface.

Using the images and the 9×9 grid, we will now go through the surface estimation procedure that was detailed above.

Figure 7 shows the result of using the standard spline interpolation to expand the 9×9 grid to the full resolution of the surface. The result is a smooth surface showing the major features, but note that it contains no more information than the coarse surface.

Keeping the heights fixed at this surface, we then use the images to infer initial values for the albedos. The result is shown in figure 8. Note that this is *not* simply the back-projection of the of the images onto the surface, The information in both images has been optimally combined to give the albedo estimates. This surface is now a passable approximation to the original surface, as it has high resolution albedo information providing rich visual detail, but clearly it contains no topographic detail.

Figure 9 shows the final inferred surface. This is much improved over the surface in figure 8. It shows that much of the detail of the topography has been extracted from the data and incorporated into the model. The error surfaces show in figures 10 and 11 show clearly the improvement in the surface estimate. These error surfaces show both the height error and the albedo error as a shaded surface – the topography shows the height error, and the colour of the surface shows the

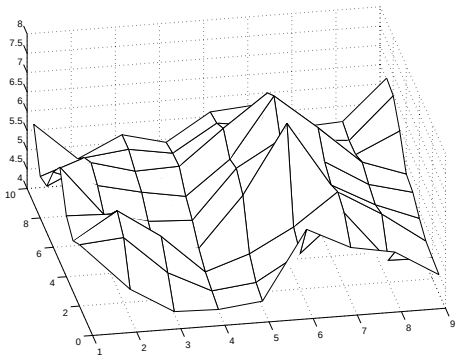

Figure 6: Grid from the 9×9 simulated laser altimeter measurements.

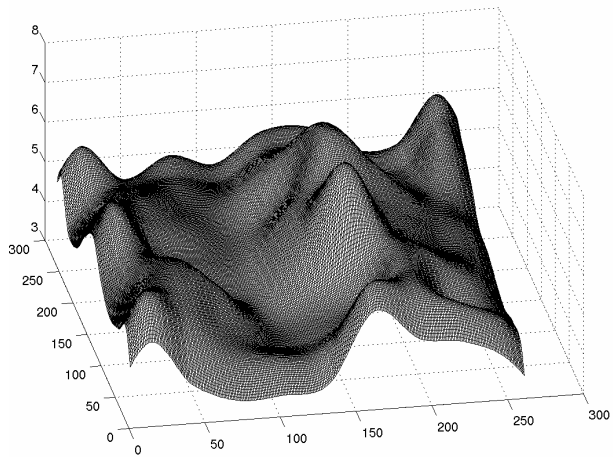

Figure 7: Spline interpolation of the synthetic laser altimeter measurements.

albedo error. The rms errors for the interpolated surface are 0.64 (per vertex) for the heights and 2.6×10^{-5} and for the final infered surface are 0.01 for the heights and 1.3×10^{-5} for the albedos. Note that the albedo values from the initialization are already quite good (as can be seen on figure 8, however the inference process produces a topography which is very significantly more accurate.

6 CONCLUSIONS AND FUTURE EXTENSIONS

We have presented the theory and practice of using Bayesian methodology to combine the information in laser altimeter measurements and visible images into a single, high resolution surface model. We have shown on synthetic data that the two data sets can be combined into a single high resolution model that is more detailed than could be provided by either data stream alone.

Current work is proceeding towards applying the demonstration system to real data, including NASA mission data. Work in this area is devoted to sensor modeling (producing the synthetic images and derivative matrices for the actual imaging sensor, rather than an idealization of it), estimation of the camera positions to sub-pixel accuracy, better control of the smoothness prior on the surface, and better initialization of the optimization procedure.

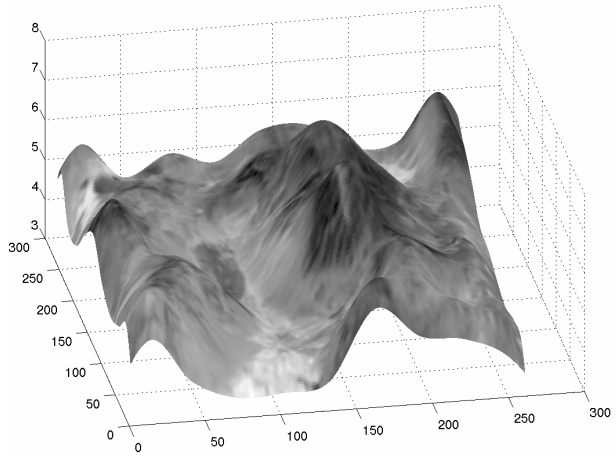

Figure 8: Interpolated surface with inferred albedos.

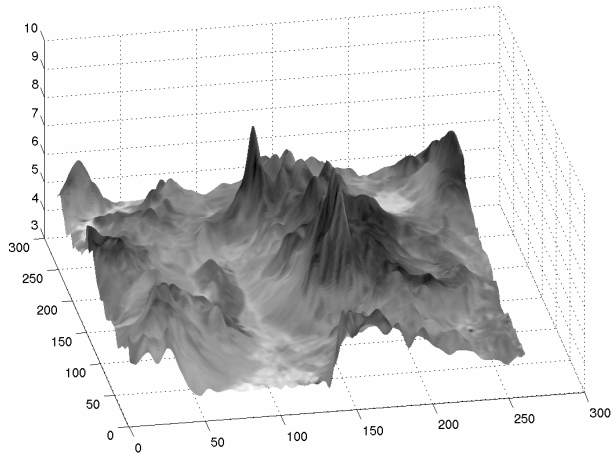

Figure 9: Final inferred surface using the Bayesian approach to combining the laser altimeter and visible images

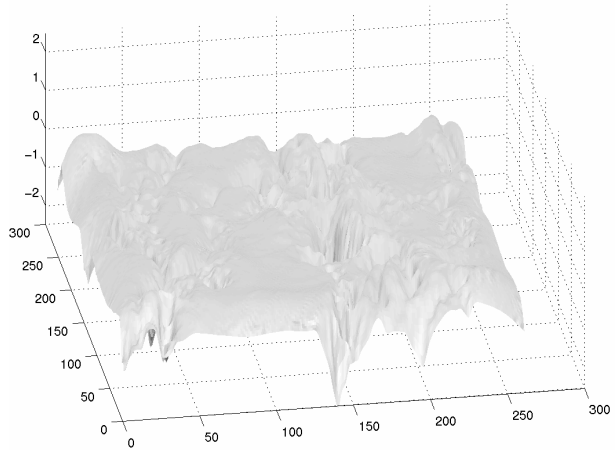

Figure 10: Error surface for the interpolated surface

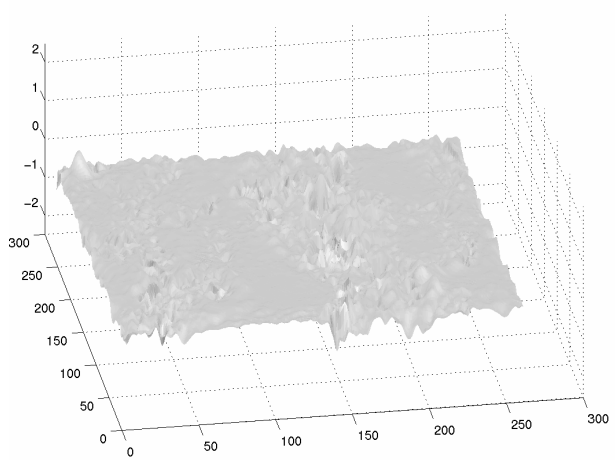

Figure 11: Error surface for the inferred surface

REFERENCES

Bernardo, J. and Smith, A., 1994. Bayesian Theory. Wiley, Chichester, New York.

Foley, J., van Dam, A., Finer, S. and Hughes, J., 1990. Computer Graphics, Principles and Practice. Addison-Wesley, 2nd edition.

Hartley, R. and Zisserman, A., 2000. Multiple View Geometry in Computer Vision. Cambridge University Press.

Morris, R.D., Smelyanskiy, V.N., Cheeseman, P., 2001. Matching Images to Models – Camera Calibration for 3-D Surface Reconstruction. Proceedings of EMMCVPR 2001, Springer LNCS volume 2134.

Press, W.H., Teukolsky, S.A., Vetterling, W.T., Flannery, B.P., 1992. Numerical Recipes in C. Cambridge University Press, 2nd edition.

Rees, W., 1990. Physical Principles of Remote Sensing. Cambridge University Press.

Smelyanskiy, V.N., Cheeseman, P., Maluf, D.A., Morris, R.D., Bayesian Super-Resolved Surface Reconstruction from Images. Proceedings of Computer Vision and Pattern Recognition 2000.

Smelyanskiy, V.N., Morris, R.D., Maluf, D.A., Cheeseman, P., 2001. (Almost) Featureless Stereo – Calibration and Dense 3D Reconstruction Using Whole Image Operations. Technical Report, RIACS, NASA Ames Research Center.

ACCURACY STUDY OF AIRBORNE LASER SCANNING DATA WITH PHOTOGRAMMETRY

Toni Schenk[1], Suyoung Seo[1], Beáta Csathó[2]

[1]Department of Civil and Environmental Engineering and Geodetic Science
[2]Byrd Polar Research Center
The Ohio State University
Columbus, OH 43210
schenk.2@osu.edu, Seo.1@osu, csatho.1@osu.edu

KEY WORDS: Photogrammetry, Laser Ranging, DTM generation, Surface Reconstruction, Calibration, Segmentation, Fusion

ABSTRACT

This paper describes an accuracy study of airborne laser scanning data obtained by the Airborne Topographic Mapper (ATM) laser system over Ocean City, Md. The ATM is a conical scanning laser altimeter developed by NASA for precise measurement of surface elevation changes in polar ice sheets, ocean beaches and drainage systems. First, we determine the “internal" accuracy of the system by comparing data from different flight missions. This is followed by a comparison of the merged laser data sets with surface elevations obtained by photogrammetry. Large-scale aerial photographs have been acquired over the test area and an aerial triangulation was performed to determine the exterior orientation parameters. The comparison consists of several experiments that were performed with the digitized photographs and the laser points. First we determine how well the laser points agree with the visible surface as defined by two overlapping images (stereopsis). This is accomplished by backprojecting the laser points to the images based on their exterior orientation parameters. The location of the laser points in the images serve as initial approximations for image matching. We use an adaptive least-squares matching procedure with a variable template size. A non-zero matching vector indicates discrepancies between laser points and photogrammetry. The purpose of the second experiment is to estimate the horizontal accuracy of laser points. One way to accomplish this is to extract linear features and to compare them. Linear features in laser point data sets can only be determined indirectly, e.g. by intersecting planar surface patches. In contrast, linear features in aerial images can be determined directly by an edge operator. We used the Canny operator to extract edges in the images and feature-based matching to find corresponding edges in the stereopair. After describing the procedure, experimental results are reported.

1 Introduction

Laser altimetry is a new technology for rapidly capturing data on physical surfaces. An ever increasing range of applications takes advantage of the high accuracy potential, dense sampling, and the high degree of automation that results in a quick delivery of products derived from the raw laser data. Airborne laser altimetry offers many advantages, including the high precision of the laser points. It appears at the outset that the elevation accuracy is limited by the range accuracy which is assumed to be better than one decimeter. Planimetric errors are often disregarded with the argument that they do not matter on flat surfaces. This view is too simple—the error budget of laser points is far more complex (*Schenk* (2000)). It is important to distinguish between the accuracy potential and the actual results achieved with today’s systems.

Several papers report about errors encountered in laser points or surfaces derived from laser points. In The Netherlands, for example, airborne laser altimetry has been extensively used on a nation-wide scale for establishing DEMs and for monitoring coastal erosion. *Huising and Gomes Pereira* (1998) identified elevation errors in overlapping strips on the order of a few decimeters and planimetric errors of more than one meter. Similar elevation errors are also reported in *Crombaghs et al.* (2000).

We present in this paper an accuracy study of airborne laser scanning data obtained by the Airborne Topographic Mapper (ATM) laser system over Ocean City, Md. The ATM is a conical scanning laser altimeter developed by NASA for precise measurement of surface elevation changes in polar ice sheets, ocean beaches and drainage systems. The accuracy of the laser points is estimated by a comparison with elevations and features derived from aerial images by photogrammetric means. Since laser points are not physical tangible it is impossible to carry out an error analysis on a point to point bases. The second section describes a procedure that we call backprojection. Here, laser points are projected back to aerial images that cover the same surface. This backprojection can be thought of as an image formation process—the location of the footprint is imaged just like any other point on the surface. Now we check with a modified least-squares matching approach if the backprojected laser points are in fact conjugate with respect to the gray values that represent the true surface.

The third section is concerned with the planimetric accuracy of laser points. We propose a method whereby linear features are extracted from both sources. This is not directly possible with laser points, however. First, planar surface patches must be found, for example by way of segmentation. This is followed by grouping planar surfaces that most likely belong to the same object. In this case, two neighboring surfaces are intersected resulting in an object boundary. The same boundary can be determined from the aerial images. Here, edges are extracted, matched, and represented in object space. The two edges in object space should be identical in an ideal world. Comparing corresponding edges allows to estimate the planimetric accuracy of laser points.

2 Elevation accuracy obtained by backprojection

2.1 Principle

Fig. 1 illustrates the principle of checking the accuracy of laser points by photogrammetric means. Let $L = \mathbf{l}_1, \mathbf{l}_2, \ldots, \mathbf{l}_n$ be the laser point cloud with $\mathbf{l}_i = [xl_i\ yl_i\ zl_i]^T$ the i^{th} laser point and let s', s'' be an oriented digital stereopair. The location $\mathbf{p}_i$ of laser point $\mathbf{l}_i$ in an image can be determined by the collinearity equation given below in vector notation.

$$\mathbf{p}_i = \lambda \mathbf{R}(\mathbf{l}_i - \mathbf{c}) \tag{1}$$

with $\mathbf{p}_i = [x_i\ y_i\ -f]^T$ the image coordinates (f = focal length), $\mathbf{R}$ an orthogonal rotation matrix defined by attitude (three angles) of the image, and $\mathbf{c}$ the position of the perspective center. $\mathbf{R}', \mathbf{c}'$ and $\mathbf{R}'', \mathbf{c}''$ are the six exterior orientation parameters of the two images s', s''.

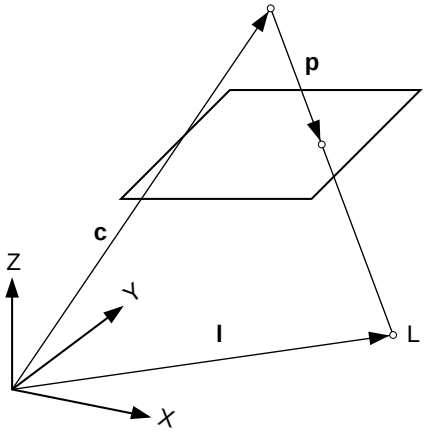

Figure 1: Principle of backprojection. Laser point $\mathbf{l}_i$ is "imaged" in point P_i. The location is found by intersecting line (C, L) with the image plane, mathematically performed by eq. 1.

Images are central projections of the visible surface of the object space. In general, laser points are also on this surface. Hence, when backprojected to the images, one cannot only visualize where the laser footprint was but determine if the computed positions of laser points are really on the surface.

Suppose that laser point L is not on the visible surface as shown in Fig. 2. The computed image positions by eq. 1 are in L' and L'', respectively. At the image location L', surface point A is imaged, however. Likewise, at image location L'', point B is shown. The corresponding point to image point $L' = A'$ is in fact image point A'' and not L''. The difference between L'' and A'' can be determined automatically by area-based image matching (see *Schenk* (1999)).

2.2 Implementation of Backprojection

We have implemented the backprojection method by a modified least-squares matching (LSM) approach. LSM minimizes gray level differences between a template (window in image s' and a matching window of the same size in image s''. The matching window is moved and shaped until the gray level differences reach a minimum. A brief description of the major steps follows.

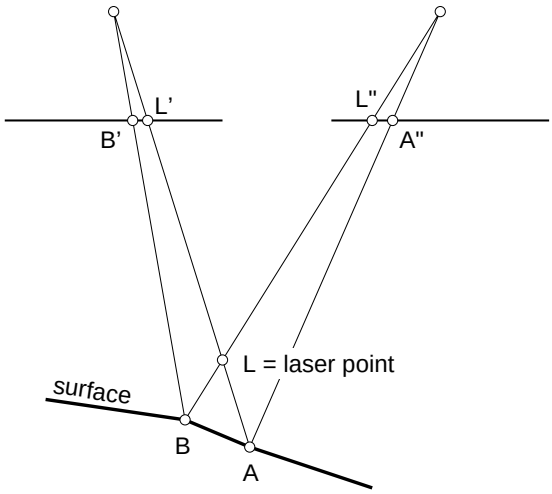

Figure 2: Illustration of the effect of a laser point D that is not on the visible surface. Its backprojected location in the images are in D' and D'', respectively. At these locations, surface points A and B are imaged, however. The corresponding point to $D' = A'$ is A'' and not D''.

1. Backproject laser point $\mathbf{l}_i$ to images s', s'' with eq. 1, using the exterior orientation of the respective images. Convert photocoordinates $\mathbf{p}_i'$ and $\mathbf{p}_i''$ to pixel coordinates row$_i'$, col$_i'$ and row$_i''$, col$_i''$ using the affine transformation parameters of the images' interior orientation.
2. Select a template window, centered at row$_i'$, col$_i'$ that has a distinct gray level distribution. The template size ranges from 9×9 to 23×23 pixels, depending on the gradiants and the entropy. The success of area-based matching depends on distinct gray level variations within the template. If the upper window size is reached without an acceptable entropy, matching is not performed and the method proceeds with the next laser point.
3. Start the iterative LSM approach with the initial position of the matching window centered at row$_i''$, col$_i''$. In each iteration, a new position of the matching window is determined. The translation parameters are real values and the gray levels in the new matching window are found by a bi-linear interpolation. The termination criterion is reached if the shift between successive iterations is less than 0.1 pixel.
4. The matched location in s'' is converted to photocoordinates $(\mathbf{pm}'')$ and intersected with $\mathbf{p}'$—the corresponding point in image s'. This intersected point in object space refers to point A of Fig. 2. The difference between this point and the laser point is used as a quality control measure.

2.3 Experimental Results

A multisensor data set has been collected over Ocean City, Maryland, under the auspices of ISPRS WG III/5, the Geomatics Laboratory for Ice Dynamics of the Byrd Polar Research Center, and the Photogrammetry Laboratory of the Department of Civil and Environmental Engineering, OSU.

The data set comprises aerial photography, laser scanning data, and multispectral and hyperspectral data. *Csathó et al.* (1998) provide a detailed description.

For the experiments we used an aerial stereopair, scanned from the original film negatives with a pixel size of 28 μm. The large scale aerial photographs were flown by the National Geodetic Survey (NGS) at a flying height of 372 m (photo scale approx 1 : 2,435). Thus, the ground pixel size is about 7 cm. We have performed an aerial triangulation of one strip with GPS ground control points. NASA Wallops made several laser data sets available, using the Airborne Topographic Mapper (ATM) laser system. The ATM is a conical scanner, developed by NASA for the purpose of measuring ice sheet surfaces. Recently, other applications have been pursued with this system, for example beach mapping.

The exterior orientation of the photographs is in the same reference frame as the laser points. Consequently, features derived from both data sets can be compared directly.

Fig. 3(a) provides an overview of the test site for the accuracy study. Six areas have been selected. They are highlighted and numbered from 1 to 6. The sub-images are approximately 2×2 cm^2 corresponding to 700×700 pixels. Fig. 3(b) and (c) depict a detail view of area 4. The two sub-images are extracted from the two overlapping digital images that form the stereo model. Superimposed as blue dots are the backprojected laser points. A close visual inspection reveals that the laser points in both images are in fact at corresponding locations. The dense distribution of the laser points results from combining several laser flight missions.

Fig. 3(d) shows the right sub-image. It has been used as the matching image. As described in the previous section, every laser point projected to the left sub-image served as the center of a template while the corresponding point in the right sub-image was used as the starting position of the matching window. In the LSM scheme, the matching window is moved until the gray level differences between template and matching window reach a minimum in the least-squares sense. The red dots in Fig. 3(d) indicate the starting position in the matching window. The end of the red lines depict the final position (matching vector). All the matching vectors are almost horizontal because we applied the epipolar line constraint which forces the match along epipolar lines. Epipolar lines are nearly parallel to the $x-$direction in aerial images. Note that out of 860 backprojected laser points, only 106 could be matched. All the other points did not satisfy the strict criteria imposed on the matching scheme, for example sufficient gray level variation in the template. A good example where this criterion is not met are the laser points on the road. Here, the gray levels within the template and/or matching window are very homogenous and thus not suitable for area-based matching. The same is true for laser points on roofs. Only the building in left upper corner of the sub-image has enough texture to allow matching.

A non-zero matching vector indicates differences between the laser points and the aerial images. We would expect a random error, σ_d of this difference of

$$\sigma_d = (\sigma_a^2 + \sigma_L^2)^{1/2} \quad (2)$$

with σ_a the standard deviation of an elevation derived from photogrammetry and σ_L the standard deviation of an elevation error of a laser point. σ_a largely depends on the flying height, the matching method used, and the pixel size. Taking these factors into account we obtain $\sigma_a = \pm 4$ cm. A good estimate for the accuracy of the laser points comes from the comparison and merging of the different laser missions. *Csathó et al.* (2001) provide a detailed report about this comparison from which we assume $\sigma_L = \pm 8$ cm. Hence, the difference should have a standard deviation of $\sigma_d = \pm 9$ cm.

area	#laser points	#matched points	σ_d [m]	bias [m]
1	2870	502	0.12	-0.33
2	2235	461	0.08	-0.42
3	750	217	0.07	-0.02
4	860	106	0.10	0.07
5	1344	207	0.15	-0.33
6	757	108	0.09	0.07

Fig. 3(e) shows the result of the matching procedure. On the horizontal axis are the laser points in ascending order (point number). The blue dots show the difference between laser point elevation and elevation established by matching. The gaps in the horizontal axis indicate points that could not be matched. For an example, see points with a number around 500. The plot reveals a fairly even distribution of the elevation differences around zero. The mean is approximately 7 cm and $\sigma_d = \pm 10$ cm. There are also a couple of outliers clearly visible. For example, point 98 has a $z-$difference of 1.41 m. This point is on the roof of the third building from the top, right upper corner.

In the interest of brevity we omit detailed comments on the other five sub-images. Table 1 summarizes the most important results.

Analyzing Table 1 reveals an average standard deviation of the $z-$differences in all 6 areas of $\sigma_d \approx 11$ cm. This is just about what we have estimated a priori. It confirms the high accuracy of laser points if the systems are well calibrated. The last column of Table 1 contains the bias between laser points and photogrammetry. In some areas, the bias is much larger than the standard deviation. Examining the bias and the corresponding areas suggest that there is a tilt about the $x-$axis of the images (flight direction). Comparing the different laser missions did not indicate a problem of that nature. However, when carefully checking the aerial triangulation results we found that the stereomodel used in this investigation was the last in the strip and it had insufficient elevation control points. Thus, the biases discovered are caused by strip deformation.

Finally, we computed a relative orientation with the total of 1601 matched laser points. The average $y-$parallax was $\pm 2.8\,\mu$m which is exactly $1/10^{\text{th}}$ of the pixel size. This high accuracy does not necessarily reflect the elevation accuracy, however, because errors in the $x-$direction, causing elevation errors, remain undetected.

3 Planimetric accuracy assessment

The planimetric accuracy of laser points has not been thoroughly investigated as judged by the lack of publications dealing with this problem. The primary interest is in elevations and planimetric errors are often neglected with the

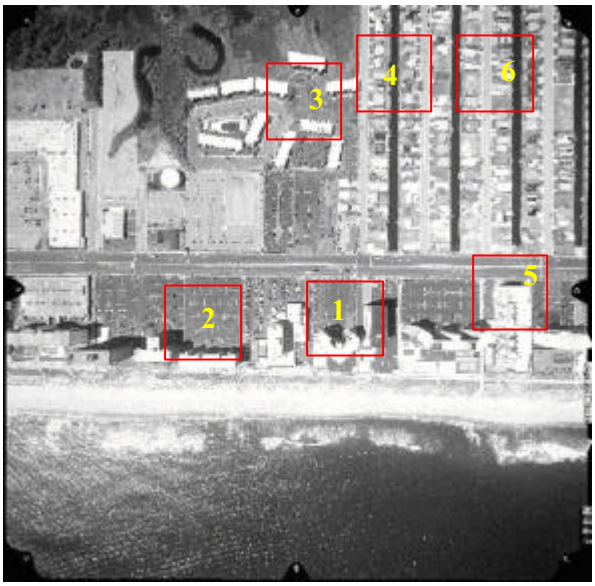

a

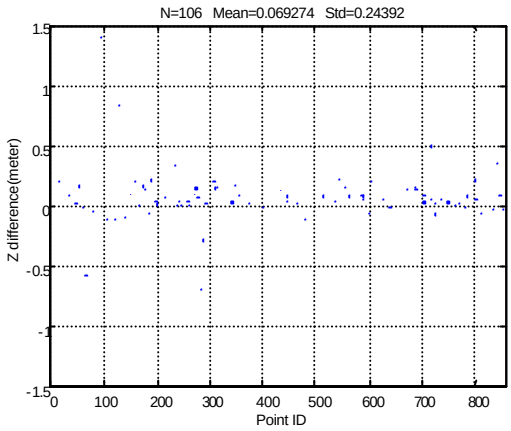

(e)

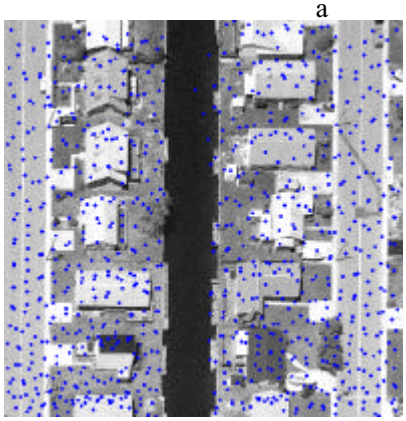

(b)

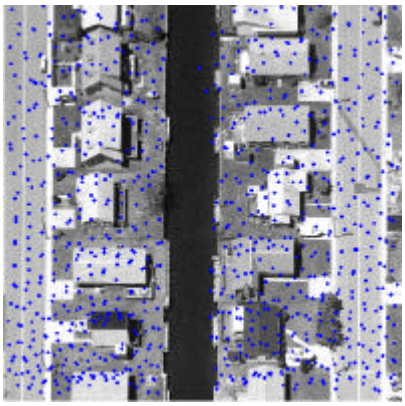

(c)

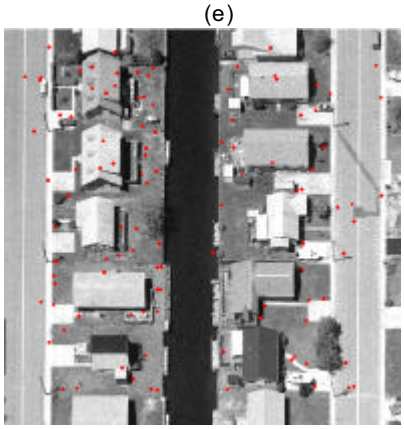

(d)

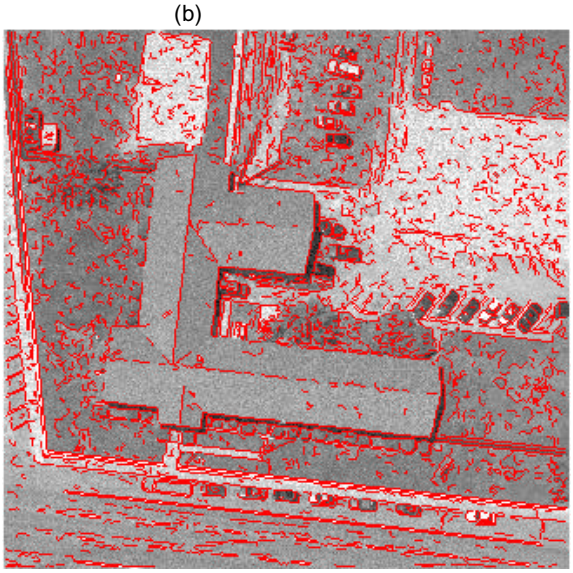

(f)

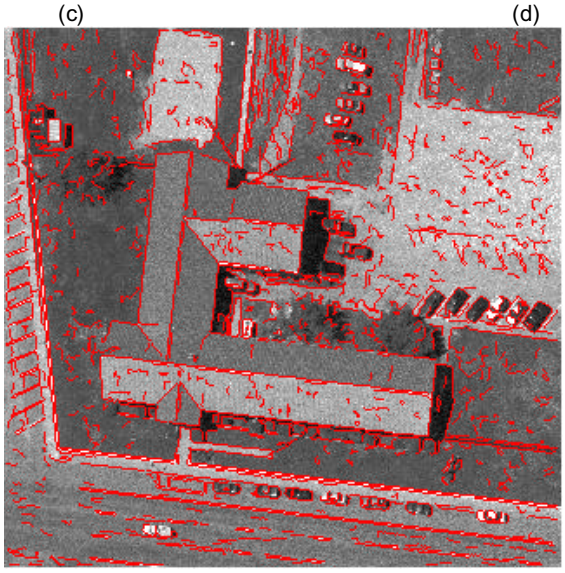

(g)

Figure 3: (a) shows the 6 selected sub-areas for checking laser points by the method of backprojection. The backprojected laser points of sub-area 4 are shown in (b) and (c)–a stereopair. The backprojected laser points that passed the criteria for least-squares matching are shown in (d). The z–differences between laser points and matched points in the stereopair are shown in (e). Finally, (f) and (g) shows edges extracted with the Canny operator.

argument that horizontal error components do not cause significant changes in the surface derived from laser points. While this may be true for profiling systems and fairly flat, horizontal surfaces, planimetric errors need attention when scanning systems are used to derive surfaces in rugged topography. Planimetric errors become the primary concern if objects are extracted from a cloud of laser points.

The problem of assessing planimetric errors is rooted in the fact that laser points do not carry semantic information that would allow their physical identification on the ground. By and large, laser points are only defined by location—additional information, such as “top of chimney", “corner of building", “street center line", is missing. Laser footprints are not visible and it will not be possible to directly determine the difference between the footprint (physical location of laser beam on the reflected surface) and the computed laser point.

We describe in this section how to extract physical features from laser points that would allow a comparison with independent determination of the same features.

3.1 Invariant features

Since it is impossible to carry out the accuracy analysis on the level of the original data, one way to solve the problem is to extract invariant features. With this we mean features that are related to object space (visible surface) phenomena. If sensory input data do not contain intrinsic information about the same object space phenomena, tasks such as registration or error analysis cannot be performed. Fortunately, ALS and photogrammetry have implicit information about common features in object space.

We concentrate on linear features, such as object boundaries. Object boundaries are abundant, especially in urban scenes, where man-made objects typically have straight-line or second order curve boundaries. The quest is to determine the same (physical) boundary reliably and automatically from laser points and from aerial images.

Extraction of linear features from laser points There are several ways to determine linear features from a laser point cloud. One possibility, proposed by several researchers, is to interpolate the laser points into a regular grid, and to convert elevations into gray levels (range image), followed by detecting edges in the range image. The rationale is that edges in object space are manifest by abrupt elevation changes. The success of this simple approach hinges on the density of the laser points and the interpolation method used for the conversion of the irregularly distributed points to an image. Unless sophisticated interpolation methods are used that try to avoid interpolating over breaklines, the edges to be detected in the range image are blurred and make it harder to detect them reliably as pointed out, e.g. by *Vosselman* (1999) and *McIntosh et al.* (1999).

Another—in our view better—approach is to compute edges from extracted planar surface patches. This is a lot more robust and leads to edges of superior accuracy as can be shown by simple error propagation. Surface patches (planar or second order surfaces) can be extracted from laser points by way of segmentation. Several segmentation procedures have been proposed (see *Lee and Schenk* (2001) for an overview). A popular approach is to generate a range image for employing segmentation methods developed in image processing. We prefer segmentation methods that work directly with the irregularly distributed 3D points to avoid potential problems related to the interpolation, however. *Lee and Schenk* (2001) present a multi-stage segmentation scheme with the goal to find a 3D perceptual organization of surface patches.

After having extracted planar surface patches the next problem is to determine which patches should be intersected to generate 3D lines. The challenge is to identify patches that belong to the same object and share a common boundary. Consider a building with a saddle roof, for example. The two planar surface patches extracted from the laser points intersect in the roof line. This is a physical edge, defined by the intersection of two physical planes. Imagine now the intersection of one roof plane with the parking lot next to the building. This intersection also involves two physical planes but it is not physically manifest in the object space. We call this non-physical line a *virtual line (edge)*. Virtual lines may also be useful for establishing planimetric accuracies, however, they are only useful if the same planes can be determined from aerial images.

Apart from topological constraints (adjacent planes in one object), there are also geometric considerations for computing 3D lines. Let us go back to the saddle roof for a moment. The accuracy of the ridge depends on how well the two roofs are determined (e.g. number and distribution of points, fitting plane) and on the intersecting angle, defined by the pitch of the roof. In that regard, virtual edges offer more flexibility in that topological constraints are waived and any two planar surface patches with favorable conditions (their accuracy and intersecting angle) can be chosen.

Extraction of linear features from aerial images Extracting linear features from aerial images is straightforward. There are numerous edge operators available that detect discontinuities in the gray levels, link edge pixels to edges, and assign various attributes, such as strength, orientation, and sign. Figs. 3(f,g) show edges in two overlapping image patches, extracted with the Canny operator. The roof boundaries are successfully detected, but a closer examination reveals that there are gaps in the edges. Also, there are differences between the edges in the left and right image.

The challenge in determining 3D lines from images is in the matching of matching, that is, in the identification of corresponding edges. We employ a feature-based, relational matching scheme and perform the segmentation of matched edges to straight lines in object space, although it is conceivable to determine straight edge segments in image space, before matching.

3.2 Experimental results

We have selected several sub-areas from the same Ocean City data set, described in the previous section. The subareas were selected to ensure that planar surface patches could be extracted from the laser point cloud and overlapping aerial images.

Lee and Schenk (2001) describe in detail the procedure of segmenting the laser points into planar surface patches and to group them according to geometric and topologic criteria. The paper also presents results of the segmentation, using the same data set. The planes selected for the experiments described here contained typically more than one hundred points. The fitting error for all planes was less than ± 10 cm,

in many cases as low as ± 5 cm. Thus, a high accuracy for the lines as intersection of two planes can be expected.

The accuracy of lines determined by photogrammetry from aerial images depends on the accuracy of extracted edges in the images, on the exterior orientation parameters, and on the segmentation in object space (fitting a straight line). Taking all these factors into account we can expect the same high accuracy as for lines determined from laser points.

The planimetric accuracy that resulted from comparing eight lines was not consistent. For some lines, the error is slightly higher than expected (about ± 20 cm) while for three lines the error was 40 cm. A closer examination revealed the following interesting problem. The roof ridges computed as intersection of roof planes are not necessarily identical with the physical ridges because they have constructive elements that are not part of the roof planes. This is also apparent in the extracted roof edges. The error of fitting a straight line through the edge pixels in object space also indicates that the physical ridge is not necessarily very straight.

These findings would suggest to avoid a comparison of edges determined by direct measurements of the physical edge (extracting edges in images) with indirectly determined edges (intersection of planes). The dilemma is that physical edges are not directly “mapped" by laser points. On the other hand, determining indirectly edges from images would require point measurements on surfaces, such as roof planes. This, in turn is often times not feasible because many roof planes appear quite homogenous in aerial images (see Fig. 3(f,g) for an example).

4 Conclusions

We have presented an accuracy study of laser points which is based on comparing elevations and features in aerial images with their counterparts in the laser point cloud. The proposed procedure with backprojecting laser points into oriented stereopairs is very successful. The automatic procedure allows to check thousands of points and gives direct information about discrepancies between the laser points and the visible surface as defined by overlapping aerial images. The average elevation difference between 1601 laser points and the photogrammetric surface (stereo) was ± 9 cm. This error consists of errors in photogrammetrically determined points and errors in laser points. Considering the photogrammetric point error we conclude that the laser points have an elevation accuracy of about ± 7 cm.

The method is also suitable for checking the accuracy of DEMs. Here, the grid posts can be backprojected and checked in the same fashion.

Assessment the horizontal accuracy of laser points is an intriguing problem. It can be approached by extracting linear features which are then compared with their “true" location. This is a two step process because linear features can hardly be directly retrieved from laser points. We propose to segment the laser points into planar surface patches and to compute straight lines by intersecting topologically related planes, such as roofs. It is important to realize, however, that these intersecting lines are not necessarily identical with the physical lines. A roof ridge, for example, may be slightly different to the intersection of the roof planes.

We are currently investigating other features that may serve as control information. The prime motivation is to find useful features for fusing aerial images, as well as multispectral and hyperspectral images with laser points obtained from airborne laser scanning systems.

5 Acknowledgement

The laser data sets used in the experiments was made available by NASA Goddard Space Flight Center, Wallops Flight Facility. We acknowledge the support of William Krabill and Serdar Manizade to who helped us to process the data. The aerial photography was made available by the National Geodetic Survey (NGS).

REFERENCES

Crombaghs, M.J.E., R. Brügelmann, and E.J. de Min, (2000). On the adjustment of overlapping strips of laser-altimeter height data. *ISPRS Journal of Photogrammetry & Remote Sensing*, **54**(2-3),164–198.

Csathó, B., Y.R. Lee, T. Schenk, W. Krabill and J. McGarry (2001). Creation of high-resolution, precise digital elevation models of Ocean City and Assateague Island, Md. In *International Archives of Photogrammetry and Remote Sensing*, **34**(3/W4), this proceedings.

Csathó, B., W. Krabill, J. Lucas and T. Schenk (1998). A multisensor data set of an urban and coastal scene. In *International Archives of Photogrammetry and Remote Sensing*, **32**(3/2), 588–592.

Huising, E.J. and L.M. Gomes Pereira, (1998). Errors and accuracy estimates of laser data acquired by various laser scanning systems for topographic applications. *ISPRS Journal of Photogrammetry & Remote Sensing*, **53**(1998),245–261.

Lee, I. and T. Schenk (2001). 3D Perceptual Organization of Laser Altimetry Data. In *International Archives of Photogrammetry and Remote Sensing*, **34**(3/W4), this proceedings.

McIntosh, K., A. Krupnik and T. Schenk, (1999). Utilizing airborne laser altimetry for the improvement of automatically generated DEMs over urban areas. In *International Archives of Photogrammetry and Remote Sensing*, **32**(3/W14), 89–94.

Schenk, T. (2000). *Modeling and Analyzing Systematic Errors in Airborne Laser Scanners*. Technical Report Photogrammetry No. 19, Department of Civil and Environmental Engineering and Geodetic Science, OSU, 39 pages.

Schenk, T. (1999). *Determining transformation parameters between surfaces without identical points*. Technical Report Photogrammetry No. 15, Department of Civil and Environmental Engineering and Geodetic Science, OSU, 22 pages.

Schenk, T. (1999). *Digital Photogrammetry.* TerraScience, Laurelville, Ohio, 428 p.

Vosselman, G. (1999). Building reconstruction using planar faces in very high density height data. In *International Archives of Photogrammetry and Remote Sensing*, **32**(3-2/W4), 383–388.

LAND SURFACE MAPPING AND CHARACTERIZATION USING LASER ALTIMETRY

SESSION 5

DATA MODELING

MODELING LIDAR WAVEFORMS USING A RADIATIVE TRANSFER MODEL

B. Peterson[1],W. Ni-Meister[2], J.B. Blair[3], M.A. Hofton[1], P. Hyde[1] and R. Dubayah[1]

[1]Department of Geography
University of Maryland
College Park, MD 20742
USA

[2]Goddard Earth Sciences and Technology Center (GEST)
and Hydrological Branch
NASA/Goddard Space Flight Center
Greenbelt, MD 20771
USA

[3]Laser Remote Sensing Branch
Laboratory for Terrestrial Physics
NASA/Goddard Space Flight Center
Greenbelt, MD 20771
USA

KEY WORDS: Lidar, Radiative transfer modeling, Canopy structure

ABSTRACT

In the past, obtaining reliable measurements of key forest canopy metrics has been difficult, even after the development of remote sensing technology. Fortunately, next-generation lidar systems are proving to be useful tools for deriving critical canopy measurements, such as height, structure and biomass. These studies have all focused on empirical comparisons between basic lidar-derived and field-sampled measurements. The results of these studies have shown that lidar remote sensing instruments can successfully measure forest canopy characteristics. However, physically-based remote sensing models are necessary to more fully understand and interpret the interactions of the laser energy with the forest canopy. In this study the Geometric Optical and Radiative Transfer (GORT) model is used to model lidar waveforms. GORT is capable of modeling lidar returns from canopies with clumped multiple layers and multiple species. For this study, GORT was used to model waveforms over the Sierra National Forest in California. Field data input into GORT are a representative sample of the different vegetation types found in the forest. The modeled waveforms are then validated against actual lidar data collected by the Laser Vegetation Imaging Sensor (LVIS) which mapped the area in October 1999. By modeling lidar waveforms based on the physical principles of radiative transfer, GORT fills a missing link between the remotely sensed and actual canopy structure. The results of this study will also aid in future large-scale land surface mapping by developing a link between lidar and other remote sensing data.

1 INTRODUCTION

Forest canopy structure is one of the least studied aspects of the forest ecosystem (Van Pelt and North, 1996; Yang et al. 1999). This lack is often attributed to the difficulty of working in forest canopies (Parker et al. 1992; Weishampel et al. 1996). Remote sensing of forest canopy structure overcomes many of the obstacles inherent in ground-based sampling and has been identified as a valid method for obtaining a variety of canopy data for regions all around the world (Weishampel et al. 1996; Hyyppä et al. 2000). Indeed, remote sensing has been called the only practical way of acquiring quantitative information about the biophysical and biochemical properties of forests (Danson and Curran 1993).

Next-generation, large-footprint lidar systems in particular provide a direct and elegant means to measure the structure of vegetation canopies. These large-footprint, waveform-digitizing systems have been optimized for the measurement of forest vegetation (Blair et al. 1994; Blair et al. 1999). Canopy height, basal area, canopy cover and biomass have all been successfully derived from large-footprint lidar waveform data (Means et al. 1999; Lefsky et al. 1999; Drake et al. in press; Peterson 2000). However, to take full advantage of the wealth of data contained in the lidar waveforms, the interaction between the laser energy and the structural elements of the canopy must be better understood. To this end, this study uses a physically-based remote sensing model to model lidar waveforms in a coniferous forest in the Sierra Nevada.

The model used in this study is the Geometric Optical and Radiative Transfer (GORT) model. It combines the theories of geometric optics and radiative transfer. It was originally developed to study the effects of the canopy architecture of discrete canopies on the radiation environment and to describe the heterogeneous radiation environment in natural vegetation (Li et al. 1995). GORT models the integrated radiation regime within forest canopies at the stand level. The inputs are distribution functions of tree geometry parameters (e.g. mean tree size, shape and density) and the spectral properties of the canopy and the background (Ni-Meister et al. in press). Specifically, GORT calculates the probability of individual photons finding within-crown or between-crown gaps in the canopy. These gaps represent pathways through which the photons can pass through the canopy and reach the ground beneath. GORT models total gap probability as a function of height. A detailed description of the model and how it can be used to model lidar waveforms is provided in Ni-Meister et al. (in press). The GORT model has been validated using field data from the BOREAS study and has also been used to model lidar waveforms from the SLICER instrument that collected data over the BOREAS field sites (Ni-Meister et al. in press).

2 DATA COLLECTION

2.1 LVIS Data

In October 1999 the LVIS instrument mapped a large area of the Sierra National Forest in California. LVIS is a pulsed laser altimeter that records the travel time of a laser pulse to a reflective surface as well as the shape of the output and return waveforms, thereby allowing the heights of the reflecting surfaces within each footprint to be determined (Blair et al. 1999). The system has a vertical precision of approximately 30 cm. The ranging data are combined with airplane roll, pitch and bearing data and GPS data to locate each individual laser footprint on the surface to within 1 m. Flying onboard a NASA C-130 at 8 km above ground level and operating at 320 Hz, LVIS produced 12.5 m-diameter footprints at the surface, overlapping by 50% across track and contiguous along track. In total, an area approximately 180,000 km^2 wide was mapped by LVIS in the Sierra Nevada study area.

2.2 Field Data

Field data for this study were collected in the summer of 2000 in the Sierra National Forest as part of a larger, on-going research study conducted by the U.S. Forest Service, the University of Michigan and the University of Maryland and are a representative sample of the different vegetation types found in this area. Circular plots centered on lidar footprints measured 15 m in diameter. Within these plots all trees over 10 cm dbh were sampled. Measurements included: total tree height, height to partial crown, partial crown wedge angle, height to full crown, four crown radius measurements and distance and azimuth relative to the plot center. Tree crown shape and species were also recorded.

Leaf Area Index (LAI) measurements were also taken in these plots. These measurements were taken at 61 points located every 3 m up to 15 m on transects radiating from the plot center at every 30 degrees and at the plots center. The LAI measurements were taken with two LICOR LAI-2000 instruments - one in the plot taking below-canopy measurements at the 61 points (four measurements at each point) and one located a short distance away logging clear sky data. The data from the two sensors were merged using the LICOR C2000 software and used to calculate LAI for each of the 61 points.

3 METHODS

Because each field plot was centered on the location of one footprint, there was one LVIS waveform to which to compare the data from the field. A total of 16 plots were included in this analysis. For each plot, the associated waveform was normalized and the canopy portion of the waveform was identified by removing the last peak in the waveform, which corresponds to the ground portion of the return signal. This method is comparable to that described by Means et al. (1999), although nothing was done to compensate for any difference in reflectance for the ground versus the canopy. Because the ground returns for this data set were relatively strong, this method of obtaining the canopy portion of the return was considered robust. The canopy return of the normalized waveform was then compared to the GORT output and a crown volume profile constructed from the field data.

The field data were used to calculate parameters to initialize the GORT model. The model requires the following tree geometry parameters: upper crown center height boundary (h2), lower crown center height (h1), average crown radius (R), and crown depth/crown radius ratio (e) and crown count density (ë). Values for these tree geometry parameters are provided for one example plot in Table 1. The tree geometry parameters and their derivation are described in Ni-Meister et al. (in press). Foliage area volume density (favd) was derived from the LAI data. The favd was calculated through the following equation:

$$favd * 4/3 * ë * ð * R^2 * b = LAI, \qquad (1)$$

where b is vertical crown radius (all variables were obtained for each plot from the field data).

Table 1: Input tree geometry parameters for the GORT model for a single plot in the study area

ë	h1	h2	R	e	favd
0.13	4.36 m	27.15 m	1.89 m	2.47	0.3

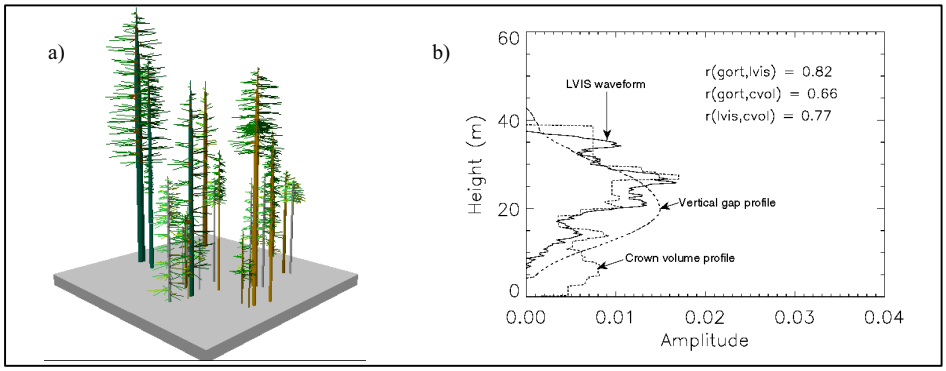

Figure 1. a) Profile view of a sample plot in the study area. The tree geometry parameters for the GORT model are given in Table 1. (This image was created with the Stand Visualization System developed by the U.S. Forest Service.) b) The lidar canopy return for this same plot is shown along with the GORT-generated vertical gap profile and the vertical crown volume profile. (All profiles normalized). The correlation coefficients are shown in the top right corner.

All the input parameters for the GORT model were calculated from the field data for each individual plot. The model was run separately for each plot. Each model run produced between-crown and within-crown gap probabilities for each height interval (set at 30 cm to correspond with the vertical resolution of LVIS) in the canopy. Total gap probability was calculated by adding between-canopy and within-canopy gap probabilities. A vertical profile of total gap probability was constructed by calculating total gap probability as a function of height. The normalized vertical profile was compared to the normalized LVIS canopy waveform for each plot.

Crown volume profiles were also calculated from the field data. Crown cross-sectional area was calculated at 30 cm height intervals for the entire canopy down to the ground. The individual crowns were assumed to be cylindrical in shape, however partial crown height, full crown height and partial crown wedge measurements were used to adjust for cases in which the crown cross-sectional area would not be adequately modeled as a circular disk. In this way the crown volume profile adjusted for anomalies in crown shape. The normalized crown volume profiles were also compared to the normalized GORT gap probability profile and the normalized lidar canopy waveform.

4 RESULTS

The similarities between the LVIS waveform, vertical profile of gap probability and crown volume profile for each plot were assessed by calculating correlation coefficients (Pearson's r) between these different profiles (Figure 1). Histograms showing the distribution of correlation coefficients for all the plots are shown in Figure 2. The mean values of the correlation coefficients were 0.61, 0.54, and 0.67 for the LVIS waveform/vertical gap profile, LVIS waveform/crown volume profile and vertical gap profile/crown volume profile pairs respectively. The best overall correlation was between the crown volume profiles and the gap probability profiles.

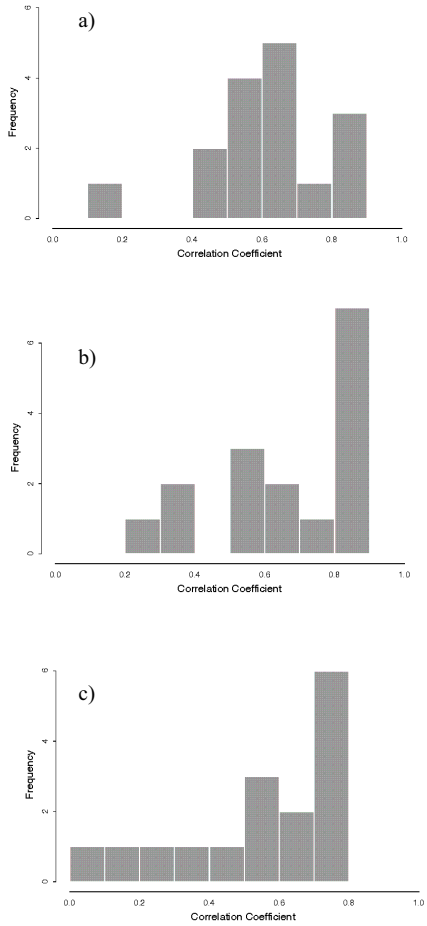

Figure 2. Histograms showing the distribution of the correlation coefficients for the LVIS waveform/vertical gap profile (a), vertical gap profile/crown volume profile (b) and the LVIS waveform/crown volume profile (c) relationships.

5 DISCUSSION AND CONCLUSION

The results show that GORT was able to model the LVIS waveforms for the Sierra Nevada field sties. This model validation demonstrates that GORT was able to characterize lidar waveforms using a few tree geometry parameters and the spectral properties of the canopy leaves as derived from LAI measurements in the field. The current tree geometry calculations are based on observations that are characteristic of the boreal forest in central Canada rather than the forests of the Sierra Nevada. Revisions to the equations used to derive the tree geometry for the plots in this study could improve the relationship between the vertical gap profiles, LVIS waveforms and the crown volume profiles. These results are also based on a relatively small sample size. Once further data are included in the study the overall results may improve.

In general, the lidar waveforms tend to show a concentration of material near the top of the canopy, whereas the vertical gap profiles indicate a more evenly spread out canopy (Figure 2). This discrepancy should be examined in greater detail. There are two approaches to this: 1. The GORT model should be rerun several times for each plot using different input parameters to test the sensitivity of the shape of the gap profile to factors that influence tree geometry (e.g. presence or absence of a layer of dominant and co-dominant trees or tree species). 2. Previous research has shown that upper layers in the canopy may obscure lower layers, thereby reducing the amount of energy reflected back by the lower portions of the canopy and resulting in erroneously weak lower canopy returns (Means et al. 1999; Lefsky et al. 1999). Methods to address for this have been developed (Means et al. 1999; Lefsky et al. 1999) and should be applied to the lidar waveforms in this study to see if this would improve the correlation between them and vertical gap profiles. This may then lead to the development of a 'correction factor' that could be applied to the vertical gap profile to create more realistic waveforms. Establishing whether or not these approaches improve the relationship between the lidar waveforms and the vertical gap profiles will greatly aid in the understanding of how the energy interacts with the elements of a natural vegetation canopy. The

comparisons of the vertical gap profiles and lidar waveforms to the crown volume profiles can also aid in determining which elements of the canopy influence their shape. These comparisons also demonstrate that traditional canopy volume profiles may not adequately capture the heterogeneity of natural canopies in terms of the vertical distribution of reflecting surfaces in the canopy and light penetration.

The results of this study will help develop a better understanding of the interactions between the energy of a lidar laser beam and the forest canopy. By modeling lidar waveforms based on the physical principles of radiative transfer, GORT fills a missing link between the remotely sensed and actual canopy structure. The results of this study will also aid in future large-scale land surface mapping by developing a link between lidar and other remote sensing data. If lidar waveforms can be modeled from field data or other remote sensing data then it will be possible to derive a better three-dimensional picture of the structure of the Earth's vegetated surface, even in areas that have not been mapped by a lidar instrument.

ACKNOWLEDGEMENTS

The authors wish to thank Carolyn Hunsaker and Wayne Walker for organizing and leading the collection of the field data in the Sierra National Forest. They also thank Nancy Casey-McCabe, David Rabine and David Kendig for their work collecting and processing the LVIS data.

REFERENCES

Blair, J.B., Coyle, D.B., Bufton, J., and Harding, D., 1994. Optimization of an airborne laser altimeter for remote sensing of vegetation and tree canopies. *IEEE International Geoscience and Remote Sensing Symposium*, 2:939-941.

Blair, J.B., Rabine, D.L., and Hofton, M.A., 1999. The Laser Vegetation Imaging Sensor (LVIS): A medium-altitude, digitization-only, airborne laser altimeter for mapping vegetation and topography. *ISPRS Journal of Photogrammetry and Remote Sensing*, 54:115-122.

Danson, F.M., and Curran, P.J., 1993. Factors affecting the remotely sensed resonse of coniferous forest plantations. *Remote Sensing of Environment*, 43:55-65.

Drake, J.B., Dubayah, R.O., Clark, D., Knox, R.G., Blair, J.B., Hofton, M., Chazdon, R.L., Weishampel, J.F., and Prince, S., in press. Estimation of tropical forest structural characteristics using large-footprint lidar. *Remote Sensing of Environment*.

Hyyppä, J., Hyyppä, H., Inkinen, M., Engdahl, M., Linko, S., and Zhu Y-H., 2000. Accuracy comparison of various remote sensing data sources in the retrieval of forest stand attributes. *Forest ecology and Management*, 128:109-120.

Lefsky, M.A., Harding, D., Cohen, W.B., Parker, G., and Shugart, G.G., 1999. Surface lidar remote sensing of basal areas and biomass in deciduous forests of eastern Maryland, USA. *Remote Sensing of Environment*, 67:83-98.

Li, X., Strahler, A.H., and Woodcock, C.E., 1995. A hybrid geometric optical-radiative transfer approach for modeling albedo and directional reflectance of discontinuous canopies. *IEEE Transactions of Geoscience and Remote Sensing*, 33:466-480.

Means, J.E., Acker, S.A., Harding, D.J., Blair, J.B., Lefsky, M.A., Cohen, W.B., Harmon, M.E., and McKee, W.A., 1999. Use of large-footprint scanning airborne lidar to estimate forest stand characteristics in the western Cascades of Oregon. *Remote Sensing of Environment*, 67:298-308.

Ni-Meister, W., Jupp, D.L.B., and Dubayah, R., in press. Validation of the GORT model for lidar waveforms in discrete and discontinuous plant canopies. *IEEE Transactions of Geoscience and Remote Sensing*.

Parker, G.G., Smith, A.P. and Hogan, K.P., 1992. Access to the upper forest canopy with a large tower crane. *BioScience*, 42:664-670.

Peterson, B., 2000. Recovery of forest canopy heights using large-footprint lidar. M.A. Thesis, University of Maryland at College Park.

Van Pelt, R. and North, M., 1996. Analyzing canopy structure in Pacific Northwest old-growth forests with a stand-scale crown model. *Northwest Science*, 70:15-30.

Weishampel, J.F., Ranson, K.J., and Harding, D.J., 1996. Remote sensing of forest canopies. *Selbyana*, 17:6-14.

Yang, X., Witcosky, J.J., and Miller D.R., 1999. Vertical overstory canopy architecture of temperate deciduous hardwood forests in the eastern United States. *Forest Science*, 43:349-358.

EVALUATION OF GEOSCIENCE LASER ALTIMETER SYSTEM (GLAS) WAVEFORMS FOR VEGETATED LANDSCAPES USING AIRBORNE LASER ALTIMETER SCANNING DATA

Claudia C. Carabajal[1] and David J. Harding[2]
[1]NVI, Inc. @ NASA/Goddard Space Flight Center, Space Geodesy Branch – Code 926
Greenbelt, MD 20771, U.S.A.
claudia@stokes.gsfc.nasa.gov
[2]NASA/Goddard Space Flight Center, Geodynamics Branch – Code 921
Greenbelt, MD 20771, U.S.A.
harding@core2.gsfc.nasa.gov

Commission III, Working Group 3

KEY WORDS: LIDAR, laser altimetry, laser waveform analysis, waveform simulations, topography, vegetation

ABSTRACT

The Geoscience Laser Altimeter System aboard NASA's Ice, Cloud and land Elevation Satellite will record the height distribution of laser energy reflected from surfaces within 70 m diameter footprints. For land surfaces, post-processing of this waveform data will be used to estimate the within-footprint mean elevation and surface relief due to ground slope and roughness, vegetation cover, buildings and other structures. A methodology is described for validating the derived surface properties for vegetated and urbanized landscapes using a GLAS waveform simulator applied to high-resolution, airborne, scanning laser altimeter data being acquired by the Puget Sound Lidar Consortium (PSLC) in northwestern Washington state. The GLAS waveform simulator is being modified to operate on 3-dimensional representations of topography and vegetation cover with the incorporation of digital elevation models derived from the airborne laser data and representations of the spatial distribution of surface reflectance, the transmitted laser energy measured on a per-pulse basis by the GLAS instrument, and detector's field-of-view responsivity. The attributes of the PSLC airborne laser mapping data are also described.

1 INTRODUCTION

The Geoscience Laser Altimeter System (GLAS) is a NASA Earth Observing System facility instrument planned for launch in the summer of 2002 aboard the Ice, Cloud and land Elevation Satellite (ICESat). The ICESat mission will measure polar ice-sheet topography and temporal changes in topography, cloud heights, planetary boundary heights, aerosol vertical structure, and land and water topography. GLAS will operate continuously in a 600 km, 94 degree inclination orbit, acquiring globally distributed elevation profiles consisting of 70 m diameter laser footprints spaced every 175 m along the profile. Precise pointing control of the ICESat spacecraft will enable specific ground tracks to be profiled repeatedly with a cross-track location accuracy of 30 m (1 sigma). Geolocation processing will yield footprint position and elevation accurate to 5 m and 13 cm, respectively (1 sigma for flat surfaces). A waveform recording laser backscatter energy as a function of time will be digitized for each footprint with a vertical sampling of 15 cm. The waveform, a measure of the height distribution of laser-illuminated surfaces, will be used to quantify within-footprint relief (i.e. vertical structure) due to surface roughness, slope, vegetation cover, and man-made features.

Laser profile and waveform matching to a Puget Sound airborne lidar data set has been proposed to validate ICESat footprint products [Schutz et al., 2000]. Comparison of laser altimetry profile geolocation results to topographic profiles derived from accurate digital elevation models (DEMs) has shown to be useful in assessing the absolute accuracy and systematic errors of the laser footprint position [Rowlands et al., 2000; Luthcke et al., 2001]. An additional geolocation comparison can be done based on matching synthetic waveforms produced from DEMs of high-resolution and accuracy to the backscatter energy digitized by the laser instrument at the footprint location [Blair and Hofton, 1999]. Waveform-to-DEM matching can also be used to validate parameters related to the quality of the laser beam, such as pulse width, footprint diameter and circularity. In addition, quantities derived from the footprint, like mean elevation, slope, roughness and vegetation height, can be validated. Well characterized DEMs of very high accuracy and spatial resolution covering large areas with significant relief, varying on short spatial scales, are the best suited for profile and waveform matching purposes. The Puget Sound data set possesses these characteristics.

Simulated laser waveforms can be made using the technique first described by Blair and Hofton (1999). They used a 33 cm horizontal spacing, 10 cm vertical accuracy DEM of dense, tropical rainforest in Costa Rica derived from a FLI-MAP helicopter-based, high-resolution laser altimeter survey to construct simulated waveforms that were then compared to waveforms for 25 m diameter laser footprints acquired by the Laser Vegetation Imaging Sensor (LVIS). Maximizing a Pearson correlation coefficient for all waveforms was used to estimate goodness of the agreement. Shifts in the horizontal and vertical direction, pulse width and footprint diameter variations yielded well defined correlations, which showed 0.01 m precision for the vertical shift and pulse width variation, and 0.1 m precision for the east, west and diameter parameters.

Because the waveforms to be provided by ICESat will cover approximately 8 times the area of an LVIS footprint, they will typically have a smoother distribution of surface elevations with fewer well-defined waveform peaks, and thus will likely yield less precision when matched to high-resolution DEMs. None-the-less, waveform to DEM matching should provide a useful evaluation of ICESat geolocation, laser beam quality, and derived surface properties. Simulated waveforms will also be used to

evaluate the GLAS on-board acquisition algorithm prior to launch and during mission operations.

Here we describe a methodology for validating ICESat products using a GLAS simulator to generate synthetic waveforms from high-resolution DEMs. The GLAS simulator incorporates a representation of terrain elevation and reflectivity and models all the components of the instrument including transmitter characteristics and detector and digitizer responses. We describe the original simulator version and some of its applications, modifications that have been implemented to date, and future plans that will make this tool evolve into a more useful estimator of the instrument and processing algorithms performance. The characteristics of the Puget Sound data set will also be presented, as it will serve as the primary data set to be used for ICESat calibration and validation of products generated for vegetated and urbanized terrains.

2 THE GLAS WAVEFORM SIMULATOR

The GLAS simulator was developed as a first-generation tool to explore the relationship between the altimeter design, performance, and terrain characteristics [Abshire et al., 1994]. The original version of the simulator calculates the performance of the altimeter in a simplified two-dimensional measurement geometry (elevation vs. along track distance). The simulator includes the entire optical laser path and detector propagation paths, also calculating an estimate of the receiver's noise. The optical intensity waveform of the laser altimeter is calculated as it propagates to and from the terrain surface and, through the altimeter's receiver after detection of the laser energy. The transmit signal has a specified energy, duration (pulse width), angular width (beam divergence) and angular pointing offset from Nadir.

As designed originally, time is quantized in 100 psec bins (1.5 cm in range), and the transmit beam's intensity and far-field pattern are assumed to be Gaussian. The laser's optical wavefront is approximated by a finite number of rays distributed in the along-track angle, calculating the range delay and intensity for each one. The interaction with the terrain surface is calculated by projecting the beam in the along-track direction, ignoring any cross-track terrain height variations. Instrument parameters such as the transmitter's wavelength, divergence angle, and tilt angle of the altimeter can be specified. It assumes the terrain encountered by the laser beam is a diffuse reflector, and the height and reflectivity can be specified for every point along track. The receiver model includes a telescope, an optical band-pass filter, with the option to use either a photomultiplier or an avalanche photodiode optical detector, a low-pass filter, a timing discriminator, a time interval unit and a digitizer. The signal collected at the receiver is calculated based on 3-D diffuse scattering and a 3-D receiver telescope, and includes solar illumination effects. For every shot, it independently calculates the receiver waveform by adding the signal with the appropriate delays and the background light. The noise-only portion of the received waveform is used to calculate the threshold detector for the receiver. The received waveform is low-pass filtered to account for detector bandwidth, producing a smoothed version of the input waveform, and the simulated digitizer response is then calculated. The digitizer's sampling rate, number of bits and voltage scaling can be specified. A coarse estimate of the range is calculated from the time between the laser fire and the first threshold crossing. Fine range corrections can be calculated from the digitized waveform using different estimators (50% rise-time, midpoint, center of area, mean and peak of the received waveform). An estimate of the received energy can be inferred from its proportionality to the pulse area. Atmospheric refraction effects are not included in the calculations.

Csathó and Thomas [1995; 1997] have developed an algorithm to determine sea ice roughness from altimeter waveforms, based on the knowledge of sea ice properties (reflectance, surface roughness). They used the 2-D simulator to evaluate estimates of surface roughness from waveforms generated for a set of sea ice models and profiles acquired by airborne laser altimeter surveys. Spectral albedos observed under different conditions were used in creating realistic sea ice surface models. For horizontal surfaces with Lambertian reflectance, the RMS surface roughness (standard deviation of elevations within the footprint) is estimated from the mean-square width of the received pulse [Gardner, 1982]. Equivalent horizontal, Lambertian, random rough surfaces producing the same RMS laser pulse width can be defined. Decoupling surface roughness from slopping terrain effects on the waveforms represents a problem, and equivalent roughness estimates are obtained for different models indicating that further studies are needed to understand the influence of the various factors in the accuracy of the determination. These factors include the scale at which roughness contributes to pulse spreading, and the need for a more accurate description of elevation changes within the footprint.

Yi and Bentley [1999] studied the relationship between surface topography and laser waveforms using theoretical 3-D surface topographies and a Gaussian beam pattern and pulse shape to simulate waveforms. A non-linear least square minimization scheme was used to compare the derived surface roughness and slope parameters derived from the generated waveforms to the ones derived from various theoretical models. Their study illustrated the difficulties in de-coupling the slope and roughness effects, even when theoretical models are used. In addition, atmospheric forward scattering effects (which depend on cloud height, optical depth, cloud particle size and shape, and receiver field of view) can be a significant source of error in the elevation estimates, as well as in the slope and roughness estimates derived from waveform pulse widths [Duda et al., 2000; Mahesh et al., 2001].

To model the expected GLAS response to the intercepted surfaces in vegetated and urbanized sites, the current version of the GLAS waveform simulator is being modified to input 3-D terrain surfaces, incorporating the ingestion of DEM and surface reflectance surfaces gridded at 1 m resolution. Furthermore, instrument characteristics that convolve with the terrain properties are being incorporated in the modified simulator. These include a non-Gaussian laser spatial energy distribution, which for GLAS will be measured on a shot-by-shot basis by the instrument's Laser Profiling Array (LPA) which records a two-dimensional image of the transmit laser energy. In addition, the detector's responsivity across the field-of-view will be simulated to assess potential boresight misalignment between the transmit beam and detector. Surface elevation, reflectance, transmit beam spatial energy, and detector sensitivity all are input into the simulation as gridded, spatially varying parameters. No immediate inclusion of atmospheric effects is planned, but it would clearly be useful to use the simulator to re-create the effects of multiple scattering under various conditions.

3 THE PUGET SOUND DATA SET

Airborne LIDAR mapping in the Puget Sound region, is now being conducted by the Puget Sound Lidar Consortium (PSLC) [Harding and Berhoff, 2000]. The PSLC is an association of local government agencies, the United States Geological Survey, and NASA, which has contracted with Terrapoint, LLC to acquire and process multi-return laser altimeter data, yielding 'bald Earth' and 'canopy top' Digital Elevation Models (DEM) gridded at 6 ft resolution. To date 4,000 km^2 of the Puget

Lowland region has been mapped during leaf-off conditions. The data is being collected for a variety of purposes, including topographic mapping, identification of landforms related to active faults, hydrologic modeling, flood plain assessment, and urban planning. For the nominal flight conditions at 920 m altitude and 150 knots ground speed, a 600 m wide swath results in 0.9 m diameter footprints spaced 1.5 m along- and across-track. The Terrapoint ALTMS laser transmitter operates at 20 KHz and 1064 nm, with an 8 ns FWHM (full width at half maximum) pulse. The ±18° scan mirror operates at 50 Hz. About thirty percent of the laser swath is illuminated by the footprints, and up to 4 returns from vertically separated surfaces (with a minimum separation of 1.4 m) are collected per laser pulse. Using 50% overlap between adjacent swaths, the footprint density is doubled and all areas are imaged at two scan angles, providing multi-return laser data with dense sampling and very high spatial resolution.

The region being mapped includes a diverse assemblage of land cover types, including forests, agricultural pastures and fields, and suburban and urban communities [Harding and Berghoff, 2000]. The expected character of GLAS waveforms for a diverse set of vegetation cover and ground slope conditions will be illustrated in order to assess retrieval of ground elevation, vegetation height, and canopy structure. Point clouds of individual, geolocated laser returns acquired by Terrapoint are aggregated over 70 m diameter footprints, into height distributions that approximate the within-footprint relief to be detected by GLAS waveforms. The Terrapoint 1.5 m laser shot spacing within a swath nominally yields 1,700 laser shots per height distribution. Comparisons of height distributions obtained from the two overlapping swaths demonstrate good reproducibility of the height distributions.

The point cloud of all laser returns is classified into returns thought to be from vegetation and from ground by means of a Virtual Deforestation (VDF) filter discussed in Haugerud and Harding [2001, this volume]. A 'bald Earth' DEM gridded at 6 ft resolution is then constructed from those returns classified as ground. The accuracy of the 'bald Earth' DEM has been established by comparison to ground control points established by Global Position System (GPS) surveying in five land cover classes (three non-forested: bare, tall grass, and urban; two forested: coniferous and deciduous). The mean and RMS difference of the Ground Control Point (GCP) elevations with respect to the DEM interpolated to the GCP locations for a total of 36 sites is –2.3 cm and 17.4 cm, respectively. As expected, the results for 23 non-forest sites (0.6 and 10.6 cm) are better than for 13 forested sites (-7.5 and 25.3 cm) where in several cases the derived DEM is above the actual ground surface due to the presence of dense understory vegetation. A histogram of GCP elevation differences is shown in Figure 1.

For input into the GLAS waveform simulator, a DEM gridded at 1 m is constructed by nearest-neighbor resampling of the complete all-return Terrapoint point cloud. Nearest neighbor resampling is used to preserve the original data's height distribution, rather than introducing heights not actually present as is caused by interpolation schemes. The type (ground versus not-ground) of each 1 m DEM cell is identified based on the VDF classification of the nearest-neighbor return, so that the elevation of the ground surface in the simulated GLAS waveform can be tracked.

In order to use the Puget Sound data as a basis for modeling GLAS waveforms, it is assumed that the surface is uniformly sampled spatially and that individual returns represent illuminated surfaces of equivalent area. Although the former assumption is well justified by the laser shot density and distribution, the latter is not well established. The Terrapoint ALTMS system uses a constant-fraction discriminator threshold detection scheme to identify multiple returns. The sensitivity of detection may not be equal for each return in a sequence of multiple returns. Furthermore, for a complete simulation, the spatial variation of surface reflectance must be minimal or independently known, because the simulated return intensity depends on the reflectance of the surface elements. Use of high-resolution, multi- and hyper-spectral imaging data is being considered as a source for the necessary reflectance information.

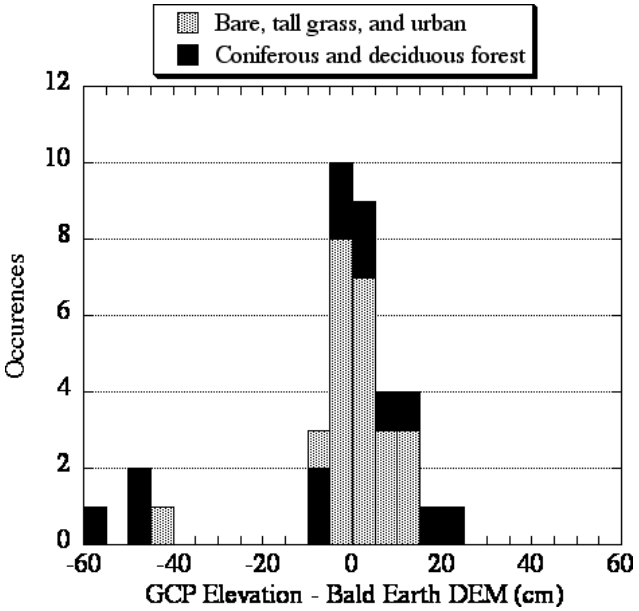

Figure 1. Elevation difference between 36 GCPs established by GPS surveying and the Puget Sound 'bald Earth' DEM, gridded at 6 ft resolution and then projected to the GCP location using bilinear interpolation.

4 PRODUCTS TO BE VALIDATED

The products to be validated by profile and waveform matching are the x and y horizontal geolocation of ICESat footprints, and the land parameters derived from the waveform. The latter are parameters like the mean, minimum, and maximum elevation, slope, roughness, vegetation height, and Gaussian fits to the multiple within-footprint surfaces [Brenner et al., 2000]. Because the Terrapoint data is classified as returns from ground and non-ground surfaces, using these data will enable the assessment of which peaks in the GLAS waveforms correspond to the actual ground surface as a function of vegetation cover and slope conditions. This measurement in turn allows for validation of GLAS derived vegetation height measurements, since it greatly depends on the correct identification of the ground return in the waveform. The transmit beam quality can also be validated, including the FWHM (full width at half maximum) of the pulse, and the diameter and circularity of the footprint energy distribution.

The steps to accomplish this validation will consist of first matching GLAS elevation profiles to the Puget Sound DEM to test the geolocation accuracy of the laser footprints [Rowlands et al., 2000; Luthcke et al., 2001]. Second, observed GLAS waveforms will be matched to synthetic waveforms created using

the GLAS simulator applied to the Puget Sound laser point cloud data to refine the geolocation test. Having established the best footprint geolocation, the surface parameters derived from the observed waveforms via the GLAS processing procedures will be evaluated with respect to the known surface properties defined by the Puget Sound high-resolution data.

The diversity of land cover types, and the relief complexity at GLAS footprint scales introduced by local variations in building and tree heights, provides an ideal opportunity to use the well characterized Puget Sound data set for waveform matching purposes along ICESat tracks.

REFERENCES

Abshire, J. B., J. F. McGarry, L.K. Pacini, J. B. Blair, and G. C. Elman, 1994. *Laser Altimetry Simulator, Version 3.0 User's Guide,* NASA Technical Memorandum 104588, NASA/GSFC, Greenbelt, MD, 70p.

Blair, J. B. and M. A. Hofton, 1999. Modeling Laser Altimeter Return Waveforms Over Complex Vegetation using High-Resolution Elevation Data, Geophysical Research Letters, Vol. 26, No. 16, pp. 2509-2512.

Brenner, A. C., H. J. Zwally, C. R. Bentley, B. M. Csathó, D. H. Harding, M. A. Hofton, J. B. Minster, L. A. Roberts, J. L. Saba, R. H. Thomas and D. Yi, 2000. Derivation of Range and Range Distributions From Laser Pulse Waveform Analysis for Surface Elevations, Roughness, Slope, and Vegetation Heights, *Geoscience Laser Altimeter System (GLAS) Algorithm Theoretical Basis Document*, Version 3.0, 93p.

Csathó, B. and R. H. Thomas, 1995. Determination of Sea Ice Surface Roughness from Laser Altimetry Waveform, *Byrd Polar Research Center Technical Report Number 95-03*, The Ohio State University, Columbus, Ohio, 44p.

Csathó, B. and R. H. Thomas, 1997. Geoscience Laser Altimeter System: Surface Roughness of Sea Ice, *Geoscience Laser Altimeter System (GLAS) Algorithm Theoretical Basis Document*, Version 0.2, 16p.

Duda, D. P., J. D. Spinhirne and E. W. Eloranta, 2000. Atmospheric Scattering Effects on GLAS Altimetry. Part I: Calculations of Single Pulse Bias, IEEE Trans. Geoscience and Remote Sensing, Vol. 39, pp. 92-101.

Gardner, C. S. 1982. Target Signatures for Laser Altimeters: An Analysis, Applied Optics, Vol. 21, No. 3, pp. 448-453.

Harding, D. J and G. S. Berghoff, 2000. Fault Scarp Detection Beneath Dense Vegetation Cover: Airborne LIDAR Mapping of the Seattle Fault Zone, Bainbridge Island, Washington State, Proceedings of the American Society of Photogrametry and Remote Sensing, Washington, D.C., May, 2000, 9p., also available at http://pugetsoundlidar.org.

Haugerud, R. A. and D. J. Harding, 2001. Some Algorithms for Virtual Deforestation (VDF) of Lidar Topographic Survey Data, International Archives of Photogrametry and Remote Sensing, this volume.

Luthcke, S. B., C. C. Carabajal and D. D. Rowlands, 2001. Enhanced Geolocation of Spaceborne Laser Altimeter Surface Returns: Parameter Calibration from the Simultaneous Reduction of Altimeter Range and Navigation Tracking Data, submitted to the Journal of Geodynamics Special Issue on Laser Altimetry, 32p.

Mahesh, A., J. D. Spinhirne, D. P. Duda, and E. W. Eloranta, 2001. Atmospheric Multiple Scattering Effects on GLAS Altimetry Part II: Analysis of Expected Errors in Antarctic Altitude Measurements, submitted to IEEE Trans. Geoscience and Remote Sensing.

Rowlands, D. D., C. C. Carabajal, S. B. Luthcke, D. J. Harding, J. M. Sauber, and J. L. Bufton, 2000. Satellite Laser Altimetry: On-Orbit Calibration Techniques for Precise Geolocation, The Review of Laser Engineering, Vol. 28, No. 12, pp. 796-803.

Schutz, R. E. et al., 2000. *GLAS Altimeter Post-Launch Calibration/Validation Plan*, Version 0.99, Section 6.7.7, pp. 58-61.

Yi, Donghui and C. R. Bentley, 1999. Geoscience Laser Altimeter System Waveform Simulation and its Applications, Annals of Glaciology, Vol. 29, pp. 279-285.

LAND SURFACE MAPPING AND CHARACTERIZATION USING LASER ALTIMETRY

SESSION 6

FORESTRY APPLICATIONS

MEASURING FOREST CANOPY HEIGHT USING A COMBINATION OF LIDAR AND AERIAL PHOTOGRAPHY DATA

Benoît A. St-Onge and Nora Achaichia
Department of Geography
Université du Québec à Montréal
Canada
st-onge.benoit@uqam.ca

Commission III, Working Group 3

KEY WORDS: lidar, photogrammetry, forest, aerial photography, canopy, height.

ABSTRACT

It has been demonstrated that the height of forest canopies can be measured with a good accuracy using small footprint lidars. This is essentially accomplished by subtracting the last return altitude (ground) from the corresponding first return altitude (canopy surface). The technique is considered superior to photogrammetric methods mainly because the ground level, which is difficult to see on aerial photos of densely forested areas, can be well identified using small footprint lidars. However, lidar cannot be used to characterized past forest states, while these can be assessed, and photogrammetically measured, in the wealth of historical aerial photographs most developed countries possess. Our goal is to replace the first return lidar data by altitude models derived from aerial photos in order to map forest canopy height changes of the past decades. This paper presents the first methodological steps which consist in comparing canopy heights obtained from lidar data only to a combination of lidar and photogrammetry data. The lidar data was acquired over an area of the boreal forest in Quebec, Canada, in 1998, using Optech's ALTM1020 flying at an altitude of 700 m. Two stereo-pairs of aerial black and white photographs were used: 1) a pair of 1:15,000 photos taken in 1994, and 2) a pair of 1:40,000 photos taken in 1998. A lidar canopy height model (CHM) was created by subtracting ground altitudes from canopy altitudes. Aerial photo altitude models were derived using the image correlation methods of Virtuozo 3.2 software. The ground level altitudinal fit between the aerial photo altitude model and the lidar data was checked on rock outcrops. A photo CHM was created by subtracting the lidar ground altitude model from the aerial photo altitude model. The photo CHM and the lidar CHM show a good degree of correlation.

RÉSUMÉ

Il a été démontré que la hauteur des couverts forestiers peut être mesurée avec une bonne exactitude à l'aide de lidars à petite empreinte. Ceci s'effectue en soustrayant l'altitude des derniers retours (sol nu) des altitudes correspondantes du premier retour (surface du couvert). La technique est considérée comme étant supérieure aux méthodes photogrammétriques en ce qu'elle permet d'identifier correctement le niveau du sol nu alors que ce dernier est rarement visible sur les photos aériennes de zones de forêts fermées. Toutefois, le lidar ne peut être utilisé pour caractériser des états forestiers antérieurs alors que ces derniers peuvent être observés et mesurés photogrammétriquement à partir des nombreuses photos aériennes historiques que possèdent la plupart des pays développés. Notre but est de remplacer les premiers retours du lidar par des modèles d'altitude dérivés de photos aériennes de manière à cartographier l'évolution de la hauteur des couverts forestiers des dernières décennies. Cet article présente les premières étapes méthodologiques qui consistent en une comparaison des hauteurs de couvert dérivées des données lidar de celles produites par la combinaison des données lidar et photographiques. Les données lidar d'une zone de forêt boréale du Québec, Canada, ont été acquises en 1998 à l'aide du capteur ALTM1020 de la compagnie Optech à partir d'une altitude de 700 m. Deux couples stéréo de photo aériennes noir et blanc ont été employées : 1) une paire de photos au 1 :15,000 acquises en 1994 et 2) une paire de photos au 1 :40,000 acquises en 1998. Un modèle lidar de hauteur du couvert (MHC) a été créé en soustrayant les altitudes du sol nu de celles de la végétation. Des modèles d'altitude ont été dérivés des photos en ayant recours à des méthodes de corrélation d'images du logiciel Virtuozo 3.2. L'ajustement altitudinal du niveau sol nu entre les modèles altimétriques photographiques et lidar a été vérifié sur des affleurements rocheux. Un MHC photo a été créé en soustrayant le modèle d'altitude lidar du sol nu du modèle d'altitude de la végétation dérivé des photos. Les corrélations entre les CHM photo et le CHM lidar montrent un bon degré de corrélation.

1 INTRODUCTION

Problem statement

Forest management relies on accurate and up to date spatial information on forest structural characteristics: height, density, timber volume, etc. It is widely recognized that obtaining this information through ground measurements is time consuming and costly. Aerial photo interpretation and photogrammetry have for this reason been widely used. Because the cost of interpreting aerial photos is also high, alternative remote sensing methods were sought. Despite decades of efforts involving the development of new sensors and processing methods, monoscopic remote sensing exploiting the spectral features of images did not succeed in providing reliable measurements of three dimensional forest characteristics at the stand level scale. Tree height in particular is difficult to evaluate from monoscopic vertical images of the forest. Recent progress in three dimensional remote sensing include mainly digital stereophotogrammetry, radar interferometry, and lidar. Sensors producing three dimensional data theoretically provide a better assessment of structural aspects of forests than do monoscopic sensors, an hypothesis that was verified on

different occasions (see Hyyppä et al., 2000, and Lefsky et al., 2001 for a comparison).

Digital stereophotogrammetry and radar interferometry can provide maps of the altitude of the canopy surface but usually not accurate canopy height, especially in dense forest environments where the bare earth level remains invisible. It has indeed been know for a long time that "seeing" this level at locations close to a tree is necessary if the height of that tree, i.e. the altitude difference between its top and base, is to be measured (Spurr, 1960; Howard, 1970). Possible confusion of the ground level with the surface of close-by low vegetation can also make height measurements unreliable. Small footprint lidar provides canopy altitude and heights, the latter being the altitude difference between the top of canopy altitude and the bare earth altitude. The very small divergence of laser impulses indeed allow the coherent energy to penetrate dense canopies from place to place. However, lidar surveys are still expensive due to the high number of flight lines needed to cover a given area (due to the lidar narrow swath width), such that forest companies are reluctant to pay for such surveys for large areas, mostly because the huge costs involved will have to be invested at a regular multi-year interval. Also, efficient scanning lidars being fairly recent, the record of past lidar databases is extremely tenuous. Historical monitoring of past forest states using lidar is clearly impossible.

Objectives

To produce the canopy surface and bare earth altitude dual layers from which one can obtain canopy height by simple subtraction, we here investigate the replacement of lidar-produced canopy altitudes by the stereoscopic surface reconstruction from scanned aerial photos. We thus evaluate the potential of combining lidar and digital photogrammetry as a mapping tool of forest structural characteristics, and investigate the effect of air photo scale by testing 1:15,000 and 1:40,000 scales. This relies on the assumption that the ground topography remains essentially unchanged over decades. This study is also a first step to map out the processing steps needed to achieve good results and identify needed improvements before historical studies can be carried out.

2 STUDY AREA

Data and methods have been developed and tested for the *Training and Research Forest of Lake Duparquet* (TRFLD), located in western Quebec, Canada (approx. 48°30' N, 79°22' W). This 80 square km territory is covered by softwood, hardwood and mixed stands typical of the balsam fir-white birch domain of the Canadian Shield. The study area is populated by mature to over mature dense stands, some of which show openings that originated from an spruce budworm outbreak (*Choristoneura fumiferana* [Clem.]), a coniferous defoliator that mostly affects balsam fir, that occurred in the 1980s. The topography is characterized by gentle hills with occasional steeper drops. The altitudes inside the study perimeter vary from 228 m to 335 m above sea level.

3 DATA

Lidar

The lidar survey was carried out on June 28th 1998 using Optech's ALTM 1020 instrument on a Piper Navajo plane flown at 700 m by LaserMap Image Plus. To obtain the desired hit density, two passes were carried out for the first return (canopy) and one for the last return (bare earth). Flight and lidar characteristics are presented in Table 1. Vegetation/ground separation was carried out by the survey provider using Optech's REALM software. No subsequent filtering was done. The average distance between two consequent hits was of 1 m for vegetation, and 3.0 m for the ground. The accuracy is of approximately 20 cm for the altitude values, and of 70 cm for the X,Y values.

Aerial photos

Two stereo-pairs of aerial photos were used in this study. The first was acquired at the scale of 1:15,000 on July 11th 1994 at an above sea level (ASL) altitude of 2600 m. The second was captured at a scale of 1:40,000 on May 8th 1998, i.e. less than two months before the lidar dataset, at altitude of 6400 m ASL. Unfortunately, hardwoods are barely starting to grow leaves at that date produce, which does not provide the best conditions for crown surface reconstruction by image matching. It also important to note that because the study perimeter is close to the 1:15,000 edge, i.e. far from the principal point, tree leaning is quite pronounced. Table 2 presents the detailed characteristics of the photos and figure 2 shows one photo of each pair. Both aerial coverage were produced by contract with the Province of Quebec Ministry of Natural Resources (MRNQ) by Hauts-Monts Inc. independently of this research project's purpose. The two pairs were scanned using a Epson 836XL scanner at a resolution of 1200 dpi. Combined with the two abovementioned photo scales, this yields ground pixel sizes of 0.3 and 0.85 m for 1994 and 1998 respectively. The choice between uniform scanning resolution (which is the case here) and uniform ground pixel size among the photo sets, both of which have advantages as the former "transfers" the original scale of the hardcopy photo to the softcopy while the latter produces a uniform ground pixel size, useful in a comparison, was settled on technical considerations. Optical distortions may indeed occur at resolution greater than 1200 dpi on the particular scanner we used. We hypothesized that the highest resolution allowing optically correct scans should give the best results possible at the image correlation stages on both datasets.

The aerial camera calibration reports were obtained from the MRNQ (see table 2 for details). Unfortunately, an ambiguity in the fiducial marks locations in the 1994 report could not be resolved in time for this study, so the values found in the 1998 report were used temporarily instead. The same aerial camera model had been flown on both years although different units were involved. The consequences of this are discussed in the results section.

Field data

The height of individual trees was measured on the ground using a standard clinometer method. Two measures were taken from different vantage points separated by at least 90 degrees to insure independence between the two measures. Trees for which the two height measures differed by more than 3 meters or by more than 15% were discarded so that errors in comparing lidar-derived heights to actual heights can mostly be attributed to the lidar. These two heights for all well measured trees were later used to assess the accuracy of ground measurements. The study focused on two species: Trembling Aspen (Populus tremuloides [Michx]) and White Spruce (Picea glauca [Moench], Voss.) but some other species were measured. After measurement error filtering, 36 trees remained (12 hardwoods and 24 softwoods). These trees were localized on the lidar dataset by using a combination of high precision GPS and visual analysis of the lidar image and low altitude photography.

4 METHODS

Processing of the lidar data

Generation of the canopy height model The lidar canopy height model (lidar CHM) was obtained by subtracting the interpolated ground-classified hits (lidar ground altitude model, or GAM) from the interpolated vegetation-classified altitudes (lidar canopy altitude model, or lidar CAM – see figure 2a). To create both surfaces, triangulated irregular network (TIN) interpolation of the X,Y,Z lidar hits was converted into a 50 cm pixel size grid.

Validation of lidar canopy heights The lidar CHM gives the interpolated height of all points in the canopy in the form of a regularly spaced grid with a 50 cm pixel size. The height of a tree was defined as the pixel having the highest value in a high-valued pixel cluster corresponding to a crown. This "top pixel" is normally situated near the center of the crown but can sometime be found a few pixels away from the center in the case of large hardwood trees. Linear regression was performed between ground-measured heights and lidar predicted heights (see St-Onge, 1999 for details). The mean of the two height measures done in the field for these trees was regressed against the corresponding height read from the CHM for the 36 trees. The linear model yielded a R^2 of 0.90 (significant at α=0.01). For this reason, we consider lidar derived heights as a surrogate for ground truth in the assessment of the accuracy of the digital stereophotogrammetry results.

Processing of the aerial photo data

Generation of the canopy altitude model The generation of the photo-derived canopy altitude model (photo CAM) was carried out using Virtuozo v. 3.2 from Supresoft. The hierarchical image correlation algorithms employ both statistical correlation and feature base matching to achieve the photo CAM. It is known that, while supervised tree height measurements made using softcopy photogrammetry packages are accurate, current commercial packages are not designed for precise automated crown shape reconstruction (Sheng et al., 2001). This problem lead these authors to develop a crown shape model-based reconstruction method. This method, while very successful in some conditions, is not currently operationally implemented.

The exact values from the camera calibration reports were input in Virtuozo. The relative orientation control points were produced by Virtuozo and were not modified by manual edits. Nine X,Y,Z control points coordinates were read on the lidar data on bare ground (rock outcrops, rocky shores, etc.) and associated with single pixels on the scanned photos. This theoretically constrains the stereo-photo model to fit with the lidar model. The points were spread out as evenly as possible over the studied sector (around the edges, and on the interior). The CAM was created with a 0.5 m pixel size and a 0.1 m Z precision and transferred from the Virtuozo format to a binary floating point number grid format for the further processing steps.

Generation of the aerial photo canopy height models The aerial photo CHM was generated by subtracting the lidar GAM from the photo CAM of each stereo-pair. The result shows the variations of canopy height on a 0.5 m pixel basis according to the surface reconstructed from the photos.

5 RESULTS AND DISCUSSION

General observations

The CHM created using only lidar, and a combination of the aerial photos and the ground altitude given by lidar are presented in figure 2 b-d (where brightness is proportional to height). We can see that the patterns determined by variation of tree height, crown size and density are very similar from one CHM to an other. It appears that the canopy surface altitude was correctly reconstructed by the image matching process and that the achieved resolution is quite good. We also see that the lidar CHM is quite crisp compared to the 1:15,000 photo CHM and that the definition of the 1:,40,000 photo CHM is still lower than its 1:15,000 counterpart, as could be expected based on the resolution of the original documents.

Close-up observations

Figure 3 shows three close-ups of the CHMs. These reveal that the resolution of the photo CHMs is high enough to resolve tree clusters, and, especially for the 1:15,000 photo CHM, individual trees. We also see that the crown sizes and heights, as perceived via the diameter and brightness of the spots on the lidar and 1:15,000 photo CHMs look very similar, suggesting that these two parameters could be measured on photo CHMs with a certain level of accuracy. A closer look at the lidar and 1:15,000 CHMs reveals some differences. The latter seems “fuller” than the lidar CHM, i.e., the crowns are less defined but more rounded and often wider. We hypothesize that the relatively low lidar hit density (the lidar used for the study was built in 1995; impulse frequencies have since then increased by a factor of 8) results in crowns being hit partially, some smaller crowns being entirely missed. The lidar CHM thus shows “choked” crowns. The 1:15,000 photo CHM was built using high resolution pictures that show the entire crowns (except for the shaded parts). It is therefore not surprising that this photo CHM shows a more closed canopy than the lidar CHM. We can expect a closer resemblance between the lidar CHMs produced by 33KHz lidars and 1:15,000 photo CHMs.

There are also some discrepancies between the summer CHMs (lidar and 1:15,000 photo) and the spring CHM (1:15,000). One is quite obvious on figure 3 (middle row) in the dense patch of forest at the extreme left of each CHM. This patch is completely closed in the summer CHM but has important gaps in the spring CHM. The most plausible explanation for that is that the almost leafless state of hardwood on May 8 1998 (1:40,000) left some foliage free gaps in otherwise closed mixed canopies.

Quantitative comparison: a first assessment

Bare earth level Due to the unresolved ambiguity in the precise locations of the fiducial marks of the 1:15,000 photos, we preferred to postponed a complete quantitative assessment of the canopy height error of the photo CHMs. We did however checked a certain number of pixel values to get a rough idea of the quality of the photo CHMs. A first test consisted in comparing the Z co-registration of the ground level of all CHMs. This test was conducted by first identifying patches where the ground level could be seen. These patches have approximately equal first and last returns lidar altitudes. We compared the lidar ground altitude to the altitudes given by the photo CHMs for the same locations. The altitudes given by the 1:40,000 photo CHM where clearly closer to the (true) lidar altitudes than where the 1:15,000 photo altitudes, which where consistently higher (approx. 8-12 m higher). The altitudes of

the 1:40,000 photo altitudes were often within 2-3 m of the lidar altitude on bare ground. We believe that the fact that the fiducial mark locations of the 1998 photos where used for the computation of the interior orientation of the 1994 photos is responsible for these discrepancies. This leads us to think that the co-registration of lidar and photo GAMs can be quite accurate.

Canopy and tree height We define canopy height as the height of the foliage source above ground for any point of the canopy. Tree height is the height of the tree apex (topmost point) above ground. We first assume that in general, the lidar canopy height is quite close to the true height. However, the height value of single trees is often lower in a lidar CHM than in reality because the tree apex, especially of a softwood tree, is quite narrow, and for this reason often missed by lidar hits, thus truncating the tree top. In an earlier study (St-Onge, 1999), we developed a correction equation for this phenomena in the same study region. The tree heights read on the lidar CHM were first corrected using this equation before they were compared with the photo CHM tree heights. In comparing canopy heights between lidar and photo CHMs, one must be sure that the X,Y coregistration of the CHMs is nearly perfect because of the very high spatial frequencies of the height variations. In other words, one should avoid comparing the altitude of the top of a tree on one CHM with the side of that same tree on an other CHM. Because we did not assess the accuracy of the X,Y co-registration, we only compared very broad canopy height variations using a low-medium-high height classification. A more precise study will be carried out later. We found that these broad height variations are very similar on both the lidar and the 1:15,000 CHMs. This corroborates the visually observed high correlation between the brightness levels of these CHMs. The 1:40,000 photo CHM does show height similarities with the lidar CHM, but to a lesser degree. The fact that the leafs were not fully grown on this CHM does not provide us with good comparison conditions, so we did not pursue the comparison further. The major differences between the lidar and 1:15,000 CHMs occurred at gap locations on the lidar side. As said earlier, we believe that most tree crown diameters are shrunk and that some trees are entirely missed because of the relatively low hit density of the ALTM 1020. For this reason, and because of tree leaning on the 1:15,000 photos, there are some cases where there appears to be a tree on the photo CHM and a gap on the lidar CHM. The height discrepancies are of course very high in theses cases.

Conclusion

Even though a detailed quantitative assessment of the accuracy of canopy height models derived from a combination of lidar and photo based surface reconstruction still as to be carried out, the initial observations we made lead us to conclude that:

- lidar altitude models can be co-registered in X,Y,Z to aerial photo derived altitude models,
- general canopy patterns, tree clusters, and on many occasions individual trees are correctly represented in photo CHMs
- photo scale is determinant in the effective resolution of the CHMs
- the height of the canopy and of certain individual trees can be estimated from the photo CHMs, although with a currently unknown level of accuracy.

Its seems reasonable to think at this point that the evolution of the structure of forest canopies over time (height and density increments, gap dynamics, etc.) could be studied using diachronic photo CHMs with a single lidar coverage. These diachronic studies would be possible from past to present states, and, provided the photogrammetrical problems can be solved, the full record of stereo air photos, starting around 1920 for some regions in North America, could be used for this purpose.

Further studies will include full quantitative assessment of canopy height measurements derived from photo CHMs, more precise evaluation of the X,Y,Z co-registration of CHMs, more control over photogrammetrical and image matching parameters, the use off older photos for diachronic studies, and possibly a link to model-based surface reconstruction.

ACKNOWLEDGMENTS

We thank the National Science and Engineering Research Council of Canada, and the Network of Centres of Excellence on Geomatics for Informed Decisions (GEOID). Our gratitude also goes to LaserMap Image Plus (Boisbriand, Québec, Canada) for providing the laser survey at a significantly discounted price.

Date of survey: June 28th 1998
Laser sensor: Optec's ALTM1020
Laser wavelength: 1047 nm
Impulse frequency: 4000 Hz
Scan frequency: 16 Hz
Flight altitude for vegetation and ground: 700 m
Footprint size: 0.19 m
Maximum scan angle from nadir : 10 degrees
Approximate Z accuracy: 20 cm
Approximate X,Y accuracy: 70 cm
Number of passes for first return: 2
Number of passes for last return : 1
Average hit density for vegetation: 1 hit/m^2
Average hit density for ground: 1 hit/2.5 m^2
Vegetation/ground separation : Optec's REALM

Table 1 Lidar characteristics

Nominal scale	**1:15,000**	**1:40,000**
Acquisition date	July 11, 1994	May 8, 1998
Camera	Wild RC 10	Wild RC 10
Calibrated focal length	153.234 mm	153.107 mm
Flight altitude over ground level	2600 m asl	6400 m asl
Scanning resolution	1200 dpi	1200 dpi
Nominal ground pixel size	32 cm	85 cm

Table 2 Aerial photos characteristics

REFERENCES

Howard, J.A., 1970. Aerial Photo-Ecology. Elsevier, New York.

Hyyppä, J., Hyyppä, H., Inkinen, M., Engdahl, M., Linko, S., and Yi-Hong, Z., 2000. Accuracy comparison of various remote sensing data sources in the retrieval of forest stand attributes. Forest Ecology and Management, 128, pp. 109-120.

Lefsky, M.A., Cohen, W.B., and T.A. Spies, 2001. An evaluation of alternate remote sensing products for forest inventory, monitoring, and mapping of Douglas-fir forests in western Oregon. Can. J. of For. Res., 31, pp.78-87.

Sheng, Y., Gong, P., and Biging, G.S., 2001. Model-based conifer-crown surface reconstruction from high-resolution

aerial images. Photogrammetric Engineering and Remote Sensing, 67(8), pp. 957-965.
Spurr, S.H., 1960. Photogrammetry and Photo-interpretation., Ronald Press Company.
St-Onge, B. 2000. «Estimating individual tree heights of the boreal forest using airborne laser altimetry and digital videography». *Workshop of ISPRS WG III/2 & III/5 : Mapping surface structure and topography by airborne and spaceborne lasers.* 7-9.11.1999 La Jolla (Californie): Int. Arch. of Photog. & Rem. Sens. Vol. 32 no 3-W14 p. 179-184.

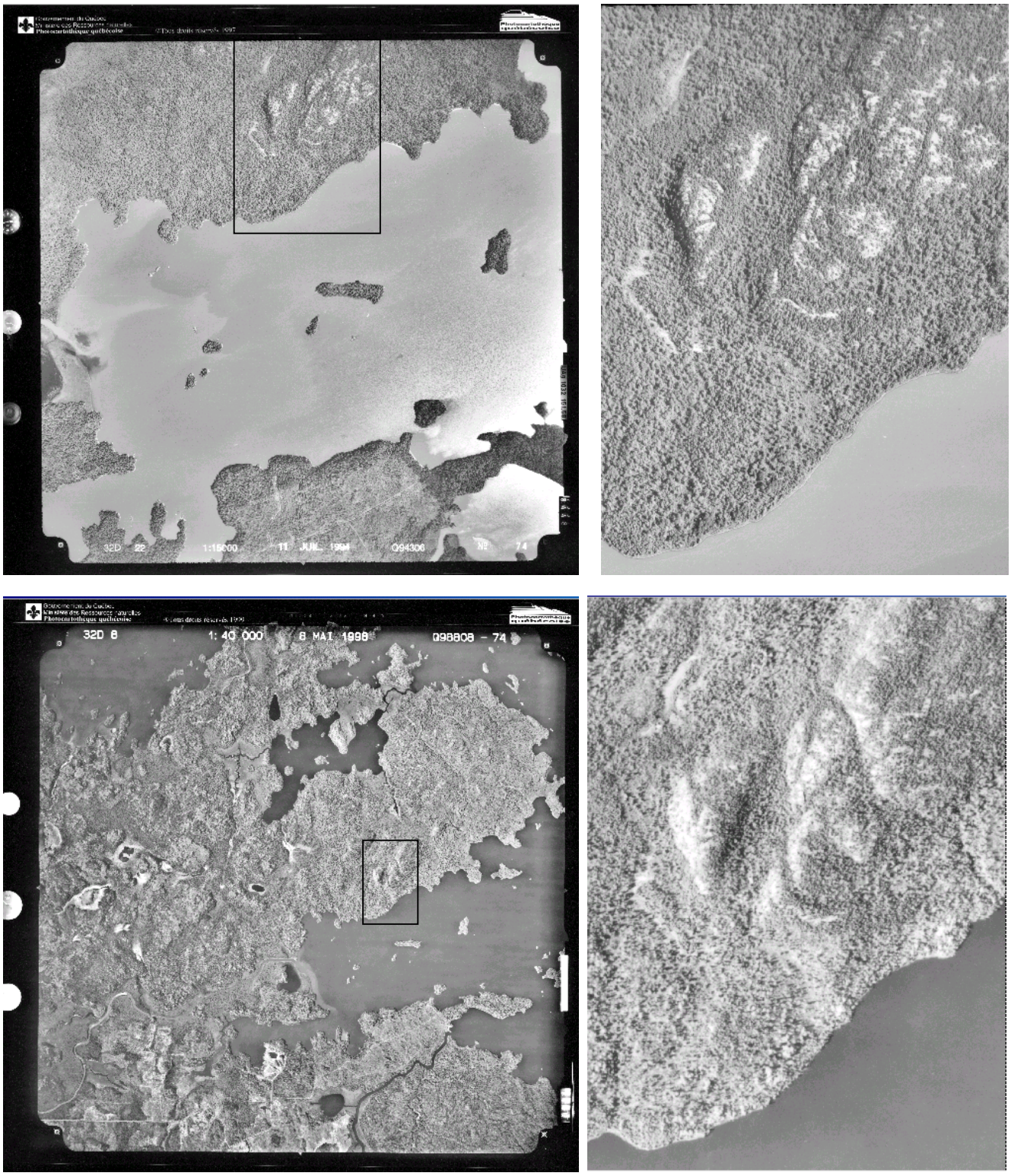

Figure 1 Aerial photos used to create the canopy height models. Top row: one of the 1:15,000 photos with close-up on the study region (rectangle). Bottom row: same for the 1:40,000 photos.

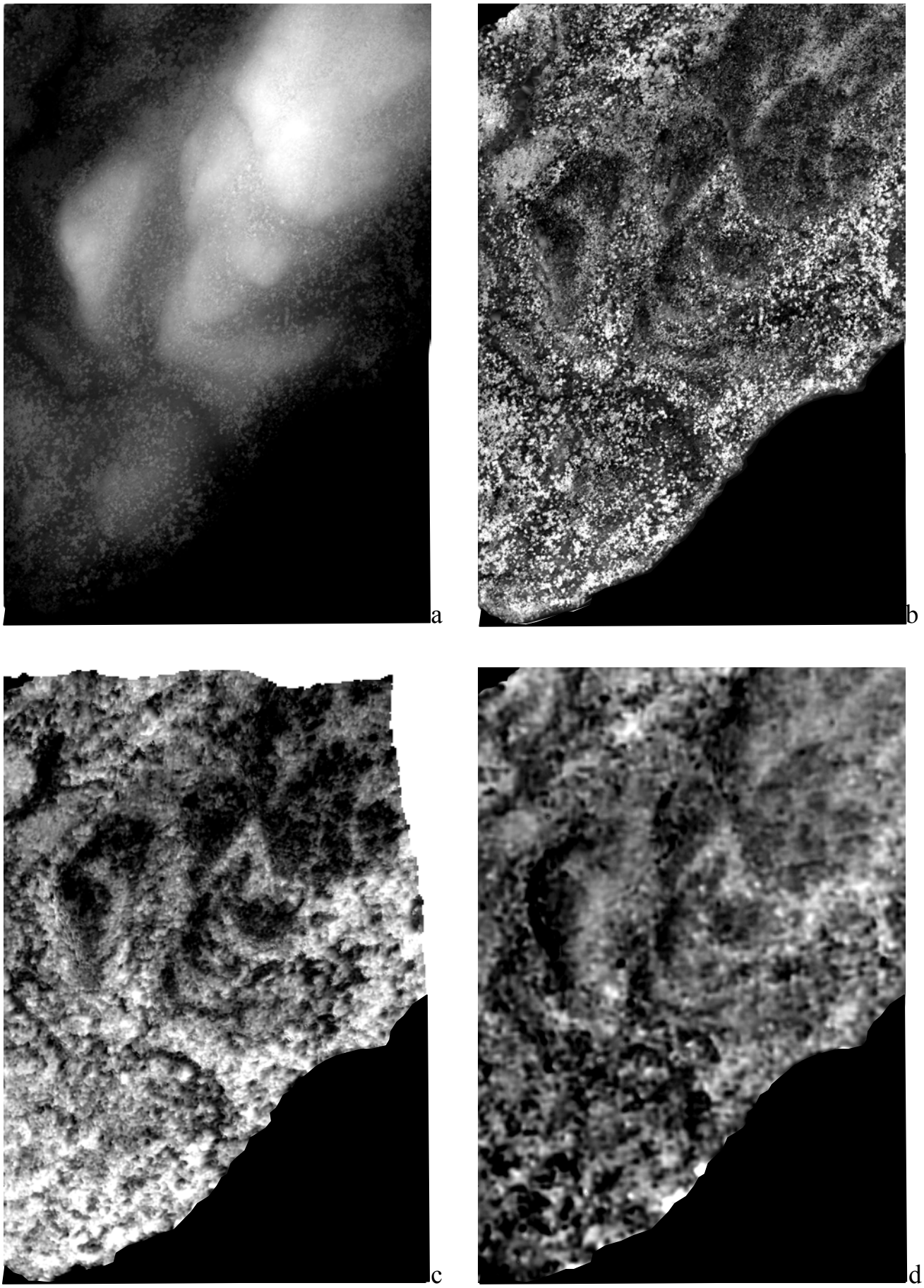

Figure 2 Lidar canopy altitude model (a), lidar CHM (b), 1:15,000 photo CHM (c), 1:40,000 photo CHM (d)

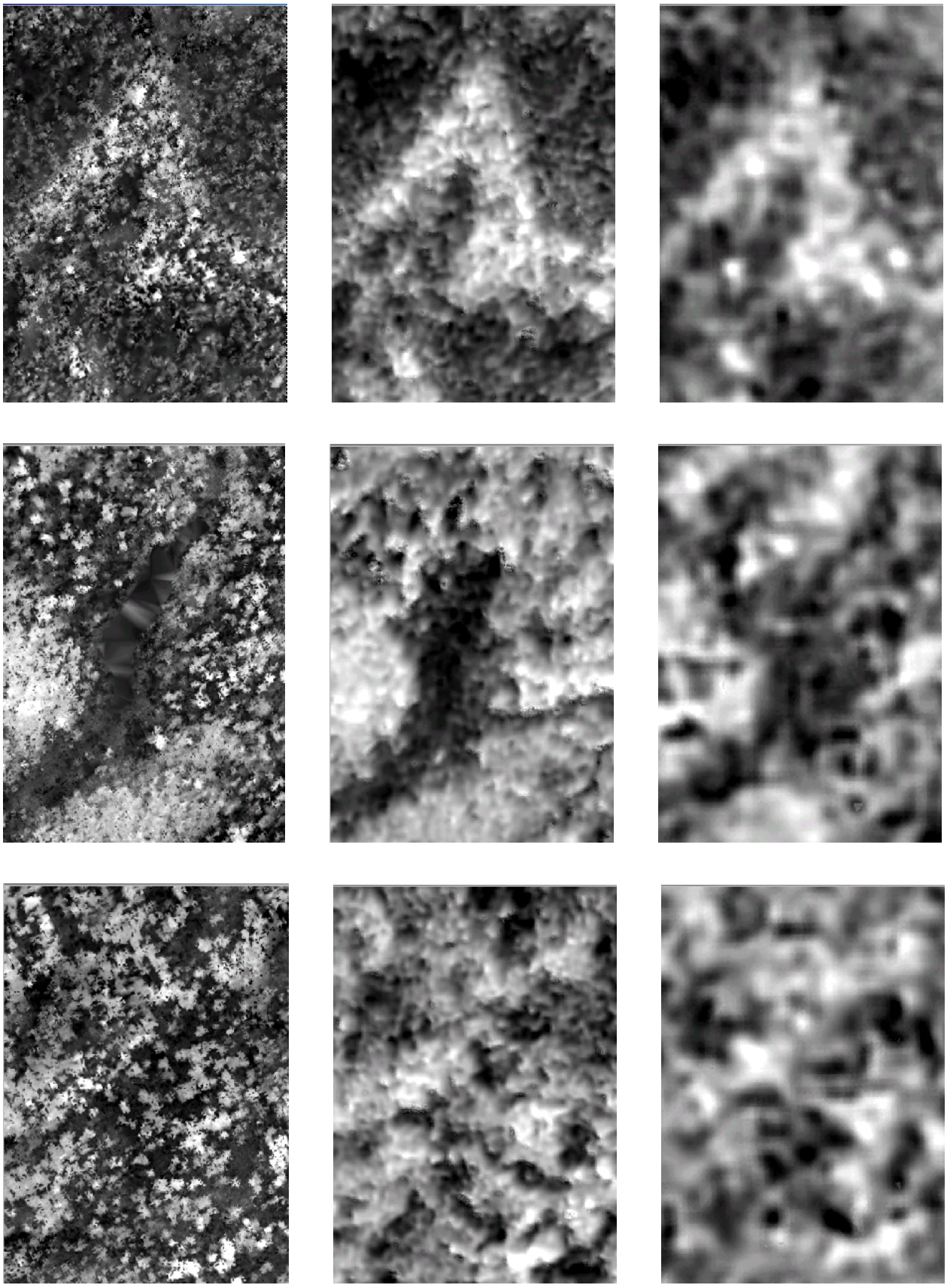

Figure 3 Each row represents a different close-up view. The left column shows the lidar CHM, the middle column the 1:15,000 photo CHM, and the right column the 1:40,000 photo CHM.

Investigation of Measuring Accuracy of Forest Area by Means of Airborne Laser Scanner

Manabu FUNAHASHI, Masahiro SETOJIMA, Yukio AKAMATSU and Yasuteru IMAI
Department of Global Environmental Research
Kokusai Kogyo Co., Ltd.
12-1 Goban-cho, Bancho Kaikan 7th Floor Chiyoda-ku, Tokyo, 102-0076
JAPAN
manabu_funahashi@kkc.co.jp

Masahiro AMANO, Toshio KATSUKI, Miki FUKUDA
Forestry and Forest Products Research Institute
1 Matsunosato, Kukisaki-cho, Inashiki-gun Ibaraki, 305-8687
JAPAN

Commission III, Working Group 3

KEY WORDS: airborne laser scanner, sinks, global warming, tree height measurement, measuring accuracy

ABSTRACT

It is an important subject to accurately measure forests that serve as sinks since the global warming is taken up as a serious problem in recent years. Tree height and so on have so far been measured by the conventional direct or indirect measuring method. Presently, however, the measuring accuracy by airborne laser scanner has been improved and it is now reaching the stage of practical use for measuring forests as well. For this study, we selected the forest of Tama Forest Science Garden (Hachioji, Tokyo) of Forestry and Forest Products Research Institute as an investigation field where various types of trees grow and a database is constructed. Then we compared the data obtained with the laser scanner with the results of topographic survey and tree height measurement conducted at the investigation field of a specific range and investigated the accuracy of measuring the forest area. According to the verification result relating to the DEM accuracy, the error of the DEM made from the laser scanner to the actually measured value was about 50cm(min.). As a result of accuracy investigation of tree height, a large difference was found in measuring error depending on the growth condition of trees (tree shape). At a place where trees grow almost vertically, the difference between the DSM and tree height value actually measured was small. However, at places where trees grow obliquely or trees are intertwined in a complicated way, the measuring error was large.

1. INTRODUCTION

The interests and expectation of our nation have been increasing to the forest in recent year. Especially, along with the improvement of quality of life and increase of leisure time, diversification of sense of value, recognition of natural environment, and enhancement of orientation towards health and rest, there is an increasingly strong tendency to attempt the sustainable forest management by restoring the places where the human and nature can co-exist through utilization and management of Satoyama coppice forests which have been highly devastated so far. To this end, it is required to make measurement and analysis of forests including those of Satoyama (Shigematsu et al., 1997).

Also, in the various movements in recent years around the Kyoto Protocol as the countermeasure against global warming, a high expectation is accorded to the absorption and fixation function of forest as one of the means to reduce the carbon dioxide among the green house effect gas. Therefore, it has become an urgent issue to establish measurement technology and method for the forests (Oguma et al., 2000 ; Yamagata et al., 2001).

In case where the forest area is selected as the object of study, the ground height, tree height, tree crown and species can be pointed out as spatially effective information. Sueta applied Fourier analysis to the vertical cross section of ground surface vegetation measured by infrared laser instrument mounted on airplane and assumed the existing volume of vegetation by analyzing the structure of forest over the wide area (Sueta et al., 1998). In this study, the improvement in the accuracy of land surface is pointed out as the future issue. Tamura made an experiment of tree height measurement at Tomakomai experimental plantation of Hokkaido University using airborne laser scanner (Tamura et al., 2000). As a result, the difference between the laser scanner data and actually measured data was in an allowable error of 1m at 67 out of 89 measuring points, namely 75% of the measuring points, and they reported that it was possible to measure the tree height distribution over the wide area with fairly high accuracy. Omasa made 3 dimensional measurement of tree crown height using laser scanner mounted on helicopter (Omasa et al., 2000). In this study, they reported that the difference of crown height between the laser data and actually measured data was 47cm(max.) in case of coniferous trees for which the measuring error is generally large, and 19 cm in case of RMSE.

In our present study, based on the study results on the

applicability of airborne laser scanner, and presuming that this technology is actually used for Satoyama coppice forests, we selected the forest area having the aspects close to Satoyama coppice forests, and verified its applicability to ground surface measurement and tree height measurement based on the data obtained by airborne laser scanner and the analysis made on such data (Funahashi et al., 2001).

2. CONFIGURATION OF THE STUDY

This study is composed of 1) discussion on the ground height measurement and 2) comparison and discussion of tree height measurement (see Fig. 1).

2.1 Discussion on the ground height measurement

The purpose of this discussion was to determine by what extent of accuracy it is possible to assume the ground surface from the data obtained from airborne laser scanner. Namely, we assumed the ground surface by filtering the obtained data and verified the applicability of airborne laser scanner to the ground surface measurement by comparing the data with the results of actual topographic survey. We also compared the data with the ground surface obtained from the existing topographic maps (Tokyo topography at the scale of 1/2500, surveyed in 1999, published by Tokyo City Planning Bureau). The applicability was examined from both comparison and discussion based on ground DEM (we specified the data of airborne laser scanner as LSDEM, those of actual topographic survey as actual measurement DEM, and those obtained from topographic map as topographic map DEM) and comparison and discussion based on the topographic cross section.

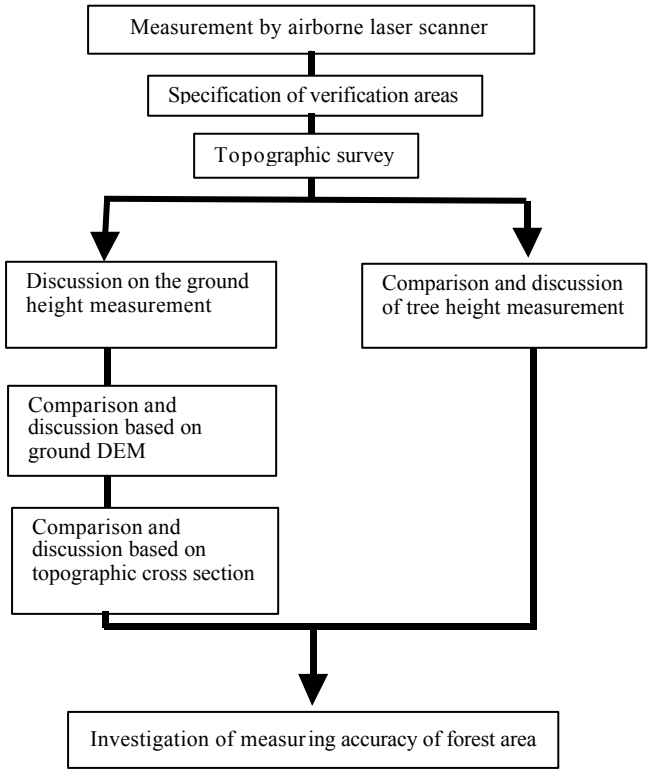

Fig. 1: Structure of the study

2.2 Comparison and discussion of tree height measurement

We compared actual tree height with LSDSM(we specified the first pulse data of airborne laser scanner as LSDSM) and discussed the applicability of this method. As for the applicability, we discussed the influence on the tree height measuring results of the difference of the topography of slope area as well as the difference of composition species (deciduous broad-leaved forest, evergreen/deciduous mixed forest, artificial forest of cedar and cypress).

3. SELECTION AND NOTION OF VERIFICATION AREA

Tama Forest Science Garden of Forestry and Forest Products Research Institute which we selected as the verification area is a hill land of about 57ha with the altitude around 200m located at east edge of mountain mass abutting on Mount Takao in west side of Tokyo. Among this hill land, we specified the verification areas as follows (Photos 1 and 2) considering (1) forest type with different species (cedar artificial forest, deciduous broad-leaved forest, evergreen/ deciduous mixed forest) and (2) different topographic type (steep slope area, gentle slope area and flat area).

ST – 1: This is a steep slope area with dense forest of mature-aged cedar, and one measuring line (A–B section) was specified along the woodland path which runs almost orthogonally against the most steep slope for the comparison of topographic cross section.

ST – 2: This is a area with sparse forest deciduous broad-leaved trees (cherry tree preservation forest), and one measuring line was specified (A–B section) along the direction of most steep slope area for the comparison of topographic cross section.

ST – 3: This is a area composed of flat area and steep cliff on which evergreen/deciduous dense forest is growing. One measuring line was specified (A–B section) on the flat area for the comparison of topographic cross section.

4. MEASURING SENSORS AND OBTAINED RESULTS

4.1 Airborne laser scanner and obtained data

The airborne laser scanner used for this study is RAMS (made by EnerQuest Systems), which can, different from the conventional systems, record maximum 5 reflection pulses against the irradiated laser beam. Monochrome digital camera of 4,096 x 4,096 pixels was also mounted on the aircraft so as to acquire the image data simultaneously with the laser data. The coordinates information of measuring points and picture taking point is recorded at 200Hz by GPS and IMU incorporated in the system. These data enable us to calculate the inclination of digital camera, and make orthophoto without placing ground marks on the land. The measurement by airborne laser scanner was made on October 11, 2000 at the whole areas of Tama Forest Science Garden according to the details as shown in Table 1. Measuring course is

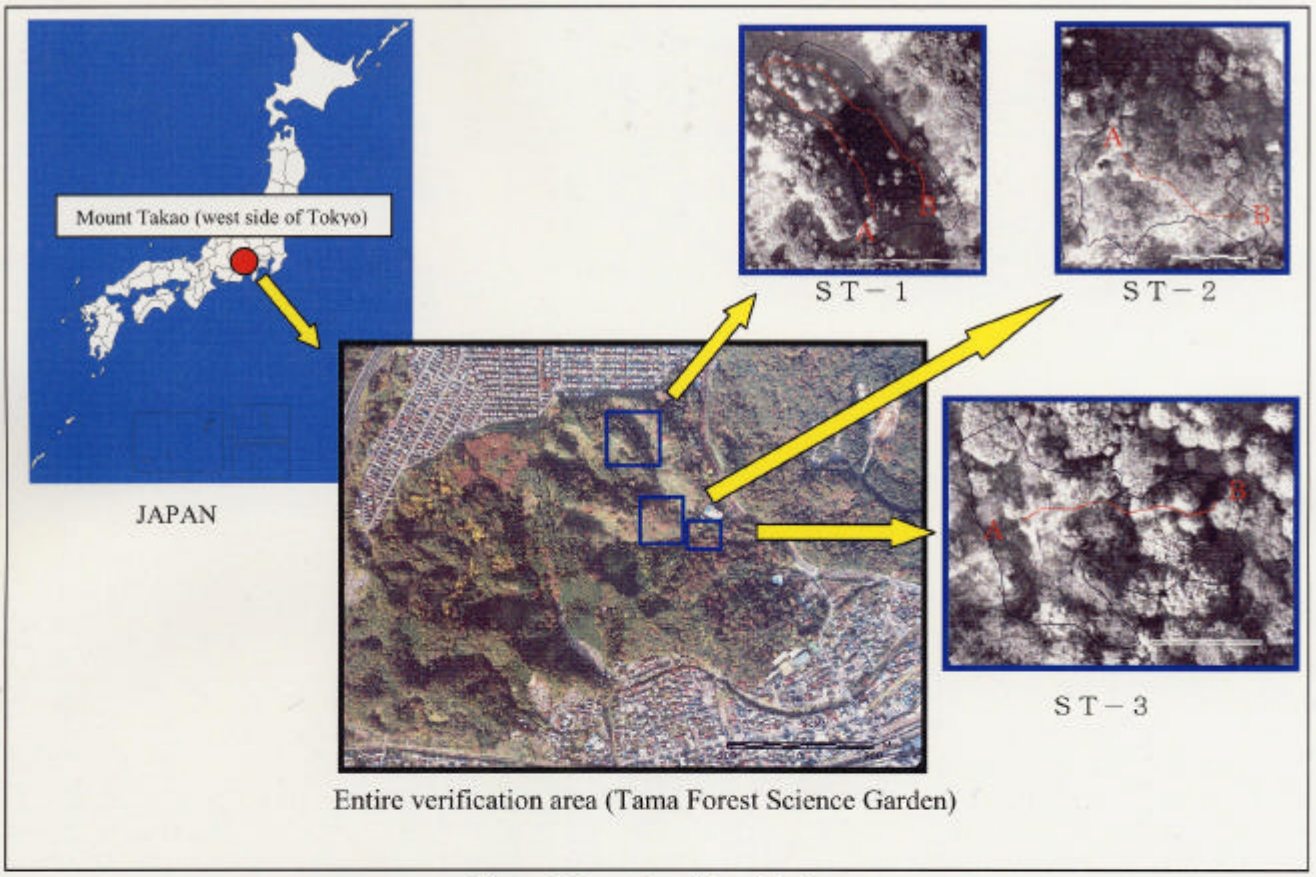

Photo 1: Location of verification areas

ST – 2: Condition at the site (sparse deciduous broad-leaved forest (cherry tree preservation forest), slope area)

ST – 1: Condition at the site (dense cedar forest, steep slope area)

ST – 3: Condition at the site (evergreen/ deciduous mixed dense forest, flat area and steep cliff)

Photo 2: General conditions of verification areas (Tama Forest Science Garden)

shown in Fig. 2 (only the data of verification areas were used in this study). When the data is acquired with these conditions, the width of area which can scanned at one flight is about 650m, and therefore, we made measurement by dividing the area into three courses; the laser irradiation density at this time was 1 laser per 2m square.

4.2 Topographic survey

We made topographic survey in the mid winter (February 8 and 9 , 2001) when the land surface is most exposed. We measure at the interval of 1m at the places where the topography changed steeply and at the interval of 2m at the places where the topography changed gentle.

We used Total Station (GT – 1002) made by Topcon for the topographic survey and tree height meter (VERTEX III) made by Timbertech for the measurement of tree height (Table 2).

Table 1: Measuring specifications of airborne laser scanner used for the study

Conditions	Set value
Data acquisition altitude	2500 (m)
Flying speed	200 (km/h)
Scanning angle	15 (deg.)
Scanning width	650 (m)

Table 2: List of measuring instrument used for the topographic survey

GPT – 1002 Topcon	Resolution of telescope	2.5”
	Distance measuring unit (prism)	6,000 m
VERTEX III Timbertech	Measuring distance	30 m
	Measuring range	-55°~ +85°
	Distance resolution	1 cm
	Angle resolution	0.1°
	Height resolution	10 cm

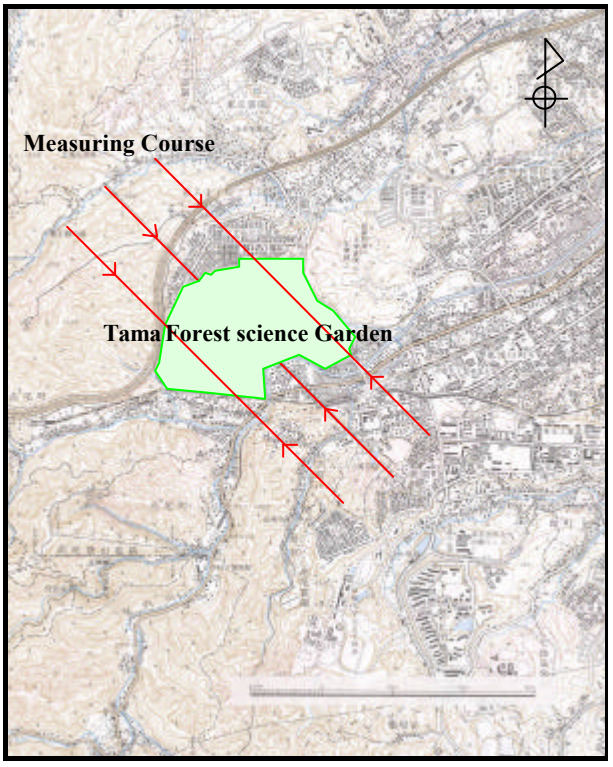

Fig. 2: Measuring course of airborne laser scanner

5. RESULTS AND CONSIDERATION

5.1 Discussion on the ground height measurement

In this stage of study, we made consideration both from comparison with ground DEM and comparison with topographic cross section. The actual measurement DEM of 2m interval was interpolated to 1m interval and compared and checked with LSDEM. Especially, we paid attention for the conformity of both DEM’s influence by the differences of composition species and shale of slope area. In the comparison of topographic cross section, we analyzed the conformity of topographic cross section obtained from LSDEM, actual measurement DEM and topographic map DEM (made at the interval of 1m) along the measuring lines specified in verification areas ST – 1 ~ 3.

5.1.1 Comparison and discussion based on ground DEM

In ST-1 (Photo 4), there are many points where the difference between LSDEM and actual measurement DEM is within 1m showing relatively high coincidence. However, some fluctuation is observed partially such that LSDEM is rather higher than actual measurement DEM in the north edge of the area while LSDEM is somewhat lower than actual measurement DEM at the central part of the area. It is considered that there is dense forest of matured age trees having large diameter and therefore the laser beam did not reach the land surface being influenced by them, and as a result, LSDEM values were calculated rather higher. Also, the multiple layered forest is formed in this range being dominated by evergreen shrub such as aucuba, which may have given an influence on the calculation results. On the other hand, there is dense forest of juvenile trees at the central part, and therefore, there are only a small number of measuring points where the laser beam can reach the ground surface. In addition, the fine topography could not expressed adequately because many measuring points were erased by the filter processing.

In ST-2 (Photo 3) , the difference between LSDEM and actual measurement DEM is within 1m throughout almost all the area, and the coincidence is highest among three ST’s. This is considered because, since this is an area of sparse forest of deciduous broad-leaved trees (cherry tree preservation forest), the laser beam easily reached the ground surface, and also because it is gentle slope area and topography could be adequately express even by the data thinned out by the filter processing. However, there are points where LSDEM differs from actual measurement DEM at a part of north edge of this area. The cause of this anomaly is considered to be that many measuring points were thinned out by filter processing because many trees of large diameter distribute in these points, and the topography is complicated as there is steep cliff at the edge of gentle slope area.

In ST-3 (Photo 5), good coincidence is observed between

LSDEM and actual measurement DEM at the west edge of area, but the difference is large at other parts. Especially, ground DEM is calculated higher at south part and north edge and lower at east part of the area. The land surface is almost flat at the west edge of area being occupied by mixed forest evergreen broad-leaved and deciduous broad-leaved trees and the density of tree crown is relatively sparse, which is considered to have resulted in the higher accuracy ground DEM calculation. On the other hand, since tall trees are growing at high density at other parts of this area, the laser beam did not reach the land surface and the topography is complicated being composed of steep cliffs and steep slope, and therefore, the topography was not expressed adequately by the data of measuring points thinned out by filter processing.

It is known from the comparison of results of ST's that there is a difference in the applicability to the compilation of LSDEM by the form of land surface. The applicability is relatively high at the homogeneous topography such flat area in ST- 3 and gentle slope in ST-2, while the applicability is rather low at the complicated topography where the change is steep such as steep slope in ST-1 and steep cliff in ST-3. This tendency is especially conspicuous at the place where the density of tree crown is high. This is because only the measuring points where the laser beam reached the land surface are picked up by the filer processing for making LSDEM, and as a result, the number of measuring point that can actually be used is substantially reduced; and DEM obtained by interpolation is not adequate to express the complicated and steeply changing topography. It is difficult to draw an absolute conclusion as the tendency may vary according to the density of tree crown, but in general, it can be said that the applicability of data of airborne laser scanner to the compilation of LSDEM will be lower as the topography becomes more complicated with steep slope and steep cliff.

It is clear from the comparison of results by ST's that the composition species give a great influence on the applicability to LSDEM compilation. LSDEM coincides fairly well with actual measurement DEM at deciduous broad-leaved forest in ST-2 and mixed forest of deciduous broad-leaved / coniferous trees in ST-3, but the conformity is rather low at a part of ST-1 and ST-3 which is dominated by coniferous forest or mixed forest of deciduous broad-leaved / coniferous trees where the density of tree crown is high. This is considered because the points where the laser beam reaches the ground surface is small at the places of species having high density of tree crown, and the actual topography cannot be adequately expressed by DEM which is created by interpolation. Also, there is a possibility that LSDEM is calculated higher at the places of multiple layered forest such as ST-1 due to the influence of middle ~ low trees. On the other hand, the actual topography was expressed accurately in a part of ST-2 and ST-3 which include deciduous broad-leaved forest probably because the leaf falling had already begun and laser beam reached the land surface at many points. As stated in the

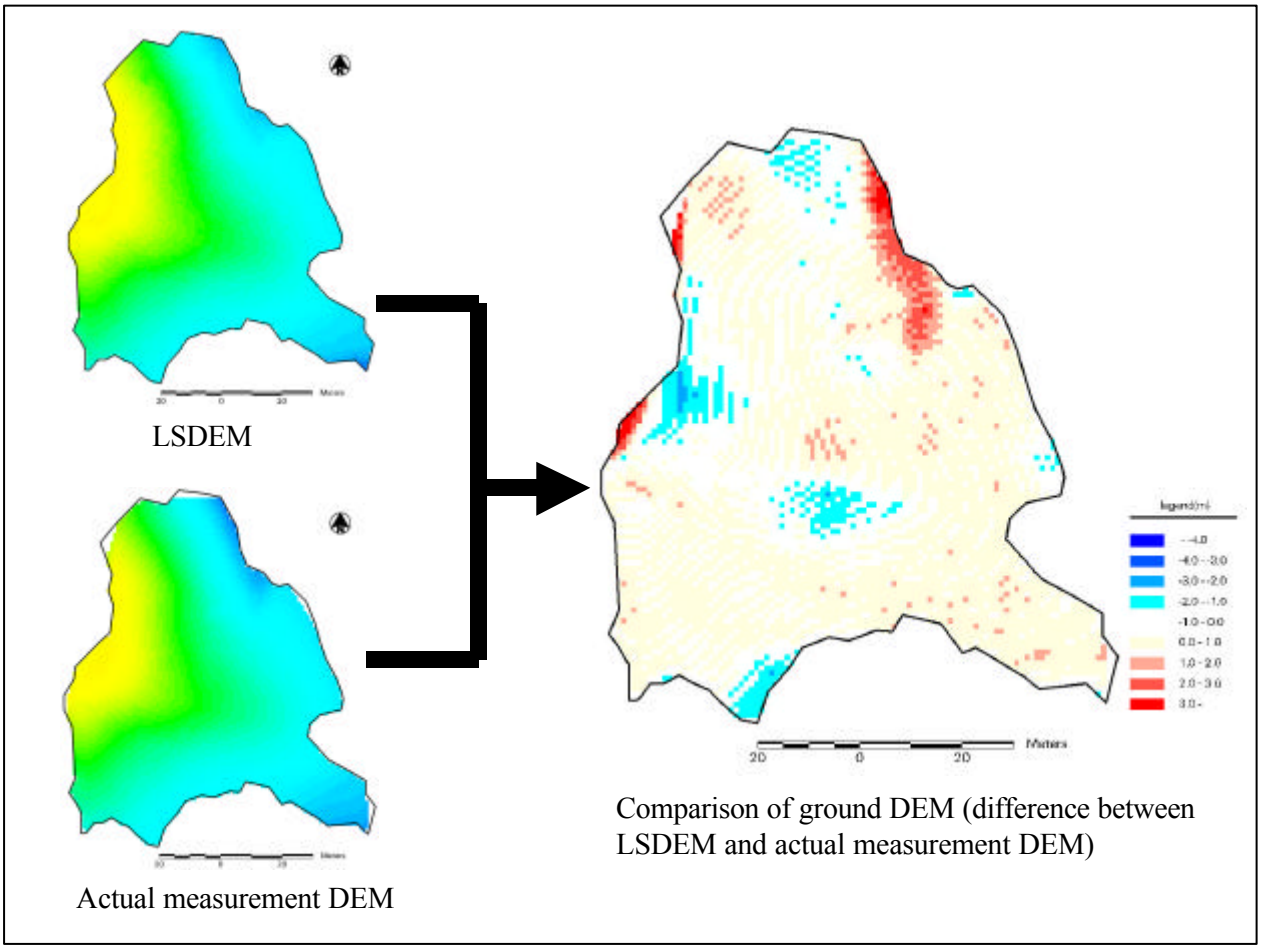

Photo3: Comparison and verification of LSDEM and actual measurement DEM

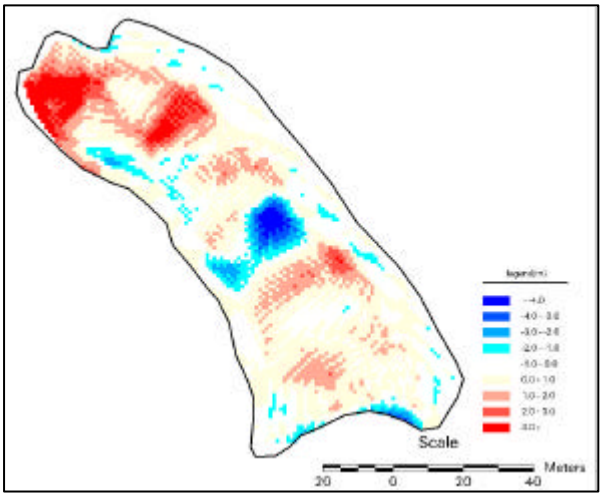

Photo4: Points where there is difference between LSDEM and actual measurement DEM (in case of ST-1)

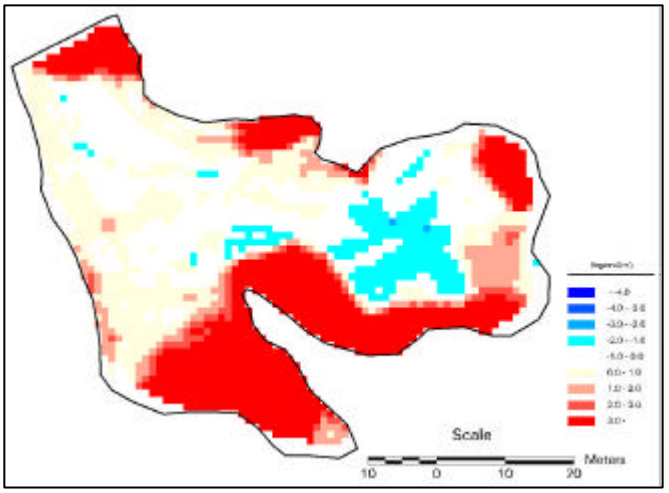

Photo 5: Points where there is difference between LSDEM and actual measurement DEM (in case of ST-3)

above, not only the composition species but also the density of tree crown and condition of trees due to the time of survey (season) give influence on the applicability of airborne laser scanner to the compilation of LSDEM.

5.1.2 Comparison and discussion of topographic cross section

The results of comparison of topographic cross section between LSDEM and actual measurement DEM are shown by ST in Figs. 3 to 5. As seen in comparison result of ST-1 consisting of steep slope, a good coincidence is observed between LSDEM and actual measurement DEM with the error of around 1 ~ 2m in general, which is almost the same accuracy of DEM compiled from topographic map. On the other hand, there are points where a large difference in the topographic cross section between the both, but the relationship between its distribution and topography is unknown. As seen in the comparison result of ST-2 consisting of gentle slope, the coincidence between LSDEM and actual measurement DEM is high with the difference within 1m throughout the area, and the lad surface is expressed more accurately than those expressed by DEM made from topographic map (topographic map DEM). It is considered that accurate LSDEM can be produced at gentle slope area as there is no difference in the topographic cross section as seen at the steep slope area. In addition, as seen in the comparison result of ST-3 consisting of flat area, it is clear that the shape of land surface is expressed more accurately than those expressed by topographic map DEM similarly as in the case of gentle slope area.

It was understood from the comparison result stated in the above that, in the comparison of topographic cross section, the accuracy of LSDEM is influenced by the topography of study area, and also that it is possible to express the topography more accurately than those expressed by topographic map DEM.

5.2 Comparison and discussion of tree height

The comparison of tree height between airborne laser scanner and actual measurement by ST's is shown in Figs. 3 to 5. In ST-1, the difference of tree height between airborne laser scanner and actual measurement is 1 ~ 2m showing good coincidence in general. However, there is a tendency that LSDSM is somewhat lower than actual measurement, and when we consider that the height is calculated rather higher by LSDEM comparing with actual measurement, we can understand that the tree height is calculated rather lower. Also, there are some places, although very rare, where tree height calculated by LSDSM is substantially higher than actual measurement; this is considered because the low tree actually measured was concealed by the crowns of surrounding taller tree, which was measured by airborne laser scanner.

In ST-2, it is known that LSDSM coincides quite well with actually measured tree height excepting some exceptional points. Taking into account the good coincidence between LSDEM and actual measurement DEM as stated before, it is considered that the tree height can be measured with high accuracy. On the other hand, the trees are growing upright as shown in Photo 6 in many cases where the tree height obtained by airborne laser scanner coincide with the actual measurement, while the difference is observed between the two in many cases where the trees are growing obliquely (Photo 7).

Similarly to ST-2, LSDSM shows quite good coincidence with the actually measured tree height in ST-3 excepting some parts (Photo 8). Taking into account the good coincidence between LSDEM and actual measurement DEM as stated before, it is considered that the tree height can be measured with high accuracy.

6. CONCLUSION

The outcomes obtained by our present study are summarized as follows:

1) In the spatial comparison of ground height by DEM, it was understood that the applicability of this technique to LSDEM compilation may vary according to the shape of land surface. The applicability to LSDEM is high at gentle slope area or the area having the homogeneous topography, but problems remains for the application of it to the complicated topography including the land having steep cliffs or steep change in the slope.

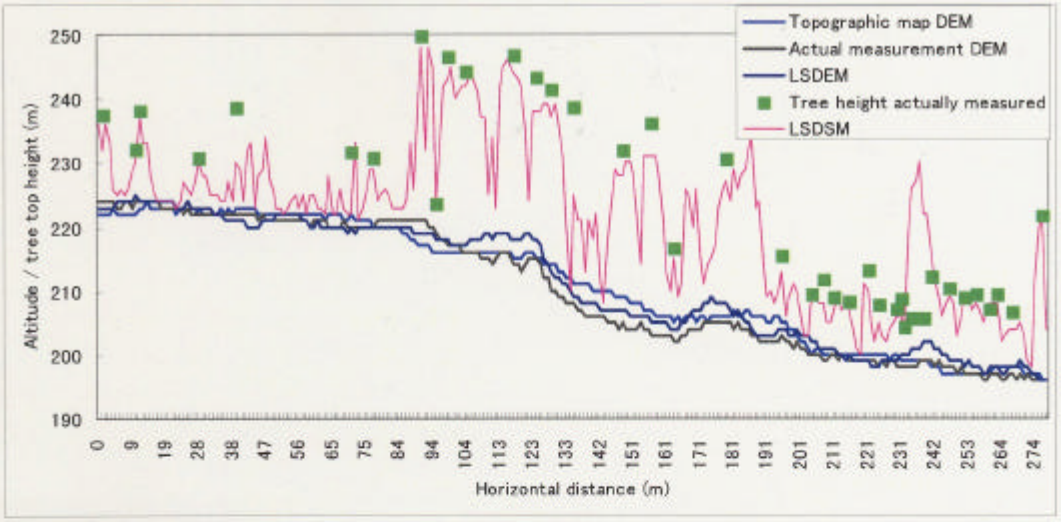

Fig. 3: Comparison of topographic cross section in ST –1

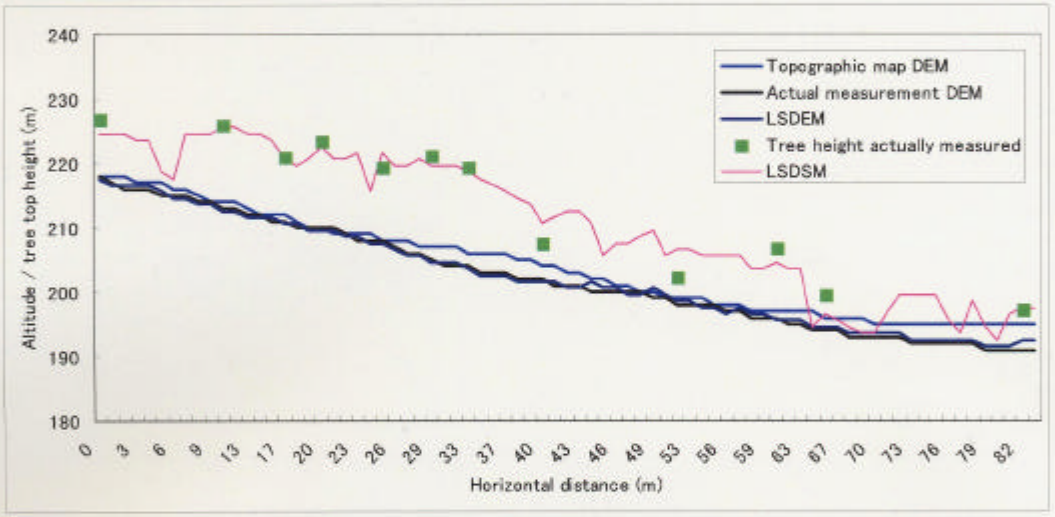

Fig. 4: Comparison of topographic cross section in ST – 2

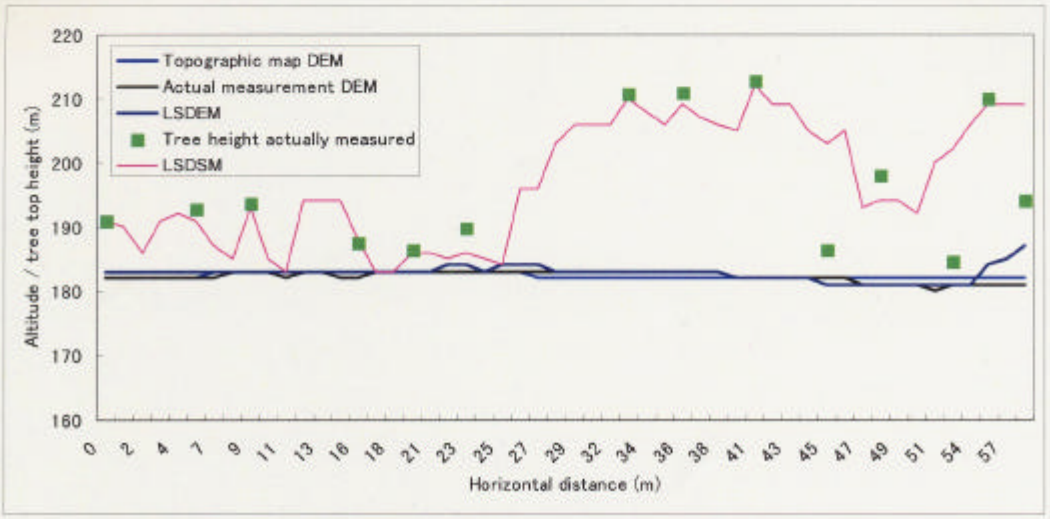

Fig. 5: Comparison of topographic cross section in ST – 3

2) As for the relationship between LSDEM and composition species, the coincidence is high with the actual measurement DEM at the homogeneous deciduous broad-leaved forest and artificial forest where the growth of low layer vegetation is small, but there is an influence of evergreen trees of the low layer at the multiple layer forest where the lower layer is covered by middle and low trees.

3) In the comparison of topographic cross section, there is a tendency that the accuracy of LSDEM is influenced by the topography of study area, but it is considered to be possible to express the topography more accurately than those expressed by existing topographic map DEM at gentle slope and flat area.

4) The conformity with the actual measurement is good in general in the measurement of tree height. Especially the conformity is high at the place where the trees are growing vertically, but the difference from the actual measurement becomes larger where the trees are standing obliquely.

Photo 6: Point of conformity in ST – 2

Photo 7: Point of non-conformity in ST – 2

Photo 8: Point of non-conformity in ST – 3

REFERENCES

[Shigematsu et al., 1997] Shigematsu, T., Asahiro, K., Setojima, M., Makita, F., 1997. Basic studies on a dynamic vegetation mapping system and its utilization as a tool for rural country land conservation. Journal of The Japanese Institute of Landscape Architecture, vol.60-5, 527-530.

[Oguma et al., 2000] Oguma, H., Yamagata, Y.,2000. Estimation crown cover ratio with remote sensing data (The establishment of the remote sensing technique to contribute to the Kyoto Protocol) . Journal of the Japan Society of Photogrammetry and Remote Sensing, vol.39-2, pp.82-89.

[Yamagata et al., 2001] Yamagata, Y., Oguma, H., Tsuchida, S., Sekine, H., Rokugawa, S., 2001. The role of remote sensing for monitoring and verification of the carbon sinks under the Kyoto Protocol. Journal of The Remote Sensing Society of Japan, vol.21-1, pp.43-57.

[Sueda et al., 1998] Sueda, T., Fukushima, Y., 1998. Estimation of biomass by fourier analysis of forest longitudinal section. The Ministry of Education science research-funds subsidy foundation research report (A) (1), pp14-26.

[Tamura et al., 2000] Tamura, M., Takatsuki, S., 2000. Tree height measurement by airborne laser scanner. Journal of the Japan Society of Photogrammetry and Remote Sensing, vol.39-2, pp.8-13.

[Omasa et al., 2000] Omasa, K., Akiyama, Y., Ishigami, Y., Yoshimi, K., 2000. 3-D remote sensing of woody canopy heights using a scanning helicopter-borne lidar system with high spatial resolution. Journal of The Remote Sensing Society of Japan, vol.20-4, pp.34-46.

[Funahashi et al., 2001] Funahashi, M., Setojima, M., Akamatsu, Y., Imai, Y., Amano, M., 2001. Verification about the use of Airborne Laser Scanner in Forest area. Proceedings of spring conference of JSPRS, pp.49-52.

RELATIONSHIP BETWEEN LIDAR METRICS AND ABOVEGROUND BIOMASS IN CLOSED-CANOPY NEOTROPICAL FORESTS

Jason B. Drake[1], Ralph Dubayah[1], Robert G. Knox[2], David B. Clark[3], Richard Condit[4]

[1] Department of Geography
University of Maryland
College Park, MD 20742

[2] Biospheric Sciences Branch
NASA's Goddard Space Flight Center
Greenbelt, MD 20771

[3] Department of Biology
University of Missouri-St. Louis
St. Louis, MO 63121

[4] Center for Tropical Forest Science
Smithsonian Tropical Research Institute
Unit 0948, APO AA 34002-0948, USA

KEY WORDS: lidar, aboveground biomass, carbon stocks, tropical forest structure

ABSTRACT

Previous studies have shown that canopy metrics from lidar data are highly correlated with aboveground biomass in a variety of closed-canopy forests, however the generality of these site-specific relationships has remained untested. In this study, we compare relationships between lidar canopy metrics and forest structural summaries from a tropical wet forest site in Costa Rica and across a series of tropical moist forest field sites in Panama. We found that in both regions lidar metrics were strongly correlated with forest structural summaries including mean stem diameter, basal area and aboveground biomass. We also showed that the relationships differed between these regions unless deciduousness of canopy trees in Panama was considered. Adjusting for leaf-drop removed statistically significant differences between the two regions in the relationships between a lidar metric and both mean stem diameter and basal area. The relationships between lidar metrics and aboveground biomass, however, remained significantly different between the two study areas because of different general allometric relationships used to estimate aboveground biomass in tropical wet forests and tropical moist forests. Future efforts should continue to examine climatic factors that may influence the generality of the relationships between lidar metrics and forest structural characteristics, and address the dearth of allometric data on the very large trees that can dominate the biomass of primary tropical forests.

1 INTRODUCTION

Aboveground biomass (the total amount of oven-dried biological material present above the soil surface in a specified area) estimates in forest ecosystems are critical for carbon dynamics studies at multiple scales. These estimates provide initial conditions for ecosystem and biogeochemical models (e.g., Foley et al., 1996; Friend et al., 1997; Hurtt et al., 1998; Potter, 1999) that simulate the exchange of carbon and energy between the atmosphere and forest canopies through time. In addition, knowledge of forest carbon stocks are necessary for carbon flux estimates from deforestation, land cover change, and other disturbances (e.g., Houghton, 1991).

Changes in vertical canopy structure typically accompany changes in aboveground biomass in forest ecosystems. For example, as forests recover from past disturbance events, there are often changes in both the horizontal and vertical distribution of forest structure that are associated with an overall increase in aboveground biomass (Aber, 1979; Bormann and Likens, 1979; Oliver and Larson, 1990; Richards, 1996). Additionally, variability in environmental conditions (e.g., climatic, edaphic) and disturbance regimes may result in differences in the spatial distribution of aboveground biomass and vertical canopy structure (e.g., Clark and Clark, 2000; Laurance et al., 1999; Lieberman et al., 1996; Yamakura et al., 1996). For example, in nutrient poor areas, forests typically are lower-stature and contain less aboveground biomass than in nutrient rich areas (Kimmins, 1997; Oliver and Larson, 1990).

Lidar (**li**ght **d**etecting **a**nd **r**anging) remote sensing has proven to be an efficient tool for the characterization of forest structure in a variety of forest environments (Drake et al., In press; Magnussen et al., 1999; Means et al., 1999; Nelson et al., 1988). Because lidar instruments sample the vertical distribution of canopy (e.g., leaves and branches) and ground surfaces (Blair and Hofton, 1999; Dubayah and Drake, 2000; Dubayah et al., 2000; Harding et al., 2001) and because of ecological and

biomechanical links between biomass and vertical structure (Franco and Kelly, 1998; Givnish, 1986; King and Loucks, 1978; O'Neill and DeAngelis, 1981; Oohata and Shinozaki, 1979), recent studies have found a strong correlation between lidar metrics and aboveground biomass (Drake et al., In press; Lefsky et al., 1999; Means et al., 1999; Nelson et al., 1988).

However, the relationships that have been developed between lidar metrics and aboveground biomass (e.g., Means et al. 1999, Drake et al. In press) are site specific and there have been no attempts to compare relationships developed in areas with different environmental conditions. Global terrestrial biomass estimates from future spaceborne lidar instruments such as the Vegetation Canopy Lidar (Dubayah et al., 1997) and the Ice, Cloud, and Land Elevation Satellite (Schutz, 1998) depend on an examination of the generality of these relationships in different regions and biomes.

In this study we examine the relationship between lidar metrics and aboveground biomass in closed-canopy Neotropical forest areas with different environmental conditions. We focus on a tropical wet forest (sensu Holdridge et al., 1971) area in Costa Rica, and on a tropical moist forest area in Panama that receives 50-75% less rainfall on average. First we test for differences in the relationships between lidar metrics and forest structural characteristics such as basal area and aboveground biomass at the two study areas. We also explored other factors (e.g., environmental characteristics) that could help explain any differences in the relationships at the two study areas.

2. METHODS

Field data

Data collected as a part of different ongoing field studies at two Central American study area was used in this study. The first study area is the La Selva Biological Station in the Atlantic lowlands of northeastern Costa Rica (McDade et al., 1994). La Selva is a 1540 ha research facility that is comprised of a mixture of primary and secondary tropical forest, agroforesty, and current or abandoned pasture areas. This area receives approximately 4200 mm rainfall per year (OTS, 2001; Sanford Jr. et al., 1994) and is classified as "tropical wet forest" according to the Holdridge classification method (Holdridge et al., 1971).

The second study area is centered on the Isthmus of Panama along the Panama Canal. This area spans a precipitation gradient ranging from approximately 2000 mm rainfall per year on the Pacific coast of Panama to 3000 mm rainfall per year on the Atlantic side (Condit et al., 2000; Pyke et al., In press) and is classified as lowland "tropical moist forest" (Holdridge et al., 1971). Within this broad area, we focus on a series of 1 ha plots distributed throughout this precipitation gradient (Pyke et al., In press), and on the 50 ha research site on Barro Colorado Island (Condit, 1998).

In the Costa Rica study area, field data were collected in eighteen 0.5 ha primary forest plots (Clark and Clark, 2000), and 3 secondary forest areas of 14, 22 (Guariguata et al., 1997; Nicotra et al., 1999) and 31 (Pierce, 1992) years since abandonment as of March 1998. In addition, published data for 6 agroforestry plots (Menalled et al., 1998) were included.

At the Panama study area, field data from nineteen 1 ha research plots near the Panama Canal (Pyke et al., In press) were used in this study. Four of these sites are mature secondary forests, and the rest are primary forest (Table 1). The remaining field data in Panama were from the 50 ha plot on Barro Colorado Island (BCI, Condit 1998). The 50 ha plot was first divided into 50 1 ha square plots. Next, the spatial correlation length of the lidar metrics used in this study (metrics discussed below) was determined to be approximately 90 m so every other 1 ha plot was discarded to maintain relative independence of the independent variable in the regression analysis. This left a total of 25 1 ha plots from BCI in a checkerboard pattern.

Table 1. Forest structural summaries for all field data used in this study.

Study Site	Land Cover Type	Number of Sites	Mean QMSD (cm)	Mean Basal Area ($m^2 ha^{-1}$)	Mean Estimated AGBM ($Mg ha^{-1}$)
BCI, Panama	Primary Forest	25	28.16	26.27	286.77 *
Panama Canal Plots	Primary Forest	15	26.69	25.23	257.73 *
	Secondary Forest	4	24.35	26.89	277.91*
La Selva Biological Station, Costa Rica	Primary Forest	18	20.76	23.6	160.5**
	31 yr Secondary Forest	1	22.24	26.71	147.7**
	22 yr Secondary Forest	1	12.85	22.05	129.4**
	14 yr Secondary Forest	1	10.46	14.28	78.5**
	Agroforesty	6	9.03	14.48	34.3

* Estimated aboveground biomass (Mg/ha) using general equation for tropical moist forests (Brown 1997)
** Estimated aboveground biomass (Mg/ha) using general equation for tropical wet forests (Brown 1997)

In all forest plots at both study areas, stem diameters were measured in a marked location either at breast height or, when necessary, above buttressing (see methods in Clark and Clark, 2000; Condit, 1998). Stem diameter measurements were used to estimate aboveground biomass values for each measured tree using general allometric equations (Brown, 1997) for tropical wet forests (Equation 1) at the Costa Rica study area, and for tropical moist forests (Equation 2) at the Panama study area. Stem diameters were also used to calculate quadratic stem diameter and basal area for each plot.

Equation 1. $\mathbf{AGBM_s} = 21.297 - 6.953(\mathbf{D}) + 0.740(\mathbf{D}^2)$

Where **D** is the stem diameter in cm, and **AGBMs** is the estimated oven-dried AGBM for the stem in kg

Equation 2. $\mathbf{AGBM_s} = \exp(-2.134 + 2.530 * \ln(\mathbf{D}))$

Where **D** is the stem diameter in cm, and **AGBMs** is the estimated oven-dried AGBM for the stem in kg

Plot-level values of estimated aboveground biomass were then calculated by summing all estimated stem-level aboveground biomass values and converting to standard units (Mg/ha). Sixteen plots at the Panama study area contained stems whose diameters were larger than the maximum diameter used to develop the original allometric equation (Equation 2), therefore, only plots that contained stems within this regression range (<150 cm) were used in the regression analysis comparing lidar metrics with EAGB. However, all plots were used in the regression analysis involving lidar metrics and QMSD or basal area.

Lidar data

Lidar data were collected over both study areas in March 1998 using the Laser Vegetation Imaging Sensor (LVIS, Blair et al., 1999; Dubayah et al., 2000). LVIS is an airborne scanning laser altimeter that measures the roundtrip time for pulses of near-infrared laser energy to travel to the surface and back. The incident energy pulse interacts with canopy (e.g., leaves and branches) and ground features and is reflected back to a telescope on the instrument. Unlike most other laser altimeters, LVIS digitizes the entire time-varying amplitude of the backscattered energy (in 30 cm vertical bins). This yields a "waveform" or profile related to the vertical distribution of intercepted surfaces from the top of canopy to the ground within each 25 m footprint (Blair et al., 1999; Dubayah and Drake, 2000; Dubayah et al., 2000). LVIS scanned across a swath of approximately 1 km with a 50% overlap of footprints across swath, and contiguous along-track footprint spacing. At both study areas, only LVIS footprints that were entirely coincident with field plots were included.

The lidar metric that is used in this study is the height of median energy (HOME). HOME is calculated by first identifying the location of the median of the entire signal (i.e. above the noise level), including the energy from both canopy and ground surfaces (Drake et al., In press). This location is then referenced to the ground (the center of the last Gaussian pulse) to derive a height. Plot-level means for HOME were then calculated for all shots that fell within each plot.

Adjustment of lidar HOME for deciduousness in Panama

When the lidar flights occurred in late March 1998, the Panama study area was at the end of its dry season and leaf loss from canopy-forming trees was extensive in some areas. As a result, more of the lidar energy was able to penetrate through the upper canopy, thereby reducing the lidar HOME metric relative to the Costa Rica study area. To compensate for this effect, a proportional adjustment to the HOME metric was made based on the estimated fraction of crown area that was deciduous (FCAD).

The first step was to linearly interpolate between data points for precipitation and the fraction of crown area deciduous as listed in Condit et al. (2000). The relationship (Equation 3) was then used to interpolate FCAD from average precipitation values for all Panama field plots. Lidar HOME was then proportionally adjusted in these Panama plots by the fraction of crown area deciduous using the relationship in Equation 4.

Equation 3. **FCAD**= -0.02 ***Rainfall** + 60.27
where **Rainfall**=mm/yr and **FCAD**= fraction of crown area deciduous (developed from Condit et al. 2000)

Equation 4. **HOME′** = **HOME**/(1-**FCAD**)
where HOME= lidar height of median energy (m) and **FCAD**= fraction of crown area deciduous

Data analysis

A linear regression analysis was used to develop relationships between plot-level averages of lidar HOME and field-derived QMSD, basal area and EAGB for each study area. For each forest structural characteristic (e.g., QMSD), an analysis of covariance (ANCOVA) was then performed to test for significant differences in the slope and intercept of the relationships (Zar, 1996) developed for each site. This process was used for both the normal and deciduous adjusted HOME metrics.

3. RESULTS AND DISCUSSION

Lidar HOME vs. estimated aboveground biomass

The lidar metric HOME is highly correlated with estimated aboveground biomass (EAGB) in both study areas (Figure 1). In the Panama study area, the R^2 value is 0.66 for plots whose tree diameters are all within the range of the general allometric equation (Equation 2), and 0.82 for all Panama plots, with RMSE values of 31.52 Mg/ha and 39.10 Mg/ha respectively. For the Costa Rica relationship, the R^2 value is 0.89 and the RMSE is 22.54 Mg/ha.

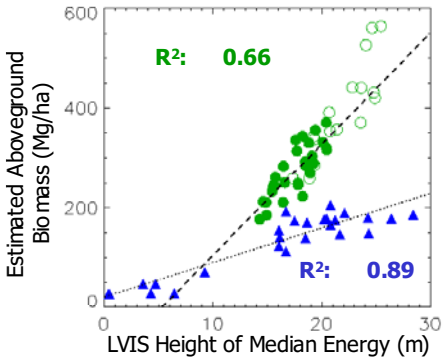

Fig 1. Regression analysis for lidar height of median energy (m) vs. plot-level allometrically-estimated aboveground biomass (Mg/ha) for study areas in Panama (circles, dashed line, upper left R^2) and Costa Rica (triangles, dotted line, lower right R^2). The open circles in the Panama regression relationship indicate plots that contain stems whose diameters are larger than the original distribution sampled to develop the allometric equation (equation 2) and were not included in the regression analysis.

However, there is a great deal of divergence between the relationships for the two study areas (Figure 1). The slope is much greater in the Panama relationship (22.33) compared to the Costa Rica relationship (6.33). The Panama regression equation also has a negative intercept, probably the result of only sampling within relatively high biomass areas. An analysis of covariance (ANCOVA) shows that the slopes and intercepts of these two equations are significantly different ($p<0.01$).

Lidar HOME vs. basal area and QMSD

Lidar HOME is strongly correlated with quadratic mean stem diameter (QMSD) in both study areas (Figure 2a). The level of variation in QMSD explained by the HOME metric (i.e., the R^2 value) is approximately 92% in the Costa Rica study area compared to 66% in the Panama study area. However, the RMSE in Panama (1.89 cm) is somewhat lower than the value from the Costa Rica relationship (2.09 cm). HOME is also strongly correlated with basal area in both areas (Figure 2b). In this case the level of variation explained is approximately equal for both areas (~70%).

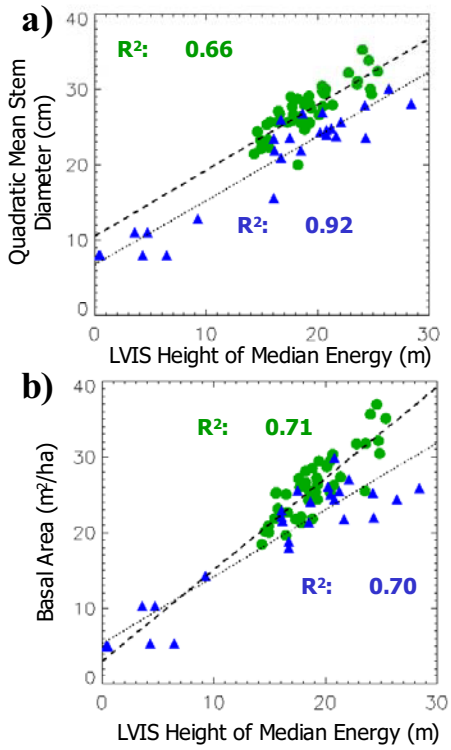

Fig 2. Regression analysis for lidar height of median energy (m) vs. **a)** plot-level quadratic mean stem diameter (cm) and **b)** plot-level basal area (m^2/ha) for study areas in Panama (circles, dashed line, upper left R^2) and Costa Rica (triangles, dotted line, lower right R^2).

The relationships between lidar HOME and QMSD (Figure 2a) and between HOME and basal area (Figure 2b) are not as divergent at the two study areas as were the relationships between HOME and EAGB (Figure 1). The slopes of the relationships between HOME and QMSD are similar at both sites, and were not found to be significantly different ($p=0.55$) in an ANCOVA analysis. Intercepts for the HOME-QMSD relationships, however, were found to be significantly different ($p<0.01$), indicating that the relationships are not equivalent between study sites. Similarly, both the slopes and the intercepts of the HOME-basal area relationships were found to be significantly different between the two study areas, however the y-intercept term in the Panama linear regression relationship was not significantly different from zero ($p=0.19$).

There are two possible reasons for differences in the HOME-basal area and HOME-QMSD relationships between study areas. First, tree diameters could be larger for a given tree height on average at Panama. An analysis of the relationship between stem diameter and stem height from both Panama (based on allometry from BCI in Bohlman et al., In review) and La Selva supports this trend (Drake et al., In review). It is possible that this individual-level relationship could influence the plot-level relationships between lidar HOME and either basal area or QMSD. A second possible explanation is that the drier conditions at Panama resulted in more leaf loss, which in turn lowered lidar HOME values. The HOME metric is determined by the vertical distribution of canopy elements (e.g., leaves and branches), therefore a reduction in leaf abundance of canopy-forming trees in drought-deciduous areas (Condit et al., 2000) would allow more energy to penetrate further into the canopy, thereby lowering the HOME value. We therefore next examine the effect of this deciduousness on the relationship between HOME and forest structural summaries.

Deciduous-adjusted HOME vs. basal area and QMSD

The relationships are much more similar between the two study areas after the proportional adjustment of HOME for the effect of leaf loss of canopy trees (Figure 3a and b). The slope and the intercept from both HOME′-QMSD relationships are not significantly different using an ANCOVA test ($p=0.85$ and 0.21 respectively). Similarly, the difference in slope from the HOME′-basal area relationships in the two study areas is smaller and not significantly different ($p=0.06$). The intercepts in the HOME′-basal area relationships were found to be significantly different ($p<0.01$) however where the data cover the same range of HOME′ and basal areas, the two point clouds now overlap more completely and appear similar (Figure 3b).

Thus, proportional adjustment of lidar HOME metrics by simple fraction of crown area deciduous values eliminated much of the difference between HOME-basal area and HOME-QMSD relationships at both Costa Rica and Panama plots. The minor remaining differences may be the result of small differences in diameter vs. height relationships in both study areas (discussed above) or a difference in the ranges of conditions studied combined with a modest nonlinearity in the underlying causal relationship. In either case, leaf loss in canopy trees at the end of the dry season in Panama was responsible for much of the difference between relationships in these two tropical regions that we found with unadjusted lidar data.

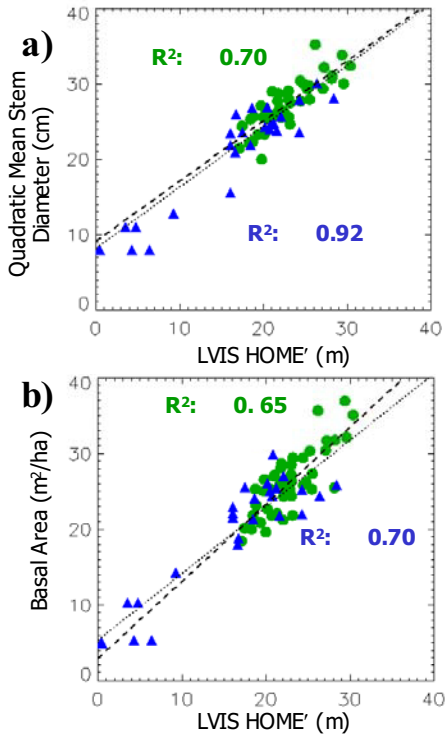

Fig 3. Regression analysis for deciduous-adjusted lidar height of median energy (m) vs. **a)** plot-level quadratic mean stem diameter (cm) and **b)** plot-level basal area (m^2/ha)for study areas in Panama (circles, dashed line, upper left R^2) and Costa Rica (triangles, dotted line, lower right R^2).

Deciduous-adjusted HOME vs. estimated aboveground biomass

The proportional adjustment of lidar HOME did not affect the strength of the relationship between HOME and EAGB at both study areas (Figure 4). The R^2 and the RMSE stayed approximately the same (66% and ~31Mg/ha respectively) after HOME values were adjusted. However, although the adjustment did slightly reduce the slope of the Panama relationship (from 22.33 to 21.46), the relationships from the two study areas were still significantly different in both slope and the intercept ($p<0.01$, from ANCOVA).

The differences in relationships between HOME′ and EAGB for the two study areas are most likely the result of using different allometric equations to estimate aboveground biomass from stem diameter in each area. At nearly the same total basal area, Panama sites are calculated to have much larger biomass than nearly all similar sites in Costa Rica (Table 1). This is despite having only minor differences in HOME′-QMSD (Figure 3a) and HOME′-basal area (Figure 3b) relationships after adjustment for leaf loss. As a result, sites at Panama and Costa Rica with nearly identical basal areas and HOME′ values may have very different EAGB values.

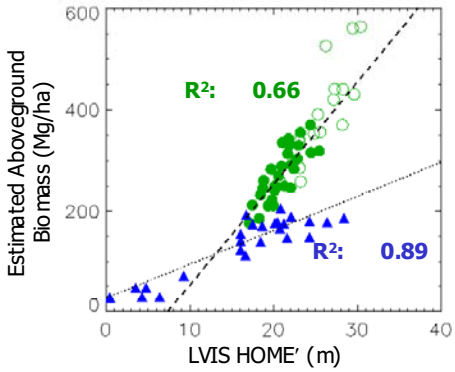

Figure 4. Regression analysis for deciduous-adjusted lidar height of median energy (m) vs. plot-level allometrically-estimated aboveground biomass (Mg/ha) for study areas in Panama (circles, dashed line, upper left R^2) and Costa Rica (triangles, dotted line, lower right R^2). The open circles in the Panama regression relationship indicate plots that contain stems whose diameters are larger than the original distribution sampled to develop the allometric equation (equation 2) and were not included in the regression analysis.

4. CONCLUSIONS

Our results show that relationships between a simple lidar metric (height of median energy) and directly measured forest structural characteristics, such as basal area and QMSD, are nearly identical at both Costa Rica and Panama study areas after accounting for the extensive leaf loss of canopy-forming trees in Panama during the study period (Figure 3a and b). There is still a subtle difference in the HOME′-basal area relationships from the two study areas that could be attributable to differences in the individual-level diameter vs. height allometric relationships for the two sites. Nevertheless, these results illustrate that the same lidar metric, HOME, is strongly correlated with basal area and QMSD. In addition, the relationships appear to be general across both tropical wet and tropical moist forest life zones.

The relationships between lidar metrics and allometrically estimated aboveground biomass are significantly different, however, for these two study areas. Although adjustment for leaf loss slightly improved the agreement between the two site-specific relationships, the two different allometric equations (Equations 1 and 2) used to estimate aboveground biomass lead to significant differences at both study areas.

An assessment of the applicability of these general allometric equations vs. locally-derived allometric equations (cf. Keller et al., In Press) would be beneficial because remotely sensed estimates of biomass (and carbon) are ultimately dependent on allometric relationships. We therefore join with other authors (Brown et al., 1995; Clark and Clark, 2000) who have called for more destructive sampling, especially of sparsely sampled large trees, in different tropical life zones to more rigorously assess the robustness of general allometric equations. Ultimately, this will allow for better broad-scale, remotely sensed aboveground biomass estimates.

Assuming that the general allometric equations used in this study are reasonably accurate, these results have significant implications for how global observations from future spaceborne lidar instruments (e.g., VCL) should be used to produce global estimates of terrestrial aboveground biomass. Our results show that it will likely be necessary to develop unique relationships between lidar metrics and aboveground biomass in different bioclimatic life zones.

Future work in other tropical and extra-tropical forest environments may reveal that it is possible to develop a relatively simple algorithm or model to estimate terrestrial aboveground biomass globally from a suite of lidar and climatic metrics. In more open tropical woodlands, it is likely that additional lidar metrics such as canopy top height and a canopy cover index will be necessary to estimate aboveground biomass accurately. We also expect that the fusion of lidar data with high spatial and temporal satellite imagery will further extend the utility of these data.

ACKNOWLEDGEMENTS

We thank J. Bryan Blair, David Rabine, Michelle Hofton, Nancy Casey-McCabe and Dave Kendig for their help in collecting and processing the LVIS data. We thank Robin Chazdon for the use of her secondary forest field data. We are especially grateful to all those who were involved in the collection of the field data at both study areas. We also thank S. Hubbell and R. Foster for initiating the BCI 50 ha plot. Our special thanks also go to the the Organization for Tropical Studies, the Carbono Project (funded by DOE, NSF and the Andrew W. Mellon Foundation), the Center for Tropical Forest Science of the Smithsonian Tropical Research Institute, the Wallops Flight Facility Aircraft Programs Office, the National Geographic Institute of Costa Rica and the Governments of Costa Rica and Panama. This project is funded by a NASA contract to the University of Maryland for the implementation and execution of the Vegetation Canopy Lidar Mission under the Earth System Science Pathfinder program. In addition, J. Drake is funded through a NASA Earth System Science Fellowship.

REFERENCES

Aber, J. D., 1979. Foliage-height profiles and succession in Northern hardwood forests. *Ecology,* 60: 18-23.

Blair, J. B., and Hofton, M. A., 1999. Modeling laser altimeter return waveforms over complex vegetation using high-resolution elevation data. *Geophysical Research Letters,* 26: 2509-2512.

Blair, J. B., Rabine, D. L., and Hofton, M. A., 1999. The Laser Vegetation Imaging Sensor (LVIS): A medium-altitude, digitization-only, airborne laser altimeter for mapping vegetation and topography. *ISPRS Journal of Photogrammetry and Remote Sensing,* 54: 115-122.

Bohlman, S. A., Condit, R., O'Brien, S. T., Foster, R. B., and Hubbell, S. P., In review. Using species-specific allometric equations to predict canopy structure on Barro Colorado Island, Panama.

Bormann, B. T., and Likens, G. E. 1979. *Pattern and Process in a Forested Ecosystem*. Springer-Verlag, New York.

Brown, I. F., Martinelli, L. A., Thomas, W. W., Moreira, M. Z., Ferreira, C. A. C., and Victoria, R. A., 1995. Uncertainty in the biomass of Amazonian forests: An example from Rondonia, Brazil. *Forest Ecology and Management,* 75: 175-189.

Brown, S. 1997. Estimating biomass and biomass change of tropical forests: A primer. *UN-FAO Forestry Paper 134*, Rome, Italy.

Clark, D. B., and Clark, D. A., 2000. Landscape-scale variation in forest structure and biomass in a tropical rain forest. *Forest Ecology and Management,* 137: 185-198.

Condit, R. 1998. *Tropical Forest Census Plots*. Springer-Verlag, Berlin, Germany.

Condit, R., Watts, K., Bohlman, S. A., Perez, R., Foster, R. B., and Hubbell, S. P., 2000. Quantifying the deciduousness of tropical forest canopies under varying climates. *Journal of Vegetation Science,* 11: 649-658.

Drake, J. B., Dubayah, R. O., Clark, D. B., Knox, R. G., Blair, J. B., Hofton, M. A., Chazdon, R. L., Weishampel, J. F., and Prince, S., In press. Estimation of tropical forest structural characteristics using large-footprint lidar. *Remote Sensing of Environment*.

Drake, J. B., Knox, R., Dubayah, R., Clark, D., and Condit, R., In review. Aboveground biomass estimation in closed-canopy Neotropical forests using lidar remote sensing: Factors affecting generality of relationships. *Global Ecology and Biogeography*.

Dubayah, R., Blair, J. B., Bufton, J. L., Clark, D. B., JaJa, J., Knox, R. G., Luthcke, S. B., Prince, S., and Weishampel, J. F. 1997. The Vegetation Canopy Lidar mission. Pages 100-112. *Land Satellite Information in the Next Decade II: Sources and Applications*. American Society for Photogrammetry and Remote Sensing, Bethesda, MD.

Dubayah, R. O., and Drake, J. B., 2000. Lidar remote sensing for forestry. *Journal of Forestry,* 98: 44-46.

Dubayah, R. O., Knox, R. G., Hofton, M. A., Blair, J. B., and Drake, J. B., 2000. Land surface characterization using lidar remote sensing. Pages 25-38 in M. J. Hill and R. J. Aspinall, eds. *Spatial Information for Land Use Management.* Gordon and Breach Science Publishers, Australia.

Foley, J. A., Prentice, I. C., Ramankutty, N., Levis, S., Pollard, D., Sitch, S., and Haxeltine, A., 1996. An integrated biosphere model of land surface processes, terrestrial carbon balance, and vegetation dynamics. *Global Biogeochemical Cycles,* 10: 603-628.

Franco, M., and Kelly, C. K., 1998. The interspecific mass-density relationship and plant geometry. *Proceedings of the National Academy of Sciences, USA,* 95: 7830-7835.

Friend, A. D., Stevens, A. K., Knox, R. G., and Cannell, M. G. R., 1997. A process-based, terrestrial biosphere model of ecosystem dynamics (Hybrid v3.0). *Ecological Modelling,* 95: 249-287.

Givnish, T. J., 1986. Biomechanical constraints on self-thinning in plant populations. *Journal of Theoretical Biology,* 119: 139-146.

Guariguata, M. R., Chazdon, R. L., Denslow, J. S., Dupuy, J. M., and Anderson, L., 1997. Structure and floristics of secondary and old-growth forest stands in lowland Costa Rica. *Plant Ecology,* 132: 107-120.

Harding, D. J., Lefsky, M. A., Parker, G. G., and Blair, J. B., 2001. Laser altimeter canopy height profiles: Methods and validation for closed-canopy, broadleaf forests. *Remote Sensing of Environment,* 76: 283-297.

Holdridge, L. R., Grenke, W. C., Hatheway, W. H., Liang, T., and J. A. Tosi, J. 1971. *Forest Environments in Tropical Life Zones: A Pilot Study*. Pergamon Press, New York, NY.

Houghton, R. A., 1991. Tropical deforestation and atmospheric carbon dioxide. *Climatic Change,* 19: 99-118.

Hurtt, G. C., Moorcroft, P. R., Pacala, S. W., and Levin, S. A., 1998. Terrestrial models and global change: challenges for the future. *Global Change Biology,* 4: 581-590.

Keller, M., Palace, M., and Hurtt, G. C., In Press. Biomass estimation in the Tapajos National Forest, Brazil: Examination of sampling and allometric uncertainties. *Forest Ecology and Management*.

Kimmins, J. P. 1997. *Forest Ecology: A Foundation for Sustainable Management*. Prentice-Hall, Inc., Upper Saddle River, NJ.

King, D., and Loucks, O. L., 1978. The theory of tree bole and branch form. *Radiation and Environmental Biophysics,* 15: 141-165.

Laurance, W. F., Fearnside, P. M., Laurance, S. G., Delamonica, P., Lovejoy, T. E., Rankin-de Merona, J., Chambers, J. Q., and Gascon, C., 1999. Relationship between soils and Amazon forest biomass: A landscape-scale study. *Forest Ecology and Management,* 118: 127-138.

Lefsky, M. A., Harding, D., Cohen, W. B., Parker, G., and Shugart, H. H., 1999. Surface lidar remote sensing of basal area and biomass in deciduous forests of eastern Maryland, USA. *Remote Sensing of Environment,* 67: 83-98.

Lieberman, D., Lieberman, M., Peralta, R., and Hartshorn, G. S., 1996. Tropical forest structure and composition on a large-scale altitudinal gradient in Costa Rica. *Journal of Ecology,* 84: 137-152.

Magnussen, S., Eggermont, P., and LaRiccia, V. N., 1999. Recovering tree heights from airborne laser scanner data. *Forest Science,* 45: 407-422.

McDade, L. A., Bawa, K. S., Hespenheide, H. A., and Hartshorn, G. S., eds. 1994. *La Selva: Ecology and Natural History of a Neotropical Rain Forest.* University of Chicago Press, Chicago.

Means, J. E., Acker, S. A., Harding, D. J., Blair, J. B., Lefsky, M. A., Cohen, W. B., Harmon, M. E., and McKee, W. A., 1999. Use of large-footprint scanning airborne lidar to estimate forest stand characteristics in the Western Cascades of Oregon. *Remote Sensing of Environment,* 67: 298-308.

Menalled, F. D., Kelty, M. J., and Ewel, J. J., 1998. Canopy development in tropical tree plantations: A comparison of species mixtures and monocultures. *Forest Ecology and Management,* 104: 249-263.

Nelson, R., Krabill, W., and Tonelli, J., 1988. Estimating forest biomass and volume using airborne laser data. *Remote Sensing of Environment,* 24: 247-267.

Nicotra, A. B., Chazdon, R. L., and Iriarte, S. V. B., 1999. Spatial heterogeneity of light and woody seedling regeneration in tropical wet forests. *Ecology,* 80: 1908-1926.

Oliver, C. D., and Larson, B. C. 1990. *Forest Stand Dynamics*. McGraw Hill, New York.

O'Neill, R. V., and DeAngelis, D. L., 1981. Comparative productivity and biomass relations of forest ecosystems. Pages 411-449 in D. E. Reichle, ed. *Dynamic properties of forest ecosystems*. Cambridge University Press, Cambridge.

Oohata, S., and Shinozaki, K., 1979. A statical model of plant form– Further analysis of the pipe model theory. *Japanese Journal of Ecology,* 29: 323-335.

OTS, Organization for Tropical Studies 2001 La Selva Biological Station: Meterological data (1957-2001), Available at: http://www.ots.duke.edu/en/laselva/

Pierce, S., 1992. La Selva Biological Station history: colonization/landuse/deforestation of Sarapiqui, Costa Rica. M.S. thesis, Colorado State University. Fort Collins, CO.

Potter, C. S., 1999. Terrestrial biomass and the effects of deforestation on the global carbon cycle - Results from a model of primary production using satellite observations. *Bioscience,* 49: 769-778.

Pyke, C. R., Condit, R., Aguilar, S., and Lao, S., In press. Floristic composition across a climatic gradient in a neotropical lowland forest. *Journal of Vegetation Science*.

Richards, P. W. 1996. *The Tropical Rain Forest: An Ecological Study*. Cambridge University Press, New York.

Sanford Jr., R. L., Paaby, P., Luvall, J. C., and Phillips, E., 1994. Climate, geomorphology and aquatic systems. Pages 106-119 in L. A. McDade, K. S. Bawa, H. A. Hespenheide, and G. S. Hartshorn, eds. *La Selva: Ecology and Natural History of a Neotropical Rain Forest.* University of Chicago Press, Chicago.

Schutz, B. E., 1998. Spaceborne laser altimetry: 2001 and beyond. in H. P. Plag, ed. *Book of Extended Abstracts, WEGENER-98.* Norwegian Mapping Authority, Honefoss, Norway.

Yamakura, T., Kanzaki, M., Itoh, A., Ohkubo, T., Ogino, K., Chai, E., Lee, H. S., and Ashton, P. S., 1996. Forest structure of a tropical rain forest at Lambir, Sarawak with special reference to the dependency of its physiognomic dimensions on topography. *Tropics,* 6: 1-18.

Zar, J. H. 1996. *Biostatistical Analysis*. Prentice-Hall, Upper Saddle River, NJ.

Lidar Remote Sensing of Aboveground Biomass in Three Biomes

M.A. Lefsky
Oregon State University
Forest Sciences Laboratory
3200 SW Jefferson Way
Corvallis, OR, 97331
lefsky@fsl.orst.edu

Warren B. Cohen
USDA Forest Service, Forest Sciences Laboratory
3200 SW Jefferson Way, Corvallis, OR, 97331

David J. Harding
Goddard Space Flight Center, Geodynamics Branch
Mail Code 921, Greenbelt, MD 20771

Geoffery G. Parker
Smithsonian Environmental Research Center
P.O. Box 28, Edgwater, MD 21037

Steven A. Acker
National Park Service
909 First Avenue, Seattle, WA, 98104

S. Thomas Gower
Department of Forest Ecology and Management
University of Wisconsin, Madison, WI, 53706

Commission III, Working Group 3

KEY WORDS: Laser altimetry, lidar, forest, biomass

ABSTRACT

Estimation of the amount of carbon stored in forests is a key challenge for understanding the global carbon cycle, one which remote sensing is expected to help address. However, direct estimation of carbon storage in moderate to high biomass forests is difficult for conventional optical and radar sensors. Lidar (light detection and ranging) instruments measure the vertical structure of forests and thus hold great promise for remotely sensing the quantity and spatial organization of forest biomass. In this study, we compare the relationships between lidar-measured canopy structure and coincident field measurements of aboveground biomass at sites in the temperate deciduous, temperate coniferous, and boreal coniferous biomes. A single "simplified" regression for all three sites is compared with equations derived for each site individually. The simplified equation explains 84% of variance in aboveground biomass ($p<0.0001$) and shows no statistically significant bias in its predictions for any individual site.

INTRODUCTION

Accurate estimates of terrestrial carbon storage over large areas are required to determine its role in the global carbon cycle, estimate the degree that anthropogenic disturbance (i.e., land use / land cover change) is changing that cycle, and for monitoring mitigation efforts that rely on carbon sequestration through reforestation. Remote sensing has been a key technology involved in existing efforts to monitor carbon storage and fluxes (Cohen et al. 1996, Running et al. 1999), and has been identified as a likely tool for monitoring carbon related treaties such as the Kyoto protocol (Ahern et al. 1998).

Nevertheless, direct estimation of carbon storage in moderate to high biomass forests remains a major challenge for remote sensing. While remote sensing has had considerable success in measuring the biophysical characteristics of vegetation in areas where plant canopy cover is relatively sparse, quantification of vegetation structure where leaf area index (LAI) exceeds three has been less successful (Carlson and Ripley 1997, Turner et al. 1999, Waring et al. 1995). High LAI forests, which generally have high aboveground biomass, occur in the boreal, temperate and tropical regions. These forests cover less than 35 % of the Earth's terrestrial surface, yet account for 67 % of terrestrial NPP, and 89 % of terrestrial biomass (Waring and Schlesinger 1985). Given their prominent role in global biogeochemistry, and the likelihood that these high productivity areas will be prime areas for carbon sequestration efforts, better characterization of high biomass forests using remotely sensed data is desirable. One promising technique is lidar.

	Number of Plots	Mean	Minimum	Maximum
Canopy Cover (m^2m^{-2})				
Temperate Deciduous	112	0.853	0.607	0.938
Temperate Coniferous	21	0.696	0.285	0.876
Boreal Coniferous	16	0.312	0.168	0.472
Mean Canopy Height (m)				
Temperate Deciduous		28.6	9.7	39.5
Temperate Coniferous		35.6	15.3	53.2
Boreal Coniferous		7.3	2.2	11.0
Aboveground Biomass ($Mgha^{-1}$)				
Temperate Deciduous		312.5	11.4	716.3
Temperate Coniferous		602.0	135.6	1329.0
Boreal Coniferous		29.9	0.0	58.5

Table 1. Plot Characteristics

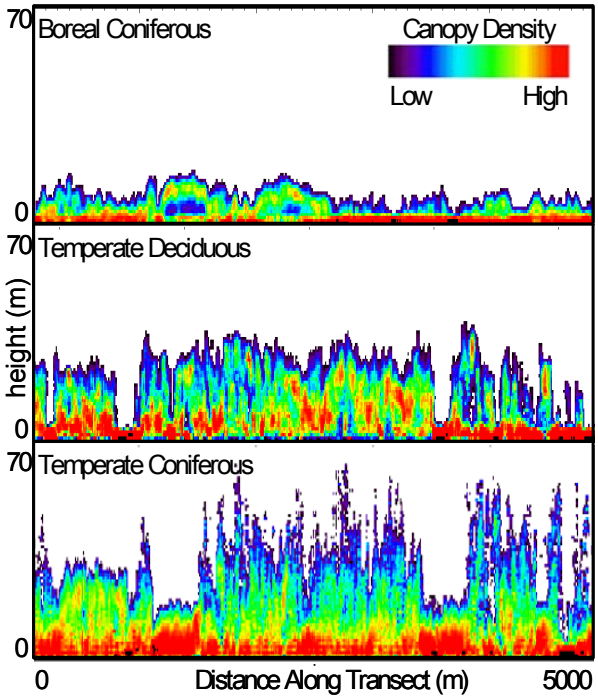

Figure 1. Measurements of canopy structure made using NASA's SLICER (Scanning Lidar Imager of Canopies by Echo Recovery) remote sensing device. SLICER operates by measuring the vertical distribution of energy returned to the sensor when a short-duration pulse of laser light is reflected off the forest canopy. Data are then transformed to correct for the occlusion of far surfaces by those closer to the instrument to create an estimate of canopy density (yellow and red indicate high canopy density, blue and black indicate low canopy density) . Top panel shows data from a boreal coniferous sites in northern Manitoba, with simple canopy structure and maximum heights of 18 m. Middle panel shows data from a temperate deciduous forest near Annapolis, MD., with regenerating gaps and complex canopy structure. Bottom panel shows data from a temperate coniferous forest on the western slope of the Cascades in Oregon, and shows both younger (shorter) stands with simple canopy structure, and an old-growth forest (middle third of panel) with extremely complex canopy structure and especially high diversity of canopy heights.

Lidar instruments directly measure the vertical structure of forests by estimating the distance between the sensor and a target through the precise measurement of the time between the emission of a pulse of laser light from the sensor and the time of detection of light reflected from the target. Waveform-sampling lidar systems, such as the SLICER device used in this work (Blair et al. 1994, Harding et al. 1994, Harding et al. 2001) and the VCL satellite (Dubayah et al. 1997) now scheduled for launch in 2003, employ multiple measurements of both distance to and amount of energy reflected from the many surfaces of a geometrically complex target. When this distribution of return energy, the lidar waveform, is measured over a vegetation canopy, it records the vertical distribution of light reflected back to the sensor from vegetation and soil surfaces from the top of the canopy to the ground. For forests, relating these waveforms to conventional, primarily non-spatial, measurements of forest structure, such as aboveground biomass and stand basal area, has been a primary research goal (Drake et al. 2001, Lefsky et al. 1999a, Lefsky et al. 1999b, Means et al. 1999). In this study, we compare the relationships between lidar-measured canopy structure and coincident field measurements of aboveground biomass at sites in the temperate deciduous, temperate coniferous, and boreal coniferous biomes. A single equation derived from regression analysis using data from all three sites is compared with equations derived for each site individually. The goal of the work is a simplified method to estimate aboveground biomass at all three sites. The existence of such a method could reduce the amount of fieldwork, with attendant effort and expense, required to develop global biomass estimates from satellite lidar data. We focus on the estimation of aboveground biomass because it is closely related to aboveground carbon storage, and allometric equations for its estimation are readily available. While belowground carbon pools are often as large or larger than aboveground storage, no existing remote sensing system can estimate their magnitude directly.

METHODS

Coincident field plots and lidar data were collected in three distinct sites in the boreal coniferous (Northern BOREAS study area), temperate coniferous (H.J. Andrews Experimental Forest) and temperate deciduous (Smithsonian Environmental Research Center) biomes. Estimates of aboveground biomass were calculated using established allometric equations using stem data collected using fixed or nested plot designs. Estimates of canopy height, canopy cover and a variety of canopy density weighted heights were calculated from the lidar data.

	Boreal Coniferous	Temperate Deciduous	Temperate Coniferous	ALL
Canopy Cover (%)	0.837	0.112 n.s.	0.633 †	0.372
Maximum Height (m)	0.665 †	0.765	0.909	0.885
Mean Canopy Height (m)	0.743 ††	0.792	0.92	0.868
Mean Canopy Height Squared (m)	0.701 †	0.79	0.929	0.914
Mean Canopy Profile Height (m)	0.781 †	0.746	0.774	0.812
Quadratic Mean Canopy Profile Height (m)	0.741 ††	0.804	0.825	0.841
Cover x Maximum Height (m)	0.853	0.744	0.921	0.839
Cover x Mean Canopy Height (m)	0.872	0.509	0.923	0.662
Cover x Mean Canopy Profile Height (m)	0.877	0.716	0.810	0.761
Cover x Quadratic Canopy Profile Height (m)	0.874	0.773	0.854	0.785

Unless otherwise noted, all relationships are significant at P<0.0001
† Denotes P<0.01
†† Denotes P<0.001

Table 2. Correlation coefficients (r) between height indices and aboveground biomass.

Study Areas

Field data for the temperate coniferous plots were collected in and near the H.J. Andrews Experimental Forest, located on the west slope of the Cascade Range in Oregon (Van Cleve and Martin 1991). Douglas-fir (*Pseudotsuga menziesii*) is the dominant species in these stands, contributing 90 % of all basal area in young stands, and 64 % in old-growth stands. Western hemlock (*Tsuga heterophylla*) in the second most important species, and occurs mostly in later succession, contributing 29 % of total basal area in old-growth stands (Lefsky et al. 1999a). Data from temperate deciduous plots were collected in and near the Smithsonian Environmental Research Center, located on the western shore of Chesapeake Bay, near Annapolis, MD. They are mixed deciduous forest with an overstory dominated by *Liriodendron tulipifera* (Lefsky et al. 1999b). Plots for the boreal coniferous type were collected at the Northern Old Black Spruce (NOBS) study area established as part of NASA's BOREAS study; plot data was collected as part of the BigFoot study (Cohen and Justice 1999). Major cover types at the site include muskeg, black spruce (*Picea mariana*) forest, and wetlands; infrequent patches of jack pine (*Pinus banksiana*) and aspen (*Populus tremuloides*) also occur.

Field Data Collection

Existing publications describe the field data collections for the boreal coniferous (Campbell et al. 1999), temperate deciduous (Lefsky et al. 1999b) and temperate coniferous stands (Lefsky et al. 1999a). Generally, fixed or nested plots were used to tally stems, and appropriate allometric equations were used to predict aboveground biomass. At the boreal coniferous site, the 25 x 25 m field plots put in as part of the BigFoot (Cohen and Justice 1999) study were used as a source of field data. The location of existing SLICER waveforms were compared to the locations of 107 field plot and any plot with more that 5 waveforms within its boundaries was considered as part of this analysis, a total of 16 plots.

SLICER Data Collection and Processing

SLICER data were collected at the temperate coniferous, boreal coniferous and temperate deciduous sites in September 1995, July 1996, and September 1997, respectively. To estimate canopy height profiles (CHPs, the vertical distribution of foliage and woody surfaces) from the raw SLICER waveforms, we adapted (Harding et al. 2001) the transformation method developed by MacArthur and Horn (MacArthur and Horn 1969). The resulting CHPs serve as a common measurement of forest canopy structure at the three sites. One key factor in the CHP algorithm is a coefficient calculated as the ratio of the average reflectance (at 0° phase angle) of the ground and canopy at the laser wavelength. For the temperate deciduous and temperate coniferous sites, the ratio of ground and canopy reflectance is assumed to be 2.0. Use of this assumption has been supported by fieldwork comparing lidar estimates and field measurements of canopy cover at these sites (Lefsky 1997, Means et al. 1999). At the boreal coniferous site, the existence of a high ground-level cover of herbaceous and fern species and a small dataset of coincident lidar and field measurements of cover imply that this ratio should be close to 1.0, the value used in calculations for this site.

Canopy structure indices used in this study were calculated from CHPs (Lefsky et al. 1999a). Measurements of mean canopy height are not available from the field measurements of canopy structure made at some of the temperate deciduous plots; a regression between quadratic mean canopy height and mean canopy surface height was developed using the another set of plots at the same site, and applied to these plots to predict mean canopy height.

RESULTS

Plot Characteristics

Mean canopy height at the sites follows the expected order, with boreal coniferous having the shortest maximum and mean heights, temperate coniferous having the tallest, with the temperate deciduous site in the middle (Table 1). Values for

canopy cover for the temperate deciduous site occupy a narrower range than either of the coniferous sites due to the high cover associated with even the youngest of these sites, and the absence of significant disturbance. Mean, minimum and maximum cover are lowest in the boreal coniferous plots, as a consequence of the low productivity of this site, and the juxtaposition of closed forest

and open forest / muskeg conditions. Site maxima for aboveground biomass range from 58.5 Mg ha^{-1} for the boreal coniferous plots to 1329.0 Mg ha^{-1} for the temperate coniferous forest; again the temperate deciduous plots occupy an intermediate position. Figure 1 illustrates characteristic transects of lidar measured canopy structure at each study site.

Correlation of Canopy Structure Indices and Aboveground Biomass

Nearly all the canopy structure indices were significantly correlated with aboveground biomass (Table 2), with the exception of canopy cover for temperate deciduous plots. This is likely due to the narrow range of canopy cover conditions observed in those plots. Otherwise, there were few patterns in the correlations that were consistent between all three biomes. For the boreal coniferous site, the product of cover and several of the height indices performed better than the height indices alone. At the temperate deciduous site, the reverse was true, again probably due to the low range of canopy cover, and the resulting non-significant correlation between cover and biomass. At the temperate coniferous site, no clear difference between the two sets of indices is clear. When all sites are considered together, mean height squared is the best overall predictor of aboveground biomass.

Regression Analysis

The correlation analysis identified the mean height squared as the variable with the highest correlation with aboveground biomass for all sites considered together. Analysis of the residuals of the resulting equation

$$AB = 0.378*MCH2, \quad (r^2=84\%, P<0.0001)$$

where:

AB is aboveground biomass (Mgha-1), and

MCH^2 is mean canopy height (m) squared.

Analysis of the residuals resulting from the equation indicates that product of Mean Canopy Height and Cover had the highest correlation (r=0.18) with those residuals, and this variable was added to the equation, resulting in

$$AB= 0.342* MCH^2 + 2.086*COVCHPX, \quad (R^2=0.84, P<0.0001)$$

where:

COVCHPX is the product of mean cover and mean canopy height.

Although the addition of the COVCHPX variable does not improve the overall fit of the model, it does improve the residuals associated with the boreal sites, and so it was left in. Regressions between the predicted values from this equation and the observed aboveground biomass were calculated separately for each site, and tested to see if the resulting regression lines were significantly different from an identify line (Figure 2). In all three cases, neither the slope nor intercepts were significant different (Table 3). Stepwise multiple regression was also performed for each site individually, and the resulting R^2 are presented in Table 3. Only in the case of the boreal coniferous site did the general equation predict considerably less of the overall variance than did the individual site equation.

DISCUSSION

The results of this study indicate that a single equation can be used to relate remotely sensed canopy structure to aboveground biomass in three distinctly different forested communities. Clearly, this result must be considered preliminary. Tropical systems are not discussed at all, and ultimately it would be necessary to have replicated studies from each climatic and physiognomic zone before the implied hypothesis-- that this result is applicable to forested ecosystems generally—could be accepted. The primary value of this work, in our opinion, is that it indicates that research into that hypothesis is reasonable. Forests of the type describe in this paper cover 16% of the global land surface, and 50% of the forested land surface. If the relationship between forest canopy structure and the aboveground biomass contained within are as consistent as suggested in this study, then the estimation of global forest carbon storage, and the monitoring of its change in time, may be greatly simplified. Adoption of a modeling approach would further improve the confidence associated with a simplified relationship. Simple models, starting with the known allometric properties of plants, and incorporating competition for light and space, have already demonstrated that they can reproduce emergent community level relationships (Enquist and Niklas 2001). Such an approach should be adaptable to this problem, and could provide the necessary confidence to interpret the global dataset anticipated from the Vegetation Canopy Lidar mission, with a minimum of additional fieldwork.

	Intercept (b_0)	Slope (b_1)	$P(b_0 \neq 0)$	$P(b_1 \neq 1)$	Simplified Equation R^2	Individual Site Equation R^2
Boreal Coniferous	10.11	0.75	0.09	0.19	56%	76%
Temperate Deciduous	11.10	0.93	0.62	0.29	65%	65%
Temperate Coniferous	61.55	0.98	0.30	0.81	87%	87%
All	-3.34	1.01	0.81	0.84		

Table 3. Slope and intercepts of general biomass equation applied to each site individually, Observed=B_0+ (B_1 x Predicted)

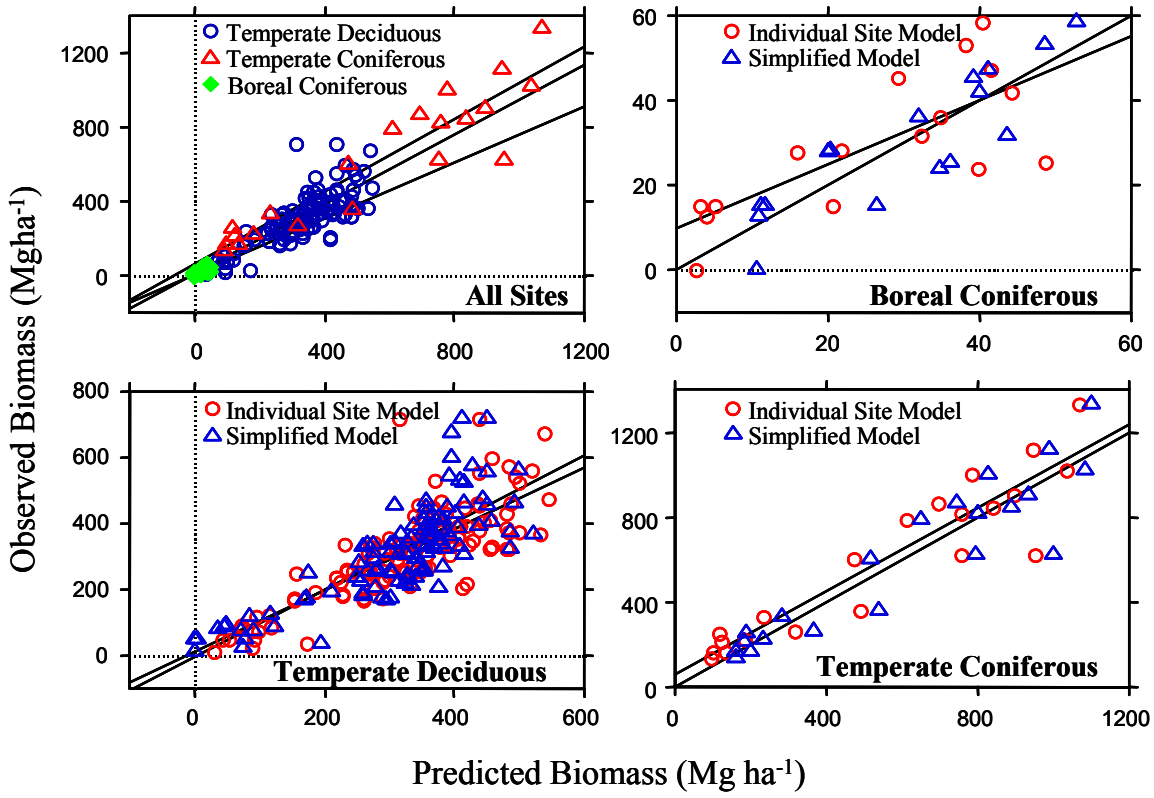

Figure 2. Comparison of predicted and observed aboveground biomass from simplified and individual equations for all sites (upper-left), and each site separately.

REFERENCES

Ahern, F. J., A. C. Janetos, and E. Langham. 1998. Global Observation of Forest Cover: one component of CEOS' Integrated Global Observing Strategy. Pages 1-5. *27th International Symposium on Remote Sensing of Environment*, Tromsø, Norway.

Blair, J. B., D. B. Coyle, J. L. Bufton, and D. J. Harding. 1994. Optimization of an airborne laser altimeter for remote sensing of vegetation and tree canopies. *Proceedings of IGARSS'94.*

Campbell, J., S. Burrows, S. Gower, and C. WB. 1999. Bigfoot: Characterizing land cover, LAI, and NPP at the Landscape Scale for EOS/MODIS Validation. Field Manual 2.1. Oak Ridge National Laboratory, Environmental Science Division.

Carlson, T. N., and D. A. Ripley. 1997. On the relation between NDVI, fractional vegetation cover, and leaf area index. *Remote Sensing of Environment* 62: 241-252.

Cohen, W. B., M. E. Harmon, D. O. Wallin, and M. Fiorella. 1996. Two decades of carbon flux from forests of the Pacific Northwest. *Bioscience* 46: 836-844.

Cohen, W. B., and C. O. Justice. 1999. Validating MODIS terrestrial ecology products: linking in situ and satellite measurements. *Remote Sensing of Environment* 70: 1-3.

Drake, J., R. Dubayah, D. Clark, R. Knox, J. Blair, M. Hofton, R. Chazdon, J. Weishample, and S. Prince. 2001. Estimation of tropical forest structural characteristics using large-footprint lidar. *Remote Sensing of Environment* In Press.

Dubayah, R., J. B. Blair, J. L. Bufton, D. B. Clark, J. JaJa, R. Knox, S. B. Luthcke, S. Prince, and J. Weishample. 1997. The Vegetation Canopy Lidar Mission. Pages 100-112. *Land Satellite Information in the Next Decade II: Sources and Applications*. ASPRS, Washington D.C.

Enquist, B., and K. J. Niklas. 2001. Invariant scale relations across tree-dominated comunities. *Nature* 410: 655-660.

Harding, D. J., J. B. Blair, J. G. Garvin, and W. T. Lawrence. 1994. Laser altimeter waveform measurement of vegetation canopy structure. *Proceedings of IGARSS'94.*

Harding, D. J., M. A. Lefsky, G. G. Parker, and J. B. Blair. 2001. Lidar Altimeter Canopy Height Profiles: Methods and Validation for Closed Canopy, Broadleaf Forests. *RSE* 76: 283-297.

Lefsky, M. A. 1997. Application of lidar remote sensing to the estimation of forest canopy and stand structure. *Department of Environmental Science,*. University of Virginia, Charlottesville, Virginia.

Lefsky, M. A., W. B. Cohen, S. A. Acker, G. G. Parker, T. A. Spies, and D. Harding. 1999a. Lidar remote sensing of the canopy

structure and biophysical properties of Douglas-fir western hemlock forests. *Remote Sensing of Environment* 70: 339-361.

Lefsky, M. A., D. Harding, W. B. Cohen, G. Parker, and H. H. Shugart. 1999b. Surface lidar remote sensing of basal area and biomass in deciduous forests of eastern Maryland, USA. *Remote Sensing of Environment* 67: 83-98.

MacArthur, R. H., and H. S. Horn. 1969. Foliage profile by vertical measurements. *Ecology* 50: 802-804.

Means, J. E., S. A. Acker, D. A. Harding, B. J. Blair, M. A. Lefsky, W. B. Cohen, M. Harmon, and W. A. McKee. 1999. Use of large-footprint scanning airborne lidar to estimate forest stand characteristics in the western Cascades of Oregon. *Remote Sensing of Environment* 67: 298-308.

Running, S. W., D. D. Baldocchi, D. P. Turner, S. T. Gower, P. S. Bakwin, and K. A. Hibbard. 1999. A global terrestrial monitoring network integrating tower fluxes, flask sampling, ecosystem modeling and EOS data. *Remote Sensing of Environment* 70: 108-127.

Turner, D., W. Cohen, R. Kennedy, K. Fassnacht, and J. Briggs. 1999. Relationship between leaf area index and Landsat TM spectral vegetation indices across three temperate zone sites. *Remote Sensing of Environment* 70: 52-68.

Van Cleve, K., and S. Martin. 1991. Long-term ecological research in the United States. Long-Term Ecological Research Network Office.

Waring, R. H., and W. H. Schlesinger. 1985. *Forest Ecosystems: Concepts and Management*. Academic Press, Orlando, Florida.

Waring, R. H., J. Way, E. R. Hunt, L. Morrissey, K. J. Ranson, J. F. Weishampel, R. Oren, and S. E. Franklin. 1995. Imaging radar for ecosystem studies. *BioScience* 45: 715-723.

LAND SURFACE MAPPING AND CHARACTERIZATION USING LASER ALTIMETRY

SESSION 7

MAPPING GEOSURFICIAL PROCESSES

LASER MONITORING OF ICE ELEVATIONS AND SEA-ICE THICKNESS IN GREENLAND

R. Forsberg, K. Keller, S. M. Jacobsen
Geodynamics Dept., National Survey and Cadastre (KMS)
Rentemestervej 8, DK-2400 Copenhagen NV, Denmark
rf@kms.dk

KEY WORDS: Laser altimetry, laser scanning, SAR interferometry, glaciers, sea-ice.

ABSTRACT

A low-cost Twin-Otter based laser altimetry and scanning system have been set up by KMS in several different commercial aircraft, and flown extensively in connection with airborne gravity activities in the Arctic Ocean north of Greenland, as well as on various research projects on the ice sheet and coastal glaciers in Greenland. The hardware system is based on a Riegl laser swath scanner or Optech laser altimeter combined with numerous GPS receivers. Roll and pitch are provided by either a medium-grade commercial INS or a low-cost custom-made IMU with fiber-optics gyros. The whole system is designed for use on non-dedicated aircraft, with a minimum of set-up time. In the paper we outline the hardware setup, processing schemes and give some examples of field campaigns and estimated accuracies. Measurements over sea-ice in the Polar Sea north of Greenland have shown that sea-ice freeboard can readily be measured combining laser altimetry and a local geoid model, yielding an indirect measurement of sea-ice thickness. Over land ice laser results have, a.o., been used to study radar penetration effects of airborne SAR interferometry, showing large height-dependent variations, corresponding to changes in snow facies.

1 INTRODUCTION

Airborne remote sensing is an efficient way to determine the elevations of the Greenland ice sheet, the surface elevations representing a delicate balance between ice flow, firn compaction, precipitation, and ice flow. The heights of the ice sheet may be determined by numerous methods: GPS and surface surveys, satellite altimetry, airborne laser altimetry and airborne or satellite SAR interferometry. Each of the methods has different accuracy and effective footprint size, and the radar methods further have varying degree of penetration into the firn.

In this paper we will primarily describe the gradual evolvement of a low-cost, easy-to-install airborne remote sensing system, used in commercial non-dedicated charter aircraft. The system has evolved slowly since 1996 based on experience from an airborne gravity and geoid project (AGMASCO, cf. Forsberg et al., 1996), smaller national Danish ice sheet mapping projects (Keller et al., 1997; Lintz et al., 1999), and a major program to map the marine areas around Greenland and Svalbard with airborne gravimetry, carried out with support mainly from the US National and Imagery Mapping Agency (Forsberg et al., 2001).

In the sequel we outline a few examples of Greenland laser projects, mainly carried out in connection with climate-related research projects in local areas. For different regions operations have been carried out in cooperation with the Technical University of Denmark (Danish Center for Remote Sensing), and the glaciological groups of the University of Copenhagen, and the Geological Survey of Denmark and Greenland. We especially have used laser methods in connection with satellite and airborne SAR interferometry, and give an example of the validation of the performance of the DTU EMISAR system (Madsen et al., 1996) for mapping ice sheet heights by intercomparison to laser heights. We will also give some examples of the potential of airborne laser measurement of sea-ice freeboard heights, allowing the measurement of ice thickness through assumptions of isostatic equilibrium. The sea-ice freeboard data have been collected since 1998 as a by-product of airborne gravity measurements in the sea-ice of the Polar Sea north of Greenland and the Fram Strait.

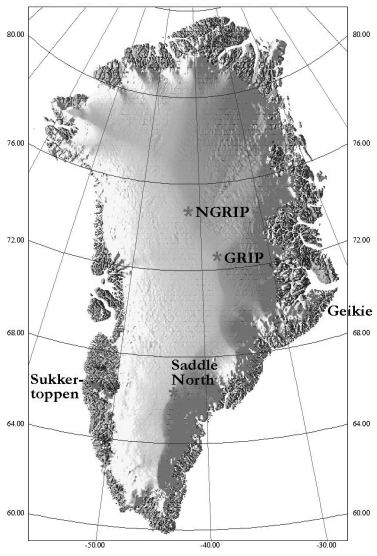

Fig. 1. Main ice sheet field sites

2 HARDWARE SYSTEM SETUP

The KMS airborne laser system has been set up to be easily installable in various airplanes. In Greenland most installations have been done in a Greenlandair Twin-Otter (OY-POF), normally used as a freight airplane (Fig. 2). The aircraft is for survey flights equipped with 2-3 geodetic GPS receivers, sharing two GPS antennas mounted on top of the aircraft. Attitude of the aircraft is determined by inertial sensors: For early flights (1996) a clinometer assembly was used, which together with horizontal GPS accelerations allowed a crude roll and pitch to be estimated; in 1997 a low-cost strap-down prototype fiber-gyro IMU (Inertial Measurement Unit) made by Greenwood Engineering was added to the system; and finally in 2000 a proper medium-grade INS (Honeywell H-764G) was used for superior determination of attitude angles. The H-764G incorporates an embedded GPS receiver, making time synchronization much simpler than in the early flights.

Fig. 2. Twin-Otter aircraft at Station Nord, May 2001

Laser units flown include single-beam laser altimeters from Optech, Inc., and – since 2001 – a swath laser scanner manufactured by Riegl, Austria. The Riegl scanner is a linear scanner used a rotating mirror, generating a software-controllable linear cross-pattern. In the sea-ice tests north of Greenland and tests in Denmark reported here a 40 Hz scan rate and 8kHz data rate is used, which at 1000 ft flight elevation and typical airspeeds corresponds to a distance between points on the ground of roughly 1.5 m.

All laser and INS data are logged on laptops and partially also on an integrated data logger and IMU control unit, manufactured by Greenwood Engineering. For airborne gravimetry a modified Lacoste and Romberg marine gravimeter (S-99) is added to the system. Other equipment flown includes ice-penetrating radar, fed from a simple dipole antenna mounted through a tie-down point through the aircraft tail. Depending on the project, equipment is typically installed in 1-2 days, and operated in flight by a single person. On some Danish tests with other aircraft (two different photogrammetric planes) installation times have been as low as a few hours.

3 LAND ICE APPLICATION EXAMPLE

To study the performance of airborne SAR interferometry, a laser survey and surface GPS survey including a strain net and positioning of radar corner reflectors was done on the Geikie Ice Plateau, East Greenland. The measurements were done in cooperation with the Danish Center for Remote Sensing, cf. Dall et al., 2000.

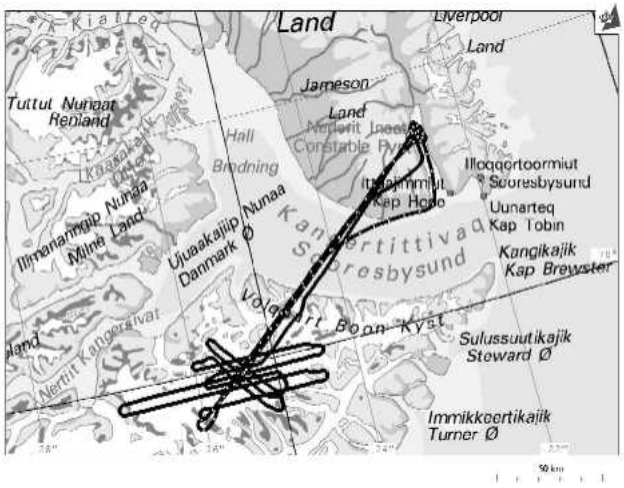

Fig. 3. Airborne laser tracks, Geikie ice cap

The Geikie ice plateau is an elongated, narrow ice-dome, located at more than 2000 m elevation on top of the northern terminus of the steep tertiary basalt province just south of Scoresbysund. It is a region of extreme topography and the poorest mapped part of Greenland. The Geikie operations took place 1996-98, and included repeated GPS measurements at the assumed top of the plateau and four surrounding points, repeated mapping by airborne laser altimetry, and the positioning by GPS of corner reflectors for airborne SAR operations. In addition a shallow ice core was extracted and the subsurface bedrock mapped by ice radar. Due to weather and logistical constraints not all repeated measurements were carried out as planned, and evaluation of results are still ongoing.

Fig. 4. Radar reflector on Geikie ice cap

The Geikie ice cap shows very large changes in ice velocity and elevations due to the fairly high yearly accumulation (3-4 m of snow). It is therefore a special target area for the

investigations of SAR interferometry, and both elevation- and ice velocity models have been derived based on ERS tandem mission SAR interferometry combing descending and ascending passes using the method of Mohr et al. (1997). The conversion of the SAR satellite data into heights and velocities are complicated significantly by the extreme topography (south of Geikie some valleys are flanked by 1000 m vertical walls), which produce radar shadows and layovers, and makes the unwrapping of interference fringes ambiguous.

Fig. 5. G3 with EMISAR XTI radar

Airborne SAR C-band interferometry has the advantage over satellite data of higher accuracy and resolution, and by using dual antennas (cross-track interferometry, XTI) the uncertainties connected with ice movements disappear and radar interferogram fringes represent topography (and errors) only. Over Geikie both XTI and RTI (repeat track interferometry) was flown in 1997 and 1998 using the EMISAR system of the Danish Center for Remote Sensing, DCRS, (Madsen et al., 1996), mounted in a Gulfstream jet of the Royal Danish Air Force. Radar reflector GPS positions were used to calibrate the airborne SAR data in the sense of fitting an overall bias in the elevations, but otherwise the corner reflector GPS coordinates were not used for SAR calibration. The SAR data were processed at DCRS in a 5 m-resolution grid subsequently averaged to 25 m. At present only the XTI 1997 data have been processed.

The SAR data was evaluated primarily using airborne laser altimetry. A single-beam laser altimeter (Optech 501SX) was used in combination with kinematic GPS positioning and aircraft attitude information to map the ice surface with an error of around 50 cm, as evidenced from laser track cross-overs. The main part of this error is probably due to kinematic GPS, as the reference GPS site used was more than 150 km away (at the airport of Constaple Pynt). A part of the error is due to insufficient roll and pitch of the aircraft. In the first flight (1996) we did not have a proper INS available, but only a horizontal accelerometer unit, which combined with GPS accelerations, can give a somewhat noisy roll and pitch signal (the influence of roll and pitch was limited flying a draped survey at a nominally 300 ft terrain clearance). In 1997 a prototype fiber-gyro IMU manufactured by Greenwood Engineering was used to provide high-resolution roll and pitch and a more safe flight elevation was used. Unfortunately bad weather prevented laser operations in 1998. The laser data were measured at 10 or 50 Hz, and averaged to 1 sec averages, corresponding to 60 m on the ground.

Since the laser-SAR DEM comparison is critically dependent on the correct processing of the kinematic GPS surveys, including sensor offsets, the airborne laser altimetry was checked by comparing to overflights of the Constaple Pynt runway. A dense geometric pattern of points was independently established on the surface of the runway using a kinematic GPS survey by car. The runway comparison is shown in Table 1, and shows a good fit (20 cm), indicating no gross errors in the GPS processing. At the longer baseline lengths to Geikie the accuracy will degrade, however, but airborne GPS results should still be accurate well below half a meter or so.

The comparisons between the laser altimetry in two consequent summer surveys (1996 and 1997), as well as comparisons between laser altimetry and airborne SAR interferometry and ERS satellite tandem interferometry are additionally shown in Table 2. The laser internal cross-over errors are in part due to a large laser sampling interval (60 m on the ground). The laser intercomparison between 1996 and 1997 show height changes on the order of 0.5-1 m, which is in accordance with the general variations in the snowfall. The annual snow accumulation is 2-3 m, as inferred from a shallow ice core taken in 1998. Overall the snow surface increased by roughly 0.5 m from 1996 to 1997, a number confirmed by static GPS measurements at the radar reflectors, and explained by a relatively large snowfall in the 1996-97 season.

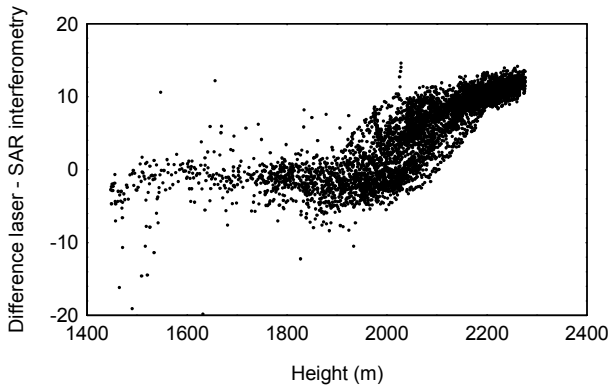

Fig. 6. Difference between laser altimetry and SAR interferometry, Geikie ice cap (outliers are mainly rocks)

The comparison to the airborne SAR interferometry shows that a 4.7 m r.m.s. agreement has been obtained, with a bias of 7 m. The bias is mainly due to penetration effects of the radar signals into the ice sheet. The bias turns out to be height dependent, with shallow penetration (virtually no bias) below 1900 m, and a 10 m bias above 2100 m. This probably corresponds to the difference between the lower-elevation percolation zone (where the firn contains ice layers

due to yearly melting/refreezing of the snow) and the upper-elevation dry-snow zone, where little melting occurs, and volume scattering thus is the predominant mechanism for the radar return.

When restricting the SAR interferometry to the dry-snow zone, an r.m.s. fit of 1.9 m is obtained between laser and SAR, so at present airborne SAR interferometry may be assumed to be just barely useful for detecting climate-related height changes, but extremely useful for precise DEM determination for mapping. Satellite SAR interferometry are also useful for this purpose, showing a fit over Geikie of 14 m r.m.s. (the bias value is not significant as the SAR DEM was fitted to the average level of the static GPS at the radar reflector elevations).

Table 1. Comparisons of laser altimetry and SAR interferometry at Geikie Ice Cap, East Greenland.

Comparison (units: m)	Mean	Std. dev.
Airborne laser vs. Airport runway kinematic GPS	0.16	0.25
Internal accuracy of laser survey (1996; 87 cross-overs)	0.02	0.63
Do. (1997; 130 cross-overs)	-0.01	0.65
Laser altimetry 1997 minus 1996 (545 crossings)	0.47	0.94
Laser altimetry minus airborne SAR interferometry (1997)	7.06	4.67
Do., above 2100 m only	9.89	1.90
Laser altimetry minus ERS satellite interferometry	-3.48	13.75

4 ACCURACY OF LASER SCANNING

A Riegl laser scanner unit have been flown over major part of the Arctic Ocean area north of Greenland during April/May 2001, and also used for digital elevation model tests in Denmark.

To obtain a quantitative estimate of the accuracy of laser scanning, a number of tests have been done in connection with overfligths of airport runways, as well as buildings, as measured in detail with kinematic GPS methods. Table 2 gives some results of overflights over the Kangerlussuaq airport, western Greenland (May 2001), as well as overflights of Roskilde Airport, Denmark (July 2001, Piper Navajo aircraft installation). In both cases reference GPS stations were close by, so that GPS errors play a minor role, and comparisons where done by interpolating the surface "ground truth" data to the location of the laser points, if the points were sufficiently close (< 1 m).

The results show an excellent performance in the tests in Denmark (< 10 cm accuracy), whereas the Greenland comparisons are much poorer, likely a consequence of some inconsistencies in timing and coordinate offsets, and a suspected lack of rigidity in the improvised scanner mount of the Greenland 2001 campaign. Overflights over Longyearbyen airport, Svalbard, showed even larger comparison error values (90 cm r.m.s.), and work is in progress to try and solve the problems.

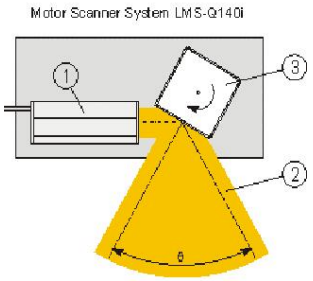

Fig. 7. Riegl laser scanner principle

Table 2. Comparisons of airborne laser scanning and runway kinematic GPS car surveys

Comparison (units: m)	Mean	Std. dev.
Kangerlussuaq: 2000 runway survey vs. 2001 laser scanning	0.24	0.32
Roskilde: Runway road survey vs. Laser scanning	-0.03	0.04
Roskilde: Comparison of two separate laser scanning flights	-0.04	0.10

5 SEA-ICE LASER MEASUREMENTS

In the period 1998-2001 the Greenland coasts have been mapped with airborne gravimetry at roughly 10 n.m. line spacing, with laser altimeters routinely collecting data over the ocean as well, and – since 2001 – also a Riegl laser scanner. Because of fog and limited visibility not all tracks have given useful data. Flights have been flown at low elevations (500 to 1000 ft), and GPS tracked from a number of base stations at the various airports in the area. GPS heights are generally accurate only at the 0.3-0.5 m level due to the long baselines and ionospheric conditions.

The laser altimetry measurements provide a direct

measurement of ice freeboard heights, which might be useful, e.g. for validation of future satellite missions such as Icesat and CryoSat, as well as for general studies of sea-ice thickness changes. The basic principle is

$$F = h_{GPS} - H_{laser} - N$$

where F is the ice free-board height, h the height of the aircraft, H the measured range to the ice surface and N the geoid. To this equation should be added the instrument offsets, measurement errors, tides, and permanent sea-surface topography, the latter assumed to be small and of relatively long wavelength. It is therefore possible to correct for these errors by filtering and adjusting data to a "lowest level" representing open water or new ice. The ice freeboard values may subsequently be converted to total ice thickness, based on assumption of isostatic equilibrium between the sea-ice (normal density 915 kg/m^3) and the water (density 1024 kg/m^3). A constant freeboard to thickness ratio K around 7.84 has been taken from a model presented in Wadhams et al. (1992). The K factor is a mean value for the season, and depends on the thickness and density of overlying snow, as well as on variations on the density of the sea-ice itself or the ocean density.

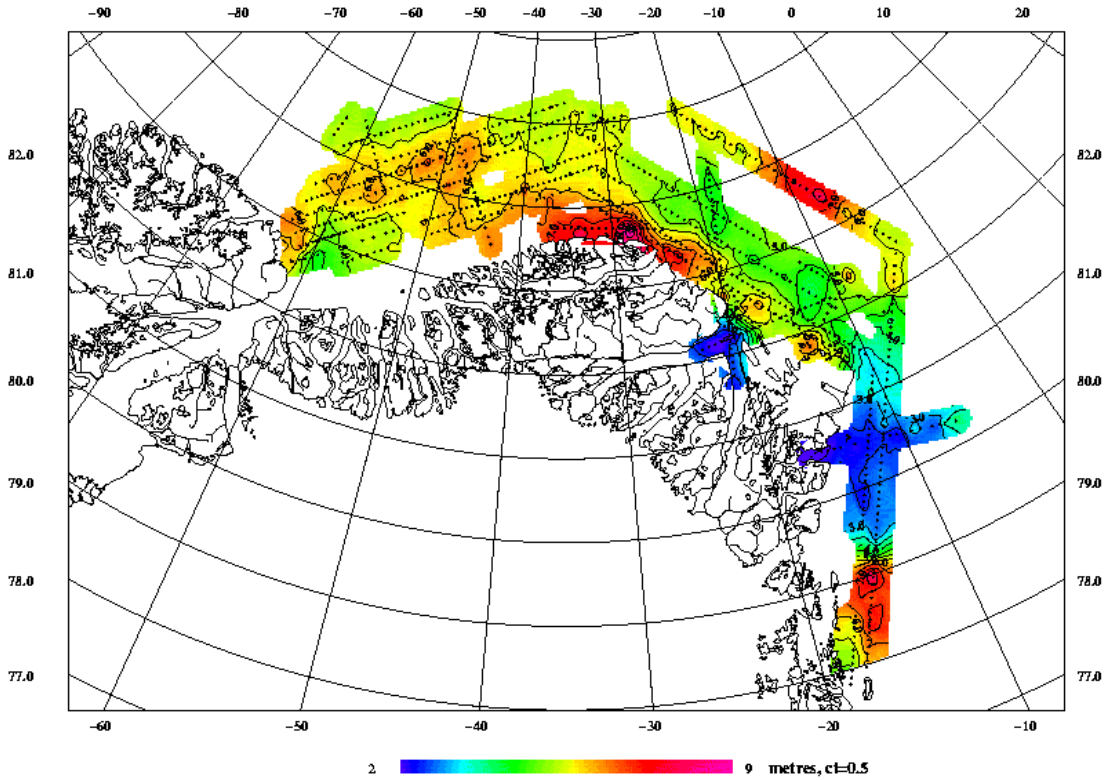

Fig. 8. Sea-ice thickness north of Greenland determined from airborne laser measurements

Fig. 8 shows an example of ice thickness for the Polar Sea north of Greenland, derived from June 1998 laser profile measurements. Data have been processed onto a 0.1° resolution grid from available fog-free filtered laser track data, using a geoid model derived from the airborne gravity measurements. The thick accumulation of sea-ice north of Greenland is likely due to compression and ridging due to the dynamics from the Transpolar current. Investigations are ongoing to analyze 1999 and 2001 data and compare with remote sensing imagery. The use of laser scanner data provides an additional capability to map the ice floe geometries in greater detail, including the study of pressure ridges and leads.

Fig. 9. Polar pack sea-ice north o f Greenland

Fig. 10 shows an example of the ice freeboard field for a region of the Arctic Ocean north of Greenland, as mapped by airborne laser scanning using the Riegl system. The plot shows the actual measured freeboard heights along a typical track north of Greenland. The laser scanning freeboard data clearly shows the typical 50-100 m-scale individual ice floe features, as well as pressure ridges between floes. Work is currently ongoing at KMS to analyze the sea-ice laser scanning data, along with analysis of onboard video data collected and remote sensing data from ERS-2 and Radarsat.

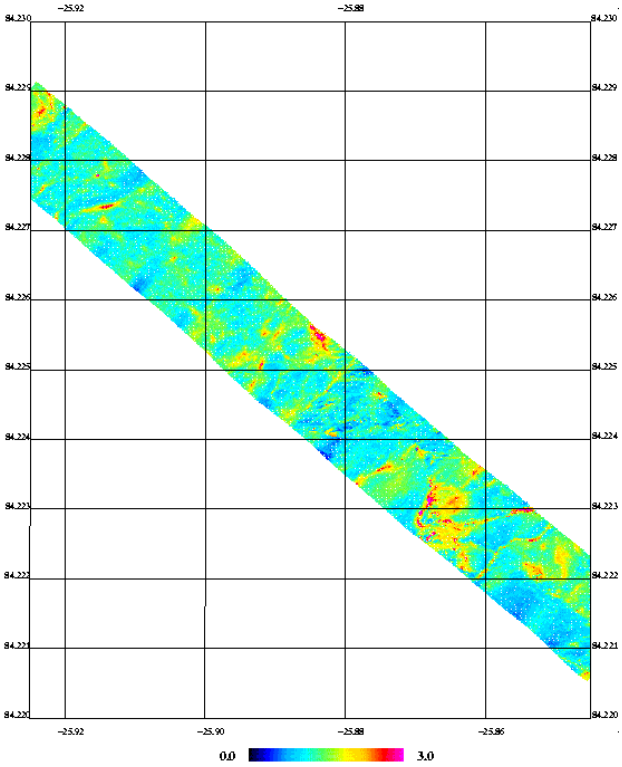

Fig. 10. Ice freeboard heights (m) of Arctic pack ice. Swath width is approximately 150 m (flight elev. 500 ft)

6 CONCLUSIONS

We have outlined some examples and results of Greenland laser projects, based on a low-cost Twin-Otter system setup. We are currently refining and developing software and tools, a.o. to provide estimation of laser scanner orientation angles, changing with every new installation and field project. In Danish tests the used Riegl scanner system have obtained very good results (accuracy down to the 5 cm level), whereas Greenland applications have generally been noisier. Applications of laser scanning for sea-ice studies appears very promising, and airborne measurements can provide a good understanding of the signatures of the future satellite missions such as Icesat and CryoSat, and help in studying climate-induced changes in the polar sea-ice cover.

REFERENCES

[Dall et al., 2001] Dall, J., S. N. Madsen, K. Keller, R. Forsberg: Topography and penetration of the Greenland ice sheet measured with airborne SAR interferometry. Geophysical Research Letters, vol. 28, no. 9, p. 1703, 2001.

[Forsberg et al., 1996] Forsberg, R., K. Hehl, L. Bastos, A. Giskehaug, U. Meyer: Development of an airborne geoid mapping system for coastal oceanography (AGMASCO). Proc. International Symposium on Gravity, Geoid and Marine Geodesy, Tokyo, Sept. 1996, Springer Verlag IAG series vol 117, pp. 163-170.

[Forsberg et al., 2001] Forsberg, R., A. V. Olesen, K. Keller, M. Møller, Arne Gidskehaug, D. Solheim: Airborne Gravity And Geoid Surveys in the Arctic And Baltic Seas. Proceedings of International Symposium on Kinematic Systems in Geodesy, Geomatics and Navigation (KIS-2001), Banff, June 2001, pp. 586-593.

[Keller et al., 2001] Keller, K., R Forsberg,, C S Nielsen: Kinematic GPS for Ice Sheet Monitoring and SAR Interferometry in Greenland. In: M.E. Cannon and G. Lechapelle (eds.). Proc. Int. Symp. on Kinematic Systems in Geodesy, Geomatics and Navigation, Banff, Canada, June 3-6, 1997, Publ.Univ. of Calgary, pp. 525-528, 1997.

[Lintz et al, 2000] Lintz, E., N. Reeh, R. Forsberg, J. H. Jørgensen, N. Skou, K. Woelders: *A low cost glacier mapping system.* Accepted for publication, Journal of Glaciology, 2000.

[Madsen et al., 1996] Madsen, S. N., N. Skou, J. Granholm, K. Woelders, E. L. Christensen: *A System for Airborne SAR Interferometry.* Int. J. of Electronics and Communications, Vol. 50, No. 2, pp 106-111, 1996.

[Mohr et al., 1997] Mohr, J., S. N. Madsen, N. Reeh: ERS tandem study of glacier dynamics in NE Greenland. In: Proc. 3rd ERS symp. on space at the service of our environment, ESA SP-414, pp. 989-993, 1997.

[Wadhams et al, 1992] Wadhams, P., W. B. Tucker, W. B: Krabill, R. N. Swift, J. C. Comiso, N. R. Davis: Relationship between sea-ice freeboard and draft in the Arctic Basin, and implications for ice thickness monitoring. Journal Geoph. Res., vol. 97, C12, pp. 20325-20334, 1992.

Quantifying River Bank Erosion with Scanning Laser Altimetry

David P. Thoma, Satish C. Gupta, Marvin E. Bauer
Department of Soil, Water and Climate and Department of Forestry
University of Minnesota
U.S.A.
dthoma@soils.umn.edu

KEY WORDS: Bank erosion, bank collapse, scanning laser altimetry, non-point source pollution.

ABSTRACT

Detailed topographic data collected with an airborne laser scanner can help determine the extent of bank erosion and identify banks that are more vulnerable to bank collapse and thus require stabilization efforts. The Minnesota River which flows through a 95% agricultural watershed has been ranked among the top 20 most polluted rivers in the U.S. Greater than 50% of the sediment load carried by the river at Mankato, MN is delivered by a single tributary, the Blue Earth River. A 56km length of the main stem of the Blue Earth River corridor was scanned April 2001 with an helicopter mounted Topeye laser system. The database includes X, Y, Z coordinates of laser returns from the river valley plus return intensity. Other data collection included ground elevation measurements for two banks using a total station, and vegetation density at eight locations along the river. A bare earth model was constructed by removing returns from vegetation and is currently being tested against the ground elevation measurements. Plans are to make another scan in a year or more to calculate volumetric change in the river valley due to bank erosion / bank collapse. This volume change along with soil bulk density along the river corridor will be used to assess the extent of bank erosion. The mass wasting rates will then be converted to total suspended sediments assuming fine silt and clay fractions are most likely to be transported.

1 INTRODUCTION

Nutrients, pesticides and sediment from agricultural activities are the leading surface water pollutants in the U.S. At the root of the water quality issue are agricultural practices that allow sediment and nutrient transport to surface water bodies. Soil cultivation and drainage are such practices that are often necessitated by the climate and soils in the region. Cultivation exposes soil to forces that can dislodge and transport it, whereas drainage provides a conduit for transport of sediment and soluble nutrients to surface waters.

Many of the same agricultural activities are linked to declines in water quality in the eight corn belt states that account for 80% of U.S. agricultural production (Fausey et al. 1995). The interaction between cultivation of 55.7 million hectares and drainage on 20.6 million hectares has affected the hydrologic regimes and water quality of several rivers in the mid-west United States.

One such river is the Minnesota River that flows through a relatively flat agricultural landscape, but is fed by tributaries that are incised with steep and unstable stream banks. According to one estimate, the Minnesota River carries between 0.2 and 2 million tons of suspended sediment per year at Mankato, MN. Approximately 55% of that sediment is contributed by a single tributary, the Blue Earth River (Payne, 1994).

The Minnesota Pollution Control Agency (MPCA) has stated that a 40% reduction in sediment load is required to meet federal water quality standards in the Minnesota River. But it is not known what proportion of the load is from surface runoff versus stream bank collapse. Gupta and Singh (1996) estimated the bank erosion contributions at 48-55% of the total sediment load in the Minnesota River at Mankato. Bauer (1998) estimated that 36 to 84% of the sediment in the Blue Earth River was from bank erosion. Based on ground surveys of a few banks, Sekely (2001) estimated that bank erosion varied between 31 to 44% of the total suspended sediment load from the Blue Earth River. However, most of the above estimates are based on assumptions that have not been tested.

To achieve the sediment reduction goal MPCA recommends conservation tillage adoption in as much of the Basin as possible. An assumption implicit in this recommendation is that most of the sediment in the river has its source in the uplands. This logic has been applied to soil erosion from agricultural landscapes for many years at considerable expense but with little improvement in water quality (Wilkin and Hebel, 1982).

In order to implement effective management practices to address pollution sources there must be a clear understanding of which mechanisms are the largest contributors. If monitoring showed for instance that large quantities of sediment were being contributed from stream bank collapse some effort could be re-directed to focus more attention on hydrologic processes both in-stream and via drainage networks that influence channel morphology. However, quantification of bank erosion is difficult due to the remote location of river banks. The process is also time consuming if done manually. Airborne scanning lasers provide a convenient, efficient, and cost effective means to monitor bank erosion / bank collapse.

The objective of this research is to determine the potential of laser scanning altimetry to provide comprehensive stream reach mass wasting estimates. Airborne laser altimetry measurement for stream bank mass failure rates has not been attempted to our knowledge, yet it has great potential for government agency and commercial application in erosion and water quality management. Advancements in techniques for measuring river bank erosion and channel migration have been slow to evolve (Lawler, 1993). The successful outcome of this research will demonstrate this technology is a viable method for estimating bank erosion and channel migration at an unprecedented level of detail and geographic extent.

2 THEORY

The premise behind airborne laser scanning for calculating mass wasting

rates is to construct a bare earth digital elevation model (DEM) at two times bounding an interval during which erosion occurs. The difference in surface elevations between the two models then reflects the volume change due to bank erosion / bank collapse.

In airborne laser scanning, thousands of pulses per second are fired at the ground. The sensor receives multiple echoes from each returning laser pulse. Typically the first returned pulse is the top of vegetation canopy while the last is usually the ground. In situations where the last echo return is not from the ground, filtering must be employed to remove these elevation data if interest is purely in the bare earth elevations (Ritchie, 1994). The elevation of the earth surface is determined as the difference between platform elevation above a reference ellipsoid and platform height above the earth surface. Platform height is a function of the time it takes a laser pulse to be transmitted to the land surface and then reflect back to the sensor. Lateral positions of laser pulses are georeferenced using a global positioning system (GPS) and an intertial navigation system (INS) (Krabill and Martin, 1987; Wehr and Lohr, 1999).

3 METHODS

This study was conducted on the main stem of the Blue Earth River, a tributary of the Minnesota River. Bauer (1998) identified 136 eroding stream bank sites along 157 km of the Blue Earth River between Mankato and Blue Earth, MN. This stretch of the Blue Earth River has steep (up to 90^{o}) and unstable banks as high as 30m (Figure 1). The eroding stream banks range in area of 102 to 18364 m^2. Bauer classified banks into minor, moderate and severely eroding. We focused on river reaches between the confluence of the Blue Earth and Wantonwan rivers and Amboy (~56km river length) which contain 10 minor, 30 moderate, and 15 severely eroded sites greater than 3m high.

Figure 1. Eroding river bank on the frozen Blue Earth River with farm buildings for scale.

Field Work

In February 2001, 56km of the river between Rapidan Dam and Vernon Center were mapped with a March III GPS to 5m accuracy and stream banks on either side of the river were photographed and categorized qualitatively by size, erosion activity, and vegetation coverage. The start and end points of all large banks were recorded. This data is being used to aid interpretation of the laser scan and to independently compute bank lengths.

Two stream banks were surveyed with a total station during February 2001. These surveys are being used as reference standards to determine absolute accuracy of the airborne

scanning laser system. On April 28 and 29, 2001, eight locations representing various vegetation cover types were also surveyed for vegetation canopy density using a Geographic Resource Systems densitometer.

Laser Scanning

On April 24 and 25, 2001 Aerotec Inc. completed a 56 km scan of the river corridor using the Saab Topeye laser range finding system.

The scan specifications were:
flight platform – Eurocopter Astar 350 series helicopter
flight altitude - 375 m
flight speed - < 25 m/s
distance between foot prints - 0.305 m
laser foot print diameter - 0.116 m
laser pulse rate – 7000 Hz
returned echoes - 5
scan width - 273 m
scan angle - 20 degrees
mirror frequency 12.5 Hz
ground reference station - Trimble 4000 SSi dual frequency receiver

4 RESULTS

The data was filtered by Aerotec to remove reflections from vegetation resulting in a bare earth model which was then gridded and contoured to derive topographic maps. Figure 2 shows an example of a scanned river bank along the Blue Earth River. Usually, water bodies absorb infrared laser pulses, but some reflections occurred from the Blue Earth River due to high sediment loads in the water. We are in the process of comparing the elevation measurements from the laser scan against the total station derived elevations and are currently building DEM's (Figure 3) that will be used for volume change estimates when a second scan is completed. The DEM constructed from the April 2001 scan is also being used to create a 3-D fly-through animation of the river valley. The animation will be used as a tool to demonstrate the significance of bank erosion problems in the Minnesota River Basin.

A second scan of the same 56km length of the river will be made in about a year. The difference in DEM's will provide a measure of sediment volume change in the river valley. Sediment bulk density will be determined to convert volume change into mass wasting. The contribution of suspended sediment from bank erosion will be estimated as a portion of fine silt plus clay in the mass wasted materials. These estimates will then be compared against the suspended sediment load from river monitoring to estimate the proportion of sediment from upland versus stream bank erosion.

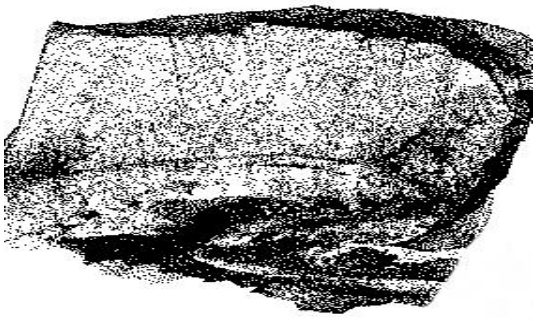

Figure 2. Raw laser data 'image' of an eroding river bank. The X, Y, Z point data is used to construct gridded elevation model and topographic map products. This view has a perspective similar to Figure 1.

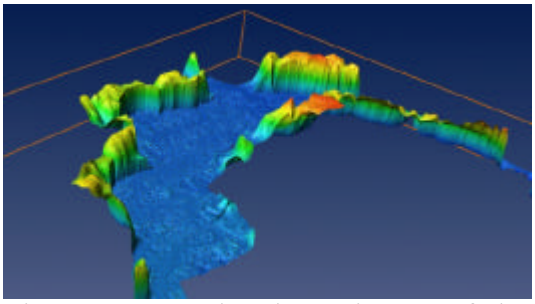

Figure 3. Rendered 3-D image of the Blue Earth River valley used in an animated fly-through movie. Color is used to represent elevation. Height is not to the scale.

5 CONCLUSIONS

Improved understanding of sediment sources and delivery mechanisms is important to efficiently allocate resources for mitigation of sediment pollution in rivers and lakes. This project is examining the potential of scanning laser altimetry to measure comprehensive mass wasting rates from actively eroding river banks, an heretofore improbable task using traditional surveying means. Once successful, this tool will provide not only a means to measure bank erosion but also a means to determine allocation of resources to projects that have the greatest potential for non-point source pollution abatement. Additionally, quantifying upland contributions by subtracting stream bank inputs from total sediment load will help determine effectiveness of current upland soil erosion control practices.

6 ACKNOWLEDGEMENTS

The research was in part supported by funds from the Water Resources Center and the Graduate School of the University of Minnesota, the Minnesota Corn Council, the Minnesota Soybean Council, and the University of Minnesota Supercomputing Institute. The authors gratefully acknowledge the computer rendering of the laser scanning data by Cal Kirchhof of the Supercomputing Institute.

7 REFERENCES

Abdalati, W. and W.B. Krabill 1999. Calculation of ice velocities in the Jakobshavn Isbrae area using airborne laser alitmetry. Remote Sensing of Environment, (67) pp. 194-204.

Bauer , D.W. 1998. Stream bank erosion and slumping along the Blue Earth River. M.S. thesis Dept. Soil, Water and Climate. University of Minnesota, pp. 2-72.

Fausey, N.R., L.C. Brown, H.W. Belcher, and R.S. Kanwar 1995. Drainage and water quality in great lakes and cornbelt states. Journal of Irrigation and Drainage Engineering July/August, pp. 283-288.

Gupta, S.C., and U.B. Singh 1996. A review of non-point source pollution models: Implications for the Minnesota River Basin. Department of Soil, Water, and Climate, College of Agricultural, Food, & Environmental Sciences, University of Minnesota, St. Paul, MN.

Krabill, W.B., R.H. Thomas, C.F. Martin, R.N. Swift, and E.B. Frederick 1995. Accuracy of airborne laser altimetry over the Greenland ice sheet. International Journal of Remote Sensing, (16)7, pp. 1211-1222.

Krabill, W.B., and C.F. Martin, 1987. Aircraft positioning using global positioning system carrier phase data. Navigation: Journal of the Institute of Navigation, (34)1, pp 1-21.

Lawler, D.M., 1993. The measurement of river bank erosion and lateral channel change: A review. Earth Surface Processes and Landforms, (18) pp. 777-821.

Minnesota Pollution Control Agency (MPCA) 1994. Minnesota River Assessment Project Report: Volume II, Physical and Chemical Assessment. Report to the Legislative Commission on Minnesota Resources, pp 12-38.

Payne, G.A. 1994. Sources and transport of sediment, nutrients, and oxygen-demanding substances in the Minnesota River Basin, 1989-1992. In Minnesota River Assessment Project Report, Vol II: Physical and Chemical Assessment. MPCA.

Ritchie, J.C., E.H. Grissinger, J.B. Murphey, and J.D. Garbrecht, 1994. Measuring channel and gully cross-sections with an airborne laser altimeter. Hydrological Processes (8) pp. 237-243.

Sekely, A. 2001. Stream bank slumping and its contribution to the phosphorus and suspended sediment loads of the Blue Earth River. M.S. Thesis, University of Minnesota, St. Paul.

Vaughn, C.R., J.L Bufton, W.B. Krabill, D. Rabine, 1996. Georeferencing of airborne laser alitmeter measurements. International Journal of Remote Sensing (17)11 pp. 2185-2200.

Wehr, A., and U. Lohr, 1999. Airborne laser scanning-an introduction and overview. ISPRS Journal of Photogrammetry & Remote Sensing (54) pp. 68-82.

Wilkin, D.C., and S.J. Hebel, 1982. Erosion, redeposition and delivery of sedimnent to Midwestern streams. Water Resources Research, (18)4 pp. 1278-1282.

Mapping the Surface of Sheet Flow Water in the Everglades

William Carter, Ramesh Shrestha, Grady Tuell, David Bloomquist, and Michael Sartori
University of Florida, Department of Civil and Coastal Engineering
GeoSensing Systems Engineering, Gainesville, FL, 32611
e-mail: bcarter@ce.ufl.edu

KEY WORDS: Mapping, Airborne, Laser, Intensity, Nadir Points, Sheet Flow Water

ABSTRACT

University of Florida (UF) researchers used airborne laser swath mapping (ALSM) to map the height of vegetation, relative to the surface of sheet flow water, in the Everglades. In less than three hours of flying, ALSM provided sub-decimeter precision measurements of the height and slope of the water surface over an area greater than 50 square kilometers. The RMS scatter of the measurements about the best fitting slope along a 14 kilometer transect was less than 4 cm. Two features of the UF ALSM system were of particular advantage in this project: coverage of the nadir provided by the oscillating mirror scanner, and intensity values of the return signals. Openings in the grasses allowed a small percentage of laser shots, at the nadir of the aircraft, to be reflected from the calm surface of the slowly flowing water. These nearly specular reflections produced intensity values five to ten times as strong as the diffuse reflections from the grasses. The ALSM observations had to be carefully calibrated for the unusually strong return signals, but once this was done the signal-to-noise ratio was excellent and the geometry could not have been better for determining the height of the water surface. This project demonstrated the unique capabilities of ALSM to quickly and accurately map remote wildlife habitats, in this case that of the Cape Sable Seaside Sparrow, an endangered species that builds nests within 15 cm of the surface of the water. Managers hope to use such measurements to plan and control the release of water in order to avoid inundating nests, hopefully helping the Cape Sable Seaside Sparrow to avoid extinction.

BACKGROUND

The conceptual basis for Airborne Laser Swath Mapping (ALSM), which is also referred to as LIDAR (light detection and ranging), LADAR (laser detection and ranging), and airborne laser altimetry, has existed for at least two decades. However, until a few years ago only federal agencies such as the Department of Defense and the National Aeronautics and Space Administration could afford to build and operate the large, heavy, power demanding early generation instrumentation. The development of compact energy efficient diode pumped Nd:YAG lasers, Inertial Measurement Units (IMU) composed of fiber optic gyroscopes and solid state accelerometers, and high performance personal computers during the mid 1990's suddenly made it possible to build ALSM units that could be operated from light dual, or even single, engine aircraft. The attendant order-of-magnitude drop in operating costs for the first time allowed academic researchers access to this powerful technology, setting off a remarkable growth in studies of Earth's topography, bridging such traditional specialties as geodesy, geophysics, hydrology, civil engineering and biology (Gutelius et. al., 1998; Carter et. al., 1998: Shrestha, et. al., 1998)

In March, 1999, the University of Florida (UF) and Florida International University, took delivery of the first ALSM unit, an Optech Inc. model ALTM 1210, to be purchased by an academic institution in the United States (Shrestha et. al., 1999). Researchers at these universities have completed more than twenty research projects, funded by a wide variety of federal, state and county agencies. In this paper we report results from an ALSM survey conducted in the Florida Everglades, funded by the U.S. Geological Survey, to explore the capabilities of the technique to map the height of vegetation (most particularly of grasses that grow in areas of shallow surface sheet flow of water) relative to the surface of the water.

INTRODUCTION

The U.S. Congress has appropriated billions of dollars to restore large portions of the Florida Everglades. Dikes, canals and locks constructed by the U.S. Army Corps of Engineers to manage surface water will be removed, restoring the natural sheet flow of water across thousands of square kilometers of grass lands. Cape Sable Seaside Sparrows build their nests in the grass, just above the surface of the water. U.S. Park Service personnel estimate that an increase in the height of the water surface of just 15 centimeters, while the nests are in use, can result in their inundation, reducing the ability of this endangered species to reproduce. The primary focus of the UF research was to determine if ALSM could provide precise measurements of the grass water interface, and the height of the vegetation above that interface.

The Everglades project extended over a nearly rectangular block, approximately 9.5 kilometers by 10 kilometers, located just west of Homestead, Florida (Figure 1.). The ALSM data were collected in a single flight of approximately three hours, with less than two hours of laser "on" time. Table 1. summarizes the primary specifications associated with the data collection. Two features of the UF/FIU ALSM system were used to advantage in this project: coverage of the nadir provided by the oscillating mirror scanner, and measurement of the intensities of the return signals.

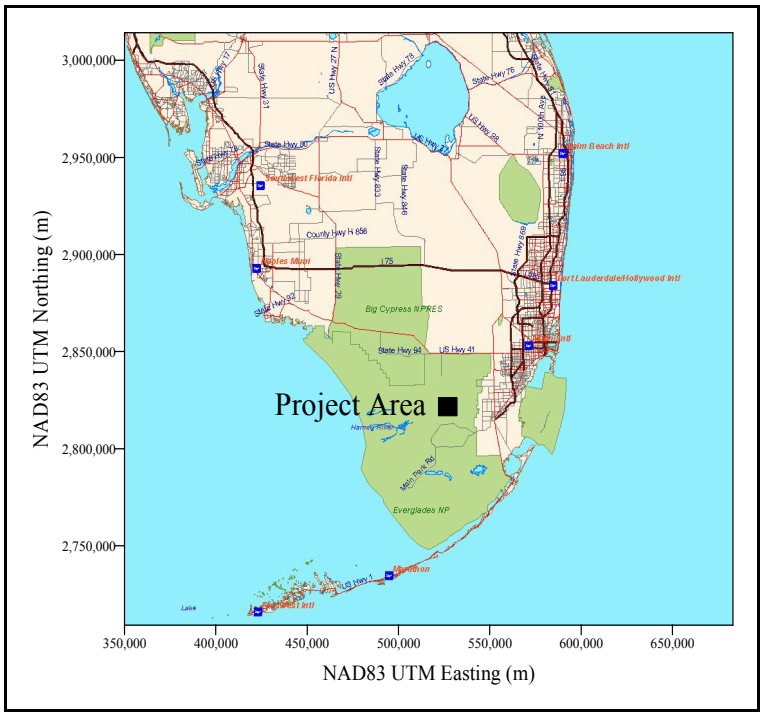

Figure 1. Map showing the location of project area in the Florida Everglades.

Table 1. Everglades Data Collection Specifications

Flying height:	487m	Number of flight lines:	30
Flying speed:	60 m/sec	Total number points:	46,000,000
Scan angle:	±19 degrees	Water surface points:	25,905
Scan rate:	30 Hz	DEM interpolation:	Kriging

EXTRACTING WATER SURFACE POINTS

Oscillating Mirror Scanner

The UF/FIU ALSM unit uses a simple oscillating mirror scanner to distribute the laser pulses along a line at right angles to, and extending equally on either side of, the longitudinal axis of the aircraft. The forward motion of the aircraft creates a saw-tooth pattern of laser points on the surface, within the swath covered by a single pass. The width of the swath, the spacing of laser points along each scan line, and the spacing between tips of the saw-tooth pattern depend on the flying height and speed of the aircraft, as well as the scan rate and angle selected. The features of the oscillating mirror scanner generally considered as positive include the simplicity and relatively low cost of the scanner instrumentation, and the ease of changing the scan rate and angle, which provide the user freedom to choose the distribution of laser point spacing within the saw-tooth pattern. By selecting a slow scan rate (few Hz) the spacing of adjacent points along the scan lines can be minimized, providing improved spatial resolution across the swath. Spatial resolution is sacrificed in the along track direction, but that may be acceptable if the primary interest is in mapping lineal features, such as the edges of highways, the front edges of dunes along a beach, or the wet water line on a beach. Conversely, by selecting a high scan rate (tens of Hz) the spatial resolution in the along track direction can be improved, at the cost of reducing the across track resolution. Intermediate scan rates can be used to generate a pattern with nearly equal spacing of points across and along the track, for general mapping and the production of Digital Elevation Models (DEM).

The negative aspects of the oscillating mirror scanner most generally cited include the concentration of points near the tips of the saw-tooth pattern, and the large change in the angle of incidence of the laser pulses with the surface of the terrain. The concentration of points near the edges of the swath is undesirable not only because the information gained tends to be redundant, but also because the dynamics involved in stopping and reversing the direction of the scanning mirror and angular encoder may degrade the positional accuracy of the points. Often, points near the edges of the scan are simply discarded, to avoid these problems. The UF/FIU unit has a low mass beryllium mirror that minimizes the problem of reversing directions, and we usually truncate only a fraction of a degree, perhaps 0.1 to 0.25 degree, depending on the scan rate. Dealing with the problems created by large variations in the angle of incidence is more difficult. Large changes in the angle of incidence can result in large variations in the amplitude of the laser returns,

with equally large variations in the signal level from the detector. The greater the dynamic range that must be accommodated, the more sophisticated the electronics must be to obtain consistent range measurements. The UF/FIU unit has two time interval measurement modules to handle high and low signals separately, and uses constant fraction discriminators to further reduce the effects of the large range in the amplitudes of the return pulses. Sorting the returns into two channels, based on amplitude, addresses problems related to the overall signal range, but introduces the possibility of a range bias between the high and low level signals. And, even after splitting the high and low level signals, the variations within each of the channels is still sufficient that residual non-linearity of the sensor/electronics must be calibrated and corrections applied, using a unit specific lookup table. The lookup table must be changed when components are changed, and may need to be refined as components age, or perhaps even to compensate for changes in operating conditions, such as the ambient temperature inside the aircraft.

Not withstanding the negative features outlined above, the oscillating mirror scanner had one feature that was necessary for mapping the undisturbed surface of the slowly moving sheet flow water through the grasslands – the scan pattern includes points at, or very near, the nadir of the aircraft. A small percentage of laser shots directed toward the nadir of the aircraft passed through small openings in the vegetation and were reflected from the glassy calm surface of the water. These nearly specular reflections produced intensity values five to ten times as strong as the diffuse reflections for the grass. The signal-to-noise ratio was high and the geometry could not have been better for determining the height of the water surface.

Intensity Values

When UF researchers first began exploring the applications of ALSM five years ago, we immediately concluded that some measurement of the amplitude of the return laser pulses would be valuable for certain, if not all applications. For example, to detect paint stripes on highway pavement. In a more general sense, we thought that intensity values would help with the classification, either computer automated or interactive, of surface materials – certainly among pavement, roof tops, sand beaches, lawns, brush, and forests, but perhaps even among types of trees, or healthy and diseased trees.

The leased unit used for our early projects did not record any information on the strength of the return signals, but the manufacturer determined that it would be relatively easy to sense the peak voltage from the Avalanche Photodiode (APD), convert it to a digital value, and record the value on the data tape. The high and low signal channels were equipped with 8 bit analog-to-digital converters, and with overlap, this provides approximately 12 bits of usable range, from zero to several thousand. The intensity value recorded is essentially an uncalibrated number that might be thought of as a proxy for relative surface reflectivity at 1.064 micrometer wavelength. Strictly speaking, the intensity value is not a reliable indicator of the surface reflectivity because of a variety of effects peculiar to the individual pulses, such as change in the laser energy from pulse to pulse, atmospheric scattering and absorption, variations in the angle of incidence caused by the scanner, and localized tilting of the surface on the scale of the laser footprint. Nonetheless, because the nearly specular returns from the surface of the water were five to ten times the amplitude of the diffuse returns from the vegetation, the intensity values could be used to identify the water surface returns with near one hundred percent accuracy. Figure 2. is a gray scale image created from the intensity values for all of the laser returns in the area of the coverage. The extraordinarily bright returns along the nadir of the flight path are immediately obvious. The nadir line is not always centered on the swath, because uncompensated roll of the aircraft displaces the swath relative to the true nadir line.

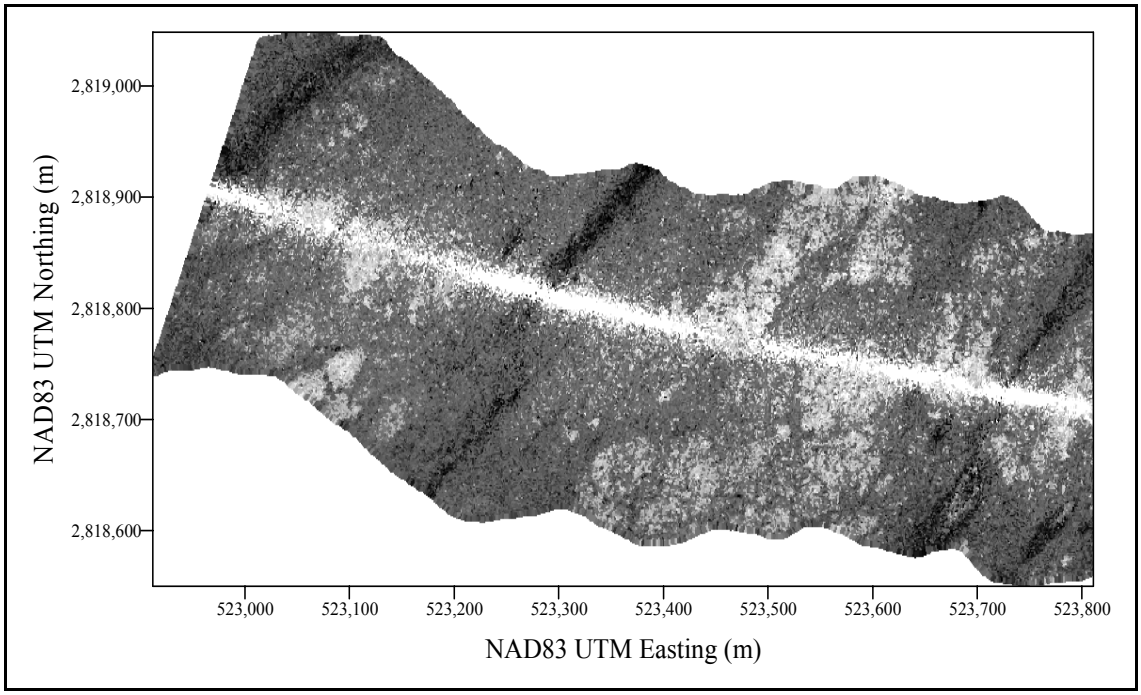

Figure 2. Gray scale image made from ALSM intensity values.

REFINING THE RANGE CALIBRATION VALUES

Figure 3a. is a shaded relief image of the topography created from a DEM derived from the ALSM horizontal position and height values. Imperfect calibration values in the lookup table used to correct the raw range measurements (discussed above) cause the positions, and most particularly the heights, of the high intensity returns to be systematically biased. In the shaded relief image, this results in a narrow "trail" along the nadir line. Figure 3b. shows the same area after refinements have been made to the calibration lookup table. The corrections were derived simply by cutting several cross sections through the nadir line (which extended several tens of meters on each side of the nadir line) plotting the surface and determining the corrections needed to flatten the trail. The refined calibration values were linear over a range of intensities of 1500 to 2500, into which most of the nadir water surface returns fell. The corrected lookup table was used to process all of the data from the project and, based on samples examined from other swaths, generally reduced any remaining apparent height biases to about three to five centimeters. Because of the large size of the data set, we limited our examination to a small sampling, but after applying the corrections, the trails were greatly diminished, and in most cases could no longer be seen in the shaded relief images.

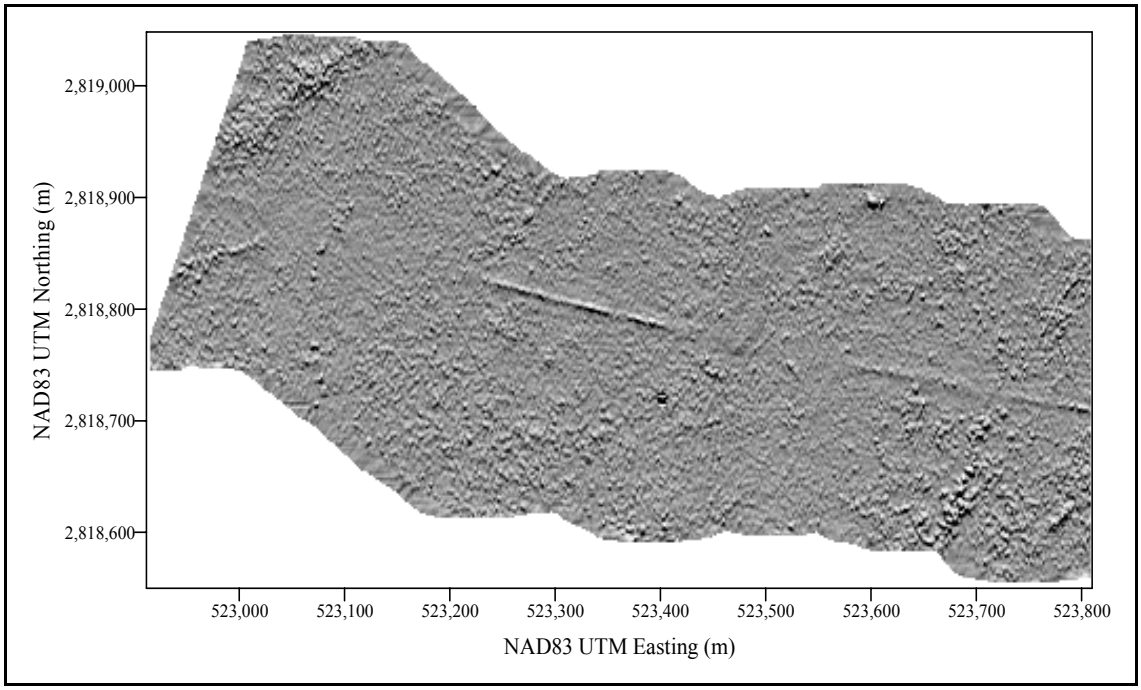

Figure 3a. Shaded relief image showing the trail caused by intensity calibration error.

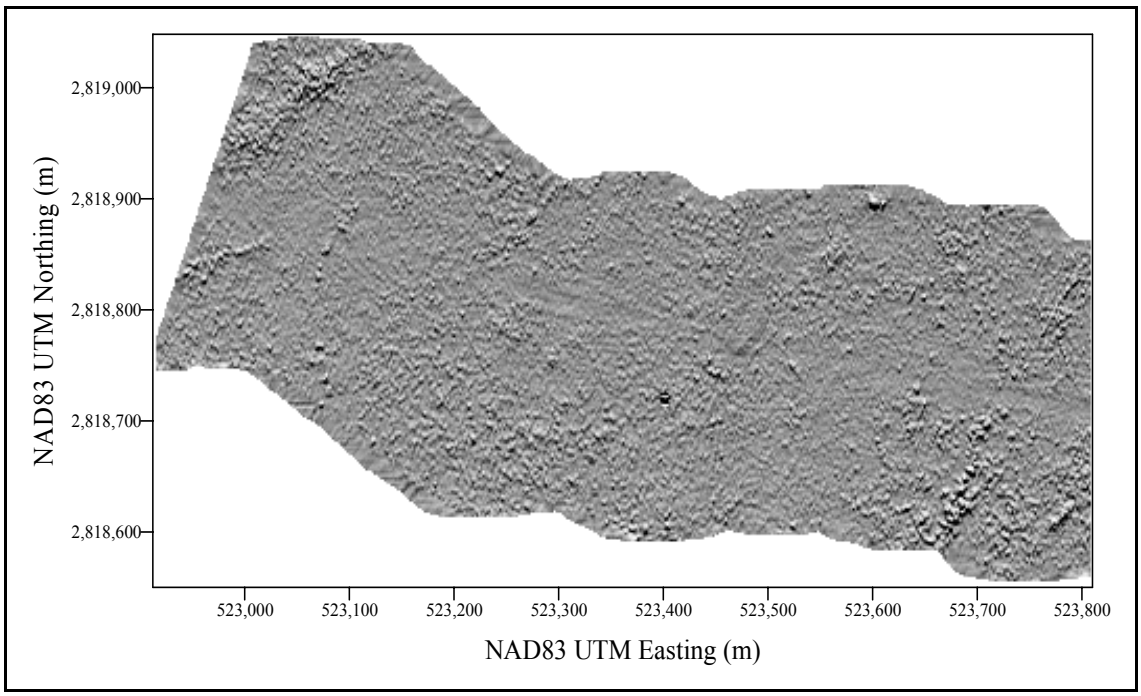

Figure 3b. Shaded relief image of the same area in Figure 3a after correcting intensity calibration.

FINAL PRODUCTS

Figure 4. shows a plot of the 25,905 nadir water surface points extracted from the total data set. The distribution along each flight line varies, depending on the density of the vegetation and the amount of open water. Kriging was used to interpolate heights at grid points to generate a DEM, and that DEM was used to compute height contours. Figure 5. shows a color filled contour map of the project area. An apparent slope of the water surface, from a high in the northeast to a low in the southwest, is immediately apparent.

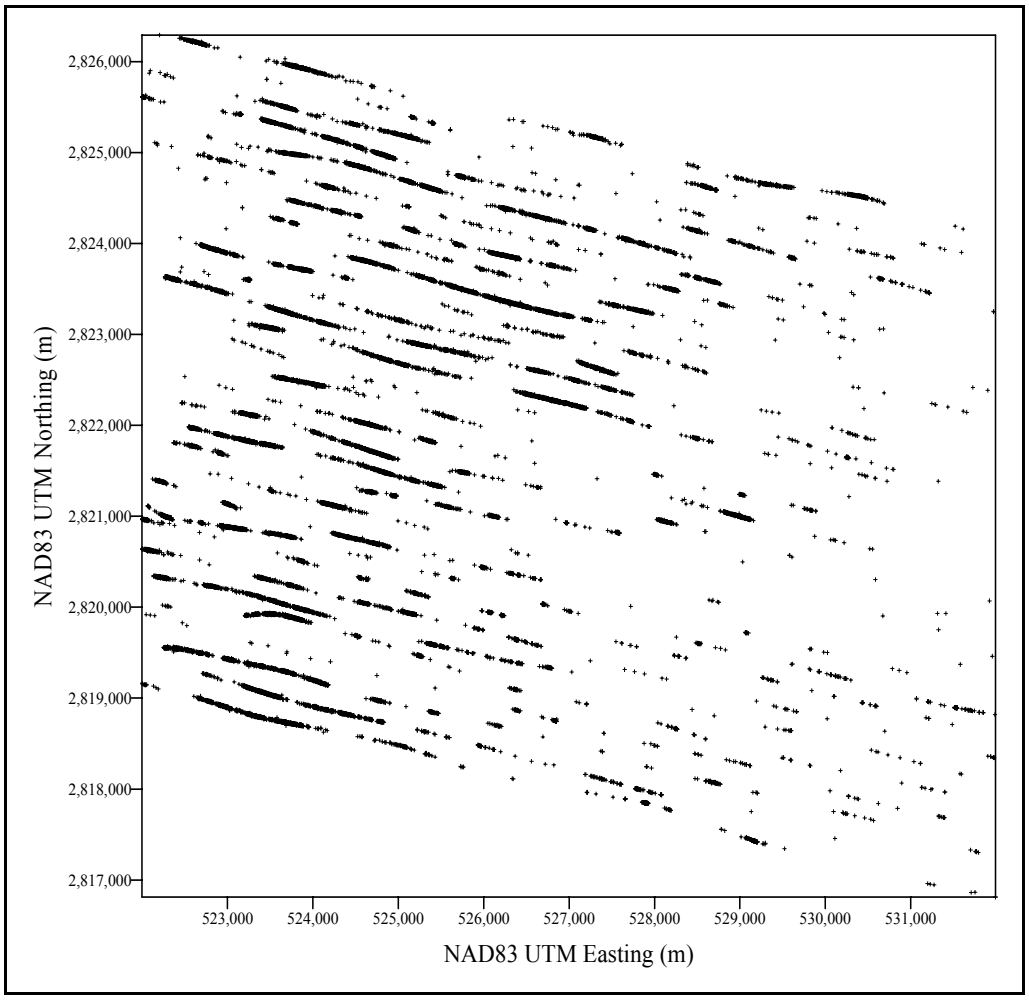

Figure 4. A plot of the 25,905 nadir water surface points extracted from the total data set.

CONCLUDING REMARKS

We conclude from this initial test that ALSM, with intensity capability, offers a convenient and reliable method of determining the precise height of the surface of sheet flow water in areas such as the Florida Everglades. While the Everglades are unique in certain aspects, there are other types of terrain where intensity values can be used to advantage. In fact, UF researchers first experienced and became aware of the potential value of water surface nadir returns while working along the intra-coastal waterway in Pinellas County, Florida. In that setting, they provided an accurate record of the surface of the tidal waters relative to the land, at the time of each of the data collection sessions. Similarly, in surveying tidal marsh areas along the coastline, the specular returns from nadir water surfaces help capture details of the complex drainage patterns in these environmentally sensitive areas, and document the height of the tidal water at the time of the mapping, with a precision of a few centimeters.

The use of ALSM in areas such as the Everglades or coastal marshes, where vegetation and water surfaces are closely intermixed in complex patterns, is not without problems. At angular distances of more than a few degrees from the nadir, the laser pulses reflected from the water surface are directed away from the aircraft and no return signals are detected, unless the reflected pulses strike vegetation. The laser light scattered from the vegetation may be sufficient to be detected by the ALSM sensor. We found a small percentage of such “multi-path” returns in the Everglades observations. These points could be identified because the anomalously long ranges yield height values below the surface of the water. Even with the increased processing required to remove multi-path points and perform extensive quality control procedures, ALSM is less expensive, faster and more accurate than traditional ground surveying and photogrammetric methods in these remote settings, and should prove invaluable in the restoration of the Everglades and coastal marsh areas.

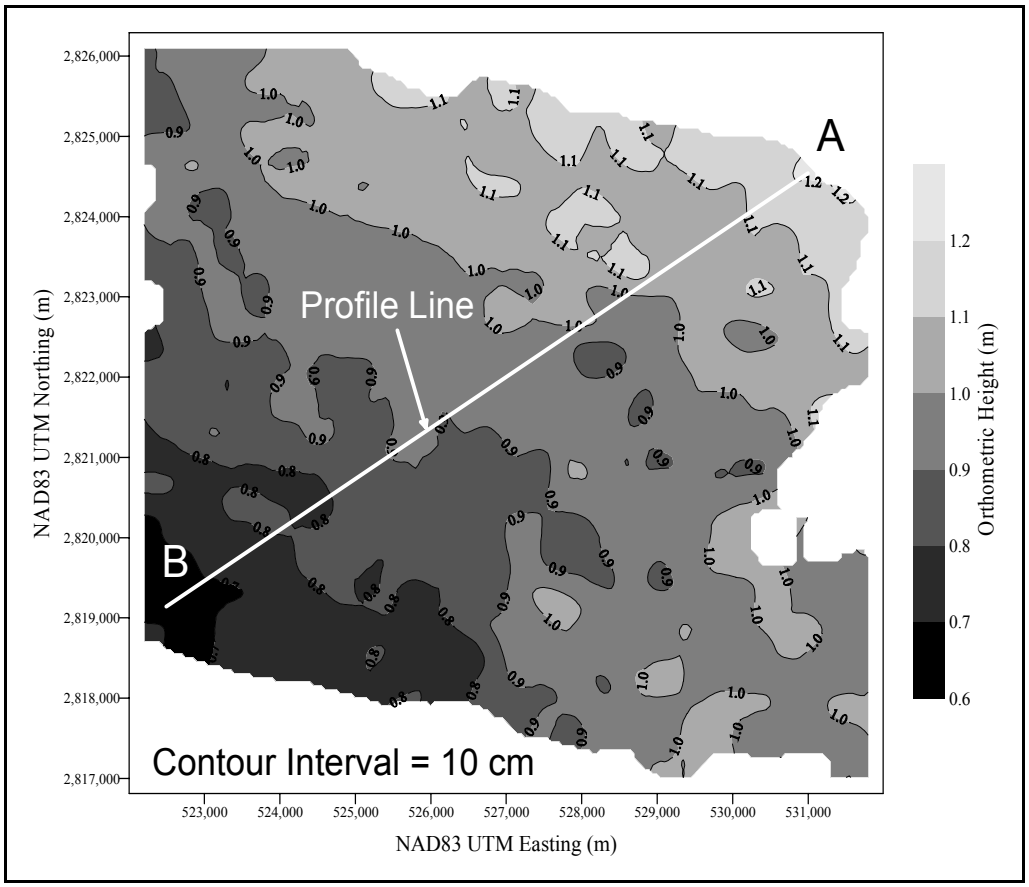

Figure 5. The height of the surface of sheet flow water through an area of the

Another step in the evaluation of ALSM for applications related to the restoration of the Everglades was recently announced by the South Florida Water Management District (SFWMD). It involves tests to determine if the technology might prove useful to monitor the evolution of tree islands scattered throughout the submerged grasslands. The goal is to be able to detect changes in the size of the tree islands, and in the health of the trees and shrubs on the islands. A contract to collect and analyze ALSM observations of the tree islands has been awarded to a private sector company. Unfortunately, it appears that the contractor will not collect intensity values. UF researchers think that this is a serious mistake, which will ultimately limit the usefulness of the data collected for the SFWMD project, and we are currently seeking the resources to map some number of the tree islands with the UF/FIU system.

ACKNOWLEDGMENTS

The research results presented in this paper were supported in part by the U.S. Geological Survey.

REFERENCES

Shrestha, R.L., W.E. Carter, M. Lee, P. Finer and M. Sartori, Airborne Laser Swath Mapping: Accuracy Assessment for Surveying and Mapping Applications, Journal of American Congress on Surveying and Mapping, Vol. 59, No. 2, pp. 83-94, 1999.

Carter, W. E., R.L. Shrestha and S. P. Leatherman, Airborne Laser Swath Mapping: Applications to Shoreline Mapping, Proceedings of International Symposium on Marine Positioning (INSMAP '98)**,** Melbourne, FL, Nov. 30 - Dec. 4, 1998.

Shrestha, R.L. and W.E. Carter, Instant Evaluation of Beach Storm Damage Using Airborne Laser Terrain Mapping, EOM, The Magazine for Geographic, Mapping, and Earth Information, pp. 42-44, 1998.

Gutelius, G, W.E. Carter, R.L. Shrestha, E. Medvedev, R. Gutierez, and J.G. Gibeaut, Engineering Applications of Airborne Scanning Lasers: Reports from the Field, HIGHLIGHT ARTICLE, PE&RS, The Journal of American Society for Photogrammetry and Remote Sensing, Vol. LXIV, No. 4, pp. 246-253, 1998.

LASER PULSE CORRELATION: A METHOD FOR DETECTING SUBTLE TOPOGRAPHIC CHANGE USING LIDAR RETURN WAVEFORMS

Michelle A. Hofton
Department of Geography, University of Maryland, College Park, MD 20742 USA
mhofton@geog.umd.edu

J. Bryan Blair
Laser Remote Sensing Branch, NASA Goddard Space Flight Center, Greenbelt, MD 20771 USA
bryan@avalon.gsfc.nasa.gov

KEYWORDS: LIDAR, laser altimetry, waveforms, natural hazards, surface deformation

ABSTRACT

We present a technique for using the recorded laser return pulse as a raw observation to detect centimeter-level vertical topographic change from large footprint airborne and spaceborne laser altimetry. We use the correlation of waveforms from coincident footprints as an indication of the similarity in structure of the waveforms from epoch to epoch, and assume that low correlation is an indicator of vertical structure or elevation change. Thus, using vertically and horizontally geolocated waveforms as raw observables (i.e., waveforms tied to a common reference ellipsoid), we assess whether epoch-to-epoch vertical ground motion results in a decrease in the correlation of coincident waveforms over time, and whether this can be used to quantify the magnitude of the deformation. Results of computer models and an example over an area of eroded beachfront are described.

1 INTRODUCTION

Laser altimeters provide a precise and accurate method for mapping topography at fine horizontal and vertical scales. A laser altimeter provides range by measuring the round-trip flight time of a short pulse of laser light from the laser altimeter instrument to the target surface. This range is then combined with ancillary information describing the position and attitude of the laser at the time of each shot to derive the horizontal and vertical position of each laser footprint relative to a known reference surface (i.e., WGS-84) (e.g., Hofton et al., 2000b).

Newer generations of airborne (e.g., Blair et al., 1999) and spaceborne (e.g., Dubayah et al., 1997) laser altimeters measure the range by recording the shape and time of the outgoing and received laser pulses. The shape of the return pulse provides unique information about the vertical structure of material such as vegetation within each laser footprint. The shape of a return pulse can be as simple as closely resembling the shape of the outgoing laser pulse, or extremely complex (containing multiple modes) and temporally distorted. Distortion of the return pulse is caused by the time-distributed reflections from vertically distinct layers of material within the footprint. While extremely small diameter footprints typically return simple pulses, larger footprints (10 – 100m in diameter) can contain numerous vertically distinct target surfaces and thus provide the potential for producing complex return pulses.

Interpreting the return pulse from laser altimeters has evolved from methods involving real-time analog timing between thresholds, constant-fraction discriminators, multi-stop time interval units, and using post-processed range-walk corrections, to actual recording of the time varying return pulse intensity, i.e., the return waveform. Post processing of the waveform can involve thresholding the return pulse to identify timing points, calculating a centroid to find the "center", or fitting one or more gaussian pulses to the signal to separate the individual surface reflections (Hofton et al., 2000a). The laser derived elevations resulting from these interpreted laser ranges are used for a variety of purposes, from producing topographic data sets for scientific or commercial studies, to providing ground truth for the validation and calibration of other remote sensing data sets. Due to the inherent precision and accuracy of laser-derived topography, these data enable unique studies of topography including the detection of topographic change over relatively small horizontal scales and small vertical change over large areas.

2 DETECTING ELEVATION CHANGE

Natural hazard monitoring requires repeated measurements of surface topography whose change reflects some geologic or hydrologic process. A simple and direct method for detecting vertical topographic change is to sample the elevation at two separate epochs and difference the coincident measurements (dubbed spot comparison method). This method has been used successfully in regions of simple terrain, for example, to precisely detect vertical elevation changes at Mt. St. Helens (Garvin et al., 1996), Assateague Island, MD (Krabill et al., 1999), and on the Greenland ice cap (Krabill et al., 1995). Problems can arise however if the laser return pulse is complex in shape or noisy, resulting in misinterpretation of the return pulse (either in real-time or post-processing) and a decrease in accuracy of the laser altimeter elevation measurement.

An alternative approach involves the return pulse correlation method (Hofton and Blair, 2000) which uses the shape similarity of near-coincident, vertically-geolocated laser return waveforms from two observation epochs to detect vertical change. A similar method was used previously by Blair and Hofton (1999) to assess laser footprint geolocation accuracy. The shape similarity of two coincident waveforms from different measurement epochs is assessed using the Pearson correlation, a ratio between the shared variance of the two waveforms and their individual variances (Figure 1). If no

change in the vertical structure within the footprint area occurred between measurement epochs within the vertical and horizontal extent of the waveforms, then two coincident, temporally distinct, geolocated waveforms will have a high level of correlation. Poorly correlating waveforms indicate that either vertical ground deformation or some kind of vertical structure change (for example, vegetation growth or loss) has occurred. The benefit of the pulse correlation method is that it eliminates subjective interpretation of individual waveforms and the errors resulting from any misinterpretation, especially in circumstances where the waveform is extremely complex.

For this initial study to estimate the capability to detect centimeter-level ground deformation, we assume that the ground deformation is the dominant source of vertical change within the area of the laser footprint (otherwise we risk confusing the ground elevation change with surface structural change such as tree growth). Consequently, we assume that changes in surface elevation result in corresponding changes in the elevations of all reflecting surfaces within the laser footprint between measurement epochs. That is, that all the modes within the waveform are moved up or down relative to the reference surface by an amount corresponding to the ground deformation that occurred. The amount of ground deformation is determined by calculating the correlation of the geographically coincident waveforms from different measurement epochs as the waveforms are vertically shifted relative to each other. The vertical shift at which the maximum correlation occurred indicates the amount of vertical change that occurred between the two epochs at that location. This forms the basis of the pulse correlation method.

Notice that we perform no interpretation of the laser waveform itself, even if the elevation of the desired reflecting surface has previously been misinterpreted (e.g. during real-time processing on the instrument). Thus, we are using an unbiased representation of the surface from which to extract elevation change. A constant bias or offset between the data sets is likely an indication of a systematic error or measurement bias that is easily removed, whereas variations in the vertical offset within or across an area may indicate actual vertical ground deformation signal.

3 RESULTS OF COMPUTER SIMULATIONS

To assess the sensitivity of the pulse correlation technique across an image of return waveforms, we generated a simulated set of laser altimeter waveforms from a series of surfaces with varying roughness and slope characteristics using the method of Blair and Hofton (1999). The surfaces were then deformed using the equation for a Mogi point source to simulate the effect of volcanic intrusion beneath the surface. A second set of waveforms, corresponding to the deformed surface, were then generated. We compared the two sets of waveforms using the pulse correlation method in order to recover the applied deformation signal. Waveforms correspond to 25m-wide footprints, with a laser pulse width of 0.6893m, and digitizer bin width of 0.2997m. Centimeter-level deformation is clearly visible in the results (Figure 2). To assess the potential for this technique under what may be more realistic data collection circumstances, the co-location between the two sets of waveforms (corresponding to the original and the deformed surfaces) was varied to evaluate the degradation of vertical sensitivity resulting from any misalignment between data sets. The results show that moderate horizontal offsets (i.e., several meters) between footprints from the two epochs do not degrade the vertical precision of change detection significantly. Although some horizontal averaging is required to improve the vertical resolution, we can clearly see centimeter-level deformation in the simulated data.

4 BEACH EROSION RESULTS

Assateague Island, MD, is an area that has been extensively surveyed on an almost annual basis using the small-footprint Airborne Topographic Mapper (ATM) system (Krabill et al., 1999). The island is a highly dynamic barrier island of the Atlantic coast, and is characterized by high levels of coastal change in which tens of meters of land can be lost or gained in a matter of months. Return waveforms were synthesized from the 1996 and 1997 ATM data sets using the method of Blair and Hofton (1999) to assess the feasibility of using the laser pulse correlation method to detect vertical change using large footprint laser data in an actively deforming region. The deformation results obtained using the pulse correlation method

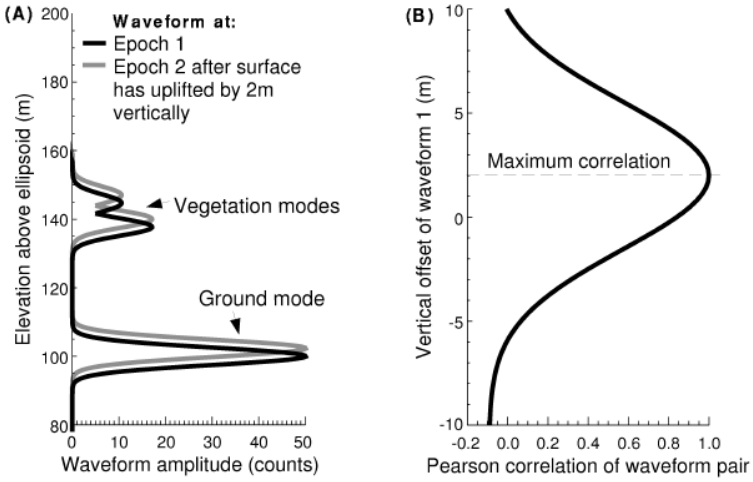

Figure 1. Overview of the pulse correlation method. (a) Two example, geolocated return laser waveforms from the same location but at different measurement epochs showing the effect on the individual waveform modes of 2m of surface uplift occurring between the two measurement epochs. The waveforms contain ground and vegetation modes. The modes within the return waveform collected at the later epoch are higher relative to the reference ellipsoid than at the first measurement epoch. (b) The Pearson correlation of the waveform pair versus their vertical offset. The maximum correlation occurs when the earlier-collected waveform is shifted up by 2m relative to the ellipsoid, i.e., this is the amount of uplift that occurred between the observation epochs.

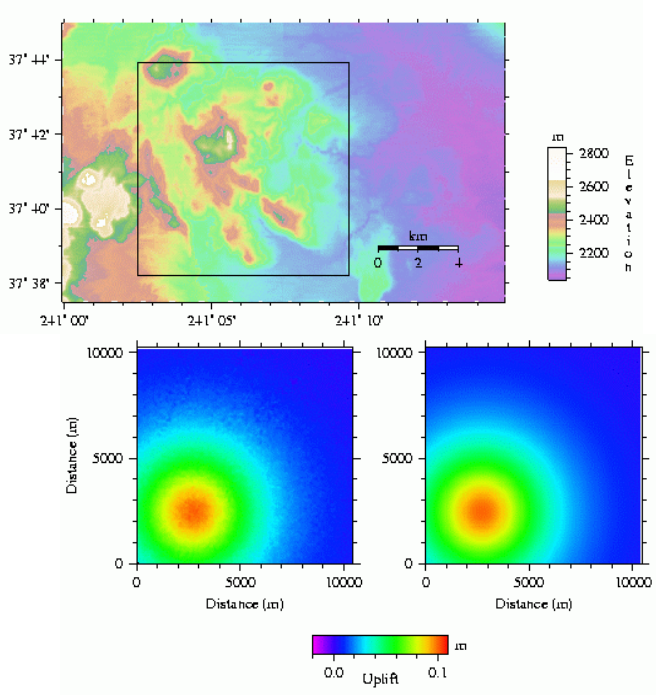

Figure 2. DEM of Long valley, CA. Topographic elevation is colored using the scale on the right. The box indicates the area whose surface elevations were deformed using a Mogi point source. Waveforms corresponding to both the undeformed and deformed elevation surface were synthesized, and compared using the pulse correlation method. The recovered and applied deformation fields are shown in the lower left and right of the figure respectively. The images are shaded according to the amount of uplift. The root mean square (RMS) difference is 0.014 cm.

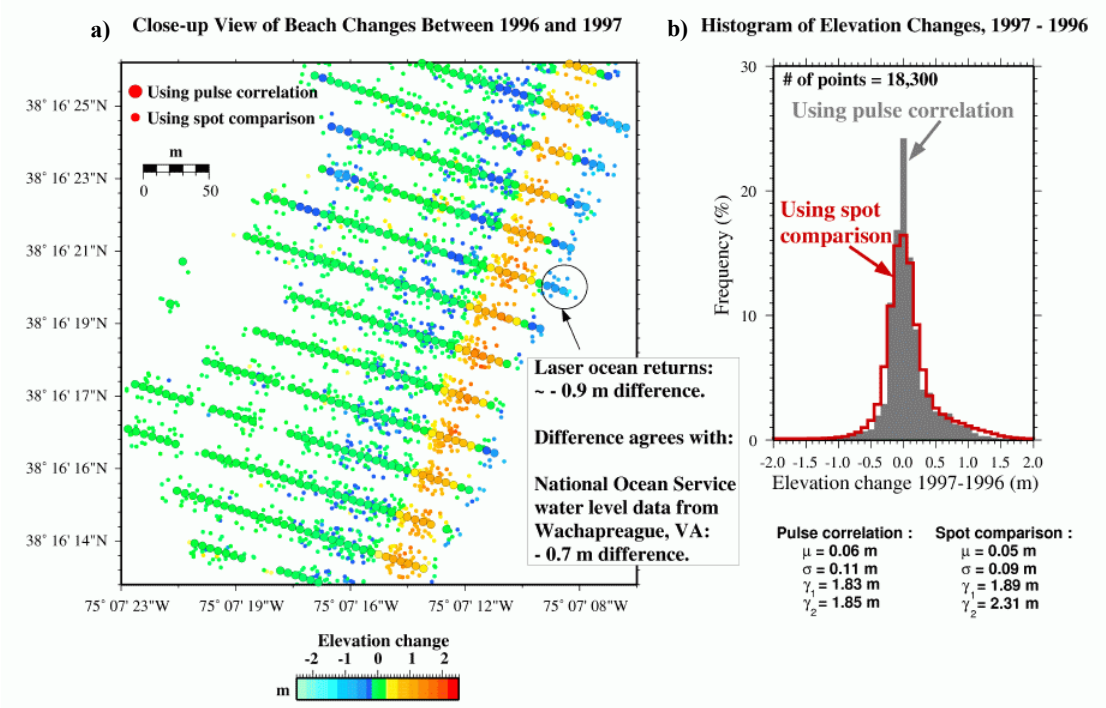

Figure 3. (a) Vertical elevation change detected along part of the Assateague Island beach, 1997-1996. The footprints within which waveforms were synthesized are outlined in black and colored using the amount of change detected using the pulse correlation method. The smaller footprints are those of the ATM, colored using the amount of change detected using the spot comparison method. Neither footprint set is drawn to scale. The elevation change scale bar is shown bottom right. (b) Distribution of vertical elevation change estimates along Assateague Island from 1996 to 1997 determined using the spot comparison (open histogram) and pulse correlation (shaded histogram) methods. The mean, standard deviation, skewness and kurtosis are denoted by ì , ó, ã$_1$, and ã$_2$ respectively.

are also compared to deformation results obtained from the comparison of spot elevation measurements on a footprint-by-footprint basis to establish the accuracy of the laser pulse correlation method relative to a more traditional technique.

Along the ~18 km-long stretch of coastline studied, up to 1.5 m of accretion occurred along the beach front from 1996 to 1997, with the widest zone of accretion occurring to the north. The majority of the area west of the beachfront underwent little or no change, except in the southern part of the surveyed region, where erosion of up to 0.5 m occurred immediately behind the beachfront. A small area (400m by 200m) of the beach front is shown in Figure 3. The amount of vertical elevation change detected using pulse correlation within each laser footprint is shown. For comparison, the elevation change from 1996 to 1997, derived by subtracting the elevation of the 1996 ATM spot closest (within a 1 m search radius) to each 1997 ATM spot are also shown. Similar patterns of deformation to that detected using the pulse correlation method are observed. Areas of deposition and erosion correspond and are of similar magnitude. Some ocean returns remained in the data. These show approximately -0.9 m of vertical change (Figure 3) because of the difference in tides at the times of the 1996 and 1997 surveys. This difference is consistent with that obtained from the differencing of water level data collected by the National Ocean Service (NOS) station at Wachapreague Island, VA, (~60km south west of Assateague Island), a difference of about -0.7m in elevation between the times of the ATM surveys in 1996 and 1997 (NOS, 2001). The difference between these predictions likely results from the proximity of the ocean returns to the shore and the distance of the water level station from the laser measurements. The distributions of elevation changes from 1996 to 1997 using the pulse correlation and spot differencing methods are similar in shape and have similar mean changes, standard deviations, and skewness values (Figure 3). The use of the pulse correlation method gives nearly identical vertical ground deformation estimates to those derived using a spot comparison method in this actively deforming region (Hofton and Blair, 2001).

5 SUMMARY

We show that by treating large-footprint laser altimeter return waveforms as "raw observations" we can potentially detect centimeter-level vertical change in topography and greatly reduce the potential for misinterpretation of the return waveforms. It is hoped that this technique will allow precise vertical topographic change detection from large-footprint, spaceborne laser altimeter data. Since this method is not restricted to use only under "bare Earth" conditions, it could potentially be used to complement change detection data collected by Interferometric Synthetic Aperture Radar, the current baseline measurement in natural hazards and surface change detection. The use of laser pulse correlation with medium-large (i.e., 10-100 m diameter) footprint laser altimeter waveforms cuold enable some altimeter system requirements such as footprint diameter and laser pulse-width to be relaxed to allow faster and easier change detection data collection over wider areas.

ACKNOWLEDGEMENTS

The authors would like to thank W. Krabill, E. Frederick, and the ATM group; and the members of the VCL team, in particular S. Luthcke, R. Dubayah, R. Knox, N. Casey-McCabe and D. Rabine. This work was funded as part of the calibration/validation activities of the Vegetation Canopy Lidar Science Team.

REFERENCES

Blair, J.B., Rabine, D.L., and Hofton, M.A., 1999. The Laser Vegetation Imaging Sensor (LVIS): A medium-altitude, digitization-only, airborne laser altimeter for mapping vegetation and topography. ISPRS J. Photo. Rem. Sens. 54, 115-122.

Blair, J.B., and Hofton, M.A., 1999. Modeling Laser Altimeter Return Waveforms Over Complex Vegetation Using High-Resolution Elevation Data. Geophysical Research Letters 25, 2509-2512.

Dubayah, R., Blair, J.B., Bufton, J.L., Clark, D.B., Ja Ja, J., Knox, R., Luthcke, S.B., Prince, S., and Weishampel, J., 1997. The Vegetation Canopy Lidar mission. In: Land Satellite Information in the Next Decade II: Sources and Applications. American Society for Photogrammetry and Remote Sensing, Bethesda MD, pp. 100-112.

Garvin, J. B., 1996. Topographic characterization and monitoring of volcanoes via aircraft laser altimetry. Geological Society of London Special Publication 110, 137-153.

Hofton, M.A., Minster, J.-B., and Blair, J.B., 2000b. Decomposition of Laser Altimeter Waveforms, 2000a, IEEE Transactions of Geoscience and Remote Sensing.

Hofton, M.A., Blair, J.B., Minster, J.-B., Ridgway, J.R., Williams, N.P., Bufton, J.L., and Rabine, D.L., 2000b. An airborne scanning laser altimetry survey of Long Valley California. International Journal of Remote Sensing 21, 2413-2437.

Hofton, M.A., and Blair, J.B., 2001. Detecting surface elevation change using laser altimeter return pulses, submitted to Journal of Geodynamics.

Krabill, W.B., Thomas, R.H., Martin, C.F., Swift, R.N., and Frederick, E.B., 1995. Accuracy of airborne laser altimetry over the Greenland ice sheet. International Journal of Remote Sensing 16, 1211-1222.

Krabill, W.B., Wright, C.W., Swift, R.N., Frederick, E.B., Manizade, S.S., Yungel, J.K., Martin, C.F., Sonntag, J.G., Duffy, M., Hulslander, W., and Brock, J.C., 1999. Airborne laser mapping of Assateague National Seashore Beach. Photogrammetric Engineering and Remote Sensing 66, 65-71.

NOS, 2001. NOAA National Ocean Service Center for Operational Oceanographic Products and Services, 2001. http://co-ops.nos.noaa.gov/co-ops.html.

PRECISE AIRBORNE LIDAR SURVEYING FOR COASTAL RESEARCH AND GEOHAZARDS APPLICATIONS

Roberto Gutierrez, James C. Gibeaut, Rebecca C. Smyth, Tiffany L. Hepner, John R. Andrews
Bureau of Economic Geology, The University of Texas at Austin, Austin, Texas, USA
oskar@mail.utexas.edu
Christopher Weed
Center for Space Research, The University of Texas at Austin, Austin, Texas, USA
William Gutelius
Optech, Inc., Toronto, Canada
Mark Mastin
U.S. Geological Survey, Tacoma, Washington, USA

KEYWORDS: LIDAR, laser, ALSM, calibration, natural hazards, shoreline mapping

ABSTRACT

The monitoring and analysis of many natural hazards requires repeated measurements of a topographic surface whose change reflects some geologic or hydrologic process. The development of airborne laser surface mapping (ALSM) allows the study of natural hazards over areas tens to hundreds of kilometers in extent with a horizontal resolution of 1 meter or less and a vertical accuracy of 0.10-to-0.15m. Change detection requires that repeated ALSM surveys be precise and accurate. Repeatability is a function of the stability and calibration of the instrument, the accuracy of GPS aircraft trajectories, the density and completeness of ALSM data coverage, the availability of "ground truth" information, and the accuracy and flexibility of ALSM data classification. Since 1997 The University of Texas at Austin (UT) has mapped various portions of the Texas Gulf coast using several small-footprint, scanning ALSM systems developed by Optech, Inc. During summer 2000, UT comprehensively mapped the Texas coast from Sabine Pass on the Texas-Louisiana border to the mouth of the Rio Grande River. These data provide a series of Gulf shorelines for estimating beach erosion rates and computing volumetric sand loss. The high-resolution beach and dune topography derived from ALSM will help characterize the susceptibility of the coast to hurricane overwash and storm-related flooding. In another project UT collaborated with Optech and the U.S. Geological Survey in March 2000 to survey fifteen municipalities in Honduras with ALSM as part of the USAID Hurricane Mitch Recovery program. Digital elevation models produced from these data are being used for flood and landslide hazard analysis. During these and other projects, UT began implementing procedures for instrument calibration, data classification, and ground GPS surveying that enhance the repeatability of our ALSM surveys.

1 INTRODUCTION

The Bureau of Economic Geology (BEG), a geologic and environmental research group within the University of Texas at Austin (UT), is the state agency responsible for providing shoreline information to the Texas legislature and state regulatory agencies. Because of the requirement for accurate shoreline data, the BEG began a program in airborne laser surface mapping (ALSM) in collaboration with the UT Center for Space Research, and Optech, Inc. This program began with a shoreline survey in December 1997 using an ALSM system provided by Optech (Gutierrez et al, 1998). In July 2000, UT acquired an Optech ALTM 1225 instrument, a 25kHz scanning laser mapping system. In this paper we describe our current ALSM program and how we are implementing geodetic techniques into our operations. We also discuss some results from our Texas shoreline mapping and a flood-hazard mapping project in Honduras, C.A.

2 METHODS

NASA began developing ALSM technology in the 1980's and several instruments (RASCAL, SLICER, AOL, LVIS, ATM) were developed for terrain, vegetation, and ice sheet mapping (Rabine et al, 1996; Harding et al, 2000; Krabill et al, 1995; Blair et al, 1999, Krabill et al, 2000). Commercial ALSM systems became available as the technology matured. Optech developed the ALTM 1020, a compact scanning ALSM system with a 5kHz laser repetition pulse rate, in 1995. Increases in laser power, laser pulse rate, and overall system performance were incorporated by Optech in subsequent models with the ALTM 1225 system appearing in 1999. The ALTM 1225 has the following specifications:

- Operating altitude 410-2,000 m AGL
- Laser pulse rate 25 kHz
- Laser scan angle variable from 0 to ± 20° from nadir
- Scanning frequency variable, 28 Hz at the 20° scan angle.
- Beam divergence 0.2 milliradian (half angle, 1/e)

The ALTM 1225 does not digitize and record the waveform of the laser reflection, but records the range and backscatter intensity of the first and last laser reflection using a constant-fraction discriminator and two Timing Interval Meters (TIM).

ALSM elevation points are computed using three sets of data: laser ranges and their associated scan angles, platform position and orientation information, and calibration data and mounting parameters (Wehr and Lohr, 1999). Global Positioning System (GPS) receivers in the aircraft and on the ground provide platform positioning. The GPS receivers record pseudo-range and phase information for post-processing. Platform orientation information comes from an Inertial Measurement Unit (IMU) containing three orthogonal accelerometers and gyroscopes. An aided-Inertial Navigation System (INS) solution for the aircraft's attitude is estimated from the IMU output and the GPS information.

2.1 Calibration

There are no standard instrument calibration procedures, each equipment manufacturer and ALSM group have developed its own techniques (Wehr and Lohr, 1999). The instrument calibration for our Optech ALTM 1225 includes the estimation of the scanner roll

and pitch bias corrections, a scanner scale correction, and a timing correction for each TIM. These corrections were initially measured in the manufacturer's laboratory facility and refined by flight testing. In the laboratory, range corrections were also tabulated for varying intensities of laser backscatter. We re-estimate the instrument calibration by flight-testing before and after an ALSM survey. Estimating GPS datum or ranging errors requires flying the instrument against "ground truth" - an area (e.g. road or airport runway) surveyed by ground GPS or conventional means. However, the scanner roll, pitch and scale biases can be accurately estimated through the careful comparison of overlapping flightlines (Burman, 2000).

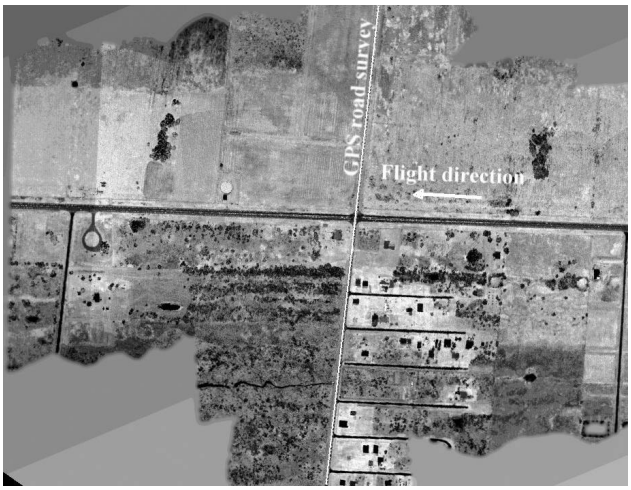

Figure 1. Laser backscatter intensity image of calibration area.

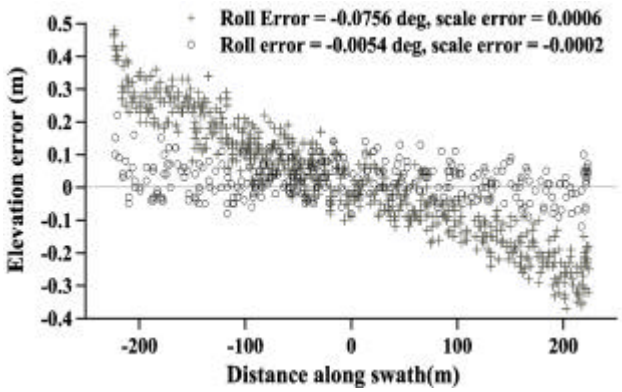

Figure 2. Roll and scale errors before and after adjustment.

Figure 1 is a laser backscatter intensity image constructed from several flightlines on the Texas coast. Indicated on the image is a kinematic GPS ground survey on a paved road oriented normal to the direction of four crossing flightlines. Figure 2 shows the elevation differences (+) between the ground GPS and one of these crossing ALSM flightlines processed using nominal calibration settings. We estimated calibration corrections from four flights spaced over two weeks (July 12 through July 27, 2001) of surveying. Plotted for comparison are the elevation differences (O) between the ground GPS and the same flightline after calibration adjustment. The consistency of the four calibration flights indicates that the ALSM system's pointing accuracy has a RMS of ≤0.01° and a scanner scale RMS of ≤0.0006.

2.2 GPS

The absolute positioning of the ALSM platform comes from GPS. Therefore planning the GPS component of the ALSM survey, operating the air and ground GPS equipment, and estimating the aircraft trajectory from the GPS observations are critical steps. We conduct ALSM surveys during periods when the Dilution of Precision (DOP) is ≤3.5 as estimated for a 15° elevation mask. We occupy ground GPS base stations that have an unobstructed sky-view down to 10°-to-15° above the horizon and are free of RF interference or significant multi-pathing. We use dual-frequency, 12-channel GPS receivers in the aircraft (Ashtech Z-12) and on the ground (Ashtech Z-12 or Trimble 4000SSi) to record data at 1Hz. The ground receivers use Dorne & Margolin chokering antennas to reduce multi-pathing and a Dorne & Margolin C146-2-1 antenna is mounted in the aircraft. All antennas have been calibrated by the National Geodetic Survey's (NGS) Geosciences Research Division. The NGS measures the antenna's L1 and L2 phase center variations as a function of GPS satellite elevation (see figure 3). Unless our GPS observations are corrected for these phase center variations, errors as large as a decimeter can be introduced into the height component of the aircraft trajectory.

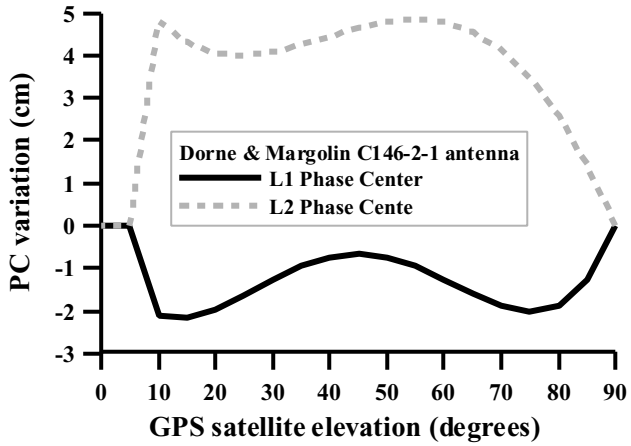

Figure 3. Phase center error as a function of satellite elevation for the C146-2-1 antenna.

We use the NGS's kinematic GPS processing software, KARS (Mader, 1992), to estimate a double-differenced, ionospherically-corrected (L3), ambiguity-fixed, phase solution for the aircraft trajectory. We use precise GPS ephemerides, computed by the International GPS Service (IGS) or the NGS, instead of the broadcast orbits in the trajectory solution.

On July 17, 2001, we mapped the Texas shoreline from Sabine Pass to Galveston Island (see figure 4). A Trimble 4000SSi receiver occupied a tide gauge benchmark at Sabine Pass and an Ashtech Z-12 occupied a tide gauge benchmark at Port Bolivar. During the almost three-hour survey, the aircraft was always within 50 km of one GPS base station, but could be as far as 150 km from the other basestation (see figure 5).

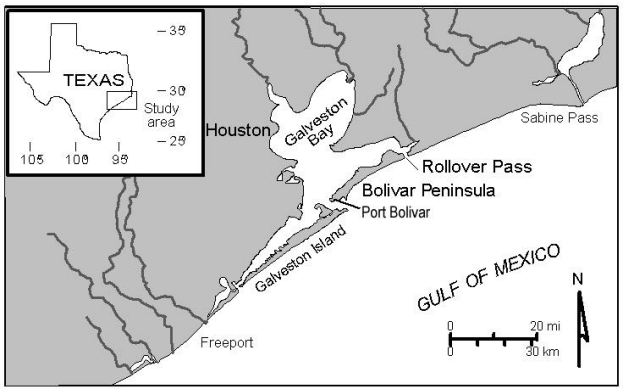

Figure 4. The Galveston Bay - Bolivar Peninsula area.

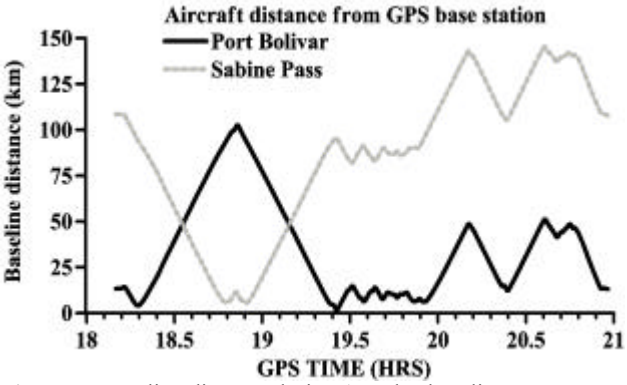

Figure 5. Baseline distance during 17 July shoreline survey.

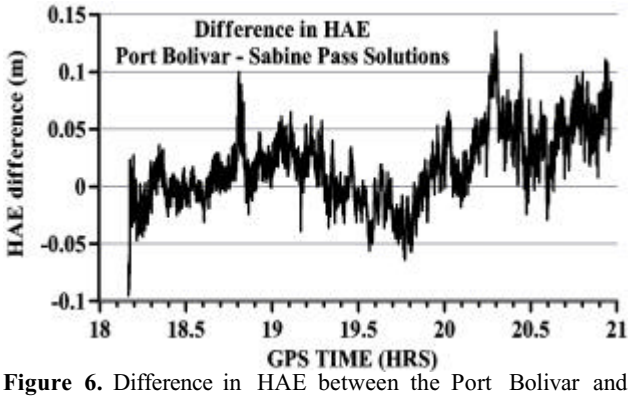

Figure 6. Difference in HAE between the Port Bolivar and Sabine Pass aircraft trajectories for July 17, 2001 shoreline survey.

We computed KARS trajectories for the aircraft using both the Port Bolivar and Sabine Pass GPS base station data. The differences between the two trajectories in the east and north, components are under 0.05m. The HAE differences between the two trajectories are under 0.05m when the aircraft is within 50km of both base stations. The HAE differences are under 0.10m even when the aircraft is more than 100 km from one of the base stations (see figure 6).

2.3 Data Coverage

Small foot-print ALSM systems operating with a 25kHz or higher laser pulse repetition rate can generate ALSM coverage with a sub-meter laser point spacing during a single pass. However, vegetation, buildings, and topography can cause shadowing that may significantly reduce the ground surface coverage. For area surveys we fly an orthogonal grid, two sets of flightlines at right angles, to minimize data gaps. Scanning from a number of different aircraft positions allows us to more accurately reconstruct the morphology of topographic or cultural features. For ALSM surveys that are route-oriented, e.g. a shoreline survey, parallel swaths can be spaced laterally so as to scan both sides of a route-parallel obstruction such as a dune line.

2.5 Ground Truth

We conduct ground GPS surveys within each ALSM survey area to acquire ground "truth" information. We re-occupy the ALSM GPS base stations and survey an open area with an unambiguous surface (road, soccer fields, large building) using kinematic GPS techniques. The ALSM data are sorted to find LIDAR points that fall within 0.5m of a ground GPS survey point. The mean elevation difference between the ALSM (last returns only) and the ground GPS are used to estimate and remove an elevation bias from the ALSM. The standard deviation of the elevation differences provide an estimate of the LIDAR precision. Selected portions from each ALSM data set (last return only) are used to generate a high-resolution (1m $\times$ 1m or 0.5m $\times$ 0.5m) digital elevation model (DEM) or laser intensity image. The kinematic GPS data are superimposed on the DEM or intensity image and examined for any horizontal mismatch.

Figure 7 is a 0.5m $\times$ 0.5m laser backscatter intensity image of the soccer field in Juticalpa, Honduras. The chalk markings on the field are discernible. On the right panel, the survey points from a GPS survey of the chalk marks and two transects across the field are superimposed on the intensity image. The GPS and ALSM match to within the resolution of the image indicating an ALSM horizontal error of <0.5m. There were 417 ALSM points that fell within 0.5m of a GPS ground survey point on the soccer field. The mean elevation difference between the GPS and ALSM was –0.169m with a RMS of 0.088m.

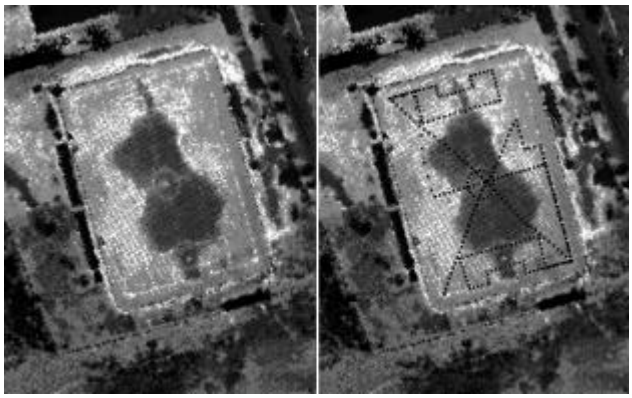

Figure 7. Intensity image of soccer field with GPS ground survey overlain.

2.4 Data classification

ALSM generates a semi-random cloud of elevation points that requires classification into reflections from ground and vegetation. As a preliminary step towards constructing digital elevation

models, we have classified ALSM data using algorithms developed by TopScan GmbH (Petzold et al, 1999) and by the UT Center for Space Research (Neunschwander et al, 2000). The TopScan algorithm identifies points as either "ground" or "non-ground" by iteratively improving an initial terrain surface. The initial terrain surface is generated from the minimum value of elevation points within a large, moving window. All the elevation points that exceed a specified threshold above the terrain are classified as non-ground points and removed. Using a smaller moving window, the remaining elevation points are used to create a new terrain surface. The ALSM data are again compared to a threshold value and the non-ground points are removed. This process is repeated for a set number of iterations. The window size and threshold values are terrain-dependent and require a high level of user interaction.

The UT method classifies elevation points as ground, vegetation, or buildings using an image-based processing algorithm. The ALSM data are gridded to create a high-resolution topographic image. The average topographic surface is estimated and subtracted from the high-resolution image. The resulting residual image contains the high-frequency content of the vegetation and the building edges. The lower envelope of high-frequency residuals represents the ground surface in the signal. Using the lower envelope, an initial ground surface is estimated. A gradient-based method is used to detect and remove any large buildings remaining in the estimated ground surface. After interpolating across gaps, the final ground surface is used to classify the ALSM data. Building classification is accomplished by first detecting planar surfaces representing roofs. The building boundaries are delineated by extending the edges using a gradient-flood fill method. The building surface is then used to classify ALSM points as man-made features. A building outline can be distorted by laser multi-pathing, therefore ALSM first-returns are used for building classification.

Figure 8 is a 1m × 1m DEM constructed from first-return ALSM data of the Mayan ruins at Copan, Honduras. An aerial photograph is shown for comparison. Figure 9 is a 1m × 1m DEM of the Copan ruins constructed from last-return ALSM data filtered to remove the trees using the envelope detector and gradient based method developed at UT. The elevation points representing the Mayan archeological structures were classified and added to the ground points before the DEM was computed. For comparison is a site map constructed from a Harvard University ground survey.

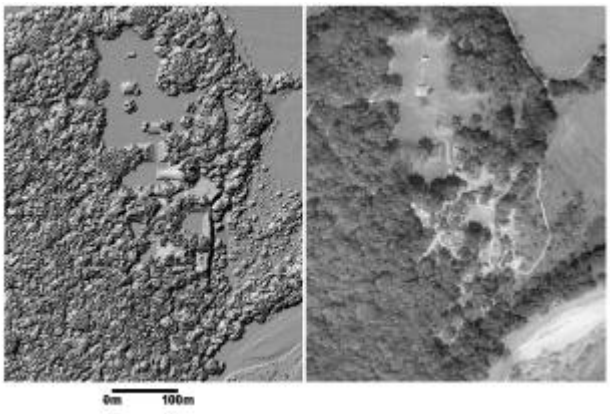

Figure 8. Left: ALSM DEM of Copan. Right: aerial photograph.

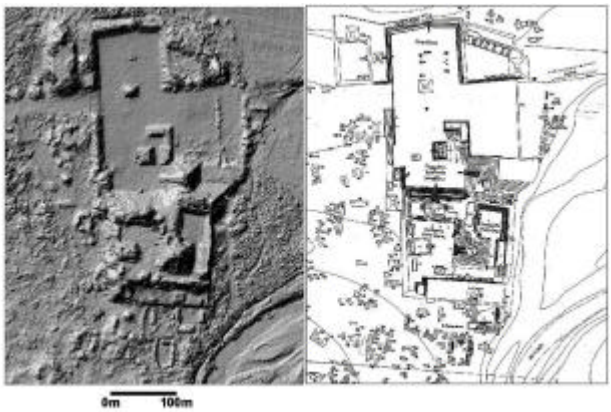

Figure 9. Left: vegetation-filtered ALSM. Right: ground survey.

3 COASTAL MAPPING

3.1 Texas Gulf Shoreline Change Project

In 1999, with the support of the Texas General Land Office, the BEG developed the Texas Shoreline Change Project. The project's goal is to establish a state-of-the-art regional shoreline-monitoring and shoreline-change analysis program that will help solve coastal erosion and storm hazard problems along the bay and Gulf shorelines of Texas. ALSM is a key component of the Texas Shoreline Change Project; it is important in identifying "critical coastal erosion areas" and in the monitoring of historical shoreline erosion rates.

During 2000 we mapped the entire Texas Gulf shoreline using the Optech 1225 system from Sabine Pass, at the Texas-Louisiana border, to the mouth of the Rio Grande River, a distance of over 600 kilometers. We mapped the shoreline in three sections: Sabine Pass to Freeport (212km), Freeport to Corpus Christi (215km), and Corpus Christi to the Rio Grande (174km). During a typical shoreline survey, the aircraft flew two to four passes along the shoreline with parallel swaths overlapping by about 50 percent. The survey altitude varied from 450m to 760m AGL and the ground speed was usually held to 51m/sec (100 knots). The resulting ALSM coverage of the beach, dunes, and back-barrier area is 500m to 700m wide and has an average ground point spacing of <1m.

Three ground GPS receivers, Ashtech Z-12 or Trimble 4000SSi, operated during the ALSM mapping. One GPS receiver was situated at each end of the 200km section of coastline and the third was located approximately in the middle of the survey area. Six of the nine GPS base stations occupied benchmarks at NOAA or Texas Coastal Ocean Observation Network (TCOON) tide gauges. These gauges are at Sabine Pass, Port Bolivar, Port O'Connor, Port Aransas, Port Mansfield, and South Padre Island. The remaining three GPS ground stations were monuments established by either the NGS, the U.S. Army Corps of Engineers, or UT.

GPS data processing was conducted in the International Terrestrial Reference Frame 1997 (ITRF97) and the ALSM elevation points were output in Universal Transverse Mercator (UTM) coordinates and height above the GRS-80 ellipsoid (HAE). The ALSM data were compared to GPS ground surveys for the estimation of

ALSM elevation biases. Shorelines were delineated from 1m × 1m digital elevation models (DEM). Long and short ALSM ranges (e.g. clouds, birds, and multi-paths) were edited and ALSM elevation biases were removed. The edited and bias-corrected ALSM data were then imported into ARC/INFO and interpolated using the TOPOGRID module, which is based on the ANUDEM interpolation method of Hutchinson (1989). The DEM's were converted from HAE to orthometric height using the G99SSS gravimetric geoid model (Smith and Roman, 2000) and adjusted vertically so that the zero-elevation conformed to mean sea level (MSL) at the nearest tide station.

3.2 Rollover Pass

Rollover Pass is a small artificial inlet on the southeast Texas coast that connects East Bay of the Galveston Bay system with the Gulf of Mexico. The channel was dredged across a narrow portion of Bolivar Peninsula in 1954/55 and has stabilized at a width of 61m. Bolivar Peninsula is an area of naturally high erosion rates, however the shape of the shoreline shows that the artificial inlet has altered rates of shoreline movement by changing the littoral drift rate in the area.

From 1996 to 1999, Tropical Storms Josephine and Frances caused a total of 27m of scarp retreat 3.2km to the west of Rollover Pass. The process of shoreline retreat in the Rollover Pass area involves episodic and dramatic scarp retreat during storms followed by post-storm recovery and widening of the beach in front of the scarp. Eventually, the long-term erosion process resumes and the beach begins to narrow, allowing a subsequent storm to erode the scarp again.

We collected ALSM data along Bolivar Peninsula before Tropical Storm Frances on August 6, 1998, and after the storm on September 17, 1998 using an Optech 1020 ALSM system. All the HAE were transformed into orthometric heights using the National Geodetic Survey G96SSS geoid model. All the ALSM data were adjusted by –0.35m vertically so that the zero-elevation would conform to the local mean sea level as measured at the Port Bolivar tide gauge.

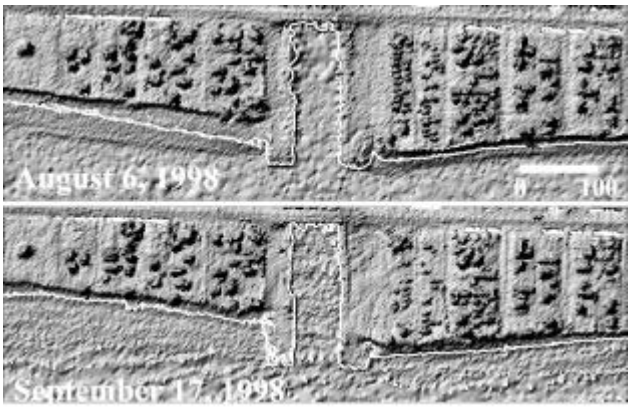

Figure 10. ALSM shaded relief images of Rollover Pass. Upper panel is the pre-Tropical Storm Frances shoreline with the 1m contour in white. The lower panel is the post-Frances shoreline.

We computed pre- and post-Frances 2m × 2m DEMs from the vertically adjusted data sets. Figure 10 shows the coastal topography at Rollover Pass before and after Frances. The 1m elevation is the white contour line on both shaded relief images. We digitized the 1m contour lines along the beach for a distance of 10km on either side of Rollover Pass. Figure 11 shows the shoreline change as represented by the movement of the 1m contour from August 6 to September 17, 1998. The shoreline data show a complex pattern of erosion. This pattern reflects the interaction of factors including offshore topography and wave refraction, piers and other man-made shoreline structures, and pre-storm beach morphology in determining the response of the beach to the storm. Except for a small area within 300m west of Rollover Pass where as much as 30m of retreat occurred, it appears that the pass had no unusual effect on beach erosion during this storm.

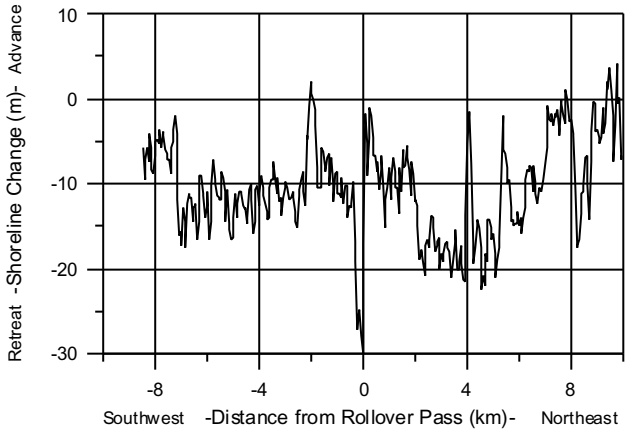

Figure 11. Change in 1m contour at Rollover Pass during due to Tropical storm Frances.

Figure 12. Geotube installed in front of the beach scarp at Bolivar Peninsula during July 2001

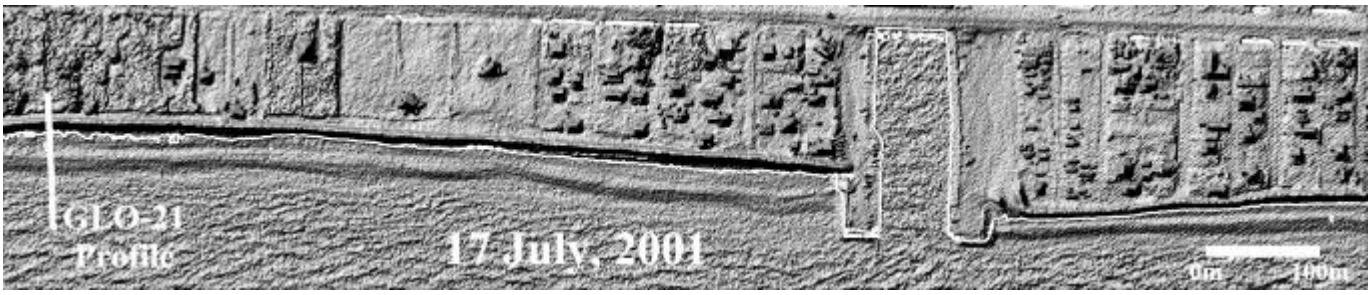

Figure 13. ALSM shaded relief image of Rollover Pass on 17 July 20001 showing geotubes installed behind the beach and in front of the eroding beach scarp. The 1m elevation contour is shown in white. A shore-normal beach profile (GLO-21) is to the left of Rollover Pass.

In 1999, communities on Galveston Island and Bolivar Peninsula began installing geotextile tubes (geotubes) along the most erosion-prone stretches of shoreline. The geotubes are sand-filled sleeves of geotextile fabric with an approximately 4m oval cross section (see figure 12). The ALTM 1225 system was used to map the Galveston and Bolivar shorelines, including the geotubes, on 17 and 18 July, 2001 (see figure 13).

Kinematic GPS and a total station were used to measure a set of shore-normal profiles after the ALSM surveys were flown. The profiles extended across the geotubes, the beach, and for 100-200m offshore. Figure 14 compares the topography measured by ALSM with the total station profile at location GLO-21 (see figure 13). The ALSM elevations agree well with the ground control except were dense vegetation behind the geotubes masks the true ground surface. Thick deposits of sargassum on the back-beach also cause the ALSM elevations to be slightly higher than the true ground surface. These new data will be used to study the response of the beach and geotubes to coastal processes.

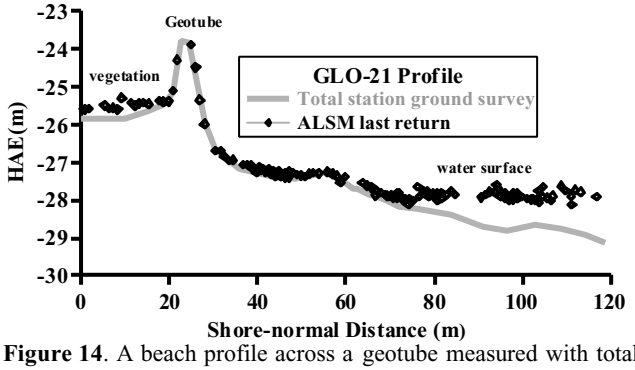

Figure 14. A beach profile across a geotube measured with total station on 19 July, 2001 is compared to ALSM data collected on 17 July, 2001.

4 FLOOD HAZARD MAPPING

4.1 Hurricane Mitch

From October 27 to November 1, 1998, Central America was devastated by Mitch, a category 5 hurricane on the Saffir-Simpson scale with winds up to 155 mph. Mitch is responsible for over nine thousand deaths, making it one of the deadliest Atlantic tropical cyclones in history and comparable to the great Galveston storm of 1900. In Honduras, the human toll is an estimated 5,000 deaths. Whole villages were washed away and an estimated 70-to-80 percent of the transportation infrastructure was destroyed. At least 70 percent of the crops were destroyed; an estimated $900 million loss. Honduras is still rebuilding the housing and infrastructure destroyed by Hurricane Mitch. To minimize future flood disasters, the Honduran government needs maps that accurately delineate probable areas of inundation by flooding.

From February to March 2000, the BEG, the U.S. Geological Survey (USGS) and Optech collaborated to map the channel geometry of the floodplains within 15 Honduran municipalities using ALSM. Between January 7-21, 2001, the USGS and BEG collaborated again to measure the geometry and location of 21 bridges in these 15 municipalities using a total station and GPS equipment. The USGS will use the bridge geometry and ALSM data to generate new, accurate 50-year flood inundation maps for each Honduran municipality.

The construction of the Honduran inundation maps involved three general steps. We estimated the 50-year stream discharges for the rivers in each municipality using a statistical analysis of precipitation and a rainfall-runoff model. We then computed water-surface elevations using channel geometry information from ALSM-derived DEM's and the HEC-RAS hydraulic simulation model (U.S. Corps of Engineers, 1998). HEC-GeoRAS, an ArcView extension, was used to define the stream thalweg, banks, overbank centerlines, and extract channel cross-sections from the DEM's (U.S. Corps of Engineers, 2000). Often a shaded relief image of the DEM was used as background to help locate these various lines. Manning roughness coefficients, n, were estimated by the hydrologists from field observations or by reviewing a shaded relief image of the DEM. The shaded relief image gave a good view of the density of vegetation in the stream channel – the higher densities were given higher n values. Finally, the simulated water levels from the hydraulic mode were plotted as depth and area of inundation over the DEM.

4.2 Tegucigalpa

We installed the ALTM 1225 system in a Beech King Air A-90 aircraft in the U.S. and ferried the aircraft to Toncontin Airport in Tegucigalpa, Honduras. Tegucigalpa was mapped during 1-2 March, 2000. We operated the instrument at a laser repetition rate of 25kHz, a laser scanning rate of 28Hz, and a laser scan angle of ±20° off nadir. We flew the aircraft at an average airspeed of 140 knots (72 m/s). This resulted in a spacing of about 2.6m between laser scan lines. The aircraft altitude varied between 800m to 1200m above ground level (AGL). To generate an approximately 1m × 1m ground point spacing, we mapped the city with a grid of orthogonal flight lines with approximately 30 percent side-lap between adjacent swaths (see figure 15).

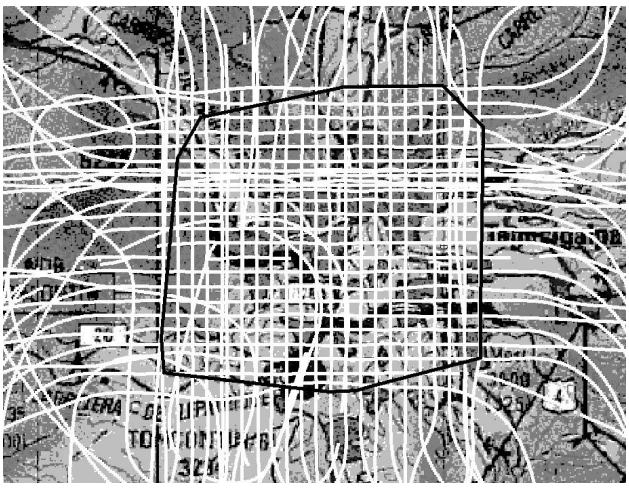

Figure 15. Flightlines over the 10 km x 10 km survey area for Tegucigalpa, Honduras.

These flights produced a uniform and dense ALSM data point coverage over an approximately 10km × 10km area of Tegucigalpa. Figure 16 shows the point "cloud" distribution over the city center at the confluence of the Rio Grande O Choluteca and the Rio Guacerique. The only data gaps are on the rivers where the water surface was often too specular to provide good laser returns.

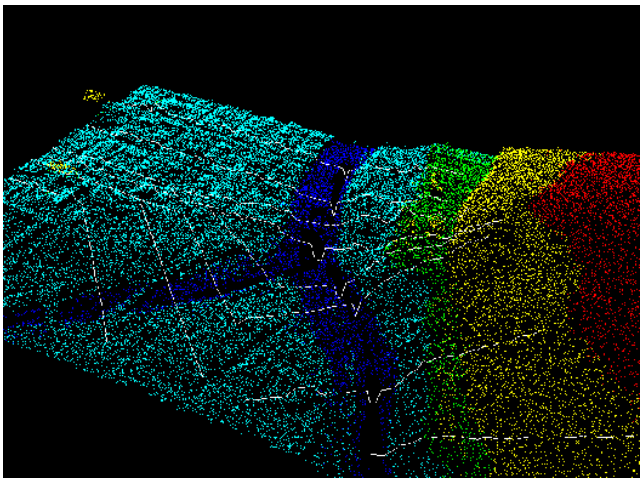

Figure 16. ALSM point cloud for central Tegucigalpa. The individual laser returns are colored to represent elevation. Channel cross-sections are shown in white.

We edited the ALSM data, compared them to ground surveys, and corrected for elevation biases. We generated a 1.5m × 1.5m "all points" DEM using all the ALSM last-return data. We then applied the TopScan vegetation-filtering algorithm to the last-return ALSM data. The filter parameters were chosen so that reflections from trees were removed, but most reflections from the ground surface and buildings were retained. We constructed a second, 1.5m × 1.5m "vegetation-removed" DEM from the filtered ALSM data. We then used HEC-GeoRAS to define the river channels and extract cross-sections from the "vegetation-removed" DEM' (see figure 16).

Heavy rains associated with Hurricane Mitch caused three major landslides in Tegucigalpa. The most devastating slide occurred on the Cerro Berrinche in northwest Tegucigalpa. The El Berrinche landslide destroyed an entire hillside community and dammed the Rio Grande O Choluteca causing significant flooding in the city center. Figure 17 shows the topography of the El Berrinche landslide after mitigation. The toe of the landslide has been cut into a series of steps and stabilized with gabions.

Figure 17. Shaded relief image of the El Berrinche landslide in Tegucigalpa.

5 DISCUSSION

Erosion along the Texas coast caused by the recent tropical storms in the Gulf of Mexico has intensified efforts to save property and houses. ALSM can provide the topographic models needed for geomorphic analysis and the delineation of areas particularly susceptible to storm damage. Post-storm ALSM surveys allow rapid and quantitative assessment of the amount of erosion and vulnerability of the coast to subsequent storms. In the past, coastal geologists and engineers have either conducted regional studies with sparse data or local studies with detailed data. With ALSM, however, it is possible to acquire detailed and accurate topographic data over a broad coastal region allowing geomorphic analysis across the continuum of spatial scales.

Landslide and flooding risks are strongly dependent on topography. With ALSM it is possible to characterize topography over large areas with sufficient resolution and accuracy to model hydrologic and geomorphic processes with unprecedented detail. New, quantitative models for hydrologic and surficial processes can be developed and tested using high-resolution topographic data.

6 REFERENCES

Blair, J.B., D. L. Rabine, and M. A. Hofton, 1999, The Laser Vegetation Imaging Sensor: a medium-altitude, digitization-only, airborne laser altimeter for mapping vegetation and topography, ISPRS Journal of Photogrammetry and Remote Sensing, vol. 54, no.2-3, pp.115-122.

Burman, H., 2000, Adjustment of laser scanner data for correction of orientation errors, International Archives of

Photogrammetry and Remote Sensing, Vol. 23, Part B3, pp.125-132.

Gutiérrez, R., J. C. Gibeaut, M. M. Crawford, M. Mahoney, S. Smith, W. Gutelius, D. Carswell, and E. MacPherson, 1998, Airborne laser swath mapping of Galveston Island and Bolivar Peninsula, Texas, in Proceedings of the Fifth International Conference for Remote Sensing for Marine and Coastal Environments, San Diego, CA., vol. I, pp. 236-243.

Harding, D.J., J.B. Blair, D.L. Rabine, and K.L. Still, 2000, SLICER airborne laser altimeter characterization of canopy structure and sub-canopy topography for the BOREAS Northern and Southern Study Regions: Instrument and Data Product Description, Volume 93 in Technical Report Series on the Boreal Ecosystem-Atmosphere Study (BOREAS), F.G. Hall and J. Nickeson, Eds., NASA/TM-2000-209891, Vol. 93, 45 pp.

Hutchinson M.F., 1989, A new procedure for gridding elevation and stream line data with automatic removal of spurious pits, Journal of Hydrology, vol.106, pp211-232.

Krabill, W.B., R.H. Thomas, C.F. Martin, R.N. Swift, and E.B. Frederick, 1995; Accuracy of Airborne Laser Altimetry Over the Greenland Ice Sheet, International Journal Remote Sensing, Vol. 16, No. 7, pp. 1211-1222.

Krabill, W., W. Abdalati, E. Fredrick, S. Manizade, C. Martin, J. Sonntag, R. Swift, R. Thomas, W. Wright, J. Yungel, 2000, Greenland Ice sheet: high–elevation balance and peripheral thinning, Science, pp.428-430.

Mader, G. L., 1992, Rapid static and kinematic Global Positioning System solutions using the ambiguity function technique, Journal of Geophysical Research, vol. 97(B3): pp.3271-3283.

Neunschwander, A., M. Crawford, C. Weed, and R. Gutierrez, 2000, Extraction of digital elevation models for airborne laser terrain mapping data, Geosciences and Remote Sensing Symposium, 2000, Proceedings, IGARSS 2000, IEEE 2000 International, vol.5, pp.2305-2307.

Petzold, B., P. Reiss, and W. Stössel, 1999, Laser scanning – surveying and mapping agencies are using a new techniques for the derivation of digital terrain models, ISPRS Journal of Photogrammetry and Remote Sensing, vol. 54, no.2-3, pp.95-104.

Rabine, D. L., J. L. Bufton, and C. R. Vaughn, 1996, Development and test of a raster scanning laser altimeter for high-resolution airborne measurements of topography, IGARSS96.

Smith, D.A., and D.R. Roman, 2001, GEOID99 and G99SSS: One arc-minute models for the United States, Journal of Geodesy, in press.

Wehr, A. and U. Lohr, 1999, Airborne laser scanning - an introduction and overview, ISPRS Journal of Photogrammetry and Remote Sensing, vol. 54, no.2-3, pp.68-82.

U.S. Corps of Engineers, 1998, HEC-RAS River Analysis System, Hydraulic Reference Manual version 2.2, Hydraulic Engineering Center, Davis, California, 237p.

U.S. Corps of Engineers, 2000, HEC-GeoRAS, An extension for support of HEC-RAS using ArcView, User's Manual version 2.2, Hydraulic Engineering Center, Davis, California, 96p.

LAND SURFACE MAPPING AND CHARACTERIZATION USING LASER ALTIMETRY

SESSION 8

SURFACE RECONSTRUCTION II

DIGITAL TERRAIN MODELS IN DENSE URBAN AREAS

F. Dell'Acqua, P. Gamba, A. Mainardi
Department of Electronics
University of Pavia
Pavia, Italy
{f.dellacqua,p.gamba}@ele.unipv.it

Commission III

KEY WORDS: DTM extraction, Laser scanning, image processing, urban remote sensing.

ABSTRACT

In this paper we consider the problem of DTM extraction in dense urban areas. To this aim, we need valuable and reliable data in the tiny open areas among buildings, and a suitable algorithm to reconstruct the terrain discarding these same structures. So, we compare first LIDAR and aerial photogrammetry by evaluating the relative accuracy of the three-dimensional reconstructed surface in the small open areas in the town center. Then, we characterize the digital terrain model (DTM) of the whole town using a filtering and building detection approach. It comes out, as expected, that the best filter width depends on the terrain and built structure characteristics, and we show that, after training on test areas comprising all possible combination, it is possible to obtain highly precision DTMs filling the built areas with surrounding terrain without significantly affecting the open areas.

1 INTRODUCTION

Historical centres in European Towns are often crowded with buildings, grouped in small or large blocks and separated by very narrow roads. This situation provides a formidable challenge to Digital Terrain Model extraction tools, both automatic and semi-automatic. Indeed, in this area we have bunches of points only in a few parts of the area, and the definition of the digital terrain model (DTM) should be considered by interpolation or substitution techniques. This, in turn, requires that these points must be detected with extreme precision in the 3D space to provide a sufficient basis for the extraction of the surrounding areas.

Usually these points can be retrieved by using automatic or semi-automatic photogrammetric tools, and, recently, by LIDAR systems. Current laser ranging systems allow measuring terrain points at approximately one point each 0.5 x 0.5 m^2 and a vertical accuracy in the order of 0.3 m and are therefore suitable for this task.

A first aim of this work is to make a quantitative evaluation in a dense urban area of the two techniques, (LIDAR and aerial photogrammetry) by computing the relative accuracy of the three-dimensional reconstructed surface in the small open areas of a dense town center.

A different but related problem of the LIDAR approach is that you need to restrict your measurements to the true terrain areas to retrieve DTM from DSM. In some sense this problem is similar to the extraction of the soil in forested areas. Indeed, the histogram technique introduced in [1] and the algorithm used in [2] are very similar in the concept, assuming that on an area of a "reasonable extension", ground points and tree/building points constitute two disjoint sets and these two sets are characterized by significantly different values of the average height. The problem is the dimension of the "reasonable extension", which heavily depends on the structure of the forest (or the city center).

The second part of this paper is devoted to the definition of a strategy to understand which is this "reasonable dimension" in a urban environment, and if it is possible to adopt a strategy to choose the parameters of a terrain point extraction procedure similar to the one discussed in [1].

2 DATA SET AND DTM EXTRACTION ALGORITHMS

For this work, a LIDAR data set has been acquired on the town of Pavia and its immediate neighbourhood in mid-November 1999 with the Toposys sensor, produced and operated by the German company Toposys, installed on a plane of an Italian company called CGR, Compagnia Generale Ripreseaeree. The flight height was around 850 meters (with the exception of two cross stripes, flight at halved height); the Toposys sensor is able to acquire, flying at that height, approximately five points per square meter, so that the one-meter grid which is usually delivered to the customers, and that we used, can be calculated with a good reliability. Up to now the Toposys instrument isn't able to measure the reflected signal intensity, so it gives pure geometric data and it can acquire first pulse or last pulse alternatively. Therefore, to test all the operational capabilities of the sensor, three different acquisitions have been performed: they are shown in Table 1. The German company delivered to us the gridded data, with 1 meter cells, as well as the so called raw data, that is, sparse points measured by the sensor. Aerial photogrammetric images were acquired during the same flight and scanned at 1200 dpi resolution, allowing a scale ratio of 1/5600 and a ground pixel size of 12 cm.

On the same area we were able to provide a large number of Ground Control Points (GCPs), in many test areas. So, we were also able to make a quantitative evaluation of the original DSM as well as the DTM extracted. This, in turn, allowed us to compute the *systematic* and *random* elevation errors ($\bar{z}$ and σ_z) and determine how the range of the input parameters of each DTM extraction algorithm could be related to the topographic characteristics of the terrain. To this aim, GCPs must be computed with extreme precision: on our test areas they were measured by means of differential GPS techniques or manual photogrammetric analysis by an expert operator.

We individuated four test areas, each covering a 400 x 400 pixel square (corresponding to 160000 m^2), shown in figure 1. In test areas (1) and (2) reference data were obtained by GPS techniques and belong to topologically flat structures, like tennis or basketball courts. In particular, the first area contains

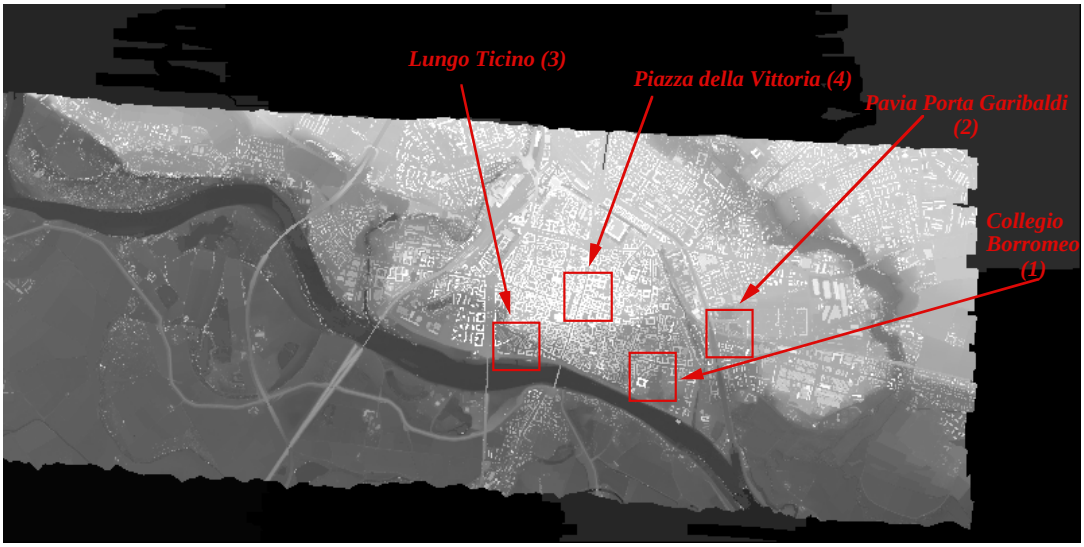

Figure 1: A bidimensional representation of the LIDAR data set over the town of Pavia, Northern Italy. The squares represent the four test area used to train the DTM extraction algorithms in this research.

the playground near the college called "Collegio Borromeo", the second one is situated near the railway station of Pavia Porta Garibaldi. Ground control points for test areas (3) and (4) were obtained by means of photogrammetric techniques and refer to a small bay in the Northern bank of the river at the border of the town and the central area near Piazza della Vittoria, respectively. All these test areas were selected following two criteria. First of all, the availability of measurements to compare with, but also the capability to cover all the topographic features which are present in the area, from residential to industrial to central areas of the town, as well as artificial or natural features of the ground. By this choice, we were able to test the DTMs in different situations of terrain topography as well as building densities. In section 4 we will evaluate only test areas (1) and (4), due to the limited space.

	T_1	T_2	T_3
Points measured in a second	80000	80000	80000
Scan lines acquired in a second	625	625	625
Acquisition mode	LP	FP	LP
Flight height	850 m	850 m	400 m
Plane speed	70 m s-1	70 m s-1	70 m s-1
Scan semiangle	7°	7°	7°
Scan line length	209 m	209 m	98 m
Distance between two points on the same line	1.66 m	1.66 m	0.78 m
Distance between homologous points belonging to two consecutive lines	0.11 m	0.11 m	0.11 m
Average density (points per square meter)	5.47	5.47	11.63

Table 1: Main parameters of the laser flights over Pavia.

As for the algorithms, we considered two different approaches to extract DTM from the original LIDAR data. They are based on three-dimensional data filtering by means of convolutional or morphological kernels (Lohman *et al.*, 2000). The workflow of these algorithms requires a first DTM estimate by means of a low pass or a morphological filter. Buildings are then individuated by thresholding the difference between the original DSM and the estimated DTM. Then the built areas are extracted and filled in the original digital surface model (DSM) using the mean height value around them or the first DTM estimate (in the low-pass and morphological case, respectively). Finally, the large buildings are extracted using the histogram technique in Hug and Wehr, 1997, where the height histogram is computed and the highest peak is associated to these structures, provided that their area is sufficiently large to justify their survival to the first processing step. To correctly apply the procedure, we need to know the kernel size that reduces as much as possible the DTM errors with respect to GCPs. Moreover, it turns out that the histogram techniques is extremely sensible to the window size where the heights are considered, and that it is difficult to define an unique size if a very rugged terrain is considered. Moreover, it is necessary to observe that, when we have buildings near steep terrain areas, the results of the histogram technique depend on the kernel size used for the first part of the procedures. Since each kernel has a different smoothing effect, this might produce an apparently similar histogram, where the threshold computed using the technique in Hug and Wehr, 1997, is actually slightly different.

So, even this very short outline of the algorithms highlights he need to provide some hints on the input parameters of the filtering procedure, as well as the dimension of the areas used to discriminate between terrain and buildings in the histogram approach. This point has been studied, for instance, in Morgan and Tempfli, 2000, where adaptive filtering has been conceived, with a morphological approach using a window whose width is ruled by sloping parameters. However, the window size and the so called "height bandwidth" in this algorithm have still to be decided from a priori knowledge of the area. What we want to discuss in this paper is if we can test the parameter choice in a few test areas and apply this values to the overall urban area.

3 LIDAR AND PHOTOGRAMMETRIC DTM COMPARISON IN SELECTED AREAS

As mentioned in the introduction, the need to provide accurate terrain height in open areas inside built area and especially city centres requires first an evaluation in selected parts of out data

set of the relative accuracy of the LIDAR data with respect to the above mentioned photogrammetric DEM.

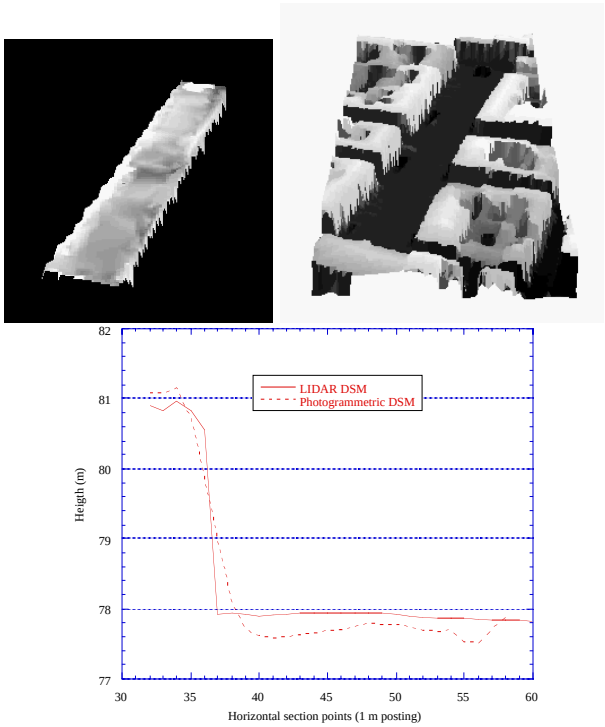

Figure.2: 3D view (on top) of the Photogrammetric and LIDAR DSM of the part of Piazza della Vittoria, where control points by analytical photogrammetry were available. Lower graph is a horizontal section of both DSMs for quantitative comparison.

A detailed analysis of the relative strengths and drawbacks of the two techniques have been already considered for extra-urban areas in *Casella et al.*, 2001, where a section of the main embankment of the river Ticino South-West of the town has been extensively studied. The conclusions were that a skilled and trained operator is able to reconstruct DTM geometry by using stereo pairs with a similar (or even superior) accuracy than the LIDAR instruments. However, the time required is extremely limiting with respect to the point number that could be made available. On the other hand, automatic extraction of photogrammetric DTM by commercial software fails in characterizing the true terrain slope, with mean absolute deviation still more than 1 meter in the best case.

We want to provide here a similar discussion for a selected area inside the city centre, where we were able to extract a sufficiently reliable photogrammetric DTM. In figure 2 we provide a 3D view and a section of a part of Piazza della Vittoria as it can be seen using the original LIDAR and the photogrammetric DSM. We note that the two DTMs are very similar as for the capability to characterize the flat square terrain, and the systematic error (nearly 20 cm) and the small random error are both evident.

Their high accuracy and reliability make the heights of the manually extracted photogrammetric points very useful as ground truth values for the LIDAR DTM. However, it is also evident that no suitable data set of GCPs will be available by photogrammetric techniques in a reasonable time, because analytical photogrammetry is a manual operation. Moreover, geometric problems due to the limited terrain areas visible in stereo views in urban zones where buildings are very dense prevent this approach to be effective other than to provide accurate reference for control points.

4 DTM EXTRACTION IN TEST AREAS

Before discussing how the DTM extraction procedures should be tuned to provide the best results in the test area, it is useful to anticipate part of the problems we will see in the results. This in order to explain the criteria used to test the algorithms in the selected areas. Sometimes, in the following graphs we will see that the altimetric values of the DTMs *inside* the building are different from those *outside* it. The causes for such behaviour are many and different. For instance, if the values inside are higher than outside, this could be due to a wrong width dimension for the filtering window, or to the variability of the terrain surrounding the structure. In some cases, this is also due to parts of the buildings at different (lower) height than the major built structure, with a non-negligible area, like terraces or porches.

Therefore, as a general rule to understand if the DTM extraction procedure has been truly successful, we will consider not only the ground control points presented in the previous section. We will also take into account a more qualitative but surely interesting approach, looking at DTM sections and

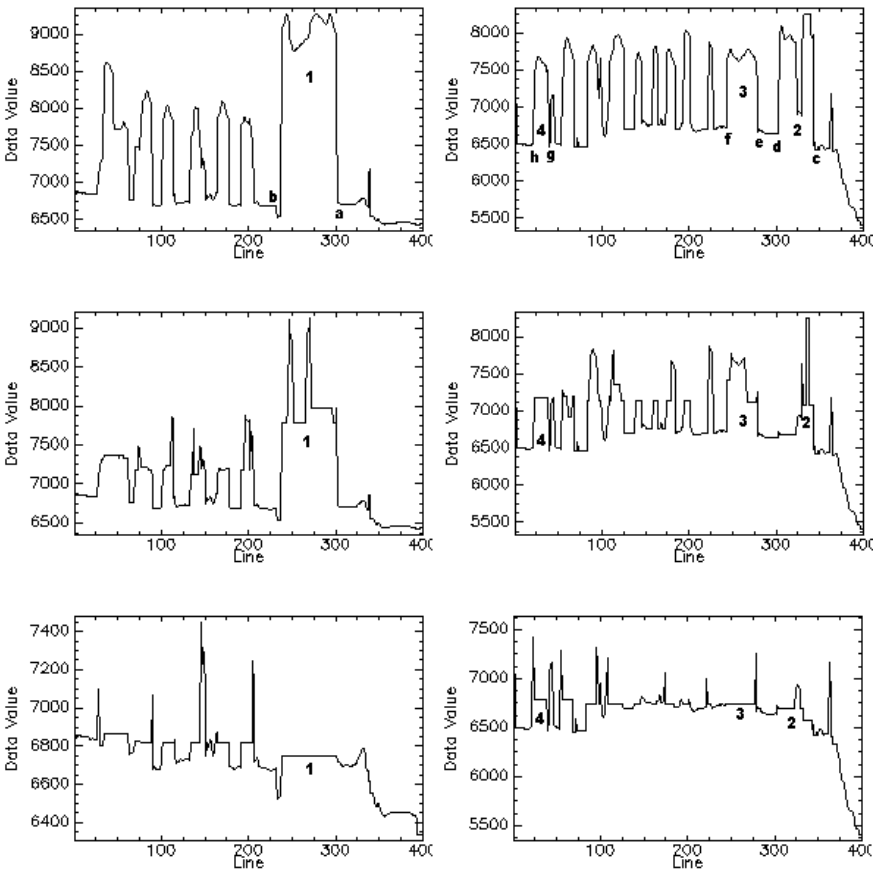

Figure 4 : From top to bottom: sections Y1 and Y2 in the initial DSM, and after low-pass filtering with a kernel size of 10 and 100 m, respectively.

evaluating how the terrain profile matches our request to have transactions as smooth as possible between non-built and built areas in the same zone.

Figure.3: The raster map (on the left) and a bidimensional representation of the LIDAR height values (on the right) for the test area near the Collegio Borromeo.

4.1 First test area (Borromeo): flat terrain with large/ sparse buildings

As already said, the first test area is located near the University College called "Collegio Borromeo", whose green park is visible in figure 2 in the lower part of the images. In the same figure we show on the right a bidimensional representation of the LIDAR data (lighter areas correspond to higher elevation values, as usual). On the left, instead, there is the same part of the town as it is represented on the raster map of the town of Pavia (1:2000 scale). In the same figure we have highlighted the playground where the ground control points were recorded during the GPS measurement campaign, while the two green lines correspond to the sections that we will consider in the following to compare the DTM estimate inside and outside the buildings. Section denoted as "Y1" give us information on the college building and the GCP test area. Section "Y2", instead depicts more densely placed buildings at the left in the figure. Note that, beyond the control zone the main structure of the college is the nearly square building at the lower left, with a large internal ground.

As a first note, we should consider that the original LIDAR DSM provides for this area a min-max difference around 5 meters. So, we may label this test area as a "flat area with large/sparse buildings".

Then, we need to consider the difference between the original LIDAR data and the GPS control points. The systematic and random errors for this set are $\bar{z}$ = 31.5000 cm and σ_z= 2.3452 cm, respectively. Since the algorithms used for DTM extraction aim at labelling building structures without changing the laser estimates on the "natural" terrain surface, these values are exactly the same also for the DTM, for any window width and any filtering choice. Indeed, the GCPs are on a flat playground, and no change in this area is expected between the DSM and the DTM. However, as we will see in a moment, there is a further processing step that we need, to complete the DTM procedure, which has the disadvantage to change the original elevation data.

So, this step does not give us any hint on the investigated matter. Still, it gives us a strong validation results, because we can compare the error values with those found in Casella, 2001 which is an extensive evaluation of the laser scanning precision on the same data set. In that work, the author finds that the systematic error should be placed in the range between 25 and 30 cm, while random error is around 5 cm. We should note that the values presented in the previous paragraph are extremely similar as for the systematic error, but they seem better for the random part. However, this is an effect of the fact that GCPs are, in this test, very near one to the other, and differential GPS allows better reducing the random error in elevation measurements.

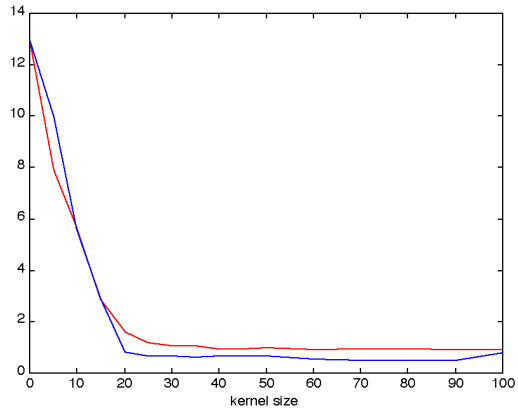

Figure 5: Mean square error between the elevation data *inside* and *outside* the buildings, computed using the data in section Y1, with respect to the filtering window width (in meters). Lower values at higher kernel sizes for morphological DTM.

Now, even if filtering does not affect the playground area, it changes the results in the building area. In figure 4 we show sections Y1 and Y2 (on the left and the right, respectively) in the original DSM as well as in two DTMs obtained with a low-pass filter and different window width (10 and 100 pixels, corresponding to 10 and 100 m). The numbers in the sections help identifying the different buildings (number 1 is the Collegio Borromeo). The letters in the first row sections, instead, correspond to point just outside the buildings (not changed by the DTM extraction procedures). In section Y1 the

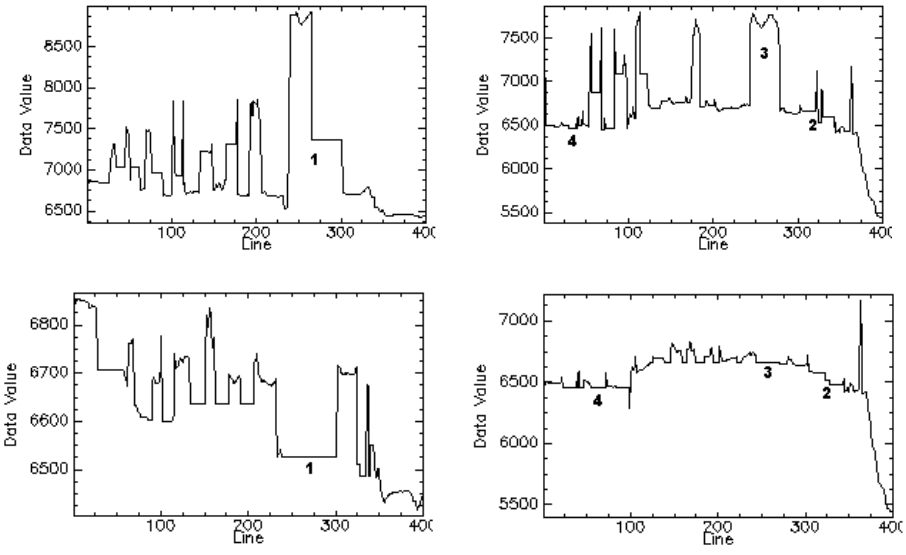

Figure 6: From top to bottom: sections Y1 and Y2 after morphological filtering with a kernel size of 10 and 100 m, respectively.

playground area correspond to the flat portion line numbers between 350 and 400.

Looking at this figure, we may first note that there are points where in both DTMs it is evident an error, or at least a different elevation value with respect to what expected (for instance, the two peaks over object #1). This situation could be labelled as "noise" and will be considered in next paragraphs. The second consideration refers to the low-pass filter window width. No doubt that the second choice (a larger width) corresponds to better results. To have a quantitative evaluation of this effect, we computed the mean value of the terrain around each structure, and compared it with the mean value inside the same structure. This is, as already discussed, a different but equally valuable way to discriminate between effective and useless DTM results. In particular, the mean value of the terrain height in the points characterized by a letter is compared with the mean elevation value of the points referring to a structure (i.e. numbers in the sections of figure 3), and the mean square difference is given as a numerical value of this assessment process. The graph in figure 4 represents this error as a function of the window width (called from now on *kernel size*). Since the result shown in figure 3 for the low-pass procedure is valid also for morphological filtering, we report in figure 5 both mean square differences. It is interesting to note that the behaviour is similar, and that for both approaches an unbearable change is obtained with kernel size lower than 20 m. More in detail, the error is 108 cm for a kernel size of 25 m, while it lowers to 95 cm for a kernel size greater or equal to 40 m. Using morphological filtering, instead, we obtain an error of 82 cm already with a kernel size of 20 m.

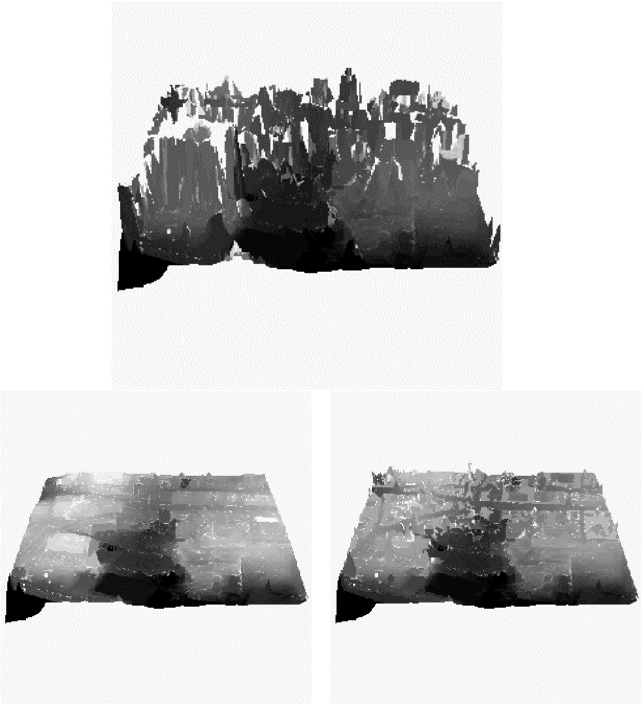

Figure 7: Three-dimensional view of the LIDAR DSM for the Collegio Borromeo (top), and of the DTMs obtained by means of low-pass (bottom left) or morphological (bottom right) filtering.

In figure 6 we show the DTM results for sections Y1 and Y2 using the morphological approach. By comparing figure 6 and 4 we should say that the former provides a smoother terrain inside the building structures (this is more evident looking at Collegio Borromeo and to building #4 in section Y2), confirming the graph in figure 5.

So, as a final statement for this point, the best achievable DTM seems to be the one with kernel size higher than 40 m for low-pass filtering and 25 m for morphological filtering. This means, by the way, that there is no simple relationship between the mean building area and the filtering window width. At least, this strongly depends on the filtering approach.

Finally, in figure 7 we show the original DSM and the DTMs obtained by means of low-pass filtering (kernel size = 100 m) or morphological filtering (kernel size = 25 m). It is evident that the building extraction software works better with larger filtering width, and therefore buildings are individuated and removed in the left image better than in the right one.

In other words, the two different DTMs present different advantages and drawbacks. The low-pass one has a larger number of "noisy parts" and a better characterization of the built structure, especially on their borders. The morphological DTM, instead, shows less local problem but also a lower definition of the built areas. Therefore, both models need a further refinement, as already noted.

The "noise" problem is related to small parts of the buildings or vegetation that have not been discarded by the previous steps. As already noted, this is indeed the case for complex structures and should be corrected. Therefore, we implemented a final low-pass filtering step on the first DTM approximation, with a window size that now should be investigated in order to change as few as possible the terrain parts untouched by the previous processing steps. To individuate the optimal kernel size, we computed the systematic and random error $\bar{z}$ and σ_z, as a function of the kernel size (figure 8).

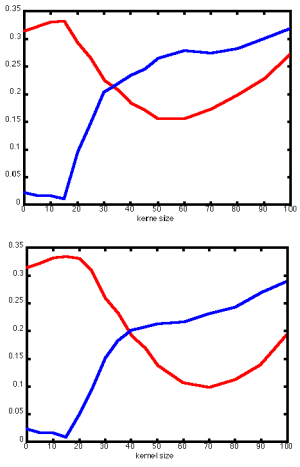

Figure 8: The absolute value of $\bar{z}$ (decreasing curves) and σ_z (increasing curves) after the final low-pass filtering step applied to the first DTM approximation in figure 7 as a function of the kernel size. The upper graph refers to low-pass DTM, the lower one to morphological DTM.

The behaviours in figure 8 are very similar for both DTMs, as expected. In particular, the absolute value of $\bar{z}$ tends to increase with larger kernel sizes, because the effect of small noisy area expands to the surrounding terrain. Instead, σ_z almost constantly decreases because of the smoothing effect of the filter. In both images the best value to reduce the systematic error is around 15 m, while for random errors the best range is between 50 and 70 meters. The two curves intersects somewhere in the middle of the 20÷40 range, suggesting that the best compromise for both error measures is 30 meters.

Applying this choice, we obtain the final DTMs, shown in figure 9.

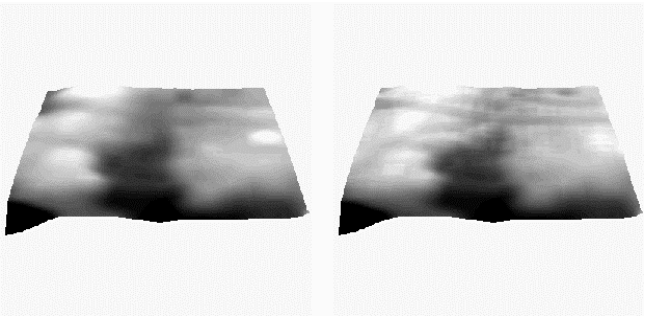

Figure 9: Final DTMs, after the final low-pass filtering with kernel size of 30 m.

3.2 Fourth test area (Piazza della Vittoria): city center

One more test area to be considered is a part of the city center, crowded with buildings and with small, short streets bordering building blocks. We focus on the main square of the old town and the surrounding built structures.

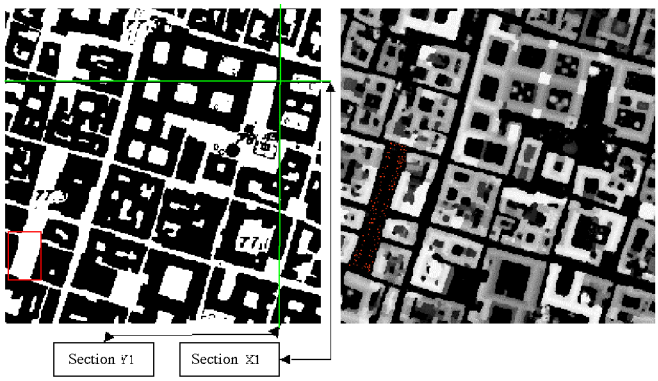

Figure 10: Raster map and LIDAR DSM of the 4th test area.

In figure 10 we show the map and the LIDAR DSM of this area, together with the locations of sections X1 and Y1, which are used to characterize building profiles after the DTM extraction. Moreover, we have highlighted the area where the GCPs have been measured. The points have been characterized by means of photogrammetric techniques, since their location do not allow to provide GPS measurements with sufficient reliability, due to the building surrounding the square.

A first analysis of the DSM height values in the area provides a max-min difference of about 8 m, due to the presence of the buildings. Indeed, this is a flat area, with no terrain slope. As for the section analysis, we should note that in this dense urban area the best result is obtained by means of the morphological filtering approach, while the low-pass technique provides an overestimate of the terrain inside the buildings, due to the insufficient smoothing effect of the filter. Indeed, partially covered, internal courts, whose effect is evident in the sections in figure 11, characterize the buildings. These parts are not easily evaluated by means of the histogram technique, if the first DTM approximation maintains information on the built structures. This effect is larger with low-pass than morphological filtering, and leads to worse building extraction in the histogram analysis and, finally, to worse DTM approximations. Quantitatively, we have systematic and random errors of 1.99 cm and 33.04 cm, respectively for the low pass DTM. This shows a good reduction of the systematic height shift but a consistent enhancement of the random errors, due to terrain fluctuations that are not real ones. Instead, the morphological DTM has for the random error a value near to the original one. A graphical evaluation of this effect may be obtained looking at section Y1 and X1 profiles in figure 19.

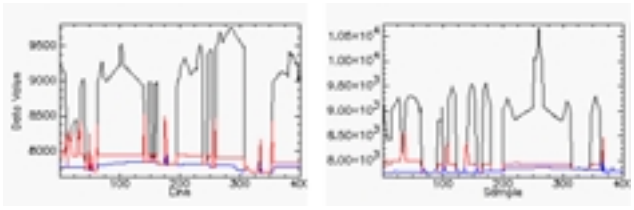

Figure 11: Section Y1 (left) and X1 (right) profiles in the original DSM of the fourth test area (tèop curve), the low-pass DTM (middle curve) and morphological DTM (bottom curve).

Finally, in figure 12 we give a three-dimensional representation of the original DSM (upper image) in comparison with the low-pass (left) and morphological (right) DTMs, before the final low-pass filtering step.

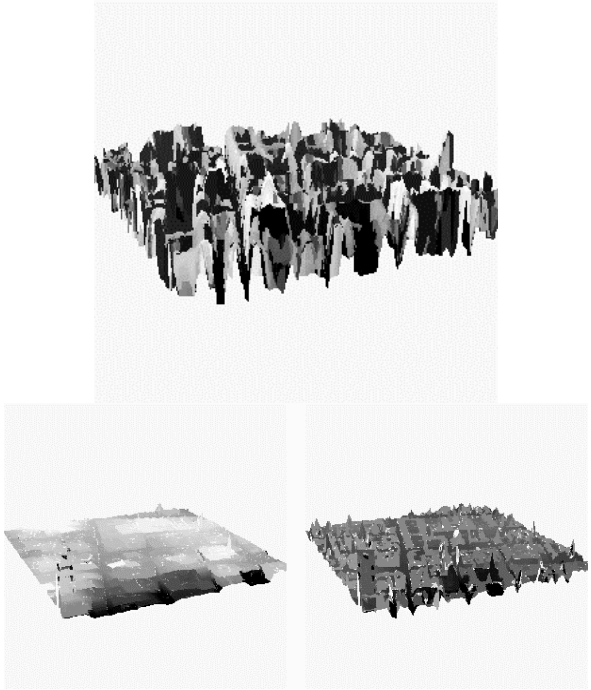

Figure 12: Three dimensional view of the original LIDAR DSM for the Piazza della Vittoria test area, together with the morphological DTM (lower left, kernel size = 25 m) and the low-pass DTM (lower right, kernel size = 100 m).

5 DTM EXTRACTION FOR THE WHOLE URBAN AREA

After the discussion of the previous section, it seems that filtering approaches followed by histogram evaluation are able to provide a sufficiently precise DTM of the whole urban area, since there is a strong similarity between the kernel size values that provide the best results in all our four test areas. Therefore, we implemented a complete DTM extraction for the whole area depicted in figure 1, with three different choices: low-pass filtering with kernel size of 25 or 100 m and morphological filtering with kernel size of 20 m.

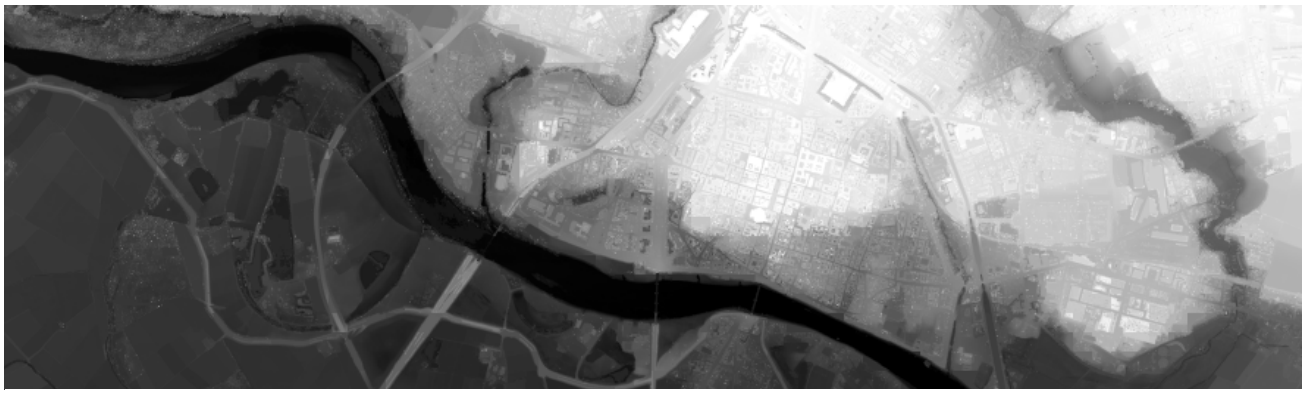

Figure 13: Low-pass DTM (kernel size = 25 m).

Figure 14: Low-pass DTM (kernel size = 100 m).

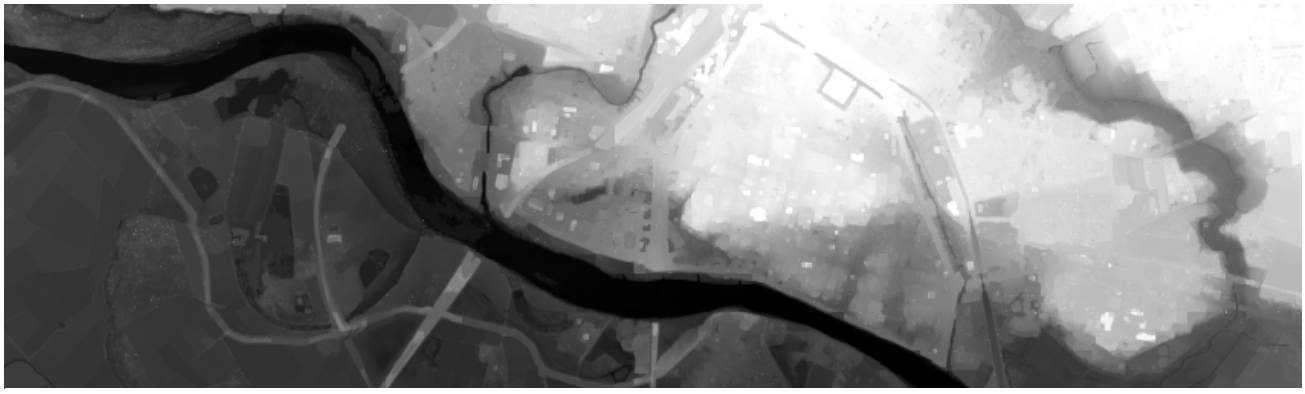

Figure 15: Morphological DTM (kernel size = 20 m).

As expected, the use of smaller kernel and low-pass filter provide smaller errors in the natural structures (like embankments) East of the town. However, in dense built areas the effect of this filter is not completely satisfying, leaving to slightly different values inside the building areas than outside them. Instead, low-pass filtering with a larger kernel helps in these areas, but tends to cancel natural features that may be of interest.

The best compromise in this sense is obtained by means of the morphological filtering approach, with small kernel size as suggested by all test areas analysis. In this case we obtained a good extraction results, both in the city center and in the areas outside the town. Moreover, given the reduced kernel size, even the computation time is lower.

This analysis is confirmed by the inspection of a horizontal section of the DTMs, shown in the following figure for the best low-pass in the urban area (100 m) and the morphological DTMs. Note that the city center area is comprised between samples 3500 and 4500.

Quantitatively, to characterize all these DTMs in a densely built part of the town, we provide here a comparison with a set of GCPs in a different part of the city center (Piazza del Duomo). The systematic and random error values are 0.20 m and 0.65 m for the original DSM, 0.14 m and 0.36 m for the low-pass DTM (kernel size = 25 m), 0.13 m and 0.32 m for the low-pass DTM (kernel size = 100 m), and 0.14 m and 0.38 m for the morphological DTM. As expected, all the DTMs have comparable good results outside of the buildings.

6 CONCLUSIONS

The present work provides a methodological approach to the extraction of digital terrain models in densely built areas. The idea is to use a filtering approach with a kernel size determined by means of a training step in some test areas.

Two filtering techniques, namely the low-pass and the morphological ones have been exploited, together with the

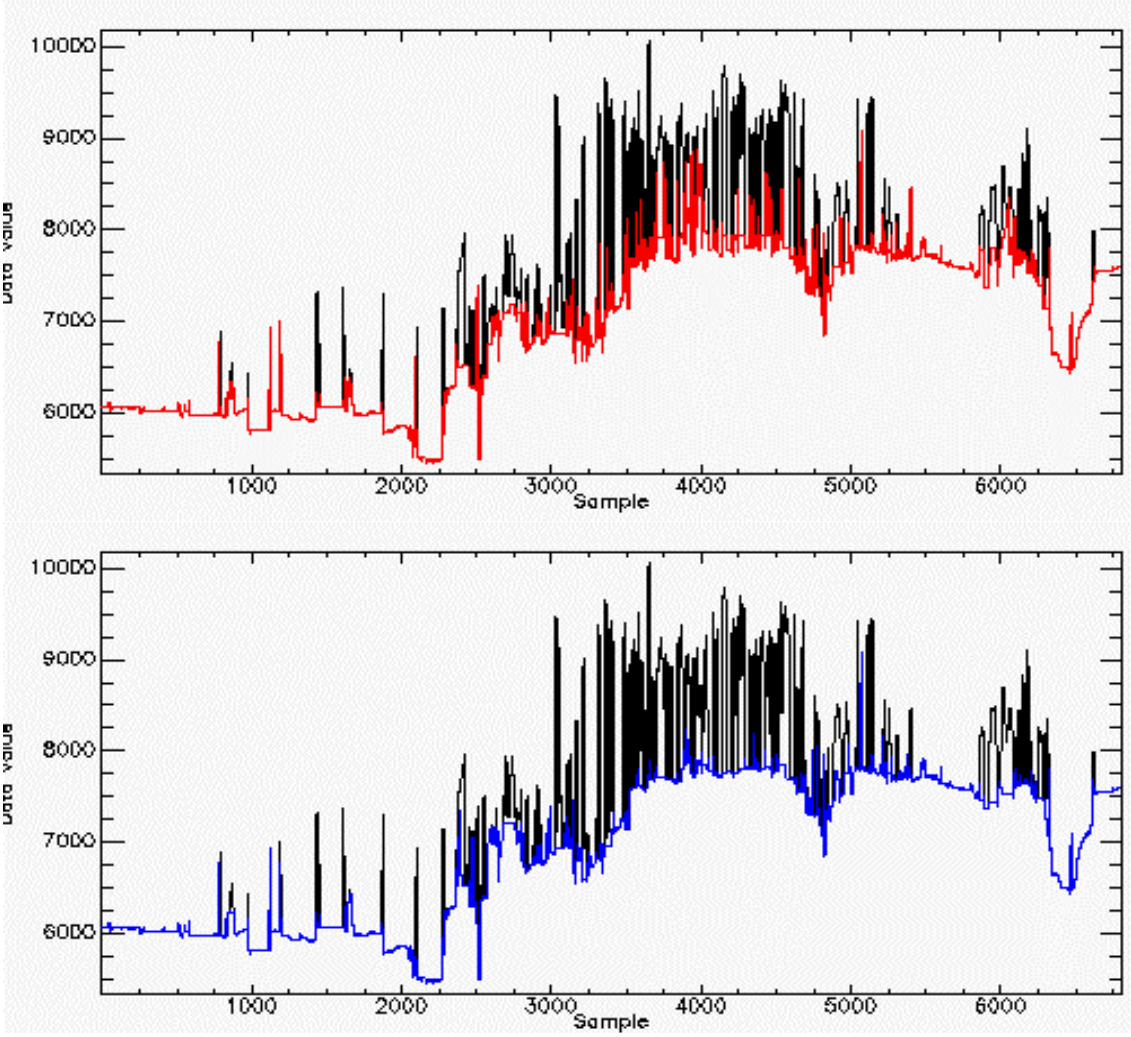

Figure 16: Comparison between the original DSM and the low-pass and morphological DTMs in a horizontal section of figures 14 and 15. In black the original DSM, in grey the low-pass and the morphological DTMs.

histogram analysis for building extraction, and reasonably good DTMs have been provided. The test area characterization proved to be an effective way to choose the input parameters of these techniques, and quantitative evaluations of the retrieved terrain height with ground control points have confirmed this assumption.

Future work will be dedicated to improve the procedure and determine a relationship between the values of the inpiut parameters and the structural characteristics of the buildings and the terrain features, so that no DTM extraction in test areas will be required, but only simpler information in the same zones.

ACKNOWLEDGEMENTS

The authors want to thank Prof. V. Casella for providing the LIDAR data as well as precious discussions on the topic. They would also like to acknowledge the work of Paolo Marchese at the analytical stereoplotter.

REFERENCES

[Casella, 2001] Casella, V., 2001. Accuracy assessment of laser scanning data: a case study, Proceedings of the 3rd International Symposium on Mobile Mapping Technology, Cairo, Egypt, 3-5 January 2001.

[Casella *et al.*, 2001] Casella, V., Zampori, B., Gamba, P., 2001. Shaping the bank of a river: laser scanning versus automated digital photogrammetry. Proceedings of Italy – Canada 2001 Workshop on 3D Digital Imaging and Modeling Applications of: heritage, industry, medicine & land, Padua, Apr. 3-4, 2001.

[Hug and Wehr, 1997] Hug, C., and Wehr, A., 1997. Detecting and identifying topographic objects in imaging laser altimeter data. IAPRS, 32 (Part3-4W2), Stuttgart, September 17-19 1997.

[Kraus and Pfeifer, 1998] Kraus, K. , and Pfeifer, N. , 1998. Determination of terrain models in wooded areas with airborne laser scanner data. ISPRS J. Photogrammetry & Remote Sensing, 53 (4), pp. 193-203.

[Lohman *et al.*, 2000] Lohmann, P., Koch, A., and Schaeffer M., 2000. Approaches to the filtering of laser scanner data, IAPRS, 33 (Part B3), Amsterdam 2000.

[Morgan and Tempfli, 2000] Morgan, M., and Tempfli K., 2000. Automatic building extraction from airborne laser scanning data, IAPRS, 33 (Part B3), Amsterdam 2000.

FILTERING OF LASER ALTIMETRY DATA USING A SLOPE ADAPTIVE FILTER

G. Sithole
Department of Geodesy, Faculty of Civil Engineering and Geosciences
Delft University of Technology
The Netherlands
g.sithole@citg.tudelft.nl

Commission III, Working Group 4

KEY WORDS: Laser, DEM, Filtering

ABSTRACT

A point set obtained by laser altimetry represents points from not only the ground surface but also objects found on it. For civil works applications points representing the surface of non-ground objects have to be removed from the point set in a filtering process. This paper describes modifications made to an existing "slope based" filtering algorithm, and presents some results obtained from the use of the filter. The "slope based" filter operates on the assumption that terrain slopes do not rise above a certain threshold, and that features in the data that have slopes above this threshold do not belong to the natural terrain surface. However, this assumption limits the use of the filter to terrain with gentle slopes. To overcome this limitation, the filter was modified in manner that the threshold varies with respect to the slope of the terrain. The results of tests carried out using the modified filter confirm that the modification reduces the number of Type I errors (ground points in steep terrain are not filtered off). Further numerical comparison of the filter output with a reference data set for the same site (obtained photogrammetrically) show that the filter generates relatively minimal Type II errors. The output of the modified slope filter was also compared with the output from a filtering found in the commercial software package, "Terrascan".

1 INTRODUCTION

Airborne laser altimetry has gradually become a mainstream tool for abstracting high accuracy and high-density digital terrain surfaces. However, the point set obtained by laser altimetry represents points from both the ground surface and objects found on the ground surface. For civil works applications points representing such objects have to be removed from the point set.

In the filtering process points classified as non-ground are discarded. The large number of points in a laser data set necessitates a high degree of automation in the classification of points. Some filtering techniques that have been developed are described in Kraus and Pfeifer 1998, Vosselman 2000, Axelsson, 2000, Elmqvist, 2001. Most of the criteria used in classifying points have focused on simple geometric characteristics of a point relative to its neighborhood. To further improve the accuracy of classification some filters iterate the classification process. Other classifiers work on the premise that ground points and non-ground points in the laser scanner data set are stochastically separable.

The filters do not work under all circumstances, and efforts have been put into improving the filters (e.g., Schickler and Thorpe, 2001). This paper describes the modification of a slope-based filter with a view to improving the performance of the filter in steep sloped terrain.

The slope-based filter developed by Vosselman (2000) uses the slope of the line between any two points in a point set as the criteria for classifying ground points. The technique relies on the premise that the gradient of the natural slope of the terrain is distinctly different from the slopes of non-terrain objects (trees, buildings, etc.). Any feature in the laser data that has slopes with gradients larger than a certain predefined threshold therefore does not belong to the natural terrain surface. However, this assumption limits the use of the filter to terrain with gentle slopes. To overcome this limitation, the filter was modified so that the threshold varies with respect to the slope of the terrain.

In the first part of this paper, the modifications to the slope-based filter are discussed. The modified filter was implemented and tested using the Vaihingen test field. The preliminary results of the tests are presented in the second part of the paper. Finally, the paper concludes by discussing the implications of the results for future filtering strategies.

2 THE MECHANICS OF THE FILTER

2.1 Slope Based Filter

The basic mechanics of the slope-based filter is illustrated in Figure 1. The vertex of an inverted cone sweeps under each point in the point-set to be filtered. Wherever the cone cuts the point set, then the point at the vertex of the cone is filtered off. In Figure 1(a) the point, p_i, at the vertex of the cone is not filtered off because the cone does not cut the surface. In the implementation of the filter, an inverted bowl whose shape is defined by a probabilistic function designed to minimize classification error replaces the cone. For simplicity, a cone is considered here.

Another way to visualize the method is shown in Figure 1(b). The curved surface shown in the Figure represents the slope of the vectors from the point, p_i, to every other point on the surface. From here, onwards this surface will be referred to as the *point-slopes* surface. The plane is the negative of the absolute value of

the gradient of the cone's generators. If the plane cuts the *point-slopes* surface point, p_i, is filtered off. In Figure 1 (b) the *cutoff* plane does not cut the *point-slopes* surface so point, p_i, is not filtered off. In the implementation the *cutoff* plane is not planar but rather curves upwards the further it gets from point, p_i. The curvature is determined by a probabilistic function derived from a training data set.

2.2 Modification

The main parameter of the slope-based filter is the gradient of the cone's generators. Adjusting this gradient has the effect of moving the *cutoff* plane up or down. The steeper the gradient the lower the *cutoff* plane and vice-versa. If the gradient of the cone's generators is such that the *cutoff* plane cuts the *point-slopes* surface point, p_i, is filtered off. This is illustrated in Figure 2. The classifier is expressed as:

$$\forall p_j \in A : hp_i - \Delta h(d(p_i, p_j), m) \leq hp_j \qquad (1)$$

Where: p_j is a point in the data set ($p_i \neq p_j$).
hp_i and hp_j are the heights of p_i and p_j respectively.
$hp_i - \Delta h(p_i,p_j)$ is the height of a point directly above or below p_j and on the lateral surface of the cone whose vertex is located at p_i.
m is the absolute value of the gradient of the cone's generators. The negative value of m is the height of the cutoff plane.
A is the set of laser points to be filtered in order to extract the DEM.

The next parameter of the filter is the radius of the base of the cone. This parameter defines the operating the range of the filter. In the examples shown in Figure 1 and Figure 2, the operating range of the filter is infinite; the *cutoff* plane extends to infinity. In the implementation, the scope of the *cutoff* plane was restricted. This is because the *point-slopes* surface tends to flatten out the further one moves away from point, p_i, thus reducing the effectiveness of the filter.

The classifier in equation 1 works well if the slope of the terrain is gentle. However, in steep sloped terrain discriminating between the ground surface and features such as buildings and vegetation becomes difficult. To overcome the problem the classifier was modified in such a way that the *cutoff* plane shifts up or down with respect to the position of the cone in the terrain. In the original filter, the *cutoff* plane is held fixed for every point in the point set.

The *cutoff* plane is tuned to the slope of the terrain at point, p_i. Phrased differently as the cone sweeps underneath each point in the point set its slope changes in tune with the maximum slope of the terrain at point, p_i.

The classifier given in equation 1 is now be expressed as

$$\forall p_j \in A : hp_i - \Delta h(d(p_i, p_j), m_i) \leq hp_j \qquad (2)$$

Where: m_i is the height of the cutoff plane.

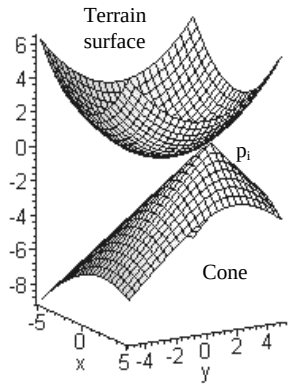

(a)

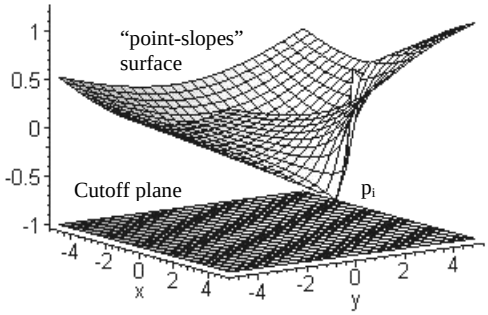

(b)

Figure 1 Mechanics of the original filter.

Choosing the value of $\mathbf{m_i}$. Setting the value of m_i equal to the maximum slope of the terrain at the point at which the cone's vertex touches the surface of the terrain is not enough. Figure 3 shows why. Shown in the Figure is a terrain x-section. The x-section of a cone is also shown. The cone sweeps underneath the surface, with its vertex always in contact with the surface. The cone is shown at three points on the surface. At each point $|m_i|$ is set equal to the maximum slope of the terrain at that point. In Figure 3(a), the cone touches the surface at a point where the

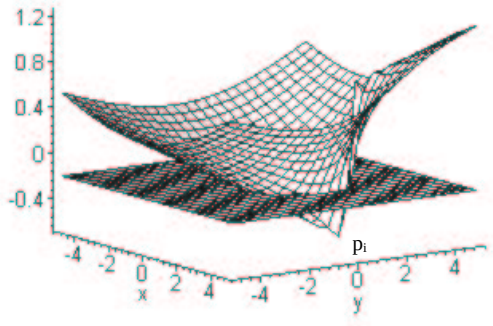

Figure 2 "Cutoff" plane cutting the "point-slopes" surface. Point, p_i is filtered.

surface is concave. The cone does not cut the surface and the point (at the vertex) is correctly accepted as a part of the surface. However, on convex slopes as shown in Figure 3(b), the cone cuts the surface and the classifier fails. In this case the slope is multiplied by a constant factor (>1). The filter can also fail in gently sloped terrain as shown in Figure 3(c). A characteristic of the terrain in this area is the small amplitude and large frequency of the surface (exaggerated in Figure 3(c)). In these areas, where the value of $|m_i|$ is small (flat ground) points will be incorrectly rejected. To overcome this problem a minimum threshold is set for m_i.

To summarize, m_i has to be pre-multiplied by a constant factor (for convex slopes) and then thresholded (for flat terrain). The classifier is now expressed as:

$$\forall p_j \in A : hp_i - \Delta h(d(p_i, p_j), m_i, s_{mi}, m_{\min}) \le hp_j \quad (3)$$

Where: m_i is the maximum slope of the terrain at the point the cone's vertex touches the surface,
s_{mi} is a predefined factor by which m_i multiplied
m_{min} is the minimum threshold for $s_{mi}*m_i$.

The DEM is expressed as:

$$DEM = \left\{ \begin{array}{l} p_i \in A \mid \forall p_j \in A : \\ hp_i - \Delta h(d(p_i, p_j), m_i, s_{mi}, m) \le hp_j \end{array} \right\} \quad (4)$$

Slopemap. To tune the cutoff plane to the surface of the terrain, a rough model of the terrain is needed. This model was generated in the form of a minimum height image in which the pixel values are local height minima (assumption: the minimum value in any neighborhood belongs to the terrain). A slopemap image was generated from the minimum height image. The values from the slopemap were then used to tune the *cutoff* plane.

The slopemap image was then dilated. This was done because the minimum height image is a discrete representation of the terrain, and as a result of this, there can be ambiguity in assigning slope values to points located at the edges of pixels. In this way, dilation ensures that the position of test points relative to the current point does not affect the classifier.

3 TEST DATA

The laser data used in the study is from the Vaihingen test field (part of the OEEPE data set). Features found on the site are urban areas, forests, hills, a river and a quarry. The outstanding feature of the Vaihingen data set is the data gaps (the result of a flight planning error) and the presence of large outliers (points with very low or very high heights). Because of the way in which the slopemap was generated the slope values calculated at the edges of gaps are very large, which makes the filter very generous at the edges of gaps. This was corrected by setting all the extremely large values in the slope map to zero.

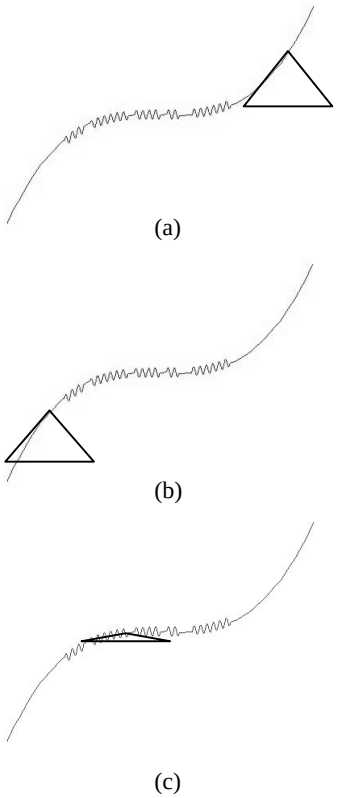

(a)

(b)

(c)

Figure 3 Mechanics of the modified filter. The slope of the cone's lateral surface adjusts to the slope of the terrain. If the slope of the cone's lateral surface is set equal to the slope of the terrain, the filter fails in cases b and c.

Using a TIN generated from the minimum height image would have avoided some of the problems associated with the slopemap. However, the slopemap was opted for, because it has fewer computational overheads.

Low lying outlying points had to be removed using a maximum height difference function (Vosselman and Maas, 2001). High outlying points were removed during normal filtering.

For ground truth a reference data set composed of 2428 points obtained by photogrammetry, from 1:13000 photography was used. The points are spread out in a regular grid pattern. The grid spacing is approximately 25m. In general the reference data is estimated to have a standard deviation of 0.25m – 0.3m. However, in some areas (with vegetation or bad texture) the standard deviation was estimated to be as much as 0.5m. There are also gaps in the reference data, located in built-up areas and areas of dense vegetation and the results presented in Table 1 should be read with this in mind.

4 RESULTS

4.1 Comparison with reference data

The data set was filtered using different parameter settings, and the filtered data were compared against the reference data. The comparison was achieved by generating a TIN from the filtered data and extracting corresponding heights for the reference points

Table 1 Filtering results (statistics in the last four columns are based on the sample after cutting off outliers)

	Min Slope	Slope Factor	Sample Count after Cutoff	RMS (m)	Mean (m)	Std. Dev. (m)	Median (m)
Slope	0.10		1226	0.2820	0.17	0.2263	0.17
	0.20		1238	0.2665	0.14	0.2241	0.14
	0.30		1241	0.2701	0.14	0.2300	0.14
Slope Adaptive	0.00	1.00	1673	0.3011	0.17	0.2465	0.17
	0.00	1.25	1718	0.2978	0.16	0.2485	0.16
	0.00	1.50	1718	0.2978	0.16	0.2485	0.16
	0.00	2.00	1718	0.2978	0.16	0.2485	0.16
	0.15	1.00	1718	0.2978	0.16	0.2485	0.16
	0.15	1.25	1789	0.2924	0.15	0.2494	0.15
	0.15	1.50	1789	0.2924	0.15	0.2494	0.15
	0.15	2.00	1799	0.2911	0.15	0.2507	0.15
	0.30	1.00	1718	0.2978	0.16	0.2485	0.16
	0.30	1.25	1799	0.2921	0.15	0.2501	0.15
	0.30	1.50	1799	0.2921	0.15	0.2501	0.15
	0.30	2.00	1798	0.2918	0.15	0.2515	0.15

from this TIN. Shown in the charts in Figure 4, are the differences (errors) of the heights in the TIN from their correspondences in the reference data.

The main characteristic of the results of the filtering where differences in a band of ±1m. However, there were a few differences (tightly bunched together) exceeding +1.5m, Figure 4(a). A visual check showed that most of these outliers were from the same area. A positive difference here means that the reference data is higher than the laser data. Considering that the reference data is older than the laser data, an explanation for the large outliers could be that there might have been an excavation in these areas after the aerial photography. Because of this, all differences beyond ±1.5m were discarded (which resulted in the loss of about 80 points). The data provided in Table 1 and the distribution shown in Figure 4(b) are from the set of differences after the ±1.5m outliers were discarded.

Table 1 shows statistics for the differences. What is noteworthy is that although the slope adaptive filter gives a high point count, the standard deviation of the filtered points does not change much. This indicates that the modifications are delivering the desired results in steeper slopes without allowing non-ground points to pass through the filter (Type II errors).

In Figure 5(a) and Figure 5(b) it can be seen that the slope adaptive filter is most effective at a minimum slope of 0.15 and a slope factor of 1.25. Using larger minimum slopes and slope factor values gives lower gains and will result in more Type II errors.

A problem with the reference data is that it generally represents areas in the terrain that are not covered by dense vegetation or human artifacts. In such areas filters have a small chance of failure. Because of this, reference data is not very useful for evaluating filters, unless the data coverage extends to built-up and vegetated areas. Therefore, the results in Table 1, Figure 4 and in

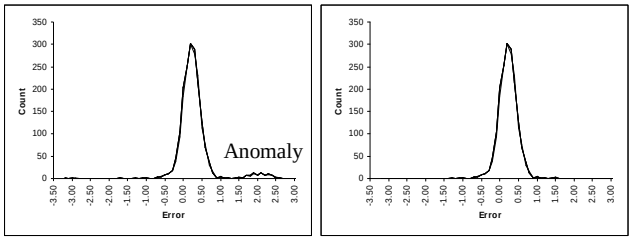

(a) Distribution with outliers (b) Distribution without outliers

Figure 4 Distribution of height differences between reference and filtered data.

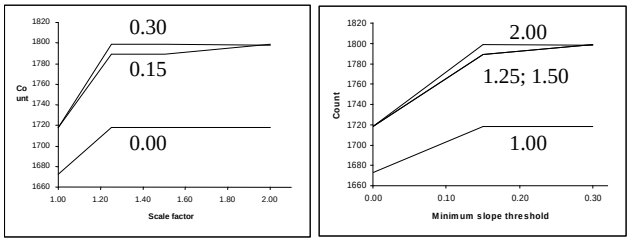

(a) Variation of slope factor (b) Variation of min. slope

Figure 5 Effect of the variation of minimum slope with respect to slope factor.

Figure 5 cannot be extended to areas covered by dense vegetation and human artifacts. For this reason, visual comparisons were done, and the results are described in the next section.

4.2 Visual Comparison

In Figure 6, the slope-based filter and the slope adaptive filter are visually compared. Figure 6(b) through Figure 6(f) are images generated from the filtered data. The areas that have pass through the filter are shown in black or gray (in the case of Figure 6(b)).

Figure 6(b) shows the result of the slope-based filter, used with a minimum slope of 0.3. The areas shaded in light gray represent points filtered by the slope-based filter when used with a minimum slope of 0.1. There are three sites (1, 2 and 3 in Figure 6(a)) were the terrain slopes are steeper than 0.3. In these sites, all points are filtered off. The minimum slope could have been increased but this would have generated many Type II errors. At site 4, there is a quarry, and here too the sides of the terraces are filtered off. The modifications to the slope-based filter are meant to avoid these incorrect rejections of terrain points on steep slopes.

Figure 6(c) and Figure 6(d) shows the same area filtered with the slope adaptive filter using a minimum slope of 0.0. Two slope factors have been used (1.0 and 1.5). Very steep slopes at sites 1 to 4 have not been filtered off. However, this gain has been at the expense of the filter's performance in urban areas. The reason for the loss of performance in urban areas is the size of buildings. The operating range of the filter is often smaller than the size of a building and consequently the slope map adapts to the roofs of the buildings. Because of this the central part of large buildings are not filtered off.

The anticipated failure of the filter in terrain with gentle slopes (Figure 3(c)), when using a minimum slope of 0.0 is seen in the appearance of furrows in Figure 6(c). Because the pixel size of the

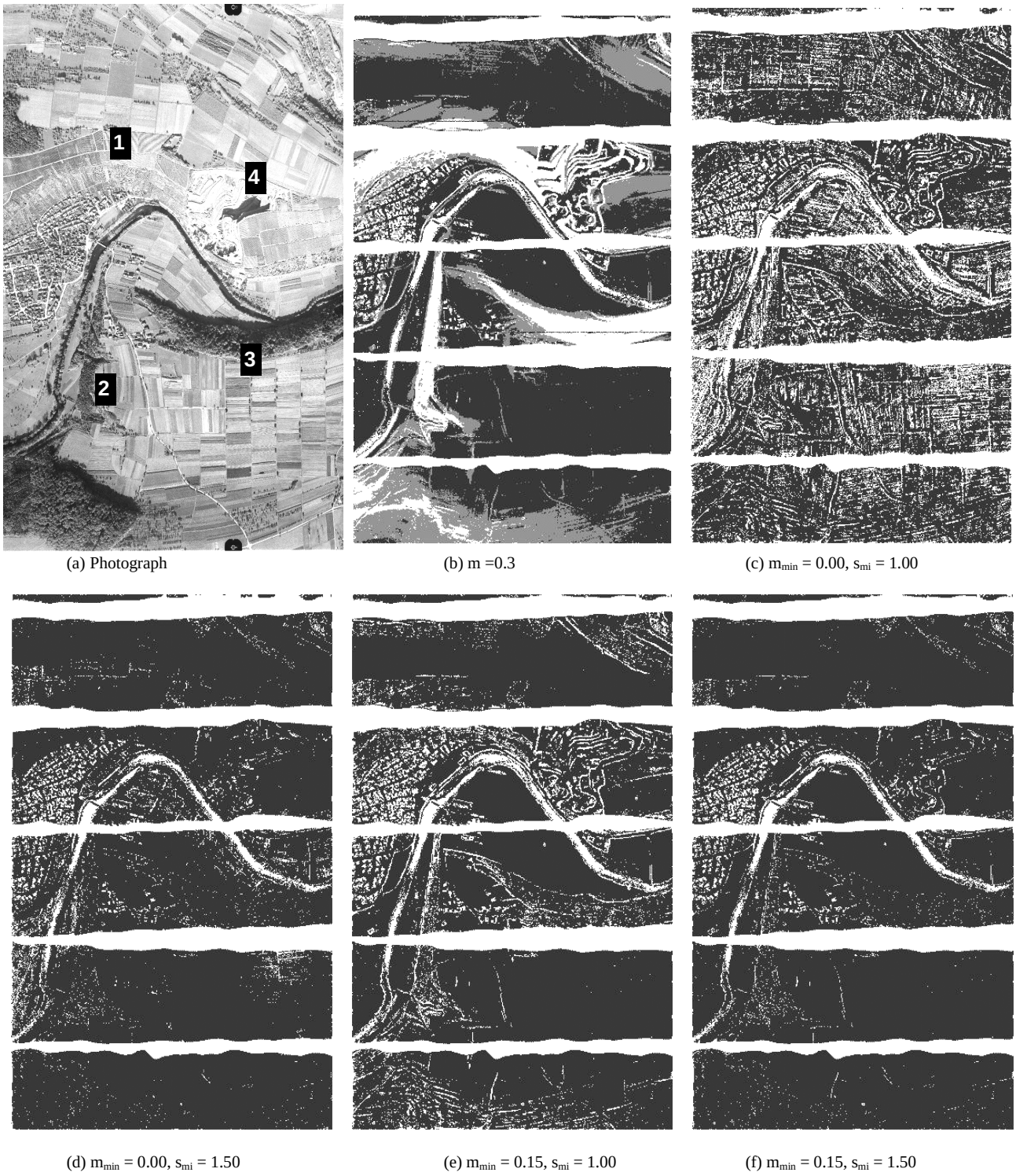

(a) Photograph (b) m =0.3 (c) m_{min} = 0.00, s_{mi} = 1.00

(d) m_{min} = 0.00, s_{mi} = 1.50 (e) m_{min} = 0.15, s_{mi} = 1.00 (f) m_{min} = 0.15, s_{mi} = 1.50

Figure 6 Comparison of filtering results

slopemap is larger than the distance between the furrows, the slope values in the slopemap will also be small (in gently sloped terrain). The problem is corrected by using a minimum slope of 0.15 as in Figure 6(e) and Figure 6(f). The effect of not using a minimum slope can also be seen when comparing figure Figure 6(d) and Figure 6(f). Although a slope factor is used, ground points are incorrectly rejected (compare right side of second strip from bottom).

A drawback of dilating the slope map is increased Type II errors at the foot of steep slopes. Because of the dilation, slope values for some of the gentler slopes will be very high (Figure 7). This effect is further worsened when the slope values are multiplied by a slope factor. It is not easily noticeable, but comparison of Figure 6(b) with Figure 6(e) shows that the modifications to the slope-based filter results in Type II errors on riverbanks and in urban areas. This effect will become more evident when examining the profiles in Figure 9.

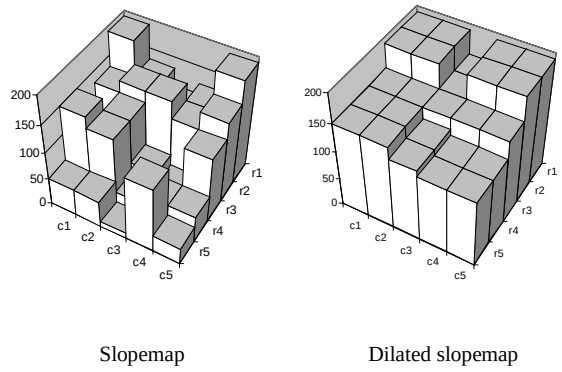

Figure 7 Slopemap (exaggerated for effect)

4.3 Comparison with Terrascan Filter

The filtering algorithm used in Terrascan (Axelsson, 2000) starts from a sparse TIN and iteratively refines it to the laser point set. At every iteration, points are added to the TIN if they are below data derived thresholds. The data derived thresholds are distances to TIN facets and angles to the facet nodes.

Figure 7 shows the results of filtering using the Terrascan filter using an iteration angle of 2 degrees and 8 degrees. The Terrascan filter was designed for urban environments and this can be seen in Figure 8. Most buildings have been filtered off. The filter also did well on the wall of the quarry. There is a very big building at the base of the quarry. The Terrascan filter completely removed this. However, it also removed surrounding terrain. The slope adaptive filter on the other hand fails to remove this building (see Figure 6, site 4).

Another interesting aspect of the Terrascan filter is its response to the gaps between the strips. When a small iteration angle is used (in Figure 8(a) it is 2) in some places, the filter erodes the edges of the strips. Increasing the iteration angle solves this problem as shown by the gray areas in Figure 8(b).

The images in Figure 6 and Figure 8 are useful for understanding the response of the filter in relation to the terrain coverage and morphology. However, they do not provide a means to examine the filtered points. For this purpose, profiles were generated, Figure 9 and Figure 10.

4.4 Profiles

Figure 9 shows three terrain cross sections. In the Figure an unfiltered section is followed by its corresponding slope adaptive filtered result (minimum slope = 0.15, slope factor = 1.0). Figure 9(a) shows a steep slope covered with high and low vegetation. The adaptive filter successfully removes high and low lying vegetation without eroding terrain points.

Figure 9(b) shows a situation in which the filter both fails and succeeds. The terrain is covered by vegetation and human artifacts. The vegetation is successfully filtered off, but not all the buildings. A slopemap with a resolution of 10m was used and because of this, buildings (size>10) are captured in the slopemap.

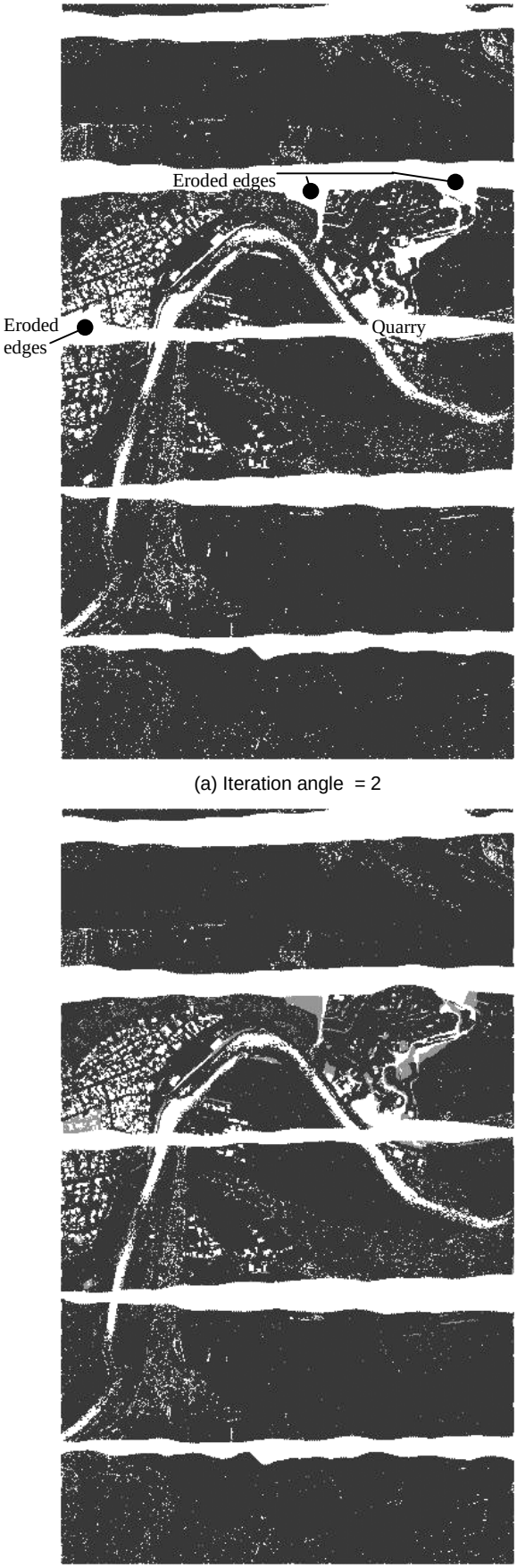

Figure 8 Difference images generated using the result of the Axelsonn filter.

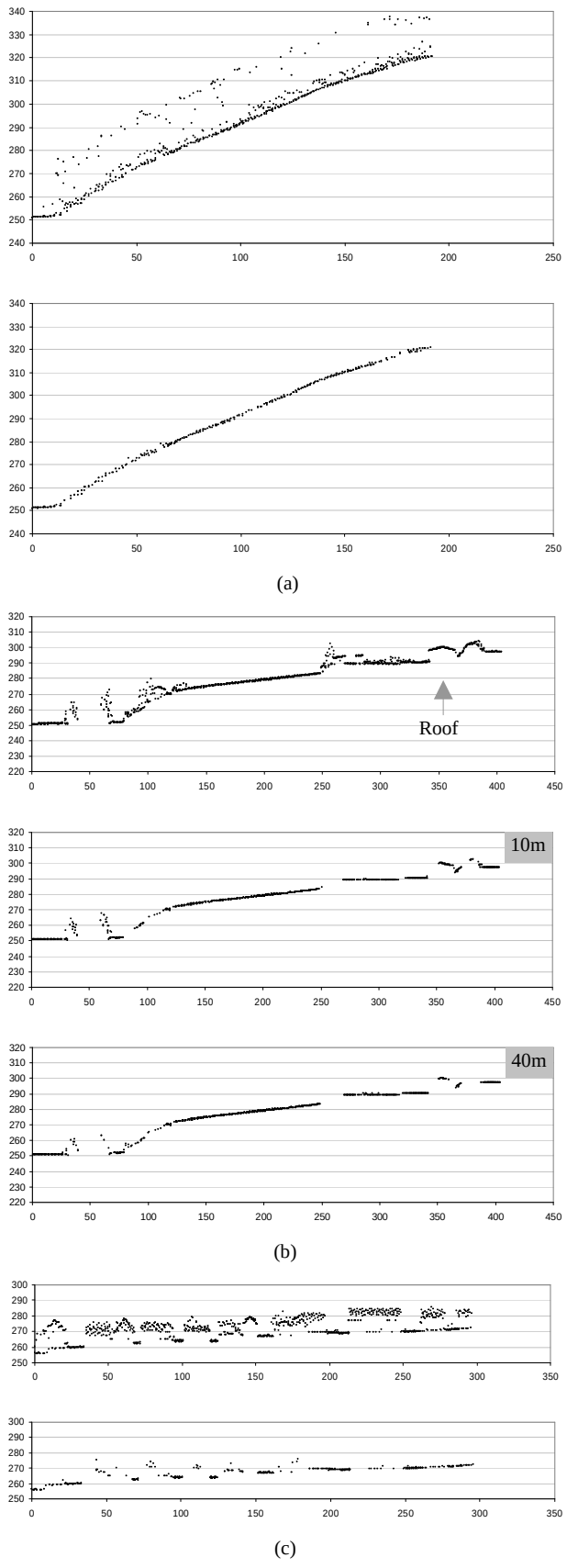

Figure 9 Unfiltered vs. filtered using slope adaptive filter

Reducing the resolution of the slopemap would result in buildings being filtered off (Figure 9 filtered using a slopemap with a pixel size of 10m and 40). However, this would result in over generalized slopes that may cause the incorrect rejection of terrain points. It can also be seen in Figure 9(b) that vegetation on riverbanks is not effectively filtered. Also, in Figure 9(c) is shown data for an area where there is low vegetation penetration. Here the filter does poorly. In both cases, the low vegetation penetration results in a slopemap that is adapted to the lowest points in the measured vegetation rather than the terrain.

Figure 10 shows more terrain profiles. Here an unfiltered section is followed by one filtered using the Terrascan filter (iteration angle = 6 degrees) and another using the slope adaptive filter (minimum slope = 0.15, slope factor = 1.0). The Terrascan filter completely removes all the vegetation if Figure 10(a). However, in the process of filtering the Terrascan filter thins the terrain points. The slope adaptive filter is not entirely successful, it removes most of the vegetation but it still leaves a few behind. A test on a few samples showed the average ratio between the slope adaptive filtrate and that from the Terrascan filter to be around 6:1.

Figure 10(b) shows the profile of a quarry. In this profile, there is very little vegetation and no buildings. What is of interest is the performance of the filters in very steep terrain. Both filters appear to capture most of the characteristics of the terrain. However, the Terrascan filter, filters off the steepest slope at the highest point in the profile. Moreover, the Terrascan filter still thins the data. Because the slope is not vertical, it is partially captured in the slopemap, and the dilation and multiplication ensures that the steep slope is not filtered off by the slope adaptive filter.

4.5 Summary

Pros. The filter does not remove steeps slopes (unlike the slope-based filter). While it is not able to correctly filter all data points, it does not thin the terrain points. This is good because it means that slope adaptive filter can be supplemented by another classifier to overcome the filter's shortcomings. If the operating range of the filter is kept low (relative to the resolution of the laser scanner data) mounds, hills, etc., are not filtered off (a problem with some filters, as noted by Huising and Gomes Pereira, 1998).

Cons. Classification is point to point. Systematic errors in a point (e.g., low points) can cause the incorrect rejection of valid terrain points. Furthermore, because the slopemap is discrete, it gives rise to side effects, which in turn have to be corrected themselves. The filter still faces problems in filtering off large buildings and areas with low vegetation penetration (forests, vegetation on riverbanks, etc.).

5 CONCLUSION

Modifications made to the slope-based filter correct the problem of Type I errors in steep sloped terrain. However, the price for this has been a small increase in the number of Type II errors and an increase in the number of filter parameters. This is unavoidable. A side effect of the increased number of parameters is that fine tuning the parameters becomes difficult, especially since it is not known if the parameters of the filter will respond similarly under different terrain conditions. Urban and vegetated areas were found to responded differently to the filter. This suggests that during

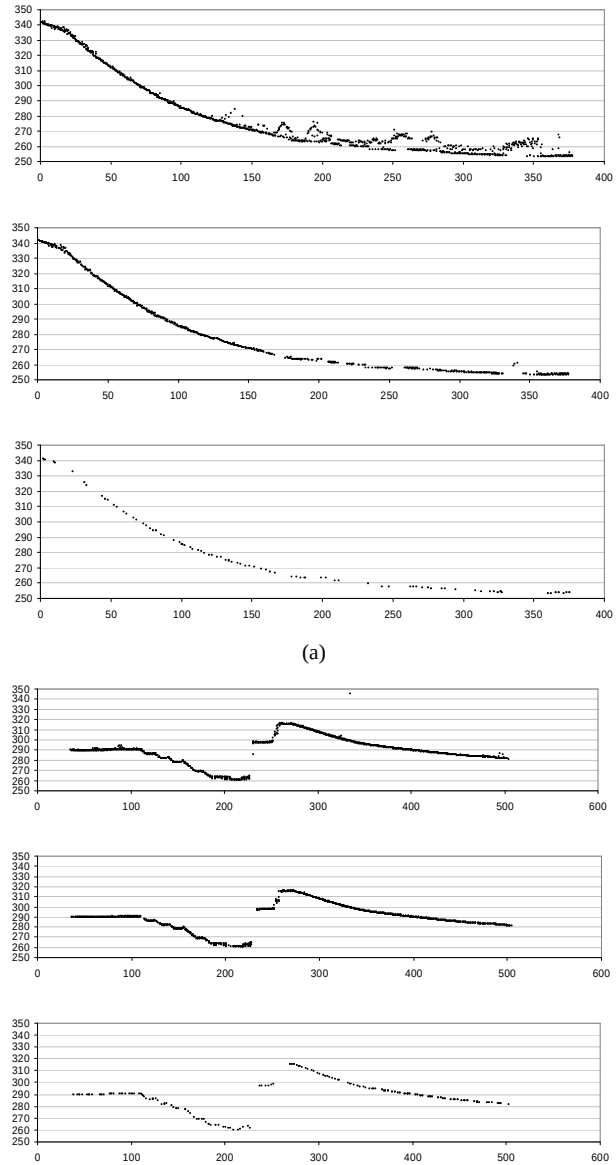

(a)

(b)

Figure 10 Unfiltered/ Slope Adaptive filter/ Terrascan filter

filtering urban and vegetated areas need to be separated (e.g. Oude Elberink and Maas, 2000) and different parameters applied for urban and vegetated areas. In the long term a filtering strategy based on using different classifiers for different terrain, coverage's may make more sense.

Another aspect of the filtering process that still needs attention is the measurement or prediction of the accuracy of filters. Currently the performance of filters is mostly reported using the rms of the filtrate or the number of points correctly classified by a filter (using a test site). The numerical and graphical comparisons presented here show that while useful, these statistics are not fully representative of the performance of the filter unless the reference data that is used is also representative of the terrain. Because of this, the approach that will be taken for assessing the accuracy of filters in future will be to determine in each data set where the filter will likely fail based on the characteristics of the filter.

REFERENCES

Axelsson, P., 2000: "DEM Generation from Laser Scanner Data Using Adaptive TIN Models. In IAPRS. Vol. 33. part B4/1, pp. 110-117.

Axelsson, P., 2001: "Ground estimation of laser data using adaptive TIN-models". Proceedings of OEEPE workshop on airborne laserscanning and interferometric SAR for detailed digital elevation models 1-3 March 2001, paper 5 (11 pages). Royal Institute of Technology Department of Geodesy and Photogrammetry 100 Stockholm, Sweden.

Elmqvist, M, 2001: "Ground Estimation of Lasar Radar Data using Active Shape Models". Paper presented at the OEEPE workshop on airborne laserscanning and interferometric SAR for detailed digital elevation models 1-3 March 2001, paper 5 (8 pages). Royal Institute of Technology Department of Geodesy and Photogrammetry 100 Stockholm, Sweden.

Huising E.J. and Gomes Pereira, L. M., 1998: "Errors and accuracy estimates of laser altimetry data acquired by various laser scanning systems for topographic applications". ISPRS JPRS, Vol. 53, no. 5. pp.245-261.

Kraus, K., Pfeifer, N., 1998: "Determination of terrain models in wooded areas with airborne laser scanner data. ISPRS JPRS. Vol. 53, pp. 193-203.

Oude Elberink, S., Maas, H, 2000: "The use of anisotropic height texture measures for the segmentation of airborne laser scanner data." IAPRS. WG III/3., Vol XXXIII, Part B3. Amsterdam, 2000. pp.678-684.

Schickler, W., Thorpe, A., 2001: "Surface Estimation Based on LIDAR". Proceedings ASPRS conference April 23-27, 20001. St. Louis Missouri. CD-ROM, 11 pages.

Vosselman, G. and Maas, H., 2001: "Adjustment and Filtering of Raw Laser Altimetry Data". Proceedings of OEEPE workshop on airborne laserscanning and interferometric SAR for detailed digital elevation models 1-3 March 2001, paper 5 (11 pages). Royal Institute of Technology Department of Geodesy and Photogrammetry 100 Stockholm, Sweden.

Vosselman, G., 2000: "Slope based filtering of laser altimetry data". IAPRS, Vol XXXIII, Part B3, pages 935-942. Amsterdam, The Netherlands.

SOME ALGORITHMS FOR VIRTUAL DEFORESTATION (VDF) OF LIDAR TOPOGRAPHIC SURVEY DATA

R. A. Haugerud[1] and D. J. Harding[2]
[1]U.S. Geological Survey c/o University of Washington, Seattle Washington 98195
rhaugerud@usgs.gov
[2]NASA Goddard Space Flight Center, Greenbelt MD 20771
harding@core2.gsfc.nasa.gov

Commission III, Working Group 3

KEY WORDS: lidar, laser scanner, filtering, vegetation, canopy, algorithm, topography, ground surface, virtual deforestation

ABSTRACT

Lidar topographic surveys of forested terrain generate XYZ positions for laser returns from numerous points, some on the ground and some from vegetation. Extracting a ground surface model from such data requires 'virtual deforestation' (VDF), preferably by automatic means. A simple error budget for lidar topography of forested terrain suggests that the dominant source of error—and the greatest room for improvement—lies in VDF procedures.

We discuss a despike VDF algorithm that classifies returns as ground or not-ground on the basis of the geometry of the surface in the neighborhood of each return. The despike algorithm is fully automatic, effective, and can recover breaklines. It fails to identify some negative blunders, rounds some sharp corners off the landscape, and as implemented is slow. There are clear paths to improve its speed. If multiple-return data are available, a no-multiple-returns VDF algorithm robustly defines areas where all returns are ground returns. Many groups are using variations on block-minimum VDF algorithms, but these do not work well on slopes and typically require substantial human involvement to adjust block size as the fraction of ground returns changes.

Fully automatic VDF algorithms are desirable not only to minimize survey costs but also to produce topography for which all necessary interpretive biases and assumptions are explicit. The development of effective VDF algorithms has been hindered by the tendency of some commercial and academic practitioners to keep their work proprietary. Open dialogue is needed.

1 INTRODUCTION

Airborne lidar (LIght Detection And Ranging, also known as ALS—airborne laser scanning or ALSM—airborne laser swath mapping) surveys promise topographic models that are more detailed and more accurate than those obtained by traditional photogrammetric methods. The potential for improvement is especially great in heavily forested areas, where the ground is poorly illuminated and particular ground points are rarely visible on both photographs of a stereoscopic pair.

On Bainbridge Island west of Seattle, WA, an initial lidar survey (described by Harding and Berghoff, 2000) serendipitously showed evidence for recent faulting (Nelson and others, 1999) despite dense forest. Subsequently, we joined local government and other USGS researchers in the Puget Sound Lidar Consortium (*http://pugetsoundlidar.org*), a cooperative effort to contract for lidar surveys of large parts of western Washington. Though our primary focus is earthquake hazards, these data will have many uses, including mapping of other hazards, geologic mapping, transportation planning, forestry, municipal planning, and fisheries.

Puget Sound Lidar Consortium members have contracted with TerraPoint LLC for surveys using a laser altimeter that covers ±17º from nadir using a rotating pyramidal scan mirror, produces a 0.9 m diameter laser beam on the surface, and records up to 4 returns for each laser pulse with a constant-fraction discriminator pulse-detection scheme. The survey is designed to yield a uniform distribution of laser pulses across a 600 m swath with across- and along-track spacing of 1.5 m. A 50% minimum sidelap between swaths ensures that all areas are covered at least twice, leading to an average pulse density of about 1/m^2. Forest cover in the Puget Lowland includes coniferous evergreen, broadleaf deciduous, and mixed stands. All data are collected in winter months to maximize ground returns. The Consortium is purchasing all-return data, classified bare-earth returns, a bare-earth surface model, and a first-return surface model. All data are delivered in State Plane projection with English units. Surfaces are gridded to 1.8 m (6 ft) cells. Approximately 4,000 km^2 of the Lowland have been surveyed to date, with another 2,500 km^2 scheduled for survey in the winter of 2001-2002.

Initial bare-earth surface models delivered by the contractor did not appear to be the best that could be obtained from these data, which prompted us to develop a new algorithm for removing returns from the forest canopy. Because we are removing trees algorithmically, rather than with chainsaws, a colleague has dubbed this post-processing 'virtual deforestation' or VDF. TerraPoint subsequently has implemented and extended our VDF algorithm for the post-processing of Consortium lidar data. This algorithm is the subject of this paper.

An error budget for lidar topography

A topographic surface is produced by measuring, with a laser scanner, the XYZ coordinates for numerous returns, some from the ground and some not; classifying these returns as ground or not-ground (vegetation, man-made structures); and interpolating from the discrete ground returns to a continuous surface. This

procedure suggests a simple error budget for the topographic surface:

$$\text{Z error} = \left[(\text{measurement error})^2 + (\text{classification error})^2 + (\text{interpolation error})^2 \right]^{1/2}$$

Measurement errors for lidar surveys are commonly estimated at about 15 cm (Z) (e.g. Huising and Gomes Pereira, 1998; Schenk and others, 1999). The average classification error is

(fraction false ground points) * (average height above ground of false ground points)

Where tree heights are many tens of meters, the classification error is potentially quite large, on the order of meters. The interpolation error is difficult to estimate without *a priori* knowledge of typical wavelengths in the topographic surface, but we do note that the probable interpretation error increases with ground-return spacing. Our experience in the Puget Lowland is that in densely forested steep areas (ravines, landslides along walls of large valleys), ground-return spacing of tens of meters commonly results in many-meter interpolation errors. Note that if interpolation error is related to surface smoothness, and if the classification of laser returns as ground or not-ground is based on smoothness of the resulting ground surface, classification and interpolation errors may be correlated and the above formula may be inadequate.

Using current technologies in forested terrain, the greatest improvement in the quality of lidar topography is likely to be achieved by reducing the misclassification of vegetation and structure returns as ground and by increasing the number of returns on the ground. The latter can be achieved both by changing the survey design (flying in leaf-off conditions, increasing pulse density) and by not misclassifying ground returns as vegetation returns.

What is ground?

In the lidar context it is useful to define the ground ("bare earth") as that surface which is continuous, is smooth, and has nothing visible below it. Note that this definition is scale dependent! With sampling at meter intervals, point returns from a hectare of forest do not constitute ground, as stem/branch/leaf returns introduce discontinuities. If the instrument could record multiple returns or the laser were aimed off-nadir, we would see many of these vegetation returns underlain by deeper returns. However, a 10 cm by 10 cm piece of tree branch, when observed with closely-spaced pulses of a millimeter-wide laser beam, may be continuous, smooth, and not underlain by any other source of returns—that is, it is "ground." Note that when observed at a large enough scale many buildings are ground by this definition, unless sharp corners catch part of a beam and lead to multiple returns.

Clearly this definition of "ground" does not meet many needs, but it (1) does match the capabilities of lidar technology and thus (2) can focus discussion of how to interpret lidar survey data. For example, this definition suggests that a filtering algorithm which preserves small details of the ground surface—pits from wind-thrown trees, glacial erratics, many break-lines—can not be expected to also identify building returns. To produce detailed, accurate bald earth surfaces (no vegetation or buildings) will require post-processing with multiple algorithms.

2 DESPIKE ALGORITHM

Smoothness—the property of the ground surface that, if sampled closely enough, it has no sharp corners—suggests a route to identifying ground points. One can search for local aberrations—points that define local strong curvatures—and remove them. Definition of ground as the lowest surface suggests that we preferentially remove points that define sharp upwards convexities. The geometry of the laser-return surface can be examined by representing it as a TIN (triangulated irregular network) constructed from the discrete returns. Because the geometry of the surface changes as we remove points, such a procedure must be iterative. That is,

```
repeat
      Build TIN
      Identify points that define strong curvatures
      Flag points as not-ground
until no or few points are flagged
```

Identifying points with strong curvatures is the nub of the problem. In ARC-INFO we have done this by

	ARC-INFO command
Convert TIN to grid1	*tinlattice*
Calculate 3x3 mean at each cell	*grid2 = focalmean(grid1)*
Convert TIN vertices to point database (Z value in item SPOT)	*Tinarc TIN cover1 point*
Calculate item SPOT2 = value of GRID2 at each point in database	*latticespot grid2 cover1 spot2*
CURVATURE = SPOT2 – SPOT	
If CURVATURE > testvalue1 or CURVATURE < testvalue2 then mark point for deletion	

`testvalue1` is chosen largely on the basis of the cell size used for grid1 and grid2. To minimize interference between neighboring points, cell size should be less than the typical point spacing for a lidar survey. With a 0.9 m laser beam diameter and average beam spacing of 1 m, we have successfully used 0.6 m (2 ft) cells. `testvalue1` is then taken at 0.2 m (0.7 ft), to accept a point on the outside shoulder of a forest road with an angle-of-

repose slope below it. Testing for `CURVATURE < test-value2` eliminates some negative blunders; this is discussed further below.

The despike algorithm can work with first returns, last returns, or multiple returns. To minimize the computational effort we use only the last return of our multi-return data. It commonly takes at least 10 iterations for the fraction of newly identified not-ground returns to drop below 0.1%, the criterion we use for convergence.

Figure 1 is a last-return surface for an area east of Seattle. Figure 2 presents the output of the despike algorithm applied to these data. Note the excellent definition of the road that traverses the scene and the good definition of the steep-sided ravine at the top of the scene. Small structures are completely removed (at **A**) or left as isolated rounded lumps (**D**, **E**). The ground surface is least satisfactorily defined in some wooded areas where few ground points remain (**B**, **C**) and at **C** this has probably resulted in truncation of the ridge crest.

Note that all the surfaces we show are produced by linear interpolation from a TIN: while other interpolation techniques may produce more realistic surfaces, conspicuous facets in a TIN-derived surface directly inform the viewer that the surveyed point density is not adequate to characterize the local curvature of the surface.

Advantages of despike algorithm

The despike algorithm creates surfaces that both look realistic and, where we have surveyed ground control, match reality. It retains large numbers of points. It requires no human intervention: to a geomorphologist concerned with understanding the processes that create the Earth's surface, this is extremely important because it means that all assumptions and biases necessary to interpret a topographic surface from raw observations are explicit in the algorithm.

If the lidar survey happens to include returns from topographic breaklines, the despike algorithm can retain them. This is an advantage over the iterative robust interpolation algorithm (Kraus and Pfeifer, 1998; Pfeifer and others, 1999), which smooths all corners.

Without complete implementations of alternate VDF algorithms (see comment below), it is not possible to judge the relative effectiveness of different algorithms at retaining ground points.

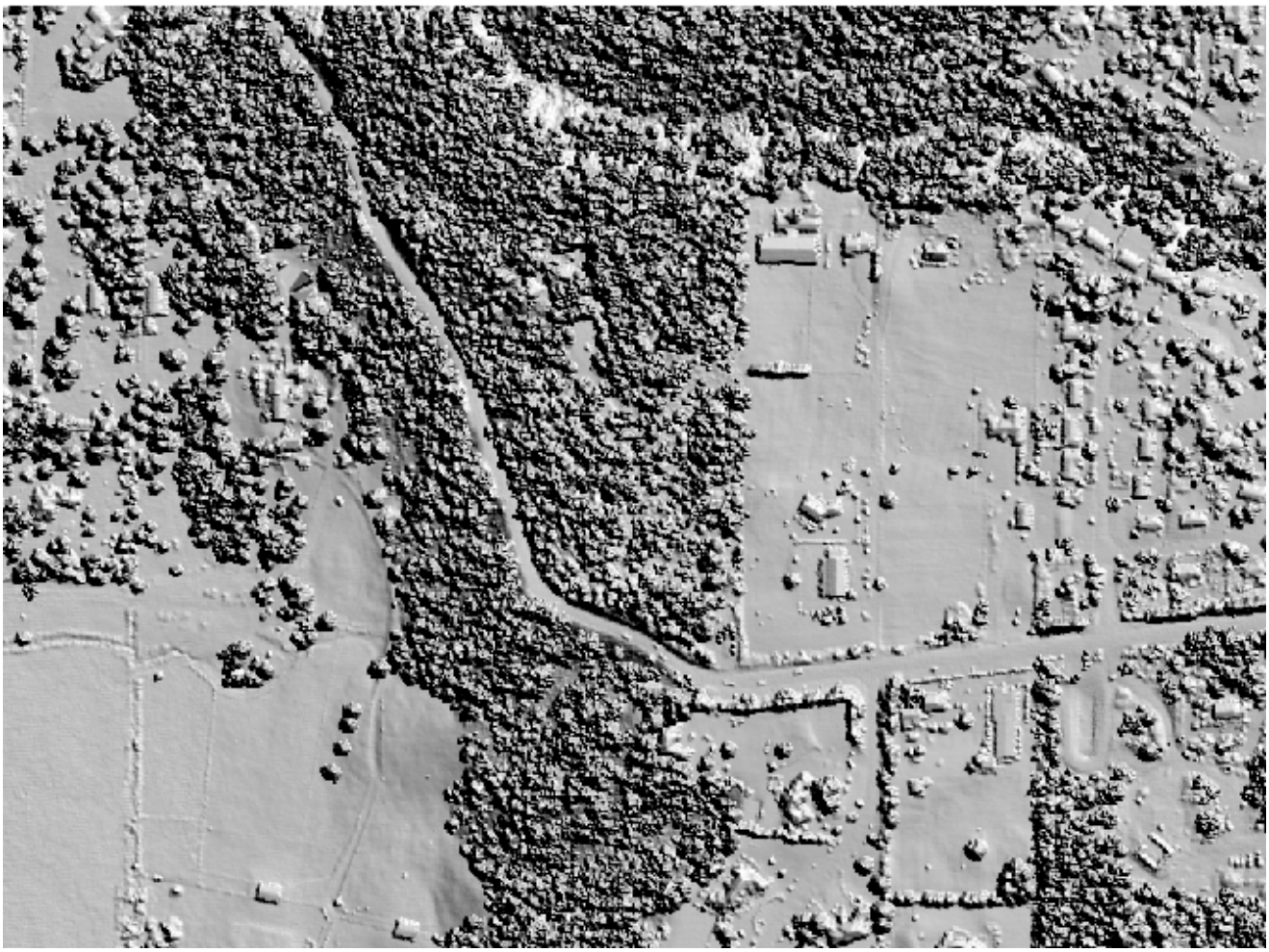

Figure 1. Last-return surface model of suburban area east of Seattle, Washington. Area shown is 850 m east-west by 760 m north-south and includes about 5 x 10^5 last-return points.

Figure 2. Surface model produced with despike algorithm, same area as figure 1. Area shown includes about 2.7 x 10^5 ground returns. See text for discussion.

The despike algorithm effectively removes small buildings and most bridges. It does not remove large-area, low-height buildings.

The despike algorithm retains more points than the block-minimum algorithms we have implemented and appears to retain more points than commercial block-minimum algorithms.

Disadvantages of despike algorithm

We have encountered three significant deficiencies of the despike algorithm.

Corner removal First, even if there are abundant returns, the despike algorithm eliminates points at the corners between near-vertical faces below gently sloping surfaces, e.g. some highway cuts in competent rock. In open (no canopy) areas this failing can be partially remedied by substituting the surface obtained with a no-multiple-returns algorithm (below). This substitution can be entirely automated.

Negative blunders The despike algorithm is especially sensitive to negative blunders. Most lidar survey data contain a few (~1 in 10^5) points dramatically lower than their surroundings and not correlated with real features.

In our experience such negative blunders are more frequent where the instrument is closer to the ground surface, are largely associated with near-nadir pulses, and are often associated with mirror-like surfaces (e.g. still water, automobiles.) Some workers (e.g. Pfeifer and others, 1999) have ascribed these negative blunders to multiple-bounce reflections—that is, reflections off more than one object in the target area. We have found negative blunders where a second reflecting surface is not evident and speculate that some negative blunders may be artifacts generated within the altimeter receiver by high-energy returns.

Processing such negative blunders with the despike algorithm can lead to distinctive 'bomb craters'—conical pits where surrounding valid ground points have been eliminated. Where the blunder is severe enough, pit diameter reflects the number of iterations of the despike process. Solitary negative blunders can be readily caught by setting `testvalue2` to 2 * grid2 cell size. Unfortunately, this occasionally discards ground returns from small ravines beneath forest canopy. Setting `testvalue2` to 4 * grid2 cell size catches some negative blunders (but not all) and appears to keep ground returns from small ravines. We have had

some success with pre-processing data to eliminate negative blunders, and further work is warranted.

Computation time The third major disadvantage of the despike algorithm is excessive computation time. Processing ~10^6 points from a 1-km^2 area takes about an hour on a dedicated single-CPU Sun Ultra 60 workstation. There is room for improvement: (1) The slowest part of the computation is building a TIN, at which ARC-INFO is not particularly efficient. (2) Within ARC-INFO the TIN data structure is not directly accessible, forcing translation of the TIN to a grid and a point set, followed by intersection of the grid and point set to evaluate curvature at each TIN node. Moving the despike algorithm to code in which the TIN data structure is directly accessible would minimize much disk I/O and reduce the amount of calculation. (3) The data could be intelligently thinned when the initial TIN is constructed. Where there are several laser returns in close proximity the lowest of these should be retained and the remainder discarded. This is not possible within ARC-INFO.

Surface roughness

Ground-surface models produced with the despike algorithm typically have widespread short-wavelength surface roughness. Enough of this roughness correlates with land cover (rough in forest, smoother in open areas) that much of the roughness probably reflects remnant vegetation. Particularly obvious are local rough areas with maximum height above the surrounding surface of 1 to 2 m. Due to pulse duration, detector bandwidth, and limitations of the ranging electronics, dual- or multi-return laser altimeters have a detection 'dead time': for a single pulse the instrument is unable to detect a return from a surface that is located closely below a surface that yields a prior return. The minimum distance between multiple returns detected by the TerraPoint system used in our project is 1.4 m, which prevents detection of returns from ground beneath some brambles and low shrubs even though the ground is illuminated by the laser.

In addition, some of the observed surface roughness reflects measurement error. This is particularly evident for very smooth surfaces where there is inconsistent navigation between overlapping flightlines. Processing data from one flightline alone reveals pavement as smooth, whereas combining two overlapping flightlines whose data are offset vertically and/or horizontally gives pavement with an orange-peel texture.

Some surface roughness is probably true ground roughness. For example, fluvial deposition may form a nearly-flat surface on a flood plain. If the flood plain is forested, toppling of trees during windstorms produces pits where the trees were rooted and hummocks where the rotting up-turned roots drop their attached soil. Human analysts commonly omit such detail as they draw contours, and we have come to assume that 'plastic' contours and the smooth surfaces they represent are more valid.

The rough area to the left of **A** in figure 2 is probably vegetation incorrectly classified as ground. But some of the high returns in this area may be from stumps that are 'ground' by the definition proposed above.

For the geologist wishing to accurately image the surface of the (forested) Earth in order to understand the processes that formed this surface, surface roughness and the uncertainty about its origin present a conundrum. Is it real and meaningful, or should it be modeled out? To make matters worse, many tools for analyzing geomorphic surfaces presume the (perhaps unreal) smoothness associated with surface models filtered through human contouring.

3 OTHER VDF ALGORITHMS

No multiple returns

The absence of multiple returns suggests that, at least locally, the laser beam has reached ground—there is nothing visible beyond this surface. Requirements that there be no multiple returns within some distance, and that contiguous areas of no multiple returns exceed some minimum dimension, quantify the "at least locally" qualification.

To implement this algorithm:

*Parse all-return data into two lists of XY locations:*First_returns *and* Other_returns

Convert these two lists to an integer grid: if there is an "other return", cell value = 1, else if a first return, cell value = 0

Expand multiple-reflection areas by `length1`. S*hrink multiple-reflection areas by* `length2`. *(*`length1` *is greater than* `length2`, `length1 - length2` *is minimum size for no-multiple-reflection areas,* `length2` *is minimum distance to a multiple-reflection area)*

Use final integer grid as mask to cut out valid part of 1st-return surface

The best values for `length1` and `length2` are subject to experimentation. We suspect they should depend on canopy type, laser spot spacing, laser beam diameter, detector sensitivity, and one's tolerance for misidentification of bare earth. (If we are willing to accept a slightly higher error level, we can identify more reflections as likely to be bare earth).

Figure 3 is an image of that part of a 1st return surface identified as ground by this algorithm.

This algorithm is exceedingly robust. With appropriate parameters it rarely misidentifies bare-earth reflections as canopy and within large bare-earth areas it doesn't falsely reject any points. It does require a multiple-return scanner with a laser beam that is sufficiently wide and powerful to create a significant number of multiple returns. And, obviously, it provides no information about the ground surface that is beneath canopy.

Block-minimum algorithms

The observation that ground points should be the lowest points in a neighborhood suggests a block-minimum function as a bare-

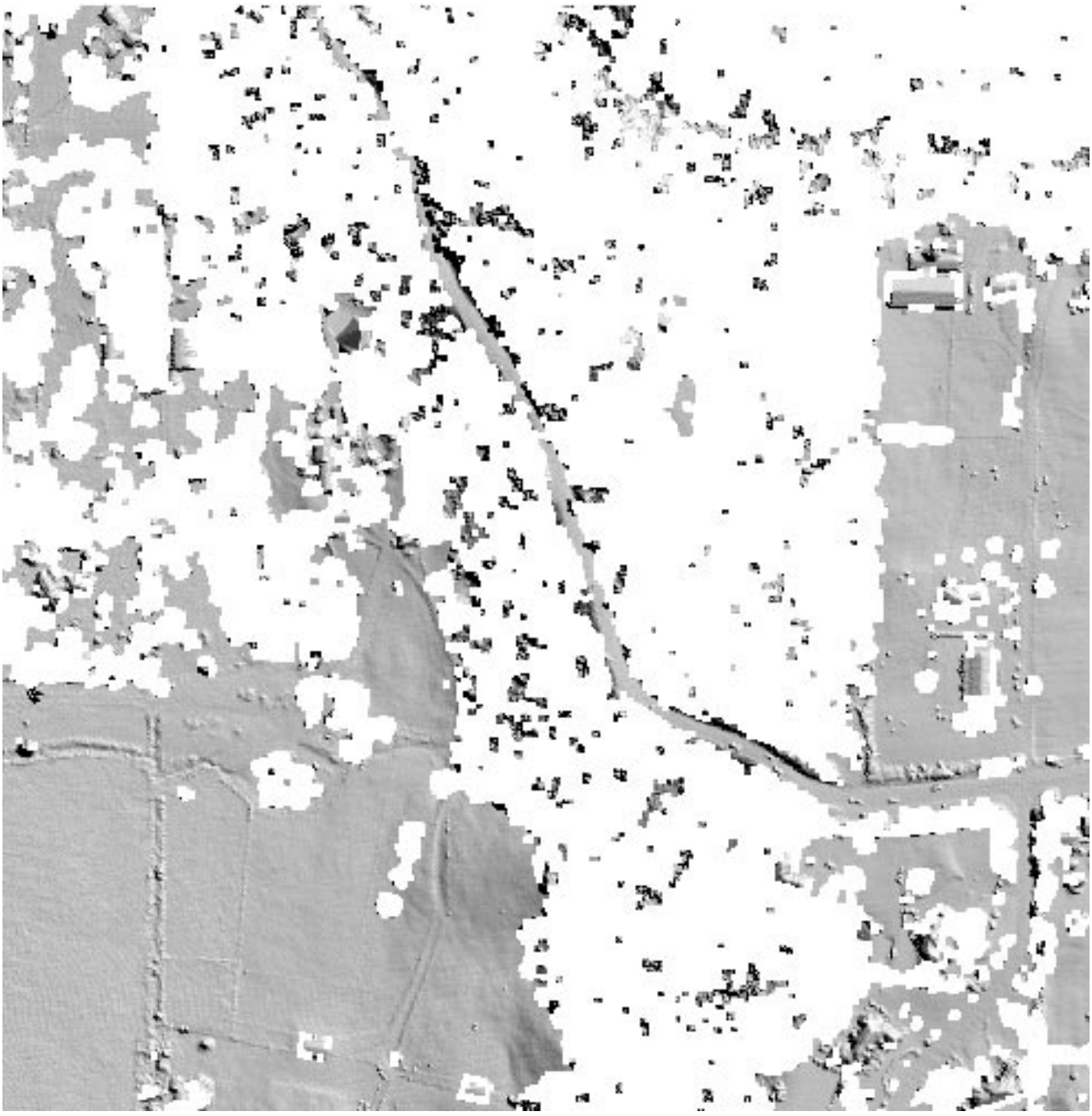

Figure 3. Surface model obtained with no-multiple-return algorithm, same area as figures 1 and 2. White areas are undefined. Model calculated with 2 ft (0.6 m) grid cells, `length1` = 10 ft (3 m) and `length2` = 6 ft (1.8 m).

earth filter. Implementations and extensions of block-minimum functions have been described by Kilian and others (1996), TerraScan (1999) and Hansen and Vögtle (1999). Proprietary algorithms used by some North American lidar survey enterprises appear to be block-minimum algorithms.

A block-minimum algorithm can be enhanced by accepting as ground returns those points that are no higher than some specified amount above the block-minimum surface. Or one can use a larger block size and take the 5th percentile (or other) elevation, thus rejecting negative blunders.

A block-minimum algorithm implemented in the raster domain can be computationally rapid, but this loses positional (XY) accuracy. The derived surface can have a tweedy appearance in steep areas. It can be biased low on slopes, as the lowest points at the edge of a block are attributed to all of a block.

Block minimum algorithms have two fundamental weaknesses. First, the necessary block size must be inversely proportional to the ground return density: areas with low density of ground returns require larger blocks. For optimum results the block size needs to be adjusted, typically with the intervention of a human operator. Second, and less obvious, block minimum algorithms

contain the implicit assumption that the ground is horizontal. They can produce acceptable results in low-slope areas; we note that some of the successful users of block-minimum VDF algorithms come from the Gulf Coast of North America.

Iterative linear prediction

Kraus and Pfeifer (1998) and Pfeifer and others (1999) described a VDF algorithm that attempts to explicitly model measurement error, derive a ground-surface model, and thus classify returns as ground or not-ground. Like our despike algorithm, it uses the smoothness of the ground as a guide to building a ground-surface model. Unlike the algorithms described above, it fits a polynomial surface to weighted laser returns, increasing the smoothness of the surface and gaining the possibility of modeling (and thus removing) random measurement errors at the price of losing all breaklines.

4 CONCLUDING REMARKS

Our experience with the despike algorithm is encouraging. Excellent ground-surface models can be extracted from lidar surveys of at least some heavily forested terrain. The classification of laser survey data into ground and not-ground returns has been almost entirely automated. Such automation is desirable not only to control the costs of lidar surveys, but also to make explicit all interpretive biases and assumptions.

The classification of lidar returns—virtual deforestation—is not yet a mature art. Topics that need further work include understanding the mechanisms that cause negative blunders, designing surveys to minimize them, and researching post-processing techniques that identify them. The identification of returns from buildings, which we have barely mentioned, needs development.

A variety of VDF algorithms are currently in use, but few are well documented in the published literature. Lidar surveys of forested terrain commonly obtain imperfect results. Together, these observations suggest that the tendency of lidar survey enterprises, whether commercial or academic, to keep their algorithms proprietary and the resulting lack of dialogue has hindered development of the robust and automatic algorithms needed for lidar surveying to reach its full potential. We urge all practitioners to publish details of their post-processing algorithms. Furthermore, we see a need for comparison of algorithms on a variety of forest and terrain types. To that end, we have posted our algorithms, sample all-return data, and derived ground surface models at *http://pugetsoundlidar.org*.

Acknowledgements:

It has been a pleasure to work with our colleagues on the Puget Sound Lidar Consortium: Erik Anderson, Phyllis Mann, and David Nash (Kitsap County), Greg Berghoff (Kitsap PUD), Ken Conradi (City of Seattle), Jerry Harless (Puget Sound Regional Council), and Sam Johnson and Craig Weaver (USGS). We thank them for their efforts in obtaining funding for data acquisition, managing the acquisition contract, and evaluating the results of our VDF research. The staff at TerraPoint LLC was impressively cooperative in incorporating our VDF algorithm in their post-processing procedures. We thank Rick Blakely and Joe Means for helpful comments on this manuscript.

REFERENCES CITED

[Hansen and Vögtle, 1999] Hansen, W., and Vögtle, T., 1999. Extraktion der Geländeoberfläche aus flugzeuggetragenen Laserscanner-Aufnahmen. Photogrammetrie Fernerkkundung Geoinformation, pp. 229-236.

[Harding and Berghoff, 2000] Harding, D.J., and Berghoff, G.S., 2000. Fault scarp detection beneath dense vegetation cover: Airborne lidar mapping of the Seattle fault zone, Bainbridge Island, Washington State. Proceedings of the American Society of Photogrammetry and Remote Sensing Annual Conference, Washington, D.C., May, 2000, distributed on CD-ROM, also available at *http://pugetsoundlidar.org*

[Huising and Gomes Pereira, 1998] Huising, E.J., and Gomes Pereira, L.M., 1998. Errors and accuracy estimates of laser data acquired by various laser scanning systems for topographic applications. ISPRS Journal of Photogrammetry and Remote Sensing, v. 53, pp. 245-261.

[Kilian and others, 1996] Kilian, J., Haala, N., and Englich, M., 1996. Capture and evaluation of airborne laser scanner data. International Archives of Photogrammetry and Remote Sensing, Vienna, Austria, v. XXXI, pt. B3, pp. 383-388.

[Kraus and Pfeifer, 1998] Kraus, K., and Pfeifer, N., 1998. Determination of terrain models in wooded areas with airborne laser scanner data. ISPRS Journal of Photogrammetry and Remote Sensing, v. 53, pp. 193-203.

[Nelson and others, 1999] Nelson, A.R., Pezzopane, S.K., Bucknam, R.C., Koehler, R., Narwold, C., Kelsey, H.M., LaPrade, W.T., Wells, S.J., and Johnson, S.Y., 1999. Late Holocene surface faulting in the Seattle fault zone on Bainbridge Island, Washington (abstract). Seismological Research Letters, v. 70, p. 233.

[Pfeifer and others, 1999] Pfeifer, N., Reiter, T., Briese, C., and Rieger, W., 1999. Interpolation of high quality ground models from laser scanner data in forested areas. International Archives of Photogrammetry and Remote Sensing, La Jolla, California, USA v. XXXII, Part 3-W14, pp. 31-36, 1999.

[Schenk and others, 1999] Schenk, T., Csatho, B., and Lee, D.C., 1999. Quality control issues of airborne laser ranging data and accuracy study in an urban area. International Archives of Photogrammetry and Remote Sensing, La Jolla, California, USA, v. XXXII, Part 3-W14, pp. 101-108.

[TerraScan, 1999] TerraScan, 1999. TerraScan for microStation, user's guide. TerraSolid Limited.

TERRAIN MODELLING AND ANALYSIS USING LASER SCANNER DATA

M. Elmqvist, E. Jungert, F. Lantz, Å. Persson, U.Söderman
FOI (Swedish Defence Research Institute)
P.O. Box 1165, SE-581 11 Linköping, Sweden
{magel, jungert, flantz, asaper, ulfso}@foi.se

Commission III, Working Group 3

KEY WORDS: airborne laser scanning, digital terrain model, ground surface modelling, single tree detection, laser data classification, terrain database, qualitative methods, resolution pyramid.

ABSTRACT

Very detailed high-resolution (3D) digital terrain models can be obtained using airborne laser scanner data. However, laser scanning usually entails huge data sets even for moderate areas, making data management and analysis both complex and time consuming. For this reason, automatic terrain modelling and efficient storage structures supporting data access are needed. In this paper a number of methods supporting automatic construction of 3D digital terrain models, especially ground surface modelling and detection and measurement of individual trees will be discussed. Furthermore automatic and/or interactive terrain feature analysis will be discussed. A special data representation structure for the terrain model allowing efficient data storage and data access will be presented. Beside this, it is possible to create a symbolic information structure from the terrain model that can be used in queries for determination of different terrain features, such as ditches or ridges etc., but also for detection of changes in the terrain.

1 INTRODUCTION

Very detailed high-resolution (3D) digital terrain models can be obtained using airborne laser scanner data. There are many applications requiring such models, both civilian and military. Visual simulation and other types of 3D-visualisations are perhaps the most prominent ones due to the growth of easy accessible powerful 3D-computer graphics hardware. However, there are many other important applications, e.g. urban planning, command and control, mission planning and preparation and various terrain analysis problems.

To support these applications development of new methods and algorithms for automatic terrain modelling, terrain feature analysis and databases are needed. Since data acquisition using airborne laser scanners usually entail huge data sets even for moderate areas it is important that computational efficiency, efficient storage and data access are considered.

This paper consists of two main parts. In the first part we will discuss methods supporting automatic construction of 3D digital terrain models, especially ground surface modelling and detection and measurement of individual trees. In the second part we will discuss terrain feature analysis for high-resolution digital terrain models. The various methods have been developed in order to support a number of specific applications where laser-radar data primarily is used

For modelling of the ground surface a method based on active contours have been developed (Elmqvist, 2001). Metaphorically, a 2.5D contour surface that acts like a sticky rubber cloth or a rubber band net is being pulled upwards from underneath the data set. The net is attracted by the data points and sticks to the points that (are assumed to) represent the true ground. The data points not representing the true ground are not reached due to the elasticity of the net. The resulting contour forms a continuous model of the ground surface. Like many other methods for ground surface modelling (Kraus and Pfeifer 1998, Axelsson, 1999, Pfeifer et al, 1999) the implementation is based on a hierarchic and iterative processing scheme. The active contour method will be presented in section 2.

Given the ground surface model, classification of ground points can be done using the distance between the raw-data points and the estimated ground surface. The remaining raw-data points can be further classified with respect to vegetation and non-vegetation using a recently developed segmentation and classification method. For vegetation data, individual trees can then be identified and tree attributes estimated using a novel method (Persson, 2001). The result can be used for construction of high-resolution 3D synthetic natural environments suitable for 3D-visualisation. Another application not covered here is forest inventory (Hyppä et al, 2000, Hyppä et al, 2001). Classification and tree identification will be discussed in section 2.

For automatic and/or interactive terrain analysis a special terrain model allowing efficient data storage and data access is necessary. For this reason the surface model, in terms of a dense regular grid, is subject to a data reduction process combined with a suitable pattern matching technique (Lantz, 2000). This results in a model with a much sparser grid combined with a set of significant irregular data points. The sparse structure corresponds to a terrain model that almost preserves the resolution without any considerable decrease in accuracy. A data reduction in the order of 90 % has been observed depending on the actual terrain. That is, a

flat terrain gives a higher reduction rate than a mountainous area. Of importance is that this data model, with its irregular data points, can be stored in a database using a regular database model. Beside this, it is possible to create a symbolic information structure from the terrain model that can be used in queries for determination of different terrain features, such as ditches or ridges etc., but also for detection of changes in the terrain. The data reduction process, storage structure and terrain analysis is discussed in section 3.

For this work we have used data from the TopEye airborne laser scanner system. This system is mainly operated carried by a helicopter. It contains a vertical scanning direct detection laser radar operating at a wavelength of 1.06um. The pulse rate is between 2 and 7 kHz and the emitted energy is about 0.1 mJ per pulse. The operational altitude is approximately 60-900m. The TopEye system is able to produce point position, intensity of reflection as well as multiple return or double echo data. The laser data used in our work was acquired at missions in 1998, 1999 and 2000. We required dense data sets and hence the mission were flown at slow speed, i.e. 10-25 m/s, and at rather low altitudes, 120-375m. Some areas were also flown in two directions perpendicular to each other. The resulting data sets have a density that varies between 2 - 16 points per square meter.

2 MODELLING AND CLASSIFICATION

2.1 Ground Surface Modelling

For the modelling of the ground surface a new surface estimation method based on active contours has been developed (Elmqvist, 2001). This method is based on the theory on active shape models (Cohen and Cohen 1993, Kass et al, 1998) which has its roots in the area of image processing where it is mainly used for detection of contours in images. Shape models are also referred to as snakes, especially when referring to two-dimensional contours. In such a case the snake is a continuous spline, open with loose ends or closed in a loop. The method for ground surface modelling described here uses a three dimensional active contour in terms of a continuous open surface.

In general, the shape of an active contour is the solution that minimizes an energy function. The function includes internal energy and a potential field. The internal energy is described using physical characteristics associated with the contour, usually material properties like elasticity and rigidity. The potential field is given by the image data, in this case height data. Since an active contour may stick to a local minimum the solution is not always the global minimum.

Metaphorically speaking, the contour used in this case acts like a sticky rubber cloth or a rubber band net that is being pulled upwards from underneath. The net is attracted by the height data points and sticks to points that (are assumed to) represent the true ground. The elasticity forces in the rubber band stops the net from reaching points not representing the true ground. The solution is a net that forms a continuous model of the ground surface. By adjusting various parameters it is possible to achieve different behaviours of the net. For example, if it is preferred that rocks in the terrain are part of the ground surface then the net should be more elastic and sense a greater attraction from the measured points. One example of using this method is illustrated in Figure 1 and Figure 2

The ground surface estimation method based on active contours has been implemented and tested in an experimental set-up. For simplicity and speed of computation the implementation only works on rectangular grid data. It is, however, straightforward to modify the implementation such that it uses the original point cloud and creates a surface in terms of a TIN.

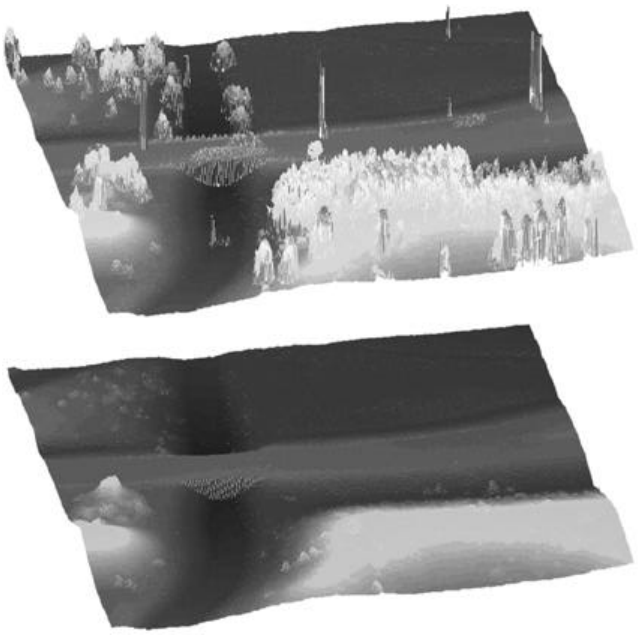

Figure 1 A test area including a road, street lamps, an underpass and a small vegetation area with small pine trees. The post spacing of the grid is 0.33m Top: raw laser data. Bottom: the estimated ground surface

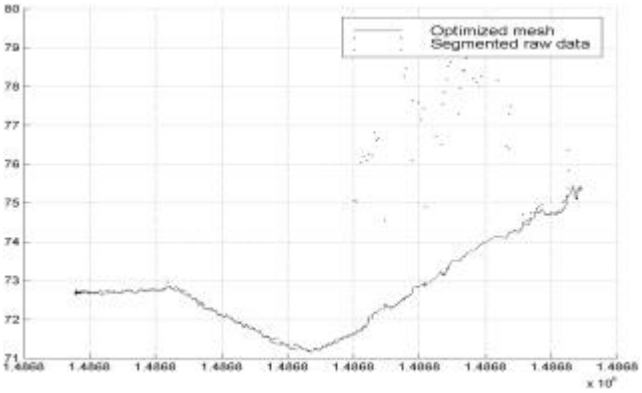

Figure 2 Estimated ground surface for a single laser radar swath. From left: the road, a ditch and a slope with trees.

2.1.1 Implementation

In the experimental implementation the raw data is first resampled in a rectangular grid. The resampling is performed in the easiest way possible. In each mesh the lowest point is selected.

The next step is the optimization of the active contour surface. This process is divided in two phases in which the net is iteratively moved and stretched towards a final solution. In this way a better approximation of the ground surface is achieved. The movement is controlled by a number of "forces" acting on the nodes of the net. In the first phase three different forces are used: elasticity, attraction and gravitation. When the net reaches the convergence criterion of the first phase the second phase starts. In the second phase gravitation is dropped and only elasticity and attraction are used. The iterations continue until the net converges at a final solution. In both phases all the forces are restricted to the z-axes component of a true three-dimensional force vector.

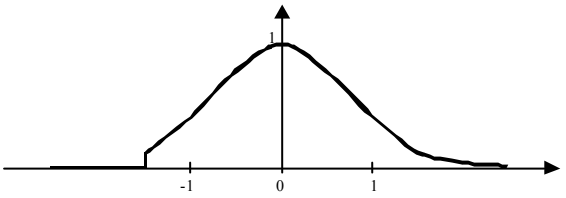

Figure 3 The attraction force as a function of attraction distance. The tail on the left is cut of at a maximum range value to prevent the net to be attracted to points too far away.

The forces are determined for each node as follows:

- Elasticity: an elasticity function is applied to all the connections between the node and its neighbours and the sum is computed. As elasticity function the arctan function is use, hence providing a strongly non-linear force.
- Attraction: an attraction function, see Figure 3**,** is applied to the distance between the node and its corresponding grid point. The force is given a sign such that it always tries to move the node towards the grid point.
- Gravitation: a negative gravitation force.

The start position for the net is set to an elevation below all points in the grid, e.g. one meter below the lowest point. The sign of the final combined force determines if the net should move up or down and the attraction force controls the length of the step. A strong attraction force means a small step; this is to prevent the net to jump past the grid point. In figure 1 one example of using this method is illustrated. Note how the properties of the contour allow the surface to stretch in a steep slope on the sides of the road underpass.

2.2 Classification of Laser Data

After the ground points are classified, the remaining raw-data points can be further classified as vegetation or buildings. Using the maximum height value in each cell, all pixels having an elevation of more than 2 meters above the ground surface are classified. The method is based on texture measures of local differences in height to distinguish artificial surfaces from the natural shape of natural objects (Maas, 1999, Hug 1997). While artificial objects such as buildings consist of continuous, compact surfaces that are bounded by discontinuous edges, natural objects such as vegetation have large vertical variations throughout the objects since the beam can penetrate the canopy of trees.

The measurements used in this method are the second derivative and the maximum slope of each pixel and its eight neighboring pixels. In vegetation, where the height between neighboring pixels varies, the second derivative and slope are larger than within buildings where the change in height of a flat or tiled roof is small. However, the second derivative and the slope are large at edges of buildings and where antennas, chimneys, etc exist. To reduce this noise, the texture measures are median filtered. Based on the two texture measures, each pixel with a height above 2 meters of the ground surface is classified as vegetation and non-vegetation using a maximum likelihood classifier.

Since the texture measures are median filtered, most buildings are correctly classified. Instead some edges of trees are misclassified. To improve the classification result, the smaller areas classified as buildings are checked to see if the area is correctly classified as a smaller building or a part of a tree that is misclassified. The mean value of the second derivative without the median filter and the number of double echoes are calculated for the values inside the boundaries of the areas. Since buildings consist of planar segments, the second derivative is close to zero within the borders of the roofs of buildings. Only at the edges large values occur. In addition, double echoes occur mainly at edges of buildings and in general not within the compact surfaces of roofs. Thus, the mean value of the second derivative and the number of double echoes using only the values inside the borders are small for buildings compared to vegetation. The two mean values are thresholded, and if any of these values are above the threshold, the area is classified as vegetation. Figure 4 shows the classification result over an area of 130x200m.

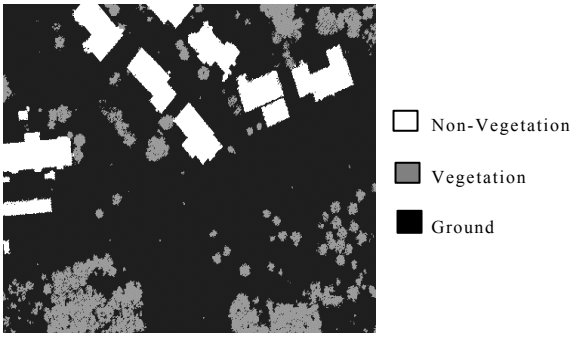

Figure 4. Laser data classification over an area of 130x200m

2.3 Detecting and Estimating attributes of Individual Trees

Using the areas classified as vegetation, individual trees are identified where the position, tree height, and crown diameter of the identified trees are estimated. The method to identify individual trees is based on three steps: 1) create a model of the canopy of trees, 2) smooth the image with different scales, and 3) select the appropriate scale in different parts of the image. The laser beam's ability to penetrate the canopy of trees may result in

large variations in height within single trees making it difficult to separate tree crowns from each other. Thus, first the pulses that have penetrated the canopy are removed to create a model of the outer part of the crowns. To remove the penetrations, the same active contour surface that is used to estimate the ground level is applied from above so that the surface follows the outer part of the crowns, see Figure 5

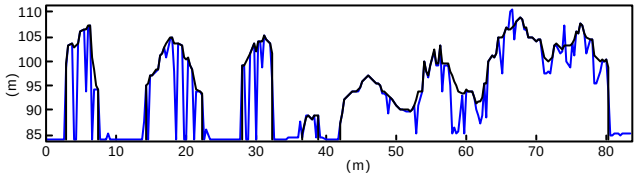

Figure 5 Removing the penetrations in the tree crowns

The process to detect single trees is based on smoothing the image and the location of the trees is estimated by identifying local height maxima. To remove height variations caused by branches within individual tree crowns so each tree has a single height maximum, a certain scale of smoothing should be used depending on the size of the trees. Three different scales are used to smooth the image. The location of the trees is estimated by searching for local height maxima in the smoothed images. Seeds are placed out in every pixel classified as vegetation and let to climb in the direction having the largest slope. When a seed reaches a position where all neighboring pixels have lower values, a local maximum is found. The crown coverage is estimated by grouping those pixels that climbs to the same maximum. The smoothing of the coarsest scale is chosen so that in general no tree has more than one maximum. The finest scale is chosen so that most trees are detected with the effect that some of the larger trees have more than one maximum.

Finally, the segmented areas of trees from the coarser scale are compared with the corresponding area from the finer scale. For cases when the finer scale have detected more than one maximum, the problem is to determine if additional maxima at the finer scale should be judged as separate trees or belong to the treetop detected at the coarser scale. Selection of the appropriate scale in different parts of the image is based on fitting a parabolic surface to the elevation data. Figure 5 shows the crown coverage (a) and the estimated positions of trees marked on the elevation data (b) when a combination of the scales is used.

The height and crown diameter of the detected trees are estimated. For each segment, the maximum height value above the ground surface is chosen as the measure of the tree height. The area of the segments is used to calculate the crown diameter as if the tree crown has the shape of a circle.

A validation of the method has been performed in cooperation with the Swedish University of Agricultural Sciences (SLU). The method was applied to data from at a test site located in southern Sweden where field measurements have been performed. The result shows that most large trees are detected. Most of the undetected trees are hidden trees with a small stem diameter that cannot be seen from above. The mean value of the difference between the estimated position of the detected trees and the field measurements is 0.51 m and the standard deviation is 0.46 m. The height and crown diameter of the detected trees were estimated with a standard error of 0.63 m and 0.61 m, respectively. These results were obtained using an elevation image having a pixel size of 0.33 x 0.33 m.

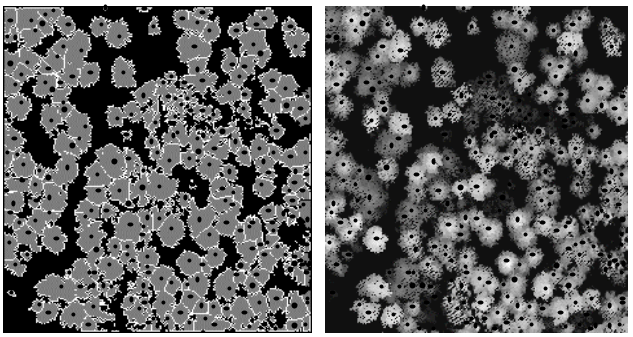

Figure 6. Estimated tree crown coverages and tree positions

2.4 Example of a high-resolution digital terrain model

The methods discussed above have been used for the construction of high-resolution models suitable for real-time 3D visualisation. An example of such a model is shown in Figure 7. This model cover 1 km x 1 km and the ground surface model used has a post spacing of 0.25 m. There are approximately 20 000 trees in the model each having the correct size and position. There are more than 50 buildings which all are reconstructed using a new method which still is under development. In Figure 8 the reconstruction of the seven buildings shown in the upper right corner of Figure 4 is illustrated.

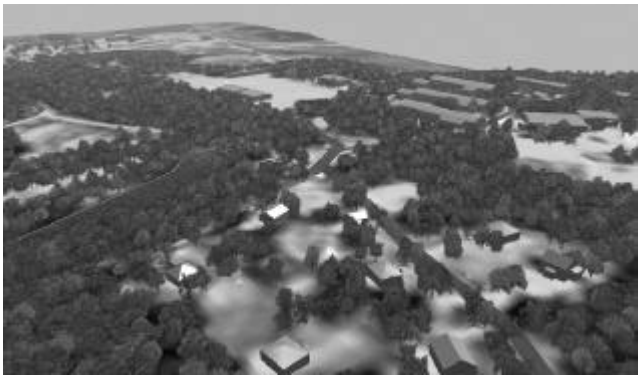

Figure 7. A high-resolution digital terrain model including trees and buildings. Besides the textures all parts of the model are derived from laser scanner data.

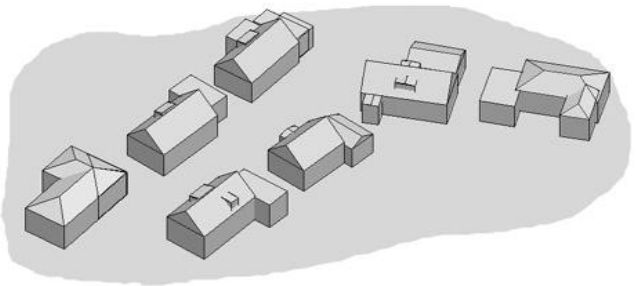

Figure 8. Reconstructed buildings from the area shown in Figure 4

3 TERRAIN ANALYSIS

3.1 Qualitative representation of the terrain in symbolic categories

To represent the terrain qualitatively the surface is partitioned into quadratic *tiles,* with 2 m sides (Lantz, 2000), that will be used as a smallest, atomic modelling element of the terrain. The purpose is to classify the tiles qualitatively into what here is called *categories*. The categories are described in terms of symbolic strings (Chang, 1996, Jungert, 2001). One of the characteristics of this qualitative modelling is that the distinctions made between different modelling elements should be *relevant*, i.e. all distinctive structures should be included without any unnecessary details. Another factor of importance, when distinguishing the characteristics of the categories depends on the uncertainty of the data. It is not appropriate to model distinctions between categories that are too small in relation to the sensor uncertainties. It is also desirable decompose the representation into subgroups that can be accessed independently. Given that a symbolic representation suppresses the unimportant details, this suppression provides data reduction in the sense that the description of the tiles will be more compact. It also reduces complexity as the number of allowed surface forms is reduced. Another advantage is that it enhances the stability of the form interpretation over time, as the distinctions made should be less sensitive to sensor uncertainties.

Which are the relevant distinctions when to query terrain objects, to perform change detection or to visualize? These operations may vary depending on their representation. Therefore, we have chosen to exclude the absolute height of the surfaces, and the magnitude of the inclination of the surface, from our qualitative representation. This does not mean that this information is disregarded; it only means that it is not interpreted qualitatively.

What is an adequate degree of modelling accuracy and what details should be suppressed? This depends on the error tolerance of the application, and on the relation between the size of the modelling elements and the resolution of the original surface. The latter determines the possible change within the tiles and thus how much structure the elements must be able to represent. A simple representation would be to approximate every square with a single plane with some inclination. This is clearly very restrictive, but even with this approximation some properties can be determined, i.e. the plane is totally determined by its normal vector which, for instance, can be split into projections along the z-axis and the xy-plane and qualitatively interpreted.

A slightly more complex approach, which allows considerably more information to be modelled, is to allow the tiles to be to be approximated by two planes. A set of restrictions, when combining the two planes, has been introduced to keep the number of categories at a manageable level. The first restriction is to allow just two types of planes, *flat* or *inclined* (although they will be to inclined in different directions). As have been mentioned, the sensor inaccuracies make it unwise to model too small height differences. Here we have chosen to ignore differences below a given threshold and tiles with less height are thus considered flat. To make qualitative distinctions between different magnitudes of inclinations is difficult. For instance, determining if a vehicle can pass a tile with a certain inclination may be difficult. E.g., a "large inclination" depends on the capacity of that vehicle. Thus, we are left with the distinctions between tiles that are flat and those that have an inclination. Another restriction on the combination of the two planes is that just categories where the edge formed by the intersection of the planes parallel to the xy-plane will be considered. These forms are by no means obvious, but after some considerations the forms described in figure 1 becomes appropriate. Other allowed forms combine planes where one of the planes is flat and cases where the inclinations of the two planes are in opposite directions. Apart from these forms and the flat category, categories with a single inclined plane will also be allowed.

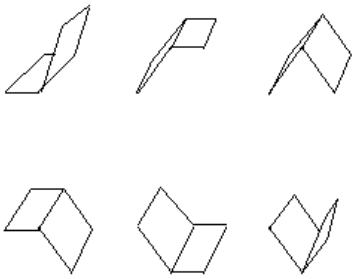

Figure 9. Basic category forms.

After this level of reduction have been reached we still have to qualitatively interpret the different ways to divide the tiles into two planes to decompose a full category description into sub indicators, that can be described in terms of symbolic strings. Of concern is to let all tiles with certain *distinct* divisions between separate planes belong to different categories. In order to determine which divisions that should be considered the tiles are split into subparts, i.e. the *corners*, the *edges* and the *interior,* as seen in Figure 10. Every division that has a start or end-point within different subparts (not considering the interior) are defined as a distinct division. Consequently, all tiles with a start point or an end point within different tile parts belong to different categories. The motivation for this division is its generality and its independence of the maximum resolution of the tile.

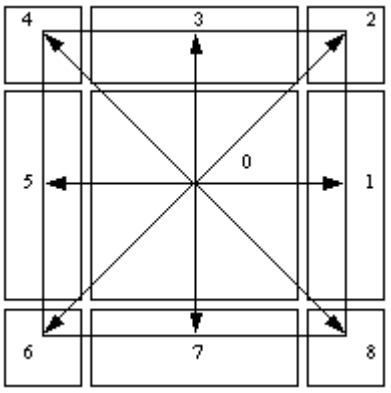

Figure 10. The sub-parts of a tile, their integer encoding and the allowed inclination directions.

As a final restriction to our representation the number of *inclination directions* allowed in a category should be restricted as well. The inclination direction is the projection of the maximal, positive tangent vector of the plane to the xy-plane. All allowed inclination directions can be seen in Figure 10. In some cases, the inclination direction is totally determined by the division of the two planes, while others are ambiguous. In all cases, but for categories determined by a single plane, there are some constraints. However, only one inclination direction for each category will be allowed. The inclination direction closest to the average inclination direction of all possible alternatives will be chosen as a representative direction. Finally, there is another type of category allowed that is not a combination of two planes. These are categories with extreme points. The reason for allowing them is that they are quite common terrain features and they will be difficult to approximate by two planes. In this case, consider two categories as different if they have extreme point in different subparts including the interior part as well. Categories with extreme points in the corners will not be accepted, as that shape is similar to the category with an edge between the borders and with the corner as a common point.

The number of categories can be calculated as follows: there are 16 ways of dividing a tile into distinct planes. Each of these has 6 possible combinations of inclined or flat planes, see Figure 9, which gives 16*6=96 categories. Adding to this is the categories with no feature, which are 9, and those with extreme points, which are 10; giving a total of 115 different categories.

3.2 Category determination and data reduction

The determination of category membership and which grid points to store for visualization and quantitative analysis can be made in many ways. This will not be discussed in this paper as it is subject to ongoing research. However, a method for categorization that is somewhat slow and primarily intended for validation, creates first a canonical representation for each category. For the categories with edges starting and ending in corner points, there is only one choice, but for all others there are more than one candidate. The number of candidates depends on the number of grid points in each category. A natural choice in this case is to use the point in the middle of each sub-part. When a canonical representation has been selected for a tile, we must transform it into a representation that allows comparison with other tiles. Note that all that is required is to find a value for a category in each grid point of the original surface. A suitable representation is then to form a sub grid (matrix) for each category. Apart from the flat category, the categories are independent of both absolute height and relative height. We can consequently choose any values, as long as they form a sampling of the plane that the grid point belongs to. The points in the canonical representations have been given canonical values. Thus the maximal value of every category is set to 1 and the minimal to 0. Then we can transform the height values in each tile to the same value range, using the minimal height and the height difference in every tile to compare with each category. Using some distance measures, for instance the L^1 norm, the comparison can be carried out simply. The result of this process can be seen as the actual *definition* of what it means to a tile to belong to a certain category. The method to determine which points to keep for visualization can also vary. Here we have chosen to keep any point that is a part of the feature, along with the corner points. Thus, there is an a priori, lower bound on the reduction determined by the four corner points, which are absolutely necessary in order to visualize a tile.

3.3 The terrain database structure

The terrain structure with its different categories is basically a grid structure completed with some irregular points. However, the main purpose of this structure is to develop a query structure that can be used for determination of different terrain features and objects represented in 3D the structure must allow objects of different size to be found. That is, small objects like ditches and large objects like canyons must be possible to find. To accomplish this, the terrain structure must be represented in different scales and the method chosen here can be seen as a generalization in 3D of the resolution pyramid [4]. The chosen grid sizes are, beside the original 2m grid, 4, 8 and 16 meters.

The terrain database must efficiently mirror the multi resolution pyramid structure permitting a formal symbolic description of the surface model at all the different resolution levels. The primary purpose of the database structure is to allow access of the symbolic categories, for operations like change detection; given two versions of the same area registered at different times, and for determination of terrain features of special interest. The latter should be determined by means of filters describing the objects; an example of such an object is a ditch. Efficient triangulation of the terrain for visualization purposes should also be possible. Consequently, the terrain data set must include information corresponding to all resolution levels with all the categories as well as their coordinate points and their elevation values. This data set can logically be described in the following terms:

x_g, y_g {the coordinates of the lower left corner of a grid area}
z_g {the elevation of the lower left corner of a grid area}
c_2, c_4, c_8, c_{16} {the category indicators of the different resolution levels}
$x_{2e1}, y_{2e1}, z_{2e1} \ldots x_{2ei}, y_{2ei}, z_{2ei}$ {The supplementary data points of the grid areas at the 2m resolution level including their altitude levels.}
$x_{4e1}, y_{4e1}, z_{4e1} \ldots x_{4ej}, y_{4ej}, z_{4ej}$ {The supplementary data points of the grid area at the 4m resolution level including their altitude values.}
$x_{8e1}, y_{8e1}, z_{8e1} \ldots x_{8ek}, y_{8ek}, z_{8ek}$ {The supplementary data points of the grid area at the 8m resolution level including their altitude values.}
$x_{16e1}, y_{16e1}, z_{16e1} \ldots x_{16el}, y_{16el}, z_{16el}$ {The supplementary data points of the grid area at the 16m resolution level including their altitude values.}

The category indicators of the different resolution levels can be split up with respect to the sub-indicators describing a category, i.e. *inclination, feature* and *orientation*. The complete category value of a grid area is a compound of these sub-indicators.

Given the information above an efficient terrain database structure that corresponds to a single flat file structure can be determined that contains all the coordinate points and their altitude for all resolution levels. Unfortunately, the category indicators cannot be stored in this structure without causing redundancy in the database. The terrain database can thus, due to its simple structure, be accessed e.g. trough a B-tree. However, to allow access of the data points of certain resolution level, the data points of the various resolution levels must be possible to distinguish. This can be accomplished by introducing a variable (*n*) that indicates the resolution level(s) of a certain data point. Since many points belong to more than one level, *n* must have a value that is simple to decode. The solution to this problem is to use a four bit binary structure. Once all the data points of a certain resolution level have been accessed they have to be sorted with respect to their grid area membership. This is a fairly simple operation since it only requires ordering of the points with respect to their grid interval in the x- and y-directions.

The category of a grid area is possible to determine for each resolution level by accessing a simple file where the key elements are the x- and y-coordinates of the lower left corner of the grid area are stored. Considering all these aspects the resulting database structure can thus be described as:

Tdb: x, y, z, n {The terrain database}
C_2DB: x_g, y_g, c_2 {the category database for 2 m grids}
C_4DB: x_g, y_g, c_4 {the category database for 4 m grids}
C_8DB: x_g, y_g, c_8 {the category database for 8 m grids}
$C_{16}DB$: x_g, y_g, c_{16} {the category database for 16 m grids}

The terrain data is also subject to various research efforts for which a number of applications are in focus. Two main applications can, beside visualization of a triangulated terrain model, be identified. These two applications are *determination of terrain features* and *detection of spatial changes over time*. The principles of these applications will be discussed. Besides this design of a query language [2] concerned with other sensor data types as well and where sensor data fusion will play a fundamental role is also going on. Access of all occurring data points, their elevation and their category types for the 2m grid can be made as follows:

$(x_{\text{lower-boundary}}, y_{\text{lower-boundary}}, x_{\text{upper-boundary}}, y_{\text{upper-boundary}}) \Rightarrow$
$\{x_g, y_g\} \Rightarrow C_2DB \Rightarrow \{x_g, y_g, c_2, n\}$
$\{x_g, y_g\} \Rightarrow$ Tdb $\Rightarrow$ {x,y,z-coordinates}
$\Rightarrow$ /triangulate and visualize /

The main operation here is obviously to access a specified area for triangulation and visualization.

Queries for the determination of different object types can basically be described in two steps. In the first step, the grid size most suitable for the requested objects is determined. In the second step object filters that describe these terrain objects or features are matched against the actual sequence of grid area categories of the area of interest (AOI). The most suitable resolution level of the resolution pyramid depends on the size of the objects and may, e.g. for ditches correspond to the 2m grid, whereas for large objects the 16m grid is better. Logically, this matching or filtering process can be described in the following high-level terms:

$(x_{\text{lower-boundary}}, y_{\text{lower-boundary}}, x_{\text{upper-boundary}}, y_{\text{upper-boundary}}) \Rightarrow$
$\{x_g, y_g\} \Rightarrow C_jDB \Rightarrow$
$\{x_g, y_g, c_j, n\}$ where $j \in \{2, 4, 8, 16\}$
$\text{Match}(\{c_j\}_{\text{feature-filter}}, \{x_g, y_g, c_j\}) \Rightarrow$
$\{x'_g, y'_g\}_{\text{succesful-match}}$

The goal here is to determine the object type filters more or less automatically from a type of formal description, which can be integrated into the query language.

Change detection means that changes of an area made over a period in time should be determined. The principle is to compare the category types of the two versions of the area against each other to determine existing changes, register their positions and eventually determine the types of changes that have occurred. For example, has a wall been built since the last registration. This can be determined by means of the filter technique at the position of change in both the generations of data. This access structure can be described as:

$(x_{\text{lower-boundary}}, y_{\text{lower-boundary}}, x_{\text{upper-boundary}}, y_{\text{upper-boundary}}) \Rightarrow$
$\{x_g, y_g\}_{\text{version-1}} \Rightarrow C_jDB \Rightarrow \{x_g, y_g, c_j, n\}_{\text{version-1}}$
where $j \in \{2, 4, 8, 16\}$
$(x_{\text{lower-boundary}}, y_{\text{lower-boundary}}, x_{\text{upper-boundary}}, y_{\text{upper-boundary}}) \Rightarrow$
$\{x_g, y_g\}_{\text{version-2}} \Rightarrow C_jDB \Rightarrow \{x_g, y_g, c_j\}_{\text{version-2}}$ where $j \in \{2, 4, 8, 16\}$
$\text{Comp}(\{x_g, y_g, c_j\}_{\text{version-1}}, \{x_g, y_g, c_j\}_{\text{version-2}}) \Rightarrow \{x'_g, y'_g\}_{\text{changed}}$

This type of matching can be made on all levels of of resolution.

4 CONCLUSIONS

In this paper methods supporting automatic construction of 3D digital terrain models - ground surface modelling and detection and measurement of individual trees - and terrain analysis have been dicussed.

A new method for modelling of the ground surface based on active contours has been presented. This method works well and is robust and creates a continuous model of the ground surface. For classification of ground points and also the remaining data points with respect to vegetation and non-vegetation a recently developed segmentation and classification method have been presented. It has been tested on several types of areas and the result is promising. A novel method for identification of individual trees and tree attribute estimation has also been presented. This method has recently been validated using field measurements and the result is very promising.

The terrain database structure described in the context of terrain analysis is basically concerned with three aspects, i.e. (1) triangulation and visualization, (2) determination of object/terrain features and (3) change detection. Of these three the first one is trivial while the two others are more complex and for this reason they are subject to further research. Furthermore, they are also based on a process of matching of elements described in terms of symbolic 3D surface categories. The advantage of this approach is that a very simple operation including very simple comparisons has been achieved. The results of these research activities are promising and especially in querying the outcome are very interesting.

REFERENCES

[Axelsson, 1999] Axelsson, P., 1999, Processing of laser scanner data – algorithms and applications, ISPRS Journal of Photogrammetry & Remote Sensing 54 (2).

[Ballard, 1982] D. H. Ballard and C. M. Brown, 1982, Computer Vision, Prentice Ha1l, pp 106-111.

[Chang, 2000] S.-K. Chang, G. Costagliola, E. Jungert, 2000, Spatial/Temporal Query Processing for Information Fusion Applications, In Advances in Visual Information Systems, R. Laurini (Ed.), Springer Verlag, Berlin, pp 127-139.

[Chang, 1996] S.-K. Chang and E.Jungert, 1996, Symbolic Projection for Image Information Retrieval and Spatial Reasoning, Academic Press, London, U.K.

[Cohen and Cohen, 1993] Cohen L. D. and I. Cohen 1993. Finite Element Methods for Active Contour Models and balloons for 2D and 3D Images. IEEE Transaction on Pattern Analysis and Machine Intelligence, PAMI-15.

[Elmqvist, 2001] Elmqvist, M., 2001, Ground Estimation of Laser Radar Data using Active Shape Models. Presented at the OEEPE workshop on Airborne Laserscanning and Interferometric SAR for Detailed Digital Elevation Models, Stockholm, Sweden.

[Hug, 1997] Hug, C., 1997, Extracting artificial surface objects from airborne laser scanner data, In A. Gruen, E.P. Baltsavias, O. Henricson, eds, Automatic Extraction of Man-Made Objects from Aerial and Space Images (II), Birkhäuser Verlag, Basel,

[Hyyppä et al, 2000] Hyyppä J., U. Pyysalo, H. Hyyppä, and A. Samberg 2000. Elevation accuracy of laser scanning-derived digital terrain and target models in forest environment. In Proceedings of the 4th EARSeL workshop on LIDAR Remote Sensing of Land and Sea, Dresden,Germany.

[Hyyppä et al, 2001] Hyyppä J., O. Kelle, M. Lehikoinen, and M. Inkinen 2001. A Segmentation-Based Method to Retrieve Stem Volume Estimates from 3-D Tree Height Models Produced by Laser Scanners. IEEE Transaction on Geoscience and Remote Sensing, Vol. 39, No. 5, May 2001, pp 969-975.

[Jungert, 2001] E. Jungert and F. Lantz, 2001, Symbolic Tile CategorieResolution, In Multimedia Databases and Image Communication, M. Tucci (Ed.), Springer Verlag, Berlin, pp 140-151.

[Kass et al, 1998] Kass M., A. Witkin, and D. Terzopoulos 1998. Snakes: active contour models. Int. J. of Computer Vision, 1:321-331.

[Kraus and Pfeifer 1998] Kraus, K., and N. Pfeifer, 1998, Determination of terrain models in wooded areas with airborne scanner data, ISPRS Journal of Photogrammetry and Remote Sens, 53.

[Lantz, 2000] F. Lantz and E. Jungert, 2000, Dual Aspects of of a Mult-Resolution Grid-Based Terrain Data Model with Supplementary Irregular Data Points, Proceedings of the 3rd Int. Conf. on Information fusion, Paris, July 0-13.

[Pfeifer et al, 1999] Pfeifer, N., T. Reiter, C. Briese, and W. Rieger, 1999, Interpolation of high quality ground models from laser scanner data in forested areas in Proceeding of the ISPRS III workshop on Mapping surface structure and topography by airborne and spaceborne lasers, La Jolla, CA.

AIRBORNE LASER SCANNING: CLUSTERING IN RAW DATA

Marco Roggero
Department of Georesource and Territory
Politecnico di Torino
Italy
roggero@atlantic.polito.it

Commission III, Working Group 3

KEY WORDS: Laser Scanning, clustering, DTM extraction, entity extraction.

ABSTRACT

We implemented a strategy for terrain, vegetation and building detection, based on laser range data only. The result was obtained by working on raw data, so we were able to take advantage of the full resolution potential of laser scanning. The detection of objects was performed in two stages: first, elevated objects and ground are separated, and then the objects are classified as vegetation or buildings. Work is still in progress, about the extraction and classification of entities. A comparative analysis of the first pulse, the last pulse and intensity data can improve the result of clustering.
Results obtained in different environments with one-meter grid laser data are shown; we have tested the algorithm on city areas, countryside, river bed, landslides, mountains and wooded terrain.

1 INTRODUCTION

Laser scanning, provides high detailed Digital Surface Models, and we are able to extract a lot of information with very simple tecniques. A gridded network model is well suited for storage in a matrix and subsequently is well organized for simple computer algorithms. For example, a matrix can be represented as a raster, and we can use image processing tecniques to extract information. However, the nodes of the gridded network have to be constructed by interpolation in the original data set. Consequently some of the information will be lost. To take advantage of the full resolution potential of laser scanning, we must work on raw data, representing them, for example, by using irregular triangular or tetrahedral networks. Triangular models have been used in terrain modelling since the 1970s. However, because of limitations of computers and the complexity of TIN data structures, gridded models were preferred to triangular models.
We implemented a strategy to classify raw data using a simple data base structure, based on gridded networks. This strategy simplifies classification algorithms. Data base structure allows direct access to data; the algorithm assigns a flag and a cluster code to all the raw data, and this information is stored in the database. Then, the classified raw data can be represented as a triangular network. Detection of clusters in raw data is performed in two stages: first, elevated objects and ground are separated, and then the objects are classified as vegetation or buildings. The first stage is based on a local minimum criterion, which excludes elevated points from analysis. Then all the points within some distance of the estimated ground surface are classified as ground points. Ground evaluation is refined in two iterations. In the second stage the algorithm classifies non ground points as vegetation or buildings with a variance criterion.

2 TERRAIN EXTRACTION

The algorithm that extracts ground points from raw data, operates as a filter, applying a local operator to all the elements of the gridded network. The target of the first stage, is to obtain a rough approximation of the DTM, excluding elevated points. Algorithm calculates the minimum height in the local operator, then assigns points to the ground if their heights are compatible with a local slope; this idea is refined in the local regression criterion, that also considers the variance of the local data set. Then, the algorithm calculates height value in the center of the operator; this value is the weighted mean of the ground point heights in the operator. Weights depends on the distance from the operator center, normalized with Gauss distribution. Maximum building size affects local operator size.
In the second stage, the algorithm uses a threshold criterion to classify points as ground or non ground. Output of this classification is stored in the database. Finally the algorithm recalculates the DTM as the wheighted mean of ground points only.
These steps are repeated once. In the second iteration, to refine the classification, all the parameters (size of local operator, local slope, coefficients of variance propagation and threshold value) are more restrictive.

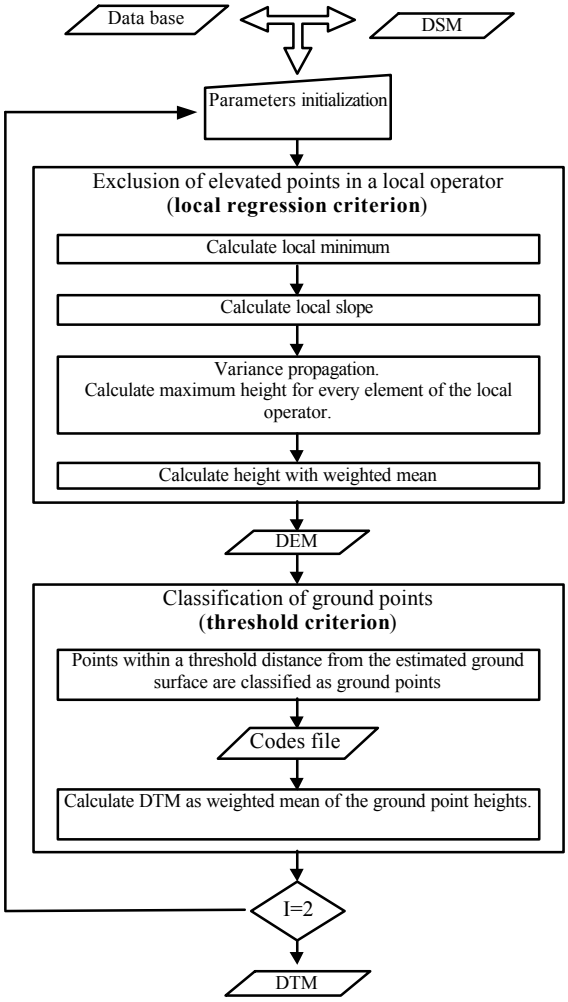

Figure 1: Algorithm flow chart.

Classification criteria

Local regression criterion. A criterion to detect ground points can be defined as a function of the maximum height difference between two points p_i and p_j in the local operator (A):

$$DTM = \left\{ p_i \in A \middle| \forall p_j \in A : h_{p_i} - h_{p_j} \le \Delta h_{\max}\left(d\left(p_i, p_j\right)\right) \right\} \quad [1.]$$

where d is the planimetric distance [Vosselmann, 2000]. We have used this criterion, studing relations between maximum height difference and points distance. We can sort points by their planimetric distance from the local minimum p_{min}. To extimate a local slope, we calculate the parameters of the linear regression of the sorted data set

$$(x, y) = \left(d\left(p_i, p_{\min}\right), \left(h_i - h_{\min}\right)\right). \quad [2.]$$

This extimate assumes that points far from minimum affect the local slope less; so data are weighted with the factor $1/\sqrt[4]{d^2 + \Delta h^2}$:

$$(x, y) = \left(d\left(p_i, p_{\min}\right)/\sqrt[4]{d^2 + \Delta h^2}, \left(h_i - h_{\min}\right)/\sqrt[4]{d^2 + \Delta h^2}\right) \quad [3.]$$

Linear regression of this population provides the parameters a (intercept), b (gradient), $s^2{}_a$ (standard deviation) and $s^2{}_b$ (gradient standard deviation). Parameters a and b and the propagation of their variance, define the local regression criterion, which links Dh_{max} to the distance d:

$$\Delta h_{\max} = a + k_a^2 \cdot s_a^2 + b \cdot d + k_b^2 \cdot d^2 \cdot s_b^2 . \quad [4.]$$

The parameters $k^2{}_a$ and $k^2{}_b$ depends on terrain typology, so their calibration is very important. Indicative values are $k^2{}_a=5$ and $k^2{}_b=0.005$.

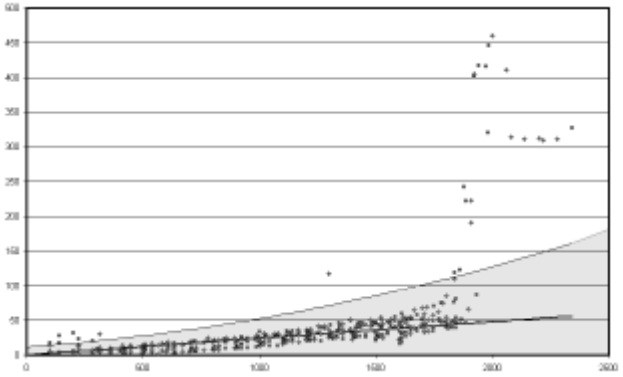

Figure 2: Linear weighted regression. Points in the grayed area are used to calculate the DTM.

Threshold criterion. The algorithm, after the computation of first approximation DTM on the basis of local regression criterion, classify raw data by vertical distance from the DTM. We define two threshold values, k_1 and k_2 (with $k_1<k_2$); the following contitions explains the classification criterion:

$h_i - h_{\min} < k_1/\cos b$ ground points

$h_i - h_{\min} > k_2/\cos b$ non ground points

$k_1/\cos b \le h_i - h_{\min} \le k_2/\cos b$ non classified points

Between k_1 and k_2, the algorithm is not able to classify points as ground or non ground. To restrict classification errors in zones with high slopes, threshold values are not constant, but depend on gradient.

3 CLASSIFICATION OF VEGETATION AND BUILDINGS

For many applications we need to detect the characteristics of scanned objects. This detection may be fully automatic. At first, classification of vegetation and buildings is very important. These two classes of objects are characterized by different values of variance in their spatial distribution, so we can use this parameter to extract vegetation and buildings from laser range data.

Fitting a local plane. Classifying the point $P(x_j,y_j,z_j)$, we consider it in relation to the N points $Q_i(x_i,y_i,z_i)$ with i=1,N, that satisfay the following condition:

$$d\left(P, Q_i\right) \le r \quad [5.]$$

where $r \in \Re$ is a parameter depending on sampling density, and $d\left(P, Q_i\right)$ is the euclidean distance

$$d(P, Q_i) = \sqrt{\left(x_P - x_{Q_i}\right)^2 + \left(y_P - y_{Q_i}\right)^2 + \left(z_P - z_{Q_i}\right)^2} . \quad [6.]$$

To fit the points Q_i and the central point P with a local plane, their distance from the plane ax+by+cz =d has been minimized. The correction to the i-th point is:

$$v_i = z_i - \left(\frac{a}{c} x_i + \frac{b}{c} y_i - \frac{d}{c}\right). \quad [7.]$$

Its variance is

$$s^2_{v_i} = \frac{a^2}{c^2} s^2_{x_i} + \frac{b^2}{c^2} s^2_{y_i} + c^2 s^2_{z_i} \quad [8.]$$

The following function must be minimized:

$$c^2(a,b,c,d) = \sum_{i=1}^{N} \frac{v_i^2}{s_{n_i}^2} = \sum_{i=1}^{N} \frac{(ax_i + by_i + cz_i + d)^2}{as_{x_i}^2 + bs_{y_i}^2 + cs_{z_i}^2} \qquad [9.]$$

Variance criterion. In any 3D point distribution we can always fitting a local plane, if we have at least three points. But this plane may be or not be significant. We can accept or reject the hypothesis that the local plane is significant, by χ^2 test on the four parameters a, b, c and d, or on any single parameter.
Then, Student's t test applied to normalized residuals tell us if the central point fits the local plane.
So, we can observe the following conditions:

1 The local plane exist, and the central point P fit the plane.
2 The local plane exist, but the central point don't fit the plane.
3 The local plane don't exist.

Classifying objects with this criterion, we can assume that in the case 1 the point belong to a building, or to another artificial structure, in the case 2 the point is an outlier, and in the case 3 belong to the vegetation.

Raw data classification. We have performed two different classifications in raw data, using local regression and threshold criteria, and using variance criterion. Now we can join the output of these two classifications, associating a decision to every couple of results. For example, if a point is classified as non ground by local regression and threshold criteria, and moreover fit a local plane, we can decide to assign it to a building. The decisions are described in table 1.

Output of local regression and threshold criteria	Output of variance criterion	Combination of criteria
Non ground	Fit the local plane	Building
	Don't fit the local plane	Outlier
	Don't exist a local plane	Vegetation
	Isolated point	Outlier
Not classified	Fit the local plane	Ground
	Don't fit the local plane	Outlier
	Don't exist a local plane	Vegetation
	Isolated point	Outlier
Ground	Fit the local plane	Ground
	Don't fit the local plane	Outlier
	Don't exist a local plane	Rough ground
	Isolated point	Ground

Table 1 – Decisions associated to every combination of classification results.

4 TESTS

We obtained DTMs in zones with very different morphology. The algorithm was tested in built-up areas, countryside, river beds, landslides, mountains and wooded areas. We performed tests on four data sets, acquired with three different scanning systems and in different sampling modes. So, the algorithm was tested in a large range of situations and applications.

TopoSys data set on Pavia town. Historical city of Pavia is a hard test area for every classification algorithm. Narrow streets and complex buildings alternate with parks and gardens, and vegetation is often close to buildings. Other sources of noise are car parks!
Table 4 report tests results. Tests 1 and 2 concerning flight T1 were performed on the same zone of Pavia city with different parameters. In this area there are no steep slopes, and the more restrictive parameters used in test 2 gave best results. Area used in test 3 has steep slopes near the castle; so we used less restrictive parameters that those used in test 1.

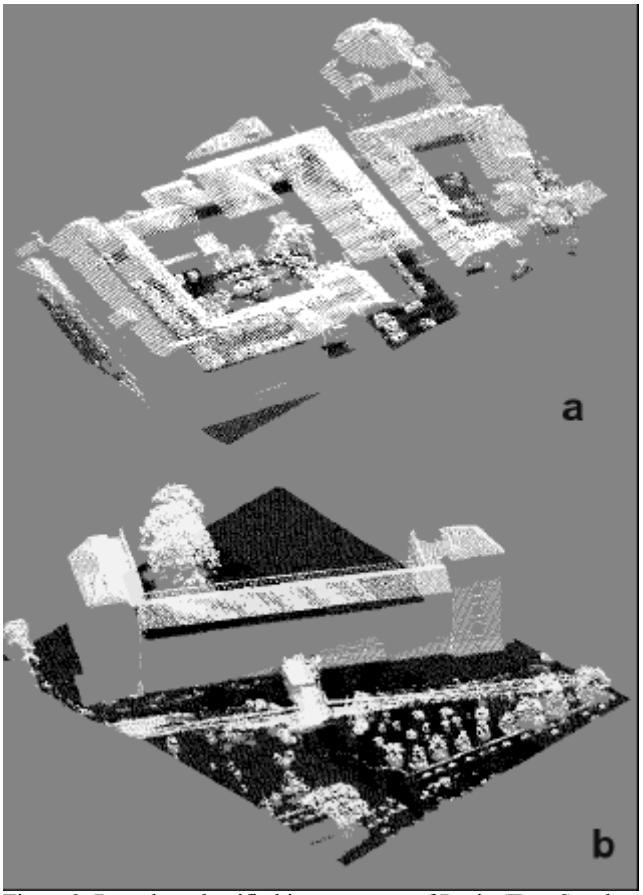

Figure 3: Raw data classified in two zones of Pavia (TopoSys data set). a) Pavia city, ground is correctly classified; here we have performed test 1 and 2. b) Castle, there are some errors in ground classification near castle moat; this is the area of test 3.

TopoSys data set on Corniglio landslide. Test zone is mountainous and densely wooded. DTM extraction is very difficult, also because we have first pulse data only. Wooded areas are very vaste, so operator size must be greater than in other cases. In tests we used a size of 41 m, but this size was not sufficient.

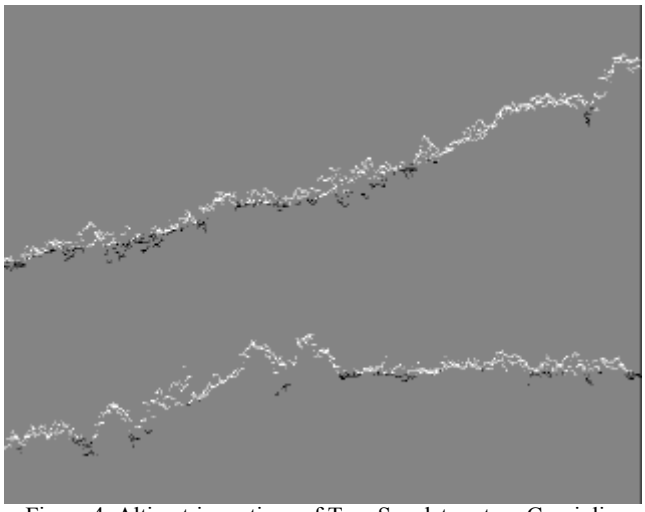

Figure 4: Altimetric sections of TopoSys data set on Corniglio landslide. Points classified as ground are in black, as non ground in white.

TopEye data set. This data set is very simple to process. Scanning system has sampled last pulse and first puls together, on a poorly wooded area. Besides, last pulse measurements has a good penetration of vegetal canopy, and give a regular representation of ground. These good conditions permit to calculate DTM classifying, in every knot of regular network, height measurements respect to median $\breve{m}$. We define DTM as:

$$DTM = \{\overline{p}_i \in A : (\breve{m} - R) \le p_i \le (\breve{m} - r)\} \quad [10.]$$

if $(\breve{m} - R, \breve{m} - r)$ is not empty

$$DTM = \{\overline{p}_i \in A : (\breve{m} - r) \le p_i \le (\breve{m} + r)\} \quad [11.]$$

if $(\breve{m} - R, \breve{m} - r)$ is empty

where r and R are two threshold values.

We have calculated DTM with the iterative algorithm too. The data set describes the ground without gaps, so the algorithm doesn't need very large operator size. Variance propagation parameters instead, need greater than average values; this is due to steep slopes ground in many zones.

The difference between the two DTMs is a few centimeters, but it is greater on slopy ground.

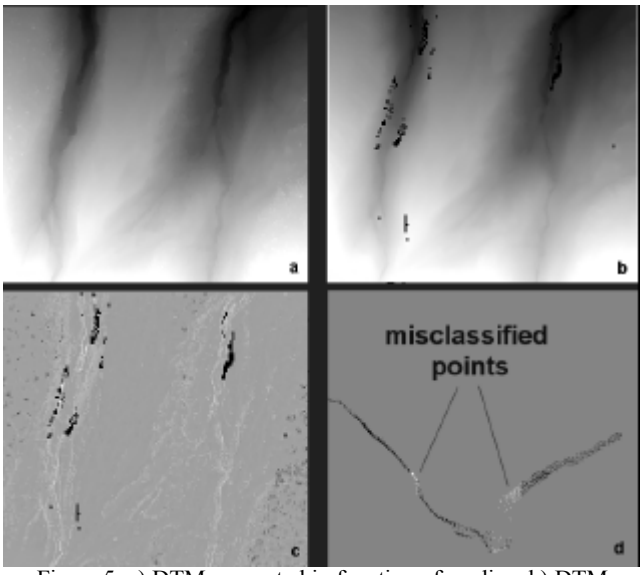

Figure 5: a) DTM computed in function of median. b) DTM calculated with iterative refinements. The zones in which the algorithm is not able to classify ground points are in black; these zones are vertical o sub-vertical ground. c) Difference between the two DTMs has an average of 7 cm and an RMS of 20 cm. d) Misclassified points.

The algorithm is not able to classify ground points correctly, if slope is vertical or sub-vertical, as you can see in figure 5d. This error has been limited by using threshold value function of slope (see threshold criterion). In the Bracigliano test area, misclassified points are 1% of total; this value may increase in mountainous areas with very uneven terrain.

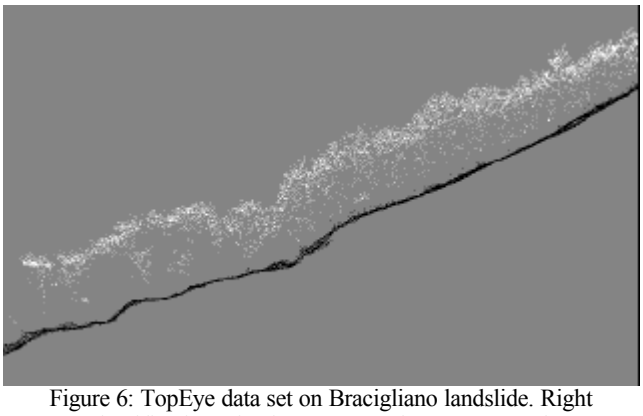

Figure 6: TopEye data set on Bracigliano landslide. Right classification of points as ground or non ground.

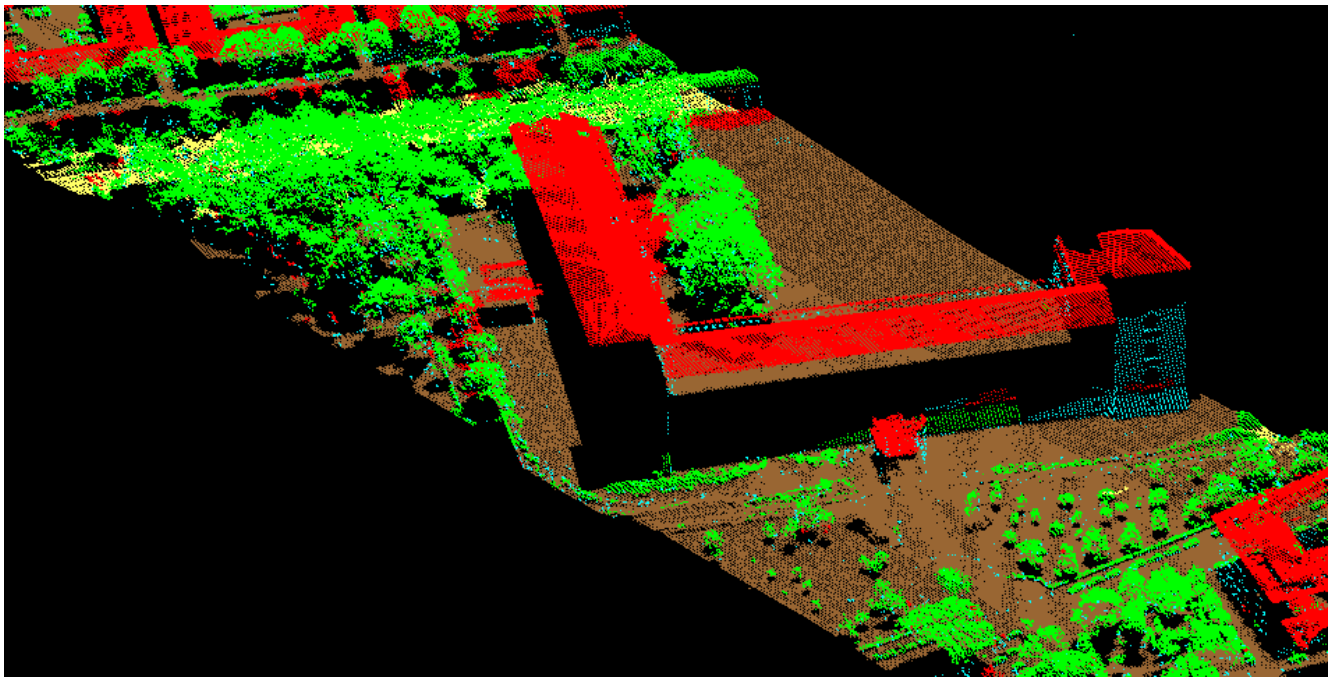

Figure 7 – Test on Pavia town, the castle (• ground, • rough ground, • vegetation, • buildings, • outliers).

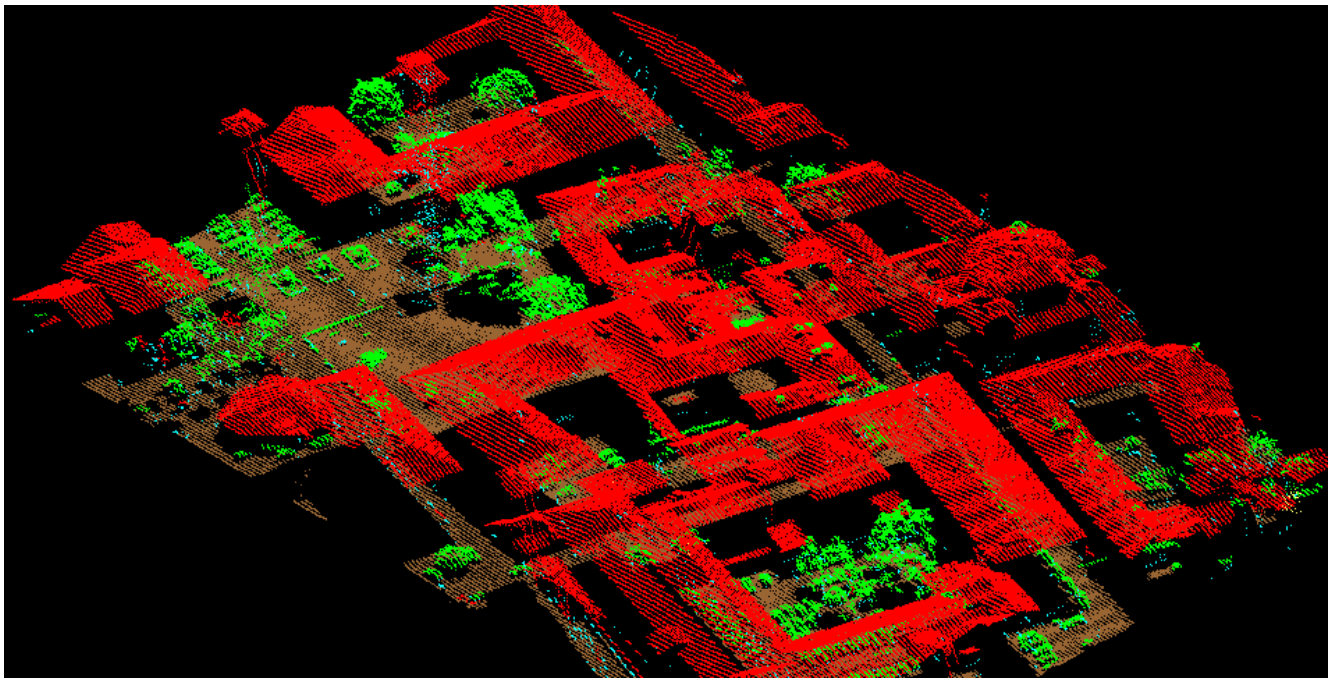

Figure 8 - Test on Pavia town, the medieval towers and the old city (• ground, • rough ground, • vegetation, • buildings, • outliers).

System	Fly zone	Fly	Frequence [kHz]	Height [m]	Sampling density [punti/m^2]	Acquisition
TopoSys	Pavia town: historic city, countryside, industrial area, Ticino river.	T1	80	400	11,6	L.P.
		T2	80	850	5,5	L.P.
		T3	80	850	5,5	F.P.
TopoSys	Corniglio landslide: mountain area; densly wooded area.	T4	80	300 ÷ 900	5 ÷ 13	L.P.
Optech	Pavia town: historic city, countryside, industrial area, Ticino river.	O1	10	600	1,0	F.P. & L.P.
		O2	10	650	0,4	F.P. & L.P.
		O3	10	500	2,8	F.P. & L.P.
TopEye	Bracigliano landslide: mountain area; wooded area.	E1		100 ÷ 200	17	F.P. & L.P.

Table 2: Data sets used in tests.

System	Fly	Test	First iteration parameters				Second iteration parameters				
			Operator size	Regression		Threshold	Operator size	Regression		Threshold	
			O	ka	kb	k1	O	ka	kb	k1	k2
TopoSys	T1	1	41·41	10	0,01	100	11·11	5	0,005	50	100
	T1	2	41·41	5	0,005	50	11·11	2	0,002	25	50
	T1	3	41·41	5	0,005	50	11·11	2	0,002	25	50
TopoSys	T4	1	41·41	20	0,02	200	11·11	10	0,01	100	200
		2	41·41	10	0,01	100	11·11	5	0,005	50	100
TopEye	E1	1	11·11	20	0,02	200	5·5	10	0,01	100	200

Table 3: Parameters values assumed in tests.

System	Fly	Test	Classified points [%]			Misclassified points [%]			Not classified points
			Ground	Vegetation	Buildings	Ground	Vegetation	Buildings	
TopoSys	T1	1	29,9	67,7		0,0	1,6		2,4
		2	27,0	71,9		0,0	0,0		1,1
		3	48,0	49,2		0,0	5,4		2,8
TopoSys	T4	1	41,4	43,9	-	~30	0,0	-	14,8
		2	17,8	75,8	-	~7	0,0	-	6,3
TopEye	E1	1	88,6	10,4	-	0,0	1,0	-	0,9
Values in this table are indicative, because referred to test areas, not to total fly.									

Table 4: Sintetic results of tests.

5 CONCLUSIONS

The most important result of the tests is that the algorithm we have proposed is very sensitive to the parameters. This fact has a negative influx on algorithm output. But algorithm has classified points successfully, if parameters were well calibrated. Safely algorithm require parameter calibration on test areas, before proceeding to whole data set processing. A comparison with other algorithms will be very useful.

We used results obtained in this study as auxiliary knowledge for data segmentation.

Algorithm is implemented in DSM_Laser software.

REFERENCES

[Agrawal, 1998] R. Agrawal, J. Gehrke, D. Gunopulos, P. Raghavan, 1998. Automatic subspace clustering of high dimensional data for data mining applications, San Jose, CA.

[Barbarella, 2001] M. Barbarella, C. Fazio, 2001. Surveying of zones at risk of landslide by laser scanning. In: OEEPE Workshop on Airborne Laser Scanning and Interferometric SAR, Stockholm.

[Forlani, 2001] G. Forlani, C. Nardinocchi, 2001. Detection and segmentation of building roofs from LIDAR data. In: Workshop on 3D Digital Imaging and Modeling, Padova.

[Roggero, 2001] M. Roggero, 2001. Dense DTM from laser scanner data. In: OEEPE Workshop on Airborne Laser Scanning and Interferometric SAR, Stockholm.

[Vosselmann, 2000] G. Vosselmann, 2000. Slope based filtering of laser altimetry data. In: International Archives of Photogrammetry and Remote Sensing, Vol. XXXIII, Amsterdam.

Land Surface Mapping and Characterization Using Laser Altimetry

PROGRAM: MONDAY 22nd OCTOBER 2001

8:00 – 9:00 **Registration** (Governor Calvert House Conference Center, Historic Inns of Annapolis)
9:00 **Welcome note**

9:15 – 12:10 SESSION 1: System Overviews
Chair: J. Bryan Blair (NASA/Goddard Space Flight Center, USA)

9:15 – 9:45 **Lidar Activities and Research Priorities in the Commercial Sector** *(invited)*
M. Flood

9:45 – 10:15 **The Vegetation Canopy Lidar (VCL) Mission** *(invited)*
R. Dubayah

10:15 – 10:45 **The ICESAT Mission** *(invited)*
J. Zwally et al.

10:45 – 11:00 BREAK

11:00 – 11:20 **Design and Performance of an Airborne Multikilohertz Photon-Counting Microlaser Altimeter**
J. Degnan, J. McGarry, T. Zagwodzki, P. Dabney, J. Geiger, R. Chabot, C. Steggerda, J. Marzouk and A. Chu

11:20 – 11:50 **Optech's View on Future Directions for Commerical Scanning Laser Systems** *(invited)*
D. Carswell

11:50 – 12:10 **Wide-Swath Imaging Lidar Development for Air and Spaceborne Applications**
J. B. Blair, S. Luthcke and M. Hofton

12:10 LUNCH

14:00 – 17:10 SESSION 2: Surface Reconstruction I
Chair: George Vosselman (Delft University of Technology, The Netherlands)

14:00 – 14:30 **Advanced DTM Generation from Lidar Data *(invited)***
K. Kraus and N. Pfeifer

14:30 – 14:50 **Creation of High Resolution, Precise Digital Elevation Models (DEM) of Ocean City and Assateague Island, MD**
B. Csatho, Y.-R. Lee, T. Schenk, W. Krabill, and J. McGarry

14:50 – 15:10 **3D Building Model Reconstruction from Point Clouds and Ground Plans**
G. Vosselman

15:10 – 15:30 **Reconstructing Textured CAD Model of Urban environment Using Vehicle-borne Laser Range Scanner and Line Camera**
H. Zhao and R. Shibasaki

15:30 – 15:50 BREAK

15:50 – 16:10 **Scanline Forced Delauney-TENs for Surface Representation**
E. Verbree and P.J. van Oosterom

16:10 – 16:30 **On the Use of Pulse Reflectance Data for Laserscanner Strip Adjustment**
H.-G. Maas

16:30 – 16:50 **3D Perceptual Organization From Laser Altimetry Data**
I. Lee and T. Schenk

16:50 – 17:10 **Comparing Probabilistic and Geometric Models on Lidar Data**
R. Fraile and S. Maybank

17:10 – 17:30 DISCUSSION
18:30 ICEBREAKER

Land Surface Mapping and Characterization Using Laser Altimetry

PROGRAM: TUESDAY 23rd OCTOBER 2001

8:30 – 9:00 **Registration**

9:00 – 11:00 SESSION 3: Data Geolocation
Chair: Toni Schenk (The Ohio State University, USA)

9:00 – 9:30 **Aspects of Processing Extra-terrestrial Lidar Data: Clementine, NEAR, MOLA** *(invited)*
G. A. Neumann

9:30 – 9:50 **Spaceborne laser Altimeter Instrument Parameter Calibration from Integrated Residual Analysis**
S. Luthcke, D. Rowlands and C. Carabajal

9:50 – 10:10 **Determining the Mounting Bias of a Laser Altimeter System by a Hough Transformation Approach**
T. Schenk

10:10 – 10:40 **Simultaneous Determination of Calibration Parameters for an Airborne Lidar System** (*invited)*
A. Borsa

10:40 – 11:00 **Recovery of Systematic Biases in Laser Altimeters Using Natural Surfaces**
S. Filin

11:00 – 11:15 BREAK

11:15 – 12:15 SESSION 4: Data Fusion
Chair: J.-Bernard Minster (University of California, San Diego, USA)

11:15 – 11:35 **Integration of Lidar and Landsat ETM Data**
A. T. Hudak, M. A. Lefsky, and W. B. Cohen

11:35 – 11:55 **High Resolution Surface Geometry and Albedo by Combining Laser Altimetry and Visible Images**
R. D. Morris, U. von Toussaint and P. C. Cheeseman

11:55 – 12:15 **Accuracy Study of Airborne Laser Scanning Data with Photogrammetry**
S. Seo, T. Schenk and B. Csathó

12:15 LUNCH

14:00 – 15:00 SESSION 5: Data Modeling
Chair: Michelle Hofton (University of Maryland, College Park, USA)

14:00 – 14:20 **Modeling Lidar Waveforms in Heterogeneous and Discrete Canopies**
W. Ni-Meister and R. Dubayah

14:20 – 14:40 **Modeling Lidar Waveforms Using a Radiative Transfer Model**
B. Peterson, W. Ni, B. Blair, M. Hofton, P. Hyde, and R. Dubayah

14:40 – 15:00 **Evaluation of Geoscience Laser Altimeter System (GLAS) Waveforms For Vegetated Landscapes Using Airborne Laser Altimeter Scanning Data**
C. C. Carabajal and D. J. Harding

15:00 – 15:20 BREAK

Land Surface Mapping and Characterization Using Laser Altimetry

15:20 – 17:10	**SESSION 6: Forestry Applications** **Chair: Michelle Hofton (University of Maryland, College Park, USA)**
15:20 – 15:40	**Measuring Forest Canopy Height Using a Combination of Lidar and Aerial Photography Data** *B. A. St-Onge and N. Achaichia*
15:40 – 16:00	**Investigation of Measuring Accuracy of Forest Area by Means of Airborne Laser Scanner** *M. Funahashi, M. Setojima, Y. Akamatsu, Y. Imai, M. Amano, T. Katsuki, M. Takahashi, and M. Fukuda*
16:00 – 16:30	**Relationships Between Lidar Metrics and Above-Ground Biomass in Closed-Canopy Neotropical Forests** *(invited)* *J. Drake, R. Dubayah, R. Knox, and R. Condit*
16:30 – 16:50	**Lidar Remote Sensing of Aboveground Biomass in Three Biomes** *M. A. Lefsky, W. B. Cohen, D. J. Harding, G. G. Parker, S. A. Acker, and S. T. Gower*
16:50 – 17:10	**Characterization of Canopy Height with Proximity to Streams and Slope Using Lidar** *D. Gillespie, R. Dubayah, M. Hofton*
16:50 – 17:30	DISCUSSION
17:30	END

Land Surface Mapping and Characterization Using Laser Altimetry

PROGRAM: WEDNESDAY 24th OCTOBER 2001

8:30 – 9:00 **Registration**

9:00 – 12:15 SESSION 7: Mapping Geosurficial Processes
Chair: Beáta Csathó (The Ohio State University, USA)

9:00 – 9:30 **Analysis of a Data Set for ICESat Cal/Val**
W. B. Krabill, S Manizade, C Martin, J Sonntag, R Swift, and J Yungel

9:30 – 9:50 **Laser Monitoring of Ice Elevations and Sea-Ice Thickness in Greenland**
R. Forsberg, K. Keller and S. M. Jacobsen

9:50 – 10:10 **Quantifying River Bank Erosion With Scanning Laser Altimetry**
D. Thoma, S. C. Gupta and M. E. Bauer

10:10 – 10:30 **Landslide Delineation Using Airborne Laser Swath Mapping**
V. R. Schaefer, S. Burckhard, D. Bloomquist and R. L. Shrestha

10:30 – 10:45 BREAK

10:45 – 11:05 **Mapping the Surface of Sheet Flow Water in the Everglades**
W. E. Carter, R. L. Shrestha, D. Bloomquist, and M. Sartori

11:05 – 11:25 **Laser Pulse Correlation: A Method For Detecting Subtle Topographic Change Using Lidar Return Waveforms**
M. Hofton and J. B. Blair

11:25 – 11:55 **Precise Airborne lidar surveying for Coastal Research and Geo-Hazards Applications**
R. Gutierrez, J. Gibeaut, R. Smyth, T. Hepner, J. Andrews, C. Weed, W. Gutelius, and M. Mastin

11:55 – 12:15 **Use of LIDAR and Other Geospatial Technologies in Support of Rescue and Recovery at the World Trade Center**
W. Decker

12:15 LUNCH

14:00 – 16:20 SESSION 8: Surface Reconstruction II
Chair: Hans-Gerd Maas (Dresden University of Technology, Germany)

14:00 – 14:20 **Digital Terrain Models in dense urban areas**
F. Dell'Acqua, and P. Gamba

14:20 – 14:40 **Filtering of Laser Altimetric Digital Surface Models**
A. Koch, K. Jacobsen, and P. Lohmann

14:40 – 15:00 **Filtering of Laser Altimetry Data Using a Slope Adaptive Filter**
G. Sithole

15:00 – 15:20 **Some Algorithms for Virtual Deforestation (VDF) of LIDAR Topographic Survey Data**
R. A. Haugerud and D. J. Harding

15:20 – 15:40 BREAK

15:40 – 16:00 **Terrain Modelling and Analysis Using Laser Scanner Data**
M. Elmqvist, E. Jungert, F. Lantz, Å. Persson, and U. Söderman

16:00 – 16:20 **Airborne Laser Scanning – Clustering in Raw Data**
M. Roggero

16:20 – 16:40 **Wavelet-based Algorithm in Segmentation of Airborne Laser Scanner Data**
M. Tokunaga and T.T. Vu

16:40 – 17:30 DISCUSSION

17:30 CLOSING REMARKS

List of Participants

Abshire, James B.
NASA/GSFC
Code 924
Greenbelt, MD 20771
USA
jabshire@pop900.gsfc.nasa.gov

Jeanne Anderson
University of New Hampshire
Complex Systems Research Center
Morse Hall
Durham, NH 03824
USA
jeanne.anderson@unh.edu

Barnard, Chris
EarthData International of Maryland
45 West Watkins Mill Road
Gaithersburg, MD 20878
USA
cbarnard@earthdata.com

Berglund, Judith
Lockheed Martin Space Operations – Stennis Programs
John C. Stennis Space Center – Bldg. 1210
Stennis Space Center, MS 39529
USA
Judith.Berglund@ssc.nasa.gov

Blair, J. Bryan
NASA/GSFC
Code 924
Greenbelt, MD 20771
USA
bryan@arthur.gsfc.nasa.gov

Boersma, Saskia
TerraImaging bv
Koningslaan 35
Amersterdam 1075 AB
THE NETHERLANDS
s.boersma@terraimaging.nl

Borsa, Adrian
Scripps Institution of Oceanography
9500 Gilman Drive, IGPP 0225
La Jolla, CA 92093
USA
aborsa@ucsd.edu

Carabajal, Claudia C.
NVI, Inc.
NASA/GSFC – Code 926
Greenbelt, MD 20771
USA
claudia@stokes.gsfc.nasa.gov

Carter, Bill
University of Florida
Department Civil & Coastal Eng.
345 Weil Hall
Gainesville, FL 32611
USA
bcarter@ce.ufl.edu

Csatho, Beata
Byrd Polar Research Center, OSU
1090 Carmack Road
Columbus, OH 43210
USA
csatho.1@osu.edu

Dabney, Philip
NASA/GSFC
Code 920.3
Greenbelt, MD 20771
USA
Philip.Dabney@gsfc.nasa.gov

Daniel, Carlton
U.S. Army Topographic Engineering Center
7701 Telegraph Road
Alexandria, VA 22315
USA
daniel@tec.army.mil

Decker, Winfield
EarthData International of Maryland, LLC
45 West Watkins Mill Road
Gaithersburg, MD 20878
USA
wdecker@earthdata.com

Degnan, John
NASA/GSFC
Code 920.3
Greenbelt, MD 20771
USA
John.Degnan@gsfc.nasa.gov

Drake, Jason
University of Maryland
Department of Geography
1158 LeFrak Hall
College Park, MD 20742
USA
jasdrak@geog.umd.edu

Dubayah, Ralph
University of Maryland
Department of Geography
1149B LeFrak Hall
College Park, MD 20742
USA
rdubayah@geog.umd.edu

Filin, S.
Delft University of Technology
Department of Geodesy
Thijsseweg 11
Delft, Zuid Holland 2629 J A
THE NETHERLANDS
S.Filin@citg.tudelft.nl

Flood, Martin
Airborne 1
5777 West Century Blvd., # 725
Los Angeles, CA 90045
USA
flood@airborne1.com

Forsberg, Rene
National Survey and Cadastre (KMS)
Rentemestervej 8
Copenhagen DK2400
DENMARK
rf@kms.dk

Fraile, Roberto
The University of Reading
Department of Computer Science
P.O. Box 225, Whiteknights
Reading RG6 6AY
UNITED KINGDOM
R.Fraile@reading.ac.uk

Friess, Peter
TopScan GmbH
Muensterstr. 19
Steinfurt 48565
GERMANY
FRIESS@TOPSCAN.DE

Funahashi, Manabu
Kokusai Kogyo Co., Ltd.
7F.12-1 Gobancho, Chiyoda-Ku
Tokyo 102-0076
JAPAN
manabu_funahashi@kkc.co.jp

Gambo, Paolo
University of Pavia
Department of Electronics
Via Ferrata, 1
Pavia 27100
ITALY
p.gamba@ele.unipv.it

Geiger, Jennifer
NASA/GSFC
Code 588
Greenbelt, MD 20771
USA
Jennifer.Geiger@gsfc.nasa.gov

Gutierrez, Roberto
The University of Texas at Austin
Bureau of Economic Geology
10100 Burnet Road, Bldg. 130
Austin, TX 78758
USA
oskar@mail.utexas.edu

Haarbrink, Roland B.
EarthData Technologies
4409 Oak Creek Ct., #503
Fairfax, VA 22033
USA
rhaarbrink@earthdata.com

Harding, David J.
NASA/GSFC
Code 921
Greenbelt, MD 20771
USA
harding@core2.gsfc.nasa.gov

Haugerud, Ralph
U.S. Geological Survey
USGS at University of Washington
Department of Earth and Space
Sciences, Box 351310
Seattle, WA 98195
rhaugerud@usgs.gov

Hofton, Michelle
University of Maryland
Department of Geography
1151 LeFrak Hall
College Park, MD 20742
USA
mhofton@geog.umd.edu

Holekamp, Kara
Lockheed Martin
Building 1210
Stennis Space Center, MS 39529
USA
Kara.holekamp@ssc.nasa.gov

Andrew Hudak
USDA Forest Service,
PNW Research Station
3200 SW Jefferson Way
Corvallis, OR 97331
USA
ahudak@fs.fed.us

Hyde, Peter
University of Maryland
Department of Geography
1158 LeFrak Hall
College Park, MD 20742
USA
phyde@glue.umd.edu

Jungert, Erland
FOI
Swedish Defence Research Agency
Box 1165
Linlöping S-581 11
SWEDEN
jungert@foi.se

Kletzli, Robert
EnerQuest Systems, LLC
7500 Jefferson Street, NE
Courtyard II, Suite 101
Albuquerque, NM 87109
USA
bkletzli@enerquest.com

Koch, Andreas
Institute for Photogrammetry &
GeoInformation (IPI)
University of Hannover
Nienburger Straâe 1,
30167 Hannover, Germany
Hannover, Lower Saxony 30167
GERMANY
koch@ipi.uni-hannover.de

Krabill, Bill
GSFC/Wallops Flight Facility
Wallops Island, VA 23337
USA
krabill@osb1.wff.nasa.gov

Kraus, Karl
Institute of Photogrammetry &
Remote Sensing of the Technical
University Vienna
Guâhausstraâe 27-29
Vienna, Austria A-1040
AUSTRIA
kk@ipf.tuwien.ac.at

Latypov, Damir
TerraPoint, LLC
4800 Research Forest Dr.
The Woodlands, TX 77381
USA
Damir.Latypov@transamerica.com

Lee, Impyeong
The Ohio State University
6068 Abbey Chapel Drive
Dublin, OH 43017
USA
lee1517@osu.edu

Lefsky, Michael
Oregon State University
Department of Forest Science
Corvallis, OR 97333
USA
lefsky@fsl.orst.edu

Liadsky, Joe
Optech, Inc.
100 Wildcat Road
Toronto, ON M3J 2Z9
CANADA
joe@optech.on.ca

Lim, Kevin
Queen's University
Department of Geography
Kingston, Ontario K7L3N6
CANADA
9kk14@qsilver.queensu.ca

Luthcke, Scott B.
NASA/GSFC
Code 926
Greenbelt, MD 20771
USA
sluthcke@xyz.gsfc.nasa.gov

Maas, Hans-Gerd
Dresden Technical University
Helmholtzstr. 10
Dresden D-01062
GERMANY
hmaas@rcs1.urz.tu-dresden.de

Mallama, Anthony
Raytheon ITSS
4400 Forbes Blvd.
Lanham, MD 20706
USA
Anthony_Mallama@Raytheon.com

Manizade, Serdar
EG&G/NASA Airborne Topographic Mapper Group
Bldg. N-159, Wallops Flight Facility
Wallops Island, VA 23337
USA
manizade@osb.wff.nasa.gov

Martin, Chreston
EG&G Technical Services
900 Clopper Road, Suite 120
Gaithersburg, MD 20878
USA
martin@wasc2.wff.nasa.gov

McGarry, Jan
NASA/GSFC
Code 920.3
Greenbelt, MD 20771
USA
Jan.McGarry@gsfc.nasa.gov

Minster, Bernard
Scripps Institution of Oceanography
9500 Gilman Drive, TGPP 0225
La Jolla, CA 92093-0225
USA
jbminster@ucsd.edu

Neumann, Gregory A.
NASA/GSFC
Code 920
Greenbelt, MD 20771
USA
neumann@tharsis.gsfc.nasa.gov

Ni-Meister, Wenge
University of Maryland
Department of Geography
1149 LeFrak Hall
College Park, MD 20742
USA
wenge@geog.umd.edu

Morris, Robin
USRA – RIACS
NASA Ames Research Center
Mail Stop 269-2
Moffelt Field, CA 94035-1000
USA
rdm@email.arc.nasa.gov

Ohring, Samuel
Raytheon
NASA/GSFC - Code 971
Greenbelt, MD 20771
USA
ohring@icesat2.gsfc.nasa.gov

Peterson, Birgit
University of Maryland
Department of Geography
1158 LeFrak Hall
College Park, MD 20742
USA
bpeterso@geog.umd.edu

Prince, Stephen D.
University of Maryland
Department of Geography
College Park, MD 20742
USA
sp43@umail.umd.edu

Roggero, Marco
Politecnico di Torino
CP 38
Santhià, VC 13048
ITALY
roggero@atlantic.polito.it

Santana, Jairo
Raytheon ITSS
3209 Shepherd Street
Mount Rainer, MD 20712
USA
Santana@terra.stx.com

Schaefer, Vernon R.
South Dakota State University
Civil & Environmental Engineering Department
Box 2219
Crothers Engineering Hall 118
Brookings, SD 57007
USA
vernon_schaefer@sdstate.edu

Tony Schenk
The Ohio State University
2070 Neil Avenue
Columbus, OH 43210
USA
schenk.2@osu.edu

Senftle, Jospeh
Advanced Power Technologies
1250 Twenty-Fourth Street
Suite 850
Washington, DC 20037
USA
jsenftle@apti.com

Seo, Suyonng
The Ohio State University
2070 Neil Avenue
Columbus, OH 43210
USA
seo.43@osu.edu

Shrestha, Ramesh L.
University of Florida
345 Weil Hall
P.O. Box 116580
Gainsville, FL 32611
USA
rshre@ce.ufl.edu

Shuman, Christopher A.
NASA/GSFC
Code 971
Greenbelt, MD 20771
USA
christopher.shuman@gsfc.nasa.gov

Sithole, G.
Delft University of Technology
Department of Geodesy
Thijsseweg 11
Delft, Zuid Holland 2629JA
THE NETHERLANDS
G.Sithole@citg.tudelft.nl

Söderman, Ulf
Swedish Denfence Research Agency
P.O. Box 1165
Linköping SE-58111
SWEDEN
ulf.soderman@foi.se

Sonntag, John C.
NASA WFF/EG&G Technical Services
900 Clopper Road, Suite 120
Gaithersburg, MD 20878
USA
sonntag@osb.wff.nasa.gov

St-Onge, Benoît
Université de Québec à Montréal
C.P. 8888 succ. Centre-Ville
Montréal Province, QC H3C 3P8
CANADA
st-onge.benoit@uqam.ca

Sun, Guoqing
University of Maryland
Department of Geography
College Park, MD 20742
USA
gsun@glue.umd.edu

Thoma, David
University of Minnesota
Department of Soil, Water & Climate
1991 Upper Buford Circle
St. Paul, MN 55108
USA
dthoma@soils.umn.edu

Tippen, Jeff
EarthData International of Maryland
45 West Watkins Mill Road
Gaithersburg, MD 20878
USA
jtippen@earthdata.com

Todd, Kent
University of Toronto
467 Atlas Avenue
Toronto, Ontario M6C 3R1
CANADA
kent.todd@utoronto.ca

Treitz, Paul
Queen's University
Department of Geography
Kingston, ON K7L3N6
CANADA
pt6@qsilver.queensu.ca

Verbee, E.
Delft University of Technology
Thijsseweg 11
Delft, Zuid Holland 2629 JA
HOLLAND
E.Verbee@geo.tudelft.nl

Vosselman, M.G.
Delft University of Technology
Department of Geodesy
Thijsseweg 11
Delft, Zuid Holland 2629 JA
THE NETHERLANDS
G.Vosselman@geo.tudelft.nl

Wicks, Donald E.
EnerQuest Systems, LLC
1991 Broadway, Suite 3200
Denver, CO 80202
USA
dwicks@enerquest.com

Zagwodzki, Thomas
NASA/GSFC
Code 920.3
Greenbelt, MD 20771
USA
Thomas.Zagwodzki@gsfc.nasa.gov

Zhao, Huijing
University of Tokyo
Institute of Industrial Science
4-6-1 Komaba, Meguro-ku
Tokyo 153-8505
JAPAN
chou@skl.iis.u-tokyo.ac.jp

Zwally, Jay
NASA/GSFC
Code 971
Greenbelt, MD 20771
USA
jay.zwally@gsfc.nasa.gov

Author Index

Achaichia N.....131
Acker S.A.....156
Akamatsu Y.....139
Amano M.....139
Andrews J.....185
Bauer M.E.....169
Blair J.B.....17, 121, 181
Bloomquist D.....67
Carabajal C.....81, 125
Carter W.E.....175
Chabot R.....9
Cheeseman P.C.....105
Chu A.....9
Cohen W.B.....95, 155
Condit R.....147
Csatho B.....31, 113
Dabney P.....9
Degnan J.....9
Dell'Acqua F.....195
Drake J.....147
Dubayah R.....121, 147
Elmqvist M.....219
Filin S.....85
Flood M.....3
Forsberg R.....163
Fraile R.....67
Fukuda M.....139
Funahashi M.....139
Gamba P.....195
Geiger J.....9
Gibeaut J.....185
Gower S.T.....155
Gupta S.C.....169
Gutelius W.....185
Gutierrez R.....185
Harding D.J.....125, 155, 211
Haugerud R.A.....211
Hepner T.....185
Hofton M.....17, 121, 181
Hudak A.T.....95
Hyde P.....121
Imai Y.....139
Jacobsen S.M.....163
Jungert E.....219
Katsuki T.....139
Keller K.....163
Knox R.....147
Krabill W.....31
Kraus K.....23
Lantz F.....219
Lee I.....57
Lee Y.-R.....31
Lefsky M.A.....95, 155
Luthcke S.....17, 81
Maas H.-G.....53
Marzouk J.....9
Mastin M.....185
Maybank S.....67
McGarry J.....9, 31
Morris R.D.....105
Neumann G.A.....73
Ni W.....121
Parker G.G.....155
Persson X.....219
Peterson B.....121
Pfeifer N.....23
Roggero M.....227
Rowlands D.....81
Sartori M.....175
Schenk T.....31, 57, 113
Seo S.....113
Setojima M.....139
Shrestha R.L.....175
Sithole G.....203
Smyth R.....185
St-Onge B.A.....131
Steggerda C.....9
Söderman U.....219
Takahashi M.....139
Thoma D.....169
Van Oosterom P.J.....45
Verbree E.....45
von Toussaint U.....105
Vosselman G.....37
Weed C.....185
Zagwodzki T.....9